Towards compact and advanced Free Electron Laser

Amin Ghaith

▶ **To cite this version:**

Amin Ghaith. Towards compact and advanced Free Electron Laser. Accelerator Physics [physics.acc-ph]. Université Paris-Saclay, 2019. English. NNT : 2019SACLS333 . tel-02375533

HAL Id: tel-02375533
https://theses.hal.science/tel-02375533

Submitted on 22 Nov 2019

HAL is a multi-disciplinary open access archive for the deposit and dissemination of scientific research documents, whether they are published or not. The documents may come from teaching and research institutions in France or abroad, or from public or private research centers.

L'archive ouverte pluridisciplinaire **HAL**, est destinée au dépôt et à la diffusion de documents scientifiques de niveau recherche, publiés ou non, émanant des établissements d'enseignement et de recherche français ou étrangers, des laboratoires publics ou privés.

université PARIS-SACLAY

NNT : 2019SACLS333

Thèse de doctorat

Towards compact and advanced free electron laser

Thèse de doctorat de l'Université Paris-Saclay
préparée à l'Université Paris-Sud

École doctorale 576 : Particules, Hadrons, Énergie et Noyaux : Instrumentation, Imagerie, Cosmos et Simulation (PHENIICS)
Spécialité de doctorat : Physique des accélérateurs

Thèse présentée et soutenue à Saint-Aubin, le 2 Octobre 2019, par

Amin Ghaith

Composition du Jury :

Victor Malka Directeur de Recherche, Laboratoire d'Optique Appliquée	Président
Toru Hara Directeur de Recherche, SPring-8/SACLA	Rapporteur
Ulrich Schramm Professeur, Helmholtz-Zentrum Dresden	Rapporteur
Gaël Le Bec Ingénieur, European Synchrotron Radiation Facility	Examinateur
Christelle Bruni Chargée de Recherche, Laboratoire de l'accélérateur linéaire	Examinatrice
Marie-Emmanuelle Couprie Directrice de Recherche, Synchrotron SOLEIL	Directrice de thèse
Olivier Marcouillé Ingénieur, Synchrotron SOLEIL	Encadrant de thèse

Contents

Chapter 1

Introduction

Ever since the discovery of the electron using a cathode-ray tube at the end of the 19^{th} century, particle accelerators have seen tremendous progress where they became widely used tools for basic research, industry, medicine, material science etc... For the past decades, innovative and compact accelerators have been developed addressing the increasing requirements in different fields. Currently, there are more than 30,000 particle accelerators in operation world wide [1]. Particle accelerators have become the essential tools for discovering new particles, where they stand at the frontiers of uncharted territories in understanding the fundamental properties of the universe. Over the last few decades, light source based accelerators have made dramatic advances that cut across many fields of research [2]. These light sources can generate photon beams ranging over a broad spectrum advancing the research in physics, chemistry [3], biology [4], medicine [5] and material science [6]. In addition, the advent of the Free Electron Lasers [7] in the X-ray domain [8], coming along with an increase of the peak brightness by several orders of magnitude, ultra short pulses, high coherence and brillance, enables to decipher the matter structure in unexplored areas and dynamics on ultra fast time scales unraveling the processes involved various domains such as complex chemical reactions [9].

1.1 Particle accelerators

1.1.1 Linear accelerators

The first linear accelerators were based on electrostatic fields to accelerate particles. A variety of techniques to obtain high voltages have been developed such as cascade generators based on voltage multiplier circuit, Van de Graaff [10] etc... Electrostatic based accelerators have a limitation due to sparks that occur at high voltage.

Very high accelerating fields can be generated by using radio-frequency (RF) cavities that by far exceed the performance of electrostatic systems [11]. These linear accelerators, commonly referred to as Linacs, are based on microwave fields injected into coaxial metallic tubes where the accelerating field is generated within the gaps between them. Conventional RF cavities can typically provide an acceleration gradient of ~10 MeV/m. Moreover, some new designs can reach up to 100 - 350 MeV/m [12, 13].

1.1.2 Circular accelerators

The first cicular accelerator was the cyclotron which was invented by Ernest O. Lawrence [14]. It consists of an alternating high voltage applied between two hollow D-shaped dipolar magnets to enable multi-pass of the particles undergoing acceleration at each pass. This type of accelerator is limited to non-relativistic particles (below 0.511 MeV for electrons and 938 MeV for protons),

because as the particle travels close to the speed of light, its mass significantly increases causing a much larger circular path. Thus, cyclotrons are commonly used for non-relativistic proton based applications. Higher energies can be achieved if the accelerated particle is kept in an orbit with a constant radius with the help of bending magnets. Synchrotrons provide a synchronization between the energy of the accelerated electron and the bending magnets to maintain its circular path. So, as the electrons are accelerated and gain momentum, the magnetic field is increased, keeping the electrons orbit constant. Most common synchrotron facilities use storage rings, where there are no accelerating sections and particles are stored at a constant energy. Table 1.1 presents some examples of synchrotron facilities built worldwide.

Laboratory	**City**	**Energy** GeV	**Circumference** m	**Status**
SPEAR/SLAC	California (USA)	3	234	In operation
ACO	Orsay (France)	0.54	-	Decommissioned
Daresbury	Warrington (UK)	2	96	Decommissioned
Super-ACO	Orsay (France)	0.8	-	Decommissioned
ESRF	Grenoble (France)	6	844	In operation
Elettra	Trieste (Italy)	2.4	260	In operation
SPring-8	Sayo (Japan)	8	1436	In operation
SOLEIL	Saint-Aubin (France)	2.75	354	In operation
Pohang Light Source II	Korea	3	280	In operation

Table 1.1: Examples of synchrotron facilities built worldwide.

The PhD is done at synchrotron SOLEIL facility. The operation energy in the storage ring is 2.75 GeV (additional beam parameters are presented in chapter 5). 29 beamlines are available for users providing a wide range of spectroscopic methods from infrared to X-rays. Figure 1.1 presents the photon brilliance produced from the beamlines ranging from 1 eV to 100 keV.

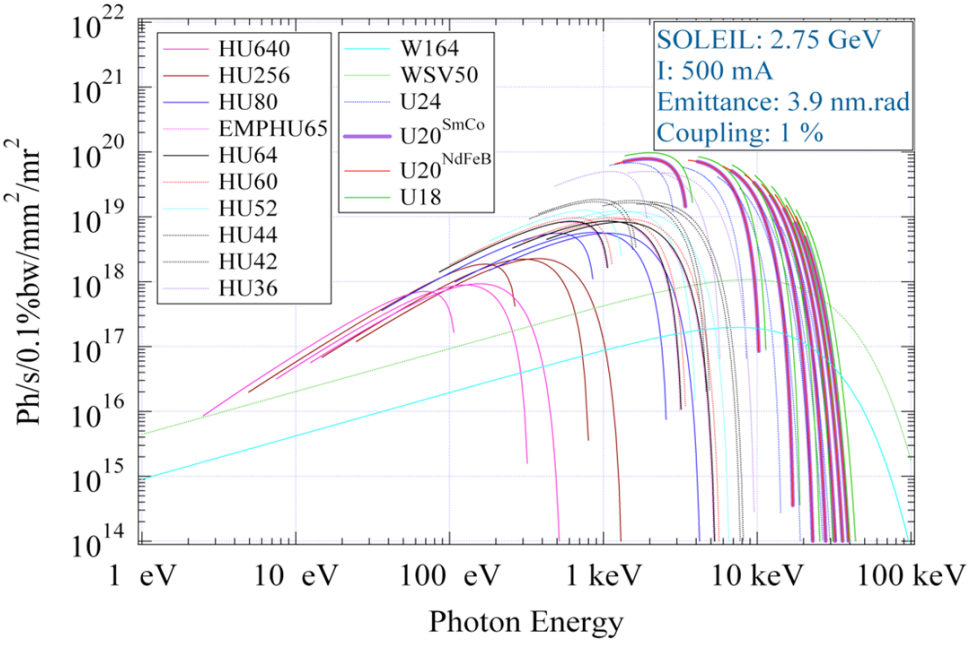

Figure 1.1: Photon brilliance generated by the different undulators installed at SOLEIL storage ring.

1.1.3 Laser plasma accelerator

Conventional Linacs are limited to tens to hundreds of MeV/m accelerating gradient by the use of RF cavities due to excessive temperature rise on the inner surface when injecting high power. Hence, the production of high energetic electrons requires a large scale and costly infrastructure. Following the rapid progress in the development of high-intensity laser systems, a new accelerating concept called Laser Plasma Acceleration (LPA) was introduced in 1979 [15]. In an LPA, an intense short pulsed laser interacts with a gas medium. Due to the high electric fields, electrons are stripped and separated spatially from the heavy ions that have a negligible response in the time-scale of the electrons response. This process creates a plasma with a disequilibrium charge distribution in the perturbed region that can be observed as a wakefield (plasma wave) following the laser. A huge gradient is created between the back of the wakefield (consists mainly of electrons) and at its center (consists mainly of ions), where electrons trapped between these two regions are subjected to an extreme electric force. This allows LPA to operate a larger gradients than ones in conventional accelerators, thus producing extremely compact sources of bright and energetic electrons [16–18]. Figure 1.2 presents a scheme of the LPA concept.

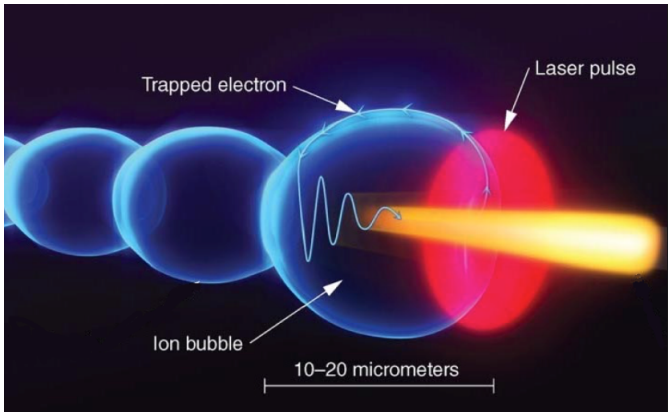

Figure 1.2: Scheme representing the laser pulse inducing plasma waves in the shape of bubbles that traps electrons and accelerate them. Figure from https://groups.physics.ox.ac.uk/norreys/ResearchWakefield.html.

LPA demonstrated its potential to become a new kind of compact electron source for synchrotron radiation applications, where electron beams of the order of hundreds MeV energies, hundreds pC charge and few milliradians divergence were reported in 2004 [19–21]. Further experimental and theoretical studies of LPA helped to identify the phenomena, which define the characteristics of the accelerated beams. In the modern LPA schemes, the accelerating structure is a non-linear plasma wave following the laser pulse (called bubble or blowout region [22–24]), and the quality of the produced beams highly depends on the injection method. In the first experiments [19–21], the injection was triggered by the plasma wave deformations resulting from the laser pulse relativistic self-focusing [25, 26]. This mechanism is now known as *self-injection* [27, 28]. More injection schemes have been demonstrated later on, including the *optical injection* using an auxiliary laser [29–31], the *ionization injection* using of the high-Z and low-Z gas mixtures [32–36], *downramp injection*, where plasma wave is locally slowed down in a density gradient [37–41], and the *shock (or density-transition) injection* triggered at the sharp transitions of plasma density [42–45].

In the experimental conditions, different injection techniques can be implemented seperately or can be combined to achieve the desired beam parameters. For example, the self-injection technique is the simplest one to produce, where its only requirement is a relatively high plasma density and has demonstrated one of the highest multi-GeV electron energies [46, 47]. Localized injection techniques, such as optical and shock injections, provide a better control of the beam character-

istics, i.e. divergence, mean energy and its spread [31]. At the same time, such techniques add complexity to the experimental setup, narrowing the choice of the targets to gas jets or gas cells, and thus limiting the maximal plasma density and consequently the accelerating gradients. Using the high-Z and low-Z gas-mixtures in either one of these schemes increase the total accelerated charge, improving source stability [44], but on the expense of a higher energy spread. Presently, significant efforts are also made to separate the injection and acceleration stages in LPA, in order to establish a robust control of source performance [35, 48, 49]. In the near future, such *multi-stage LPA* techniques promise to achieve higher energy acceleration while preserving beam quality.

It is important to note that, while the state-of-the-art LPA beam characteristics (i.e. multi-GeV energies, hundreds pC charge, sub-percent energy spread and sub-milliradian divergence) have already been demonstrated experimentally, their simultaneous reproduction and stable operation remain extremely challenging. Practically, the choice of the LPA setup with proper injection method is fundamental for a given application, as it should not only generate the beams of desired quality, but should also be reproducible and robust in the operation. To give a qualitative picture of the beam parameters obtained since the *self-injection* results of 2004 [19–21], we show in Fig. 1.3 the beam charge, energy, energy spread and divergence reported in literature up to the year 2018, for *self-injection* [19, 20, 46, 50–54], *optical injection / colliding pulse injection* [30, 31, 55], *ionization injection* [32–35], *density downramp injection* [38, 40, 56, 57], *density transition/shock injection* [42, 43], *density downramp or shock assisted ionization injection* [55, 58].

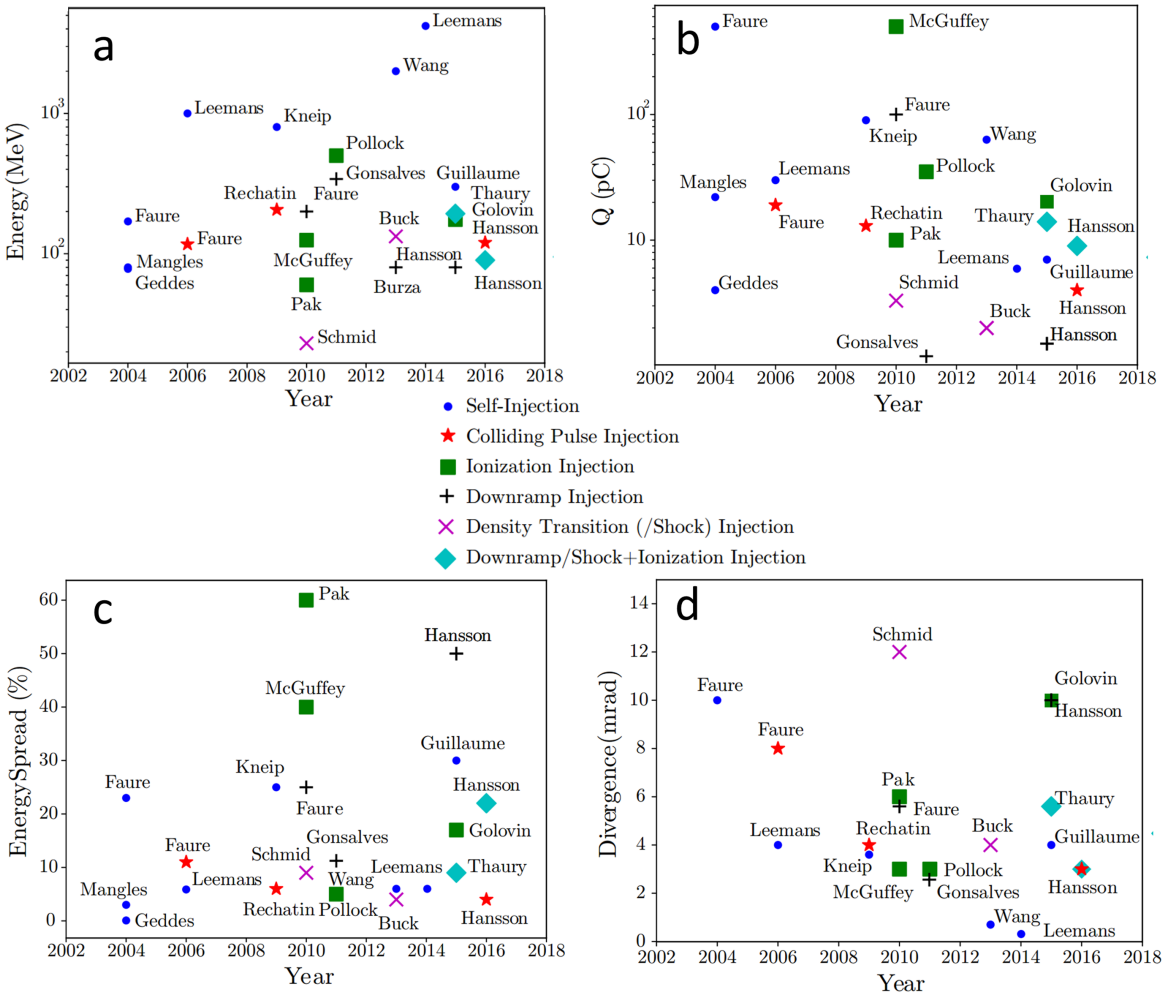

Figure 1.3: Beam energy (a), charge (b), energy spread (c) and divergence (d) reported in LPA experiments obtained through different injection techniques. Each point label is given by the first author of the corresponding reference. Figure by F. Massimo [59].

1.2 Synchrotron radiation

X-rays have been widely used in many research areas, in order to inspect materials and uncover their fundamental properties. In the year 1947, at the General Electric Company Research Laboratory in New York state, a "mysterious" white light was observed from a 70 MeV electron beam synchrotron facility [60], and was refered to as synchrotron radiation (SR). SR is emitted as a charged particle experiences an acceleration perpendicular to its motion. The wavelength of the SR changes with electron energy and is found to agree with theoretical studies done in the previous years concerning relativistic electrons acceleration. At the beginning, this radiation was kind of a nuisance due to the loss in electron energy, but as the years passed by, scientists began considering this radiation to perform experiments for applications such as microscopy, spectroscopy, atomic physics and many more. Soon after, SR developed into being a milestone in achieving a more reliable and efficient X-ray source [61]. The 3^{rd} generation of SR sources associates a high current electron beam with small emittance (a measure for the average spread of particle coordinates in position-and-momentum transverse phase space) and insertion devices. The undulator, the most common insertion device, consists of an assembly of magnets with alternating polarity producing a small period sinusoidal magnetic field. Electrons crossing an undulator are subjected to a sinusoidal trajectory and emit radiation that adds constructively from one period to another,

resulting in sharp intense narrow line spectra at the fundamental frequency and its harmonics. The undulator also serves as a crucial component in the 4^{th} generation SR sources, commonly known as Free Electron Lasers (FELs).

1.3 Conventional lasers

The invention of the laser, which is an acronym for Light Amplification by Stimulated Emission of Radiation, was laid down by Albert Einstein in the year 1917 [62]. In his article, he explains how a small packet of light, commonly known as photons, are absorbed and emitted by the electrons in an atom alongside the probabilities of these phenomena. The main aspect of his study was indeed the stimulated emission that describes how the presence of an electromagnetic wave can trigger simultaneously the decay of atoms in a higher energy state to a lower one resulting in coherent emission. With this discovery, one can pump a medium, i.e. number of atoms in higher energy state larger than the ones in the lower states, to make sure that the stimulated process dominates over the absorption and thus the light is amplified. The first Microwave Amplification by Stimulated Emission of Radiation (Maser), that is considered the forerunner of the laser, was built by C. Townes in 1953 [63]. In view of extending to the optical ranges, the pumped medium is placed between two optical mirrors (optical resonator), so that the light passes through it multiple times and gets amplified at each pass [64]. The name was then changed to laser. The first laser was built in 1960 by T. H. Maiman [65] producing light at 694 nm wavelength. Since then, the number of laser facilities have grown significantly covering a wavelength range between millimeters down to several nanometers [66]. In addition, there is another process called high harmonic generation, where an intense laser is exerted on a gas and a fraction of the laser power can be converted into higher harmonics [67, 68]. This regime allows for the creation of ultra-violet and even soft X-rays pulses.

1.4 Free Electron Laser

A relativistic electron beam traversing a sinusoidal magnetic field, generated by an undulator, emits light at each period. Photons produced by an individual electron interfere constructively resulting in sharp spectral lines. In free electron laser (FEL), the electrons interact with the radiation, where energy is transfered between the beam and the radiated wave via the so-called ponderomotive force. This process results in a low gain of the electro-magnetic wave introduced by Madey in 1971 using a quantum approach [69] and further examined by Colson with a classical approach [70]. In the undulator magnetic field, the beam energy modulation becomes a density modulation because electrons with smaller energies are affected more by the field prolonging their orbit and thus leading to a micro-bunching mechanism. Thanks to this process, the electrons are put in phase and emit coherent radiation and light intensity is amplified. The micro-bunching can be further reinforced by applying an external laser tuned at the undulator wavelength to make the process more efficient. If the radiation loses energy to the electrons, the process is known as inverse FEL and is commonly used to accelerate electrons [71, 72]. However with the right synchronization between the laser and the electron beam, an amplification can be achieved [69]. Unlike conventional lasers, where the electrons are bound to the atoms in the gain medium allowing the emission at a fixed wavelength, the FEL wavelength can be varied by changing the machine parameters such as electron beam energy or/and undulator magnetic field. The FEL has thus become a conceptual and practical alternative and has exceeded by far other lasing systems. This new laser revolution, with the advent of X-Ray FEL, opens the path for deciphering unexplored ultra-fast phenomena with unprecedented time resolution.

1.4.1 Low Gain FEL

1.4.1.1 FEL oscillator

The FEL optical resonator consists of an electron beam traversing an undulator placed between two mirrors (optical cavity) (see Fig. 1.4). This scheme is also known as an FEL oscillator that operates much like traditional lasers based on atomic transitions, where the radiation is amplified over multi passes of electron bunches through the undulator and light is stored in the optical resonator. The gain scales as $1/E^3$ as it will be discussed in chapter 2, with E the electron beam energy. To operate the FEL oscillator at shorter wavelength, a higher electron beam energy is required that deteriorates the gain. Moreover, reflective efficiency of mirrors degrades for short wavelength making the FEL oscillator operational wavelength around infrared and vacuum ultra violet region [73].

The first FEL oscillator was demonstrated at Stanford University lasing at a wavelength of 10.6 µm [74]. Then, the FEL was demonstrated at a wavelength of 3417 nm [75] by increasing the electron beam energy and followed by the visible FEL observed on ACO storage ring six years later [76].

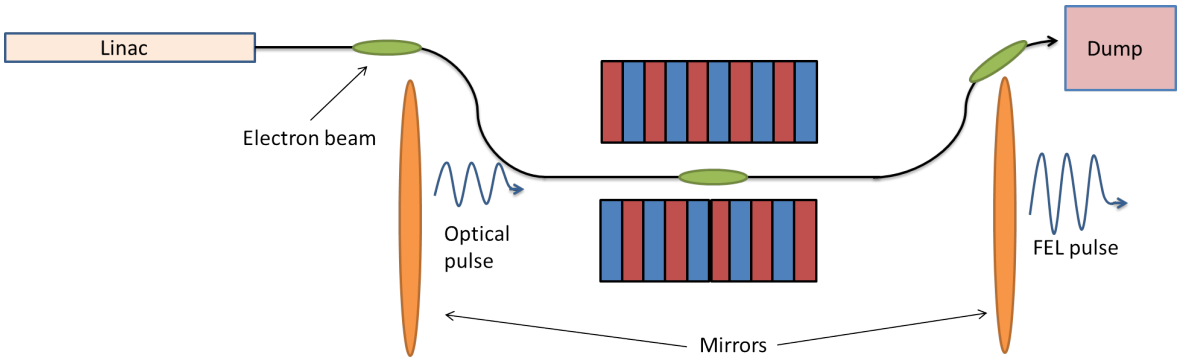

Figure 1.4: FEL oscillator schematic showing its operating principle. Starting with an electron beam (green) produced by a Linac, emits radiation in the undulator that is reflected by the optical mirrors (orange) to interact with the other electron bunch.

Table 1.2 shows some of the optical resonators built ranging from the shortest wavelength amplification achieved with FEL resonator (190 nm) up to 9 µm.

Facility	**Accelerator**	**Energy** [MeV]	**Wavelength** [nm]	**Spectral bandwidth** [nm]
Stanford University [74]	Linac	24	10600	-
Stanford University [75]	Linac	43	3400	27
Paris-Sud University [76]	Storage ring (ACO)	240	650	3
Los Alamos [77]	Linac	20	9000	-
Super-ACO [78]	Storage ring	600	350	-
CLIO [79]	Linac	60	1750	-
FELIX [80]	Linac	45	5000	50
Duke [81]	Storage ring	800	193	-
Elettra [82]	Storage ring	1000	190	0.05

Table 1.2: Examples of FEL oscillators built.

Figure 1.5-a reports on the spectral range and power covered by several FEL oscillators in the visible and vacumm ultra-violet. Due to the mirror losses, reaching a shorter wavelength is extremely difficult. The shortest wavelength was obtained on the ELETTRA FEL at 190 nm [82]. Fig-

ure 1.5-b displays relative wavelength for different FEL oscillators, where they all operate close to the Fourier limit.

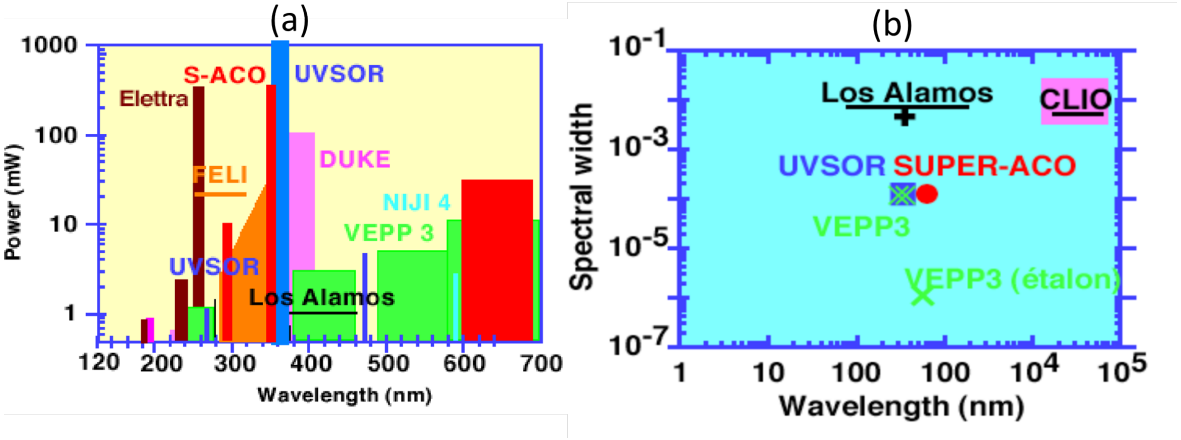

Figure 1.5: Power (a) and relative bandwidth (b) achieved in some FEL oscillators versus wavelength. Figure from [83].

In 1983, an FEL oscillator in the X-ray range was proposed, by the use of highly efficient reflectivity crystals [84], however the community at that time was intrigued to the newly discovered high gain FEL regime presented later on.

1.4.1.2 Coherent harmonic generation

Coherent Harmonic Generation (CHG) [85] can be achieved by injecting a laser tuned at the undulator resonance to enhance the FEL operation efficiency. CHG was first achieved in the UV and VUV on the ACO storage ring [85]. A Nd– Yag laser (1.06 µm wavelength, 20 Hz repetition rate, 15 MW peak power, 12 ns pulse duration) was tuned on the optical klystron first harmonic. The coherent third and fifth harmonic of Nd–Yag laser were observed, with a spectral ratio of 6000 for the third one, and 100 for the fifth one. At DUKE, the storage ring FEL in OK-4 with its sufficiently powerful super-pulses enabled to generate up to the seventh coherent harmonics in the range from 37 to 135 nm [86]. CHG was also generated at other labs: in Elettra [87], UVSOR storage ring FEL [88, 89], a test experiment in Sweden [90], at BNL [91]...

1.4.2 High Gain FEL

The success of Madey's experiments at Standford university [74, 75], where low gain FEL amplification has been achieved, attracted the attention of the scientific community by opening the path towards X-ray lasers. In the low gain theory, the FEL radiation electric field was kept constant during the interaction with the electron beam. Then a fully self-consistent theory, incorporating the radiation evolution along a single undulator pass of the electron beam, came along and led to some very interesting results.

1.4.2.1 Self-amplified spontaneous emission

A high gain regime was discovered [92–95] that allows amplification in a single electron pass, eliminating the need of optical cavities and enabling amplification in the X-ray domain. Self-Amplified Spontaneous Emission (SASE) [96–98] is based on the interaction between the electron beam and the radiation they generate while propagating in a long undulator section. The electron beam starts to micro-bunch on the scale of the radiation wavelength by interacting with the spontaneous emission. With the bunching process, the coherent radiation is increased, which in turn

enhances the micro-bunching and hence a positive feedback, referred to as a collective instability, is achieved, leading to an exponential growth of the FEL power. SASE typically starts with a shot-noise of the electron beam that emits a large degree of incoherent radiation and a small amount of coherence. Different modes radiate energy, and the mode that fits the resonance condition gets amplified along the undulator. Thus, a partial temporal coherence is achieved that results in number of the so-called SASE spikes that sit on a broad spontaneous emission radiation background. After the first demonstration in the mm range [99], the first high gain exponential regime in the infrared was observed in 1985 at Lawrence Livermore National Laboratory [100].

The SASE spectra observed on FLASH [101] are shown in Fig. 1.6. They illustrate the SASE fluctuations. The number of spikes (wave packets) is typically 2.5, leading, in using the value of the cooperation length [102], to FEL pulses of about 50 fs.

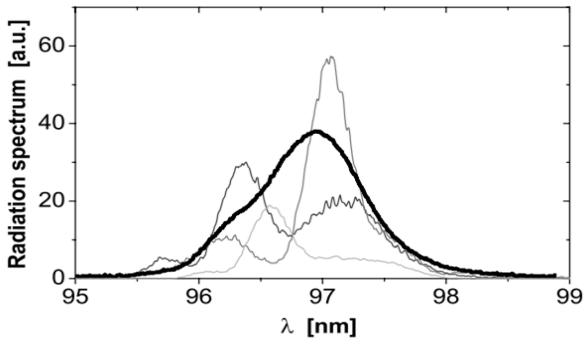

Figure 1.6: SASE spectra measured on FLASH. Thin curves: single-shot spectra, bold curve: averaged spectrum. Figure from [101].

Table 1.3 presents some of the SASE amplification and their characteristics measured at different laboratories. The gain length corresponds to the exponential growth rate and the saturation length to the distance required for the laser to saturates.

Facility	**Energy**	**Wavelength**	**Gain length**	**Saturation length**	**Saturation power**	**Gain**
	[MeV]	[nm]	[m]	[m]	[MW]	
NRL [99]	1	8×10^6	-	-	17	-
LLNL [100]	3.5	10^7	80	1.3	-	-
UCLA [103]	18	12000	2.5	-	-	10^5
BNL [104]	34	633	0.11	-	-	-
ANL [105]	217	530	1.6	-	-	-
DESY[106]	233	109	-	-	-	3×10^3
UCLA [107]	72	845	0.19	3.8	-	
LCLS [108]	13600	0.15	3	60	-	-
SACLA [109]	8000	0.06	-	-	10000	-
Pohang [110]	8000	0.14	3.43	-	-	-
SwissFEL [111]	5800	0.1	-	-	-	-
European XFEL [112]	6400	0.9	few 10^{-3}	-	-	-

Table 1.3: Examples of some Linac based SASE applications with the amplification characteristics.

1.4.2.2 Seeding

With SASE, the spike wavelengths vary from shot to shot due to the noise electron beam distribution and jitter. A seed at the resonant wavelength can thus be injected to modulate the elec-

tron beam and improve the longitudinal coherence by enhancing the bunching process efficiency [113]. Several seeding schemes aiming at enhancing the micro-bunching process are presented.

Enhanced SASE

Enhanced SASE (eSASE) consists of a modulator (can be a small undulator), installed before the radiator (undulator), to pre-modulate the electron beam [114]. This scheme, presented in Fig. 1.7, can significantly shortens the FEL gain length as comparison with normal SASE.

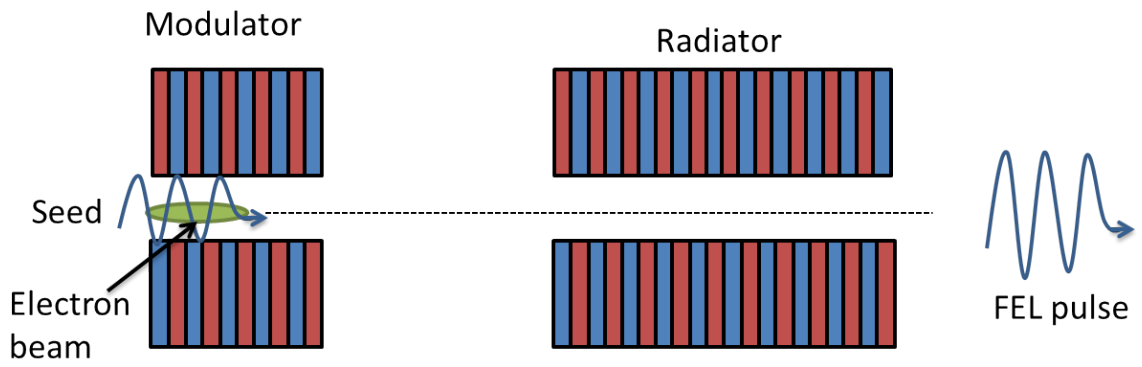

Figure 1.7: Scheme representing the enhanced SASE configuration. Seed interacting with the electron beam (green) inside the modulator.

At SLAC, the X-ray laser-enhanced attosecond pulse generation attained a single spike spectra with 5.5 eV average BW and an estimated pulse duration < 0.7 fs [115].

Self-seeding

A design to improve the spectral bandwidth of X-ray SASE amplification was presented in 1997 at DESY [116]. This scheme, known as self-seeding, consists of two undulators with an X-ray monochromator placed between them as shown in Fig. 1.8. The electron beam traverses the first undulator operating in the SASE linear regime. Then it is sent into a chicane to suppress the electron beam density modulation. The noisy SASE is cleaned in a monochromator and interacts with the electron beam in the second undulator. This process enables the second stage FEL amplifier to operate in the steady-state regime.

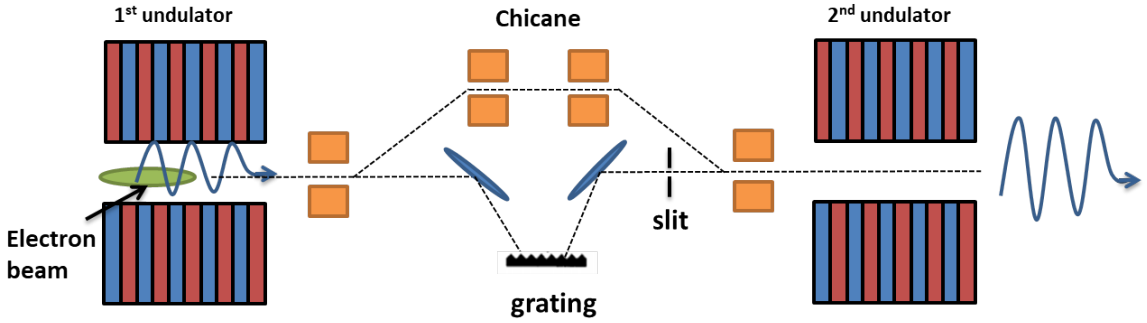

Figure 1.8: Scheme representing the self-seeding configuration.

Indeed, self-seeding suits better the hard X-ray domain by cleaning the radiation before the second amplification. Recently, self-seeding with the spectral cleaning of the SASE radiation in

a single crystal monochromator [117], appears to be very promising as experimentally demonstrated at LCLS [118, 119] and at SACLA [120].

High Gain Harmonic Generation

Much like eSASE, where a coherent seed is injected to modulate the electron beam at the start, the high gain harmonic generation (HGHG) [121] has an additional dispersive section (chicane) between the modulator and radiator as shown in Fig. 1.9. The electron beam is first modulated in an undulator with a seed laser. Then the beam is sent through a dispersive section to convert the energy modulation to density modulation. The density modulated electron beam is finally sent through a long undulator (radiator) tuned at the n harmonic of the seed laser. The resulting FEL wavelength λ_{FEL} is:

$$\lambda_{FEL} = \frac{\lambda}{n}$$

The efficiency of up-frequency conversion of this scheme is relatively low due to the high energy modulation requirement where, the increase of the slice energy spread degrades the lasing process in the radiator. Thus the harmonic number used in the classic HGHG scheme is typically lower than 10.

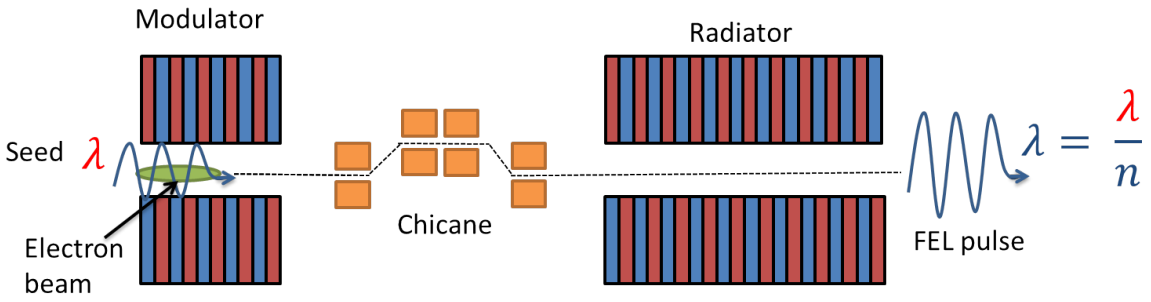

Figure 1.9: Scheme representing the high gain harmonic generation configuration. Seed interacting with the electron beam (green) inside the modulator, then dispersed in the chicane (orange) before entering the radiator.

Figure 1.10 shows a measurement at Brookhaven National Laboratory using the HGHG FEL scheme [122]. The wavelength of the seed laser is 800 nm. The amplification at the third harmonic is observed with a fine line of 0.1% relative bandwidth, and with higher spectral brightness as compared to the broad spiky SASE spectra. The HGHG width is close to one single SASE spike. An estimate of the pulse length of 0.9 ps was found, close to the 1 ps electron beam duration after compression. These results provided evidence of the high temporal coherence in the HGHG output and significant improvement due to the seeding, with respect to the SASE.

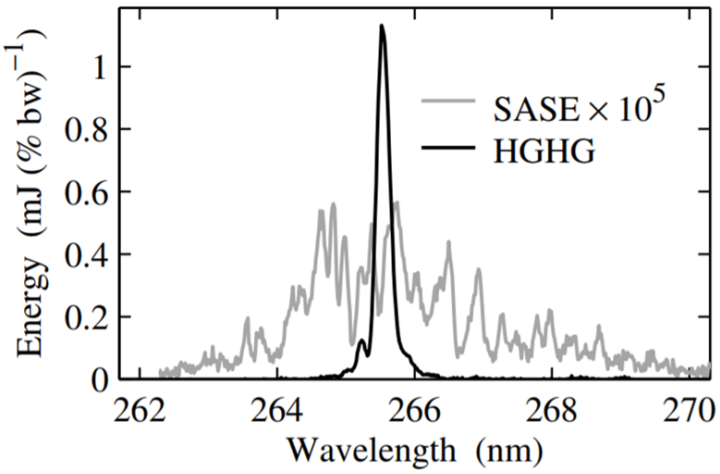

Figure 1.10: Single shot HGHG spectrum using a 800 nm laser seed compared with a SASE shot. Figure from [122].

In [123], it is discussed how the use of multiple stages of classic HGHG enhance the lasing process at higher harmonics. With this approach, the output of one HGHG stage (modulator, dispersion section, and radiator) provides the input seed to the next stage. For each stage, the frequency is multiplied by a factor of 3 to 5, where the coherent radiation produced by the prebunched beam in the radiator at the harmonic of the seed is many orders of magnitude higher in intensity than SASE. Dispersion sections are placed between stages to shift the radiation to fresh portions of the electron bunch to avoid the loss of gain due to the energy spread induced in the previous stage [113]. Shot noise at the different stages can then become an issue [124], however schemes are proposed for reducing it [125].

The FERMI-ELETTRA FEL (Trieste, Italy) is the first to implement the HGHG configuration for a user facility. The generated FEL pulses exhibits a well-defined temporal profile of ~100 fs long with a bandwidth of the order of few tens of meV [126]. The FEL section consists of two lines: The first undulator line produces coherent radiation in the spectral range from 65 nm to 20 nm by adopting the classical HGHG. The second undulator line (FEL-2) covers a spectral range between 20 nm and 4 nm using multi-cascade HGHG.

Echo Enabled Harmonic Generation

Echo-Enabled Harmonic Generation (EEHG) FEL scheme uses two laser modulators in combination with two dispersion sections to generate a high-harmonic density modulation in the electron beam (see Fig. 1.11). The echo scheme has a remarkable up-frequency conversion efficiency and allows for generation of high harmonics with a relatively small energy modulation [127]. The beam energy is tuned at frequency ω_1 in the first modulator by interacting with the first laser beam. After passing through the first dispersion section, the beam energy is then modulated in the second modulator tuned to frequency ω_2. The beam then passes through the second dispersion section, and finally into the radiator to achieve large gain at a high harmonic of the first seed laser. The amplification occurs at the wavelength λ_{FEL} expressed as:

$$\lambda_{FEL} = \frac{\lambda_1 \lambda_2}{n\lambda_2 + m\lambda_1}$$

where λ_1 and λ_2 are the wavelengths of the first and second laser seed, respectively, with n and m being integers.

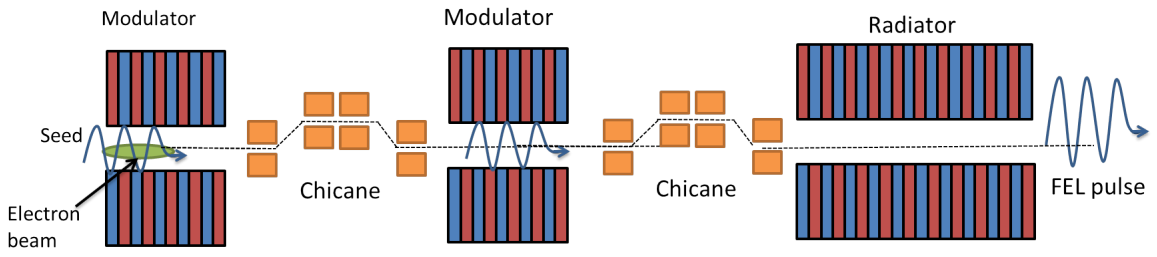

Figure 1.11: Scheme representing the echo-enabled harmonic generation configuration.

1.5 Motivation of the work: Towards compact and advanced free electron lasers

The revelation of the laser paved the way to the discovery of the FEL few years after, that consists of an electron beam and an undulator acting as gain medium, generating intense coherent radiation with tunable wavelength. The process starts from the interaction of the electron beam with the emitted radiation, where an exchange of energy occurs. This exchange leads to a micro-bunching of the electron beam on the radiated wavelength scale and achieve temporal coherence enhancing the radiation power by orders of magnitude. Different configurations can be implemented to improve the bunching efficiency and thus improve the FEL performance. For example echo-enabled harmonic generation (EEHG) can bunch the electron beam at high frequency contents and generate amplification at very short wavelength, eliminating the need of high electron beam energy that requires a very long Linac.

Five years after the FEL process discovery, the concept of LPA was introduced. This new kind of electron source is based on focusing a high power laser onto a gas, where a plasma with intense electric field is induced, and electrons can achieve GeV energies in few cm scale. LPA has demonstrated its high potential, advancing the accelerator field towards compactness. The state-of-art LPA electron source and problems are discussed in the PhD especially for FEL based applications, where the high energy spread and divergence require a specific beam line to manipulate the electron beam phase space to satisfy the FEL requirements and generate coherent emission. Different solutions to handle the divergence and energy spread have been presented.

1.5.1 Review of the general context underlying my PhD work

The particular framework of my PhD is within the context of the LUNEX5 project and its associated R&D programs. The LUNEX5 test facility is composed of two kinds of accelerators, a conventional linear accelerator (Linac) and an LPA. The EEHG configuration was targeted from the beginning on the LUNEX5 project. It was aimed at being compared to the high gain harmonic generation (HGHG) since the very efficient up frequency conversion can provide a very compact solution for reaching short wavelengths. Unfortunately, the LUNEX5 is not funded yet and the experiment comparing EEHG and HGHG could not be done in France. Meanwhile, a EEHG / HGHG test experiment was in preparation at FERMI (Italy), and we were able join the collaboration. The experiment took place in Spring and Summer 2018, and gave very promising results by getting us closer to high quality compact FEL sources.

1.5.2 Compact ancillary equipment

I have studied two specific ancillary compact equipments.

Cryogenic permanent magnet undulators (CPMUs) that take advantage of the enhanced field of permanent magnets at cryogenic temperature enable to construct a more compact undulator

with shorter period and sufficient magnetic field. The progress of CPMUs at synchrotron SOLEIL, with optimization techniques to ensure a good magnetic field quality before the undulator commissioning, magnetic design modeling, measurement methods to characterize the undulator field (Hall probe connected to a rail for the local field, a rotating coil or stretched wire for the field integrals) is presented. A CPMU of period 15 mm and 3 meters long (R&D programs), is under construction and will be optimized for the LUNEX5 project.

The second equiment is the so-called QUAPEVA, a high tunable gradient permanent magnet based quadrupole. As mentioned above, the electron beam generated from a LPA source starts with a high divergence of the orders of few mrads. To enable a good transport, the divergence should be handled at an early stage. Thus, the QUAPEVAs are a crucial components for the LUNEX5 test facility in the case of the LPA. Seven systems that been built are presented in this PhD. Modeling using RADIA and TOSCA softwares have been done alongside the magnetic field characterization using three measurements: rotating coil, stretched wire and pulsed wire. A triplet of QUAPEVAs is currently under commisioning at COXINEL for an operation energy of 200 MeV and helped us fully control the electron beam along 10 m long beam line.

1.5.3 Towards LPA based FEL

One of the R&D programs is the COXINEL experiment, where our objective is to try and achieve FEL using an LPA source. The beam line is equipped with compact high gradient permanent magnet based quadrupoles to handle the high divergence, a de-mixing chicane to reduce the slice energy spread and a compact cryogenic undulator. Another set of quadrupoles are added between the chicane and the undulator. They take advantage of the electron beam energy-position correlation induced by the chicane and allow for the so-called supermatching optics, where each energy slice is focused at a different location inside the undulator. This focusing slippage can be synchronized with the FEL wave slippage resulting in a larger FEL power.

The first milestone of the COXINEL experiment is to experimentally handle the electron beam transport. This has been covered by T. André's PhD [128]. The second milestone towards FEL studies is the achievement of proper undulator radiation at the end of the transport line. So far, undulator radiation is observed using an LPA source but with qualities, such as wavelength stability and spectral purity, that do not yet reach those achieved with conventional accelerators. Thanks to the electron beam phase space manipulation enabled by COXINEL beam line, we are able to achieve better undulator radiation qualities than what were previously reported. Simulations are done using SRW code and a satisfactory comparison is achieved with the measurements.

1.5.3.1 COXINEL progress

In march 2016, the first run of COXINEL (RUN1) took place, where the electron beam was generated by the LPA in the ionization injection configuration. The beam was rapidly transported but without correcting the dispersion. In RUN2 (November 2016), the LPA shock injection technique was carried out, where the electron beam exhibites a smaller energy spread but displayed a poor stability. Hence it was decided to operate the LPA in the ionization injection regime with the addition of an electron slit in the middle of the chicane to select a smaller energy range. During RUN3 (March 2017), a beam pointing alignment compensation was established that enabled to correct the electron beam dispersion and transport it to the undulator, enabling to map the photon transverse shape using a CCD camera. In RUN4 (November 2017), new electron beam optics had been adopted to better select a smaller energy range using the slit in the chicane. The QUAPEVAs, that had a large skew component, were corrected. Undulator radiation around 200 nm was measured using a UV spectrometer for the operating energy of 176 MeV. From day to day the maximum reachable energy was decreasing due to the degradation of the laser and its optical transport to the target. Thus it was difficult to transport a highly charged beam at the operating

energy of 176 MeV. In RUN5 (December 2018), it was decided to operate at a lower energy of 161 MeV corresponding to undulator radiation wavelength around 250 nm for a 4.7 mm undulator gap. The QUAPEVAs were moved closer to the electron generation source by 0.5 mm to achieve good focusing of this particular energy. In addition, a seed laser of wavelength 266 nm was spectrally tuned, synchronized and transversally aligned with the electron beam. In RUN6 (February 2019), we focused mainly on the synchronization and alignment of the seed laser with the electron beam aiming at measuring coherent emission but without any success.

1.6 Thesis outline

In chapter 1, particle accelerators and light sources based synchrotron radiation are introduced. The origin of the LPA and FEL are discussed starting from the invention of the laser. Different advanced FEL schemes are presented with their characteristics. I finish by the motivation of compact and advanced Free Electron Laser, which is the main aim of my PhD. Such a path is approached by different manners. The compactness is searched in investigating the replacement of FEL components such as the accelerator, the undulator or the selection of an efficient short length FEL configuration. For a compact accelerator, my work concentrates on laser plasma accelerator, that could, in addition, be qualified by the FEL application, alongside compact devices such as cryogenic undulator and permanent magnet quadrupoles.

In chapter 2, I introduce the theoretical basis required for my PhD work. It includes the electron beam dynamics through different magnetic structures, the undulator radiation produced as an electron beam propagates through it and the FEL theory including low and high gain cases.

In chapter 3, I introduce the reference of advanced and compact FEL project for my PhD work, i.e. the LUNEX5 test facility (free electron Laser Using a New accelerator for the Exploitation of X-ray radiation of 5th generation). It aims at investigating the production of short, intense, coherent FEL pulses in the 40-4 nm spectral range. It comprises a 400 MeV superconducting Linac for high repetition rate operation (10 kHz), multi-FEL lines and adapted for studies of advanced FEL schemes (HGHG and EEHG). It also consists of a 0.4-1 GeV laser plasma acceleration to investigate its qualification for an FEL application. LUNEX5 is still work under progress and my PhD work has been carried out in the frame of different R&D programs that have been launched. They include the development of a 3 m long CPMU and the test experiment of comparing echo and HGHG at FERMI. They comport also a smaller benchmark experiment COXINEL that is currently installed at Laboratoire d'Optique Appliquée (LOA), and the development of variable high gradient quadrupoles (QUAPVAs) to handle the LPA divergence. The COXINEL set-up has been defined with baseline reference electron beam parameters, that are introduced in this chapter. I also show my analytic free electron laser calculations with the Ming Xie approach for different sets of parameters.

In chapter 4, I present the design, construction and optimization of cryogenic undulators, suitable for compact light sources. I worked on the modeling with the RADIA code [129], construction and optimization of the second cryogenic permanent magnet undulator of period 18 mm at SOLEIL. I also participated in synchrotron radiation measurements in the SOLEIL storage ring of the first CPMU of 18 mm period, where we achieved results that confirmed the accuracy of our field measurements. It sets a reference quality of the undulator radiation spectrum from an LPA electron beam, on which I worked specifically with the second CPMU installed at COXINEL. I presented the progress of CPMUs at conferences (IPAC, FEL and OSA), and I wrote some proceedings regarding this matter. I was also the corresponding author of the published article [130], where I wrote the main part of it.

In chapter 5, tunable high gradient permanent magnet based quadrupoles (QUAPEVAs), of interest for handling the divergence from LPA for the COXINEL experiment, are introduced. The optimization of seven systems that have been built is done using modeling (analytics, simulations) and magnetic measurements. I compared the performance of the QUAPEVA to equivalent systems in the literature, for which I modeled multiple quadrupoles with their different designs for an unified set of parameters. I also characterized the QUAPEVAs with Radia and magnetic measurements. A triplet of QUAPEVAs are installed at COXINEL and allowed for a good handling of the beam along 10 m long transport line. I had some oral presentations and posters at different conferences regarding this device. We also published two articles, where I was the corresponding author in both. In [131], I wrote most of it and I contributed to some of the measurements. For the [132], the article was for the EAAC2017 conference, and I did it all by myself except for some measurements. Also I wrote a paper about the different designs of permanent magnet based quadrupoles to compare their performance to the QUAPEVA [133].

In chapter 6, I examine the undulator radiation in the framework of COXINEL, using SRW code [134] for the baseline electron beam reference case. I explore different approaches on how to extract the electron beam parameters such as energy spread and divergence by looking at the produced radiation.

In Chapter 7, I report about the electron beam characteristics measurements and the transport along the COXINEL line for RUN4 and RUN5. The real beam produced is quite far from the baseline case that was examined at the beginning of the project. The slice charge is one order of magnitude lower and divergence larger by a factor of 2. I contributed to the transport of the electron beam from the source down to the undulator for the photon characterization that makes a large portion of my PhD results.

In chapter 8, I present the undulator radiation measured at COXINEL using a UV spectrometer for two runs. I carried out the data analysis myself. A wavelength tunability of 100 nm and stability of 2.4% have been achieved with a minimum relative bandwidth of 5%. Also the methods introduced in chapter 7 are applied to the measurements and gave an insight on the electron beam quality. We submitted an article to Nature Scientific Reports with me being the first and corresponding author, concerning the measured undulator radiation, and it will be published in the upcoming month.

Finally in chapter 9, I discuss the echo scheme for the LUNEX5 project and for the world wide FERMI experiment, to which I participated, where we were able to achieve lasing at the 45^{th} harmonic (5.9 nm) of the laser seed. I carried myself the echo analysis on the analytic approach level.

In conclusion, I report on the progress that have been made towards advanced compact free electron laser. Using conventional acceleration, the results achieved in the frame of the EEHG FERMI collaboration make this FEL configuration very promising for an efficient up-frequency conversion, where lasing at the 45^{th} harmonic is achieved and low coherent emission has been observed on the 100^{th} harmonic of the seed laser (264 nm). The studies done on CPMUs at SOLEIL show that these devices can be properly reliable for compact constituting elements of an FEL experiment. The most challenging part of my work concerns the LPA electron beam, where we have proceeded step by step in transporting and manipulating a highly unstable electron beam at COXINEL. Undulator radiation is observed in two COXINEL runs and we were able to achieve a better photon beam quality than in the previous works. In RUN6, we attempted to observe coherent emission but with no success. Nonetheless, LPA based electron beams with parameters similar to

our baseline reference case have been reported, thus giving us the confidence that we are indeed able to achieve amplification in the years to come.

Chapter 2

Electron beam dynamics, Undulator Radiation and Free Electron Laser

In this chapter, the theoretical basis of the electron beam dynamics as it propagates through different magnetic structures is presented. A short description of undulator radiation and free electron laser in the low and high gain regime are introduced.

2.1 Beam dynamics

The electron reference path is described in a moving frame in the coordinate system shown in Fig. 2.1. The electron follows a trajectory along the longitudinal axis s with a curvature ρ and its position can be described at any point along this trajectory in the horizontal x and vertical z planes.

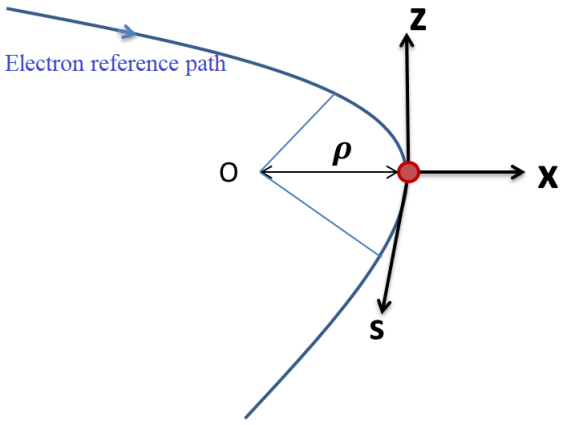

Figure 2.1: Coordinate system along the accelerator axis.

In an ideal case, all particles follow the reference electron path along the s axis. However in reality, an electron can have a deviating angle in the transverse planes with respect to the reference particle and are defined as:

$$x' = \frac{dx}{ds} \qquad \text{and} \qquad z' = \frac{dz}{ds} \tag{2.1}$$

In accelerators, magnetic fields are used to divert and focus the electron beam. The equation

of motion results from the Lorentz force:

$$\vec{F_B} = -e\vec{v} \times \vec{B} \tag{2.2}$$

where e is the elementary charge, $\vec{v}$ the electron velocity and $\vec{B}$ the magnetic field. A charged particle with a trajectory parallel to the magnetic field lines experiences no force. If the particle has an angle, it attains a gyrating orbit along the field lines. An important parameter in particle accelerator, known as the magnetic rigidity ρB, is expressed as:

$$\rho B = \frac{P}{e} \tag{2.3}$$

where $P = \gamma m v$ is the relativistic particle momentum with γ being the Lorentz factor. In practical units, for relativistic particles ($E = Pc$), the rigidity can be expressed as:

$$\rho[m]B[T] \approx \frac{1}{300}E[MeV]$$

For example, an electron beam of 200 MeV has a magnetic rigidity of 0.66 m.T and a curvature of 0.66 m for a 1 T field. The higher the particle energy, the less it gets deflected by the magnetic field.

Going from the cartesian coordinates to the cylindrical ones, the Lorentz force can be expressed as:

$$\vec{F_B} = \gamma \vec{a}_\rho = \gamma m\left[\frac{d^2\rho}{dt^2} - \frac{v^2}{\rho}\right] \tag{2.4}$$

where m is the electron mass and $\vec{a}_\rho$ the acceleration in the radial direction. Equating (2.2) and (2.4), and considering that the magnetic field is directed in the vertical axis, one gets the following:

$$\gamma m\left[\frac{d^2\rho}{dt^2} - \frac{v^2}{\rho}\right] = -eB_z v \tag{2.5}$$

By considering that the electron is deviated from the reference path by a horizontal distance x, Eq. (2.5) becomes:

$$\gamma m\left[\frac{d^2(\rho + x)}{dt^2} - \frac{v^2}{(\rho + x)}\right] = -eB_z v \tag{2.6}$$

For a small deviation from the reference path ($x << \rho$), a series expansion up to the first order can be done:

$$\frac{1}{\rho + x} = \frac{1}{\rho}(1 - \frac{x}{\rho}) \tag{2.7}$$

Thus, Eq. (2.6) takes the following form:

$$\gamma m\left[\frac{d^2}{dt^2}(\rho + x) - \frac{v^2}{\rho}(1 - \frac{x}{\rho})\right] = -eB_z v \tag{2.8}$$

Replacing Eq. (2.1) in Eq. (2.8), one arrives at:

$$x'' v^2 - \frac{v^2}{\rho}\left(1 - \frac{x}{\rho}\right) = -\frac{eB_z v}{\gamma m} \tag{2.9}$$

Considering that the field slightly varies with x, one can use Taylor expansion to write the magnetic field expression as:

$$B_z(x) = B_0 + Gx + \text{Higher orders} \tag{2.10}$$

where G, defined as the field gradient, is expressed as:

$$G = \frac{\partial B_z}{\partial x} \tag{2.11}$$

Substituting Eq. (2.10) in Eq. (2.9), one gets:

$$x'' - \frac{1}{\rho}\left(1 - \frac{x}{\rho}\right) = -\frac{eB_0}{\gamma m v} - k_q x \tag{2.12}$$

with

$$k_q = \frac{eG}{P} \tag{2.13}$$

commonly known as the quadrupole focusing strength.

Using Eq. (2.3), Eq. (2.12) becomes:

$$x'' - \frac{1}{\rho} + \frac{x}{\rho^2} = -\frac{1}{\rho} - k_q x \tag{2.14}$$

Finally, one reaches the famous Hill equation [135]:

$$x'' + Kx = 0 \qquad \text{and} \qquad K = \frac{1}{\rho^2} + k_q \tag{2.15}$$

2.1.0.1 Solution to the Hill equation

The differential equation (2.15), also known as the homogeneous Hill equation, is characterized by a harmonic oscillator where K is the frequency. In this case, K represents the focusing strength of the considered magnetic element and is composed of two terms: $\frac{1}{\rho^2}$ the weak sector magnet focusing and k_q the focusing gradient. The solution of this equation is expressed as [136]:

$$\begin{cases} x(s) = C(s)x_0 + S(s)x'_0 \\ x'(s) = C'(s)x_0 + S'(s)x'_0 \end{cases} \tag{2.16}$$

with

K > 0	**K < 0**	**K = 0**
$C(s) = \cos(\sqrt{K}s)$	$C(s) = \cosh(\sqrt{\lvert K\rvert}s)$	$C(s) = 1$
$S(s) = \frac{1}{\sqrt{K}}\sin(\sqrt{K}s)$	$S(s) = \frac{1}{\sqrt{\lvert K\rvert}}\sinh(\sqrt{\lvert K\rvert}s)$	$S(s) = s$

The solution of Hill's equation can also be determined by using a "simplified Floquet's theorem" [137]:

$$x(s) = \sqrt{\varepsilon_x \beta_x(s)}\cos(\phi_x(s)) \tag{2.17}$$

where ε_x is an invariant introduced here as the horizontal emittance and β_x the beta Twiss parameter describing a periodic oscillations commonly referred to as betatron oscillation.

By inserting the first and second derivative of Eq. (2.17) in Eq. (2.15), one gets:

$$\left(-\frac{\beta'^2}{4\beta^2} + \frac{\beta''}{2\beta} - \phi'^2 + K\right)\cos\phi - \left(\frac{\beta'\phi'}{\beta} + \phi''\right)\sin\phi = 0$$

The sum of all coefficients of the sine and cosine terms, must be equal to zero to make Eq.

(2.17) valid for all phases, thus:

$$\begin{cases} \frac{1}{2}\left(\beta\beta'' - \frac{1}{2}\beta'^2\phi^2\right) - \beta^2\phi'^2 + \beta^2 K = 0 \\ \beta'\phi' + \beta\phi'' = 0 \quad \Longrightarrow \quad \beta\phi' = 1 \end{cases} \tag{2.18}$$

The envelope equation is expressed as:

$$\frac{1}{2}\beta\beta'' - \frac{1}{4}\beta'^2 + \beta^2 K = 1 \tag{2.19}$$

Introducing the other Twiss parameters α and Υ as:

$$\begin{cases} \alpha(s) = -\frac{\beta'(s)}{2} \\ \Upsilon(s) = \frac{1+\alpha(s)^2}{\beta(s)} \end{cases} \tag{2.20}$$

and inserting them in Eq. (2.19), one gets the following relation:

$$\beta'' + 2\beta K - 2\Upsilon = 0 \tag{2.21}$$

One can note that any solution that satisfies equation (2.21) makes (2.17) a real solution of the Hill equation. Thus, one can obtain the expression of the emittance in terms of the Twiss parameters:

$$\varepsilon_x = \Upsilon x^2 + 2\alpha x x' + \beta x'^2 \tag{2.22}$$

The emittance [138] can also be defined as the area in phase space that includes the particles and generally has an elliptical shape. The geometry of the ellipse can be characterized by the Twiss parameters as shown in Fig. 2.2.

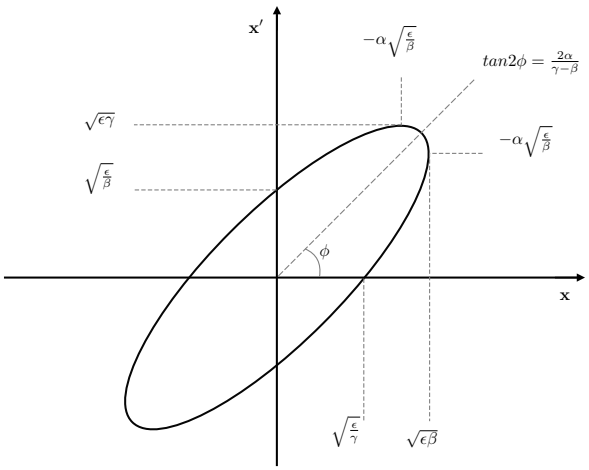

Figure 2.2: Phase space with the ellipse containing all the particles.

The horizontal phase space can be also designated by the matrix Σ_x:

$$\Sigma_x = \varepsilon_x \begin{pmatrix} \beta & -\alpha \\ -\alpha & \Upsilon \end{pmatrix} = \begin{pmatrix} \sigma_x^2 & \sigma_{xx'}^2 \\ \sigma_{xx'}^2 & \sigma_x'^2 \end{pmatrix} \tag{2.23}$$

where σ_x and σ'_x are the beam size and divergence of the electron beam, respectively, and $\sigma_{xx'}$

corresponds to the position and angle correlation. Thus:

$$\begin{cases} \sigma_x^2 = < (x - < x >)^2 > = \varepsilon_x \beta_x \\ \sigma_x'^2 = < (x' - < x' >)^2 > = \frac{\varepsilon_x}{\beta_x}(1 + \alpha_x^2) \\ \sigma_{xx'}^2 = < (x - < x >)(x' - < x' >) > = -\varepsilon_x \alpha_x \end{cases} \tag{2.24}$$

It's interesting to note that when $\alpha > 0$ the beam is converging, for $\alpha < 0$ the beam is diverging, and in the case of $\alpha = 0$ the beam size in phase space has a minimum or maximum (see Fig. 2.3).

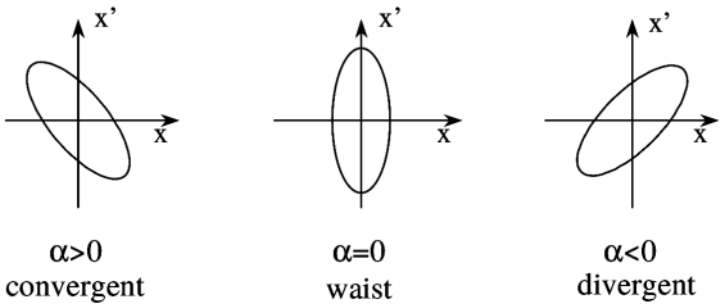

Figure 2.3: Form and orientation of the phase ellipse for different α cases.

2.1.1 Inhomogeneous Hill equation: Dispersion

The Hill equation has been solved by disregarding the transverse planes coupling induced by the variation of the magnetic field ($\frac{\partial B_z}{\partial z} = 0$). Also the energy dispersion of the beam $\delta = \frac{P - P_0}{P_0}$, with P_0 being the momentum of the reference electron, has been neglected. In reality the electron beam has an energy spread distribution. A paricle with dispersion $\delta \neq 0$ undergoes different acceleration forces induced by the magnetic elements and thus acquires a different trajectory from the reference particle. To take this effect into account, an additional term is added to equation (2.15):

$$x'' + Kx = \frac{1}{\rho}\delta \tag{2.25}$$

This equation is known as the inhomogeneous Hill equation. The solution can be written as:

$$x = x_H + x_D \tag{2.26}$$

where x_H is the solution of the homogeneous Hill equation that describes the motion of a particle with momentum P_0 presented in the previous section. x_D is the solution of $D'' + KD = \frac{1}{\rho}$ that describes the motion of a particle with momentum P. For simplicity, Eq. (2.26) can be rewritten in a matrix form :

$$\begin{pmatrix} x \\ x' \\ \delta \end{pmatrix}_s = \begin{pmatrix} C(s) & S(s) & D(s) \\ C'(s) & S'(s) & D'(s) \\ 0 & 0 & 1 \end{pmatrix} . \begin{pmatrix} x \\ x' \\ \delta \end{pmatrix}_0 \tag{2.27}$$

where $D(s)$ is known as the dispersion function and expressed as:

$$D(s) = S(s) . \int_0^s \frac{1}{\rho(t)} . C(t) dt - C(s) . \int_0^s \frac{1}{\rho(t)} . S(t) dt \tag{2.28}$$

By developing this formalism in the first order for all the coordinates characterizing the particle

beam in the 6D phase space, the transport matrix is written as:

$$\begin{pmatrix} x \\ x' \\ z \\ z' \\ l \\ \delta \end{pmatrix} = \begin{pmatrix} R_{11} & R_{12} & R_{13} & R_{14} & R_{15} & R_{16} \\ R_{21} & R_{22} & R_{23} & R_{24} & R_{25} & R_{26} \\ R_{31} & R_{32} & R_{33} & R_{34} & R_{35} & R_{36} \\ R_{41} & R_{42} & R_{43} & R_{44} & R_{45} & R_{46} \\ R_{51} & R_{52} & R_{53} & R_{54} & R_{55} & R_{56} \\ R_{61} & R_{62} & R_{63} & R_{64} & R_{65} & R_{66} \end{pmatrix} \begin{pmatrix} x \\ x' \\ z \\ z' \\ l \\ \delta \end{pmatrix}_0 \tag{2.29}$$

where l is the position deviation from the reference particle in the s axis. Keeping the approximation presented before ($\frac{\partial B_z}{\partial z} = 0$), meaning there is no coupling between the transverse planes, the matrix in (2.29) can be simplified to:

$$\begin{pmatrix} x \\ x' \\ z \\ z' \\ l \\ \delta \end{pmatrix} = \begin{pmatrix} R_{11} & R_{12} & 0 & 0 & 0 & R_{16} \\ R_{21} & R_{22} & 0 & 0 & 0 & R_{26} \\ 0 & 0 & R_{33} & R_{34} & 0 & 0 \\ 0 & 0 & R_{43} & R_{44} & 0 & 0 \\ R_{51} & R_{52} & 0 & 0 & 1 & R_{56} \\ 0 & 0 & 0 & 0 & 0 & 1 \end{pmatrix} \begin{pmatrix} x \\ x' \\ z \\ z' \\ l \\ \delta \end{pmatrix}_0 \tag{2.30}$$

By adding the dispersion terms, Eq. (2.24) becomes:

$$\begin{cases} \sigma_x^2 = \varepsilon_x \beta_x + \sigma_\gamma^2 \eta_x^2 \\ \sigma_x'^2 = \frac{\varepsilon_x}{\beta_x}(1 + \alpha_x^2) + \sigma_\gamma^2 \eta_x'^2 \\ \sigma_{xx'} = -\varepsilon_x \alpha_x + \sigma_\gamma^2 \eta_x \eta_x' \end{cases} \tag{2.31}$$

where σ_γ is the relative energy spread, η_x the horizontal dispersion and η_x' the derivative of the horizontal dispersion along s.

2.1.1.1 Transport matrices

An accelerator is composed of different magnetic elements. Each device effect on the beam can be described by a 6D matrix. The transfer matrix from one point to another inside the accelerator will be written as the product of all the matrices of the elements in between.

2.1.1.2 Drift

For example, the transfer matrix representing a drift space over a distance L can be written as:

$$M_{drift} = \begin{pmatrix} 1 & L & 0 & 0 & 0 & 0 \\ 0 & 1 & 0 & 0 & 0 & 0 \\ 0 & 0 & 1 & L & 0 & 0 \\ 0 & 0 & 0 & 1 & 0 & 0 \\ 0 & 0 & 0 & 0 & 1 & 0 \\ 0 & 0 & 0 & 0 & 0 & 1 \end{pmatrix} \tag{2.32}$$

2.1.1.3 Dipole

A dipole with a vertical magnetic field disperses the beam in the horizontal axis. For a longitudinal length L, the transfer matrix of the dipole is expressed as:

$$R_{dipole} = \begin{pmatrix} \cos\frac{L}{\rho} & \rho\sin\frac{L}{\rho} & 0 & 0 & 0 & \rho(1-\cos\frac{L}{\rho}) \\ -\frac{1}{\rho}\sin\frac{L}{\rho} & \cos\frac{L}{\rho} & 0 & 0 & 0 & \sin\frac{L}{\rho} \\ 0 & 0 & 1 & 0 & 0 & 0 \\ 0 & 0 & 0 & 1 & 0 & 0 \\ \sin\frac{L}{\rho} & \rho(1-\cos\frac{L}{\rho}) & 0 & 0 & 1 & \rho(\frac{L}{\rho}-\sin\frac{L}{\rho}) \\ 0 & 0 & 0 & 0 & 0 & 1 \end{pmatrix} \tag{2.33}$$

2.1.1.4 Quadrupole

In the case of a quadrupole with length L in the longitudinal axis that focuses in the x plane and de-focuses in the z plane:

$$M_{quad} = \begin{pmatrix} \cos\sqrt{K}L & \frac{1}{\sqrt{K}}\sin\sqrt{K}L & 0 & 0 & 0 & 0 \\ -\sqrt{K}\sin\sqrt{K}L & \cos\sqrt{K}L & 0 & 0 & 0 & 0 \\ 0 & 0 & \cosh\sqrt{|K|}L & \frac{1}{\sqrt{|K|}}\sinh\sqrt{|K|}L & 0 & 0 \\ 0 & 0 & \sqrt{|K|}\sinh\sqrt{|K|}L & \cosh\sqrt{|K|}L & 0 & 0 \\ 0 & 0 & 0 & 0 & 1 & 0 \\ 0 & 0 & 0 & 0 & 0 & 1 \end{pmatrix} \tag{2.34}$$

After having introduced the electron beam transport, let's consider now the synchrotron radiation source of interest as electrons propagate through an undulator.

2.2 Undulator magnetic field

An undulator, commonly referred to as an insertion device, is composed of an assembly of magnets with alternating poles producing a periodic magnetic field. Such devices are traditionally installed on synchrotron storage ring facilities to produce high brightness photon beams. The undulator also serves as a crucial element in the free electron laser, where it is associated with a high density electron beam to form a gain medium.

2.2.1 Planar undulator magnetic field

A planar undulator generates a sinusoidal field in one transverse plane. Consider the case of a planar undulator producing a magnetic field in the z direction as shown in Fig. 2.4. For simplicity, one can neglect the x dependence of the field at the vicinity of the electron beam. The curl of the magnetic field vanishes inside the vacuum chamber, hence Laplace equation is used to write the field as a gradient of a scalar magnetic potential ϕ_{mag}:

$$\vec{B}_u = -\vec{\nabla}\phi_{mag} \quad , \quad \nabla^2\phi_{mag} = 0$$

where $\vec{B}_u$ is the magnetic field.

For simplicity, one can also assume that the width of the magnets is much bigger than the undulator gap, hence the field dependence on the horizontal axis can be neglected. The field on-axis and the Laplacian can be written as:

$$B_u(0,0,s) = B_0\cos(k_u s)\hat{z} \qquad \frac{\partial^2\phi_{mag}}{\partial s^2} + \frac{\partial^2\phi_{mag}}{\partial z^2} = 0 \tag{2.35}$$

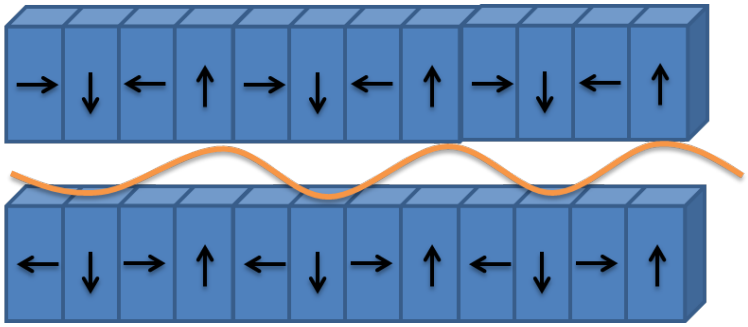

Figure 2.4: Schematic view of a planar undulator in a Halbach assembly [139] and the magnetic field generated (orange curve).

with $k_u = \frac{2\pi}{\lambda_u}$ the undulator wavenumber and λ_u the undulator period.

Taking $\phi_{mag} = f(z)\cos(k_u s)$ and replacing it in Eq. (2.35), one gets:

$$\frac{d^2 f}{dz^2} - k_u^2 f = 0 \tag{2.36}$$

By solving Eq. (2.36), the general solution can be written as:

$$f(y) = c_1 \sinh(k_u z) + c_2 \cosh(k_u z)$$

Therefore the magnetic field is expressed as:

$$\mathrm{B}_u(z,s) = k_u \left[c_1 \cosh(k_u z) + c_2 \sinh(k_u z)\right] \cos(k_u s) \tag{2.37}$$

where c_1 and c_2 are constants. For an ideal undulator, free of magnetic and mechanical errors, the field is symmetric with respect to the z = 0 plane. So by using this condition, c_2 is found to be zero. And by taking the field amplitude $c_1 k_u$ to be B_{u0}, Eq. (2.37) becomes:

$$\vec{\mathrm{B}}_u = \mathrm{B}_{u0} \cos(k_u s) \cosh(k_u z) \hat{z}$$

Figure 2.5 presents the field lines generated by an undulator computed using Finite Element Method Magnetics (FEMM) [140].

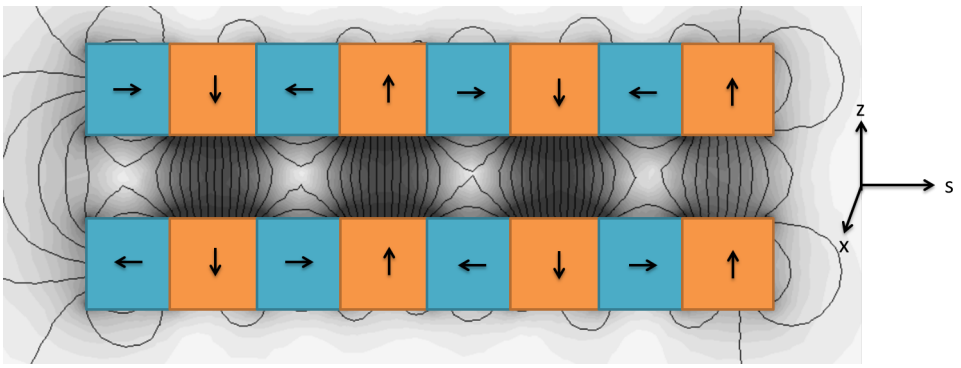

Figure 2.5: Computed field lines of a Halbach undulator [139] using FEMM software [140].

2.2.2 Electron trajectory

A relativistic electron traversing an undulator is subjected to the Lorentz force:

$$\vec{F_B} = m\gamma\frac{d\vec{v}}{dt} = e\vec{v}\times\vec{B}_u \tag{2.38}$$

Replacing the velocity v with the normalized one $\beta = v/c$ in Eq. (2.38):

$$\begin{pmatrix}\dot{\beta_x}\\ \dot{\beta_z}\\ \dot{\beta_s}\end{pmatrix} = \frac{e}{\gamma m}\begin{pmatrix}\beta_x\\ \beta_z\\ \beta_s\end{pmatrix}\times\begin{pmatrix}0\\ B_u\\ 0\end{pmatrix} \tag{2.39}$$

where the dot represents the time derivative. Taking the expression of the undulator field on-axis ($z = 0$), and considering that the longitudinal velocity β_s is constant, one is able to integrate Eq. (2.39) in the x axis and determine the transverse wiggling motion of the electron:

$$\beta_x = \frac{K_u}{\gamma}\cos(\omega_u t) + \beta_{x0}, \qquad \text{with} \quad K_u = \frac{eB_0\lambda_u}{2\pi mc} = 93.4B_0[T]\lambda_u[m] \tag{2.40}$$

where K_u is the deflection parameter, $k_u s = \omega_u t$ such that $\omega_u = k_u\beta_s c$ and β_{x0} the initial horizontal velocity.

Integrating Eq. (2.39) in the vertical axis, one gets:

$$\beta_z = \beta_{z0} \tag{2.41}$$

where β_{z0} is the initial vertical velocity. By taking

$$\beta^2 = \beta_s^2 + \beta_x^2 + \beta_z^2 = 1 - \frac{1}{\gamma^2}$$

and assuming that the electron traverse the reference path ($\beta_{z0} = \beta_{z0} = 0$), β_s is expressed as:

$$\beta_s = \sqrt{1 - \frac{1}{\gamma^2} - \frac{K_u^2}{\gamma^2}\cos^2(\omega_u t)}$$

For relativistic electrons, $1 >> \frac{1}{\gamma^2}$, hence, a series expansion can be applied and therefore the final expression of β_s is:

$$\beta_s = 1 - \frac{1}{2\gamma^2} - \frac{K_u^2}{2\gamma^2}cos^2(\omega_u t) \tag{2.42}$$

Integrating Eqs. (2.40) and (2.42), the electron trajectory motion is expressed as:

$$\begin{cases} x = \frac{K_u c}{\gamma\omega_u}\sin(\omega_u t) + x_0 \\ z = z_0 \\ s = \bar{\beta}_s c t + \frac{K_u^2 c}{8\gamma^2\omega_u}\sin(2\omega_u t) + s_0 \end{cases} \tag{2.43}$$

where (x_0, z_0 s_0) are the coordinates of the particle at the entrance of the undulator and are equal to zero in the case of the reference path and $\bar{\beta}_s$ the average velocity expressed as:

$$\bar{\beta}_s = 1 - \frac{1}{2\gamma^2} - \frac{K_u^2}{4\gamma^2} \tag{2.44}$$

Fig. 2.6 shows a planar undulator field of period 10 mm with a peak of 1 T (red) with the associated electron horizontal angle (blue) and trajectory (green). In the case of the 200 MeV beam

at COXINEL, the maximum angle reaches 2.4 mrad and the horizontal excursion 7.5 µm. In the case of the 2.75 GeV at SOLEIL, the maximum angle reaches 0.17 mrad and the horizontal excursion 0.55 µm. A steerer is normally placed at the entrance and exit of the undulator to correct the trajectory of the electron beam.

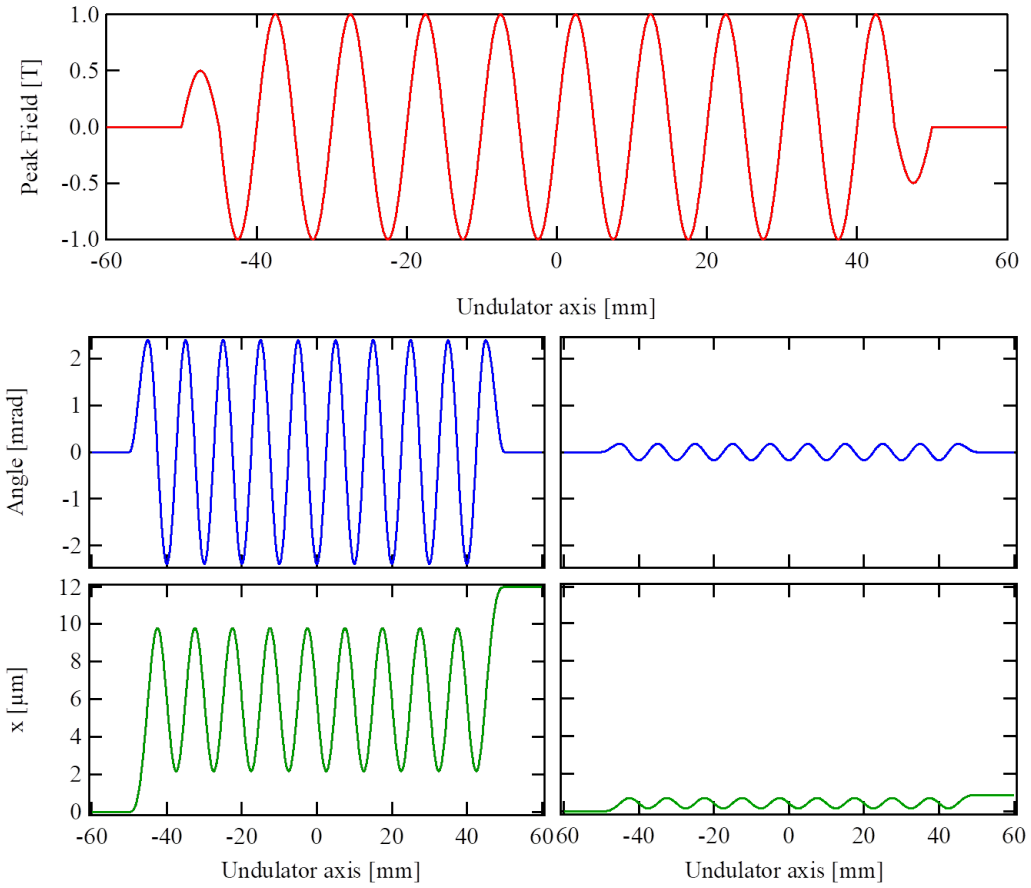

Figure 2.6: (Red) magnetic field of peak 1 T, period 10 mm. (Blue) horizontal angle for COXINEL with energy of 200 MeV (left) and at SOLEIL with energy of 2.75 GeV (right). (Green) horizontal excursion at COXINEL (left) and SOLEIL (right).

2.3 Synchrotron radiation

An electron beam traversing the planar undulator oscillates and emits linearly polarized synchrotron radiation concentrated in narrow energy bands. A relativistic particle of charge e and normalized velocity $\beta = \frac{v}{c}$ emits radiation in the straightforward direction in the shape of a cone with an angle of $1/\gamma$ (FWHM) due to Doppler effect by transforming from the particle frame to the lab frame. One first considers a relativistic electron traversing an arbitrary path as shown in Fig. 2.7. The electron emits a photon at a time t', so-called retarded time, that reaches the observer after a time t that is the observation time.

The observation time is related to the retarded time by:

$$t = t' + \frac{\vec{R}(t')}{c} \tag{2.45}$$

where $\vec{R}(t')$ the distance from the electron to the observer. By derivating Eq. 2.45 with respect to t' and substituting $\frac{d\vec{R}(t')}{dt'} = -c\vec{n}(t').\vec{\beta}(t')$, one gets:

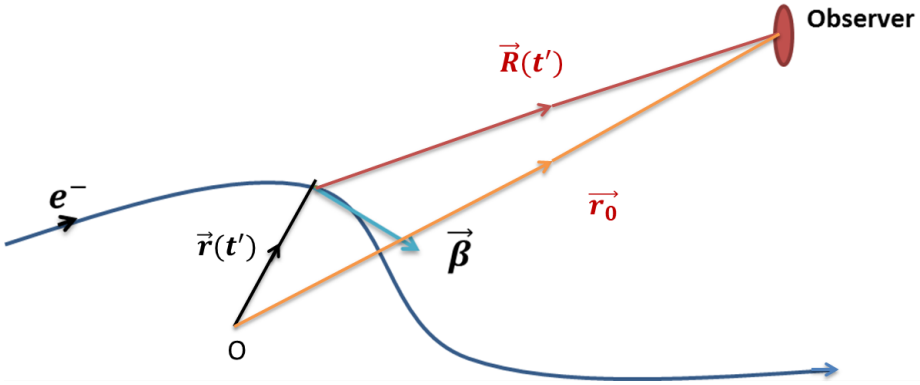

Figure 2.7: Schematic view of the electron orbitting an arbitrary path.

$$\frac{dt}{dt'} = 1 - c\vec{n}(t').\vec{\beta}(t')$$

where $\vec{n}(t') = \vec{R}(t')/R(t')$ is the unit vector pointing towards the observer along $\vec{R}(t')$.

The retarded electric field $\vec{E}(t)$ and magnetic field $\vec{B}(t)$ reaching an observer at a distance D can be derived using the Lienard-Wiechert retarded fields [141]:

$$\begin{cases} \vec{E}(t) = \frac{e}{4\pi\epsilon_0}\left[\frac{\vec{n}-\vec{\beta}}{\gamma^2 D^2(1-\vec{n}.\vec{\beta})^3} + \frac{\vec{n}\times[(\vec{n}-\vec{\beta})\times\dot{\vec{\beta}}]}{cD(1-\vec{n}.\vec{\beta})^3}\right] \\ \vec{B}(t) = \frac{\vec{n}}{c}\times\vec{E}(t) \end{cases}$$

In the electric field expression, the first term represents the near field which can be neglected in most cases considering that the observation window is quite far from the emission source. So the electric field is expressed as:

$$\vec{E}(t) = \frac{e}{4\pi c\epsilon_0}\left[\frac{\vec{n}\times[(\vec{n}-\vec{\beta})\times\dot{\vec{\beta}}]}{D(1-\vec{n}.\vec{\beta})^3}\right]$$

To examine the radiation emitted, it is better to analyze the electric field in the frequency domain. So converting from time to frequency using the Fourier Transformation:

$$\vec{E}(\omega) = \frac{1}{\sqrt{2\pi}}\int_{-\infty}^{+\infty}\vec{E}(t)\exp i\omega t dt$$

Assuming the variation of the distance D with time is constant, which is the case in the far-field approximation, the electric field becomes:

$$\vec{E}(\omega) = \frac{ie\omega}{4\pi\sqrt{2\pi}c\epsilon_0 D}\int_{-\infty}^{+\infty}(\vec{n}\times(\vec{n}\times\vec{\beta}))\exp\left[i\omega(t'+R(t')/c)\right]dt' \tag{2.46}$$

2.4 Undulator radiation

As the electron wiggles inside the undulator, radiation is emitted at each period. Fig. 2.8 presents an illustration where the radiation is emitted with an angle of observation θ. For constructive interference to occur, one should have:

$$\frac{\lambda_u}{\bar{\beta}_s} - \lambda_u\cos\theta = n\lambda \tag{2.47}$$

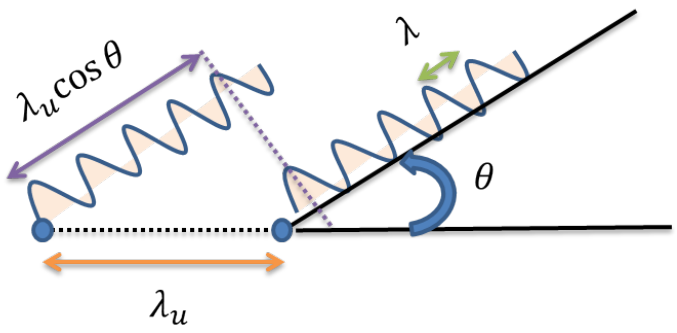

Figure 2.8: Schematic view showing the interference pattern from one undulator period to another.

where n is an integer. Substituting the average longitudinal velocity presented in (2.44) in (2.47) and considering that $\theta << 1$, i.e. $\cos\theta = 1 - \theta^2/2$, one gets:

$$\lambda_u(1 - \frac{1}{2\gamma^2} - \frac{K_u^2}{4\gamma^2})^{-1} - \lambda_u(1 - \theta^2/2) = n\lambda$$

Applying a series expansion, one arrives at the undulator radiation resonance expression:

$$\lambda = \frac{\lambda_u}{2n\gamma^2}\left[1 + \frac{K_u^2}{2} + \gamma^2\theta^2\right] \tag{2.48}$$

where n is the harmonic number. In practical units, the conversion from energy to wavelength is given by $E[eV] = \frac{1240}{\lambda[nm]}$.

2.4.1 Natural linewidth

To determine the bandwidth of the radiation, the constructive interference effect over the length of the undulator L consisting of N_u periods is examined. By multiplying Eq. (2.47) by N_u:

$$N_u n\lambda = \frac{N_u\lambda_u}{\bar{\beta}_s} - N_u\lambda_u\cos\theta \tag{2.49}$$

As for the destructive interference, it occurs at wavelength λ^* when there is a half wavelength advance over the undulator length:

$$N_u n\lambda^* + \frac{\lambda^*}{2} = \frac{N_u\lambda_u}{\bar{\beta}_s} - N_u\lambda_u\cos\theta \tag{2.50}$$

Equating (2.49) and (2.50):

$$N_u n\lambda = N_u n\lambda^* + \frac{\lambda^*}{2}$$

and so:

$$\frac{\lambda - \lambda^*}{\lambda} = \frac{1}{2nN_u + 1}$$

The spectral width, referred to as the homogeneous bandwidth or undulator natural linewidth, can be described as the distance between two dark fringes (destructive interferences), and thus:

$$\left[\frac{\Delta\lambda}{\lambda}\right]_{hom} = 2\frac{\lambda - \lambda^*}{\lambda} = \frac{1}{nN_u + 2}$$

Typically N_u is quite larger than 2, thus:

$$\left[\frac{\Delta\lambda}{\lambda}\right]_{hom} = \frac{1}{nN_u} \tag{2.51}$$

Another way to determine the natural linewidth is by looking at the generated electric field. An electron passing an undulator with N_u periods produces a wavetrain with equal number of oscillations. The electric field of the light wave is written as:

$$E(t) = \begin{cases} E_0 \exp(i\omega_l t) & \text{if } -T/2 < t < T/2 \\ 0 & \text{Otherwise} \end{cases} \tag{2.52}$$

The time duration of the wave train is $T = N_u\lambda/c$. Due to its finite length, this wave train is not monochromatic but spans over a range of frequencies. This range can be determined by applying the Fourier transformation on the electric field:

$$E(\omega) = \frac{1}{\sqrt{2\pi}}\int_{-\infty}^{\infty} E(t)e^{-i\omega t}dt$$

$$E(\omega) = \frac{E_0}{\sqrt{2\pi}}\int_{-T/2}^{T/2} e^{i\Delta\omega t}dt \qquad \text{with } \Delta\omega = \omega_l - \omega$$

Thus:

$$E(\omega) = \frac{2E_0}{\sqrt{2\pi}}\frac{\sin\Delta\omega T/2}{\Delta\omega}$$

The spectral intensity ($I(\omega)$) is proportional to $|E(\omega)|^2$:

$$I(\omega) \propto \left(\frac{\sin x}{x}\right)^2 \tag{2.53}$$

with

$$x = \Delta\omega T/2 = \frac{(\omega_l - \omega)N_u\lambda}{2c} = \pi N_u\frac{\omega_l - \omega}{\omega_l}$$

The spectral resolution or undulator homogeneous bandwidth is expressed as:

$$\frac{\Delta\lambda}{\lambda} = \frac{\Delta\omega}{\omega} = \frac{1}{N_u}$$

that is the same as the one in Eq. (2.51) for $n = 1$. For an undulator with 100 number of periods, the first harmonic natural line width is 1%.

2.4.2 Natural divergence

To examine the natural divergence of the radiation, we introduce θ^* as the angle where destructive interference occur:

$$N_u n\lambda + \frac{\lambda}{2} = \frac{N_u\lambda_u}{\bar{\beta}_s} - N_u\lambda_u\cos\theta^* \tag{2.54}$$

Equating Eq. (2.49) and (2.54), one gets:

$$\lambda = 2N_u\lambda_u(\cos\theta - \cos\theta^*)$$

For very small angles:

$$\theta^{*2} - \theta^2 = \frac{\lambda}{N_u\lambda_u}$$

For the on-axis radiation, where $\theta = 0$:

$$\Delta\theta = \theta^* - \theta = \theta^*$$

and the angle at which the intensity drops to zero is:

$$\Delta\theta = \sqrt{\frac{\lambda}{N_u \lambda_u}} \tag{2.55}$$

The angular width of the radiation, referred to as the natural divergence, can be described as the angular difference between two dark fringes, so that the term in Eq. (2.55) is multplied by 2. And by considering that the distribution in angle is a Gaussian, the rms natural divergence can be expressed as [142]:

$$\sigma'_n \approx \sqrt{\frac{\lambda}{L_u}} \tag{2.56}$$

where L_u is the undulator length. In practical units, the photon beam natural divergence is 220 µrad for a resonant wavelength of 200 nm and an undulator length of 2 m.

2.4.3 Natural beam size

The photon beam emittance ε_n emitted by a single electron is often considered to be equal to the diffraction limit [142]:

$$\varepsilon_n = \sigma'_n \sigma_n = \frac{\lambda}{4\pi} \tag{2.57}$$

Substituting the natural divergence in Eq. (2.57), the natural beam size rms is found to be:

$$\sigma_n = \frac{1}{4\pi}\sqrt{\lambda L_u} \tag{2.58}$$

In practical units, the photon beam natural size is ~140 µm for a resonance wavelength of 200 nm and an undulator length of 2 m.

Other expressions of the natural divergence and beam size can be found in [61, 143–147].

2.4.4 In-homogeneous broadening

The electron beam widens the undulator bandwidth due to the multi-electron contribution (emittance and energy spread) and reduces the radiation intensity.

2.4.4.1 Energy spread

The energy spread σ_γ widens the line symmetrically. By deriving Eq. (2.48) with $\theta = 0$:

$$d\lambda = -\frac{\lambda}{2\gamma^2}(1 + K_u^2/2)\left(\frac{2d\gamma}{\gamma}\right)$$

Thus

$$\left[\frac{\Delta\lambda}{\lambda}\right]_{\sigma_\gamma} = 2\frac{d\gamma}{\gamma} = 2\sigma_\gamma \tag{2.59}$$

For an energy spread of 0.2% rms, the contribution on the bandwidth is ~0.94% close to the natural linewidth of the 100 period undulator case.

2.4.4.2 Divergence

The divergence $\sigma'_{x,z}$ causes a red shift of the resonant wavelength and widens the bandwidth asymmetrically.

$$\lambda = \frac{\lambda_u}{2\gamma^2}(1 + K_u^2/2) + \frac{\lambda_u}{2}\theta^2$$

The deviation of the radiation wavelength with respect to the on-axis ($\theta = 0$):

$$\lambda - \lambda_{res} = \Delta\lambda = \lambda\gamma^2\theta^2/(1 + K_u^2/2)$$

Therefore

$$\left[\frac{\Delta\lambda}{\lambda}\right]_{\sigma'_{x,z}} = \frac{\gamma^2\sigma'^2_{x,z}}{1 + K_u^2/2} \tag{2.60}$$

A 0.2 mrad rms divergence contribution on the bandwidth is ~1.2% for an energy of 200 MeV and K_u of 2, slightly bigger than the natural line width of a 100 period undulator.

2.4.4.3 Vertical beam size

For short period undulators with small gaps, the field variation in the vertical axis broadens the bandwidth especially when the beam vertical size is quite large. For very small deviation in the vertical position, the undulator field can be expressed as:

$$B \propto \cosh(k_u z) \approx 1 + \frac{k_u^2 z^2}{2}$$

Deriving Eq. (2.48) on-axis ($\theta = 0$):

$$\frac{\Delta\lambda}{\lambda} = \frac{K_u^2}{(1 + K_u^2/2)}\frac{dK_u}{K_u}$$

And $\frac{dK_u}{K_u} = \frac{dB}{B} = \frac{k_u^2 y^2}{2}$ and $k_u = \frac{2\pi}{\lambda_u}$, hence:

$$\left[\frac{\Delta\lambda}{\lambda}\right]_{\sigma_z} = \frac{2\pi^2 K_u^2 \sigma_z^2}{\lambda_u^2(1 + K_u^2/2)} \tag{2.61}$$

A vertical beam size of 0.2 mm rms contribution on the bandwidth is ~1.8% for a $K_u = 2$ and $\lambda_u = 18$ mm.

2.4.5 Harmonics

The radiation emitted by an individual electron adds up from one period to another resulting in harmonics. In the on-axis direction where $\theta = 0$, only odd harmonics are observed. For $|\theta| > 0$, even harmonics are present but with a low intensity compared to the odd ones. To better understand the harmonics behaviour, one considers the angle of the electron and the electric field generated for three cases as illustrated in Fig. 2.9:

- For $K_u < 1$: the electrons maximum excursion angle is within the emitted synchrotron radiation cone $\sim 1/\gamma$, so all of the emitted radiation is seen by the observer and is thus a continuous sinusoidal electric field (see Fig. 2.9-a). Using Fourier transformation, the electric field in time domain is converted into a frequency domain and then it is clear that the pure sinusoidal field is simply a single, odd, ($n = 1$) harmonic.

- For $K_u > 1$, the angle excursion is larger than the cone angle and the observer only sees the electric field briefly as the electron wiggles through this radiation emission angle. The electric field peaks are equally spaced in time but of alternating polarity (see Fig. 2.9-b) thus the spectrum only contains odd harmonics.

- If one now considers the case where the observer is viewing the radiation from off-axis, he still sees only the electric field when the electron is within the cone angle of his observation angle, however since he is no longer on-axis, the electric field alternating pulses are not equally spaced in time with an asymmetry in the amplitude (see Fig. 2.9-c). Hence even harmonics start to be visible on the spectrum.

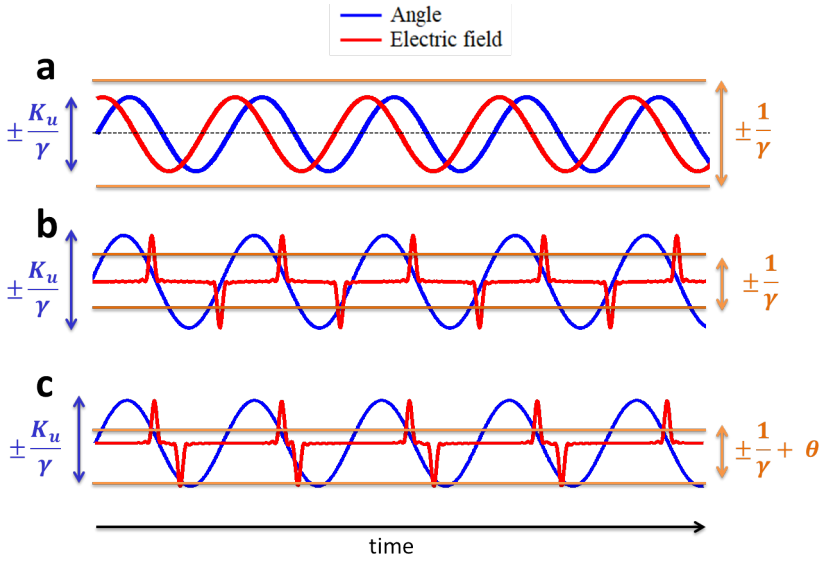

Figure 2.9: Schematic view of the electron angle (blue) and the electric field produced (Red). (a) K_u <1, (b) $K_u > 1$, (c) observation off-axis.

2.4.6 Angular spectral flux

The spectral angular flux distribution $\frac{d^2W}{d\Omega d\omega}$ radiated by one electron can be expressed as:

$$\frac{d^2W}{d\Omega d\omega} = 2\epsilon_0 c D^2 |E(\omega)|^2 \tag{2.62}$$

where ϵ_0 is the permittivity in vacuum. Substituting Eqs. (2.46)-(2.42) in Eq. (2.62) and after several mathematical steps and simplifying assumptions (details can be found in [148]) one arrives at:

$$\frac{d^2W}{d\Omega d\omega} \propto L_{\Delta\omega}$$

where

$$L_{\Delta\omega} = \frac{\sin^2(N_u \pi \Delta\omega/\omega)}{N_u^2 \sin^2(\pi\Delta\omega/\omega)}$$

the so-called lineshape function containing the radiation interference term and is plotted in Fig. 2.10. For $N > 10$, the function is independent of the number of periods and has a spectral width at the n^{th} harmonic :

$$\frac{\Delta\omega}{\omega} = \frac{1}{n\mathrm{N}_u}$$

which is in agreement with the natural linewidth expression presented in the previous section (see Eq. 2.51).

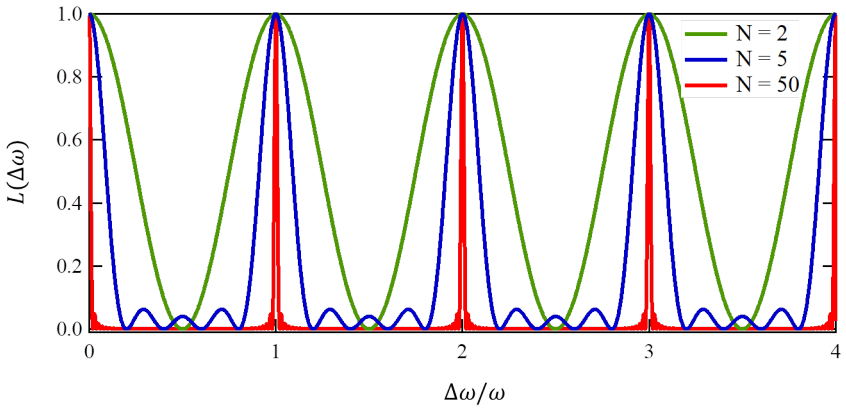

Figure 2.10: Lineshape function versus wavelength for different number of periods.

The spectral flux on-axis is expressed as:

$$\frac{d^2\mathrm{W}}{d\Omega d\omega} = \frac{e^2\mathrm{N}_u^2\gamma^2}{4\pi c\epsilon_0}\mathrm{L}_{\Delta\omega}\mathrm{F}_n(\mathrm{K}_u) \tag{2.63}$$

where

$$\mathrm{F}_n(\mathrm{K}_u) = \frac{n^2\mathrm{K}_u^2}{(1+\mathrm{K}_u^2/2)^2}\left|\mathrm{J}_{(n+1)/2}(\mathrm{Y}) - \mathrm{J}_{(n-1)/2}(\mathrm{Y})\right|^2 \tag{2.64}$$

J the Bessel function and

$$\mathrm{Y} = \frac{n\mathrm{K}_u^2}{4(1+\mathrm{K}_u^2/2)} \tag{2.65}$$

Eq. (2.64) is plotted in Fig. 2.11. The first harmonic is peaked at $\mathrm{K}_u \approx 1$ and drops for larger K_u values, whereas higher harmonics acquire more flux as shown in Fig. 2.12.

The electric field becomes sharper for larger K_u resulting in higher harmonics. In the case where K_u is very large, the number of harmonics is expanded so that the narrow sharp lines start to diminish and combine. This effect results in an overall shape of a continuous spectrum as typically observed with a dipole or a wiggler [148].

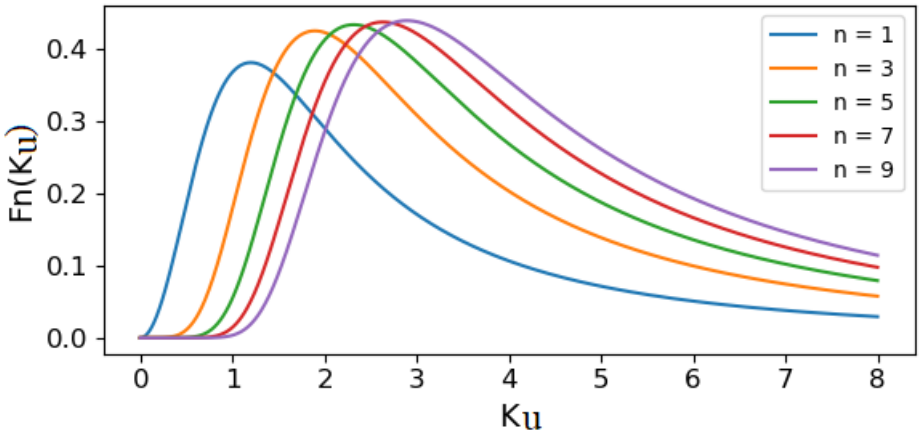

Figure 2.11: Lineshape function versus wavelength for different number of periods.

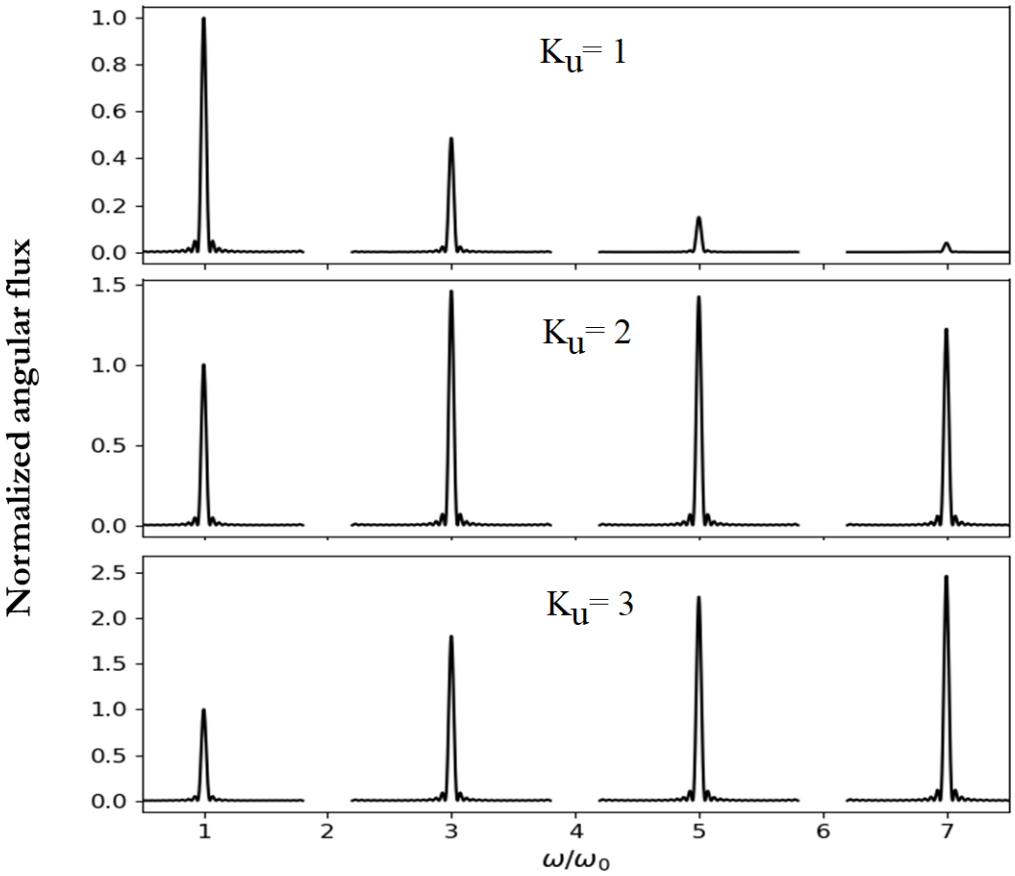

Figure 2.12: Nomalized angular flux to the intensity of the 1^{st} harmonic for different K values.

The energy emitted per electron can be converted into on-axis angular power density P by multiplying the flux density with the number of electrons per second:

$$\frac{d^2\mathrm{P}}{d\Omega d\omega} = \frac{e^2 \mathrm{N}_u^2 \gamma^2}{4\pi c \epsilon_0} \frac{\mathrm{I}_b}{e} \mathrm{L}_{\Delta\omega} \mathrm{F}_n(\mathrm{K}) \tag{2.66}$$

where I is the electron beam.

The angular power density divided by the photon energy ($h\omega/2\pi$) and integrating over all the frequencies, one gets the on-axis angular flux density expressed in pratical units as:

$$\frac{d\dot{N}}{d\Omega}[\text{ph/s/mrad}^2/0.1\%\text{BW}] = 1.74 \times 10^{14} N_u^2 E^2 [GeV] I_b [A] F_n(K) \tag{2.67}$$

where BW stands for bandwidth. The angular flux density is $\sim 4 \times 10^{19}$ ph/s/mrad^2/0.1% bandwidth with an electron beam current of 100 A and an energy of 200 MeV with an undulator of 100 periods and strength $K_u = 2$.

Integrating Eq. (2.67) over all the angles, the number of photons per second per 0.1% BW ($\dot{N}$) can be expressed as:

$$\dot{N}[ph/s/0.1\%\text{BW}] = 1.43 \times 10^{14} N_u I_b [A] Q_n(K) \tag{2.68}$$

where

$$Q_n(K) = \frac{1 + K^2/2}{n} F_n(K) \tag{2.69}$$

and is plotted in Fig. 2.13.

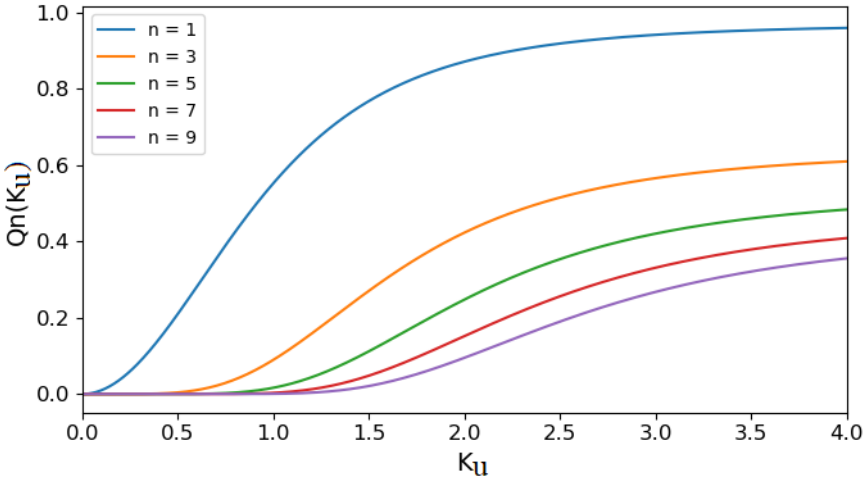

Figure 2.13: $Q_n(K_u)$ versus K from Eq. (2.69).

2.5 Free Electron Laser Concept

Relativistic electrons in an undulator act as a gain medium in the free electron laser. Previously, the magnetic field of a planar undulator and the radiation emitted as a beam of electrons traverse it were presented. In this section, a helical undulator is used to simplify the FEL calculations, where the field is exerted in both transverse planes and equal in magnitude.

2.5.1 Electron Motion in the presence of a ponderomotive force

A ponderomotive force is a nonlinear force that is applied to a charged particle, where it experiences an inhomogeneous oscillating electromagnetic field. The mechanism of the ponderomotive force can be understood by considering the motion of a charge in an oscillating electric field. In the case of a homogeneous field, the charged particle returns to its initial position after one cycle of oscillation. In the case of an asymmetric field, the force exerted on the charged particle, during the half-cycle it spends in the area with higher field amplitude, points in the direction where the

field is weaker. This force is larger than the one exerted during the half-cycle spent in the area with a lower field amplitude, which points towards the strong field area. Thus, averaged over a full cycle there is a net force that drives the charge towards the weak field area.

Starting with the relativistic equation of motion ($\vec{P} = \gamma m \vec{v}$) undergoing a Lorentz force:

$$m\Big[\frac{\partial \gamma \vec{v}}{\partial t} + \vec{v}.\nabla(\gamma \vec{v})\Big] = -e\vec{E} - e\vec{v} \times \vec{B} \tag{2.70}$$

In the case of a drift space, i.e. no electric or magnetic field, the electron velocity is not affected and continues its path along the axis which it was originally orbitting $\vec{v} = v_0 \hat{s}$.

Let us now consider a helical undulator magnetic field that can be expressed as:

$$\vec{B}_u = A_u(\hat{x} + i\hat{z}) \exp(i k_u s)$$

where $\hat{x}$ and $\hat{z}$ are the direction along the horizontal and vertical direction, respectively, and A_u is the amplitude of the undulator field. The velocity can be written as $\vec{v} = v_0\hat{s} + \vec{v_u}$, where $\vec{v_u}$ is the velocity induced by the undulator magnetic field B_u. Substituting $\vec{v}$ in Eq. (2.70) and assuming that v_0 and γ are constant:

$$m\gamma\Big[\frac{\partial \vec{v_u}}{\partial t} + (\vec{v_u} + v_0\hat{s}).\nabla(\vec{v_u})\Big] = -e(\vec{v_u} + v_0\hat{s}) \times \vec{B_u}$$

The product of two perturbed quantities are neglible, so the equation becomes:

$$m\gamma_0\Big[\frac{\partial \vec{v_u}}{\partial t} + v_0.\frac{\partial \vec{v_u}}{\partial s}\Big] = -e v_0 \hat{s} \times \vec{B_u}$$

v_u has the same dependence as B_u. So v_u can be expressed as:

$$v_u = \vec{a_u} \exp(i k_u s)$$

where $\vec{a_u}$ is the amplitude of the motion and its direction. The equation now becomes:

$$m\gamma v_0 i k_u \vec{v_u} = i e v_0 \vec{B_u}$$

so:

$$\vec{v_u} = \frac{e\vec{B_u}}{m\gamma k_u}$$

In the case of a helical undulator, the polarization of the radiation emitted is elliptical. The electric field $\vec{E_L}$ and magnetic field $\vec{B_L}$ can be expressed as:

$$\begin{cases} \vec{E_L} = A_L(\hat{x} - i\hat{z}) \exp(iks - i\omega t) \\ \nabla \times \vec{E_L} = -\frac{\partial \vec{B}}{\partial t} \end{cases} \tag{2.71}$$

where A_L is the radiation amplitude, k the wavenumber and ω the frequency. By taking $\nabla = i\vec{k}$ and $\frac{\partial}{\partial t}$ = -iω, the magnetic field becomes:

$$\vec{B_L} = \frac{ik}{\omega}\vec{E_L}$$

The velocity takes the form $\vec{v} = v_o\hat{s} + \vec{v_L}$. Substituting it in Eq. (2.70) and considering γ constant, one gets:

$$m\gamma\Big[\frac{\partial \vec{v_L}}{\partial t} + v_0.\frac{\partial \vec{v_L}}{\partial s}\Big] = -e\vec{E_L} - e v_0 \hat{s} \times \vec{B_L} \tag{2.72}$$

Solving Eq. (2.72), one gets:

$$-im\gamma\omega\vec{v}_L + im\gamma k v_0 \vec{v}_L = -e\mathrm{E}_L - e v_0 ik/\omega \hat{s}\times\vec{\mathrm{E}}_L$$

Finally:

$$\vec{v}_L = \frac{e\vec{\mathrm{E}}_L}{im\gamma\omega}$$

A linear reponse of the electron in the presence of an undulator field and an electromagnetic wave has been found independently. Now the effect when both fields are present is examined. The ponderomotive force $\mathrm{F_P}$ induced on an electron along the longitudinal direction is expressed as:

$$\mathrm{F_P} = -e\left[\vec{v}_u \times \vec{\mathrm{B}}_L - e\vec{v}_L \times \vec{\mathrm{B}}_u\right].\hat{s} \tag{2.73}$$

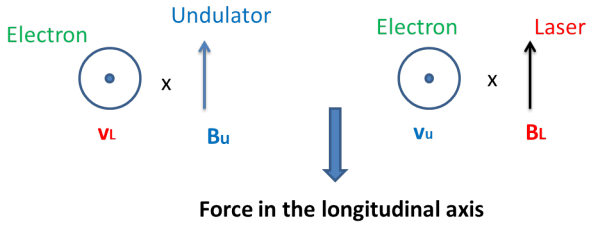

Figure 2.14: Sheme representing Eq. (2.73), where the velocity of the electron induced by one field interacts with the other field leading to a net force in the s axis.

The following equation physically represents that when the electron interacts with one of the fields, it acquires a velocity in the transverse plane. This velocity alongside the interaction with the other field yields a force in the longitudinal axis. In Eq. (2.73), the first term on the right side is the dominant one:

$$\frac{\vec{v}_u \times \vec{\mathrm{B}}_L}{\vec{v}_L \times \vec{\mathrm{B}}_u} = \frac{k}{k_u} = \frac{\lambda_u}{\lambda} >> 1$$

so by neglecting the second term, the real part of the ponderomotive force can be expressed as:

$$\vec{\mathrm{F}}_\mathrm{P} = \mathrm{A_P}\cos(\psi)\hat{s} \tag{2.74}$$

where

$$\begin{cases} \mathrm{A_P} = -\frac{2e^2 k \mathrm{A_L} \mathrm{A}_u}{m\omega\gamma k_u} \\ \psi = \omega t - (k + k_u)s \end{cases} \tag{2.75}$$

$\mathrm{A_P}$ and ψ are the ponderomotive force amplitude and phase, respectively. The phase velocity v_p of the ponderomotive force is:

$$v_p = \frac{\omega}{k + k_u}$$

The electrons interact with the wave by exchanging energies. For an efficient energy transfer between the electron and the wave over the entire undulator length, the ponderomotive phase should be constant. By deriving the phase expression in Eq. (2.75) with respect to time:

$$\frac{d\psi}{dt} = \omega - (k + k_u)\frac{ds}{dt} = 0 \tag{2.76}$$

Taking $ds/dt = c\bar{\beta}_s$ and $\omega = ck_u$, Eq. (2.76) becomes:

$$ck - c(k+k_u)\left(1 - \frac{1}{2\gamma^2} - \frac{K_u^2}{2\gamma^2}\right) = 0 \tag{2.77}$$

Note that in an helical undulator the normalized velocity takes the following expression:

$$\bar{\beta}_s = 1 - \frac{1}{2\gamma^2} - \frac{K_u^2}{2\gamma^2} \tag{2.78}$$

Replacing k and k_u by $2\pi/\lambda$ and $2\pi/\lambda_u$, respectively, Eq. (2.77) becomes:

$$\frac{2\pi}{\lambda}\left[\frac{1}{2\gamma^2} + \frac{K_u^2}{2\gamma^2}\right] = \frac{2\pi}{\lambda_u}\left[1 - \frac{1}{2\gamma^2} - \frac{K_u^2}{2\gamma^2}\right]$$

and taking $1 - \frac{1}{2\gamma^2} - \frac{K_u^2}{2\gamma^2} \approx 1$, the final resonant condition is:

$$\lambda = \frac{\lambda_u}{2\gamma^2}\left(1 + K_u^2\right)$$

which is the undulator radiation resonant wavelength on-axis for a helical undulator.

2.5.2 Low gain

The amplitude of the ponderomotive force (A_P) is proportional to the amplitude of the optical wave (A_L). The wave amplitude evolves as the pulse travels, so one has to be careful in examining the energy gained by the laser that retards the particles and increase in magnitude. For simplicity, we consider that the amplitude of the force is constant for a small distance L_s along the longitudinal direction. The ponderomotive force oscillates as shown in Fig. 2.15. In the accelerating zone, electrons experience a forward force and quickly move towards the decelerating zone, where electrons are slowed down and delayed by the negative force. Hence, due to this delay, more electrons cross from the accelerating zones to the decelerating ones leading to an accumulation of electrons and a net bunching of the beam.

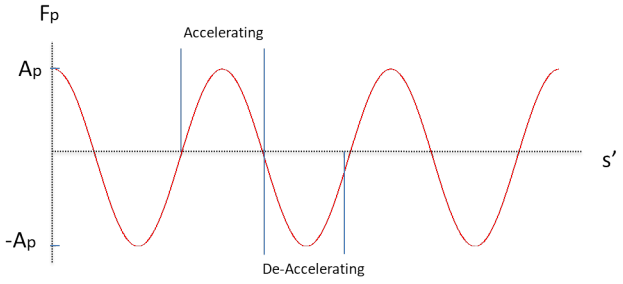

Figure 2.15: Pondermotive force along s' = $\omega t - (k + k_u)s$.

The energy transfer between an electron and the FEL radiation is examined. Starting with the derivation of the electron energy $E = \gamma mc^2$ with respect to time, one gets:

$$mc^2 \frac{d\gamma}{dt} = -e\vec{E}.\vec{v} \tag{2.79}$$

And by substituting $\vec{v} = v_0\hat{s} + \vec{v_u} + \vec{v_L}$ in Eq. (2.79) where $\vec{E}.\vec{v_u}$ is the dominant term, one gets:

$$mc^2 \frac{d\gamma}{dt} = -e\vec{E}.\vec{v_u}$$

Here we are interested in the evolution of the energy along the longitudinal axis, so replacing $\frac{d}{dt}$ by $v_0\frac{d}{ds}$, the equation becomes:

$$\frac{d\gamma}{ds} = -\frac{e}{v_0 mc^2}(\vec{E}_L.\vec{v}_u) = -\alpha\cos(\psi) \tag{2.80}$$

where

$$\alpha = \frac{2e^2 A_u A_L}{m^2c^2 v_0 \gamma_0 k_u} \tag{2.81}$$

γ decreases along s when $\cos(\psi)$ is positive implying that the FEL wave is gaining energy. Hence, the amplification highly depends on the evolution of the ponderomotive phase along s:

$$\frac{d\psi}{ds} = (k + k_u) - \omega/v_s \tag{2.82}$$

Introducing γ_r as the electron resonant energy that has the same velocity as the ponderomotive phase (v_p):

$$\gamma_r = \left[1 - \frac{\omega^2}{k_p^2 c^2}\right]^{-1/2}$$

where $k_p = k_u + k$, Eq. (2.82) becomes:

$$\frac{d\psi}{ds} = k_p(1 - \frac{\omega}{v_s k_p}) \tag{2.83}$$

By using the following approximations:

$$\begin{cases} v_s/c = \sqrt{1 - 1/\gamma^2} \approx 1 - 1/2\gamma^2 \\ \omega/k_p c = \sqrt{1 - 1/\gamma_r^2} \approx 1 - 1/2\gamma_r^2 \end{cases}$$

and introducing the energy detuning $\eta = \frac{\gamma - \gamma_r}{\gamma_r}$, Eq. (2.83) becomes:

$$\frac{d\psi}{ds} = \frac{k_p \eta}{\gamma_r^2} \tag{2.84}$$

Introducing the normalized quantities:

$$\begin{cases} \zeta = s/L_s \\ A_\alpha = L_s^2 \alpha k_p/\gamma_r^2 \\ A_\gamma = L_s k_p \eta/\gamma_r^2 \end{cases} \tag{2.85}$$

Eqs. (2.80) and (2.84) become:

$$\begin{cases} \frac{dA_\gamma}{d\zeta} = -A_\alpha \cos\psi \\ \frac{d\psi}{d\zeta} = A_\gamma \end{cases} \tag{2.86}$$

Equating the differential equations in (2.86), one arrives at the famous FEL pendulum equation:

$$\frac{d^2\psi}{d\zeta^2} + A_\alpha \cos\psi = 0 \tag{2.87}$$

Solving Eq. (2.86):

$$\frac{dA_\gamma}{d\zeta} = \frac{dA_\gamma}{d\psi}\frac{d\psi}{d\zeta} = -A_\alpha \cos\psi \tag{2.88}$$

By integrating Eq. (2.88), one gets:

$$\frac{A_\gamma^2}{2} = -A_\alpha \sin\psi + \mathbf{cst} \tag{2.89}$$

Consider at the entrance of the undulator the initial electron energy $A_{\gamma 0}$ and the initial ponderomotive phase $\psi = \psi_0$. So:

$$\mathbf{cst} = \frac{A_{\gamma 0}^2}{2} + A_\alpha \sin\psi_0 \qquad \Longrightarrow \qquad A_{\gamma 0} = \sqrt{2\left(\mathbf{cst} - A_\alpha \sin(\psi_0)\right)}$$

For:

- **cst** $> A_\alpha$: All values of ψ are permitted and in this case electrons are not trapped and do not interact with the FEL wave (passing electrons).
- **cst** $< A_\alpha$: Not all values of ψ are permitted meaning the electrons can not see the different phases of the wave, and these electrons are called trapped.
- **cst** $= A_\alpha$: $A_\gamma^2 = 2A_\alpha(1-\sin\psi)$ boundary between trapped and untrapped electrons, so-called separatrix.

Fig. 2.16 presents the ponderomotive phase. Some of the electrons with the proper phase are trapped within the ponderomotive potential well and exchange energy with the FEL wave.

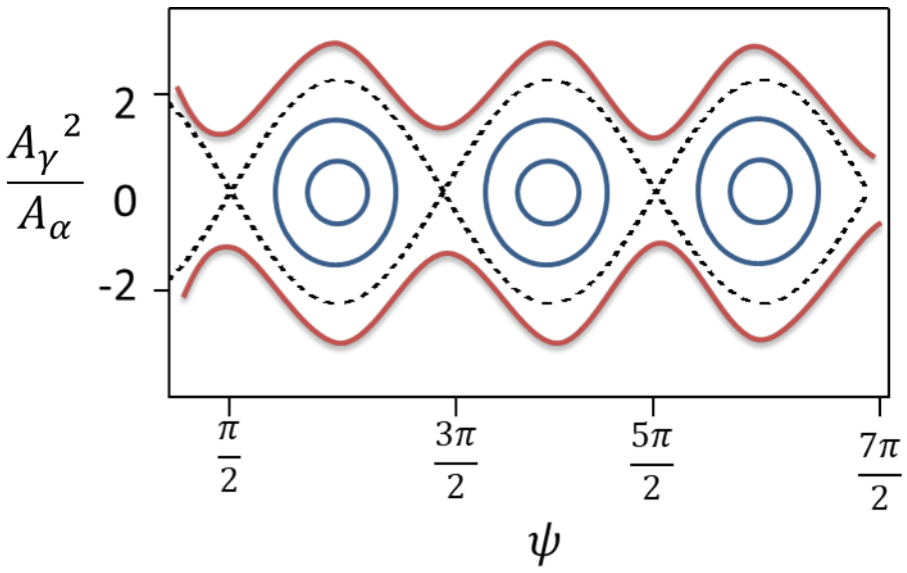

Figure 2.16: Scheme representing a phase space curves of a mathematical pendulum. (Black dashed) potential well of the ponderomotive force, (blue) trapped electrons, (red) non-trapped electrons or passing electrons.

Substituting **cst** in Eq. (2.89):

$$A_\gamma^2 = A_{\gamma_0}^2 - 2A_\alpha(\sin\psi - \sin\psi_0) \tag{2.90}$$

In the case of a weak laser field ($A_{\gamma_0} >> 2A_\alpha$), which is valid in the low gain regime, one can expand Eq. (2.90) up to the second order $\sqrt{1+x} = 1 + x/2 - x^2/8...$:

$$A_\gamma = A_{\gamma_0} - \frac{A_\alpha}{A_{\gamma 0}}(\sin\psi - \sin\psi_0) + \frac{A_\alpha^2}{2A_{\gamma 0}^3}(\sin\psi - \sin\psi_0)^2 \tag{2.91}$$

Eq. (2.91) is solved iteratively.

To the **zero order**:

$$A_\gamma^{(0)} = A_{\gamma 0}$$

and

$$\psi^{(0)} = \int A_\gamma^{(0)} d\zeta = \psi_0 + A_{\gamma 0}\zeta$$

To the **first order**, $\psi = \psi^{(0)}$ is substituted in Eq. (2.91):

$$A_\gamma^{(1)} = A_{\gamma_0} - \frac{A_\alpha}{A_{\gamma 0}}(\sin\psi^{(0)} - \sin\psi_0)$$

so:

$$\frac{d\psi}{d\zeta} = A_{\gamma_0} - \frac{A_\alpha}{A_{\gamma 0}}(\sin\psi^{(0)} - \sin\psi_0)$$

Taking $\psi = \psi^{(0)} + \psi^{(1)}$:

$$\psi^{(1)} = \frac{A_\alpha}{A_{\gamma 0}^2}\left(\cos\psi^{(0)} - \cos\psi_0 + \zeta A_{\gamma 0}\sin\psi_0\right)$$

To the **second order**, solving

$$A_\gamma = A_{\gamma_0} - \frac{A_\alpha}{A_{\gamma 0}}(\sin\psi^{(1)} - \sin\psi_0) + \frac{A_\alpha^2}{2A_{\gamma 0}^3}(\sin\psi^{(1)} - \sin\psi_0)^2$$

and taking

$$A_\gamma = A_\gamma^{(0)} + A_\gamma^{(1)} + A_\gamma^{(2)}$$

After some calculations, one gets:

$$A_\gamma^{(2)} = -\frac{A_\alpha^2}{2A_{\gamma 0}^3}(\sin\psi^{(0)} - \sin\psi_0)^2 - \frac{A_\alpha}{A_{\gamma 0}}\cos\psi^{(0)}.\psi^{(1)}$$

The normalized energy gain W of the radiation from a single electron after propagating a distance $z = L_s$ ($\zeta = 1$) is determined by integrating the energy loss of the electron over all the phases:

$$W = \frac{1}{2\pi}\int_0^{2\pi}(A_{\gamma 0} - A_\gamma|_{\zeta=1})d\psi_0 = -\frac{1}{2\pi}\int_0^{2\pi} A_\gamma^{(2)} d\psi_0 \tag{2.92}$$

Solving Eq. (2.92), one gets:

$$W = \frac{A_\alpha^2}{A_{\gamma 0}^3}\left[2\sin^2\frac{A_{\gamma 0}^2}{2} - A_{\gamma 0}\sin\frac{A_{\gamma 0}}{2}\cos\frac{A_{\gamma 0}}{2}\right]$$

By taking $x = \frac{A_{\gamma 0}}{2}$, one arrives to Madey's theorem [69] representing the FEL low gain:

$$W = \frac{A_\alpha}{8}G(x) \qquad \text{where} \qquad G(x) = -\frac{d}{dx}\left(\frac{\sin^2 x}{x^2}\right) \tag{2.93}$$

The function G(x) is plotted in Fig. 2.17, where the gain is positive when x is positive and peaked at 0.5 for $x \approx 1.3$. Thus, the electron beam should have an energy slightly above the resonance to achieve a gain. This regime is known as Madey's regime [69].

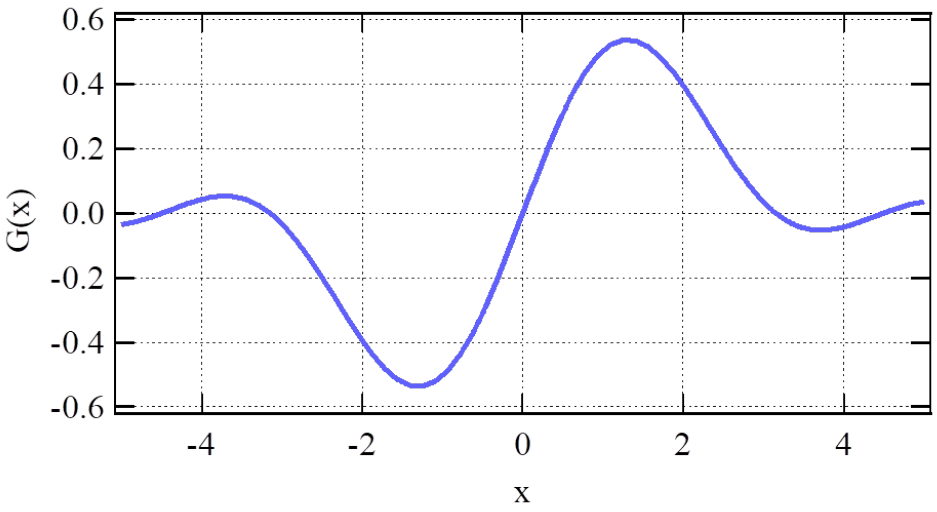

Figure 2.17: G(x) plot: The small gain function for an FEL amplifier.

The gain highly depends on the undulator and optical wave amplitudes (recall that $A_\alpha \propto A_u A_L$), and most importantly on the initial electron energy γ_0. One should always have electrons moving faster than the ponderomotive phase so that the energy gain is positive. In reality, the radiation grows at the expense of the electron beam energy, and the amplitude increases along the longitudinal axis. In the presented analytical approach, the variation of the amplitude is not taken into account.

A more traditional approach is done to derive the FEL pendulum equation in the case of a planar undulator. The electric field of the spontaneous emission (or a seed) co-propagating with the electron beam along the undulator axis can be expressed as:

$$E_x(z,t) = E_0 \cos(kz - \omega t + \phi_0)$$

The electron energy changes due to the interaction with the wave. So the energy change:

$$dW = \vec{v}.\vec{F}dt = -ev_x(t)E_x(t)dt$$

Using the horizontal velocity from the previous part, the energy transfer becomes:

$$\frac{dW}{dt} = -\frac{ecK_uE_0}{\gamma}\sin(k_u s)\cos(ks - \omega t + \phi_0)$$

By using the trigonometric relation $\sin a \cos b = \frac{1}{2}\left[\sin(a+b) + \sin(a-b)\right]$:

$$\frac{dW}{dt} = -\frac{ecK_uE_0}{2\gamma}(\sin\Psi^+ - \sin\Psi^-)$$

with:

$$\begin{cases} \Psi^+ = (k+k_u)s - \omega t + \phi_0 \\ \Psi^- = (k-k_u)s - \omega t + \phi_0 \end{cases}$$

For an efficient interaction between the electron beam and the radiation along the undulator,

the phases (Ψ^+ and Ψ^-) should be constant with time:

$$\frac{d\Psi}{dt} = 0 \Leftrightarrow [k \pm k_u]\frac{ds}{dt} - \omega = 0$$

Replacing $\frac{ds}{dt}$ with the expression of $c\bar{\beta}_s = c(1 - 1/2\gamma^2 - K_u^2/4\gamma^2)$:

$$c(k \pm k_u)(1 - \frac{1}{2\gamma^2} - \frac{K_u^2}{4\gamma^2}) - \omega = 0$$

so

$$ck(-\frac{1}{2\gamma^2} - \frac{K_u^2}{4\gamma^2}) \pm ck_u \approx 0$$

The resonant wavelength is determined:

$$\lambda = \frac{\lambda_u}{2\gamma^2}(1 + \frac{K_u^2}{2})$$

The Ψ^- is removed since we consider that the laser propagates in one direction along the electron path. For Ψ^+ to be constant, the electron should lag behind the radiation field one λ per period. The condition for resonant energy transfer all along the undulator therefore yields exactly the same light wavelength as is observed in undulator radiation emitted with a zero angle. This entitles the spontaneous emission to serve as a seed laser.

Consider a resonant energy γ_r such that electrons with the corresponding energy emit light at the wavelength of the laser seed (or resonance). The ponderomotive phase oscillates every half a period and on an average, half the electrons lose energy to the wave and the other half gain energy from it. This results in a zero net gain. To achieve a gain, electrons should have a slightly higher energy than γ_r. Introducing a relative energy deviation:

$$\eta = \frac{\gamma - \gamma_r}{\gamma_r}$$

The ponderomotive phase variation with time is no longer equal to zero for $\gamma > \gamma_r$:

$$\frac{d\Psi}{dt} = k_u c - kc\frac{1 + K_u^2/2}{2\gamma^2}$$

Replacing

$$k_u c = \frac{2\pi c}{\lambda_u} = \frac{ck(1 + K_u^2/2)}{2\gamma_r^2}$$

in the previous expression, and taking $\gamma_r + \gamma = 2\gamma_r$, $\gamma^2\gamma_r^2 = \gamma_r^4$, the ponderomotive phase variation with time becomes:

$$\frac{d\Psi}{dt} = ck(1 + K_u^2/2)\frac{\eta}{\gamma_r^2} = 2k_u c\eta \tag{2.94}$$

The energy transfer can be written as:

$$\frac{dW}{dt} = \frac{d\eta}{dt}\gamma mc^2 \Longleftrightarrow \frac{d\eta}{dt} = -\frac{eE_0K_u}{2mc\gamma^2}\sin\Psi \tag{2.95}$$

Combining Eqs. (2.94) and (2.95), the "Pendulum Equation" is determined:

$$\frac{d^2\Psi}{dt^2} + \Omega^2\sin\Psi = 0 \qquad \text{with} \qquad \Omega = \frac{eE_0k_uK_u}{m\gamma_r^2} \tag{2.96}$$

For a small value of Ω, i.e. small oscillations, the equation describes a simple harmonic oscil-

lator, where the electron is trapped and is interacting with the FEL wave. For a large value of Ω, the electron has an unbounded motion and is not trapped within the ponderomotive potential well. In the case of $\gamma = \gamma_r$, the net energy transfer is zero since electrons gaining energy are equal to the ones losing energy. For γ slightly greater than γ_r, there is a net energy transfer from the electron beam to the FEL wave.

2.5.3 High Gain FEL

The high gain FEL [97, 149–151] is based on a bright electron beam emitting radiation coherently, where the intensity is proportional to the number of electrons squared. This is possible when the beam length is shorter than the operating FEL wavelength, but the concentration of some billions of electrons into a tiny volume is not feasible at all, especially in the case of short wavelengths. To make this gain possible, instead of concentrating this large number of electrons, a temporal coherence can still do the job of achieving coherent emission. Micro-bunching, which is the main feature of the FEL, is based on the following principle: electrons in the accelerating phase of the ponderomotive force rapidly escape this region, while electrons that are in the decelerating phase traverse a sinusoidal trajectory with larger amplitude and are delayed. Thus, this process that starts with longitudinal velocity (or energy) modulation results in a density modulation, where the electrons are micro-bunched in slices separated with a distance equal to the FEL wavelength (see Fig. 2.18). In addition, the radiation emitted within a micro-bunch is coherent resulting in a stronger radiation field that furthermore enhances the micro-bunching process. A positive feedback known as "collective instability" is achieved leading to an exponential growth of the FEL radiation power.

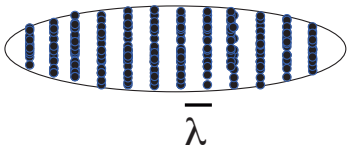

Figure 2.18: Schematic representation of the slices of length λ along a bunched electron beam.

2.5.3.1 Evolution of the light wave in the high gain regime

The FEL cubic equation

In the case of a rather small periodic density modulation, a normalized particle distribution function, obeying the Vlasov equation, is defined. After mathematical manipulation [97, 102], one can show that the radiation amplitude E_x satisfies

$$\frac{\dddot{E}_x}{\Gamma^3} + 2i\frac{\eta}{\rho_{FEL}}\frac{\ddot{E}_x}{\Gamma^2} + \left[\frac{k_p^2}{\Gamma^2} - \frac{\eta^2}{\rho_{FEL}^2}\right]\frac{\dot{E}_x}{\Gamma} - iE_x = 0 \tag{2.97}$$

where ρ_{FEL} is the so-called Pierce parameter, or FEL parameter. It depends on the electron beam density and energy and on the undulator characteristics (deflection parameter, Bessel function term, undulator wavenumber):

$$\rho_{FEL} = \left[\frac{e^2 K_u^2 [JJ]^2 n_e}{32\epsilon_0 \gamma^3 mc^2 k_u^2}\right]^{1/3} \tag{2.98}$$

Γ the gain parameter expressed as:

$$\Gamma = 2k_u\rho_{FEL}, \tag{2.99}$$

and k_p the space charge parameter given by $k_\mathrm{p} = \frac{\omega_\mathrm{p}}{c\gamma}\sqrt{\frac{2\lambda}{\lambda_\mathrm{u}}}$ with ω_p the plasma pulsation $\omega_\mathrm{p} = \sqrt{\frac{4\pi e^2 n_\mathrm{e}}{m}}$, μ_o the permeability in vacuum and n_e the electron density. In the specific case of $\eta = 0$ (on resonance) and for $k_\mathrm{p} = 0$, i.e. for negligible space charge, the cubic equation takes its simplest form, as

$$\frac{\dddot{\mathrm{E}}_x}{\Gamma^3} - \Gamma^3 \mathrm{i}\mathrm{E}_x = 0. \tag{2.100}$$

Considering the electric field expressed as $\approx \mathrm{e}^{(\mathrm{i}\kappa s)}$, it becomes $\kappa^3 = \mathrm{i}\Gamma^3$ with three solutions:

$$\kappa_1 = -\mathrm{i}\Gamma, \quad \kappa_2 = (\mathrm{i} + \sqrt{3})\Gamma/2, \quad \kappa_3 = (\mathrm{i} - \sqrt{3})\Gamma/2.$$

κ_2 leads to an exponential growth of the electric field.

FEL power growth and evolution of the light wave

The power grows as:

$$\mathrm{E}_x(s) = \mathrm{E}_{x0}\exp(s/\mathrm{L}_g), \quad \mathrm{L}_g = \frac{1}{\sqrt{3}\Gamma} = \frac{1}{\sqrt{3}}\Big(\frac{4m\gamma^3}{\mu_\mathrm{o}\mathrm{e}^2\mathrm{K}_\mathrm{u}^2[\mathrm{JJ}]^2 k_\mathrm{u} n_\mathrm{e}}\Big)^{1/3}. \tag{2.101}$$

The bunching factor evolves similarly. It is noticeable that there is amplification at resonance that differs from the small signal gain case. At the beginning of the undulator, the three terms of the cubic equation contribute to the change in the field intensity where the exponential growth is not dominant. This regime is called the 'lethargy'. Solving the cubic equation for a non-zero detuning ($\eta \neq 0$) provides the dependence of the imaginary solution with detuning, i.e. the gain bandwidth. It attains a maximum for $\eta = 0$ and decreases for $\eta \neq 0$. From the analysis of the behaviour, one can deduce that the FEL bandwidth is given by the Pierce parameter:

$$\frac{\Delta\lambda}{\lambda} = \rho_\mathrm{FEL}. \tag{2.102}$$

One estimates that the saturation power of the radiated field is the electron beam power multiplied by the gain bandwidth:

$$\mathrm{P}_\mathrm{sat} = \rho_\mathrm{FEL}\mathrm{E}\mathrm{I}_\mathrm{p}, \tag{2.103}$$

with I_p the peak current. Since the radiation pulse duration is close to that of the electron bunch, the Pierce parameter gives the efficiency of the FEL, i.e. the fraction of the beam energy given to the radiation field. Typically, the saturation power is reached after roughly 20 gain lengths, at the saturation length L_s.

$$\mathrm{L}_\mathrm{s} \approx 20\mathrm{L}_\mathrm{go} \approx \frac{1}{\sqrt{3}\Gamma} = \frac{20\lambda_\mathrm{u}}{4\pi\sqrt{3}\rho_\mathrm{FEL}} = \frac{5\lambda_\mathrm{u}}{\pi\sqrt{3}\rho_\mathrm{FEL}}. \tag{2.104}$$

So the saturation can be achieved with N_s, given by

$$\mathrm{N}_s = \frac{\mathrm{L}_\mathrm{s}}{\lambda_\mathrm{u}} = \frac{5}{\pi\sqrt{3}\rho_\mathrm{FEL}}. \tag{2.105}$$

The start-up comes from the spontaneous emission noise and followed by an exponential growth due to a collective instability (self-organization of the electrons from a random initial state). When the power saturates, there is a cyclic energy exchange between the electrons and the radiated field and a consequent change of power which corresponds to rotations in phase space. Growth and bunching also occur on the harmonics of the fundamental wavelength.

2.5.3.2 The SASE spectral and temporal properties

The uncorrelated trains of radiation, which result from the interaction of electrons progressing jointly with the previously emitted spontaneous radiation, lead to spiky longitudinal and temporal distributions, apart from single spike operation for low charge short bunch regime [152, 153]. The emission usually presents poor longitudinal coherence properties. There is some particularity of the temporal structure of the SASE pulse. Because the photons move faster than the electrons, the radiation emitted by one electron move ahead and slips by one wavelength per undulator period, and by $N_u\lambda$ for the total undulator length. The analysis [102] of the effect of slippage for an electron bunch of finite length, when the slippage effect cannot be neglected, shows that the interaction between the electrons is only effective over a cooperation length (slippage in one gain length). In a one-dimensional model the cooperation length can be written as:

$$L_{coop} = \frac{\lambda}{2\sqrt{3}\rho_{FEL}}. \tag{2.106}$$

Since the initial noise varies along the bunch length, the output radiation pulse consists of a series of spikes of random intensity separated by a distance proportional to the cooperation length [149]. For SASE at saturation, the interaction between electrons and their emitted radiation generates a number of spikes of random intensity and duration proportional to the cooperation length. The number of spikes in a pulse is given by the ratio of the bunch length to the cooperation length. The intensity in each spike fluctuates from pulse to pulse. There is no correlation between the phases of different spikes. The statistical distribution of the total intensity, summed over all spikes, is given by a gamma distribution function [153]. The spectral line width, in a SASE FEL, is inversely proportional to the spike length, and not to the bunch length. The width is of the order of the FEL parameter. In consequence, a SASE radiation pulse is not Fourier transform limited, except for the case of an electron bunch length shorter than the cooperation length, when a single spike is produced.

2.5.3.3 Ming Xi equations

In this section, the Ming Xi equations [154], that allow for a quick evaluation of an FEL performance, are presented. The study is for SASE amplification where the lasing is achieved in a single pass of a high current, high brightness electron beam through a long undulator. Starting with an ideal case (1D model), where the electron beam has a uniform transverse spatial distribution with zero emittance and energy spread, the FEL parameters are expressed as:

$$L_{1D} = \frac{\lambda}{4\pi\sqrt{3}\rho_{FEL}} \tag{2.107}$$

where L_{1D} is the gain length given by the 1D model. It can be shown that the FEL gain length can be expressed by a universal scaling function:

$$\frac{L_{1D}}{L_g} = F(\eta_d, \eta_\epsilon, \eta_\gamma) = \frac{1}{1+\eta} \tag{2.108}$$

where

$$\eta_d = \frac{\lambda L_{1D}}{4\pi\sigma_x^2} \quad , \quad \eta_\epsilon = \frac{4\pi\varepsilon_n L_{1D}}{\gamma\beta\lambda} \quad , \quad \eta_\gamma = \frac{4\pi\sigma_\gamma L_{1D}}{\lambda_u} \tag{2.109}$$

and

$$\eta = a_1\eta_d^{a_2} + a_3\eta_\epsilon^{a4} + a_5\eta_\gamma^{a_6} + a_7\eta_\epsilon^{a_8}\eta_\gamma^{a_9} + a_{10}\eta_d^{a_{11}}\eta_\gamma^{a_{12}} + a_{13}\eta_d^{a_{14}}\eta_\epsilon^{a_{15}} + a_{16}\eta_d^{a_{17}}\eta_\epsilon^{a_{18}}\eta_\gamma^{a_{19}} \tag{2.110}$$

with

$a_1 = 0.45$	$a_2 = 0.57$	$a_3 = 0.55$	$a_4 = 1.6$	$a_5 = 3$
$a_6 = 2$	$a_7 = 0.35$	$a_8 = 2.9$	$a_9 = 2.4$	$a_{10} = 51$
$a_{11} = 0.95$	$a_{12} = 3$	$a_{13} = 5.4$	$a_{14} = 0.7$	$a_{15} = 1.9$
$a_{16} = 1140$	$a_{17} = 2.2$	$a_{18} = 2.9$	$a_{19} = 3.2$	

The scaling parameters (η_d, η_ϵ, η_γ) measure the deviation of the beam from the ideal case.

- η_d: Gain reduction due to diffraction.
- η_ϵ: Gain reduction due to emittance.
- η_γ: Gain reduction due to energy spread.

The saturation power obtained from simulation is given by:

$$P_{sat} = 1.6\rho_{FEL}\left(\frac{L_{1D}}{L_g}\right)P_{beam} \tag{2.111}$$

After the calculation of L_g and P_{sat}, the saturation length is determined by:

$$L_{sat} = L_g ln\left(\frac{9P_{sat}}{P_n}\right) \tag{2.112}$$

where

$$P_n = c\rho_{FEL}^2\frac{E}{\lambda}$$

The power achieved after a certain undulator length can be determined using the following equation:

$$P = \frac{1}{9}P_n e^{z/L_g} \tag{2.113}$$

2.5.3.4 Conditions for SASE amplification

Emittance requirement

The FEL amplification efficiency highly depends on the overlapping of the electron beam and the FEL wave. Electrons follow the betatron oscillations around the undulator axis with a period larger than the undulator period that reduces the overlapping. Thus, there should be a proper transverse matching (size, divergence) between the electron beam and the FEL wave along the undulator for insuring a proper interaction. This sets the first electron beam requirement, where the normalized emittance ϵ_n should satisfy the well known Pellegrini criterion [155]:

$$\epsilon_n < \frac{\gamma\lambda}{4\pi} \tag{2.114}$$

High power short wavelength FELs require thus low emittance electron beams much smaller than 100 π mm.mrad.

Energy spread requirement

The electron beam large energy spread deteriorates the micro-bunching efficiency and smears out the electron bunch. This prevents the transfer of energy from the electron beam to the resonant

mode [156]. Hence, the electron beam should be rather cold with a relative energy spread σ_γ smaller than the FEL bandwidth:

$$\sigma_\gamma < \rho_{\mathrm{FEL}} \tag{2.115}$$

2.6 Summary

In this chapter the equation of motion of an electron beam through different magnetic structures have been introduced. The undulator radiation spectrum characteristics are discussed alongside the concept driving the free electron laser process.

Chapter 3

LUNEX5 framework

My PhD thesis aims at progressing towards advanced and compact free electron lasers and is carried out in the context of the LUNEX5 French project, which is an acronym for free electron Laser Using a New accelerator for the Exploitation of X-ray radiation of 5^{th} generation. The LUNEX5 project is introduced with the relevant R&D programs that makes a large portion of my PhD subject.

3.1 Presentation of LUNEX5 project

LUNEX5 test facility adresses the investigation of the production of short, intense, coherent Free Electron Laser (FEL) pulses in the VUV and soft X-ray spectral range (4 nm - 40 nm) [157–159]. Pilot user experiment will take advantage of the short wavelength radiation for time resolved pump-probe studies of isolated species [160, 161] as well as condensed matter imaging by exploiting the coherence to obtain single shot X-ray images of the magnetic domain structure [162].

The line design consists of two accelerators as shown in Fig. 3.1: a conventional RF linear accelerator (Linac) to drive the FEL with HGHG and EEHG schemes and compare their performance; a Laser Plasma Accelerator (LPA) to explore if FEL amplification is achievable with such a source. A common undulator line enables the comparison between high gain harmonic generation (HGHG) and echo-enabled harmonic generation (EEHG) FEL configurations.

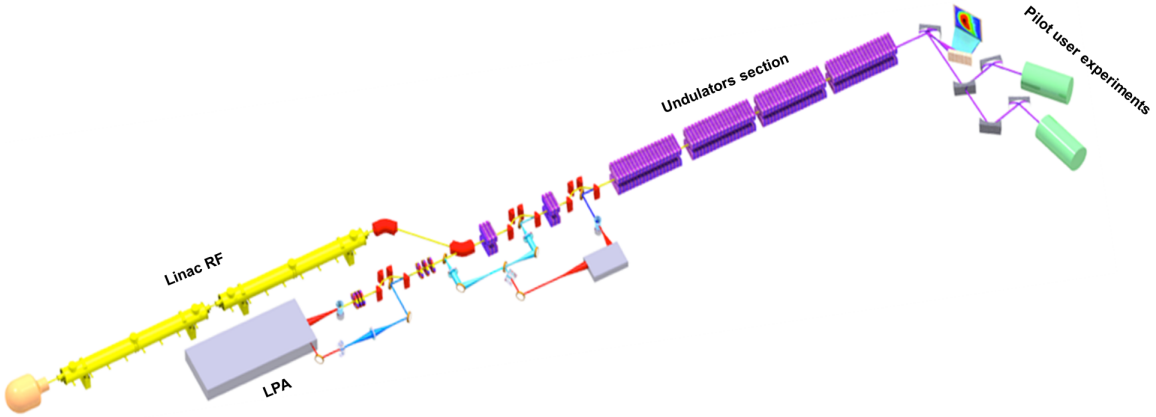

Figure 3.1: A schematic view of the LUNEX5 line. (orange) electron source, (yellow) RF cryostats, (Grey) laser hutch, (red) dipoles, (rainbow) quadrupoles, (purple) undulators.

3.1.1 LUNEX5 Accelerators

The conventional Linac under study is a 400 MeV superconducting L-band (1.3 GHz) Linac producing high average current electron beams with high repetition rate. It provides a reliable basis of the exploration of advanced FEL schemes, such as EEHG. It can also enable multi-FEL line with a fast switching of the electrons as shown in Fig. 3.2.

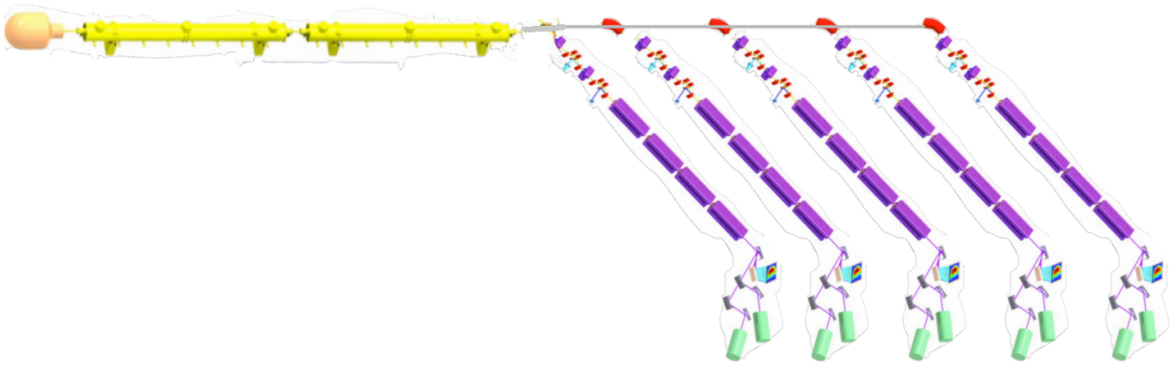

Figure 3.2: A schematic view of the LUNEX5 LINAC lines with fast switching of the electron bunches.

The LPA electron beam energy ranges from 400 MeV to 1 GeV with the use of 1 J energy, 30 fs pulse duration and multi TW or even PW power lasers. The FEL is viewed in such a case as a qualifying application of the LPA, which is a high risk and big challenge exploratory path towards the Graal of future compact FELs. Table 3.1 compares the electron beam parameters produced by the Linac and the LPA. The parameters in the LPA case are probably too optimistic, in particular the energy spread, since experiments often show few percents [163].

Parameter	Linac	LPA	Unit
Energy	400	200 - 1000	MeV
Relative energy spread (rms)	0.02	0.1	%
Normalized emittance	1.5	1	π mm.mrad
Divergence (rms)	30	1000	μrad
Beam size (rms)	60	1	μm
Bunch Length (rms)	250	1	μm
Charge	1000	15	pC
Peak current	1.2	4.5	kA

Table 3.1: Beam parameters produced at the source of the LPA accelerator [164].

3.1.2 Free electron laser line

The FEL line can be operated in the seeded (High order Harmonic in Gas seeding) and Echo Enable Harmonic Generation configurations, where the performance will be compared. Two pilot user experiments for time-resolved studies of isolated species and magnetization dynamics will take benefit of LUNEX5 FEL radiation. Studies on the FEL property manipulations are also considered, in particular two-color operation.

3.1.2.1 Undulators

The modulators for the HGHG and EEHG configurations are 27 cm long in-vacuum permanent magnet based undulators of period 30 mm. The radiators are 3 m long cryogenic permanent magnet undulators. A cryogenic permanent magnet based undulator (CPMU) of period 15 mm (U15)

is under construction at SOLEIL under the R&D programs. This device consists of Vanadium-Permendur poles and $Pr_2Fe_{14}B$ magnets. The chosen grade is characterized by a remanence field of 1.32 T and a coercitivity of 1900 kA/m at room temperature. The peak field on axis is ~1.6 T for a gap of 3 mm. After cooling down to 77 K, the peak field in increased to 1.77 T. More details on the design and optimization are discussed in Chapter 5.

3.1.2.2 Seeding

As illustrated in Fig. 3.1, a Ti:Sapphire laser oscillator (30 fs @ 800 nm) will be used for both seeding schemes (HGHG and EEHG). The laser will be sent to a regenerative and a multipass amplifier (30 fs, 800 nm, 10 mJ, 50 Hz, option at 1 kHz). For the EEHG scheme, the amplifier output is tripled to 266 nm wavelength using a crystal. As for the HGHG scheme, high order harmonics in gas [165] is intended to seed at a short wavelength ~40 nm. Pump probe experiments of the pilot users require a laser signal perfectly synchronised with the seeding laser. This laser signal can be either provided by using part of the seeding laser and transporting it to the pilot experiments or by a dedicated laser (30fs, few mJ). Extremely tight synchronisation between lasers is required. All laser characteristics are within reach of commercially available lasers.

3.1.3 LUNEX5 FEL performance

The LUNEX5 spectrum (see Fig. 3.3) covers the 4-40 nm range with the first, third and fifth harmonics, with a fundamental peak power between 10 MW and 100 MW, corresponding to more than 10^{11} photons/pulse and 10^{27} peak brightness and harmonic peak power from 1 MW down to a few hundreds W. Each wavelength can be obtained with different configurations (amplifier, multi-stage HGHG, EEHG). The FEL saturates earlier in the EEHG case than in the multi-stage HGHG (7 versus 11 m) [166], with slightly lower power (65 MW versus 0.27 GW), longer pulses (24 versus 17 fs) at the Fourier limit. LPA based FEL performance critically depends on the electron beam quality and on the optimization of the transport line.

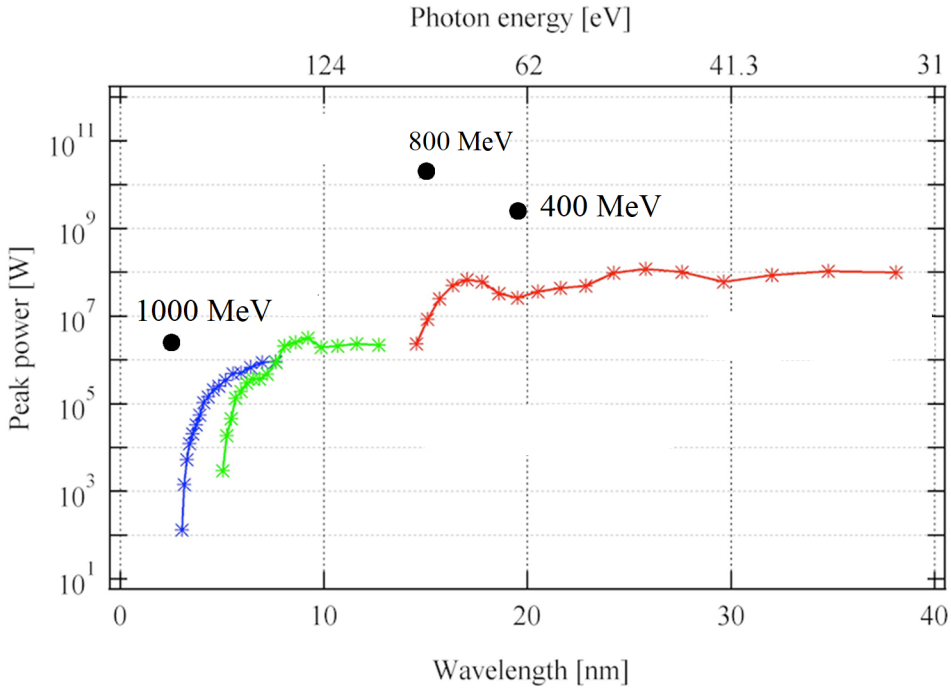

Figure 3.3: FEL peak power versus wavelength simulated using GENESIS [167]. First (red), third (green) and fifth (blue) harmonics of the FEL wavelength using the Linac accelerator at 400 MeV with beam parameters from Table 3.1. LPA at 400 MeV (second harmonic), 800 MeV and 1000 MeV (•) with parameters presented in Table 3.1. Figure from [157].

3.2 Problematics of FEL application based on LPA

This section presents the issues associated with the use of LPA driving an FEL, alongside some techniques that can be implemented to overcome this barrier to make FEL amplification possible. The baseline reference case of LUNEX5 electron beam parameters presented in Table 3.1 were very optimistic. Indeed, FEL LPA based applications remain very challenging due to the large energy spread and divergence at the source.

Recalling the emittance requirement presented in Eq. (2.114), one has:

$$\varepsilon_n < \frac{\gamma\lambda}{4\pi} \tag{3.1}$$

For a typical LPA electron beam of 500 MeV and ε_n = 1 mm.mrad at the source, the emittance requirement is satisfied for an operating wavelength $\lambda \geq 12$ nm. However, unlike beam drifts in comventional accelerators, a problem arises regarding the transport where the chromatic emittance ε_{chrom} increases quadratically with the divergence along a distance s [168–171]. Such dependence can be understood by using the general definition of the normalized emittance expressed as:

$$\varepsilon_n^2 = \langle x^2\rangle\langle\gamma^2 x'^2\rangle - \langle x\gamma x'\rangle^2 \tag{3.2}$$

Considering that there is no correlation between the energy and transverse position, i.e. drift without collective effects, one finds:

$$\varepsilon_n^2 = \langle\gamma^2\rangle\langle x^2\rangle\langle x'^2\rangle - \langle\gamma\rangle^2\langle xx'\rangle^2 \tag{3.3}$$

Inserting the energy spread relation:

$$\sigma_\gamma^2 = \frac{\langle\gamma^2\rangle - \langle\gamma\rangle^2}{\langle\gamma\rangle^2}$$

in Eq. (3.3), one gets:

$$\varepsilon_n^2 = \left(\sigma_\gamma^2\sigma_x^2\sigma_x'^2 + \varepsilon^2\right)\langle\gamma\rangle^2 \tag{3.4}$$

If the first term in Eq. (3.4) is negligible, one arrives at the conventional definition of the normalized emittance as $\varepsilon_n = \langle\gamma\rangle\varepsilon$. In the case of LPA, the generated electron beam can be considered as a point source, thus the bunch transverse size after a drift distance s becomes:

$$\sigma_x(s) = \sigma_x' s \tag{3.5}$$

Inserting Eq. (3.5) in Eq. (3.4), one gets the expression of the emittance after a drift s:

$$\varepsilon_n^2(s) \approx \varepsilon_{n0}^2 + \gamma\sigma_\gamma^2\sigma_{x,z}'^4 s^2 \tag{3.6}$$

For a typical LPA electron beam of 2 mrad divergence, 500 MeV energy and 1% spread, the emittance is increased by a factor of 80 just after 10 cm drift, thus the divergence should be handled at an early stage of the transport.

The second requirement concerning the energy spread for the FEL amplification (recall Eq. (2.115)) is given by:

$$\sigma_\gamma < \rho_{\mathrm{FEL}} \tag{3.7}$$

ρ_{FEL} is normally of the orders of 10^{-3}, so an energy spread of 0.1% and below is required to enable the FEL amplification. This condition is not acomplished by typical LPA, since energy spreads have been measured to be $\sim 10^{-2}$ for MeV-GeV electron beams [172, 173].

Furthermore, the bunch length is ultrashort of the orders of few µm. This reduces the interaction length of the radiation field with the electron bunch, leading to a degrading effect on the FEL performance.

3.2.1 Electron beam divergence handling

High energy accelerators require larger gradient quadrupoles to transport the beam around. The gradient needed for LPA beams is typically around >100 T/m. Conventional quadrupoles are generally based on electro-magnet technology that can provide intermediate gradient. Superconducting magnets come in handy for such applications but they are much more expensive than the conventional electro-magnets due to the cryogenic cost (installation and operation) and the possibility of a quench as a result of heating originating from synchrotron radiation and image charges. Thus permanent magnet based system advantages come into play with the absence of power supplies and cables, and in addition, eliminating a large element of infrastructure for the water cooling system. Permanent magnet based quadrupole can be reduced in size without losing the magnetic field strength making it suitable for future compact accelerators including LPA. However, the provided focusing is not symmetric (focusing in one plane and de-focusing in the other) and at least three systems are required to provide a round beam. Therefore, a FODO (FOcusing - DefOcusing) high gradient permanent magnet quadrupole lattice placed very close to the plasma-vacuum interface is one of the best candidates for handling and controling the LPA beam divergence.

Besides, an alternative focusing system can be implemented by the use of the plasma itself. After the emergence of the concept of magnetically self-focusing electron beam of density n_e by ions from a residual gas [174] or more generally by a plasma of density n_p, two regimes of plasma lens

can be considered. In the over-dense regime ($n_e << n_p$); the electron beam moves away due to the plasma and self generates an azimuthal magnetic field, of focusing strength $K = 2\pi r_e n_e/\gamma$ with r_e the classical radius of the electron [175]. In the under-dense regime ($n_e >> n_p$), the electron beam pass induces a strong wave in the plasma background and can be focused by the ions uniformly distributed, with a strength given by $K = 2\pi r_e n_p/\gamma$. Afterwards, Passive Plasma Lens (PPL) have been proposed and developed [176], which can provide high gradients, but the focusing properties depend on the electron beam itself and can present aberrations. PPL is further developed theoretically [177] and used for an LPA experiment [58]. Active Plasma Lens (APL), where the azimuthal magnetic field is controlled by a discharge in the plasma, has been proposed [178, 179]. APL has been applied to ion beams [178, 180] and to LPA applications [181–185]. APL provides high gradient of the order of kT/m, tunability and radially symmetric focusing, but are subjected to emittance degradation and charge reduction due to highly non-linear focusing arising from current discharge nonuniformity. Furthermore, their use in experiments that run for couple of weeks adds an additional level of risk. Plasma lenses are still under development and the use of conventional magnet can still appear to be more robust.

3.2.2 Energy spread handling

Solutions to handle the FEL second requirement are now examined. A magnetic chicane can be introduced in the line to stretch the electron beam and reduce the slice energy spread by inducing an energy-position correlation. A combined scaling law of the energy spread and bunch length is introduced in [186, 187] and showed that the FEL gain length, in the case of bunches with relative energy spreads on the order of the Pierce parameter and bunch lengths on the order of the cooperation length, can be reduced. Furthermore, a set of quadrupoles can be placed between the chicane and an undulator, taking advantage of the correlation and allowing for supermatching optics [188]. Using this optics, the different energy slices are focused at different locations inside the undulator that can be considered as a focusing slippage. The electron beam speed is less than the speed of light, so the FEL wave tends to slip over the beam. With the right synchronization between these two slippages, one is able to ensure that the FEL wave always sees the minimum slice beam size, improving the FEL perfromance.

A Transverse Gradient Undulator (TGU) can be used in the FEL based LPA line to compensate the effects of beam energy spread by introducing a transverse field variation into the undulator. By canting the poles and magnets, one can generate a linear dependence of the vertical undulator field. The electron beam is dispersed in horizontal axis so that each energy slice undergoes a different field magnitude and emit radiation at the same wavelength. This process enhances the FEL performance as shown in [189, 190].

The first step towards FEL application, using LPA source, is the transport of the higly divergent electron beam to the undulator and characterize the emitted radiation.

3.3 LPA based undulator radiation

Let's consider now what has been achieved so far concerning LPA based undulator light source application. The feasibility of achieving undulator radiation with an LPA source has been demonstrated at different laboratories.

3.3.1 Institute fur Optik und Quantenelektronik

A high-intensity Titanium:Sapphire laser of 5×10^{18} W.cm^{-2} and pulse duration of 80 fs is used to produce the relativistic electron beams. The setup of the line is presented in Fig. 3.4 [191]. The undulator is 1 m long of period 20 mm with a strength of $K_u = 0.6$.

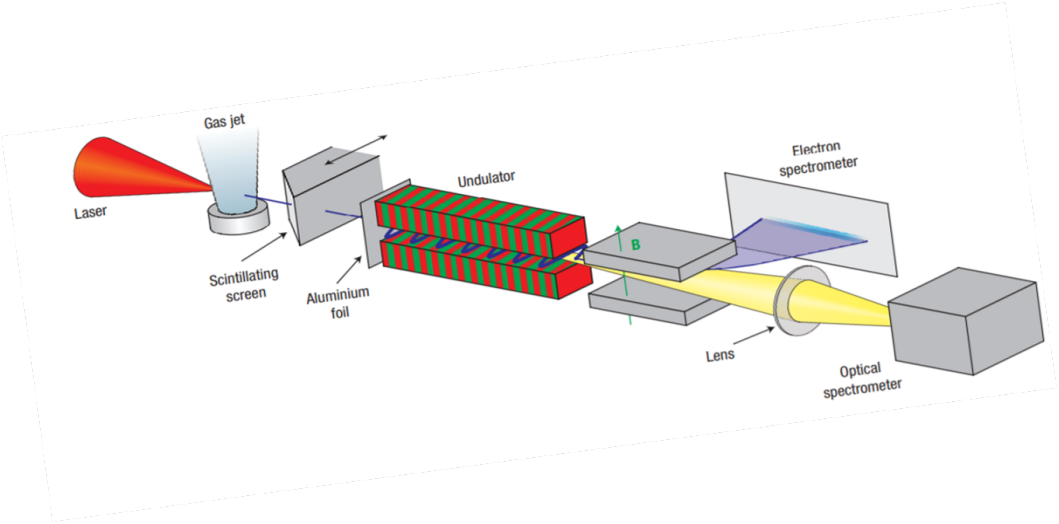

Figure 3.4: . The laser pulse is focused by an off-axis parabolic mirror into a supersonic helium gas jet where it accelerates electrons (blue line) to several tens of MeV energy. The electron beam profile may be monitored by a removable scintillating screen. The electrons propagate through an undulator, producing synchrotron radiation, and into a magnetic electron spectrometer. Radiation is collected by a lens and analysed in an optical spectrometer. The spectrometer is protected against direct laser and plasma exposure by a thin aluminium foil in front of the undulator. Figure from [191].

Figure 3.5 shows a measured electron spectrum for a single shot. The electron spectrum peaked at 64 MeV has a width of 3.4 MeV (full-width at half-maximum, FWHM), i.e. rms energy spread of ~2.3%, and contains a charge of 28 pC. The normalized emittance of the beam is estimated to be $\varepsilon_n \approx 1.3\pi$ mm.mrad, derived from beam optics simulations and the beam divergence measured from the beam size.

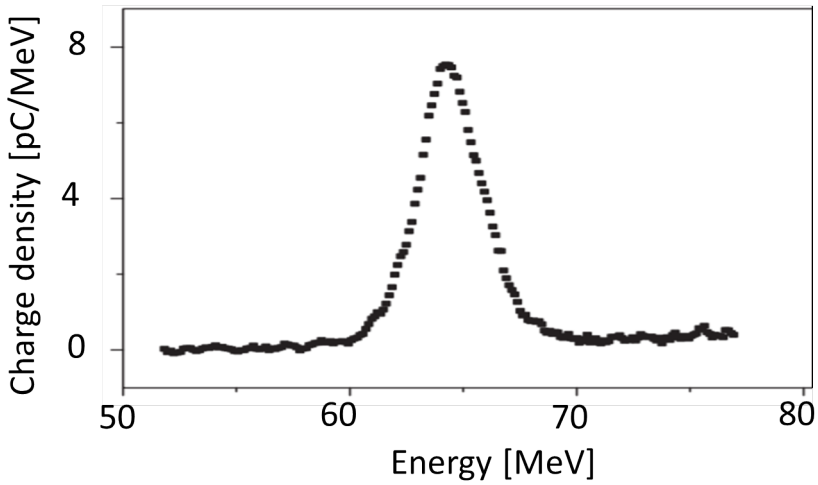

Figure 3.5: Measured electron spectrum centered around 64 MeV with a width of 3.4 MeV (FWHM), and a total charge of 28 pC. Figure from [191].

The undulator radiation is measured using a spectrometer (see Fig. 3.6) for the electron beam distribution presented in Fig. 3.5. The spectra is peaked at 740 nm with a a bandwidth of 55 nm and contains 284,000 photons (black). Another peak is observed at a wavelength of 900 nm (red) produced by a 58 MeV, 14 pC and 5% energy spread in another shot (not shown).

Figure 3.7 shows the measured electron beam and undulator radiation spectral width, simul-

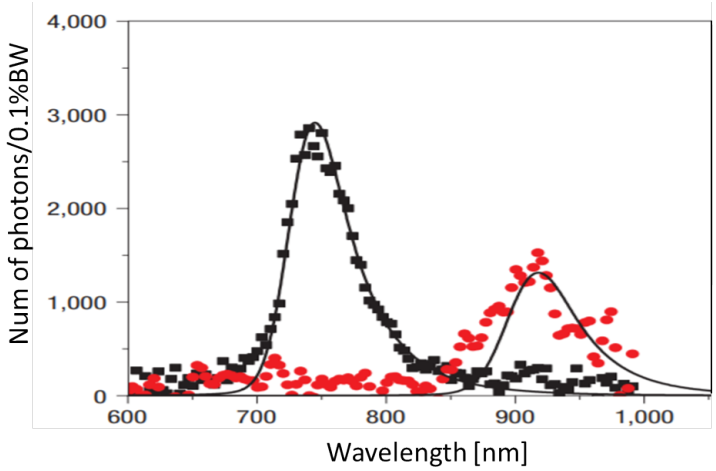

Figure 3.6: Undulator radiation spectrum (black squares) is simultaneously recorded. The peak centred at 740 nm contains 284,000 photons. The red circles show an undulator radiation spectrum from a different shot, produced by a 58 MeV, 14 pC electron bunch. The simulations of the undulator spectra (solid lines) take into account the measured electron spectrum, the undulator parameters and the optical imaging system, and compare well with the measured signals. Figure from [191].

taneously, for eight shots. The squares represent the center of the radiation spectra for each shot. The electron beam energy fluctuates between 55 MeV and 75 MeV corresponding to wavelengths between 1000 nm and 550 nm with a wavelength stability of 93 nm (over 8 shots). The peak wavelengths are in good agreement with the expected undulator wavelength (solid line).

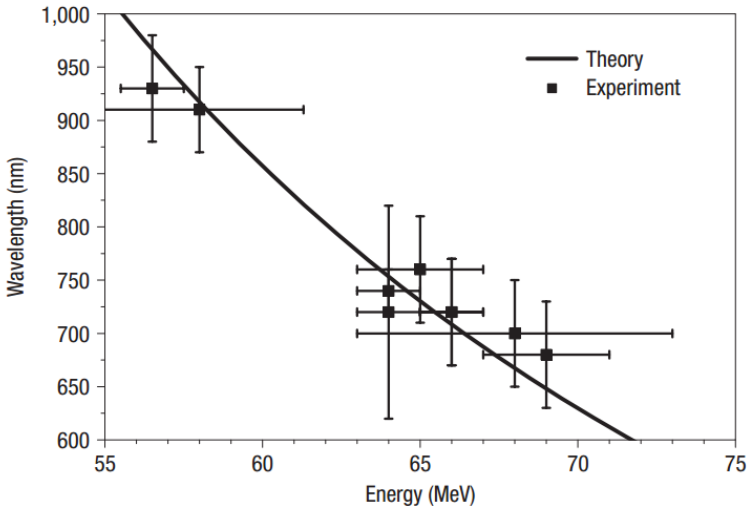

Figure 3.7: Spectral width of the undulator radiation and electron beam. Squares represent the center of the undulator spectra. (line) theoretical values. Figure from [191].

3.3.2 Max-Planck-Institut fur Quantenoptik

Figure 3.8 presents the line for the generation of soft-X-ray undulator radiation with LPA electron beams [192]. Quadrupoles of bore radius 3 mm with adjustable longitudinal position, achieving a gradient of 500 T/m, are installed after the electron source. The undulator used is 30 cm long with a period of 5 mm (60 number of periods) attaining a deflection parameter $K_u = 0.55$ at 1.2 mm gap.

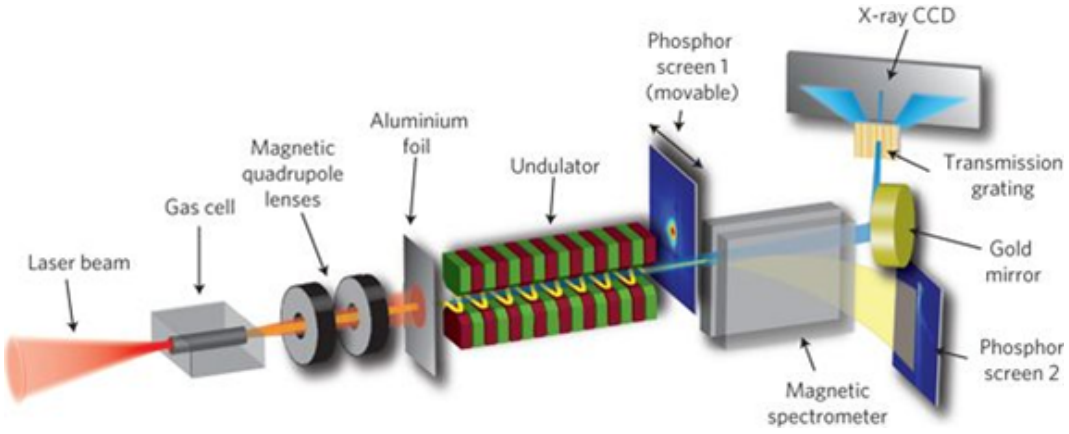

Figure 3.8: The laser pulse (red) focused on a gas cell (grey), where the electron beam is generated and then focused by two quadrupoles (black) into the undulator. Diagnostic equipments, composed of an electron and photon spectrometer, placed at the end of the line. Figure from [192].

Figure 3.9 shows a typical spectrum of undulator radiation measured with a 210 MeV electron beam energy. The first harmonic is peaked at 18 nm and a second peak near 9 nm (second harmonic).

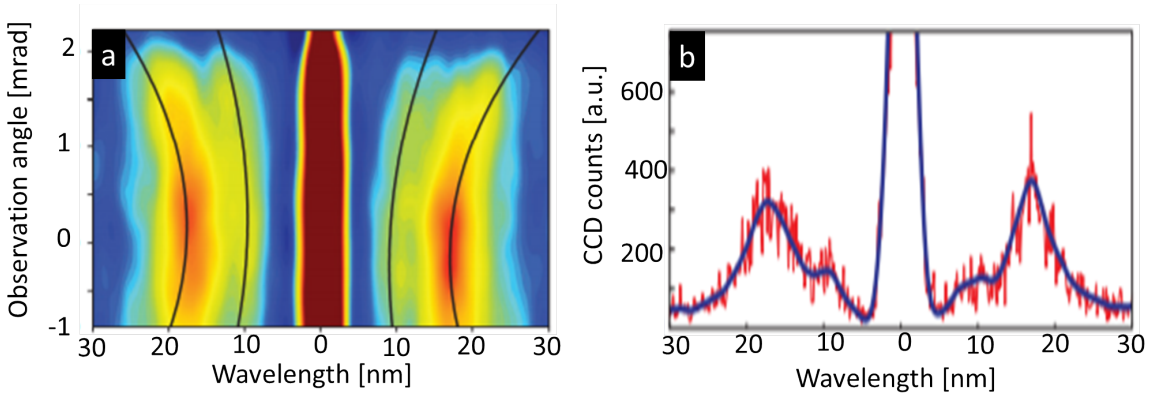

Figure 3.9: (a) Spatio spectral distribution at zero and ± first diffraction order of the monochromator measured on a CCD placed 2.6 m from the undulator center. (b) the integrated intensity of (a). Figure from [192].

Figure 3.10 shows the correlation of the peak electron energy and detected undulator radiation fundamental wavelength for two quadrupole lens positions (blue and green), i.e. focusing of different energies. The blue points (green points) measurements have an average wavelength of ~20 nm (~17.5 nm) with a standard deviation of ~1.5 nm (~1.5 nm). It thus shows a first wavelength adjustment using LPA source.

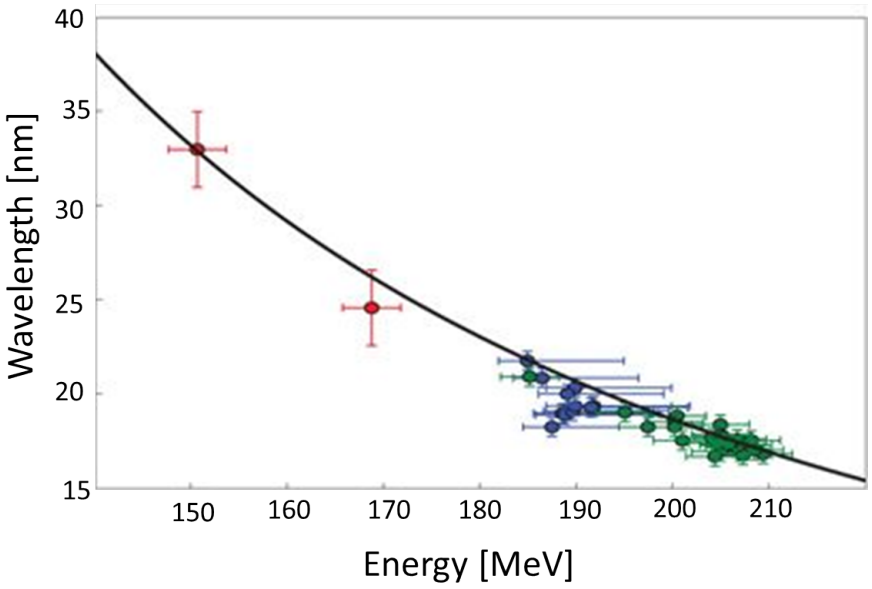

Figure 3.10: Points correspond to the central peaked wavelength of a single shot. Lines represent the error bars of the electron spectrometer, X-ray spectrometer, quadrupoles position and undulator field. (Green) and (Blue) points correspond to different positions of the quadrupoles. (Red): shots that lie outside the LPA stable regime. (line) theoretical values. Figure from [192].

3.3.3 Laboratoire d'Optique Appliquée

Figure 3.11 presents the set-up for the generation of UV undulator radiation with laser-plasma-accelerated electron beams [193]. A Titanium:Sapphire laser delivering a linearly polarized pulse at 800 nm with more than 1 J energy, about 30 fs duration is focused on a gas jet made of Helium leading to an electron density of 5×10^{18} cm^{-3}. The generated relativistic electrons pass trough a triplet of permanent magnet quadrupoles placed 15 cm from the source providing 15.4 T/m, -25 T/m and 15 T/m gradients, followed by a 0.6 m long undulator of period 18.2 mm and a deflection parameter of 1. Figure 3.12 presents the photon beam transverse shape radiation measured on the

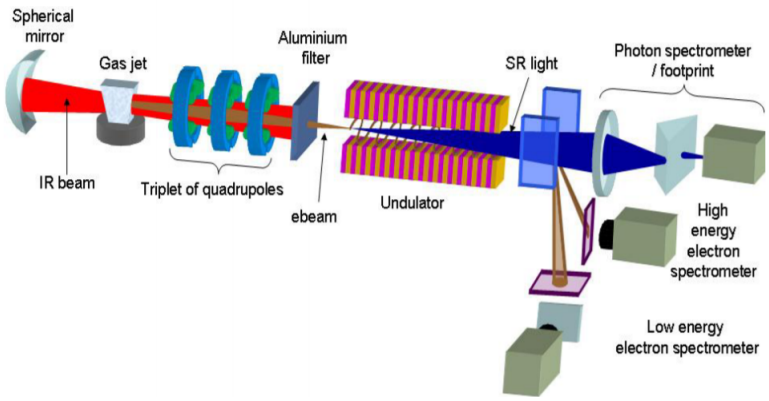

Figure 3.11: Experimental setup at LOA for generating synchrotron radiation from laser-plasma acceleration. Figure from [193].

CCD camera, which images a position corresponding to 60 cm after the end of the undulator and for an electron energy of 120 MeV energy.

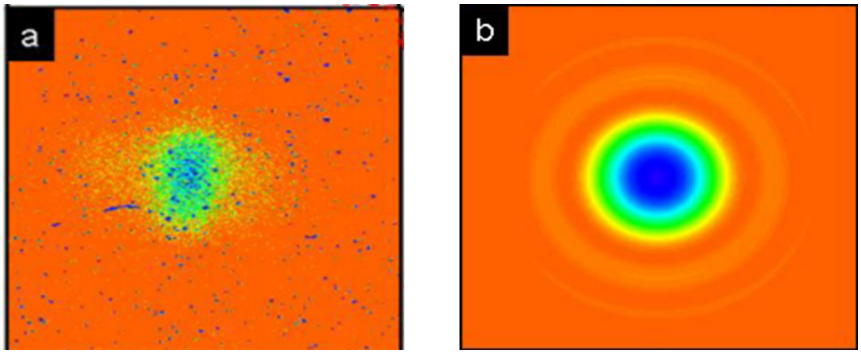

Figure 3.12: Single shot of the photon transverse shape measured on the CCD camera. (a) Experimental data. (b) Simulated synchrotron radiation from SRW software [194].

Figure 3.13 shows two single shot measurements of the electron beam energy distribution with the corresponding undulator radiation spectra. The photon spectrum presents a similar shape relative to the electron beam distribution resulting in a nice apparent correlation.

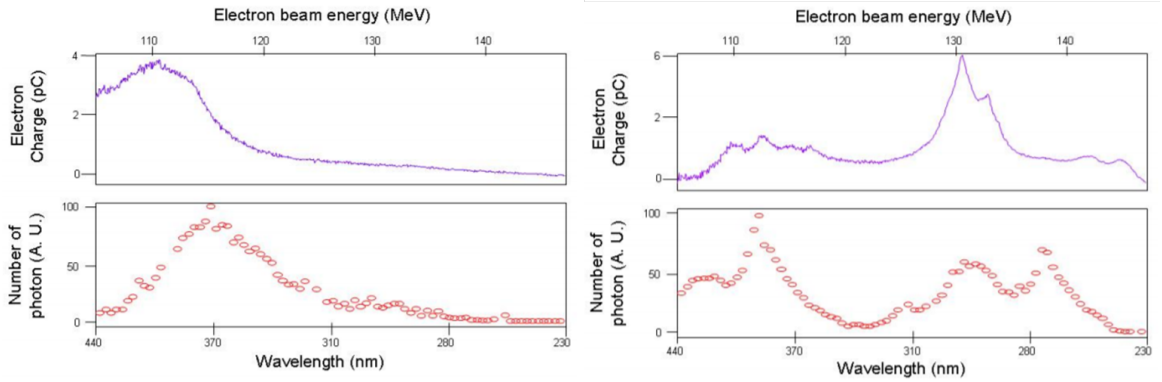

Figure 3.13: Single shot spectra of photons (red circle) and electrons (violet line) for two different shots. Figure from [193].

3.3.4 SUPA, Department of Physics, University of Strathclyde

Figure 3.14 presents the Advanced Laser-Plasma High-energy Accelerators towards X-rays (ALPHA-X) accelerator beam line [195]. A Titanium:Sapphire laser pulse centered at a wavelength of 800 nm with full-width at half-maximum duration of 36 fs and peak intensity of 2×10^{18} W.cm^{-2} is focused to a 20 µm waist at the leading edge of a 2 mm diameter Helium gas jet to form a relativistic self-guided plasma channel. The electron beams produced are initially collimated using a triplet of miniature permanent magnet quadrupoles of fixed gradients of 500 T/m. A triplet of electromagnetic quadrupoles then focuses the beam through the undulator with gradient ~2.4 T/m. The undulator is 1.5 m long with 100 number of periods and a deflection parameter $K_u = 0.38$. The distance from accelerator exit to undulator entrance is 3.52 m. Undulator output radiation is detected using a vacuum scanning monochromator and 16-bit CCD camera. The grating is positioned for a 344 nm detection bandwidth centred on 220 nm with a resolution of about 5 nm.

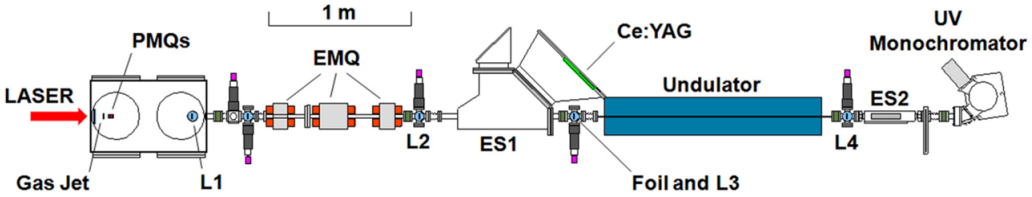

Figure 3.14: Schematic view of the line. Figure from [195].

The energy distibution measured with an electron spectrometer, placed after the gas jet (see Fig. 3.14 ES1), has a mean central energy of 104 MeV, with a 5% relative energy spread, and contains a mean charge of 1.1±0.8 pC. Figure 3.15 presents the electron beam measured after the undulator using an electron spectrometer dump (see Fig. 3.14 ES2) alongside the radiation generated measured with the CCD camera. The mean spectral bandwidth of the radiation is 69±11 nm corresponding to a relative band width of 32±7%, decreasing to as low as 16%.

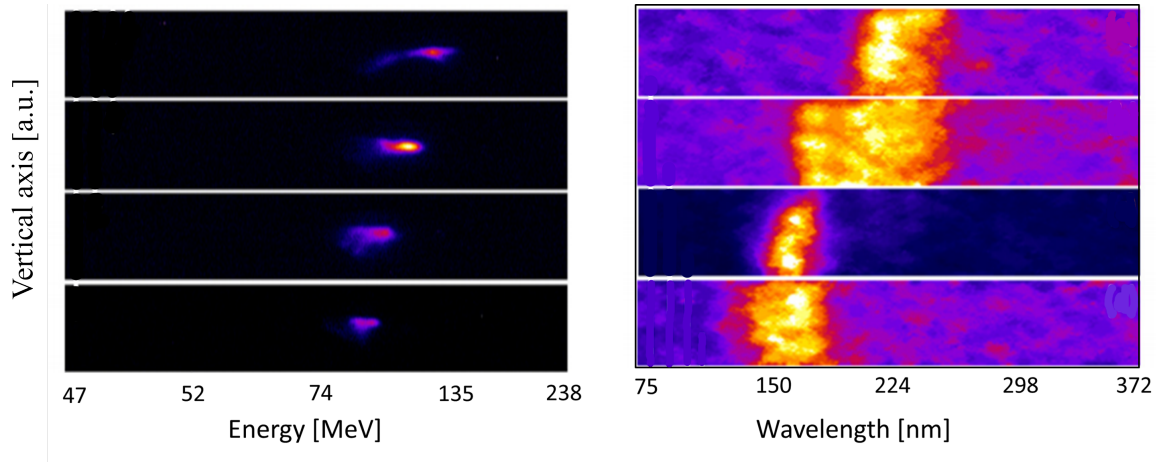

Figure 3.15: Undulator radiation single shot measurements (right) with the corresponding electron beam energy distribution measured with an electron spectrometer after the undulator (left). Figure from [195]

3.3.5 Undulator radiation summary

Table 3.2 summarize some of the undulator radiation characteristics observed so far using an LPA source. The measured radiation bandwidth is still quite wide with a rather poor wavelength stability. Wavlength tunability with undulator gap adjustment has not been shown yet. The undulator radiation quality achieved so far does not yet reach what is currently achieved on storage ring accelerator based light sources. In my PhD, I'll explore the path towards usual undulator radiation, by manipulating the phase space of the electron beam at the beam transport.

Laboratory	Energy	Wavelength	Relative bandwidth	Wavelength stability
	MeV	nm	%	nm (%)
Institut Fur Optik [191]	65	740	7.4	~ 93 (12.5)
Ludwig-Maximilians [192]	210	18	30	~1.5 (8)
LOA [193]	120	230-440	18	-
Strathclyde [195]	105	160 - 220	16	~23 (13)

Table 3.2: Undulator radiation measured from an LPA electron beam.

3.4 COXINEL transport line test experiment

COXINEL is an acronym for Coherent X-ray source inferred from electrons accelerated by laser. It is an R&D program funded by the ERC (340015) in the framework of LUNEX5 project [196]. The COXINEL experiment aims at demonstrating a full control and transport of electron beams produced by an LPA source and achieve FEL amplification at 200 nm and 40 nm. The key concept relies on an innovative electron beam longitudinal and transverse manipulation along the transport line towards the undulator. The line and FEL have been designed by SOLEIL and installed at Laboratoire d'Optique Appliquée with the 30 TW laser of Salle Jaune with the expertise of Viktor Malka and his team on LPA.

Figure 3.16 presents the experimental setup. A Titanium:Sapphire laser is focused on a supersonic gas jet where the electron beam is produced. A triplet of high tunable gradient permanent magnet based quadrupoles (QUAPEVAs) strongly focuses the electron beam and permits to handle the divergence at an early stage. The electron beam is then sent through a magnetic chicane, where an energy-position correlation is achieved sorting the electron beam in energy. Before the undulator, a set of quadrupoles are installed to enable good focusing. Finally the beam is dumped thanks to a permanent magnet dipole. Four steerers are placed along the transport line to correct the beam position.

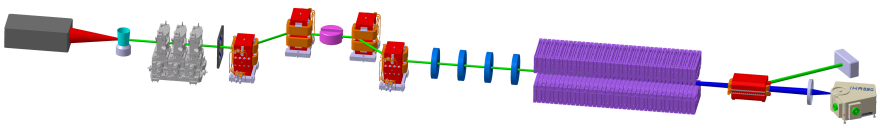

Figure 3.16: COXINEL line sheme. laser hutch (grey), gas jet (cyan), permanent magnet based quadrupoles (QUAPEVAs) (light grey), electro-magnet dipoles (red) with an adjustable slit placed at the center (pink), electro-magnet quadrupoles (blue), undulator (purple), dipole dump (red), UV spectrometer (light grey).

Table 3.3 presents the magnetic elements characteristics of the line. The QUAPEVAs achieve a maximum gradient of ~180 T/m and provide a tunability of ~90 T/m (more details are presented in chapter 6). The chicane is composed of four electro-magnet dipoles. The second set of quadrupoles used are electro-magnet based generating a maximum gradient of 20 T/m. The undulator is 2 m long and of period 18.16 mm with an adjustable magnetic gap providing a field variation (more details are presented in chapter 5).

	Unit	Value
PMQs		
Magnetic length	mm	40.7 ; 44.7 ; 26
Minimum gradient	T/m	98 ; -100 ; 90
Maximum gradient	T/m	181 ; -184 ; 165
Bore radius	mm	4
Chicane dipoles		
Magnetic length	mm	208.33
Integrated field	T.mm	130
Maximum R_{56}	mm	32
Maximum field	T	0.53
EMQs		
Magnetic length	mm	213.3
Maximum gradient	T/m	20
Bore radius	mm	12
Steerers		
Maximum integrated field	G.m	38
Undulator		
Period	mm	18.16
Number of periods	-	107
Minimum gap	mm	4.5
Maximum field	T	1.2

Table 3.3: COXINEL magnets relevant parameters. The three values for PMQs are for each PMQ of the triplet in the beam propagation order.

3.4.0.1 Electron beam transport: Super-matching optics

The COXINEL line is designed by adopting a linear optics from source to image [188]. The optics ensures a minimum beam size (waist) for the on-momentum particles (energy deviation $\delta = 0$) at the focusing point (undulator center), by setting the terms R_{12} and R_{34} in Eq. (2.29) to zero. The minimum horizontal and vertical sizes introduced as σ_{x-min} and σ_{z-min} are thus expressed as:

$$\sigma_{x-min} = R_{11}\sigma_{x0} \quad , \quad \sigma_{z-min} = R_{33}\sigma_{z0} \tag{3.8}$$

where the terms R_{11} and R_{33} represent the horizontal and vertical magnifications from source to undulator center, respectively, and σ_{x0} and σ_{z0} the horizontal and vertical initial beam sizes at the source.

By neglecting the coupling effect, Eq. (2.29), limited to the horizontal plane and chromatic terms, can be expanded up to the second order as [197]:

$$\begin{pmatrix} x \\ x' \end{pmatrix} = \left[\begin{pmatrix} R_{11} & R_{12} \\ R_{21} & R_{22} \end{pmatrix} + \delta \begin{pmatrix} R_{116} & R_{126} \\ R_{216} & R_{226} \end{pmatrix} \right] \begin{pmatrix} x_0 \\ x'_0 \end{pmatrix} \tag{3.9}$$

where the matrix R_{ij6} stands for the chromatic second order perturbation.

The COXINEL line ensures a minimum chromatic effect induced by the energy spread such that the term R_{226} in Eq. (3.9) is very small. Also, the electron beam generated by an LPA starts as a point source. Hence Eq. (3.9) becomes:

$$\begin{pmatrix} x \\ x' \end{pmatrix} = \left[\begin{pmatrix} R_{11} & 0 \\ 0 & R_{22} \end{pmatrix} + \delta \begin{pmatrix} 0 & R_{126} \\ 0 & 0 \end{pmatrix} \right] \begin{pmatrix} x_0 \\ x'_0 \end{pmatrix} \tag{3.10}$$

Considering a round Gaussian beam and approximating that $R_{22} = 1/R_{11}$ [128], the rms asso-

ciated momenta transfers at the center of the undulator can be expressed as:

$$\begin{cases} \sigma_x^2 = R_{11}^2\sigma_{x0}^2 + R_{126}^2\sigma_{x0}'^2\sigma_\gamma^2 \\ \sigma_x'^2 = \frac{1}{R_{11}^2}\sigma_{x0}'^2 \\ \sigma_{xx'} = R_{126}\sigma_{x0}'^2\sigma_\gamma/R_{11} \end{cases} \tag{3.11}$$

By multiplying σ_x and σ_x' of Eq. (3.11), the horizontal geometric emittance ε_x is calculated to be:

$$\varepsilon_x^2 = \varepsilon_{x0}^2 + \varepsilon_{chrom}^2 = \sigma_{x0}^2\sigma_{x0}'^2 + \frac{R_{126}^2}{R_{11}^2}\sigma_{x0}'^4\sigma_\gamma^2 \tag{3.12}$$

The chromatic emittance scales as the quadratic of the divergence multiplied by the energy spread. As we have seen in section 3.2, this combined effect of larger energy spread and divergence significantly enhances the emittance over a small drift distance.

For optics dedicated to FEL studies, the so-called supermatching optics is introduced [188]. With this optics, each energy slice is focused at a different location in the undulator (see Fig. 3.17).

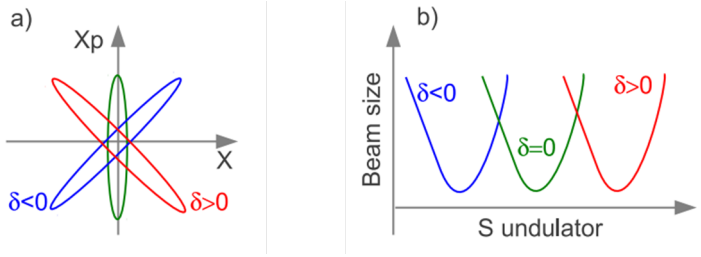

Figure 3.17: Sketches of the horizontal phasespace ellipses at the center of the undulator (a) and horizontal beam size (b) along the undulator axis for three cases of δ.

Assuming a linear chicane decompression, the bunch length σ_l, slice energy spread $\sigma_{\gamma-slice}$, slice emittance ε_{slice} and slice waist beam size $\sigma_{x-slice}$ at the center of the undulator can be expressed as:

$$\begin{cases} \sigma_l = \sqrt{\sigma_{l0}^2 + R_{56}^2\sigma_\gamma^2} & \sigma_{\gamma-slice} = \frac{\sigma_{l0}}{\sqrt{\sigma_{l0}^2+R_{56}^2\sigma_\gamma^2}}\sigma_\gamma \\ \varepsilon_{slice}^2 = \varepsilon_{x0}^2 + \frac{R_{126}^2}{R_{11}^2}\sigma_{x0}'^4\sigma_{\gamma-slice}^2 & \sigma_{x-slice} = \sqrt{R_{11}^2\sigma_{x0}^2 + R_{126}^2\sigma_{x0}'^2\sigma_{\gamma-slice}^2} \end{cases} \tag{3.13}$$

In the high gain regime (exponential growth), the FEL wave slippage over the electron beam [102] can be synchronized with the energy slice focusing by setting the chicane strength to [188]:

$$R_{56} = -R_{11}R_{126}\frac{\lambda}{3\lambda_u} \tag{3.14}$$

To operate this chromatic focusing slippage, in both horizontal and vertical planes, at least an additional triplet of quadrupoles is mandatory. With a proper synchronization, the FEL gain power is enhanced [188].

3.4.1 Baseline reference case

At the start of COXINEL project, the baseline reference parameters that were examined at the source are presented in Table 3.4, where the electron beam is considered to be a round Gaussian beam. Our aim at COXINEL is to achieve FEL amplification at 200 nm. The line is optimized in such a way that R_{11} = 10 and R_{56} = 0.4 mm. Inserting these values in Eqs. (3.13) and (3.14), one gets the beam parameters at the center of the undulator as shown in Table 3.4.

Parameters	Symbol	Source	Undulator (slice)	Unit
Energy	E	200	200	MeV
Normalized emittance	ε_N	1	1.13	π mm.mrad
Effective emittance	ε	2.6	2.8	nm
Divergence (rms)	$\sigma'_{x,z}$	1	0.1	mrad
Beam size (rms)	$\sigma_{x,z}$	2.6	30	µm
Bunch length (rms)	σ_l	1	4.3 (Total)	µm
Energy spread (rms)	$\sigma_{\gamma-slice}$	1	0.24	%
Total charge	Q	34	34 (Total)	pC
Current	I_b	4.3	1	kA

Table 3.4: Baseline reference case parameters at the generation point in the gas jet and at the undulator center for R_{56} = 0.4 mm, R_{11} = 10 and R_{126} = -4.4. In the undulator column, the energy slice parameters are displayed except for the bunch length, charge and current corresponding to the total beam.

3.4.1.1 Beam optics simulation

The electron beam is propagated from the source through the magnetic elements (QUAPEVAs, Chicane, Quadrupoles) down to the undulator using a multiparticle tracking code. The code models the transfer line up to the second order with BETA [198] and the electrons are transported through the different elements of the line. The multiparticle tracking code, based on sympletic mapping, keeps track of the electron beam in a 6D space phase which describes the position, momentum and energy at any position along the line. Each element of the line is represented by a 6x6 matrix and the product of a matrix element (drift, quadrupole, dipole, etc.) by a particle array gives the new position in the 6D space phase of the particle after interaction with the element [199]. The code has been benchmarked on COXINEL with ASTRA [200], ELEGANT [201, 202] and OCELOT [203].

Figure 3.18 presents the beam size envelopes in the horizontal (red) and vertical (blue) plane along the COXINEL line simulated in the nonlinear case with BETA code. The nominal energy is well focused at the center of the undulator in both planes.

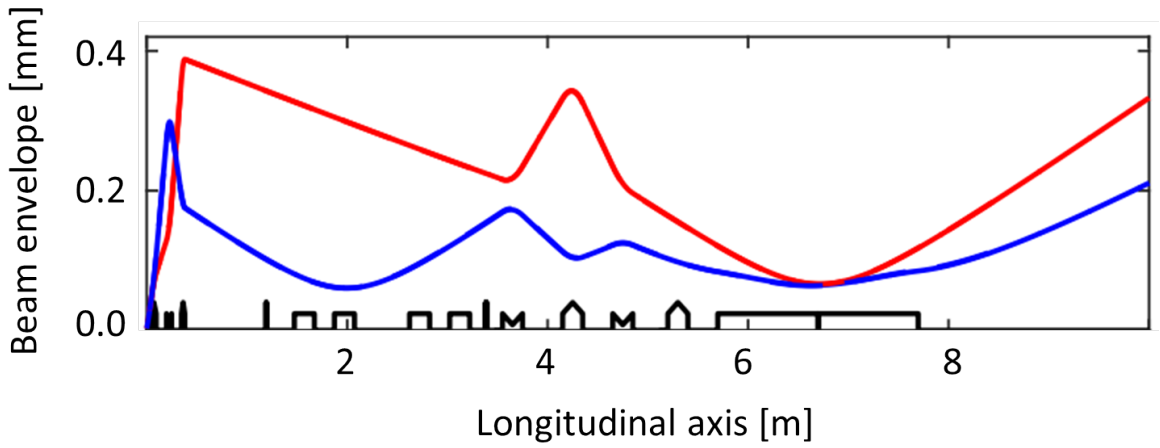

Figure 3.18: Simulated RMS horizontal (red) and vertical (blue) beam envelope from the source to the undulator using the chromatic matching optics.

The initial beam parameters of Table 3.4 are inserted in the code, and the electron beam is tracked along the line. The simulated electron beam parameters at the center of the undulator are shown in Table 3.5. The divergence and slice energy spread are reduced by a factor of ~10 and 5,

respectively. The beam is elongated by a factor of 5 in the longitudinal axis as the beam passes through the chicane, where the peak current decreases to ~430 A. The discrepency between the simulated values and calculated ones (presented in Table 3.4) is because the collective effects, space charge and CSR [204] are taken into account in the code.

Parameters	Symbol	Value	Unit
Energy	E	200	MeV
Normalized emittance	ε_N	1.37	π mm.mrad
Effective emittance	ε	3.5	nm
Divergence (rms)	$\sigma'_{x,z}$	70	μrad
Beam size (rms)	$\sigma_{x,z}$	50	μm
Bunch length (rms)	σ_l	10.1	μm
Slice Energy spread (rms)	σ_γ	0.23	%
Charge	Q	34	pC
Current	I_b	430	A

Table 3.5: Simulated parameters at the undulator center using the baseline reference case presented in Table 3.4. R_{11} = 10 and R_{56} = 0.4 mm.

3.4.1.2 Undulator radiation

The baseline reference case parameters (presented in Table 3.4) are used to examine the undulator radiation. Currently a 2 m long undulator of period of 18.16 mm with adjustable gap is installed at COXINEL (More details are reviewed in chapter 5). The FEL wavelength can thus be tuned by changing the undulator gap. The undulator has been optimized by measuring the magnetic field for gaps between 5 mm to 20 mm. The peak field B_{peak} versus gap g can be fitted using [205]:

$$B_{peak} = 3.37 \exp\left[-4.34\frac{g}{\lambda_u} + 1.12\left(\frac{g}{\lambda_u}\right)^2\right] \tag{3.15}$$

Figure 3.19 shows the peak field (a) and the corresponding resonant wavelength (b) versus gap using Eq. (7.1). A resonant wavelength of 160 nm can be achieved with a gap of 5 mm.

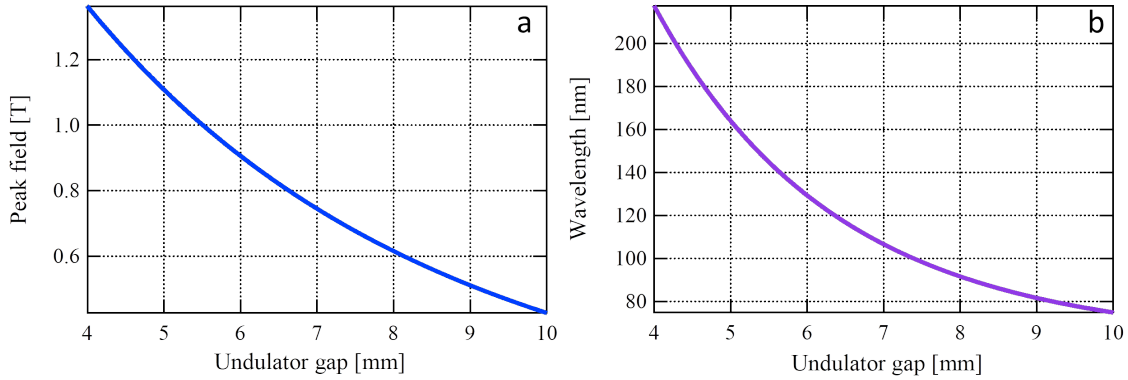

Figure 3.19: Undulator magnetic field (a) and the corresponding resonant wavelenth (b) versus gap. E = 200 MeV.

Fig. 3.20 presents the simulated spectral flux using SRW [134]. The radiation is peaked at the resonant energy (wavelength) of 7.2 eV (172 nm) with a relative bandwidth of 0.94% when using a magnetic field of 1.15 T that is achieved when setting the undulator gap at 5 mm.

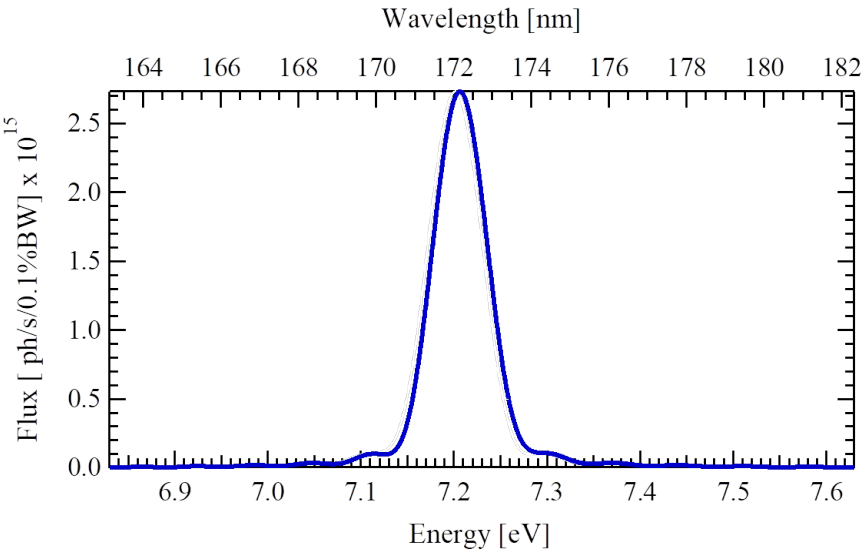

Figure 3.20: Simulated spectra flux of undulator radiation using the baseline reference case. Undulator characteristics are displayed in Table 3.3. Observation window of dimensions 1 mm x 1 mm placed 5 m from the undulator center.

3.4.2 SASE: FEL calculation

The FEL amplification is examined. The study assumes the FEL is based on Self-Amplified Spontaneous Emission (SASE) and lasing is achieved in a single pass of a laser plasma accelerator based electron beam through a planar undulator. The Ming Xi formulas, presented in chapter 2, are thus used for a quick evaluation of the FEL preformance.

The analytical beam parameters are used for the calculations. Table 3.6 presents the input values (R_{11}, R_{56}), the calculated beam parameters at the center of the undulator using Eq. (3.13) and the FEL performance using Ming Xi equations. The slice beam size and divergence highly depend on R_{11} whereas the slice enregy spread depends only on R_{56}. The P_{COX} corresponds to the power that can be observed at COXINEL after the 2 m undulator section (U18 length). It reaches a maximum for a magnification factor R_{11} = 10 and a chicane strength R_{56} = 0.2 mm.

Input			**Beam parameters**					**FEL perfomance**			
R_{11}	R_{126}	R_{56} mm	σ_L µm	σ_γ %	σ_x µm	σ'_x µrad	I_b kA	L_g m	P_{COX} MW	L_{sat} m	P_{sat} MW
5	-9.1	0.4	4.3	0.24	25.6	200	1	0.14	3	2.8	978
10	-4.5	0.4	4.3	0.24	28.2	100	1	0.12	17	2.5	1350
15	-3	0.4	4.3	0.24	39.7	66.7	1	0.14	1	3.1	1188
20	-2.3	0.4	4.3	0.24	52.3	50	1	0.17	0	3.7	1011
30	-1.5	0.4	4.3	0.24	78.1	33.3	1	0.23	0	5	737
10	0	0	1.6	1	26	100	2.8	0.17	0.2	3.5	1198
10	-1.1	0.1	1.9	0.71	27.2	100	2.3	0.13	8	2.7	1938
10	-2.3	0.2	2.5	0.45	27.9	100	1.7	0.11	70	2.4	2136
10	-9.1	0.8	8.2	0.12	28.3	100	0.5	0.15	0.5	3	583
10	-11.4	1	10.1	0.1	28.3	100	0.4	0.16	0.1	3.3	427

Table 3.6: FEL performance as the magnification of the beam (source to undulator center) and chicane strength are varied. R_{126} is calculated from Eq. (3.14).

Figure 3.21 shows that the COXINEL FEL power calculated as the beamline optics is changed

for the 2 m long undulator. The optimum case is for 0.2 mm chicane strength and 10 magnification factor, where the gain length is 0.11 m generating a power of 70 MW at 172 nm. The variation of the chicane strength provides an easy knob for FEL adjustment.

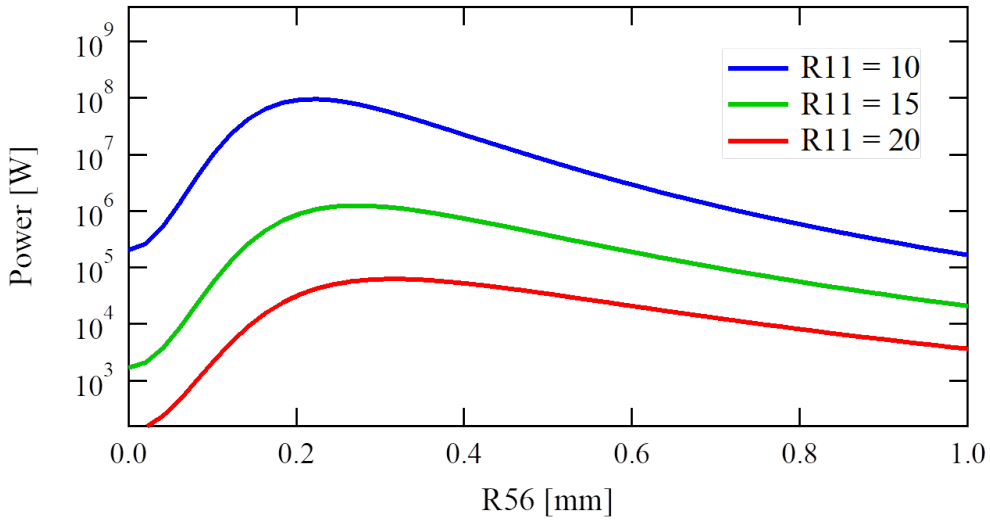

Figure 3.21: FEL power emitted after 2 m long undulator section as the magnification R_{11} and chicane strength R_{56} vary.

3.4.2.1 Beam parameter dependence

In this section, the initial beam parameters effect on the FEL performance are examined seperately while keeping the others as in the reference case (see Table 3.4). Table 3.7 and Fig. 3.22 present the power that can be measured at COXINEL for different parameters. These cases are quite optimistic and some are non realistic especially for an LPA electron beam. One can see that the power is very sensitive to the initial electron beam parameters especially the beam size.

Input		**Slice beam parameters**					**FEL perfomance**			
Initial parameter	**Value**	σ_L µm	σ_γ %	σ_x µm	σ'_x µrad	I_b kA	L_g m	P_{COX} MW	L_{sat} m	P_{sat} MW
Charge [pC]	10	2.5	0.45	27.8	100	0.5	0.31	0	6	124
	20	2.5	0.45	27.8	100	1	0.16	0.2	3.4	703
	30	2.5	0.45	27.8	100	1.5	0.12	15	2.6	1670
$\sigma_{\gamma 0}$ [%]	0.5	1.9	0.35	27.1	100	2.3	0.08	4626	1.8	4626
	1.5	3.4	0.47	28	100	1.3	0.14	1	3	1074
	2	4.3	0.49	28.1	100	1	0.18	0	3.7	593
σ'_{x0} [mrad]	0.5	2.5	0.45	26.5	50	1.7	0.11	158	2.3	2254
	1.5	2.5	0.45	29.9	150	1.7	0.12	14	2.6	1892
	2	2.5	0.45	32.6	200	1.7	0.14	1	3	1464
σ_{x0} [µm]	1	2.3	0.45	14	100	1.9	0.07	3588	1.5	3588
	2	2.4	0.45	22.3	100	1.8	0.09	2683	2	2689
	3	2.6	0.45	31.6	100	1.7	0.13	8	2.7	1815

Table 3.7: FEL performance as the electron beam parameters are changed individually while keeping the others as the baseline reference case (see Table 3.4).

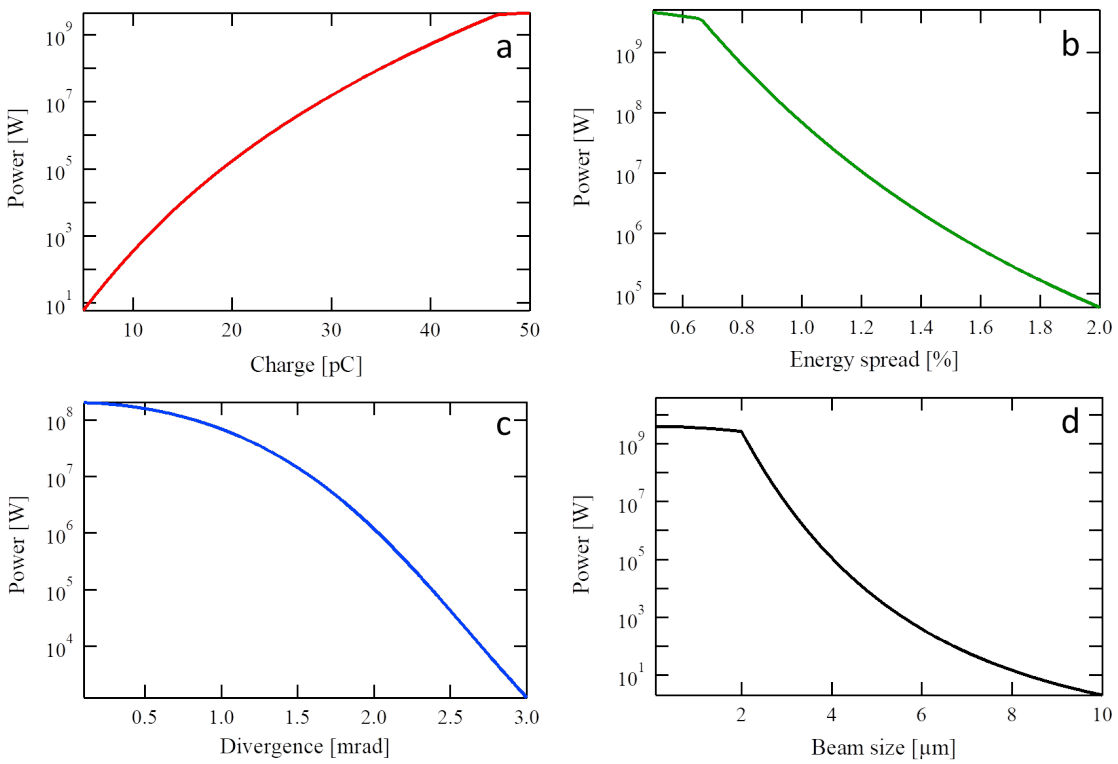

Figure 3.22: Power achieved at COXINEL as the charge (a), energy spread (b), divergence (c) and beam size (d) are changed individually while keeping the other initial parameters of Table 3.4. R_{11} = 10 and R_{56} = 0.2 mm.

3.5 Conclusion

The problems and the context of my PhD work has been described in this chapter. The path towards advanced and compact Free Electron Laser presents different approaches, such as the use of a compact undulator, that I'll describe in chapter 5, the EEHG FEL configuration as described in chapter 1, and the very challenging use of a laser plasma accelerator to drive a Free Electron Laser. The FEL studies are conducted in the case of COXINEL project using the baseline line reference parameters and its dependence on electron beam parameters. Amplification is possible using such parameters, but it is important to insist that they are rather optimistic as we shall see in chapter 8, where the real beam is introduced with different parameters.

Chapter 4

Short Period High Field Permanent Magnet Cryogenic Undulator

Large magnetic field short period undulators are of great interest for new generation of synchrotron radiation sources. These devices are of particular significance for the LUNEX5 project in view of shortening the undulator line. Cryogenic Permanent Magnet based Undulators (CPMUs) takes advantage of the enhanced performance of permanet magnets, where the magnetic field increases. With this enhancement of the peak field, one is able to shorten the periods and maintain a rather sufficient field. This enables to build more undulator periods for a given length or a more compact device [130, 206–209]. The use of Praseodymium Iron Boron $Pr_2Fe_{14}B$ operating at the liquid nitrogen temperature avoids the so-called Spin Re-orientation Transition phenomenon [210] and can be cooled down to liquid nitrogen gas 77 K (LN_2). The construction of three 2 m long 18 mm period (U18s) is presented alongside modeling of the magnetic design using RADIA code [129]. Another 3 m long CPMU and of period 15 mm U15 is being built for the LUNEX5 project. Magnetic measurements (using Hall probe and rotating coil) are carried out at room temperature, after the assembly of the magnets, to adjust the field errors. Then the undulator is cooled down to cryogenic temperature, and measurements are done to adjust the induced field errors [130, 209]. Radiation measured using a U18 undulator, installed at Synchrotron SOLEIL long-section beam line, is characterized and shows a high spectral purity [207]. The spectra can be even used for photon beam based alignment and undulator tuning for flux enhancement. These spectra give typical radiation produced in storage rings that LPA based applications aim at.

4.1 Undulator requirements

An undulator consists of periodic arrangements of dipole magnets that generate a sinusoidal magnetic field. An electron beam orbitting in an undulator produces a very intense and concentrated radiation in narrow energy bands as discussed in chapter 2. In an ideal undulator, the electron beam has a perfect sinusoidal trajectory resulting in constructive intereference of the emitted radiation at each period. For a real device, however, magnetic field errors induced by materials (magnets and poles), impurities and mechanical errors, can affect the radiation properties resulting in a degradation of the undulator performance.

4.1.1 Phase Error

Phase error arises from magnetic field errors along the undulator axis, such as variations in the peak field or the period length from one period to another [211]. In an undulator, electrons emit synchrotron radiation into a narrow cone around the forward direction. The cones overlap and photons emitted by a single electron interfere constructively from one period to another. Phase

error, resulting from magnetic imperfections, causes a change in the length of the electron tra-
1425 jectory yielding a phase lag between the electron and the photon. This lag induces destructive interference (see Fig 4.1) resulting in line broadening and intensity reduction of the emitted lines.

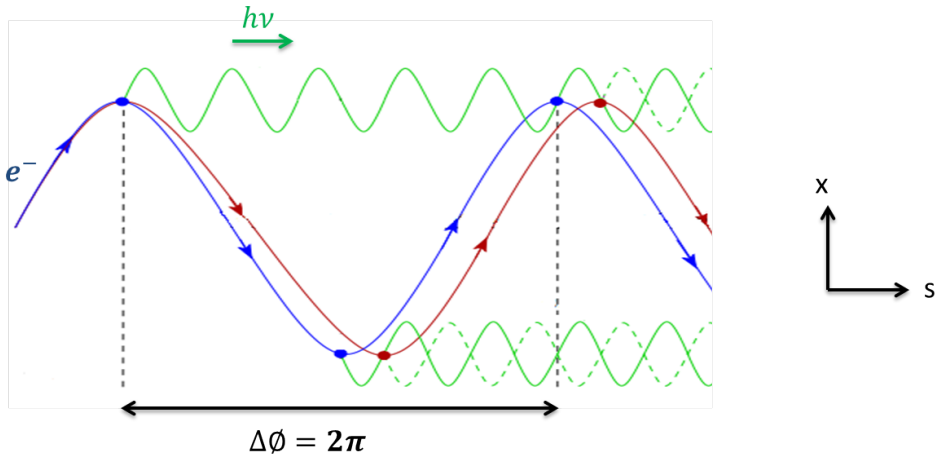

Figure 4.1: Electron trajectory in a perfect sinusoidal field (blue curve), where the emitted photons at each period add constructively. Trajectory with an error (red curve) that causes a phase slippage between the electron and the wave train, resulting in a destructive interference. Propagation of the photon emitted (green curve).

The time lag between the electron and the photon is:

$$\Delta t = t_{\gamma} - t_{e^-} \tag{4.1}$$

where t_{γ} and t_{e^-} are the time taken for the photon and electron respectively to reach point s.

Eq. (4.1) can be written as:

$$\Delta t = \frac{\phi}{\omega} = \frac{\phi\lambda}{2\pi c}$$

1430 where ϕ is the phase lag and ω the angular frequency of the emitted wave. By taking $t_{e^-} = \frac{l(s)}{v}$ and $t_{\gamma} = \frac{s}{c}$, the slippage in phase is expressed as :

$$\Phi = \frac{2\pi}{\lambda}\left(\frac{l(s)}{\beta} - s\right)$$

where $l(s)$ is the path traveled by the electron up to the point s.

The phase difference between the photon emitted and the electron for the half period of an undulator [212]:

$$\phi_i = \frac{2\pi}{\lambda_u(1+K_u^2/2)}\left(\frac{e^2}{m^2c^2}J(s_i) - \frac{K_u^2}{2}(s_i - s_0)\right) \tag{4.2}$$

where s_i and s_0 the initial and final position along the longitudinal direction, respectively, and $J(s_i)$ the second field integral expressed as:

$$J(z_i) = \int_{s_0}^{s_i} ds \int_{s_0}^{s} B_z(s')ds'$$

1435 The rms phase error ($\phi_{r.m.s}$) of an undulator is calculated as the root mean square of all phase differences in the $2N_u$ undulator half periods, and is expressed as follows:

$$\phi_{r.m.s} = \sqrt{\frac{\sum_{i=1}^{2N_u}(\phi_i)^2}{2N_u}} \tag{4.3}$$

A more efficient way to calculate the phase error for a given undulator, is by using B2E code [213], which is embedded in IGOR Pro. B2E is a software dedicated to the simulation of the radiation produced by a relativistic single electron traveling through an arbitrary magnetic field. The particle angle along the measured magnetic field is determined. Then, one can compute the produced electric field from the angle and finally the phase error is attained.

It has been shown that the reduction in on-axis brightness due to phase errors could be modeled well by the simple expression [211]:

$$\mathrm{R} = \exp(-n^2\phi_{rms}^2) \tag{4.4}$$

The intensity at high harmonics reduces drastically for large phase error (see Eq. (4.4)). For example, a phase error of 5°, the intensity reduction of the 5^{th} harmonic ($n = 5$) is 17%. Although the phase error is an important requirement and has a large effect on the radiation quality especially on high harmonics, it has been proven that its effect is less severe when electron beam emittance and energy spread are taken into account [214]. Typically a phase error of 2-5° is considered quite good for storage ring facilities. In the case of FEL, the phase error tolerance is ~10° [215] due to the fact that the FEL operates at a low harmonic.

4.1.2 Field Integrals

The electron angle, proportional to the first field integral along the undulator axis, and the position, proportional to the second field integral, should preferably remain constant as the electron exits the undulator. Thus one of the essential issues in designing an undulator involves the first $\mathrm{I}(x,z)$ and second integral $\mathrm{J}(x,z)$ along the horizontal axis that are defined as:

$$\mathrm{I}(x,z) = \int \mathrm{B}(x,s)ds$$

$$\mathrm{J}(x,z) = \int \mathrm{I}(x,s)ds$$

Concerning storage rings, the reference particle trajectory is a closed orbit along the storage ring and electrons that deviate from that orbit undergo betatron oscillations in the transverse plane. The undulator field integrals, if large, might displace the electron beam closed orbit and affect all the other users. In the case of a single pass FEL, the field integrals, in particulary the double integral, can influence the gain by dwindling the overlap of the radiation with the electron beam and prevent energy transfer to the FEL wave.

4.2 Undulator technology

The periodic magnetic field of an undulator is created by either permanent magnets or electromagnets (superconducting or normal conductors) placed next to each other and separated by equal distance. Superconductive undulators generate a sufficiently high magnetic field [216], but operate at a temperature around 4 K to enable critical current densities above 1000 A/mm^2 leading to the main setback of this device. It requires a high cost cooling infrastructure due to a great amount of heat load at temperatures where cryo-coolers are inefficient and expensive. As for permanent magnet undulators [217], they are able to function at room temperature and attain a fair magnetic field depending on the magnet material. Planar permanent magnet undulators commonly consist of two arrays of magnets positioned in a Halbach assembly [139] as shown in Fig. 4.2-a. Also introducing poles between the magnets enhances the magnetic peak field [218] (see Fig. 4.2-b). Vanadium permendur, a Cobalt-Iron-Vanadium alloy material, is commonly used for poles that saturates rather easily achieving a low permeability and high flux density.

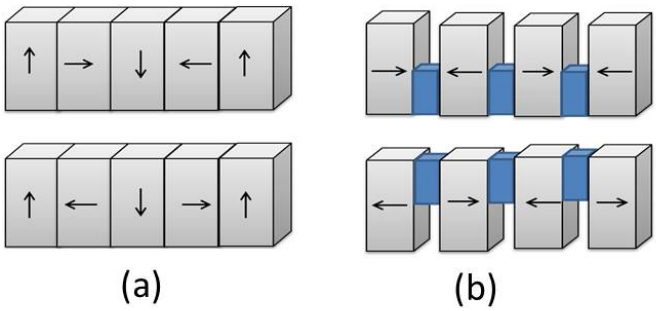

Figure 4.2: (a) Halbach geometry, (b) Hybrid.

4.2.1 Permanent magnet characteristics

Permanent magnets are characterized by their remanence field B_r, coercivity H_c (resistance against demagnetization), energy product BH_{max} (density of magnetic energy) and Curie temperature T_c (temperature at which the material loses its magnetism). Permanent magnets [219], used for undulators combine Rare Earth (R.E.) ferromagnetic elements with incomplete f-shells and transition metals with d-shells such as Iron, Nickel, and Cobalt. The rare earth magnets $RE_2Fe_{14}B$ present a crystalline structure with a very high magnetic anisotropy (stable alignment of the atoms) enable an easy magnetization along one direction. High magnetic moments at the atomic level combined with the high anisotropy results in a high magnetic field strength. Typical performance of $SmCo_5$ [220], $Nd_2Fe_{14}B$ [221, 222], and $Pr_2Fe_{14}B$ magnets are presented in Table 4.1. Magnets resistance to demagnetization [223, 224], and heat budget are an issue, for which intermediate grades of $Nd_2Fe_{14}B$ ($B_r \leq 1.26$ T; H_c =1900 kA/m) could be used. The choice of $Nd_2Fe_{14}B$ with high coercivity avoids demagnetization at ultra-high vacuum baking and radiation damage. A small inclusion of Dysprosium at magnet surface also allows for a larger coercivity with a slight decrease in remanence [225]. Typically, one should consider a coercivity larger than 1000 kA/m to avoid demagnetization at room temperature and larger than 2000 kA/m to prevent it at 120 °C (393 K), i.e. in baking conditions to improve vacuum in the case of in-vacuum undulators.

Material	B_r **[T]**	H_c **[kA/m]**	T_c **[K]**	**(BH)[kJ/m^3]**
$SmCo_5$	0.85	1400	720	150
Sm_2Co_{17}	1.1	2200	825	230
$Nd_2Fe_{14}B$	1.3	2300	585	370
$Pr_2Fe_{14}B$	1.2	1150	320	320

Table 4.1: Typical characteristics of permanent magnets used for undulators.

4.2.1.1 Permanent magnet undulators

Achieving short period undulator with sufficient magnetic field sets requirements for the magnetic material. The undulator peak field B_u can be written as a function of the undulator period λ_u and gap g with the following expression [205]:

$$B_{peak} = a.\exp[b.\frac{g}{\lambda_u} + c.(\frac{g}{\lambda_u})^2] \tag{4.5}$$

where a, b and c are constants. In the case of permanent magnet based undulators, the constants (a, b, c) typically take the values of 3 T, -4 and 1, respectively, for $0.1 < g/\lambda_u < 1$.

From Eq. (4.5), one can see that reducing the magnet size to shorten the period results in a lower magnetic field. Also increasing the magnetic remanence of a magnet is at the expense of its

coercivity (i.e. resistance against demagnetization). So in-vacuum undulators [226–228], which avoid the beam pipe undulator gap limitation, were adopted to reach a small gap with a sufficient magnetic field by placing the magnetic arrays in vacuum. The success of in-vacuum undulators has motivated to explore a novel method to fabricate undulator magnets with a very short period length, in the millimeter range. The usual permanent magnet based undulator technology employs accurately shaped magnet blocks, mounted on the non-magnetic holders, to be assembled and adjusted longitudinally on the rigid girders. For undulator periods below 1 cm, it becomes difficult to fabricate efficient magnets and poles holders for insuring the quality of the device. A first approach can consist of getting rid of the magnet holders in introducing slots onto the girder to the insertion of the magnets and poles. A more agressive solution relies on the suppression of the magnet blocks themselves, in developing a plate-type undulator magnet made of $Nd_2Fe_{14}B$ type magnetic material, thanks to an applied multipole magnetization method with a direction perpendicular to the plate surface, similarly to what is currently used for magnetic recording method in recording media [229, 230]. A 4 mm period length field has thus being acheived, with a 0.4 T peak magnetic field at 1.6 mm gap [230] with reasonable filed quality.

4.2.1.2 Cryogenic permanent magnet undulator

The idea of cooling down $RE_2Fe_{14}B$ permanent magnets, which increases the remanent field and coercivity, was proposed [206], leading to the concept of cryogenic permanent magnet undulators (CPMUs). For example, typical temperature coefficients for $RE_2Fe_{14}B$ are -0.11 %/°C for the remanent field and of -0.58 %/°C for the coercivity, i.e. decreasing the temperature by a factor of two enables to increase the remanent field by 10% and the coercivity by more than 50%. As the increase of coercivity is larger than the one of remanent field, one can even take a magnet grade that is less resistant at room temperature but with a higher remanent field. Measurements[231] of remanent field and coercivity for $Nd_2Fe_{14}B$ and $Pr_2Fe_{14}B$ grades versus temperature were performed, as shown in Fig. 4.3. For Neodymium grade at low temperature (130-140 °K), the remanent field starts to decrease due to the so-called Spin Re-orientation Transition (SRT) phenomenon [210], which exhibits a negative dependence of remanent field against temperature due to a change in the preferred direction of the magnetization with respect to the easy axis. In contrast, for the Praseodymium grades, the remanent field continues to increase at low temperatures down to 30 K. These magnets can be cooled down to lower temperature and attain a higher remanence. The coercivity of all grades maintains increasing with lower temperature.

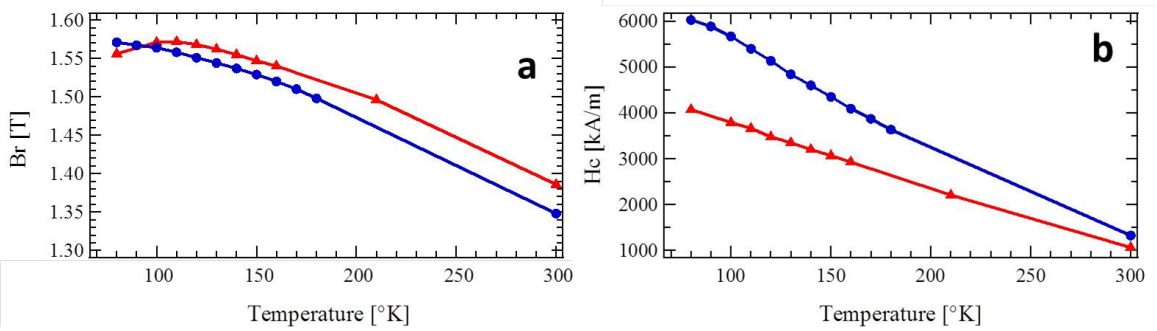

Figure 4.3: Temperature dependence of the remanent fields (a) and coercivity (b) of sintered $Nd_2Fe_{14}B$ (red) and $Pr_2Fe_{14}B$ (blue) magnets.

4.2.1.3 CPMU mechanical and thermal issues

The in-vacuum undulator operating at cryogenic temperature requires additional cooling channels where the inner components inside the vacuum chamber have to be modified so that liquid

nitrogen can be introduced for cooling down the magnets. Another solution is to implement compact cryocoolers that can cover very high heat load [206]. The operating temperature depends on the rare earth element that is used. Indeed, because of the SRT, $Nd_2Fe_{14}B$ cannot be directly operated at 77 K and thermal resistances have to be implemented. A $Pr_2Fe_{14}B$ based CPMU makes the cryogenic system simpler since the CPMU directly operates at the liquid nitrogen temperature. Between room and low temperature operation, the mechanical components are submitted to different thermo-mechanical changes, depending on the material thermal coefficients. By cooling down the system, the gap opens and the period shortens due to materials contraction at cryogenic temperature. Such a phenomenon has to be anticipated during the CPMU assembly at room temperature so that the phase error can be re-adjusted. Because of the increase in the field induces larger magnetic forces, an outer or inner spring system can be implemented to compensate the deformation of the girders [232, 233]. The majority of the CPMUs are not baked to take advantage of a high remanent field grade. Usually, the liquid nitrogen temperature performs a natural cryopumping leading to a gain of two orders of magnitude on the internal pressure when the CMPU is cooled down, and it can be then suitable for operation. The situation can be different if the temperature rises up and thus special care should be taken on the cleanliness of the separated components [234].

4.2.1.4 Issues with CPMU optimization and measurements

A crucial step in the success of the realization of a CPMU results from the measurement of the magnetic field produced at cryogenic temperature, where a specific measurement bench is needed. Standard benches usually consist of a Hall probe system and a rotating coil (or a stretched wire) for field measurements, mounted on stiff granites, enabling a precise positioning of the sensors and a sufficient reproducibility. For CPMUs, the Hall probe, including the linear motion system, has to be installed inside the vacuum chamber. It is thus needed to develop an embedded measurement bench compatible with ultra-high vacuum, cryogenic environment and small available volume.

Dedicated benches were firstly developed at SPring-8 [235, 236] with a Hall probe fixed at the extremity of a motioned tube inside the undulator prototype using bellows. At ESRF [237], the bench consists of a special vacuum chamber which includes a guide rail assembly equipped with a hall probe with a carriage that is magnetically coupled through the wall of the chamber to an external motorized axis. In addition, two stages of a stretched wire are mounted on either side of the vacuum chamber. At SOLEIL [238], a measurement system composed of a stretched wire motorized stages fixed on the undulator carriage and a Hall probe guide rail fixed on the floor through the lateral flanges of the vacuum chamber. A new bench, the so-called SAFALI, was developed [235, 236, 239] at SPring-8, consists in compensating the bad stiffness of the guide rail due to the absence of granite by an active feedback of the transverse position of the probe while propagating inside the undulator. Two laser beams that pass through two irises and illuminate position sensitive detectors measure the horizontal and vertical positions of the probe and its angle with respect to the undulator axis. The longitudinal position of the probe is acquired by an interferometer. In the second version, the whole rail guide is displaced vertically and horizontally by motorized stages to compensate the measured variations of transverse position. A Hall probe bench for CPMU measurement was also designed by HZB, taking up the feedback concept and extending it to the angle active correction [240]. In addition to the system of laser beams, irises and position sensitive detectors, the 3D interferometer returns information on the two last angles. The displacement is performed by six piezo motors embedded on the moving carriage.

4.2.1.5 Cryogenic undulator prototypes

Several Cryogenic permanent Magnet Undulators (CPMUs) prototypes were built at different laboratories.

At SPring-8, a 40 x 15 mm period $Nd_2Fe_{14}B$ based system has been built and optimized, with a rms 3.3° and 3.2° phase errors at 300 K and 130 K respectively. The temperature control at 140 K was enabled thanks to sheath heaters. It then appeared quite attracting to use $Pr_2Fe_{14}B$ magnets for being able to operate at lower temperature, thus with a larger magnetic field and coercivity.

A first prototype of 8 x 14.5 mm period using $Pr_2Fe_{14}B$ magnets (NEOMAX 53CR) and Vanadium Permendur poles has been measured in the NSLS Vertical Test Facility at liquid nitrogen and He temperatures with a slight increase of the rms phase error at lower temperature (3.1° at room temperature and 3.5° at 77 K). A second system developed at NSLS-II, using a grade of $Pr_2Fe_{14}B$ magnet that can be baked (NEOMAX CR47) led to a higher field than the previously employed grade (at 80 K : 1.12 T for the CR47 and 1.22 T for the CR53).

Three CPMU prototypes were built at SOLEIL. The first one, a 4 x 20 mm period hybrid $Nd_2Fe_{14}B$ system, shows a 11.5% increase of the magnetic field between room temperature and cryogenic temperature of 140 K the operation temperature. The second one (4x18 mm period) and the third one (4 x 15 mm period) $Pr_2Fe_{14}B$ hybrid type (NEOMAX CR53) takes advantage of the absence of SRT phenomena. The magnetic field grows by 13% between room temperature and cryogenic temperature of 77 K.

A 20 x 9 mm period $(Pr,Nd)_2Fe_{14}B$ (Vacuumschmelze /Vacoflux50) cryogenic undulator with $Co_{49}Fe_{49}V_2$ poles with saturation magnetization of 2.35 T, built jointly by Helmholtz-Zentrum Berlin and Ludwig-Maximilian-University München (LMU), shows a increase of the remanence by 20% and of the peak field at the fixed gap of 2.5 mm by 11% with partial saturation of the pole pieces from 300 K to 30 K. The second prototype with modified poles exhibits a larger field and it enables to observe synchrotron radiation using the MAMI-B beam line with 855 MeV beam.

RadiaBeam Technologies has also developed a 42 x 7 mm period cryogenic prototype using $Pr_2Fe_{14}B$ and Vanadium Permendur poles (design also considers to use textured dysprosium poles) [241]. A remaining thermal gradient was observed [242].

Table 4.2 summarizes the different CPMU prototypes built with their characteristics.

	λ_u **[mm]**	N_u	B_r **[T]**	**Gap[mm]**	B_{peak}
SPring-8	15	40	1.56	5	0.92
NSLS II	14.5	8	1.64	4.85	0.92
NSLS II n°2	16.8	8	1.4	5	1.12
SOLEIL n°1	20	4	1.58	10	0.57
SOLEIL n°2	18	4	1.58	10	0.5
SOLEIL n°3	15	5	1.55	10	0.43
HZB n°1	9	20	1.62	2.5	1.12
HZB n°2	9	11	1.62	2.5	1.28
Radiabeam	7	42	-	1.87	1.11

Table 4.2: Characteristics of developed CPMU prototypes.

4.2.2 Full scale Cryogenic Undulators

The construction of full scale devices to be installed for beamlines has started at ESRF[237, 243, 244], with a 2 m long full scale 18 mm period $Nd_2Fe_{14}B$ magnets (NEOREM 595t) hybrid CPMU. The peak field is increased by 6% when cooled down from 273 K to 150 K at gap 6 mm. The rms phase error slightly increases from room temperature (4.8°) to 150 K (5.7°), because of a residual

longitudinal temperature gradient. It was the first full scale (2 m length) CPMU to be built and installed for operation with an electron beam and a liquid nitrogen closed loop for cooling. A second CPMU has been built and installed at ESRF. Two additional $Pr_2Fe_{14}B$ based hybrid undulators are under construction.

At Paul Scherrer Institute[245, 246], a full scale 1.7 m long 14 mm period CPMU using $Nd_2Fe_{14}B$ (Hitachi NMXS45SH) magnets and Vanadium permendur poles, cooled with LN_2, had been measured with SAFALI (Self Aligned Field Analyzer with Laser Instrumentation). The measured phase error of 1.1° is similar to the one measured at room temperature, thanks to an in-situ correction method.

SOLEIL[130, 238, 247] had built and measured the first $Pr_2Fe_{14}B$ (grade CR53 with characteristics presented in Fig. 4.3) based full scale hybrid cryogenic undulator (2 m long, 18 mm period) cooled down to 77 °K with LN_2. The phase error at 5.5 mm gap at room temperature of 2.8° RMS increases up to 9° at 77 °K, but has been corrected down to 3° by shimming the rods. It is the first $Pr_2Fe_{14}B$ full scale cryogenic undulator installed on a synchrotron radiation facility, in use by Nanoscopium long beamline. Two new cryo-ready devices have been built at SOLEIL using a different $Pr_2Fe_{14}B$ grade with an enhanced coercivity (1912 kA/m) enabling to operate at room and cryogenic temperature. The first is installed for use at COXINEL project, and the second one is currently installed and in operation at SOLEIL Anatomix beamline [248]. Currently, SOLEIL is building a 3 m long CPMU of period 15 mm achieving a peak field of 1.7 T at 77 °K for a minimum gap of 3 mm.

At DIAMOND[249], a 17.7 mm period full scale $Nd_2Fe_{14}B$ (Vacodym 776TP) based hybrid CPMU has been built by Danfysik[250]. As temperature is decreased from 300 K to 157 K, the field is increased by 7.03% at 4 mm gap while for gap 10 mm the increase in field is 8.69%. At 157 K, the rms phase error is measured to be 3.5° at gap 4 mm.

Based on earlier prototypes, HZB[251, 252] currently installed a full scale cryo-cooled CPMU of 175 x 17 mm and 15 mm period length with a gap of 5 mm, investigating two cooling concepts based on liquid nitrogen and single-staged cold heads, respectively. $(Pr,Nd)_2Fe_{14}B$ magnets (Vacuumschmelze) treated with a grain boundary diffusion process for an enhanced stability, and Co-Fe poles are used. The gap size is measured using an optical micrometer. CPMU15 is developed for a plasma-driven FEL experiment in close cooperation with Hamburg University.

National Synchrotron Radiation Research Center (NSRRC) on TPS (Taiwan), in collaboration with Neomax Engineering Co [253–255] has built a 2 m long 15 mm period CPMU. it is equipped with a force compensating spring module to handle the strong magnetic forces, enabling to acheive a phase error lower than 2 ° in the 4-10 mm gap range. A CPMU magnetic measurement bench is developed and tested, with a carriage and optical components been redesigned to improve the reproducibility. New devices are foreseen.

Two CPMU have been built and measured at Shanghai Synchrotron Radiation Facility (SRRF, China) [256] in order to equip the ring with three devices. A first one (80 periods x 200 mm) uses $Nd_2Fe_{14}B$ magnets (N48H grade), and reaches a peak field of 1.07 T at 6 mm gap at cryogenic temperature. The second one uses $Pr_2Fe_{14}B$ magnets (P46H grade), and reaches a peak field of 0.91 T with a phase error of 4.4° at 6 mm gap at cryogenic temperature. Three are to be built for being installed on the ring.

Table 4.3 summarizes the different CPMU built with their characteristics.

	λ_u [mm]	N	B_r [T]	Gap[mm]	B_{peak}	Status
SLS n°1	14	120	>1.5	3.8	1.186	installed
SLS n°2-5	17					planned
ESRF n°1	18	107	1.16	6	0.88	installed
ESRF n°2	18	107	1.37	6	0.99	installed
ESRF n°3	14	140	1.62	5	1	installed
ESRF n°4	18					construction
ESRF n°5	20					construction
ESRF n°6	18					construction
ESRF n°7-9	16					construction
Diamond	17.7	113	1.32	5	1.04	installed
Diamond	17.7	113	1.32	4	1.263	installed
Diamond n°1-3	17.6	113	1.62	4.6		construction
Diamond n°4	16.7	125	1.62	4.6		construction
Diamond n°5-6	15.6	128	1.62	4.6		planned
SOLEIL n°1	18	107	1.58	5.5	1.15	installed
SOLEIL n°2	18	107	1.57	5/5.5	1.12	installed
SOLEIL n°3	18	107	1.57	5/5.5	1.12	installed
SOLEIL n°4	15	200	1.57	3		construction
IHEP	13.5	140		5	1	test
TPS	15	133	1.7	4	1.3	built
SPring-8	15	93	1.48	3	1.64	built
HZB n°1	17	88	1.62	5.5	1.12	installed
HZB n°2	15	175	1.6	2	2.08	construction
SSRF n°1	20	80	1.53	6	1.07	test
SSRF n°2	20	80		6	0.91	test
SSRF n°3						construction

Table 4.3: Characteristics of full scale CPMU developed.

4.3 Design and Construction

Let's focus now on the manufacturing of CPMUs at synchrotron SOLEIL, in which two are currently commissioned at the storage ring, one is installed at COXINEL and one is still under construction for the LUNEX5 project.

4.3.1 Undulator magnetic design

The design calculations have been done using RADIA [129], a three-dimensional program for calculation of static magnetic fields. The program uses IGOR Pro as front end and was exclusively developed for designs of insertion devices of all types.

Figure 4.4 presents the design of the magnets and poles used for three CPMUs of period 18 mm (U18).

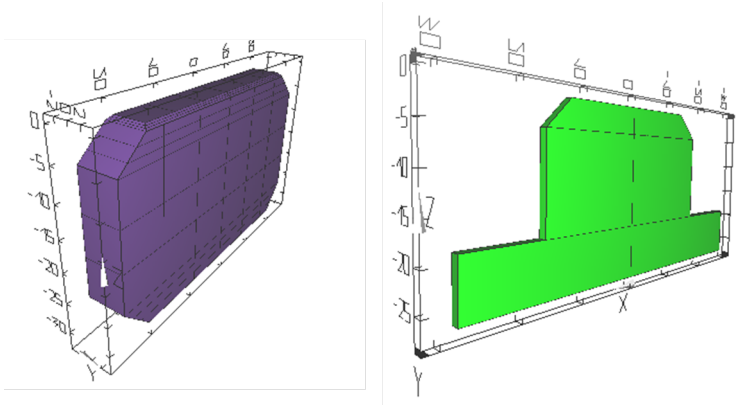

Figure 4.4: Magnet (purple) and pole (green) designs.

The first CPMU U18°1 consisted of two types of holders, a magnet and a magnet plus poles (see Fig. 4.5-a). As for the U18°2 and U18°3 one type of holders is used for a magnet and two half poles (see Fig. 4.5-b). The two half poles configuration increases the possibilities for magnet swapping during field optimization.

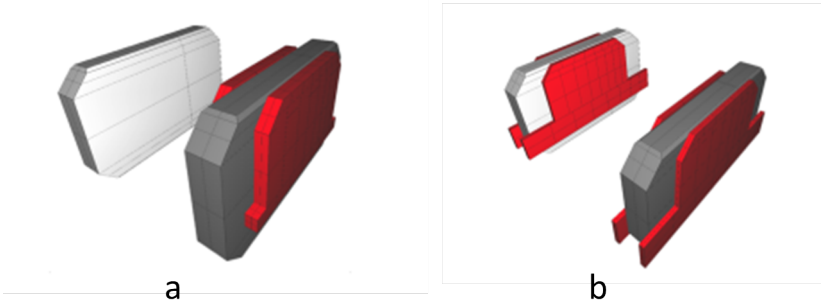

Figure 4.5: Magnet holders used for U18n°1 (a) and for U18n°2-3(b). (Grey) magnets, (red) poles.

Table 4.4 presents the undulator U18 magnet and pole characteristics used for the RADIA model shown in Fig. 4.6. For a gap of 5.5 mm, the peak field computed is around 1.05 T and increases to 1.15 T at cryogenic temperature.

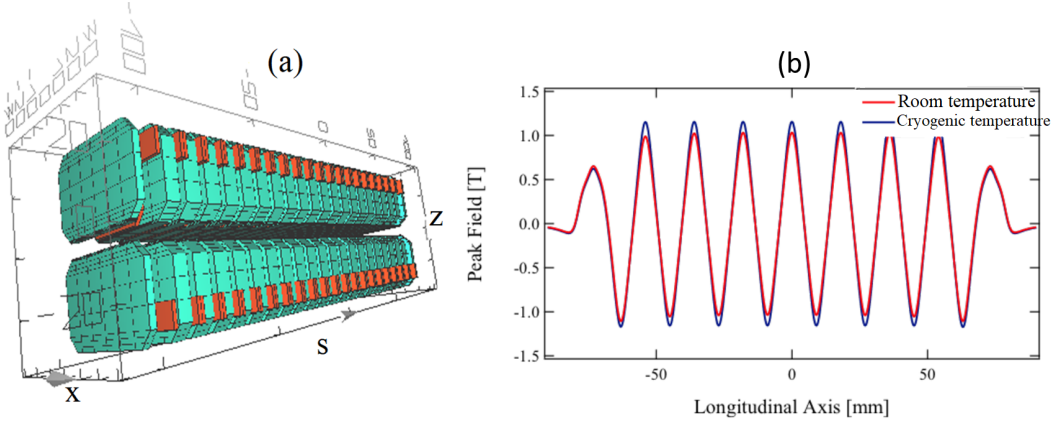

Figure 4.6: (a) Design with 10 periods length of 18.16 mm and magnetic gap of 5.5 mm. Magnet and pole charactertistics are presented in Table 4.4. (b) Magnetic field computed from the design of (a) along the undulator's axis at z = 0.

Item	Unit	Value
Technology	Hybrid	
Magnet material	$Pr_2Fe_{14}B$ (CR53)	
Remanence	1.35 at 300 °K	T
	1.57 at 77 °K	T
Coercivity	1300 at 300 °K	kA/m
	6060 at 77 °K	kA/m
Magnet size (x, z, s)	50 × 30 × 6.5	mm x mm x mm
Pole material	Vanadium Permendur	
Pole size (x, z, s)	33 × 22 × 2.5	mm x mm x mm
Period	18	mm
Gap range	5.0 - 30	mm
Length	2	m
n° of periods	107	

Table 4.4: U18 design characteristics.

Figure 4.7 displays the magnetic field as a function of the gap using RADIA model, for U18 at both room and cryogenic temperature. The field is enhanced by almost 12% from 293 K down to 77 K.

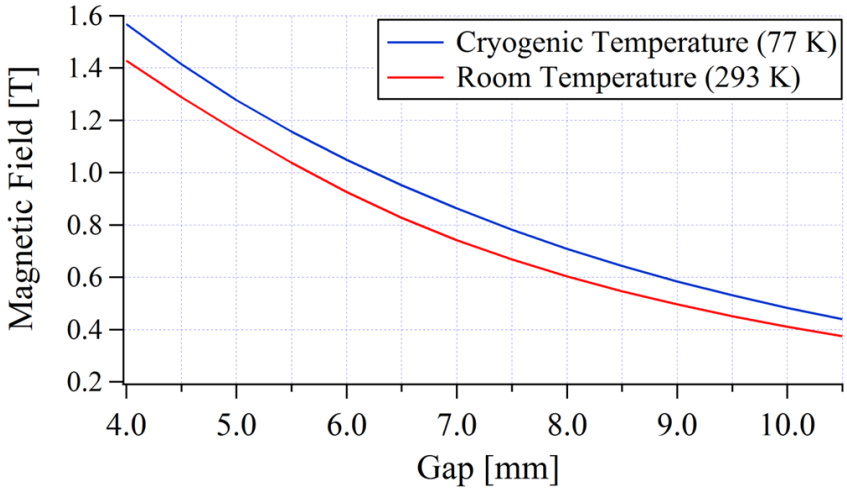

Figure 4.7: Field peak computed by RADIA as a function of the magnetic gap of the U18 undulator. Cryogenic temperature (λ_u=18 mm , B_r=1.57 T) and room temperature (λ_u=18.16 mm , B_r=1.32 T).

Table 4.5 presents the characteristics of U15 cryo-ready undulator, which is a prototype undulator for LUNEX5 project. The design is modeled using RADIA shown in Fig. 4.8 alongside the field computed along the longitudinal axis. The peak field is found to be ~ 1.5 T at room temperature and increases to 1.7 T at cryogenic temperature for a minimum gap of 3 mm.

Item	**Unit**	**Value**
Technology	Hybrid	
Magnet material	$Pr_2Fe_{14}B$ (CR53)	
Remanence	1.32 at 300 °K	T
	1.55 at 77 °K	T
Coercivity	1350 at 300 °K	kA/m
	7000 at 77 °K	kA/m
Magnet size (x, z, s)	50 × 30 × 5.5	mm x mm x mm
Pole material	Vanadium Permendur	
Pole size (x, z, s)	33 × 22 × 1	mm x mm x mm
Period	15	mm
Gap range	3.0 - 30	mm
Length	3	m
n° of periods	200	

Table 4.5: U15 design characteristics.

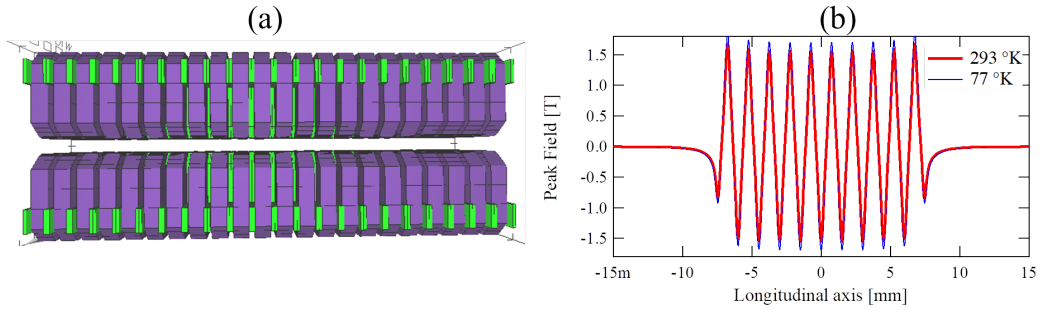

Figure 4.8: (a) Design with 10 periods length of 15 mm and magnetic gap of 3 mm. Neodymium Iron Boron material characteristics with a field remanence of 1.32 T achieved for Praseodymium magnet at room temperature. The Vanadium Permendur material characteristics as defined in Radia labeled "AFK502". (b) Magnetic field computed from the design of Figure (a) along the undulator's axis at z = 0.

CPMUs can be built with a smaller period, however the mechanical design to support the undulator gets harder. The peak fields versus gap of different period length undulators are computed with RADIA software using a newly introduced $Pr_2Fe_{14}B$ grade with remanence of 1.7 T shown in Fig. 4.9. The field dependence on the gap g can be expressed as [205]:

$$B_{peak} = a.\exp[b.\frac{g}{\lambda_u} + c.(\frac{g}{\lambda_u})^2] \tag{4.6}$$

where a, b, c are the fitting coefficients, shown in Table 4.6, that are valid for our magnet and pole geometry presented in Fig. 4.4.

Period	**Magnet width**	**Pole Width**	a	b	c
mm	mm	mm	T		
18	6.5	1.25	3.74	-4.05	0.69
15	5	1.25	3.89	-4.02	0.52
12	4	1	3.98	-4.08	0.67
10	3.5	0.75	3.53	-3.65	0.40

Table 4.6: Width of magnets and poles for different periods, as well as the coefficients of the fitting curves.

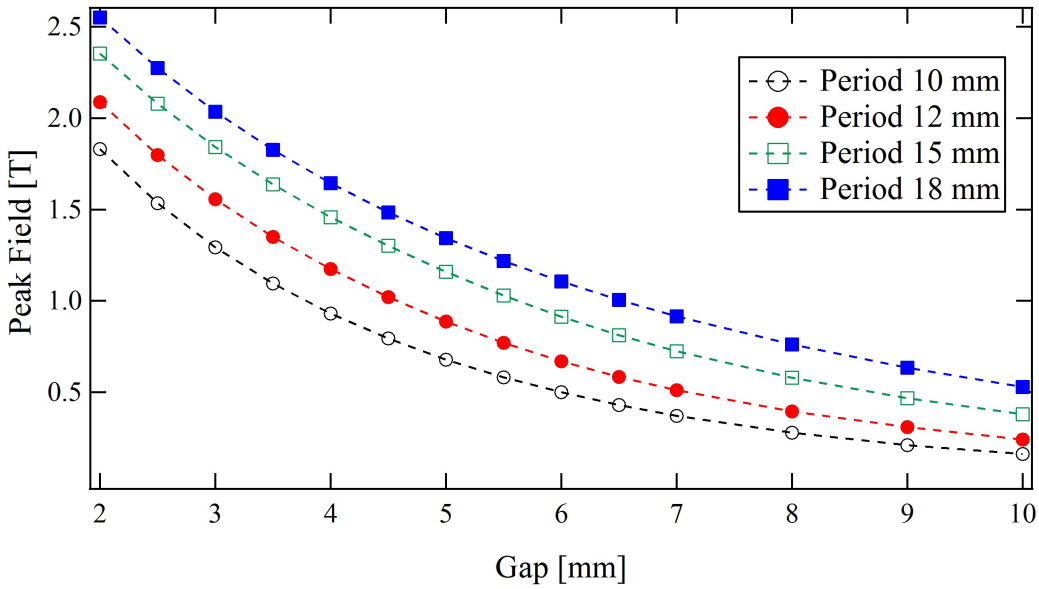

Figure 4.9: Peak field versus the magnetic gap. (■) period 18 mm, (□) period 15 mm,(•) period 12 mm, (○) period 10 mm. Magnet and pole sizes are presented in Table 4.6. Remanence field of 1.7 T. Magnet and pole geometric shape are presented in Fig. 4.4.

4.4 Mechanical Design

Figure 4.10-a presents the mechanical design of the cryogenic undulator U18 inspired from the in-vacuum undulator [257]. The carriage is constituted of a metallic base where the frame is welded. Two out-vacuum (external) girders are fixed on the frame and can move vertically thanks to two series of sliders. The magnetic systems (permanent magnets, poles and their mechanical supports) are fixed on two in-vacuum girders connected to the external ones by 24 rods. The in-vacuum girders are separated by an adjustable gap from minimum value of 5.5 mm to maximum value of 30 mm enabled by two steps motors Berger Lahr VRDM3910. A third step motor is used to move vertically the undulator over a 10 mm range in order to align it in the vertical direction with the electron beam axis. The in-vacuum girders with the magnetic system are installed in a vacuum chamber equipped with Ion pumps, Titanium sublimation pump and instrumentation to ensure an Ultra High Vacuum in the vacuum chamber during the operation with electron beam. Cu-OFHC tapers are fixed on the vacuum chamber and on the in-vacuum girders to avoid an increase of the impedance seen by the electron beam when it crosses the undulator. A copper absorber is installed at the downstream of the undulator inside the vacuum chamber to collect the undesired photon beam coming from the upstream bending magnet. The absorber is cooled down with water at room temperature. A 100 µm Cu-Ni foil is placed on the magnetic system and stretched at the extremities of the undulator by a spring tensioner system. It conducts the image current generated by the electron beam when it crosses the undulator at a very close position from the magnetic system. Permanent magnets and different parts of the undulator inside the vacuum chamber are equipped with 55 temperature sensors (thermocouples and platinum sensors PT100), which are fixed on the girders, LN2 tubes, modules holders, and directly on magnets, in order to measure the temperature during the cooling down and storage ring operation. The liquid nitrogen crosses the in-vacuum Aluminum girders through a 12 mm diameter hole, where its inner surface is cooled directly by liquid nitrogen, guaranteeing a better temperature distribution and thus a smaller thermal gradient along the magnetic system [130]. The liquid nitrogen can directly circulate inside the inner girders. The mechanical design of U15, presented in Fig. 4.10-b, still imposes difficulties due to the complexity of the device that it 3 meters long. It has more or less the same design as U18

but with 36 rods connecting the in-vacuum girders to the external ones.

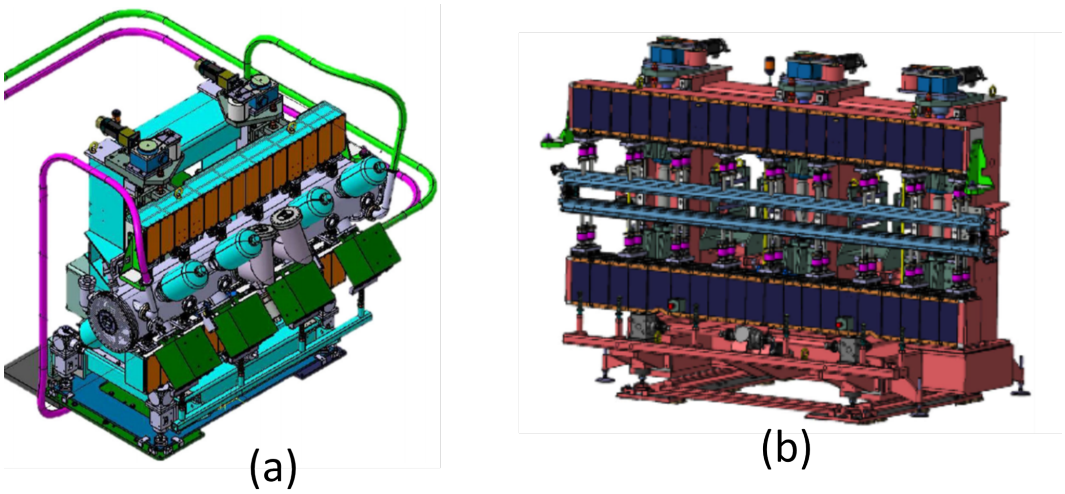

Figure 4.10: U18 (a) and U15 (b) mechanical designs.

4.5 Magnetic Measurements

In this section, the Hall probe and rotating coil concept are introduced.

4.5.1 Hall Probe

The Hall probe is a sensor that induces an electric field when there is a perpendicular magnetic field applied and used to measure the local field of a device. Consider a conducting rod (probe) connected to a power supply that delivers current through it. As it is passing through a magnetic field, the positive and negative charges are vertically separated as illustrated in Fig 4.11. Thus, a measurable potential called Hall potential is formed between the two ends of the probe and is proportional to the magnetic field.

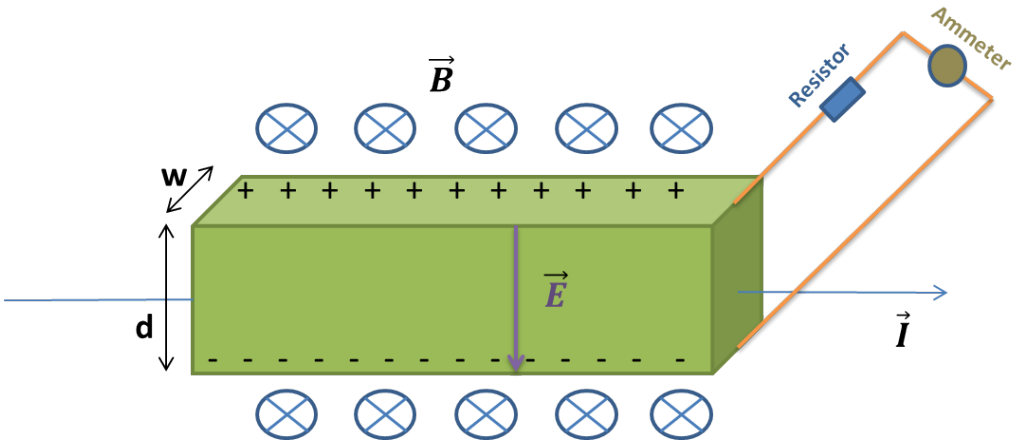

Figure 4.11: Schematic view of the physical concept behind the Hall probe. 'd' and 'w' are the thickness and width of the rod respectively, E the electric field induced, B the magnetic field, and I the current traversing the rod.

To achieve a better accuracy, one has to increase the Hall coefficient that is inversely proportional to the charge density. Thus, Hall probes are commonly made of semi conductors due to their low charge density. Another term that affects the sensitivity is the temperature. Hall effect is a temperature dependent phenomenon, so it should be equipped with a regulation system to provide a homogeneous and constant temperature. The probe can detect slow and small fluctuations in the magnetic field with a high accuracy of around 10^{-5} T.

Before undulator field optimization, the Hall probe is calibrated using a dipole and a Nuclear Magnetic Resonance (NMR).

4.5.2 Rotating coil

This device is used to measure the magnetic field horizontal and vertical field integrals produced by the undulator. The concept is to attach a conducting wire to two rotating rails, and connect it to a voltmeter as shown in Fig 4.12 in order to measure the flux variation. The coil swaps along the x axis with its surface directed in x and then in z to measure the horizontal and vertical field integrals.

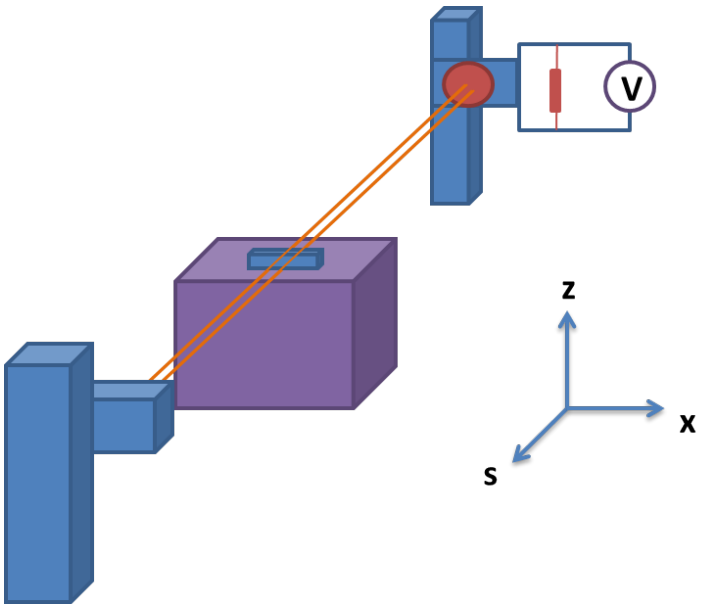

Figure 4.12: Illustration of the rotating coil connected to a voltmeter. Object to be measured (purple block).

Starting from Maxwell equation:

$$\vec{\nabla} \times \vec{E} = -\frac{\partial \vec{B}}{\partial t} \tag{4.7}$$

where S the surface area between the wires, integrating equation 4.7 over S:

$$\iint \vec{\nabla} \times \vec{E}.d\vec{S} = -\iint \frac{\partial \vec{B}}{\partial t}.d\vec{S} \tag{4.8}$$

Using the divergence theorem, one gets $\oint \vec{E}.d\vec{S} = -\frac{\partial}{\partial t}(\vec{B}.\vec{S})$. The field generated by the object and the surface area of the coil are constant. The only variable is the angle between the field and the area due to the rotation of the coil. Hence:

$$\Phi_{emf} = B.S.\omega.\sin(\omega t) \tag{4.9}$$

where Φ_{emf} the electromotive force and ω the angular velocity of the coil. So by connecting a voltmeter to the coil, one is able to calculate the induced voltage, and thus the magnetic field

integral.

4.6 Alignment tools

4.6.1 Laser Tracker

This device measures objects by determining the positions of optical targets held against them. First, the laser tracker is set on a tripod with a clear view of the object to be measured. Then a target called retro-reflector (precise machined mirrors) is taken from the base of the laser tracker and carried to the object to be measured, while moving slowly to allow the laser tracker to follow the movement of the target. Finally the target, which is a spherically mounted retro-reflector (SMR) resembling a ball bearing with mirrored surfaces, is placed against the object and prompt measurements are taken at selected points. These measurements are imported into a 3-D visual software called Innovmetric Polyworks (as shown in Fig 4.13) to plot the points and to calculate any deviation from the correct position, which is set as a reference. Laser tracker is used to measure the deformation of the girders in both the longitudinal and transverse plane. It is also used to align the Hall probe with the girders with a precision of 80 µm.

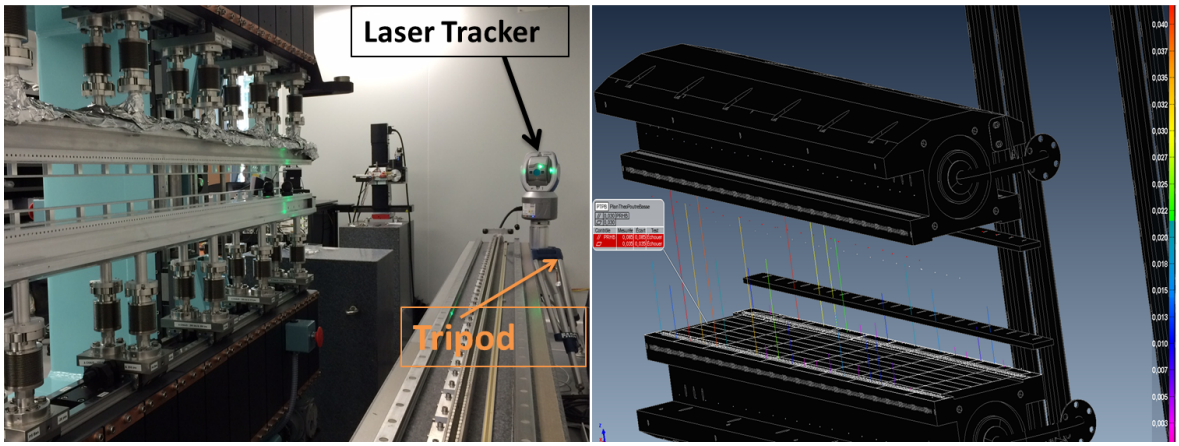

Figure 4.13: FARO Laser Tracker Vantage held on a tripod measures the position of the girders and displays them with Innovmetric Polyworks (figure on the right).

4.6.2 Comparator

The comparator is also used to double check the alignment of the laser tracker. It is connected to a rail and a carriage, which enables it to swap back and forth along the longitudinal axis of the bench. This method is to detect any deformation within the girders after placing them on the bench. This step is crucial considering the fact that the array of magnets should be as straight as possible, so any deformation will cause a change in the magnets altitude at a certain position, and thus import field fluctuations.

4.7 Undulator magnetic assembly

The first CPMU of period 18 mm (U18n°1) consisted of two magnet holders as presented in Fig. 4.5. Concerning the other CPMUs, the first step is to build modules composed of a magnet and two half poles on its side mounted on a support. A comparator is used to ensure that the magnet and poles have almost the same altitude as shown in Fig.4.14. The poles are usually higher than

the magnets by ~100 µm, so mechanical shimming is done to decrease poles height and ensure a difference no larger than 15 µm.

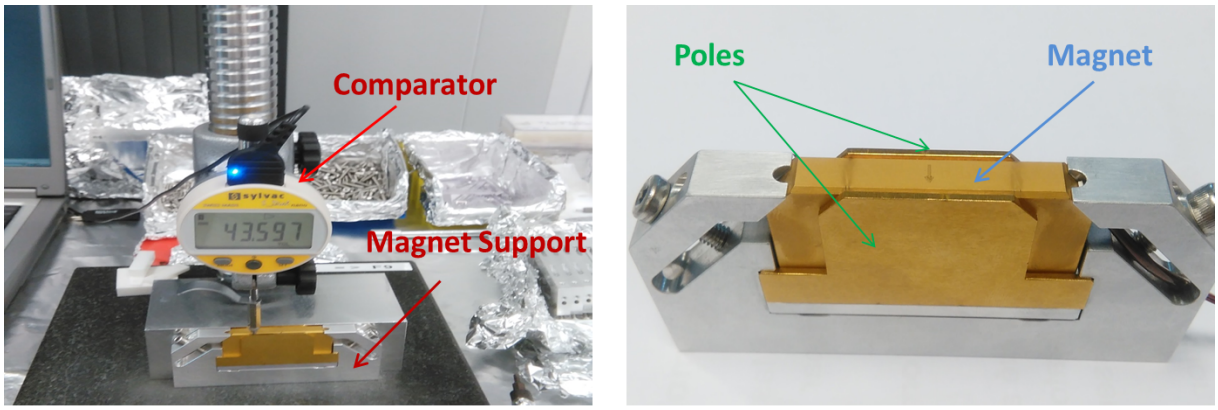

Figure 4.14: (a) Comparator (Sylvac Sdial Nano) and its dial indicator used for measurements of the poles and magnet altitude. (b) A module where the magnet and poles are built on a support.

After the mechanical shimming, each module undergoes magnetic measurements using both the rotating coils and the Hall probe. The module is placed on the bench where the Hall probe and the rotating coil are aligned to the bench as well as the rotating rails, using the laser tracker. The Hall probe covers a distance of 0.5 m across the magnetic center of the module along the longitudinal direction of the bench, and measures the local field. The rotating coil measures the first integral, in both the horizontal and vertical, by scanning across the magnet.

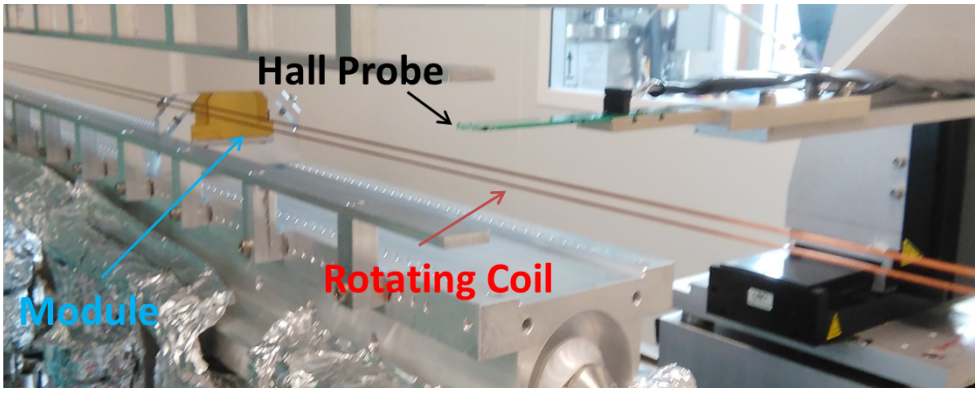

Figure 4.15: Hall probe placed on a support that can be easily adjusted in the three planes to have a good alignment with the bench.

Fig 4.16 displays a measurement on one of these modules. The field integral is null at a distance approximately 5 cm away from the magnet edges. As the Hall probe approaches the magnet, it measures both a negative and positive voltage, corresponding to the direction of the field lines, and reaches zero at the magnetic center.

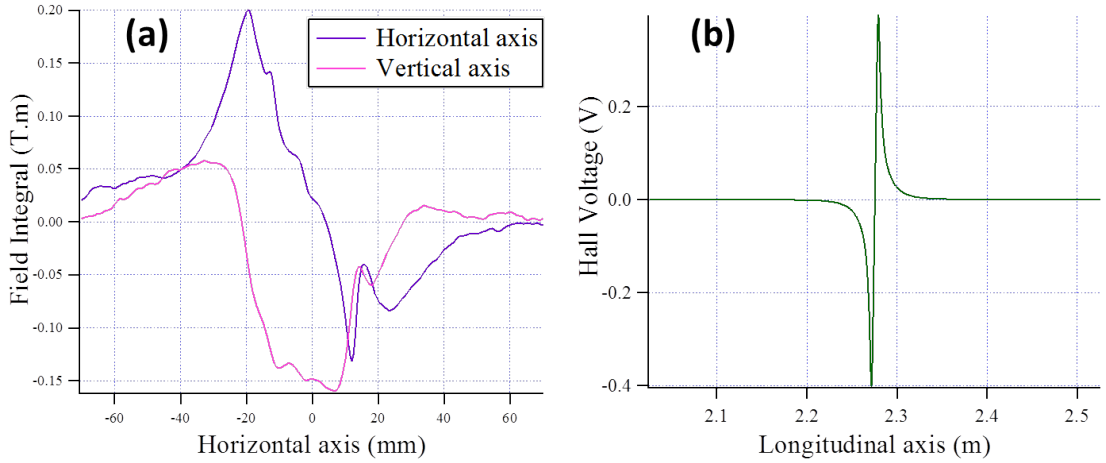

Figure 4.16: (a) Measurements of the vertical I_z (pink) and horizontal I_x (purple) field integrals of a module using the rotating coil. (b) Hall probe measurement of the same module, and by multiplying the voltage with the Hall coefficient, one is able to compute the magnetic field.

After the measurement of all the modules, a period (4 modules) are mounted on the Aluminum girders. An optimization software called ID-Builder, developed at SOLEIL [258], is used to select the most convenient position of modules to ensure the best magnetic field performance possible (low field integrals and multipoles). Then period by period the modules are sorted and mounted on the Aluminum girders.

4.8 Room Temperature measurements and optimization

After the assembly of all the modules, the undulator is optimized using magnetic measurements to correct the phase error and field integrals.

4.8.1 Phase error optimization

The phase error optimization mainly consists of mechanical shimming (adding small shims) to adjust the altitude of the poles or magnets and ensure a small deviation of the peak field from one period to another.

Table 4.7 presents the iterations done to correct the phase error of the three U18 undulators. For U18 n°1, 92 elements (magnets and pole) were shimmed individually to achieve a phase error of 2.8°. As for the other CPMUs, the phase error was quite low after the rod adjustments, thanks to the shimming process for each module before assembly as presented in section 4.7.

U18	Iteration 1	Iteration 2	Iteration 3	Phase error
n°1	Taper correction	Rods adjustment	Shimming	2.8°
n°2	Taper correction	Rods adjustment	-	2.3°
n°3	Taper correction	Rods adjustment	-	2.45°

Table 4.7: Phase error correction of the three CPMUs.

4.9 Cooling down

Figure 4.17 presents the magnet temperature and vacuum pressure variation during the cooling down of the cryogenic undulator using a cryocooler system (Cryotherm Bruker). The magnets

reach liquid nitrogen temperature of 77 K after 6 hours. The undulator was not baked in order to avoid demagnetization due to low coercivity for the selected magnet grade. However the undulator vacuum pressure drops quite rapidly due to the cold mass which acts as a cryo-pump.

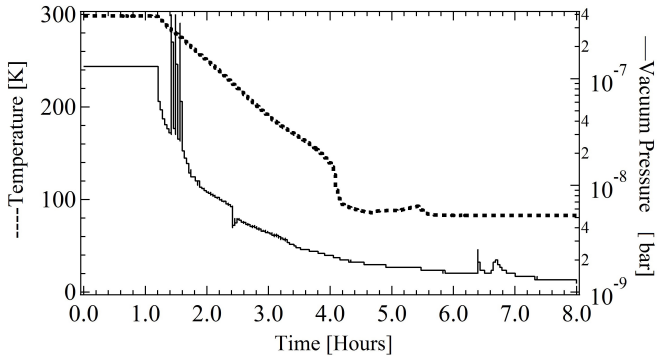

Figure 4.17: Cooling down of the cryogenic undulator. (solid line) Undulator vacuum pressure, (dashed line) permanent magnets temperature.

4.9.1 Field integral optimization

Higher order field errors arise primarily from the small minor component magnetic field errors in the permanent magnet blocks between adjacent poles, producing small field integral errors in the magnetic gap. These errors are additive and are equivalent to a single field integral error produced by a single magnetic field component. To correct it, an equal field component in the opposite sense is added to null the field integrals. This is where Multiple Trim Magnets (MTM) comes into play. MTM, also known as magic fingers, are an arrangement of magnets to correct the multipole field components in undulators. The concept behind it, is using transverse arrays of very small permanent magnets placed at the undulator extremities.

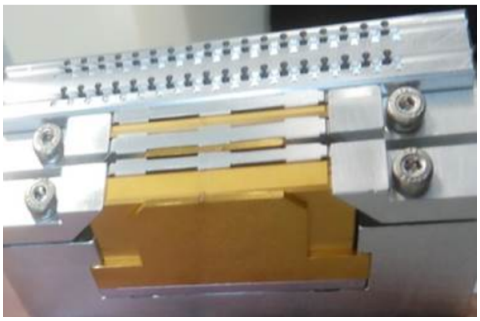

Figure 4.18: Magic fingers: Small cylindrical magnets can be added to null down the field integrals.

Figure 4.19-left presents the vertical field integral and the horizontal field integral of the three CPMUs versus transverse position at minimum gap of 5.5 mm at the end of the assembly. After the corrections, the field integrals present a smoother variation and the on-axis integral is less than 0.4 G.m and the higher off-axis field integral are reduced from 3 G.m to less than 1 G.m. Figure 4.19-right presents the electron beam trajectory calculated from the magnetic field measurements versus the longitudinal position at the end of the assembly. The horizontal position at the exit of the undulator after the use of magic fingers is kept below 2 µm.

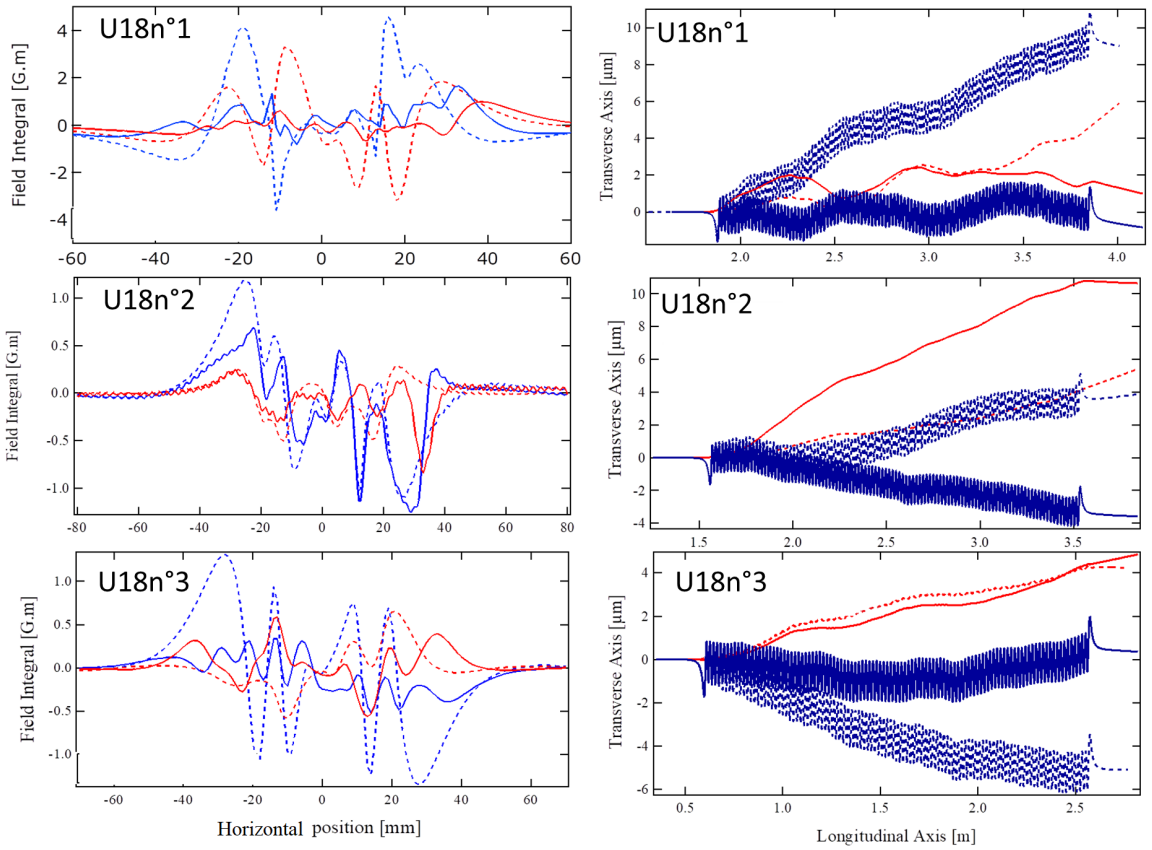

Figure 4.19: (Left) Field integrals versus horizontal position measured using a rotating coil. (Right) Calculated trajectory from the Hall probe measurements along the longitudinal axis. Measurments at 5.5 mm gap for the three U18 undulators before (dashed) and after (line) magic fingers corrections. (Red) vertical, (blue) horizontal. Field integrals precision is ~ 0.05 G.m.

4.10 Cryogenic temperature measurements and optimization

Before cooling down, the girders are dismounted to install the vacuum chamber, as well as the benches inside it to perform measurements at cryogenic temperature.

Figure 4.20 presents the electron trajectory at room temperature and cryogenic temperature calculated from the measured magnetic field. Despite the cooling down, the electrons trajectory position is kept below 4 µm along the undulator.

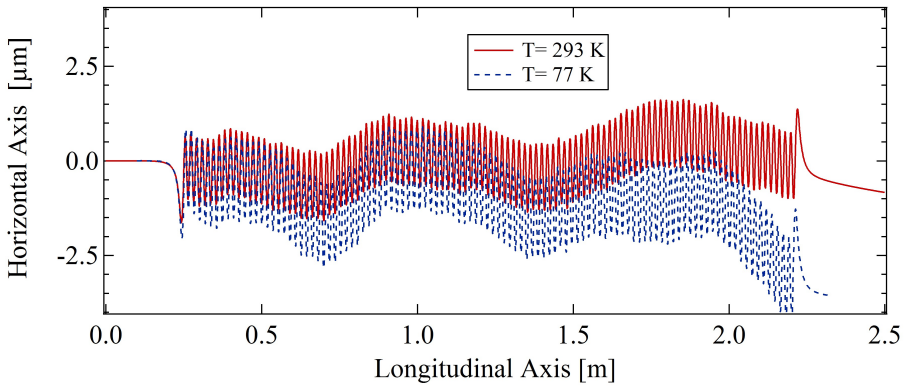

Figure 4.20: Electron beam trajectory calculated from the measured magnetic field of U18n°1. (line) at room temperature 293 K, (dashed) at cryogenic temperature 77 K after rod length correction.

In the case of U18 n°1, the phase error has been corrected (using shims) at room temperature to 2.8^o. After the cooling down, the phase error is increased to 9.1^o because of mechanical contractions of the rods that induces a periodic phase error and some local errors caused by the temperature decrease and the presence of a temperature gradient. Mechanical shims have been used to modify the vertical position of the 24 rods in order to correct the phase error and bring it down to 3^o (at gap of 5.5 mm) after 8 iterations, as presented in Fig. 4.21-a. Figure 4.21 (b) presents the phase error variation after rod length correction versus gap. The value at minimum gap of 5.5 mm is 3^o RMS and the maximum value is a 3.2^o at gap 8 mm.

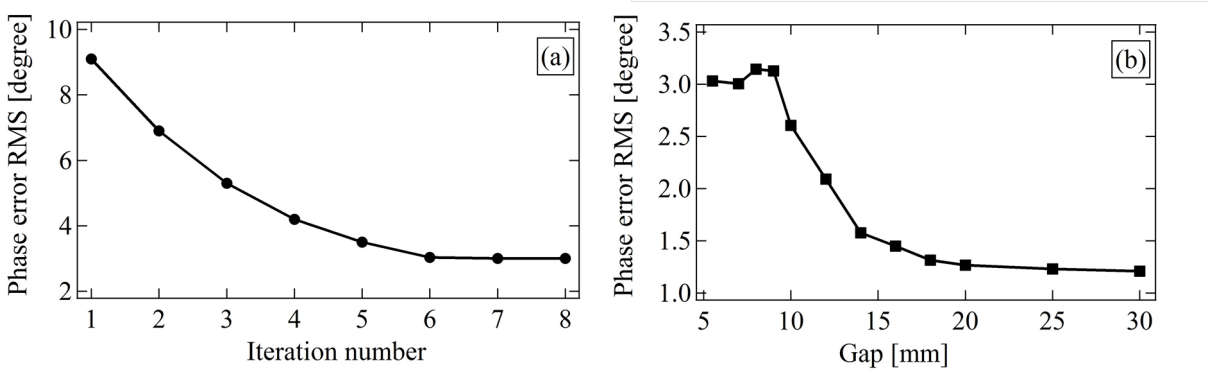

Figure 4.21: (a) Phase error corrections with rod vertical displacement at minimum gap of 5.5 mm. (b) Phase error variation versus gap after correction.

4.11 CPMU18 performance on the SOLEIL storage ring

The first 18 mm period undulator (U18n°1) built at SOLEIL, had been installed in the storage ring for the past 10 years (see Fig. 4.22). During the installation of an undulator in a storage ring, its magnetic axis should be well aligned with the electron beam, to ensure the best performance possible. After some time, misalignment might occur either in the transport line or the undulator itself. Thus, tests have been performed on the spectrum of the undulator radiation, to ensure good alignment and maximize the optical performance [130]. The characteristics of the electron beam are given in Table 4.8.

The spectrum of the undulator radiation had been monitored using the Nanoscopium long beamline with a window aperture (0.2 mm × 0.8 mm) placed 77 m away from the undulator, and

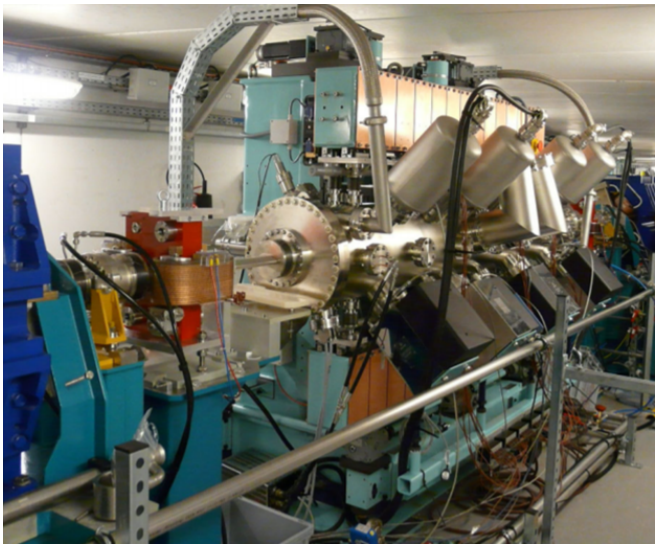

Figure 4.22: U18 n°1 installed in the long section beamline at SOLEIL.

Beam line	Values	Unit
Energy	2.7391	G*e*V
Current	0.5	A
Energy Spread	0.1	%
Emittance (x,z)	(3.9 , 0.039)	nm
Beta (x,z)	(7.507 , 2.343)	m
Alpha (x,z)	(-0.846 , 0.033)	rad
Dispersion (x,z)	(0.912 , 0)	m

Table 4.8: Electron beam characteristics in the long section of SOLEIL.

a photodiode placed at a distance of 83 m. This multimodal beamline is dedicated to scanning X-ray micro- and nanoprobe experiments in the 30 nm -1 µm spatial resolution range by combining X-ray fluorescence (XRF), absorption spectroscopy (XAS), and phase-contrast imaging.

4.11.1 Offset measurement

1845 The undulator vertical axis is varied by moving the girders up and down, while keeping the magnetic gap constant (5.5 mm). The spectrum analysis has been done on the 11^{th} harmonic as shown in Fig. 4.23-a. The shift in the resonant energy is due to the variation of the peak field. The maximum intensity with smallest bandwidth is achieved at a vertical offset of 500 µm as shown in Fig. 4.23-b.

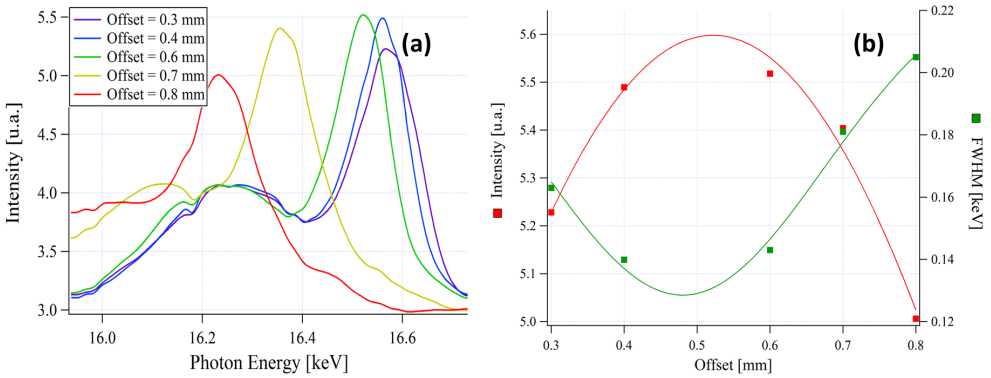

Figure 4.23: Spectrum of the 11^{th} harmonic (a) with its corresponding Full width half maximum bandwidth (b) as the vertical offset is varied.

4.11.2 Taper optimization

Undulator tapering consists in varying the peak field along the longitudinal axis. One way to modify it is to vary the gap at the exit of the undulator. The taper can be used to broaden the photon bandwidth for EXAFS experiments enabling to perform an energy scan with a more constant intensity. It can also be used in FEL to keep the emitted resonant wavelength constant as the electrons lose energy to the FEL wave as they progress along the undulator.

The taper is adjusted by observing the 11^{th} harmonic as shown in Fig 4.24. The slight change of peak energy comes from the change of the average gap and thus changing the peak field. One can see that the highest intensity with the lowest band width is at -10 µm; i.e. the girders at the end of the undulator are closed by 10 µm. This optimization was useful for the beamline and increased the flux by 0.6%.

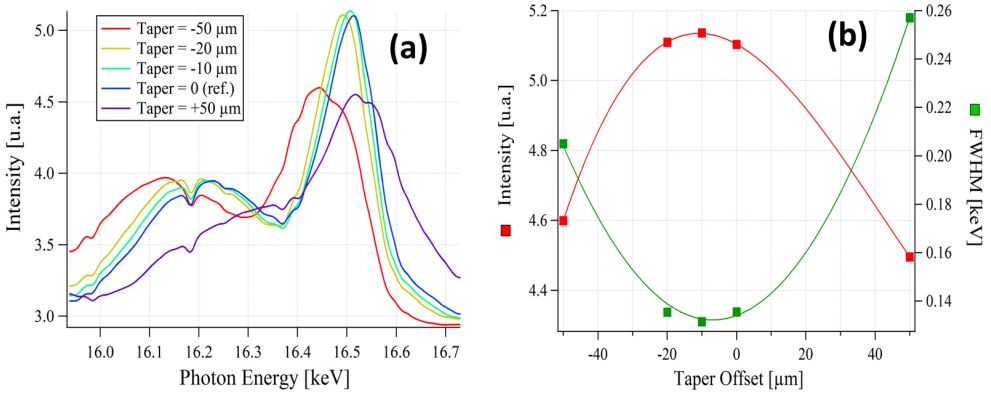

Figure 4.24: Spectrum of the 11^{th} harmonic (a) with its corresponding Full width half maximum bandwidth (b) while changing the undulator taper.

4.11.2.1 Measured undulator spectrum

The spectrum emitted by the cryogenic undulator U18n°1 has been measured on the NANOSCOPIUM long beamline. Figure 4.25 shows the photon flux on the harmonics H9, H11 and H13 of the spectrum measured on the beamline and compared to the one calculated from the magnetic measurements. A very good agreement has been found in terms of bandwidth between the measured spectrum on the beamline and the calculated one from the magnetic measurements. This result confirms that the magnetic measurements carried out had high precision.

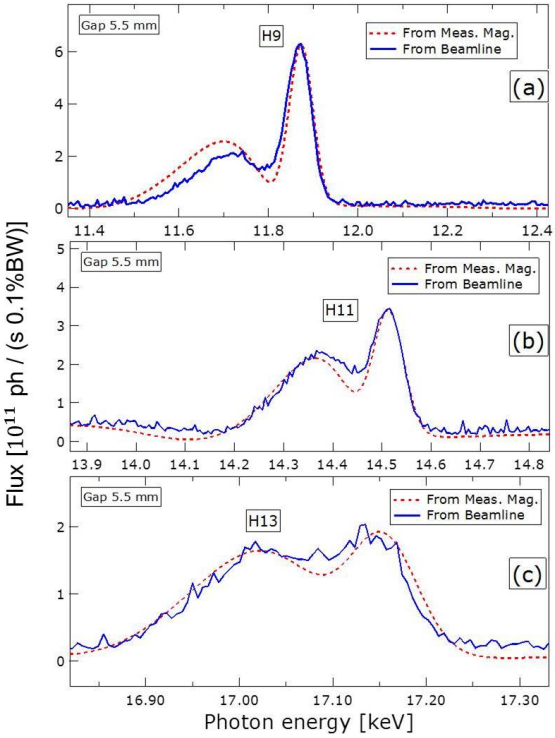

Figure 4.25: Normalized spectra measured on the beamline and calculated from magnetic measurements at 5.5 mm gap through a 0.05 mm x 0.05 mm aperture at a distance of 20.3 m from the undulator. Electron beam parameters of table 4.8, with β_x= 8.906 m, β_z= 7.216 m, α_x= -1.296 rad, α_z= -1.477 rad. (a): 9^{th} harmonic, (b): 11^{th}, and (c): 13^{th} harmonic.

Fig. 4.26 compares the measured spectra with a simulation of an ideal undulator for high harmonics (H9, H10, H11, H12, H13, H14). The intensities have been normalized to the simulated H9 peak.

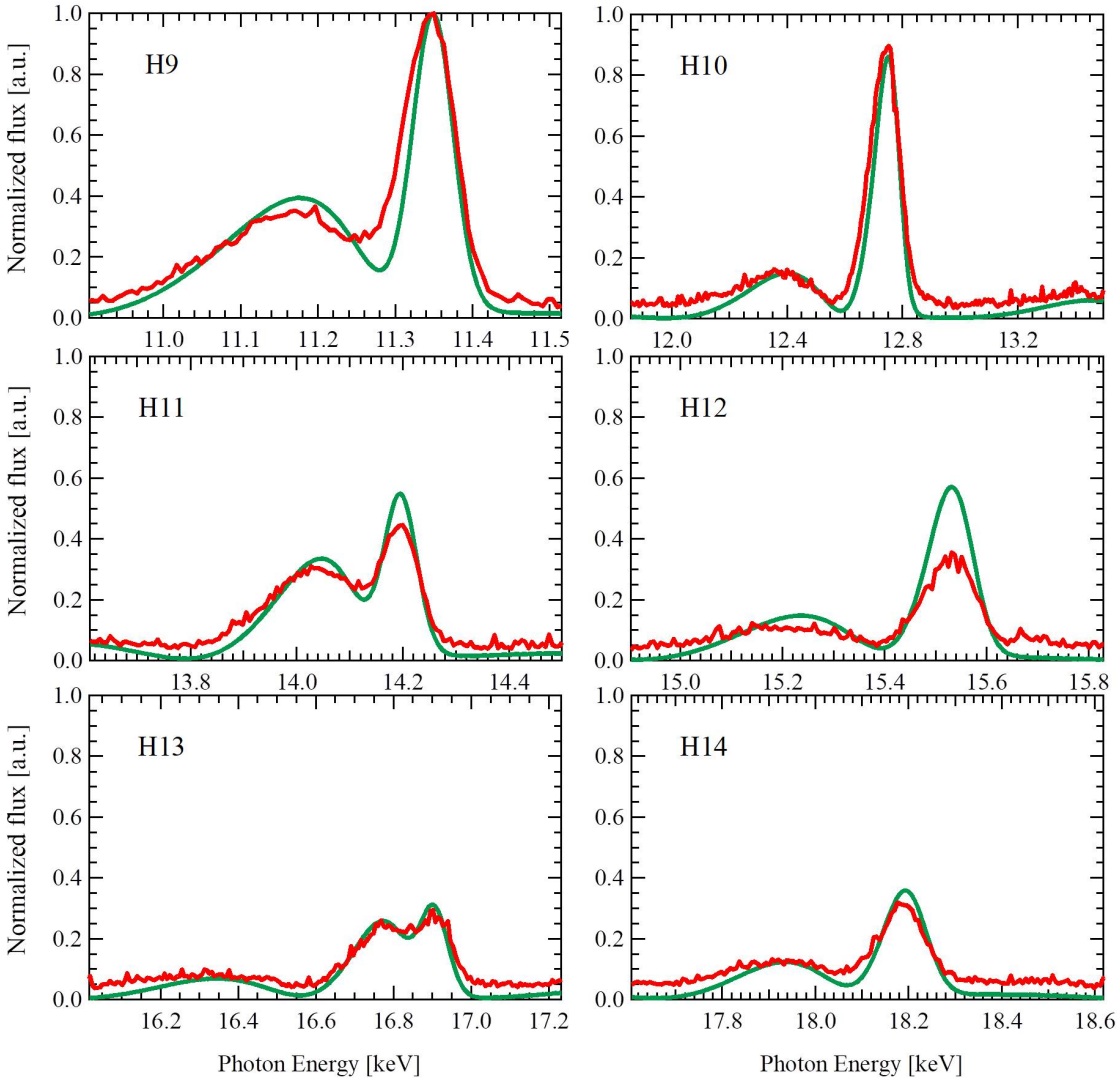

Figure 4.26: (Green) spectra computed by an ideal undulator using SRWE with beam characteristics as Fig. 4.25. (Blue) spectra from the beamline noramlized to H9 of ideal undulator.

Recalling the intensity reduction due to the phase error presented in Eq. (4.4), the measured H9 intensity I_9 can be expressed as a function of the simulated ideal case I_9^i:

$$I_9 = I_9^i \alpha = I_9^i e^{-9^2\phi^2} \tag{4.10}$$

where α is the normalization factor. Thus the intensities of the other harmonics can be written as:

$$I_n = I_n^i e^{(81-n^2)\phi^2} \tag{4.11}$$

Substituting the phase error of U18°1 (ϕ = 3° = 0.052 rad), the reduction factor $R_n = I_n/I_n^i$ calculated for the higher harmonics is compared to the measured one (see Table 4.9). Considering the assumption of Eq. (4.10), the agreement between the beamline measurements and the calculated ones using the phase error deduced from magnetic measurements is rather good. In addition, the measured and ideal harmonic line bandwidths are in good agreement as well, underlining the good quality of the undulator magnetic field.

Harmonic		H9	H10	H11	H12	H13	H14	H15	H16
Calculated	%	100	95	90	84	79	73	68	62
Measured	%	100	99	79	65	82	76	70	50

Table 4.9: Reduction factor calculated one using Eq. (4.11) and from the measured spectra.

4.12 Conclusion

Cryogenic undulator takes advantage of the enhanced performance of permanent magnets enabling the building of a compact device suitable for future radiation sources such as FEL. In this chapter, the progress of CPMUs manufacturing at synchrotron SOLEIL is discussed. Three CPMUs of period 18 mm have been contructed with very good field qualities, in which two of them (U18 n°1, U18 n°3) are installed at SOLEIL storage ring and one (U18 n°2) at COXINEL project for undulator spontaneous emission studies and FEL demonstration attempts. The U18 n°2 at COXINEL is operating at room temperature due to infrastructure reasons. A 3 m long CPMU of period 15 mm, which is one of the R&D programs, is still under contruction.

Chapter 5

QUAPEVA: Tunable High Gradient Permanent Magnet Based Quadrupole

In this chapter, a new innovative model, the so-called QUAPEVA, constructed in the view of COXINEL project achieving high gradient and tunability to handle the LPA based electron beam, is introduced. It is described after having presented the state of art of permanent magnet based quadrupoles for fixed and variable systems alongside different designs modeled with RADIA code [129]. Seven QUAPEVAs with different magnetic length have been built and three of them are commissioned at COXINEL. The QUAPEVAs are modeled using RADIA and characterized with magnetic measurements.

5.1 Quadrupole magnetic field

Quadrupoles consist mainly of four magnets with magnetization vectors directed as shown Fig. 5.1, where the dipole terms at the core of the system are canceled. In this scheme (case of an electron beam), the electron experiences an inward force towards the center in the horizontal plane and outwards in the vertical plane, thus a quadrupole focuses in one plane and defocuses in the other.

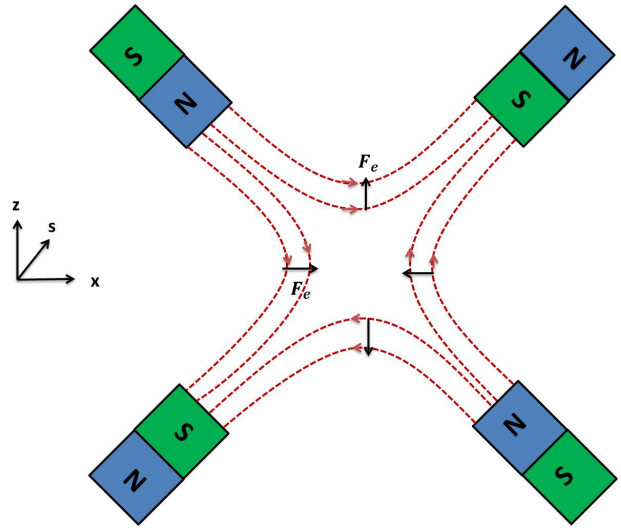

Figure 5.1: Schematic view of the quadrupole magnetic field lines (red dashed curves) and the direction of the force it exerts on electrons (black arrows) traveling along the *s* axis.

5.1.1 Gradient

In the case of permanent magnets, the current density is zero. The magnetic field $\vec{B}$ is determined using Maxwell equations:

$$\begin{cases} \vec{\nabla} \times \vec{B} = 0 \\ \vec{\nabla}.\vec{B} = 0 \end{cases}$$

Considering that the field along the longitudinal direction is zero ($B_s = 0$) and does not vary ($\frac{\partial B}{\partial s} = 0$), and neglecting higher order multipoles for small transverse displacement, one can express the field in the core of the quadrupole as:

$$\vec{B} = B_x \hat{x} + B_z \hat{z} = G(z\hat{x} + x\hat{z}) \tag{5.1}$$

where

$$G = \frac{\partial B_z}{\partial x} = \frac{\partial B_x}{\partial z} \tag{5.2}$$

is the field gradient along the horizontal axis x and vertical axis z. Eq. 5.1 is represented in Fig. 5.2 with a gradient G = 100 T/m. The field magnitude is null at the center and grows rapidly with the radial distance, so particles that are farther from the center experience a larger force.

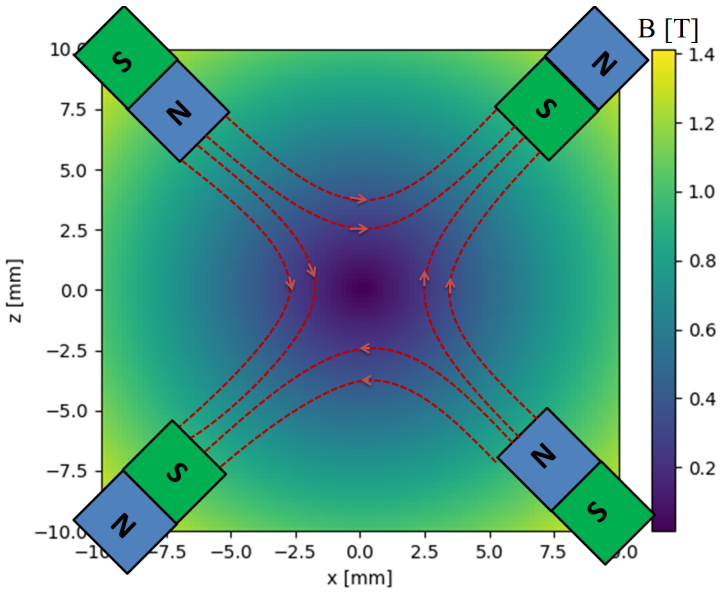

Figure 5.2: Magnetic field magnitude as a function of the transverse axes using Eq. (5.1) with a gradient of 100 T/m.

5.1.2 Multipoles

The magnetic field of realistic quadrupoles, even though designed to generate only one multipolar order, contains higher order multipoles called harmonics resulting from the structure geometry, magnetic impurities or mechanical assembly imperfections. The local field B inside a quadrupole can be expressed as a summation of all the multipole terms [259]:

$$B = B_z + iB_x = \sum_{n=1}^{\infty} (B_n + iA_n).\left[\frac{x+iz}{r}\right]^{n-1} \tag{5.3}$$

where n is the multipolar order, B_n and A_n the normal and skew multipolar coefficients respectively and r the radius for which multipolar coefficients are computed. In a 3D model, the

integrated multipole components a_n and b_n are introduced as:

$$\begin{cases} a_n = \int \mathrm{A}_n.ds \\ b_n = \int \mathrm{B}_n.ds \end{cases} \tag{5.4}$$

For a perfect normal quadrupole where n=2, the vertical and horizontal fields become:

$$\begin{pmatrix} \mathrm{B}_z \\ \mathrm{B}_x \end{pmatrix} = \begin{pmatrix} x \\ z \end{pmatrix} \frac{\mathrm{B}_2}{r}$$

The vertical field component is negative for x < 0, positive for x > 0, and null on the axis. This evolution is the same for the horizontal field along the z. The quadrupole field gradient can be calculated in 2-dimension $\mathrm{G}_{2\mathrm{D}}$ and 3-dimension $\mathrm{G}_{3\mathrm{D}}$ model:

$$\mathrm{G}_{2\mathrm{D}} = \frac{\mathrm{B}_2}{r} \qquad \text{and} \qquad \mathrm{G}_{3\mathrm{D}} = \frac{\int \mathrm{B}_2.ds}{r\mathrm{L}_{mag}} = \frac{b_2}{r\mathrm{L}_{mag}} \tag{5.5}$$

where L_{mag} is the magnetic length along the s axis.

5.1.2.1 Magnetic center excursion

In an ideal quadrupole, the magnetic center is the same as the mechanical center of the device. However in reality, some impurites in the magnets or some mechanical defects induce a shift of the magnetic center. This excursion can be determined by expanding Eq. (5.3) up to the second multipole (n = 2) and setting the field equal to zero. Thus, one gets the following:

$$\mathrm{B}_z + i\mathrm{B}_x = (\mathrm{B}_1 + i\mathrm{A}_1) + (\mathrm{B}_2 + i\mathrm{A}_2)\left(\frac{x+iz}{r}\right) = 0 \tag{5.6}$$

Separating the real and imaginary in Eq. (5.6), one gets the two equations:

$$\begin{cases} \mathrm{B}_1 + \mathrm{B}_2 x/r - \mathrm{A}_2 z/r = 0 \\ \mathrm{A}_1 + \mathrm{B}_2 z/r + \mathrm{A}_2 x/r = 0 \end{cases} \tag{5.7}$$

By solving Eq. (5.7), the magnetic center excursion is expressed as:

$$\begin{cases} x = -\frac{\mathrm{B}_1\mathrm{B}_2 + \mathrm{A}_1\mathrm{A}_2}{\mathrm{A}_2^2 + \mathrm{B}_2^2} r \\ z = \frac{\mathrm{B}_1\mathrm{A}_2 - \mathrm{A}_1\mathrm{B}_2}{\mathrm{A}_2^2 + \mathrm{B}_2^2} r \end{cases} \tag{5.8}$$

5.1.2.2 Roll angle

An ideal quadrupole has zero skew components. A real one, however, contains skew terms that give rise to a magnetic angle also referred to as the roll angle θ_{quad} and is expressed as:

$$\theta_{quad} = -\frac{1}{2}\arctan\left(\frac{\mathrm{A}_2}{\mathrm{B}_2}\right) \tag{5.9}$$

5.2 QUAPEVA specifications

Tunable high gradient quadrupoles are key components in achieving good beam characteristics, whether it is for a linear collider used as a final focus lens, a low emittance beam in a storage ring to ensure high brightness, or an LPA to focus a highly divergent beam. Fig. 5.3 presents the quadrupole gradient needed for different applications as a function of the beam energy.

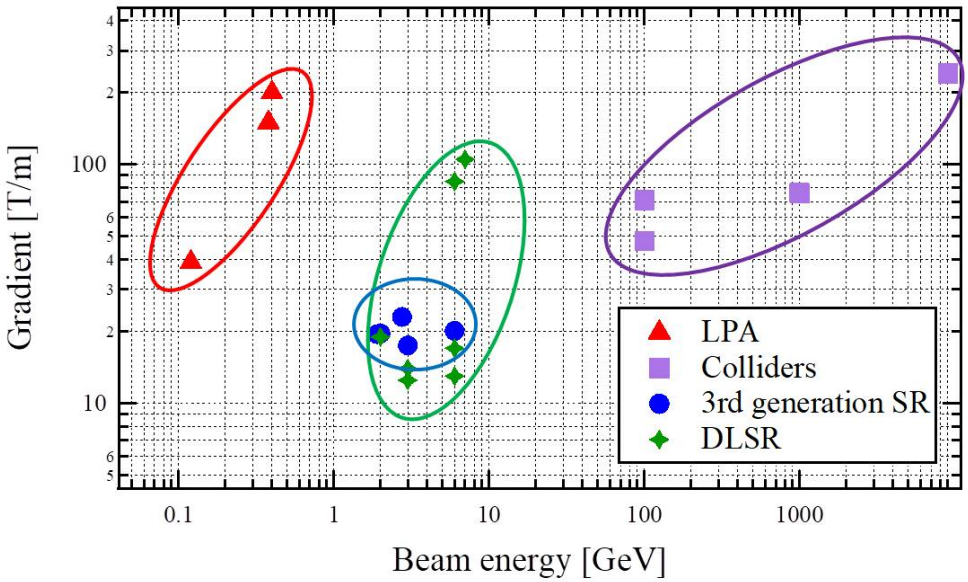

Figure 5.3: Typical quadrupole gradient required for different applications depending on the beam energy.

The specifications of the QUAPEVAs have been defined according to a Laser Plasma Acceleration beam transport for the COXINEL experiment. QUAPEVAs have to be compact due to the limited space at COXINEL and adequate to vacuum environment because of the low pressure inside the vacuum chamber. The permanent magnet quality should ensure a large coercivity to resist demagnetization due to the passage of a high powered laser (60 TW) and high current electron beam (10 kA). The magnetic design had to guarantee high gradient with a large tunability and also small harmonic components. Table 5.1 presents the detailed specifications. According to COXINEL aim to operate at two electron beam energies (180 MeV and 400 MeV), seven QUAPEVAs have been built: A prototype of magnetic length 100 mm for the design validation, a first triplet with magnetic lengths of (26 mm, 40.7 mm, 44.7 mm) for the 180 MeV beam and another one with (47.1 mm, 66 mm, 81.1 mm) for the 400 MeV operation. The 44.7 mm and 81 mm QUAPEVAs are defocusing quadrupoles, i.e. focus in the vertical and defocus in the horizontal axis.

Table 5.1: QUAPEVA specifications

Parameters	**Value**	**Unit**
Length	$\leqslant$100	mm
Cross section	90 x 90	mm^2
Gradient	$\geqslant$ 100	T/m
Gradient tunability	$\geqslant$30	%
b_6/b_2	$\leqslant$ 3	%
b_{10}/b_2	$\leqslant$ 1	%
Inner mechanical radius	5.25	mm
Inner magnetic radius (R_1)	6	mm
Outer magnetic radius (R_2)	17	mm
Cylindrical magnet radius (a)	7.5	mm

5.3 Designs of permanent magnet quadrupoles

Permanent Magnet Quadrupoles (PMQs) have evolved in the past decades to become suitable for different applications in particle accelerators. New and innovative designs are emerging where

the magnet size is reduced while maintaining a good field quality, making them suitable for future compact accelerators. In the following, different PMQ designs are compared for a given set of parameters in terms of performance.

5.3.1 Halbach designs

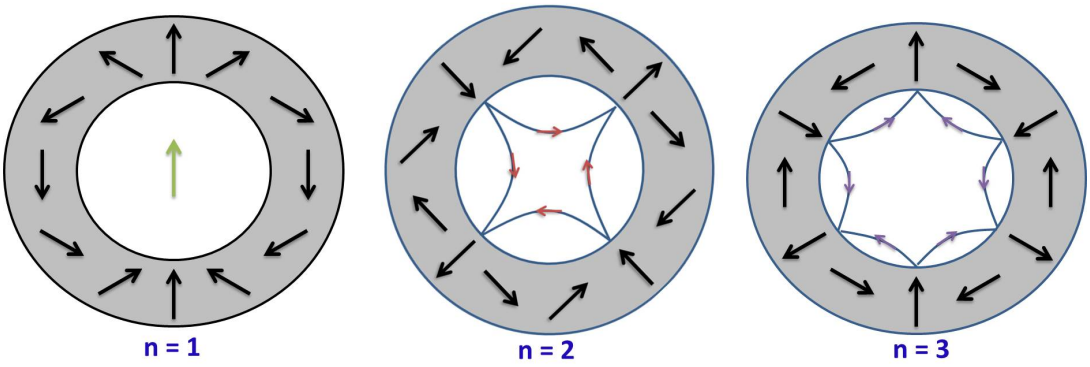

Figure 5.4: Halbach designs: (left) dipole, (middle) quadrupole, (right) sextupole.

A Halbach structure is an array of magnets with specific arrangements generating a concentrated strong magnetic field on one side whilst creating a weak stray field on the opposite side [260]. Different multipole systems can be build using such structure as displayed in Fig. 5.4 where 12 segmented magnets can be used to design a dipole, quadrupole and a sextupole.

Lets consider a Halbach ring quadrupole of inner radius R_i, outer radius R_o, M number of $Nd_2Fe_{14}B$ magnets of remanence field B_r with values shown in Table 5.2. The quadrupoles are modeled using RADIA magnetostatic code based on boundary integral method [129]. $Nd_2Fe_{14}B$ magnets are most commonly used due to their high remanent field and coercivity at room temperature [221, 261, 262] but with more sensitivity to temperature variation than SmCo grades. For

	Parameter	Notation	Value	Unit
Materials	Magnet	-	$Nd_2Fe_{14}B$	-
	Remanence field	B_r	1.26	T
	Coercivity	H_c	1830	kA/m
	Pole	-	Vanadium Permendur	-
	Saturation		2.35	T
Geometry	Inner radius	R_i	6	mm
	Outer radius	R_o	17	mm
	Magnetic length	L_{mag}	100	mm

Table 5.2: Materials with their charateristics and geometric parameters of the reference Halbach ring used for modeling.

a very long quadrupole with magnetic length $L_{mag} >> R_i$, the gradient can be expressed as follows [260]:

$$\begin{cases} G = 2B_r K_H (\frac{1}{R_i} - \frac{1}{R_o}) \\ K_H = \frac{M}{2\pi} \cos^2(\frac{\pi}{M}) \sin(\frac{2\pi}{M}) \end{cases} \tag{5.10}$$

As M tends to infinity $K_H = 1$, implying that the quadrupole gradient is enhanced for larger number of segments, but the magnet gets more complicated and expensive to manufacture.

Fig. 5.5 shows the Halbach rings for different number of segments designed by a 3D magnetostatic code based on boudary integrals approach RADIA [129]. The magnetization vectors of the magnets depends on the number of segments of the Halbach structure: The angle deviation of the magnetization vector of two consecutive magnets $\theta_i = (i\text{-}1)6^*\pi/M$, where i is an integer, for example the angle between the magnetization vectors of two consecutive magnets is 270^o for M=4, 135^o for M = 8 and 90^o for M = 12 etc...

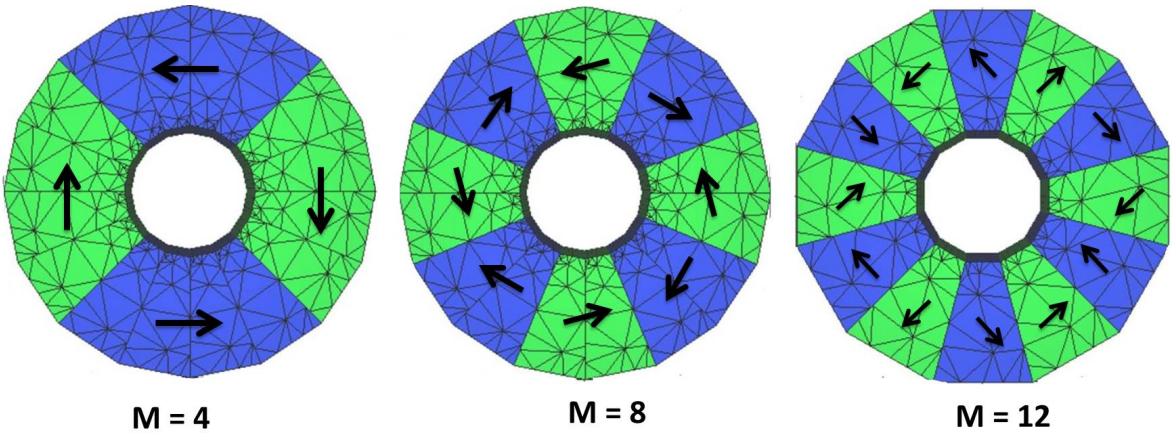

Figure 5.5: Halbach quadrupole with different number of sections with the quadrupole geometry characteristics presented in Table 5.2.

Fig. 5.6 presents a Halbach ring quadrupole with 8 magnets while changing the number of wedges within one magnet: In (a) with 1 wedge per magnet, a gradient of 175.4 T/m is obtained. In (b) with 4 wedges per magnet, the gradient is decreased to 167.4 T/m. In (c) with 8 wedges per magnet, the gradient is slightly changed to 166 T/m. For the models presented later on, the 4 wedges per magnet is chosen due to computation time consumption reason.

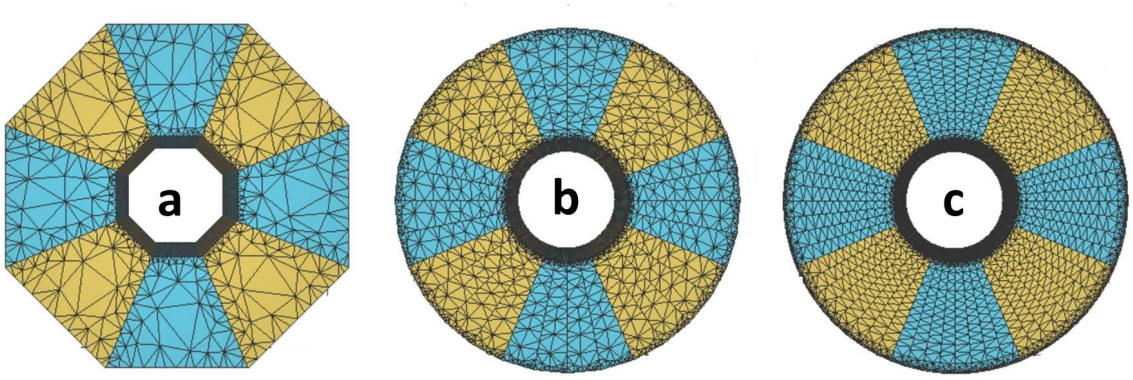

Figure 5.6: Halbach quadrupole with different number of wedges per magnet. (a) G = 175.4 T/m, (b) G = 167.4 T/m, G = 166 T/m. Quadrupole geometry characteristics presented in Table 5.2.

Fig. 5.7-a presents the computed gradient versus the mechanical length of the system that is approximately equal to the magnetic length, where Eq. (5.10) is valid for our reference parameters for a length ≥20 mm at which the gradient saturates. The gradient is computed for different number of segments and is compared to Eq. (5.10) (see Fig. 5.7-b). The gradient increases for higher number of segments. Fig. 5.7-c and d present the computed gradient for different R_0 and R_i, respectively, and show good agreement with Eq. (5.10).

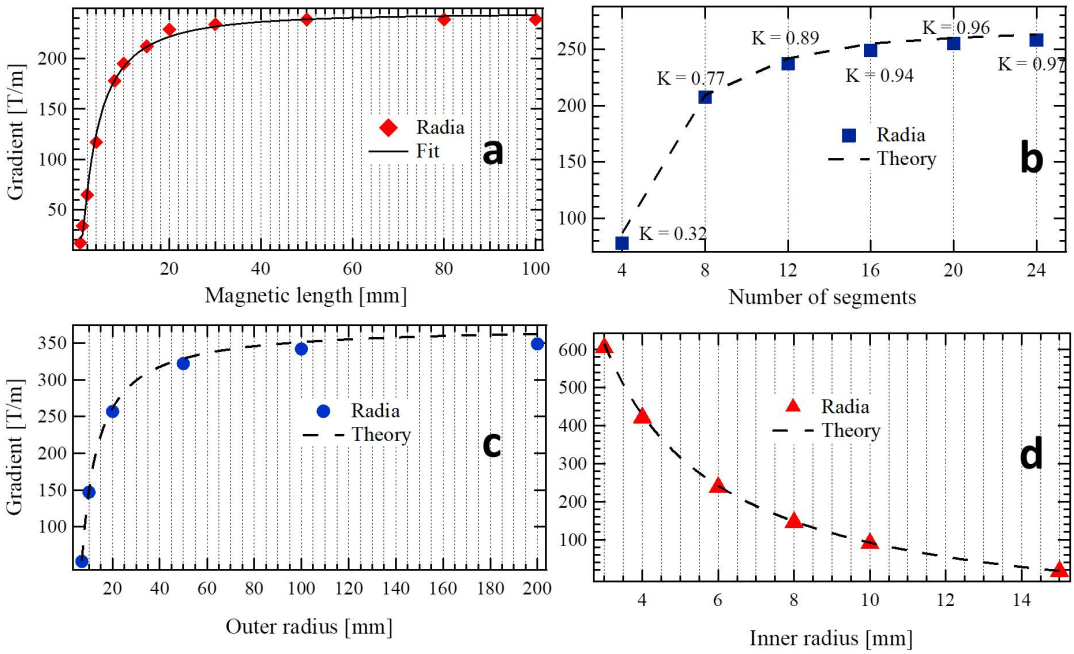

Figure 5.7: Computed gradient of Halbach quadrupole structures by changing each parameter individually (R_i, R_o, l_{mag}, K) using the reference parameters presented in Table 5.2. **a**: versus magnetic length with fit (line), **b**: versus number of segments, **c**: versus outer radius, **d**: versus inner radius. The dashed curves in b-c-d are the theoretical values calculated using Eq. 5.10.

5.3.2 Halbach hybrid designs

This section presents different quadrupole designs following a Halbach structure with the addition of poles to enhance the gradient. Fig. 5.8 shows three designs: Model **I** is composed of four magnets and four poles where the gradient is increased by almost a factor of two compared to the Halbach ring design (M = 4) presented in Fig. 5.5. Model **II** is composed of 8 magnets with poles of half the thickness (5.25 mm). Model **III** has the same design as type **II** with an additional pole ring of thickness 1.5 mm surrounding the ring to redirect the magnetic field lines back into the core.

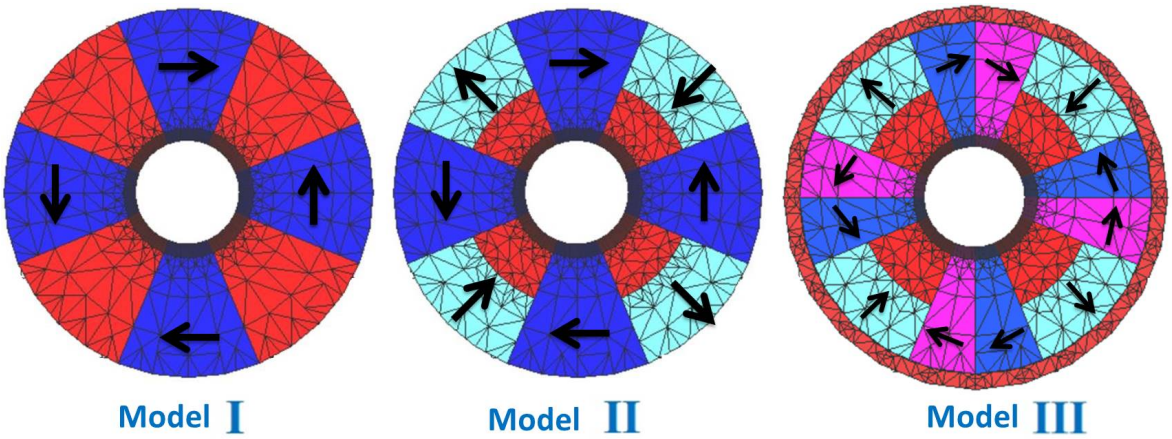

Figure 5.8: Different Halbach hybrid designs. (Red): poles, (blue): NdFeB magnets with 1.26 T remanence field. Design parameters are the reference ones in Table (5.2).

Fig. 5.9 shows the gradient computed for the three designs of Fig. 5.8 and are compared to the Halbach rings. There is a large enhancement of the gradient when the number of segments is in-

creased from 4 to 8. Using a hybrid structure enables to raise the gradient furthermore but requires a much more complex design to achieve the same gradient as the Halbach ring of 8 segments, thus for M > 8, there is no need to go to hybrid designs..

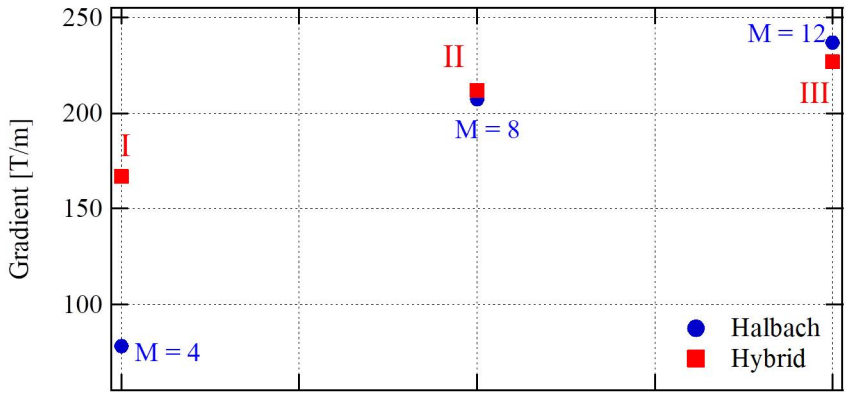

Figure 5.9: Gradient computed for the three hybrid designs compared with the Halbach structure with different number of segments.

5.3.3 Variable Systems

Permanent magnets based devices have many advantages over electro-magnets except for the tunability. In conventional electro magnets, the field, gradient etc... can be changed by varying the electric current. As for permanent magnets, it becomes much more challenging due to the requirement of mechanical motion to adjust the positions of the magnets taking into account the large magnetic forces induced by the system. Fig. 5.10 shows examples of permanent magnet based quadrupoles with variable gradient. Model **IV** is composed of a Halbach hybrid ring at the center surrounded by a Halbach ring of 12 sections, and the gradient is varied by rotating the ring. Model **V** is also a Halbach hybrid ring at the center with cylindrical magnets capable of rotating around the longitudinal axis to provide gradient tunability and the QUAPEVA design is based on this model. Model **VI** is composed of four magnetic rods (blue) build into a structure (in this case it is steel) and by moving them, the gradient can be varied.

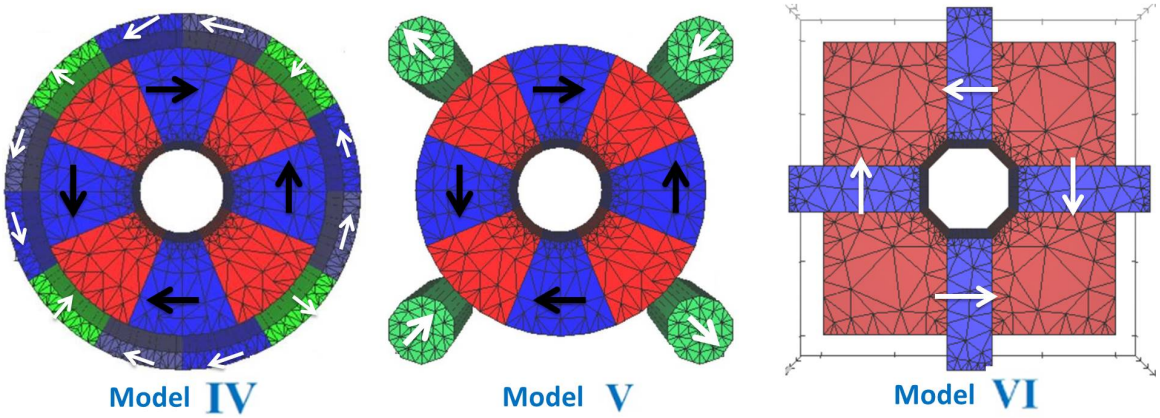

Figure 5.10: Different Halbach hybrid designs. (Red): poles, (blue): NdFeB magnets with 1.26 remanence field. Design parameters are the reference ones from Table 5.2.

Fig. 5.11 presents the gradient tunability as a function of the angle. For Type **IV** design, the outer ring is placed 2 mm away from the inner ring with a thickness of 2 mm achieving a maximum

gradient of 201 T/m and tunability of ~70 T/m. Type **V** design is composed of cylindrical magnets of radius 2 mm placed at 2 mm from the inner ring providing a maximum gradient of 185 T/m with 35 T/m tunability. Type **VI** consists of magnetic rods that can be displaced to vary the gradient from a maximum value of 100 T/m down to very low gradient.

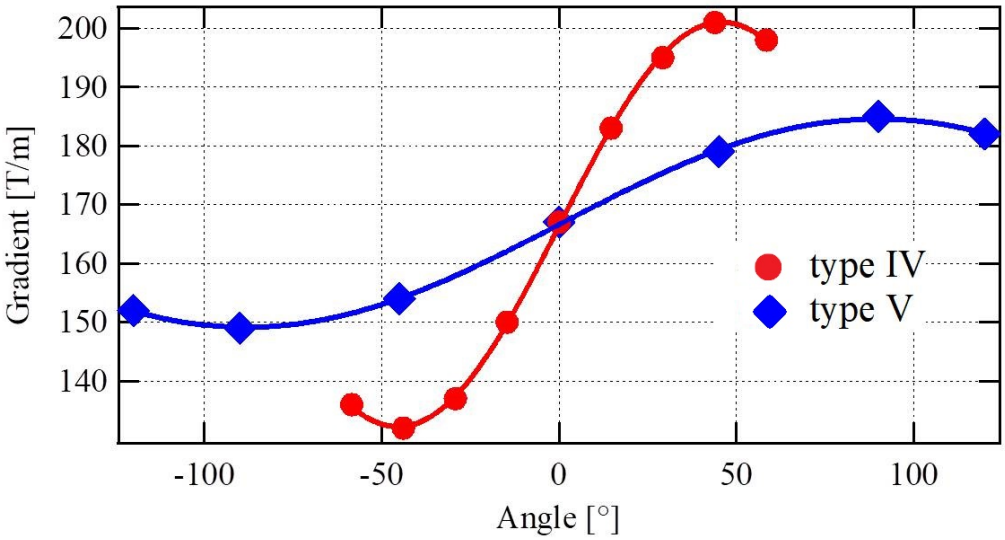

Figure 5.11: Gradient computed for the first two designs of Fig. 5.10 as a function of angle of the Halbach ring and the cylindrical magnets.

Table 5.3 summarizes the different designs of fixed and variable gradient modeled with RADIA.

Type	**n^o magnets**	**n^o poles**	G_{max} [T/m]	$\int G.ds$ [T]	**ΔG/G** [%]
Halbach	4	-	78	7.8	-
Halbach	8	-	207	20.7	-
Halbach	12	-	237	23.7	-
Hybrid-**I**	4	4	166	16.6	-
Hybrid-**II**	4 + 4 halves	4 halves	211	21.1	-
Hybrid-**III**	12	4 halves + ring	227	22.7	-
Hybrid-**IV**	4 +ring	4	201	20.1	34
Hybrid-**V**	4 + 4 cylinders	4	185	18.5	20
Hybrid-**VI**	4	Bulk	100	10	90

Table 5.3: Different PMQ designs of 6 mm bore radius modeled using RADIA. The "halves" stands for half magnet or half pole. $\Delta G/G = (G_{max} - G_{min}) / G_{max}$.

5.4 Built quadrupoles

5.4.1 Fixed gradient

Several permanent magnet quadrupoles (PMQs) with fixed gradient were built for particular applications:

- A 12 modified PM Halbach ring system in which 4 of them are half permanent magnet and half iron poles (Model **II**) is proposed at Kyoto University in collaboration with SLAC as a

final focus lens for a positron-electron linear collider accelerator [263]. The system has a bore radius of 7 mm with a magnetic length of 100 mm generating a maximum gradient of 289 T/m. At the department für Physik, in München for a Table-Top FEL application, two 12 PM sector Halbach ring system of 17 mm (15 mm) magnetic length and 3 mm bore radius achieve a gradient of 500 T/m [264].

- A 16 sector PM Halbach structure with a 33.5 mm bore radius, 92 mm magnetic length, 27.1 T/m gradient and 2.5 T integrated gradient have been built at CESR [265]. Three PMQs of the same design, each made up of a Halbach ring of 16 segments, have been installed in the PLEIADES ICS experiment as a final focus system [266]. The bore radius is very small (2.5 mm) with a magnetic length of 10.4 mm providing the largest gradient recorded using PM technology that is around 560 T/m alongside a focusing tunability through longitudinal movement of the magnets.

- A compact PMQ with a hybrid type design of interest for ultimate storage rings has been designed at ESRF [267], inspired from permanent magnet based undulator design. The magnetic structure includes rectangular permanent magnet blocks and soft iron poles. A prototype with a bore radius of 12 mm and a magnetic length of 226 mm has been built (see Fig. 5.12) provides a gradient of 85 T/m.

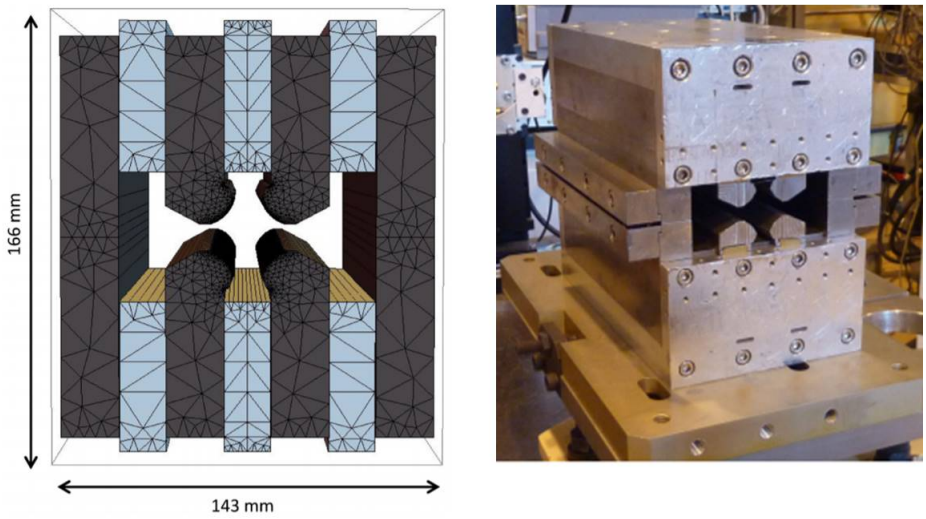

Figure 5.12: Hybrid permanent magnet based quadrupole providing a fixed gradient. Figure from [267].

5.4.2 Variable Gradient

Various original designs were proposed and developed for the permanent magnet quadrupole to provide a variable gradient:

- A double Halbach ring structure of model **IV** was fabricated at Kyoto U. / SLAC collaboration for a final focus in a linear collider. The system consists of an inner hybrid ring with 8 sectors hybrid system and the outer ring being a pure 12 magnet Halbach structure rotating around the first one resulting in gradient variation from 17 T/m up to 120 T/m for a 230 mm magnetic length and 10 mm bore radius [268].

- A super hybrid quadrupole combining permanent magnetic material, coils and soft magnetic material has been built and tested for the new Brazilian Synchrotron Light Source (Sirius) [269] (see Fig. 5.13). The system has a bore radius of 27.5 mm and a magnetic length of 288 mm providing a maximum gradient of 28 T/m with a 30% tunability.

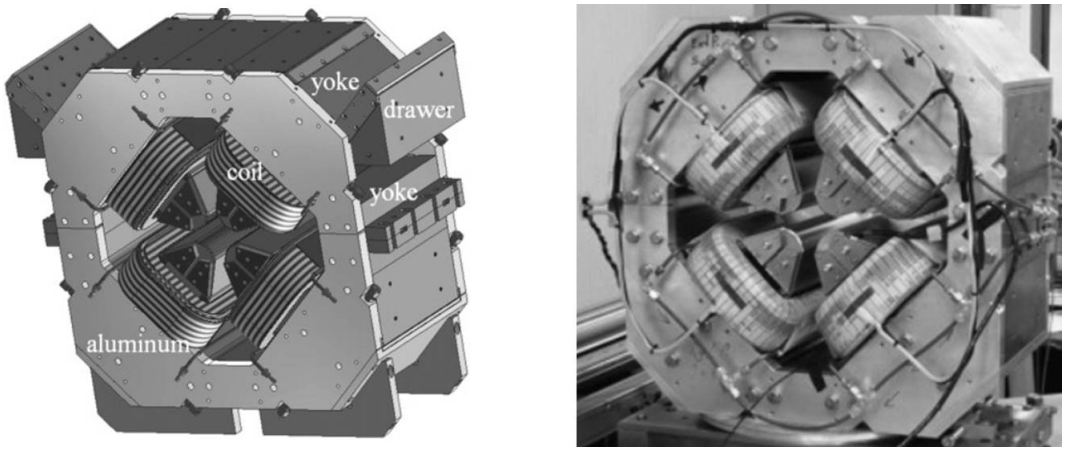

Figure 5.13: design of the super hybrid quadrupole (left) and the real system (right). Figures from [269].

- An adjustable strength PM system has been built and tested, in collaboration between SLAC and Fermilab, for the Next Linear Collider. The system is based on four PM blocks and four soft iron poles of type (**VI**), with the possibility to retract linearly the permanent magnet blocks enabling an integrated gradient variation between 7 T and 68.7 T (gradient between 13 T/m and 115 T/m) for a 6.5 mm bore radius [270].

- A modified 12 sectors Halbach design composed of 8 magnets and 4 poles surrounded by air-cooled electromagnetic coils as presented in Fig. 5.14 has been proposed in the framework of CLIC/CERN collaboration [271]. The bore radius is 4.125 mm with a magnetic length of 300 mm achieving a maximum gradient of 610 T/m with 20% tunability.

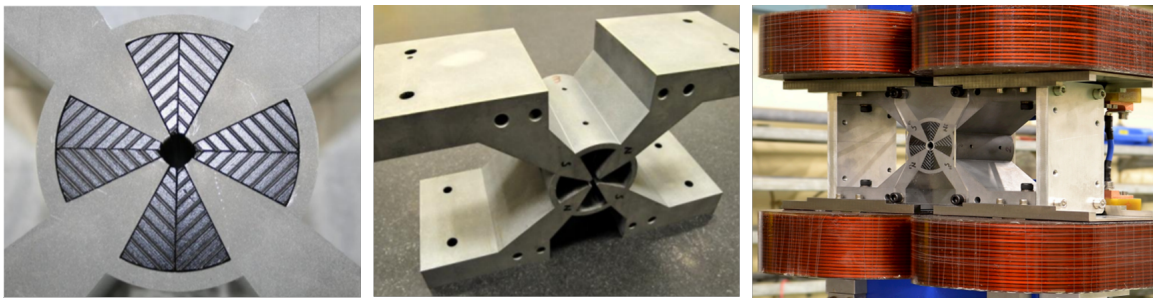

Figure 5.14: Mechanical design of the super hybrid quadrupole (left) and the real system (right). Figures from [271].

- Two variable systems have been built in a collaboration of STFC Daresbury Laboratory and CERN for the Compact LInear Collider (CLIC) project [272] with an objective to collide electrons and positrons at an energy of 3 TeV. The first design, shown in Fig. 5.15-left, provides a gradient from 15 T/m to 60.4 T/m with a magnetic length of 241 mm. The second design, shown in Fig. 5.15-right, provides a gradient from 2.9 T/m to 43.8 T/m with a magnetic length of 194 mm length. The strength is adjusted by moving the PMs vertically away from the center, and by creating an air gap the gradient is reduced.

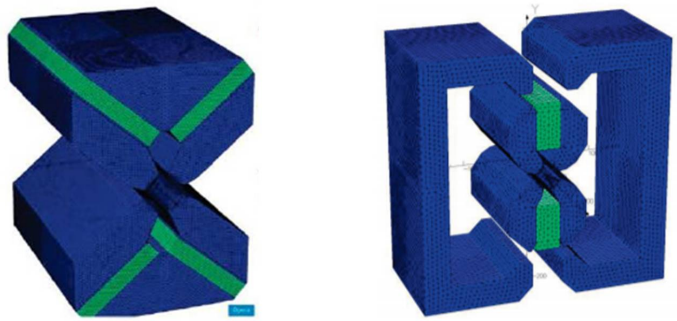

Figure 5.15: (left) high strength, (right) low strength with magnets (green) and steel structure (blue). Figures from [272].

- Two variable quadrupoles are proposed for an interdigital H-mode drift tube linear accelerator using KONUS beam dynamics [273]: The first using an external adjustable electromagnets as shown in Fig. 5.16-(left), with a bore radius of 12.5 mm providing a gradient from 50 T/m to 100 T/m. The second using internal adjustable permanent magnets as shown in Fig. 5.16-(right) that is similar to type (**IV**) but with additional number of segmented magnets. For a bore radius of 12.5 mm, the achieved gradient can be varied from 50 T/m up to 102 T/m.

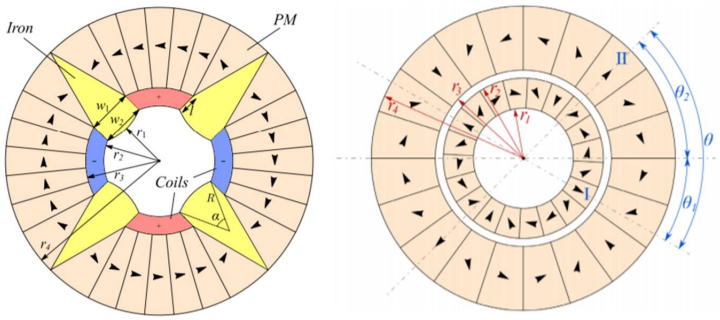

Figure 5.16: Hybrid type (left), pure permanent magnet (right). Figures from [273].

5.4.3 Summary of the built systems

Table 5.4 and Fig. 5.17 summarize the PMQs already built with their corresponding characteristics.

Project	**Lab**	R_i [mm]	L_{mag} [mm]	G_{max} [T/m]	$\int G.ds$ [T]	$\Delta G/G$ [%]	$R_i G_{max}$ [T]	**Reference**
Storage ring	CESR	33.5	92	27	2.5	-	0.9	[265]
PLEIADES ICS	Livermore	2.5	10.4	560	5.8	-	1.4	[266]
LINEAR COLLIDER	Kyoto	7	100	300	28.5	-	2.1	[274]
SPTEM	UCLA	3.5	6.16	600	3.3	-	2.1	[275]
Radiography	Tsinghua	5	20	287	5.74	-	1.4	[276]
Storage Ring	ESRF	12	226	82	18.6	-	1.0	[267]
Table-Top FEL	LMU	3	17	500	8.5	-	1.5	[264]
LPA	SPARC LAB	3	20.2	519	10.5	-	1.6	[277]
LINEAR COLLIDER	Kyoto/NIRS	10	200	120	24.2	85	0.9	[268]
CLIC	CERN	4.125	273	610	172.5	20	2.5	[271]
CLIC	CERN/STFC	13.6	214	60.4	14.6	75	0.8	[272]
CLIC	CERN/STFC	13.6	194	43.8	8.5	93	0.6	[272]
Next Linear Collider	STI/SLAC	6.5	420	163	68.7	90	1.0	[270]
COXINEL (QUAPEVA)	SOLEIL	6	100	210	21	44	1.3	[132]
linear accelerator	Peking	12.5	-	100	-	50	1.3	[273]

Table 5.4: Fixed and variable gradient PMQs. $\Delta G/G = (G_{max} - G_{min}) / G_{max}$.

Fig. 5.17 presents a summary of the PMQs already built that are presented in the previous section.

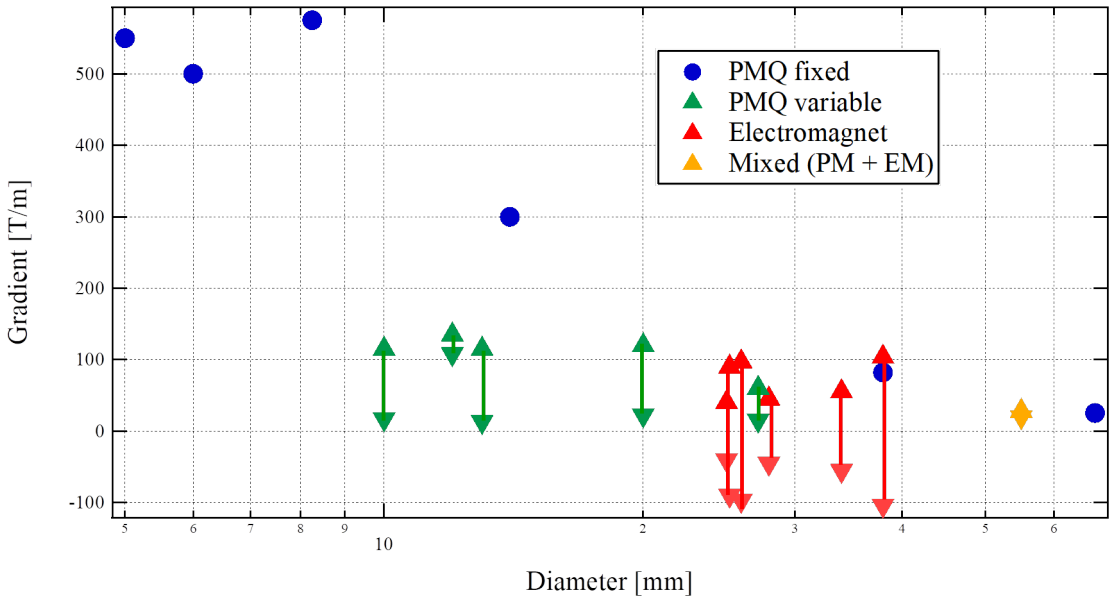

Figure 5.17: State of art summary of the gradient achieved with fixed and variable systems for the electromagnet and permanent magnet technologies.

Other characterization of a quadrupole are the systematic multipoles (b_6, b_{10}, b_{14} ...) that arise from the structure geometry and the non-systematic multipoles that emerge from magnet/pole impurities or mechanical errors. The beam quality can quickly deteriorate if these terms are not kept low; however their effect highly depends on the beam size in the quadrupole aperture and the gradient homogeneity also known as good field region. In the case of the LPA, the specifications in terms of multipoles are less stringent than a recirculating accelerator, typically by one order of magnitude. On the other hand, the gradient tunability should be larger.

5.5 QUAPEVA systems developed for the COXINEL experiment

In this section, the QUAPEVA design, similar to model **V**, is discussed, answering the specifications presented in Table 5.1 alongside construction, optimization and magnetic measurements of the different systems.

5.5.1 QUAPEVA concept

The QUAPEVA, acronym of QUdrupole à Aimants PErmanent VAriable, is made of two superimposed quadrupoles. An inner ring, with a Halbach hybrid structure consisting of $Nd_2Fe_{14}B$ and permendur poles, generates a fixed gradient. The outer quadrupole consists of four $Nd_2Fe_{14}B$ cylindrical magnets capable of rotating around their axes to provide the gradient tunability, and are shielded by permendur poles to re-direct the field lines back into the core. Fig. 5.18 presents the three particular configurations of the tuning magnets. The maximum and minimum gradient are obtained by orienting the tuning magnets easy axis towards the central magnetic poles. In these cases, the magnetic flux is either added (Fig. 5.18-a) or removed (Fig. 5.18-c) from the central poles. The average gradient is achieved when the tuning magnets are in the reference position, i.e. their easy axis is perpendicular to the central magnetic poles (Fig. 5.18-b). The QUAPEVA design has been patented (QUAPEVA program-Triangle de la Physique, SOLEIL/Sigmaphi collaboration) in europe [278].

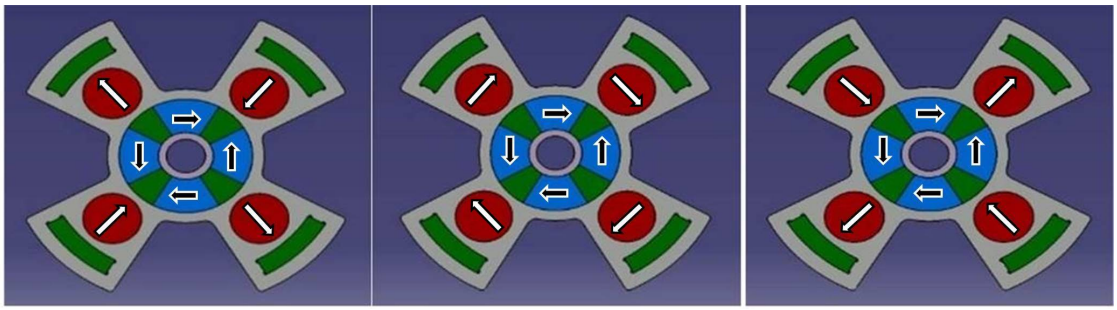

Figure 5.18: Scheme of the QUAPEVA: Permanent magnet blocks (Blue) and rotating cylinders (Red), Vanadium Premendur magnetic plates poles (Green), Aluminum support frame (Grey). (a) maximum, (b) intermediate, and (c) minimum gradient.

5.5.2 Magnetic design

5.5.2.1 2D approach

The 2D model approach considers the magnet is infinitely long in the longitudinal axis. The analytical study is the first step of the magnet optimization.

Parameter	Symbol	Value	Unit
Inner radius	R_i	6	mm
Outer radius	R_0	17	mm
Remanence field	B_R	1.26	T
Cylindrical magnet radius	a	7.5	mm
Distance between pole & cylindrical magnet	ϵ	2	mm

Table 5.5: QUAPEVA design parameters.

Inner quadrupole

The gradient generated by the inner quadrupole can be calculated using Eq. (5.10) by assuming that the poles are magnets with the same remanent field. The central magnet is then equivalent to a permanent magnet Halbach quadrupole with eight blocks. Replacing the parameters of the QUAPEVA presented in Table 5.5 in Eq. (5.10), the fixed gradient G_0 is calculated to be:

$$G_0 = 208.8 \quad T/m.$$

Another method based on Ampere's law can be used to calculated the gradient generated by the inner quadrupole by assuming that the iron permeability is infinite.

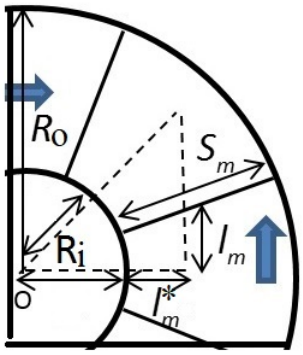

Figure 5.19: Geometrical parameters of the quadrupole 2D model with a closed contour in dashed line for Ampere's law calculation.

Ampere theorem is used by summing the integrals along the contour presented in Fig. 5.19:

$$\int_0^{R_i} H_1(r).dr + \int H_i.dl + \int_0^{l_m+l_m^*} H_m.dl + \int_{air} H_2.dl = 0, \tag{5.11}$$

Starting from the bore center O along radial direction r towards the pole:

$$\int H_1(r).dr = \int_0^{R_i} \frac{B_1(r)}{\mu_0}.dr = G_0 R_i$$

where μ_0 is the vacuum permeability. $\int_{iron} H_i.dl = 0$ due to the approximation of the irons $\mu >> 1$. Along the vertical direction l_m (see Fig. 5.19), the magnetic field is expressed as $H_m = \frac{B_m}{\mu_0} - M_R$, so:

$$\int H_m.dl = \int_0^{l_m} \frac{B_m}{\mu_0} - M_R$$

where $M_R = \frac{B_R \cos\pi/8}{\mu_0}$. The flux along the horizontal path l_m^* (see Fig. 5.19) is null because the magnetic field lines are perpendicular to this path. The same goes for $\int_{air} H_2.dl$.

B_m can be found by assuming that all the flux outgoing from the permanent magnet gets in the pole surface along the distance S_m and into the core:

$$B_m S_m = G_0 R_i^2$$

With some geometrical considerations ($l_m = \frac{\pi}{8}\sqrt{(R_i^2 - R_o^2)/2}$ and $S_m = R_o - R_i$), the final expression of the gradient is:

$$G_0 = \frac{2B_R \cos\pi/8}{R_i^2(1/l_m + 1/S_m)} \tag{5.12}$$

Taking the QUAPEVA parameters presented in Table 5.5, the gradient is calculated to be G = 203.8 T/m.

Outer quadrupole

Figure 5.20 shows a scheme of the QUAPEVA, where a the radius of the cylindrical magnets and ϵ its distance from the central ring.

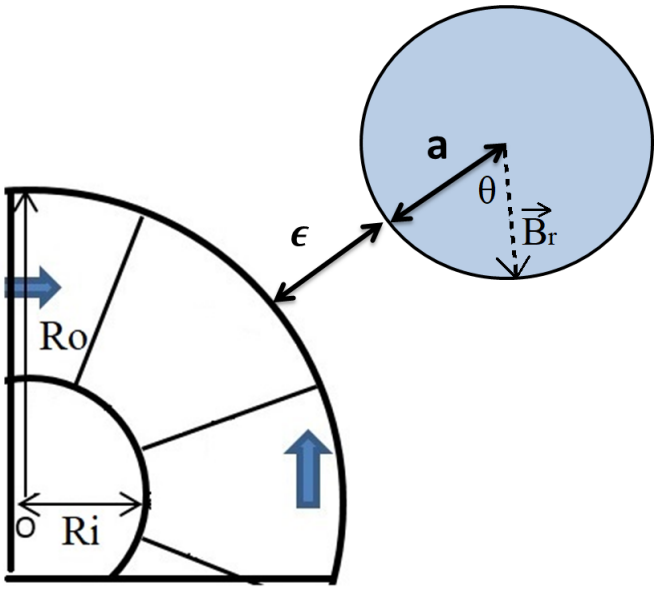

Figure 5.20: Geometrical parameters of the quadrupole.

The radial component of the magnetic field $B(r,\theta)$ produced by a cylindrical magnet at a distance r from its center is given by:

$$B(r,\theta) = \frac{a^2 B_R}{2r^2} cos(\theta)$$

where r is the distance from the center to the cylindrical magnet and θ the angle of the magnetization vector. Assuming that the pole material permeability is infinite, one gets the gradient tunability G_t expression as:

$$G_t = \frac{B(r,\theta)}{R_i} = \frac{B_R cos\theta}{2R_i(1+\epsilon/a)^2} \tag{5.13}$$

Thus, the analytical gradient achieved by the QUAPEVA is calculated to be:

$$G = G_0 \pm G_t \approx 205 \pm 45 \ \ T/m \tag{5.14}$$

Fig. 5.21-a presents the field lines produced by the QUAPEVA computed using Finite Element Method Magnetics (FEMM) [140]. Figures 5.21-b,c and d represent the field lines generated at minimum, average and maximum gradient, respectively. The gradient computed is shown in Table 5.6 to compare with the RADIA model and the analytical calculation.

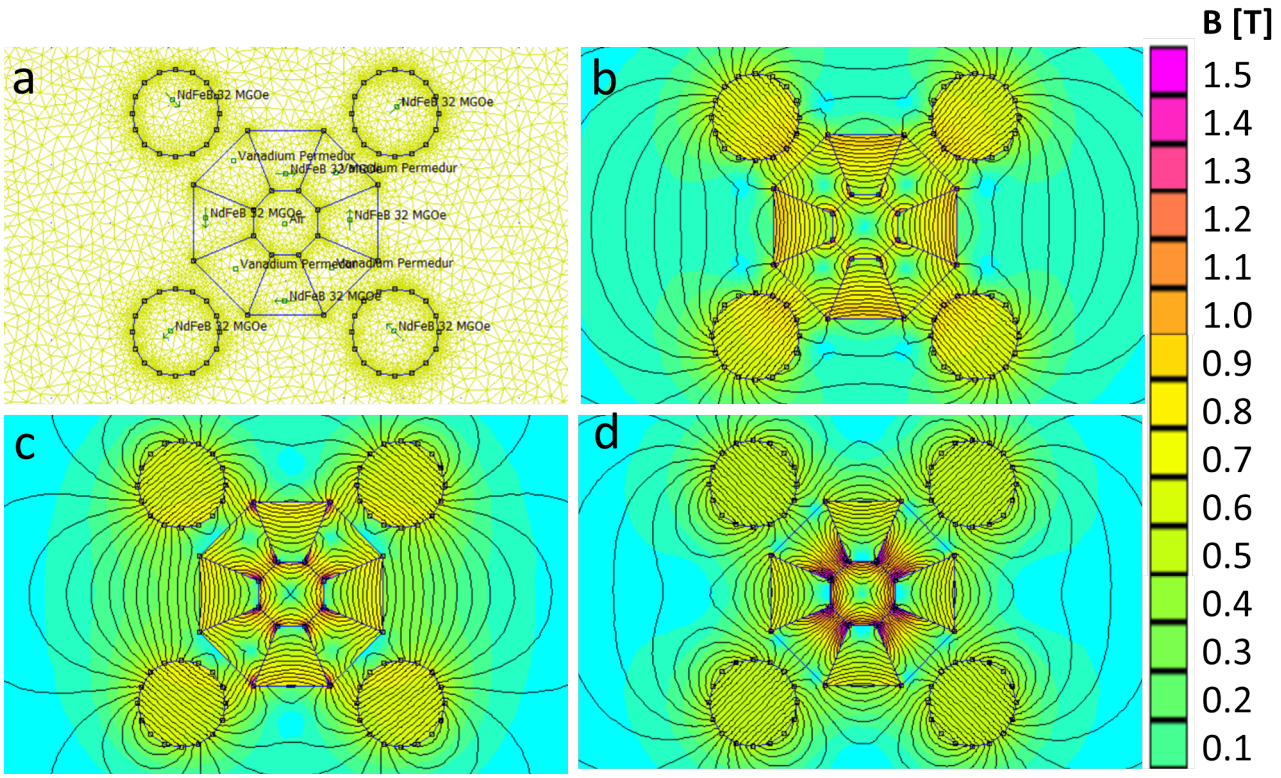

Figure 5.21: (a) QUAPEVA model using FEMM software alongside the field lines produced for the minimum (b), average (c) and maximum (d) gradients. Magnets: $Nd_2Fe_{14}B$ 32MGoe, poles: Vanadium Permendur. Core and the surrounding is air medium.

5.5.3 3D approach

The systems have been optimized using two codes. RADIA [129] and TOSCA [279] a finite element magnetostatic code based on scalar potentials for numerical solution of 3-dimensional nonlinear static. The QUAPEVA design is displayed in Fig. 5.22 using the two codes.

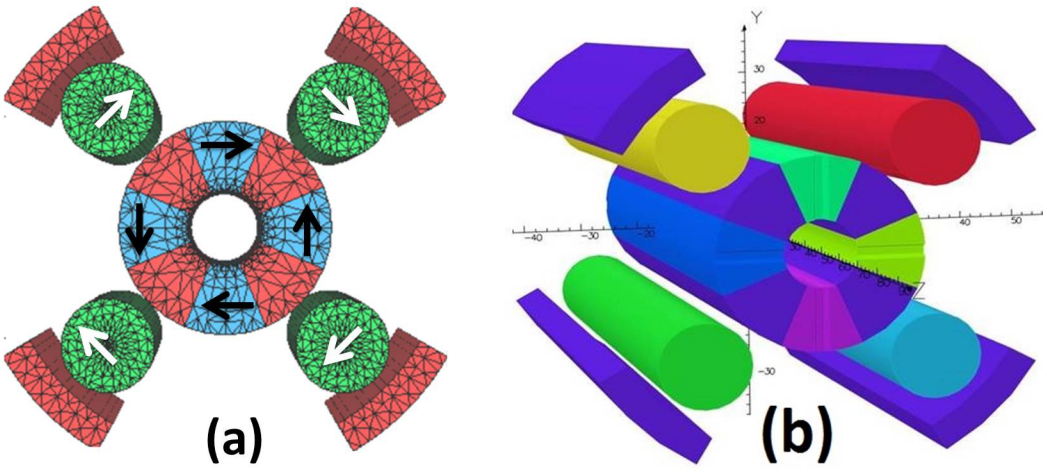

Figure 5.22: QUAPEVA model using RADIA (a) and TOSCA (b).

In the case of the QUAPEVA prototype, the gradient is computed as the cylindrical magnets are rotated from a minimum gradient of 92 T/m to a maximum gradient of ~200 T/m (see Fig. 5.23-a). The gradient tunability (±46 T/m) is in very good agreement with the analytical calculation presented in section 5.5.2.1. As for the fixed gradient, the difference is around 22% due to the approximations made regarding the saturation of the poles. The fringe field decreases in the maximum gradient case as plotted in Fig. 5.23-b

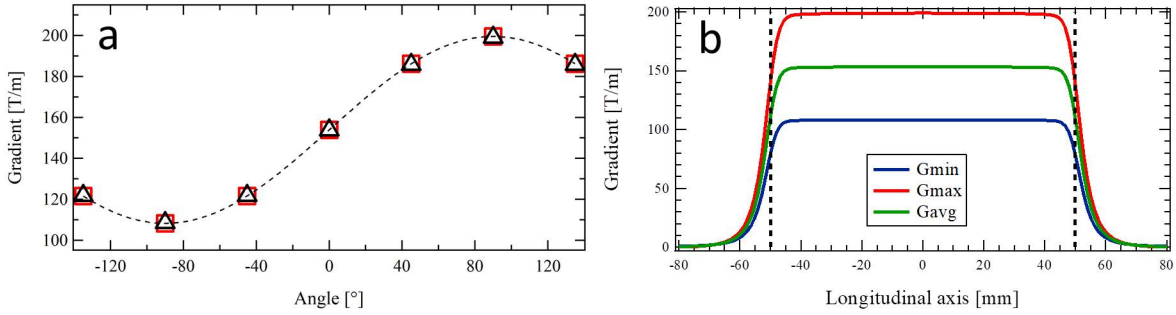

Figure 5.23: (a) Gradient computed with RADIA (□) and TOSCA (△) versus the angle of the cylindrical magnets, and are fitted with a sinusoidal curve (- - -) for the QUAPEVA prototype. (b) The minimum (blue), intermediate (green) and maximum (red) gradient computed along the longitudinal axis.

Computations are done for the QUAPEVA design with different magnetic lengths. Table 5.6 presents the computed gradient for the seven systems using RADIA software and are compared with the 2D approach considering an infinitely long magnet. The maximum gradient and tunability increase for longer magnetic lengths.

	QUAPEVA	L_{mag} mm	G_{min} T/m	G_{avg} T/m	G_{max} T/m	ΔG T/m
2D approach	Analytical	∞	160	205	250	90
	FEMM	∞	125	165	204	79
Prototype	Q0	100	110	154	200	90
	Q1	26	90	128	165	75
1^{st} Triplet	Q2	40.7	98	136	181	83
	Q3	44.7	-100	-142	-184	84
	Q4	47.1	100	143	185	85
2^{nd} Triplet	Q5	66	106	149	193	87
	Q6	81	-108	-152	-197	89

Table 5.6: Maximum gradient (G_{max}), minimum gradient (G_{min}) and average gradient (G_{avg}) alongside gradient tunability for the different systems built. The negative gradient corresponds to a defocusing quadrupole in the horizontal axis.

Table 5.7 shows the computed systematic multipole contents b_2, b_6 and b_{10} for the three gradient cases. b_6/b_2 and b_{10}/b_2 vary between 0.5-1.6% and 1.3-1.6%, respectively, satistfying the requirements presented in the specification section earlier in the chapter (see Table 5.1).

QUAPEVA	G_{min}			G_{avg}			G_{max}		
	b_2 T.mm	b_6 T.mm	b_{10} T.mm	b_2 T.mm	b_6 T.mm	b_{10} T.mm	b_2 T.mm	b_6 T.mm	b_{10} T.mm
Q0	46.5	0.52	-0.77	64.9	1.06	-1.01	83.5	1.37	-1.19
Q1	11.6	0.05	-0.18	16.3	0.17	-0.23	21.0	0.26	-0.28
Q2	18.4	0.14	-0.29	25.8	0.35	-0.38	33.4	0.48	-0.46
Q3	-20.3	-0.16	0.33	-28.5	-0.39	0.43	-36.8	-0.54	0.51
Q4	21.4	0.18	-0.34	30.1	0.43	-0.45	38.8	0.58	-0.54
Q5	30.4	0.32	-0.5	42.5	0.65	-0.65	54.8	0.86	-0.77
Q6	-37.5	-0.39	0.62	-52.4	-0.83	0.81	-67.4	-1.08	0.95

Table 5.7: Normal systematic multipoles computed with RADIA for the seven systems for the three gradient cases using a 4 mm reference radius.

5.5.4 Mechanical design

The QUAPEVAs are installed right after a gas jet where a laser plasma acceleration source generates the electrons. The mechanical structure is adapted to a laser beam passage. The motors are compact and able to handle the magnetic forces induced by the magnetic system. The chosen motors (HARMONIC DRIVE, FHA-C mini motors) have sufficient torque to counteract the magnetic forces, are very compact (48.5 x 50 x 50 mm^3), and have an encoder within a 30 µrad resolution. The magnetic system is mounted on an Aluminum frame and the motorization are placed at the four corners to avoid perturbations of the magnetic field. A non-magnetic belt transmits the rotation movement from the motor to the cylindrical magnets. The use of one motor per magnet allows for a precise positioning of each magnet and minimizes the magnetic center shift at different gradients. The quadrupole is supported by a translation table (horizontal and vertical displacement) used to compensate any residual magnetic axis shift when varying the gradient, to perform electron beam based alignment or for the magnetic measurements benches. The resulting mechanical design is shown in Fig. 5.24 (left), also an assembled QUAPEVA on the translation table in Fig. 5.24 (right).

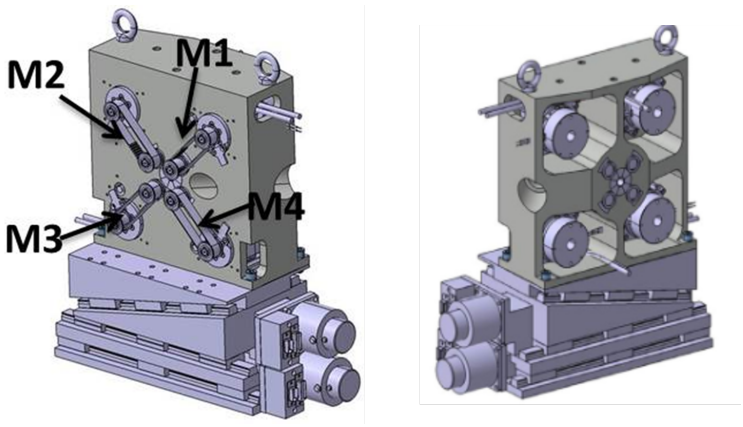

Figure 5.24: (Mechanical design (left) and an assembled QUAPEVA (right) mounted on a translation table.

5.5.5 Magnetic measurement benches

To acquire a full understanding on the behaviour of the QUAPEVAs, in terms of magnetic field multipolar components, gradient, tunability and magnetic center excursion, three magnetic measurements (a rotating coil, a stretched wire, a pulsed wire) are used.

5.5.6 Stretched wire

This method is used to measure the magnetic field integral. A conductive wire is placed in the presence of a magnetic field, and by displacing it, a voltage is induced and thus the field integral is determined.

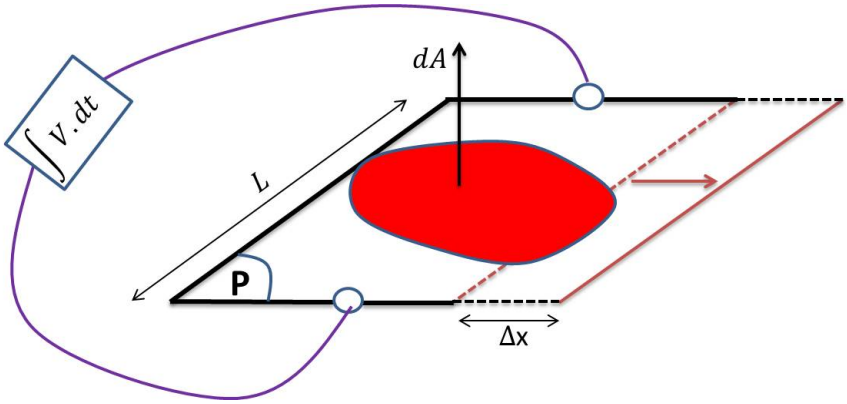

Figure 5.25: Scheme of Farady's law of induction explaining the stretched wire measurement technique.

Starting with Maxwell-Faraday law of magnetic induction ($\nabla \times \vec{E} = \frac{d\vec{B}}{dt}$), the variation of the magnetic flux (ϕ) is expressed as:

$$\Delta\phi = \int V(t).dt = \iint_S \vec{B} dA \tag{5.15}$$

where E is the electric field induced, B the magnetic field, t the time, $V(t)$ the induced voltage and A the surface area where the magnetic field lines pass (see Fig. 5.25). As the wire is moved by a value of Δx, the field integral traversing the area A is measured by:

$$\int \vec{B}.d\vec{l} = \frac{\int V(t).dt}{\Delta x} \tag{5.16}$$

The stretch-wire bench developed at ESRF [280] has been used for magnetic field integral measurements. The wire (Titanium or Beryllium Copper) corresponding to the single side of the coil is positioned inside the magnet gap. The wire resonance frequency is tuned at 300 Hz. Its sag depends on its tension. The small diameter of the wire (100 μm) allows the bench to be used for different bore and gap magnets including very small ones. Two groups of Newport linear stages driven by a Newport XPS motion controller enable the wire displacement. A voltage proportional to the variation of magnetic flux is induced and measured with a Keithley nanovoltmeter, resulting in the first field integral. A granite table supports the linear stages and the measured magnet. The stretched wire bench enables to perform fast measurement with an accuracy of a few 10^{-4} of the main multipole with a repeatability of 2×10^{-5}.

5.5.7 Rotating coil magnetic measurement

The rotating coil, similar to the stretched wire, measures the field integral by integrating the voltage induced at the edge of a coil. The rotating coil has a rectangular shape of width a and length L in the longitudinal direction. A coil of width Δx in the presence of a magnetic field generates a flux variation expressed as:

$$\int_{-L/2}^{L/2} \vec{B}.d\vec{l} = \frac{\int V(t).dt}{\Delta x} \tag{5.17}$$

A dedicated radial rotating coil (see Fig. 5.26) of 10 mm diameter was built [281] for the SOLEIL magnet characterization bench, to fit the quadrupole inner diameter of 10.5 mm. Only 0.25 mm

gap between the coil and the magnet parts is available. In order to qualify the accuracy of the rotating coil, a permanent magnet quadrupole with a 76 mm diameter bore has been measured first with a reference coil and then with the 10 mm diameter coil. The geometrical parameter of the new coil has been determined in order to find the same harmonic content with both coils at a measuring radius of 4 mm.

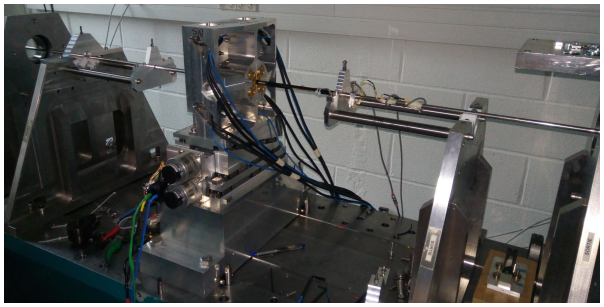

Figure 5.26: Rotating coil bench at SOLEIL with a QUAPEVA installed.

5.5.7.1 Coil Offset with respect to the bench

Before optimizing a QUAPEVA with the rotating coil bench, the coil offsets (x_{coil}, z_{coil}, θ_{coil}) with respect to the bench axis have to be determined especially the angle offset that induces false skew terms. Eqs. (5.8) and (5.9) can be written in 3D as:

$$\begin{cases} x/\mathrm{R} = -\frac{a_1 a_2 + b_1 b_2}{a_2^2 + b_2^2} \\ z/\mathrm{R} = \frac{a_2 b_1 - b_2 a_1}{a_2^2 + b_2^2} \\ \theta_{quad} = -\frac{1}{2}\arctan(a_2/b_2) \end{cases} \tag{5.18}$$

Using the QUAPEVA prototype ($\mathrm{L}_{mag} = 100$ mm), the magnetic center (x_1, z_1) and angle θ_{q1} are calculated using Eqs. (5.18), where R = 4 mm the radius of the coil. Then, the QUAPEVA is reversed along the vertical axis and re-measured to calculate the new positions (x_2, z_2) and angle (θ_{q2}). The angle and horizontal offsets of the coil are deduced using:

$$\begin{cases} x_{coil} = (x_1 + x_2)/2 \\ \theta_{coil} = (\theta_{q1} + \theta_{q2})/2 \end{cases}$$

The coil vertical offset z can not be measured using the QUAPEVA design since it can not be rotated along the longitudinal axis.

Eight measurements have been done (four before and four after reversing the QUAPEVA along the vertical axis) and are shown in Table 5.8. Taking the average of these measurements, the coil offsets are found to be:

$$\begin{cases} x_{coil} = 36 \ \ \mu\mathrm{m} \\ \theta_{coil} = 143 \ \ \mathrm{mrad} \end{cases} \tag{5.19}$$

	Measurement				Average	SD	unit
	1	2	3	4			
x_1	50.3	49.8	53.5	49.7	50.8	1.8	µm
z_1	-138	-136	-135	-137	-136.5	1.3	µm
θ_{q1}	148.8	148.4	148	148.8	148.5	0.4	mrad
x_2	38.7	35.3	32.4	38.7	36.3	3.0	µm
z_2	-139	-143	-142	-141	-141.2	1.7	µm
θ_{q2}	136.5	136.6	136.6	136.66	136.6	0.1	mrad

Table 5.8: Coil offset measurements for R = 4 mm. **SD** stands for standard deviation.

In order to verify the parameters of the coil offsets, the SOLEIL permanent magnet reference quadrupole is used. It has an octupole shape with a large core diameter of 76 mm (see Fig. 5.27).

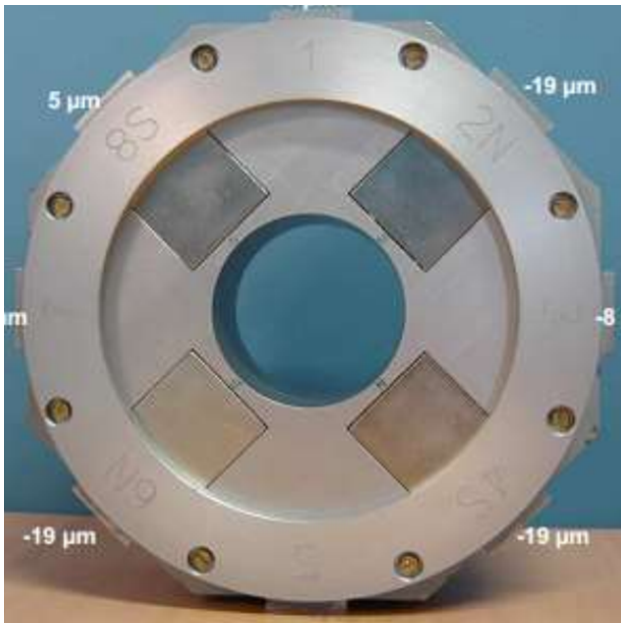

Figure 5.27: Octupole shaped quadrupole (reference quadrupole).

Table 5.9 shows the measurements for each side of the quadrupole and eight others after reversing the quadrupole around its vertical axis.

	Normal			Reverse		
Side	x [µm]	z [µ m]	θ [mrad]	x [µm]	z [µ m]	θ [mrad]
1	341	-121	137	546	-33	163
2	488	-141	-647	487	-121	-626
3	568	-56	140	310	-116	160
4	611	70	-645	226	42	-626
5	494	195	141	278	174	161
6	380	174	-645	430	209	-624
7	271	88	139	531	169	162
8	257	-46	-647	-73	-87	-624

Table 5.9: Coil offset measurements.

Fig. 5.28 plots the magnetic center variation as the reference quadrupole is rotated along its

longitudinal axis. The coil offsets are the center of the circles, and by taking the average, the coil offsets are found to be:

$$\begin{cases} x_{coil} = 426 \ \mu\text{m} \\ z_{coil} = 35 \ \mu\text{m} \\ \theta_{coil} = 148 \ \text{mrad} \end{cases} \tag{5.20}$$

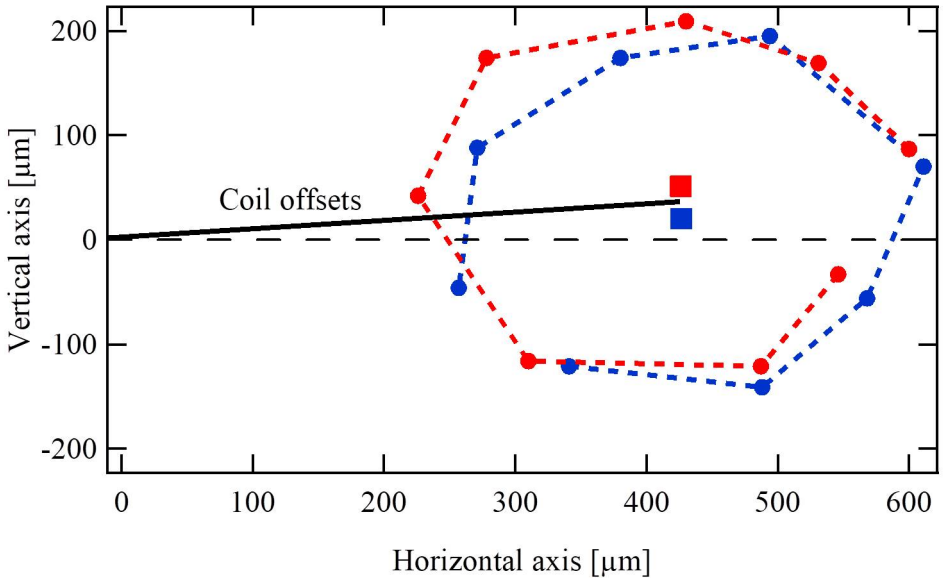

Figure 5.28: Magnetic center excursion measured for the reference quadrupole using the rotating coil bench as the quadrupole is rotated along the longitudinal axis. (Blue) the "normal position", (red) reversed along the vertical axis.

The coil offset angle is consistent between using the prototype QUAPEVA and the reference quadrupole with a difference of ~3% that is still quite large, so the one measured using the QUAPEVA prototype is taken into account. As for the horizontal offset, the value is significantly different because each quadrupole has a special support.

In summary, the coil offsets taken for the rotating coil measurements are:

$$\begin{cases} x_{coil} = 36 \ \mu\text{m} \\ z_{coil} = 35 \ \mu\text{m} \\ \theta_{coil} = 143 \ \text{mrad} \end{cases} \tag{5.21}$$

5.5.8 Pulsed wire bench

This measurement is based on applying a square current pulse through a wire placed in a magnetic field, which induces an interaction due to Lorentz force [282]. This force leads to wire displacement which is measured using a motion laser detector. The wire displacement is proportional to the magnetic field, hence it enables to measure the magnetic center of the QUAPEVA.

The pulsed-wire method has been used to align the magnetic center of the three QUAPEVAs (see Fig. 5.29 before their installation at COXINEL transport line. The wire's material is Tungsten with 125 μm thickness, and stretched with a 10 N force. The current sent through the wire is ~10 A. A reproducibility of +/-13 µm and an precision of 5 µm are achieved.

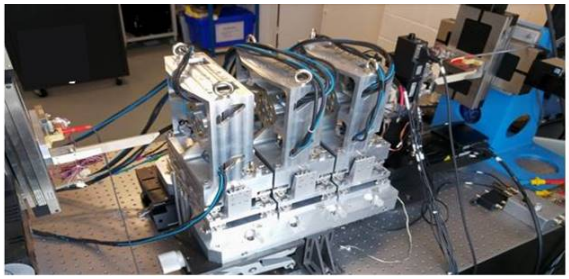

Figure 5.29: First QUAPEVA triplet placed on the pulsed wire bench to align their magnetic center.

5.6 Measurement results

The magnetic measurements of a QUAPEVA starts by calibrating the rotation of the magnets, and followed by the acquisition of multipole data.

5.6.1 Calibration of the rotating magnets

The cylindrical magnets should be well aligned in their orientation as the motors rotate in order to achieve the maximum gradient such that θ in Fig. 5.20 is equal to zero. A misalignment in one of the motors induces non-systematic multipoles especially the dipolar terms that increases the magnetic center excursion. After some time of commissioning the QUAPEVAs, the magnets might become misaligned due to the efficiency of the belts that transmit the motion from motor to magnet. So before operation at COXINEL, a calibration had to be done.

The calibration is done by measuring the normal quadrupolar term as each motor is rotated individually. Then an offset is applied to each motor to ensure that the minimum and maximum gradients are found at angles 90° and -90°, respectively. Fig. 5.30-a, b, c and d present the normal quadrupolar, skew quadrupolar, normal dipolar and skew dipolar components, respectively, as the motors are rotated after the calibration of the 26 mm QUAPEVA.

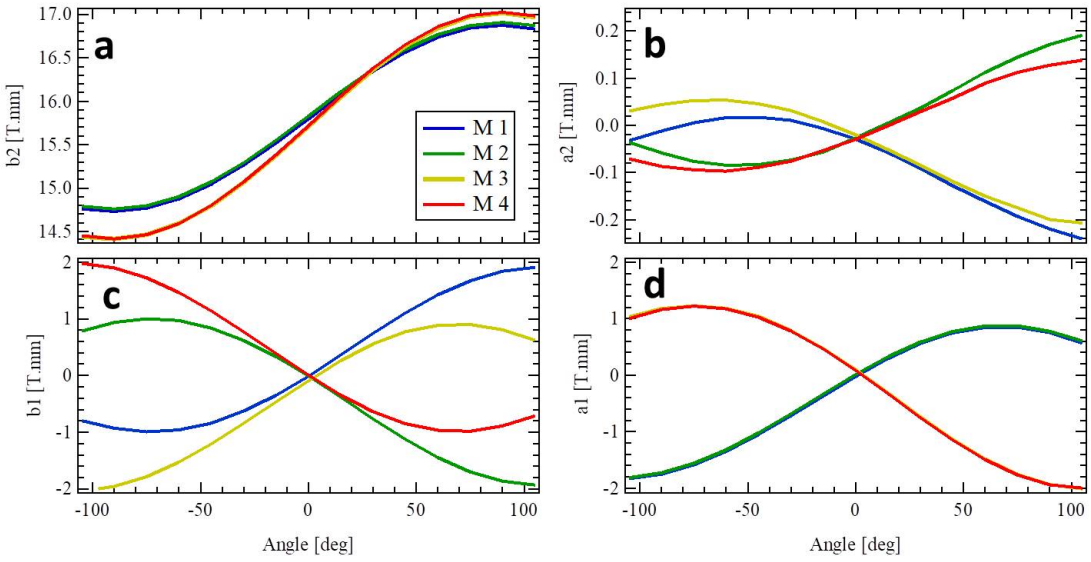

Figure 5.30: Stretched wire measurement on Q1 of the dipolar and quadrupolar terms (normal and skew) as a function of the rotation of one cylindrical magnet at a time. (M1, M2, M3, M4) are the cylindrical magnets or motors.

5.6.2 Multipoles

After the calibration of each motor, the QUAPEVA is ready to be fully characterized. Fig. 5.31 shows the variation of b_2 measured with the stretched wire, for the two triplets, as the cylidrical magnets rotate from -90^o to +90^o.

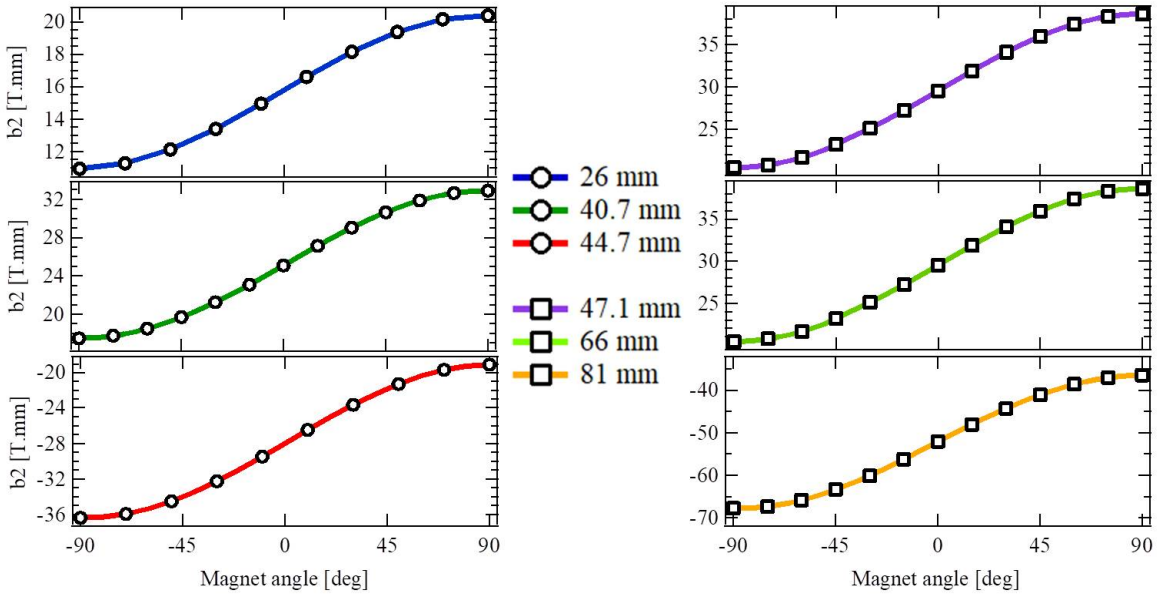

Figure 5.31: b2 measured with the stretched wire for the two triplets. QUAPEVA being referred by its magnetic length.

Table 5.10 presents the maximum gradient for the seven systems (QUAPEVAs) measured with the rotating coil and stretched wire. The difference between the two measurements can be due to the fact that the rotating coil was not perfectly centered and was touching the QUAPEVA small bore surface. The deviation of the stretched wire measurements with respect to the simulations increases for shorter magnetic length due to a notch in the poles of thickness 1 mm that is missing in the RADIA model.

QUAPEVAs	L_{mag}	b_2			Δ_{exp}	Δ_{sim}
		Rotating coil	Stretched wire	RADIA		
	mm	T.mm	T.mm	T.mm	%	%
Q1	26	20.0	20.4	21.0	2.0	-3.0
Q2	40.7	30.2	32.8	33.4	8.6	-1.8
Q3	44.7	-35.3	-36.4	-36.8	3.0	-1.1
Q4	47.1	35.5	38.5	38.8	8.5	-0.8
Q5	66	50.1	54.9	54.8	9.6	0.2
Q6	81	-66.8	-67.5	-67.4	1.0	0.1

Table 5.10: Normal quadrupolar term b_2 measured for the maximum gradient case with the rotating coil and stretched wire for the two triplets at a radius of 4 mm. Δ_{exp} the deviation of the stretched wire measurement from the rotating coil one. Δ_{sim} the deviation of the stretched wire measurement from the simulated one.

Figure 5.32 presents the systematic multipoles b_6 and b_{10} normalized with b_2 measured with the rotating coil and stretched wire. The QUAPEVAs specification, in Table 5.1, have been achieved.

In summary, due to the small bore diameter of the QUAPEVA, the stretched wire measurement is more efficient than the rotating coil, thus it is used as our reference measurement of the multipoles.

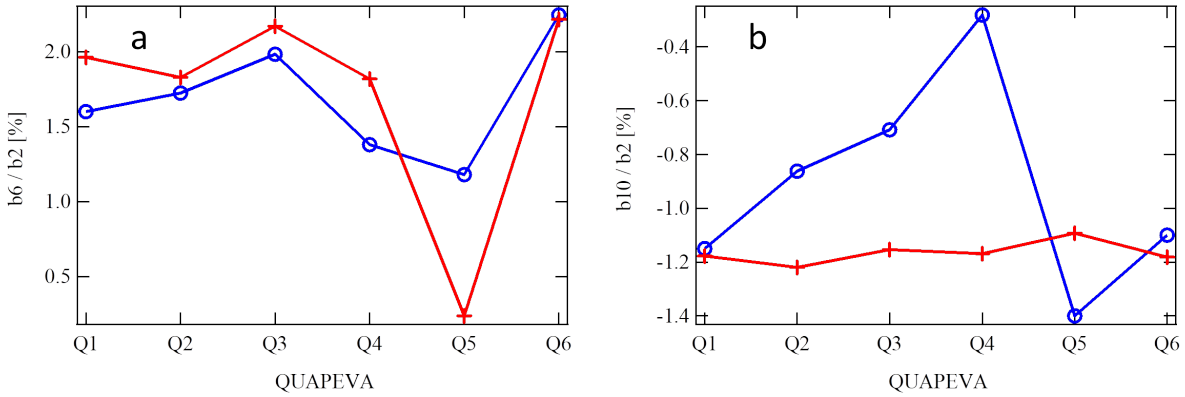

Figure 5.32: Normalized b_6 (a) and b_{10} (b) with respect to b_2 measured with the stretched wire (+), rotating coil (∘) for all the QUAPEVAs.

Tables 5.11 and 5.12 present some of the systematic and non-systematic multipoles measured with the stretched wire normalized with $b_2/10^4$. The values are quite low, corresponding to a good field quality of the quadrupoles.

QUAPEVA	G_{min}			G_{avg}			G_{max}		
	b_6	b_{10}	b_{14}	b_6	b_{10}	b_{14}	b_6	b_{10}	b_{14}
Q1	165	-108	-1	124	-77	-0.8	167	-105	0.5
Q2	190	-90	-5	165	-90	5	210	115	6
Q3	190	-130	5	350	-180	-6	220	-140	-3

Table 5.11: Systematic multipole terms for the first QUAPEVA triplet for a 4 mm reference radius. Values are normalized with $b_2/10^4$.

	b_1	b_3	b_4	b_5	a_1	a_3	a_4	a_5
Q1	-12	27	2	-122	12	27	2	-122
Q2	-2	6	7	-1	-9	15	12	-5
Q3	-83	12	12	-9	41	6	17	-8

Table 5.12: Non-systematic multipole terms at the maximum gradient for the first QUAPEVA triplet for a 4 mm reference radius. Values are normalized with $b_2/10^4$.

5.6.3 Magnetic center evolution

As the gradient of the QUAPEVA is varied by rotating the cylindrical magnets, the dipolar terms (b_1 and a_1) slightly change resulting in a magnetic center shift. Fig. 5.33 shows the magnetic center excursion measurement using the stretched wire, rotating coil and pulsed wire for the first triplet as the gradient is varied from minimum (-90^o) to maximum (90^o) before the calibration of the motors (see subsection 5.6.1). The magnetic center excursion varies between -100 µm and 100 µm. This high value is due to misalignments in one or all the rotating magnets which induces a large dipolar terms and thus shifts the magnetic center from the mechanical center.

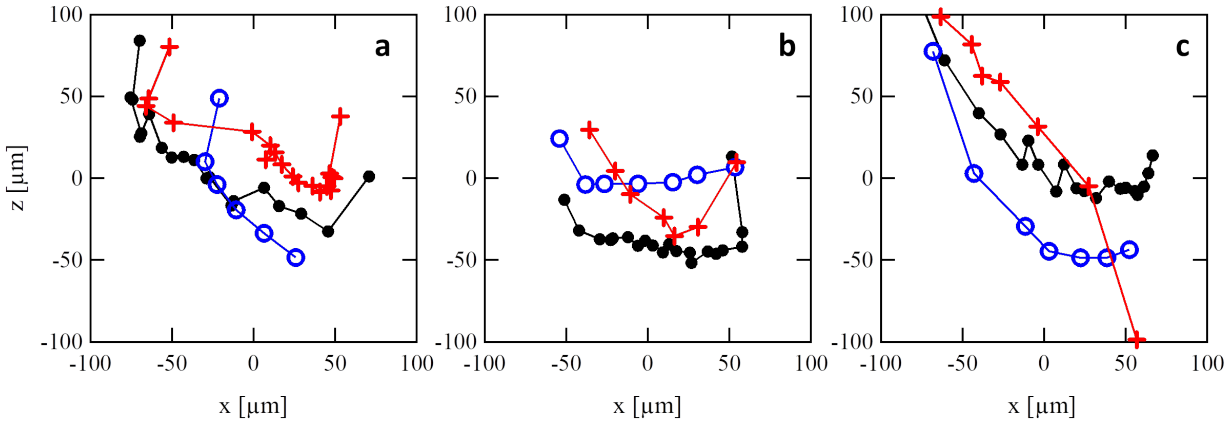

Figure 5.33: Magnetic center excursion before rotating magnets calibration measured with the stretched wire (+), rotating coil (∘) and pulsed wire (•) for the first triplet: (a) 26 mm, (b) 40.7 mm, (c) 44.7 mm.

Fig. 5.34 shows the magnetic center excursion measurement using the stretched wire, rotating coil and pulsed wire for the first triplet after the calibration of the motors. The magnetic center excursion is reduced by almost a factor of 10 after calibration.

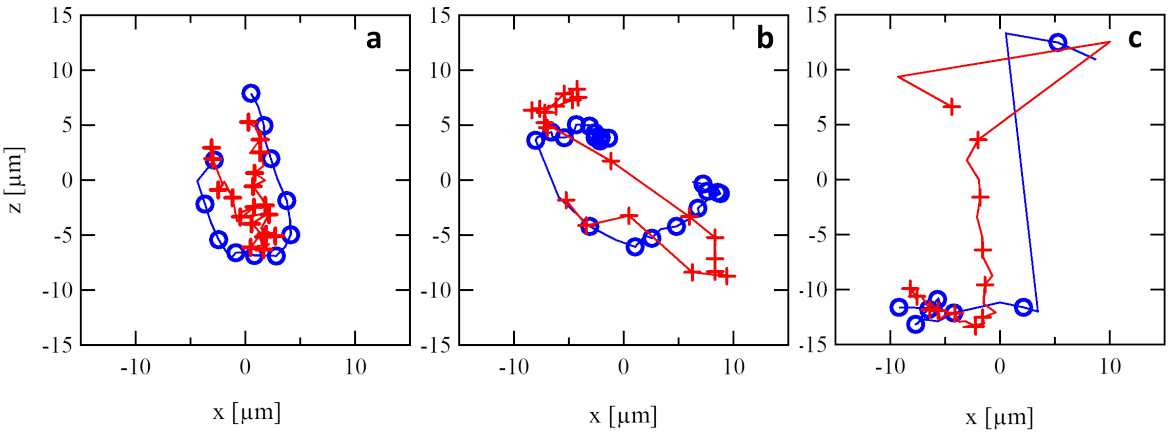

Figure 5.34: Magnetic center excursion after rotating magnets calibration measured with the stretched wire (+), rotating coil (∘) and pulsed wire (•) for the first triplet: (a) 26 mm, (b) 40.7 mm, (c) 44.7 mm.

Fig. 5.35 shows the magnetic center excursion measurement using the stretched wire for the second triplet. The magnetic center stability remains within ±8 µm in vertical and ± 4 µm in horizontal, except for the 66 mm magnetic length QUAPEVA, where it has a larger excursion (± 30 µm) which is due to the fact that the motors have not been calibrated properly for this measurement.

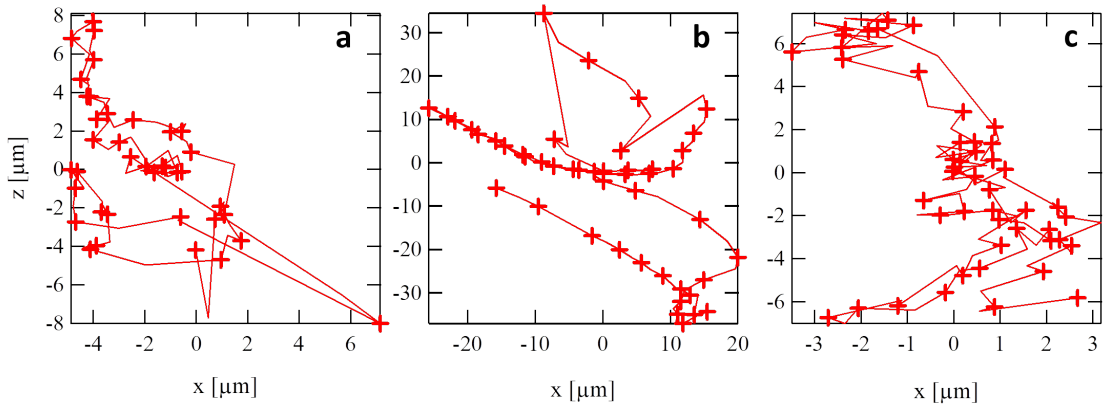

Figure 5.35: Magnetic center excursion after rotating magnet calibration measured with the stretched wire for the first triplet: (a) 47.1 mm, (b) 66 mm, (c) 81.1 mm.

5.6.4 Alignment

The use of the pulsed wire enables to check if there is not cross fields between the different magnet of a given triplet. Fig. 5.37 presents the measurement before and after adjusting the alignement of the three QUAPEVAs using the translation table. The wire displacement has decreased from a maximum value of 4 µm down to 0.2 µm.

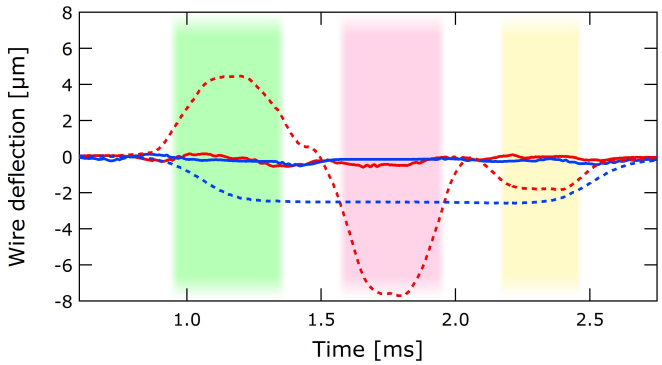

Figure 5.36: Wire displacement through the triplet (green: 44.7 mm, pink: 40.7 mm, yellow: 26 mm). (Red dashed) vertical before alignment, (Blue dashed) horizontal before alignment, (Red line) vertical after alignment, (Blue line) horizontal after alignment.

To report the fudicialization of the bench to the installation on the COXINEL line, the position of the wire on the stretched wire bench is measured with the laser tracker using the faces of the V shape mechanical, where the wire is positioned and by measuring the reference quadrupole sight also with the laser tracker.

5.6.5 Skew term compensation

Because of the inherent uncertainty of the assembly process on the positions of the central Halbach ring structures, the QUAPEVA design is subjected to a default skew quadrupole contribution a_2. After construction, the measured a_2 of the triplet presents a non-negligible contribution. This term induces a coupling effect and tilts the electron beam. It also increases the slice emittance during transport [283] that hinders the FEL performance (in case of COXINEL). The skew quadrupole components, arising from the roll angle in the QUAPEVA, are corrected by introducing a small metallic plate (called shim) as thick as 500 µm between the QUAPEVA and the base as shown in

Fig. 5.37-(left). The roll angle (QUAPEVA angle presented in Eq. (5.18)) of the three QUAPEVAs is reduced as shown in Fig. 5.37-(right).

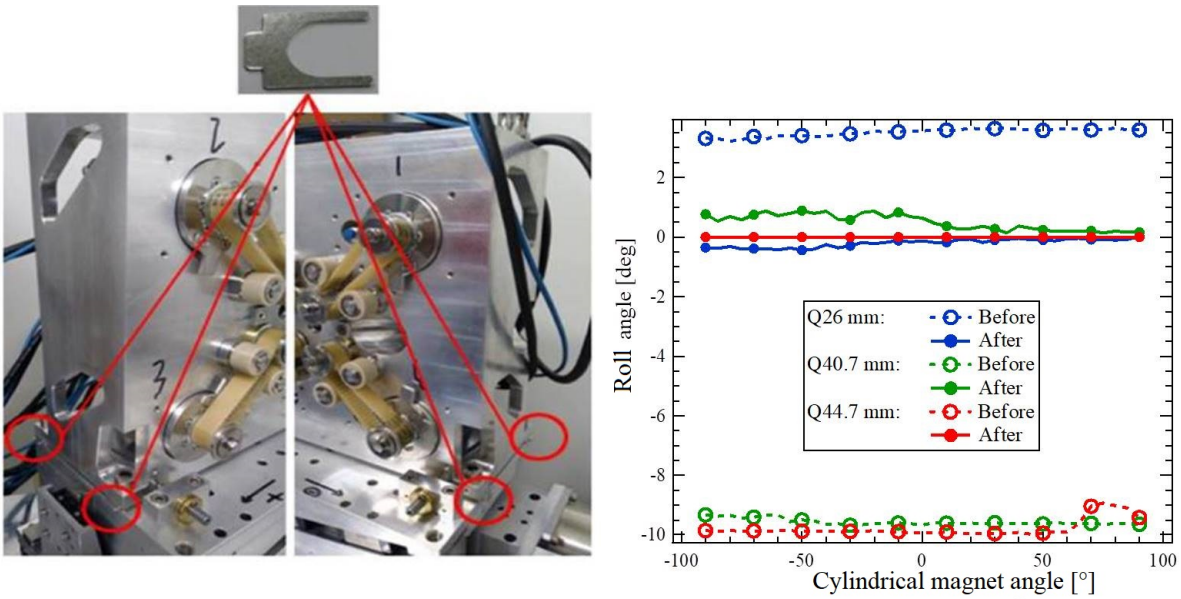

Figure 5.37: (left) mechanical shims applied to the QUAPEVAs at the four corners. (Right) roll angle of the QUAPEVA measured using the stretched wire bench before (dashed lines) and after (solid lines) shimming while varying the gradient.

Table 5.13 shows the skew terms a_2 and a_6, for the operating gradients at COXINEL, before and after applying the shims. The a_2 term is reduced by a factor of ~10 for the 26 mm and 40.7 mm QUAPEVAs and a factor of ~100 for the 44.7 mm QUAPEVA.

Magnetic length	**Before Shimming**				**After Shimming**			
	a_2 [T.mm]	a_6 [T.mm]	b_2 [T.mm]	Angle [mrad]	a_2 [T.mm]	a_6 [T.mm]	b_2 [T.mm]	Angle [mrad]
26 mm	0.073	-0.003	10.951	3.3	-0.007	-0.01	10.947	-0.3
40.7 mm	-0.325	-0.017	17.475	-9	0.027	-0	17.448	0.7
44.7 mm	0.362	0.012	-19.181	-9.4	0.003	-0.004	-19.148	0.05

Table 5.13: Multipolar terms after applying the shims.

5.7 QUAPEVAs optimization summary

Firstly, the QUAPEVAs cylindrical magnets are calibrated to ensure a small magnetic excursion as the gradient in varied. Second, mechanical shimming is applied to reduce the skew component.

5.8 Conclusion

Seven permanent magnet based quadrupoles (QUAPEVAs) of different magnetic lengths achieving a high tunable gradient have been successively built and characterized. The longest QUAPEVA (100 mm) provided a maximum gradient of 200 T/m with a 92 T/m tunability. An analytical approach is presented and compared to modeling where they are in good agreement. The measurement using different methods are consistent and in good agreement between themselves and the

simulations. The residual excursion of the magnetic center has been limited to a $\pm 10\ \mu m$ as the gradient is varied after the calibration of the rotating magnets, that in combination with the translation tables on which the QUAPEVAs are mounted, enabled to do beam pointing alignment compensation of the electron beam [284]. A new performance criterion ($G_{max} \times \Delta G$) is introduced in Fig. 5.38 and the QUAPEVA (100 mm magnetic length) is compared with the other variable PMQs presented in the state of art section where it attained the highest performance.

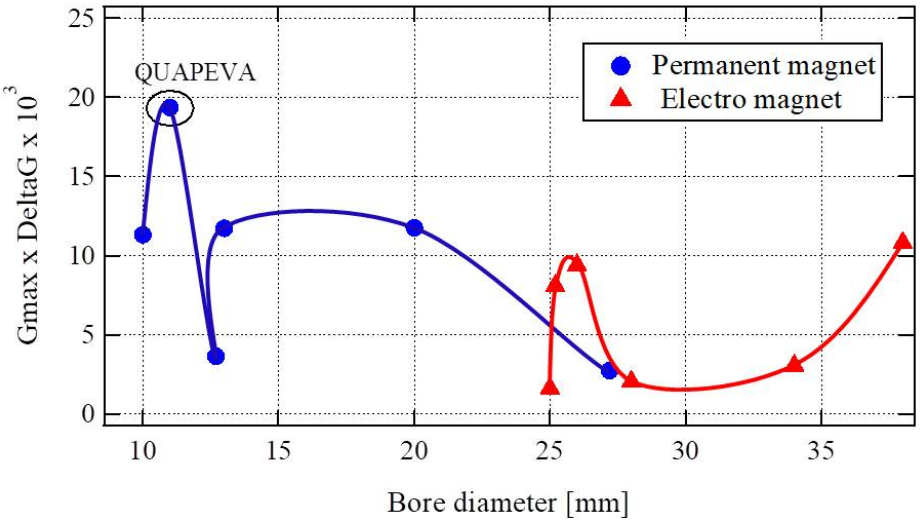

Figure 5.38: Maximum gradient multiplied by the gradient tunability for the different variable PMQs presented in the state of art.

5.9 Prospects

To improve the gradient of QUAPEVA one can integrate a cooling system at liquid nitrogen temperature [261] at 77 K and also use $Pr_2Fr_{14}B$ permanent magnets [262] with a remanent magnetization at this temperature equal to 1.7 T (1.42 T at room temperature). Simulations have been done with the QUAPEVA design for different remanent fields. The gradient increases linearly with respect to the remanent field as $G \approx 156.7 B_r$ (determined by using a fit on the simulations), so by using a $Pr_2Fe_{14}B$ magnet cooled down at cryogenic temperature (~77 K), the produced gradient is ~ 270 T/m. However, at low temperatures mechanical issues can arise concerning the cooling tube and the increase in the magnetic forces. In addition, a design with a hyperbolic shape enabling to reduce the multipole content in compromising on the gradient magnitude and variability, is of great interest for low emittance storage rings.

Chapter 6

Undulator Radiation in COXINEL framework

In this chapter, the computed undulator radiation in the framework of COXINEL is presented in details using SRW code [134]. The effect of the beam parameters (energy spread, divergence and beam size) on the spectra produced is examined and different approaches are utilized in order to estimate the parameters from the spectra.

6.1 Spectral flux

The effect of the observation aperture on the spectral flux is firstly examined. Afterwards, the energy spread and divergence effect are studied. For all the simulations, the radiation source used is the U18 undulator with parameters presented in Table 6.1. The magnetic field is set at 1 T corresponding to a K_u value of 1.7 attained with an undulator gap of 5.5 mm.

Parameter	Symbol	Value	Unit
n^o of periods	N_u	110	-
Period	λ_u	18.16	mm
Length	L_u	2	m
Gap	g_u	5.5	mm
Peak field	B_u	1	T
Deflection parameter	K_u	1.7	-

Table 6.1: U18 undulator characteristics.

The computed spectra is interpreted using the theory presented in Chapter 2. The equations describing the homogeneous bandwidth Eq. (2.51), energy spread contribution Eq. (2.59) and divergence Eq. (2.60) on the bandwidth, as presented in Chapter 2, are expressed as:

$$\begin{cases} \left[\frac{\Delta\lambda}{\lambda}\right]_{hom} = \frac{1}{nN_u} \\ \left[\frac{\Delta\lambda}{\lambda}\right]_{\sigma_\gamma} = 2\sigma_\gamma \\ \left[\frac{\Delta\lambda}{\lambda}\right]_{\sigma'_{x,z}} = \frac{\gamma^2\sigma'^2_{x,z}}{1+K_u^2/2} \end{cases} \tag{6.1}$$

With these contributions an attempt to estimate some beam parameters is done throughout the chapter. The method is first tested on the modeled case, in view of applying later on the undulator radiation measurements at COXINEL.

6.1.1 Single electron computation

The simulated radiation from a single electron traversing an undulator in SRW is computed in the near field approximation. Figure 6.1 shows the simulated spectra generated by a single electron of the COXINEL operation energy 161 MeV observed at a distance of 5 m from the undulator center. The spectrum exhibits a non-smooth shape originating from the off-axis radiation. As the aperture is reduced in dimensions, the spectrum is dominated by the on-axis radiation and a sinus cardinal shape starts to appear. Recall from Eq. (2.53) that the on-axis intensity $I_{on-axis}$ can be expressed as:

$$I_{on-axis} \propto sinc^2\left(\pi N_u \frac{\omega-\omega_r}{\omega_r}\right)$$

It has been shown in Eq. (2.48) that the undulator radiation wavelength has the following expression:

$$\lambda = \frac{\lambda_u}{2n\gamma^2}\left(1+K_u^2/2+\gamma^2\theta^2\right) \tag{6.2}$$

The flux is peaked at the resonance energy E_{res} (resonant wavlength λ_{res}) when the aperture dimensions are quite small (<1 mm x 1 mm), so that the spectrum is dominated by the on-axis radiation. As for large window apertures, the flux is peaked at a slightly detuned energy E_{peak}.

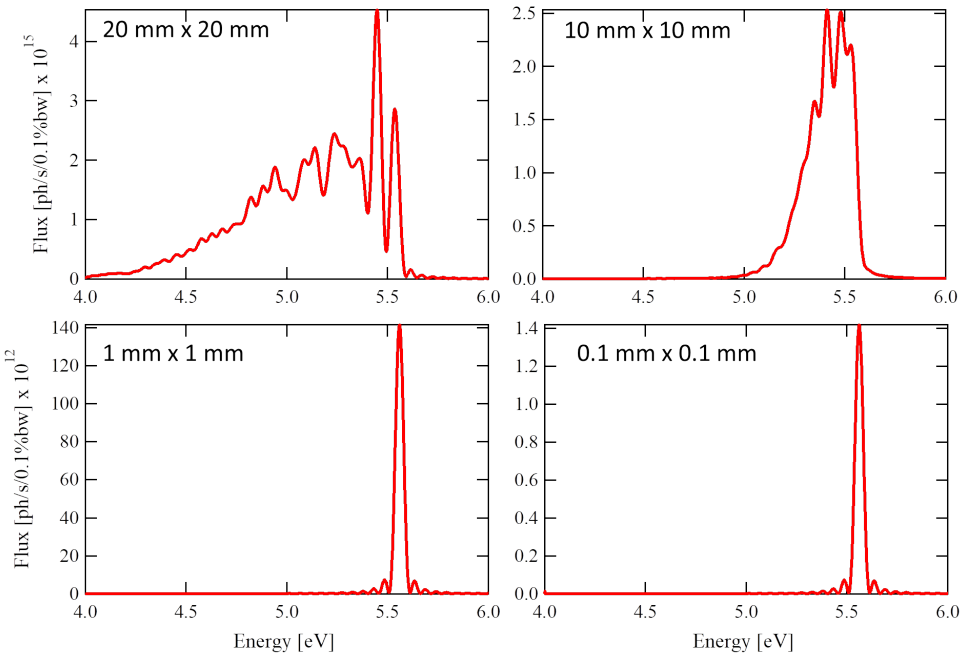

Figure 6.1: Near-field SRW simulated spectral flux captured for different window apertures (appended) placed at a distance of 5 m from the undulator center. Single electron E = 161 MeV. Undulator: λ_u = 18.16 mm, B = 1 T, K_u = 1.7, N_u = 110.

Table 6.2 shows the full width half maximum bandwidth $\Delta\lambda$, peaked energy (wavelength) E_{peak} (λ_{peak}) and relative bandwidth $\Delta\lambda/\lambda$ for different window apertures. The peaked energy (wavelength) of the first harmonic (n = 1) is found to be 5.56 eV (223 nm) equal to the resonance calculated one using Eq. (6.2) for θ = 0. The bandwidth is constant for a window aperture of dimensions smaller than 1 mm x 1 mm, meaning that for this aperture dimension and distance, the window is close to a pinhole observation. The simulated bandwidth is found to be ~0.83% close to the natural linewidth introduced in Eq. (2.51) as $1/N_u$ = 0.9%. Hence, the spectral bandwidth (FWHM) for a single electron emission is taken to be equal to the natural linewidth.

Aperture	Δλ		E_{peak}	λ_{peak}	Δλ/λ
mm x mm	[eV]	[nm]	[eV]	[nm]	[%]
20 x 20	-	-	5.4	229	-
10 x 10	0.25	10.5	5.45	227	4.6
1 x 1	0.04	1.83	5.56	223	0.83
0.1 x 0.1	0.04	1.83	5.56	223	0.83

Table 6.2: FWHM bandwidth and resonance of the radiation captured by different window apertures. Single electron E = 161 MeV. Undulator: λ_u = 18.16 mm, B = 1 T, K_u = 1.7, N_u = 110.

6.1.2 Multi-electron computation

The undulator radiation emitted by a thick electron beam (non-zero emittance and energy spread) observed through a rectangular aperture is computed with SRW in the far-field approximation. This type of computation is less accurate than the near-field one but saves a lot of time. Table 6.3 presents the reference electron beam parameters, same as COXINEL baseline reference case but with lower energy (see Table 3.4).

Parameters	**Symbol**	**Value**	**Unit**
Energy	E	161	MeV
Energy spread (rms)	σ_γ	0.1	%
Beam size (rms)	$\sigma_{x,z}$	0.1	mm
Divergence (rms)	$\sigma'_{x,z}$	0.1	mrad

Table 6.3: Reference beam parameters at the center of the undulator.

Figure 6.2 compares the spectra computed in the near field (red) and far field (blue) approximations for two cases of window aperture: (a) 20 mm x 20 mm and (b) 1 mm x 1 mm. In the near field, the radiation of 100 single electrons is computed and then the intensity is added. The parameters of each electron follow Gaussian distributions with standard deviations equal to the reference beam parameters (see Table 6.3). In the far-field, the flux captured by a large aperture presents a smoother shape than the near-field one due to the low number of electrons. For a small aperture, the near-field and far-field are the same, signifying that the far-field computation is precise enough to conduct futher studies. The spectral flux captured by the window of dimensions 1 mm x 1 mm. The spectra is peaked at the resonance energy of 5.56 eV (223 nm) with a bandwidth of 0.91% $\approx 1/N_u$. These beam parameters are considered to be our reference case where the bandwidth of the spectra produced is very close to the natural linewidth.

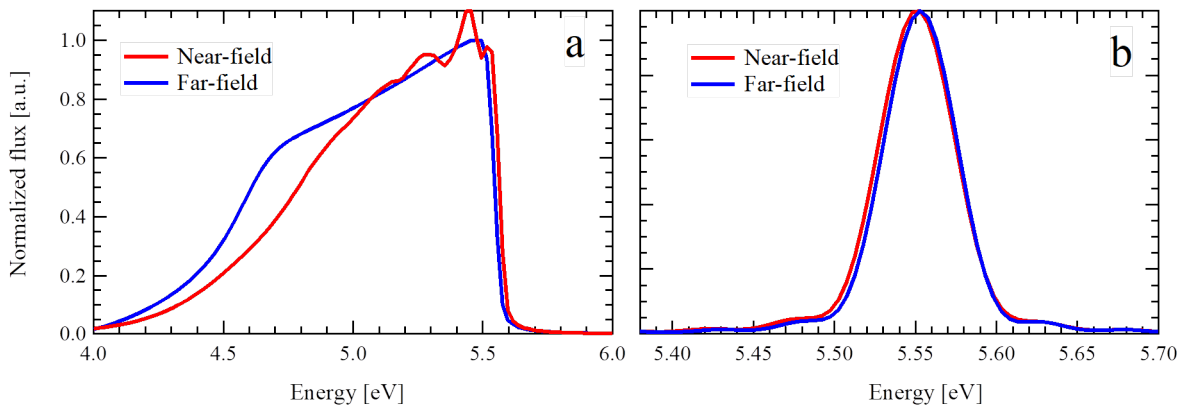

Figure 6.2: SRW simulated spectral flux using the near-field and far-field approximations for window aperture of dimensions 20 mm x 20 mm (a) and 1 mm x 1 mm (b) placed at a distance of 5 m from undulator center. Electron beam: E = 161 MeV, σ_γ = 0.1%, $\sigma_{x,z}$ = 0.1 mm, $\sigma'_{x,z}$ = 0.1 mrad. Undulator: λ_u = 18.16 mm, B = 1 T, K_u = 1.7, N_u = 110.

6.1.3 Effect of the window aperture on the spectral flux for the reference electron beam

Fig. 6.3 displays the spectral flux captured by a window aperture of different dimensions. The horizontal and vertical apertures have more or less the same effect on the spectra, where the bandwidth is broadened on the red-side (low energies) for large window apertures due to the $\gamma^2\theta^2$ term in Eq. (6.2).

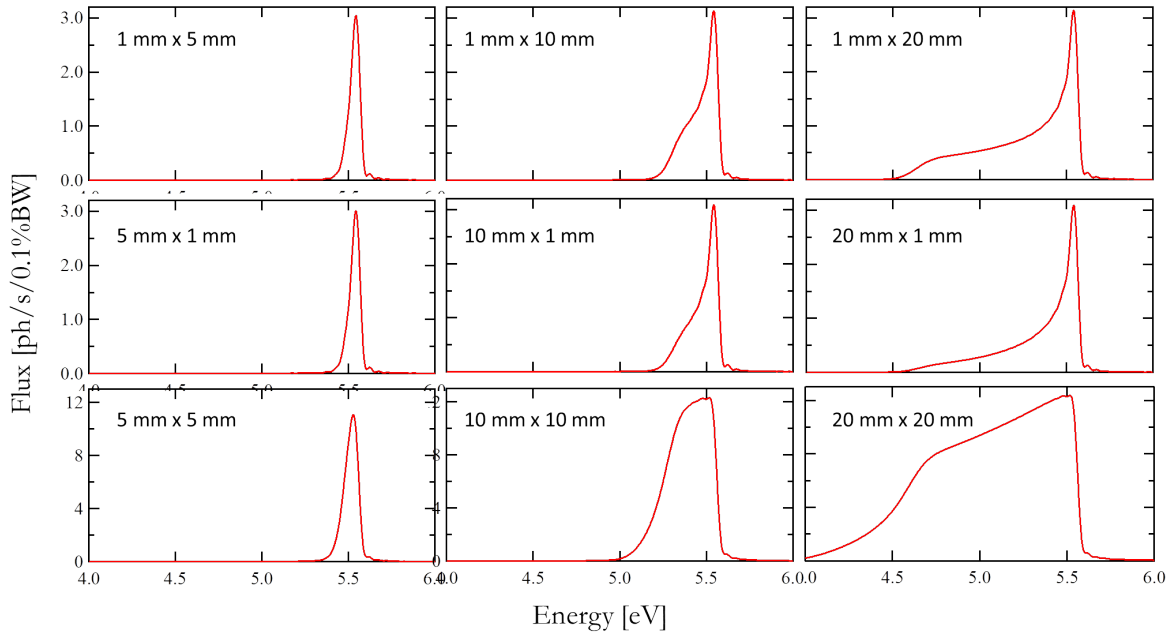

Figure 6.3: Simulated spectral flux captured with a window aperture of different dimensions (horizontal x vertical) placed 5 m from the undulator center. Electron beam: E = 161 MeV, σ_γ = 0.1%, $\sigma_{x,z}$ = 0.1 mm, $\sigma'_{x,z}$ = 0.1 mrad. Undulator: λ_u = 18.16 mm, B = 1 T, K_u = 1.7, N_u = 110.

Table 6.4 shows the characteristics of the spectra presented in Fig. 6.3. The E_{peak} is slightly detuned from E_{res} and expressed as [148]:

$$E_{peak} \approx E_{res}(1 - 1/N_u) \tag{6.3}$$

In our case, the peaked energy (wavelength) is 5.51 eV (225 nm).

Aperture	**Bandwidth**		E_{peak}	λ_{peak}	$\Delta\lambda/\lambda$
mm x mm	[eV]	[nm]	[eV]	[nm]	[%]
1 x 1	0.052	2.1	5.56	223	0.94
1 x 5	0.071	2.86	5.54	224	1.28
1 x 10	0.109	4.46	5.54	224	1.97
1 x 20	0.11	4.49	5.54	224	1.99
5 x 1	0.07	2.83	5.54	224	1.26
10 x 1	0.099	4.03	5.54	224	1.79
20 x 1	0.1	4.05	5.54	224	1.8
5 x 5	0.095	3.88	5.53	224	1.72
10 x 10	0.31	13.17	5.5	225	5.64
20 x 20	0.941	45.42	5.48	226	17.17

Table 6.4: FWHM bandwidth and resonance of the spectra presented in Fig. 6.3. Electron beam: E = 161 MeV, σ_γ = 0.1%, $\sigma_{x,z}$ = 0.1 mm, $\sigma'_{x,z}$ = 0.1 mrad. Undulator: λ_u = 18.16 mm, B = 1 T, K_u = 1.7, N_u = 110.

Figure 6.4 shows the simulated spectral flux with an observation aperture of different dimensions. The intensity remains constant for an aperture greater than ~10 mm but drops fast at a cut-off energy E_{cutoff} (wavelength λ_{cutoff}) that depends on the window aperture dimensions. From Eq. (6.2), θ_{cutoff} can be written as:

$$\theta_{cutoff} = \pm\sqrt{\frac{2\lambda_{cutoff}}{\lambda_u} - \frac{1}{\gamma^2} - \frac{K_u^2}{2\gamma^2}} \tag{6.4}$$

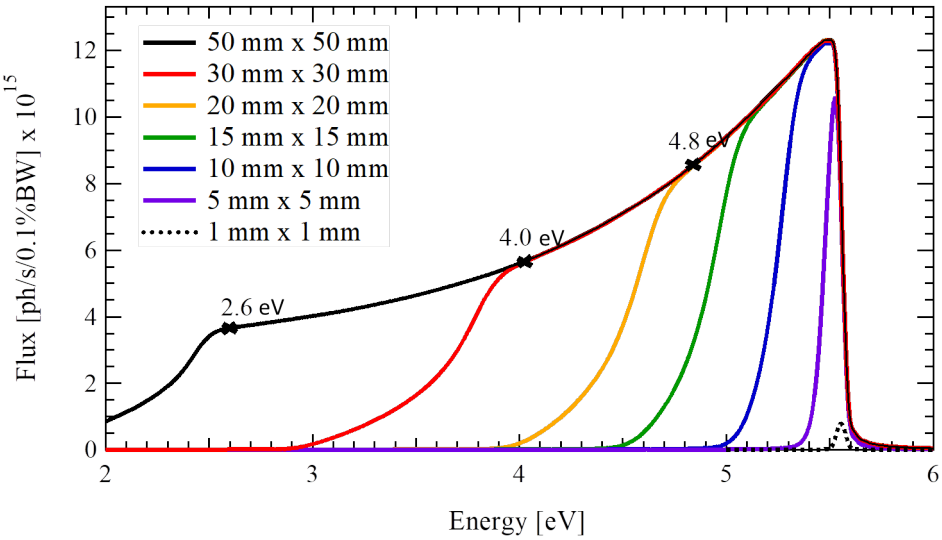

Figure 6.4: Spectral flux for different window apertures placed 5 m from the undulator center. Appended values are the energies at which the flux intensity drops. Electron beam: E = 161 MeV, σ_γ = 0.1%, $\sigma_{x,z}$ = 0.1 mm, $\sigma'_{x,z}$ = 0.1 mrad. Undulator: λ_u = 18.16 mm, B = 1 T, K_u = 1.7, N_u = 110.

Table 6.5 shows the E_{cutoff} from the simulated spectra in Fig. 6.4 alongside the θ_{cutoff} calculated using Eq. (6.4). By multiplying θ_{cutoff} with the distance of the observation window from the undulator center (5 m), one can retrieve the aperture dimensions (see Table 6.5 for values).

Window Aperture mm x mm	E_{cutoff} eV	λ_{cutoff} nm	θ_{cutoff} mrad	$D \times \theta_{cuttoff}$ mm
20 x 20	4.8	258	±1.9	±9.5
30 x 30	4.0	310	±3.0	±15
50 x 50	2.6	477	±5.3	±26.5

Table 6.5: Energy cut of the spectral flux and the angle at which the intensity of the flux starts to drop calculated using Eq. (6.4).

6.1.4 Effect of the energy spread on the spectral flux

The energy spread of the reference electron beam is varied to study its impact on the spectra. Fig. 6.5 shows the computed spectral flux for different energy spreads and window apertures with their effect on the spectrum characteristics presented in Table 6.6. The shape is symmetric for most of the cases, meaning that the energy spread contribution is dominating the spectra. In the case of 20 mm x 20 mm with small energy spread, the off-axis radiation starts to break the symmetry.

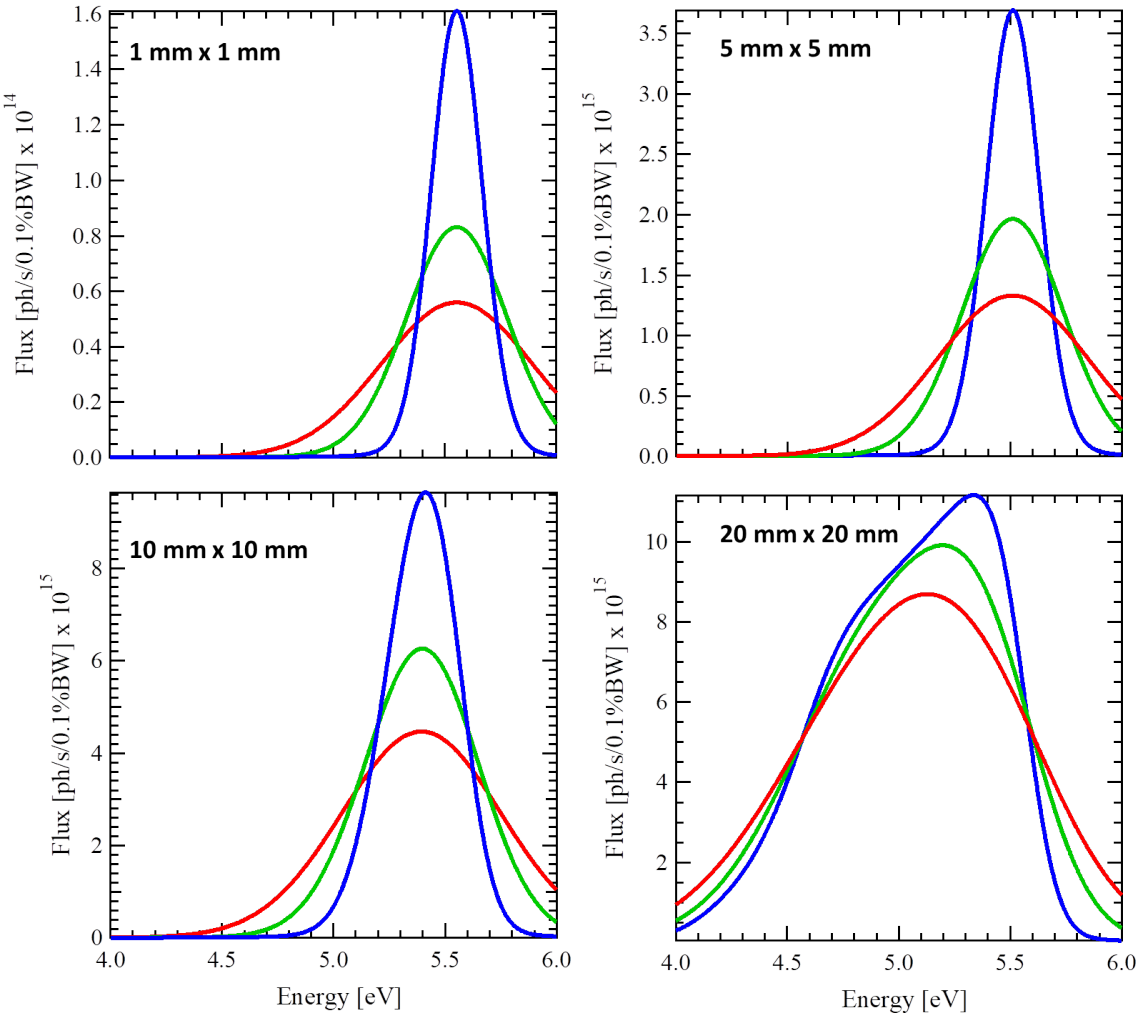

Figure 6.5: Simulated spectral flux captured with a window aperture of different dimensions while varying the energy spread rms: (blue) 1%, (green) 2%, (red) 3%. Electron beam: E = 161 MeV, $\sigma_{x,z}$ = 0.1 mm, $\sigma'_{x,z}$ = 0.1 mrad. Undulator: λ_u = 18.16 mm, B = 1 T, K_u = 1.7, N_u = 110

Energy spread	**Aperture** mm x mm	**Bandwidth** [eV]	[nm]	E_{peak} [eV]	λ_{peak} [nm]	$\Delta\lambda/\lambda$ [%]
	1 x 1	0.052	2.1	5.56	223	0.9
	5 x 5	0.095	3.88	5.53	224	1.7
0.1%	10 x 10	0.31	13.17	5.5	225	5.6
Reference	20 x 20	0.941	45.42	5.48	226	17.2
	50 x 50	1.301	67.91	5.51	225	23.6
	1 x 1	0.272	10.93	5.55	223	4.9
	5 x 5	0.284	11.59	5.51	225	5.2
1%	10 x10	0.388	16.5	5.41	229	7.2
	20 x 20	0.98	47.36	5.34	232	18.4
	50 x 50	1.505	81.1	5.34	232	28.2
	1 x 1	0.533	21.47	5.55	223	9.6
	5 x 5	0.539	22.06	5.51	225	9.8
2%	10 x 10	0.596	25.49	5.4	230	11.1
	20 x 20	1.056	51.2	5.2	239	20.3
	50 x 50	1.805	101.55	5.21	238	34.7
	1 x 1	0.795	32.11	5.55	223	14.3
	5 x 5	0.799	32.78	5.51	225	14.5
3%	10 x 10	0.838	35.93	5.4	230	15.5
	20 x 20	1.18	57.52	5.13	242	23.0
	50 x 50	2.152	126.96	5.11	243	42.2

Table 6.6: FWHM bandwidth and resonance of the radiation captured by different window apertures. Electron beam: E = 161 MeV, $\sigma_{x,z}$ = 0.1 mm, $\sigma'_{x,z}$ = 0.1 mrad. Undulator: λ_u = 18.16 mm, B = 1 T, K_u = 1.7, N_u = 110.

In view of electron beam diagnostics, one attempts to retrieve the energy spread from the spectra observed using the contributions presented in Eq. (6.1). By applying the quadratic sum and neglecting the divergence and beam size, the bandwidth can be expressed as:

$$\frac{\Delta\lambda}{\lambda} = \sqrt{\left[\frac{\Delta\lambda}{\lambda}\right]^2_{\sigma_\gamma} + \left[\frac{\Delta\lambda}{\lambda}\right]^2_{hom}} \tag{6.5}$$

Replacing the contributions of Eq. (6.1) in Eq. (6.5), one can get the energy spread, according to:

$$\sigma_\gamma = \frac{1}{2}\sqrt{(\Delta\lambda/\lambda)^2 - (1/N_u)^2} \tag{6.6}$$

Using Eq. (6.6), the energy spread is estimated as shown in Fig. 6.6 for different window apertures. A precise value can be determined in the case of an aperture smaller than 5 mm x 5 mm and an energy spread larger than 0.5%, and the discrepency increases for larger apertures due to the increasing contribution of the off-axis radiation.

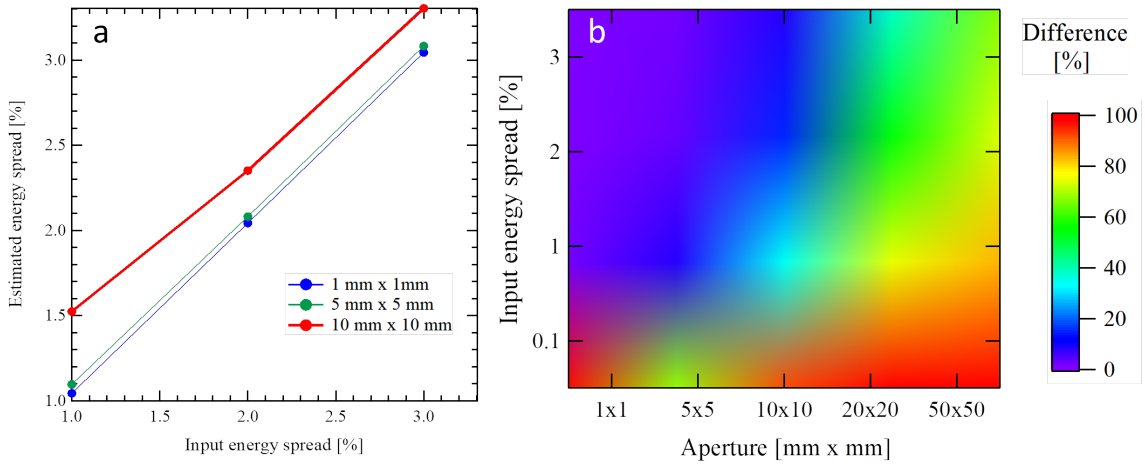

Figure 6.6: Estimated energy spread using Eq. (6.6) with the bandwidth presented in Table 6.6. (b) deviation of the estimated energy spread from the input value for different obervation window apertures.

6.1.5 Effect of the divergence on the spectral flux

In this section, the divergence of the reference electron beam is varied to examine the effect on the spectrum. Fig. 6.7 presents the spectral flux observed through a window of different dimensions as the horizontal and vertical divergence are varied simultaneously to the same value. For small apertures, the flux is very sensitive to the divergence in terms of intensity, where it reduces by a factor of ~10 from 0.5 mrad to 2 mrad. For large apertures, the reduction factor is decreased.

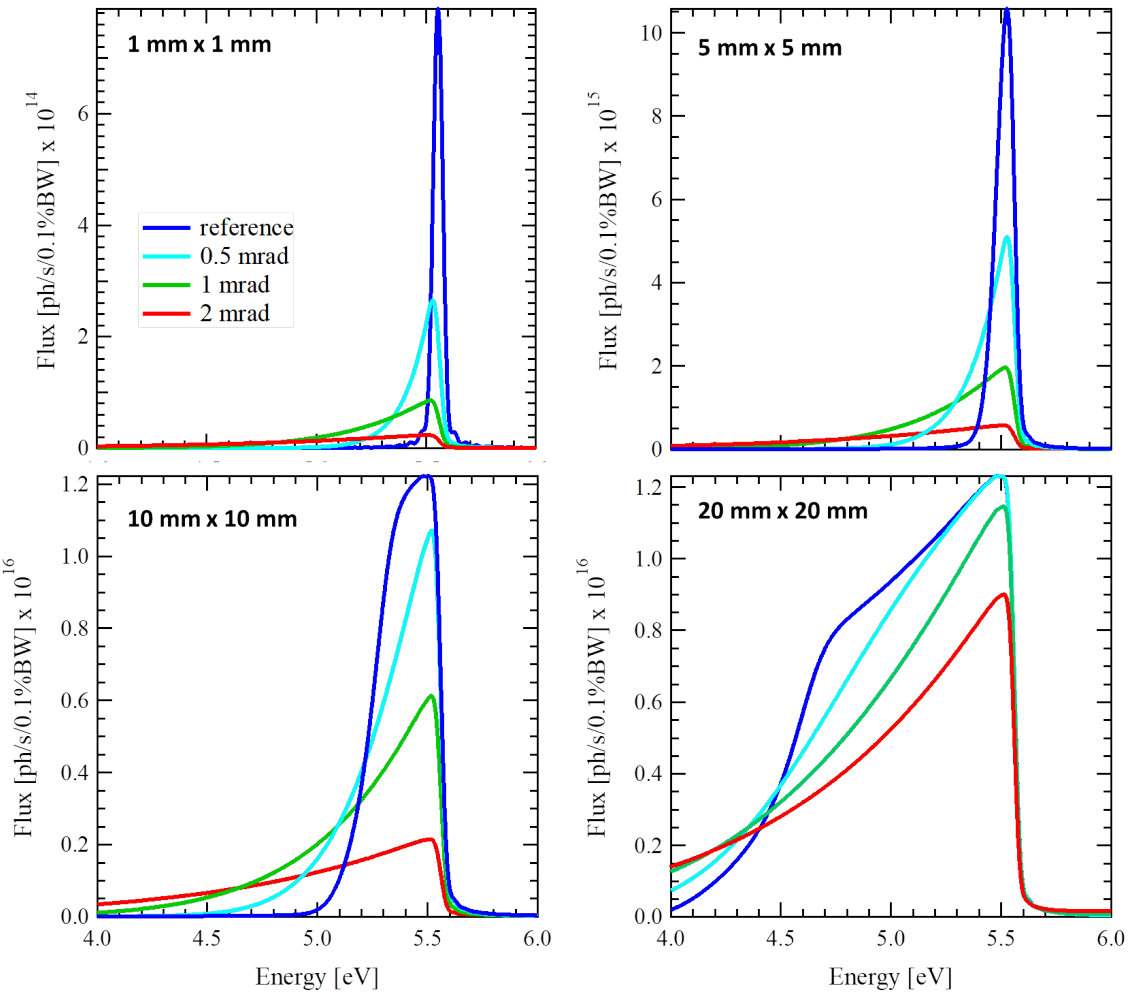

Figure 6.7: Simulated spectral flux captured with a window aperture of different dimensions placed 5 m from the undulator center while varying the horizontal and vertical divergence simultaneously. Electron beam: E = 161 MeV, σ_γ = 0.1%, $\sigma_{x,z}$ = 0.1 mm. Undulator: λ_u = 18.16 mm, B = 1 T, K_u = 1.7, N_u = 110.

Table 6.7 presents the characteristics of the spectra shown in Fig. 6.7. The bandwidth increases for larger divergence, except in the case of the 50 mm x 50 mm aperture, where the bandwidth slightly decreases because the electron beam contributes to the small energy tail and the flux reduces near the half maximum.

Applying the quadratic sum on the relative bandwidth, and neglecting the contributions of the energy spread and beam size, one gets:

$$\frac{\Delta\lambda}{\lambda} = \sqrt{\left[\frac{\Delta\lambda}{\lambda}\right]^2_{\sigma'_{x,z}} + \left[\frac{\Delta\lambda}{\lambda}\right]^2_{hom}} \tag{6.7}$$

Replacing the contributions of Eq. (6.1) in Eq. (6.7), the total divergence $\sigma'_{tot} = \sqrt{\sigma'^2_z + \sigma'^2_x}$ can be estimated by:

$$\sigma'^2_{tot} = \frac{1 + K_u^2/2}{\gamma^2}\sqrt{(\Delta\lambda/\lambda)^2 - (1/N_u)^2} \tag{6.8}$$

The estimated σ'_{tot} is presented in Table 6.7. Figure 6.8 shows the difference of the estimated

Divergence	**Aperture** mm x mm	**Bandwidth** [eV]	[nm]	E_{peak} [eV]	λ_{peak} [nm]	$\Delta\lambda/\lambda$ [%]	**Est.** σ'_{tot} mrad
0.1 mrad Reference	1 x 1	0.05	2.1	5.56	223	0.94	0.11
	5 x 5	0.09	3.88	5.53	224	1.72	0.25
	10 x 10	0.31	13.17	5.5	225	5.64	0.50
	20 x 20	0.94	45.42	5.48	226	17.17	0.87
	50 x 50	1.30	67.91	5.5	225	23.63	1.02
0.5 mrad	1 x 1	0.12	5.15	5.53	224	2.28	0.30
	5 x 5	0.16	6.54	5.53	224	2.87	0.35
	10 x10	0.292	12.33	5.52	225	5.28	0.48
	20 x 20	0.81	37.87	5.48	226	14.73	0.81
	50 x 50	1.35	71.52	5.48	226	24.64	1.04
1 mrad	1 x 1	0.30	12.86	5.52	225	5.5	0.49
	5 x 5	0.32	13.72	5.52	225	5.85	0.51
	10 x 10	0.38	16.71	5.52	225	7.03	0.55
	20 x 20	0.67	30.96	5.51	225	12.31	0.74
	50 x 50	1.34	70.88	5.49	226	24.46	1.04
1.5 mrad	1 x 1	0.49	21.53	5.51	225	8.89	0.63
	5 x 5	0.50	22.08	5.51	225	9.09	0.63
	10 x 10	0.538	23.86	5.51	225	9.76	0.66
	20 x 20	0.69	31.55	5.51	225	12.51	0.74
	50 x 50	1.28	66.74	5.5	225	23.32	1.01
2 mrad	1 x 1	0.65	29.54	5.51	225	11.81	0.72
	5 x 5	0.65	29.89	5.51	225	11.93	0.73
	10 x 10	0.679	31.01	5.51	225	12.33	0.74
	20 x 20	0.76	35.63	5.51	225	13.91	0.78
	50 x 50	1.20	61.86	5.5	225	21.96	0.99

Table 6.7: FWHM bandwidth and resonance of the radiation captured by different window apertures. Electron beam: E = 161 MeV, σ_γ = 0.1%, $\sigma_{x,z}$ = 0.1 mm. Undulator: λ_u = 18.16 mm, B = 1 T, K_u = 1.7, N_u = 110.

divergence (absolute value) from the input value in the simulation taking $\sigma'_x = \sigma'_z = \sigma'_{tot}/\sqrt{2}$. The difference is quite large showing that Eq. (6.8) is not efficient.

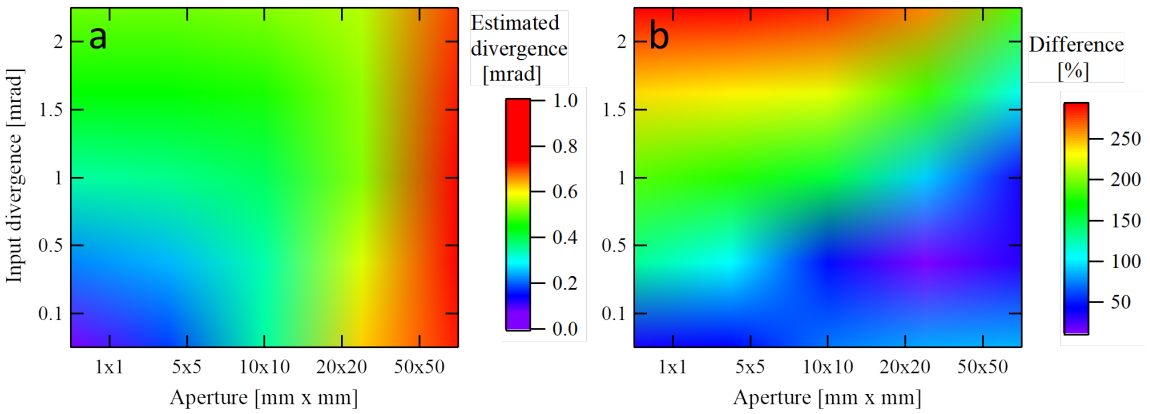

Figure 6.8: Estimated divergence (a) and deviation from the input value (b) for different input values and window apertures.

6.1.6 Effect of the beam size on the spectral flux

In this section, the beam size of the reference electron beam is varied to examine the effect on the spectrum. Fig. 6.9 presents the spectral flux observed through a window of different dimensions as the horizontal and vertical beam sizes are varied simultaneously to the same value.

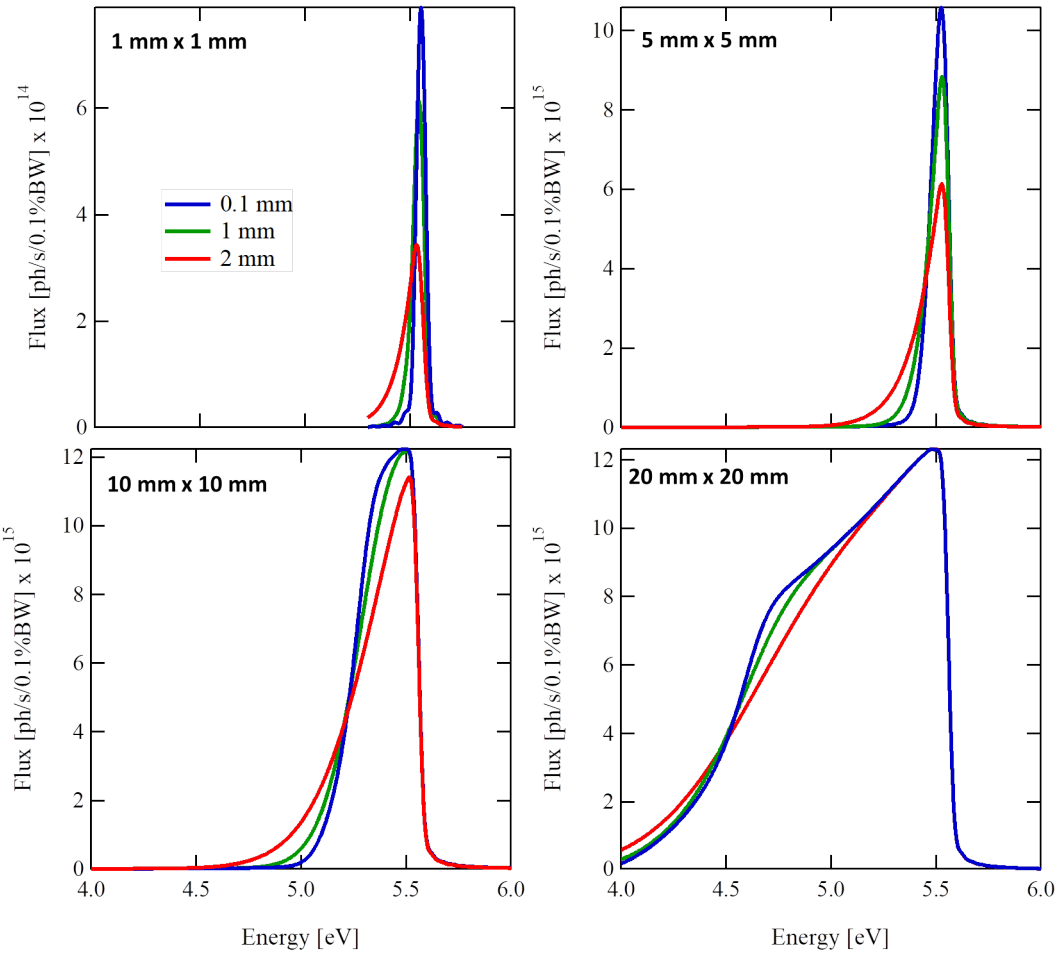

Figure 6.9: Simulated spectral flux captured with a window aperture of different dimensions placed 5 m from the undulator center while varying the horizontal and vertical beam size simultaneously. Electron beam: E = 161 MeV, $\sigma_\gamma = 0.1\%$, $\sigma'_{x,z} = 0.1$ mrad. Undulator: $\lambda_u = 18.16$ mm, B = 1 T, $K_u = 1.7$, $N_u = 110$

Table 6.8 shows the characteristics of the spectra displayed in Fig. **??**. In the case of small aperture, the radiation of the off-axis electrons that pass through the observation window is red-shifted leading to slightly increased bandwidth and intensity reduction. For large apertures, the beam size has no big effect on the spectrum. In SRW code, the magnetic field in the transverse planes is constant. In a real undulator with a small magnetic gap, the magnetic field changes with vertical position that leads to a red shift of the radiation and induces a larger effect on the spectra than the one presented.

Divergence	Aperture	Bandwidth		E_{peak}	λ_{peak}	$\Delta\lambda/\lambda$
	mm x mm	[eV]	[nm]	[eV]	[nm]	[%]
0.1 mm	1 x 1	0.052	2.1	5.55	223	0.94
	5 x 5	0.095	3.88	5.53	224	1.72
	10 x10	0.31	13.17	5.5	225	5.64
	20 x 20	0.941	45.42	5.48	226	17.17
1 mm	1 x 1	0.063	2.54	5.54	224	1.14
	5 x 5	0.107	4.35	5.53	224	1.93
	10 x 10	0.303	12.83	5.51	225	5.5
	20 x 20	0.907	43.41	5.48	226	16.54
2 mm	1 x 1	0.102	4.15	5.53	224	1.84
	5 x 5	0.138	5.66	5.53	224	2.49
	10 x 10	0.29	12.26	5.52	225	5.26
	20 x 20	0.84	39.66	5.48	226	15.33

Table 6.8: FWHM bandwidth and resonance of the spectra presented in Fig. **??**. Electron beam: E = 161 MeV, σ_γ = 0.1%, $\sigma'_{x,z}$ = 0.1 mrad. Undulator: λ_u = 18.16 mm, B = 1 T, K_u = 1.7, N_u = 110.

6.1.7 Simultaneous effect of the energy spread and divergence on the spectral flux

This section analyzes the combined effect of the energy spread and divergence on the spectral flux. Figure 6.10 presents the spectra generated with the U18 undulator observed through a 1 mm x 1 mm window aperture placed at a distance of 5 m while changing the energy spread and divergence (in both planes). For a divergence of 0.5 mrad, the spectra is symmetric with respect to the resonant energy when the energy spread contribution is dominating (σ_γ = 2%). And as the divergence increases or the energy spread decreases, the symmetry starts to break and the intensity at low energies enhances.

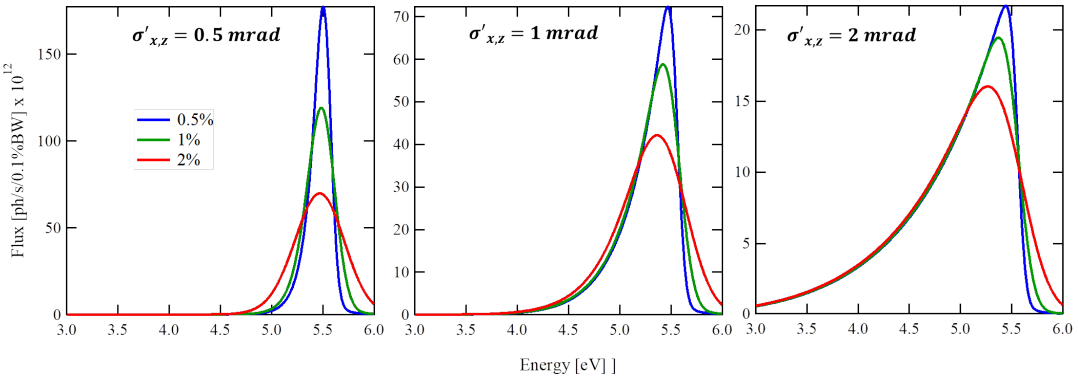

Figure 6.10: Spectral flux computed while varying of the energy spread and divergence in both planes. Window aperture of dimensions 1 mm x 1 mm placed at a distance of 5 m from the undulator center. Electron beam: E = 161 MeV, $\sigma_{x,z}$ = 0.1 mm. Undulator: λ_u = 18.16 mm, B = 1 T, K_u = 1.7, N_u = 110.

An attempt of distinguishing between the energy spread and divergence contribution on the spectral flux is examined by applying a new method, with the approximation that the divergence contributes only on the red side of the spectra, whereas the energy spread symmetrically widens the line. Thus, one can approximate the following:

$$\left[\frac{\Delta\lambda}{\lambda}\right]_{Blue} = \frac{1}{2}\sqrt{\left[\frac{\Delta\lambda}{\lambda}\right]^2_{\sigma_\gamma} + \left[\frac{\Delta\lambda}{\lambda}\right]^2_{hom}} \tag{6.9}$$

and

$$\left[\frac{\Delta\lambda}{\lambda}\right]_{Red} = \sqrt{\frac{1}{4}\left[\frac{\Delta\lambda}{\lambda}\right]^2_{\sigma_\Upsilon} + \frac{1}{4}\left[\frac{\Delta\lambda}{\lambda}\right]^2_{hom} + \left[\frac{\Delta\lambda}{\lambda}\right]^2_{\sigma'_{x,z}}} \tag{6.10}$$

where $\left[\frac{\Delta\lambda}{\lambda}\right]_{Blue}$ and $\left[\frac{\Delta\lambda}{\lambda}\right]_{Red}$ are the blue side half width and red side half width (pinhole observation so that the natural off-axis radiation is cut), respectively, represented in Fig. 6.11.

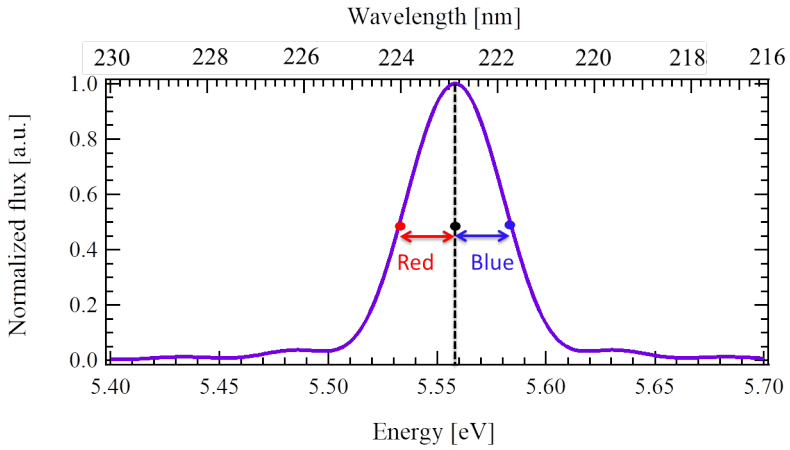

Figure 6.11: Simulated spectral flux captured with a window aperture of dimensions 1 mm x 1 mm placed at 5 m from the undulator center. Electron beam: E = 161 MeV, σ_Υ = 0.1%, $\sigma_{x,z}$ = 0.1 mm, $\sigma'_{x,z}$ = 0.1 mrad. Undulator: λ_u = 18.16 mm, B = 1 T, K_u = 1.7, N_u = 110

Using the derived contributions of the energy spread and divergence, presented in Eq. (6.1), one can use the following expressions to determine the energy spread and divergence:

$$\begin{cases} \sigma_\Upsilon = \frac{1}{2}\sqrt{4\left[\frac{\Delta\lambda}{\lambda}\right]^2_{Blue} - \left[\frac{1}{N_u}\right]^2} \\ \sigma'^2_{x,z} = \frac{1+K_u^2/2}{\Upsilon^2}\sqrt{\left[\frac{\Delta\lambda}{\lambda}\right]^2_{Red} - \left[\frac{\Delta\lambda}{\lambda}\right]^2_{Blue}} \end{cases} \tag{6.11}$$

Table 6.9 presents the spectra characteristics for different energy spread and divergence alongside the estimated values. The estimated energy spread deviation from the input value is less than 10% when the divergence is ~0.5 mrad. And as the beam divergence increases, the resonant wavelength is red-shifted increasing the blue bandwidth part and thus estimating a larger energy spread value (see Table 6.9).

Input values		**Characteristics**			**Estimate**	
σ_γ	$\sigma'_{x,z}$	$\Delta\lambda/\lambda$	$\frac{\Delta\lambda}{\lambda}\|_{blue}$	$\frac{\Delta\lambda}{\lambda}\|_{red}$	σ_γ	$\sigma'_{x,z}$
%	mrad	%	%	%	%	mrad
	0.5	3.75	1.58	2.17	0.64	0.18
0.5	1	6.89	1.98	4.91	0.82	0.32
	2	13.2	2.35	10.85	0.98	0.48
	0.5	5.92	2.78	3.15	1.17	0.18
1	1	8.95	3.36	5.59	1.42	0.32
	2	15.35	4.03	11.36	1.69	0.49
	0.5	10.44	5.13	5.31	2.17	0.17
2	1	13.36	5.95	7.41	2.52	0.31
	2	19.85	7.06	12.79	3.02	0.49
	0.5	15.07	7.5	7.57	3.19	0.15
3	1	17.91	8.43	9.48	3.58	0.31
	2	24.51	9.92	14.59	4.22	0.49

Table 6.9: Relative bandwidth of the radiation captured by a window aperture of 1 mm x 1 mm while changing the divergence and energy spread, alongside the estimated values using Eq. (6.11).

6.2 Transverse beam shape

The photon transvserse beam shape is computed using SRW. The radiation is captured by an observation window of dimensions 50 mm x 50 mm placed at a distance of 5 m from the center of the undulator. The U18 undulator is used with a peak field of 1 T. As presented, the radiation at the on-axis resonant wavelength is emitted within a cone of angle equal to the natural divergence and beam size of the photon beam (RMS values):

$$\begin{cases} \sigma'_n = \sqrt{\frac{\lambda}{L_u}} \\ \sigma_n = \frac{\sqrt{\lambda L_u}}{4\pi} \end{cases} \tag{6.12}$$

The resonant wavelength in our case is 223 nm (5.56 eV) and the undulator length is 2 m. Thus the natural divergence and beam size are calculated to be:

$$\begin{cases} \sigma'_n = 330 \ \ \mu\text{rad} \\ \sigma_n = 50 \ \ \mu\text{m} \end{cases} \tag{6.13}$$

First, a comparison between the single electron and our reference multi-electron beam is examined. Figure 6.12-a shows the transverse beam shape integrated flux (from 190 nm to 310 nm) produced by a single electron in the near-field approximation. Two optical filters, centered at the resonant wavelength (223 nm), are applied to the transverse beam shape with a bandwidth of 10 nm (Fig. 6.12-b) and 1 nm (Fig. 6.12-c). The transverse shape is elongated in the vertical axis and reduces in the case of optical filters.

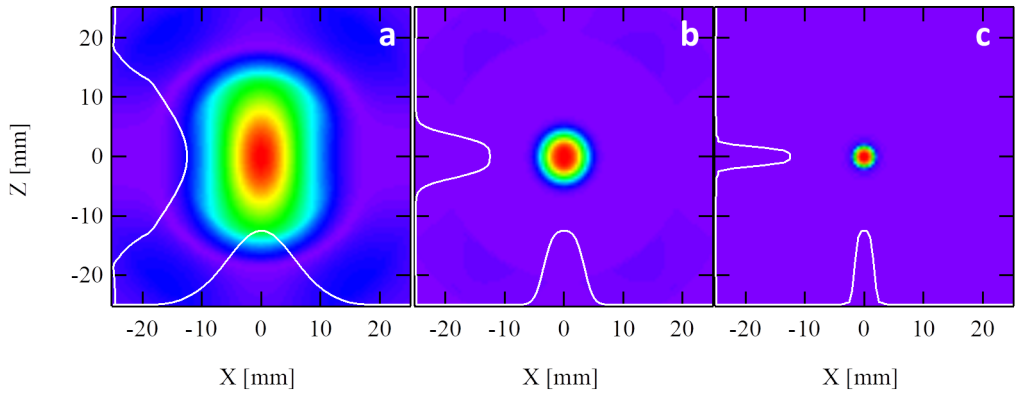

Figure 6.12: Transverse beam shape simulated in the near-field approximation for a single electron with integrated flux over the first harmonic from 190 nm to 350 nm (a) and applying filters: a 10 nm (b) and 1 nm (c) bandwidth FWHM. Window aperture of dimensions 50 mm x 50 mm placed at a distance of 5 m from the undulator center. Single electron E = 161 MeV. Undulator: λ_u = 18.16 mm, B = 1 T, K_u = 1.7, N_u = 110.

Fig. 6.13 shows the transverse beam shape integrated flux (from 190 nm to 310 nm) produced by the reference electron beam in the far-field approximation. Two optical filters, centered at the resonant wavelength (223 nm), are applied to the transverse beam shape with a bandwidth of 10 nm (Fig. 6.12-b) and 1 nm (Fig. 6.12-c). For the single electron case, the transverse shape is elongated in the vertical axis and reduces when applying optical filters. The only observable difference is that the ring of the second harmonic.

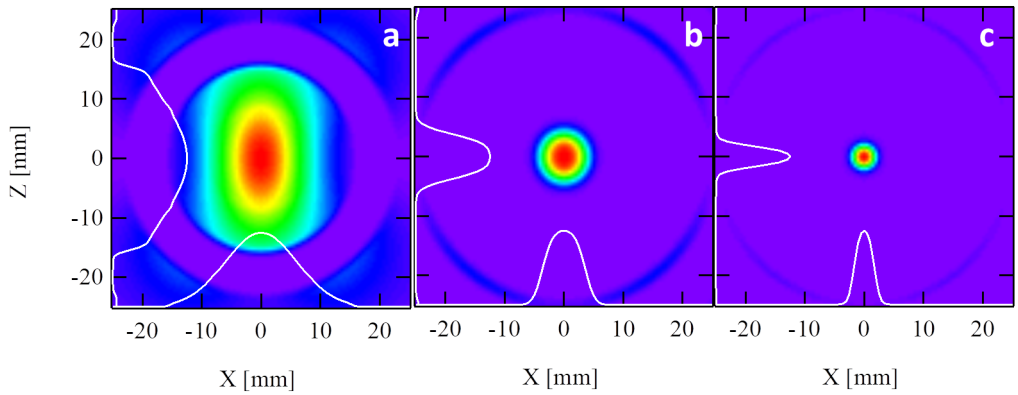

Figure 6.13: Transverse beam shape simulated in the far-field approximation for the reference electron beam presented in Table 6.3 with integrated flux over the first harmonic from 190 nm to 350 nm (a) and applying filters: a 10 nm bandwidth (b) and 1 nm bandwidth (c) centered at the resonant energy. Window aperture of dimensions 50 mm x 50 mm placed at a distance of 5 m from the undulator center. Electron beam: E = 161 MeV, σ_γ = 0.1%, $\sigma_{x,z}$ = 0.1 mm, $\sigma'_{x,z}$ = 0.1 mrad. Undulator: λ_u = 18.16 mm, B = 1 T, K_u = 1.7, N_u = 110.

The photon beam size in horizontal $\sigma_{p,x}$ and vertical $\sigma_{p,z}$, produced by the single electron and multi-electron beam, is presented in Table 6.10 for the three filter cases. The beam size produced by the multi-electron is larger than the one generated by a single electron due to the energy spread and emittance.

Beam	**No filter**		**10 nm filter**		**1 nm filter**	
	$\sigma_{p,x}$ mm	$\sigma_{p,z}$ mm	$\sigma_{p,x}$ mm	$\sigma_{p,z}$ mm	$\sigma_{p,x}$ mm	$\sigma_{p,z}$ mm
Single Electron	13.5	27.7	6.9	7.3	3.3	3.3
Multi-electron beam	15.1	30.4	7.1	7.5	3.4	3.5
Analytical	-	31.7	-	5.3	3.8	3.8

Table 6.10: Photon beam size of the radiation in both transverse planes by taking the FWHM of the cut at the center. No filter: 190 nm to 350 nm. $\sigma_{p,x}$ and $\sigma_{p,z}$ are the simulated FWHM beam size in horizontal and vertical, respectively.

Recalling that the radiation is emitted within a cone of angle $\pm 1/\gamma$ (FWHM), the FHWM beam size can be analytically determined by:

$$\sigma_{p,z} = \frac{2}{\gamma} D \tag{6.14}$$

where D is the distance of the observation window from the undulator center.

In the case of the 1 nm filter, the resonant wavelength is emitted within an angle equal to the natural divergence (see Eq. (6.13)). By neglecting the natural size (see Eq. (6.13)), one can calculate the FWHM photon beam size at the resonant wavelength using:

$$\sigma_{p,z} = 2.35 \sigma'_n D \tag{6.15}$$

where the 2.35 factor is to convert from RMS to FWHM. The analytical calculations of the total beam size and the resonant one are displayed in Table 6.10.

A dim ring surrounds the central radiation, as shown in Fig. 6.13, that corresponds to the second harmonic off-axis radiation. The higher the harmonic number n the larger the ring radius. Consider the m^{th} harmonic radiation emitted with an angle θ_m, such that it has a wavelength equal to the on-axis radiation of the n^{th} harmonic:

$$\lambda_m = \frac{\lambda_u}{2m\gamma^2}(1 + K_u^2/2 + \gamma^2\theta_m^2) = \frac{\lambda_u}{2n\gamma^2}(1 + K_u^2/2)$$

θ_m can be written as:

$$\theta_m = \sqrt{\frac{1}{n\gamma^2}(m-n)(1 + K_u^2/2)}$$

The radius R_m of the m_{th} harmonic cone, observed on a screen placed at a distance D from the center of the undulator, can be determined by setting $n = 1$. Hence:

$$R_m = D\theta_m = \frac{D}{\gamma}\sqrt{(m-1)(1 + \frac{K_u^2}{2})} \tag{6.16}$$

By inserting $\gamma = 315$, $K_u = 1.7$ and $D = 5$ m in Eq. (6.16), the radius of the second harmonic R_2 is calculated to be 24.8 mm that is in good agreement with the simulations presented in Fig. 6.12.

6.2.1 Effect of the energy spread on the photon beam transverse shape

The energy spread effect on the transverse beam shape is examined. The window aperture is still placed at 5 m from the U18 undulator center with a peak field of 1 T. Fig. 6.14 presents the transverse beam shape with different optical ranges using the reference beam (see Table 6.3) while changing the energy spread. The transverse beam shape of the captured total radiation changes in shape at its core but the size stays more or less the same (see Table 6.11 for values). Also the second harmonic ring gets thicker.

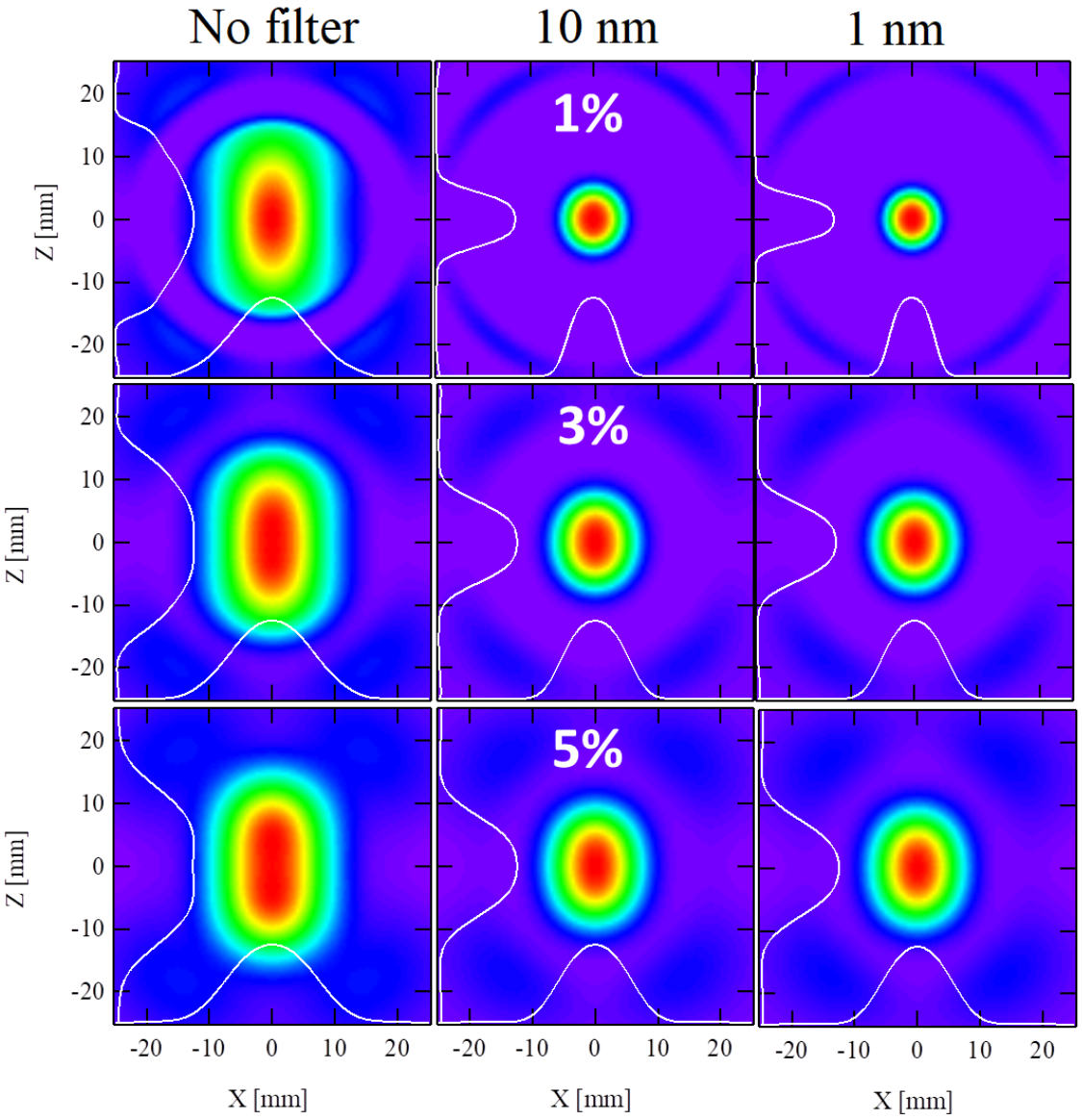

Figure 6.14: Transverse beam shape as the rms energy spread is varied with the value appended. (Left) integrated flux between 205 nm and 310 nm (left) covering the first harmonic, (middle) optical filter of 10 nm bandwidth applied, (right) optical filter of 1 nm bandwidth applied. Window aperture of dimensions 50 mm x 50 mm placed at a distance of 5 m from the undulator center. Electron beam: E = 161 MeV, $\sigma_{x,z}$ = 0.1 mm, $\sigma'_{x,z}$ = 0.1 mrad. Undulator: λ_u = 18.16 mm, B = 1 T, K_u = 1.7, N_u = 110.

In the case of an optical filter, the photon beam size increases especially in the 1 nm bandpass filter case because the high energy electrons (E > 161 MeV) emit photons with wavelength shorter than the resonance (223 nm) but with an angle that causes a red shift. Taking this into account, an

	No filter		10 nm		1 nm	
Energy spread	$\sigma_{p,x}$	$\sigma_{p,z}$	$\sigma_{p,x}$	$\sigma_{p,z}$	$\sigma_{p,x}$	$\sigma_{p,z}$
%	mm	mm	mm	mm	mm	mm
0.1	14.2	26.9	7.1	7.5	3.4	3.5
0.5	14.3	26.8	7.5	8.0	5.4	5.6
1	14.3	26.7	8.3	8.9	7.2	7.6
2	14.5	26.1	9.8	11.1	9.5	10.6
3	15.1	25.8	11	13	10.6	12.4
4	15.6	25.8	11.8	14.7	11.7	14.5
5	15.8	25.8	12.4	16.1	12.3	15.9

Table 6.11: FWHM of the cut at the center of the transverse beam shape. No filter case corresponds to integrated intensity from 205 nm to 310 nm. $\sigma_{p,x}$ and $\sigma_{p,z}$ the simulated FWHM beam size in horizontal and vertical planes, respectively. Window aperture of dimensions 50 mm x 50 mm placed at a distance of 5 m from the undulator center. Electron beam: E = 161 MeV, $\sigma_{x,z}$ = 0.1 mm. Undulator: λ_u = 18.16 mm, B = 1 T, K_u = 1.7, N_u = 110.

attempt to determine the energy spread from the transverse beam shape in the 1 nm filter case is done. The wavelength (λ_H) of the higher energies (γ_H) emitted with an angle (θ_H) is equal to the resonance:

$$\lambda_H = \frac{\lambda_u}{2\gamma_H^2}[1 + K_u^2/2 + \gamma_H^2\theta_H^2] = \frac{\lambda_u}{2\gamma^2}[1 + K_u^2/2] \tag{6.17}$$

Eq. (6.17) can be written as:

$$\frac{1}{\gamma_H^2} = \frac{1}{\gamma^2} - \frac{\theta_H^2}{1 + K_u^2/2} \tag{6.18}$$

which gives:

$$\sigma_\gamma = \frac{\gamma_H - \gamma}{\gamma} = \left(\frac{1 + K_u^2/2}{1 + K_u^2/2 - \gamma^2\theta_H^2}\right)^{1/2} - 1 \tag{6.19}$$

θ_H can be determined by using a quadratic substraction on the beam size FWHM in the 1 nm optical filter case as:

$$\theta_H = \frac{1}{D}\sqrt{\sigma_{p,z}^2 - (D\sigma_n')^2} \tag{6.20}$$

where $\sigma_{p,z}$ is the simulated vertical beam size. Substituting Eq. (6.20) in Eq. (6.19), one gets:

$$\sigma_\gamma = \frac{\gamma_H - \gamma}{\gamma} = \left(\frac{1 + K_u^2/2}{1 + K_u^2/2 - \gamma^2(\sigma_{p,z}^2/D^2 - (\sigma_n')^2)}\right)^{1/2} - 1 \tag{6.21}$$

Figure 6.15 shows the estimated energy spread from the transverse beam shape using Eq. (6.21) divided by half due to the fact that the energy spread symmetrically widens the photon transverse shape. The value is estimated to a good extent for energy spread between 1% and 3%.

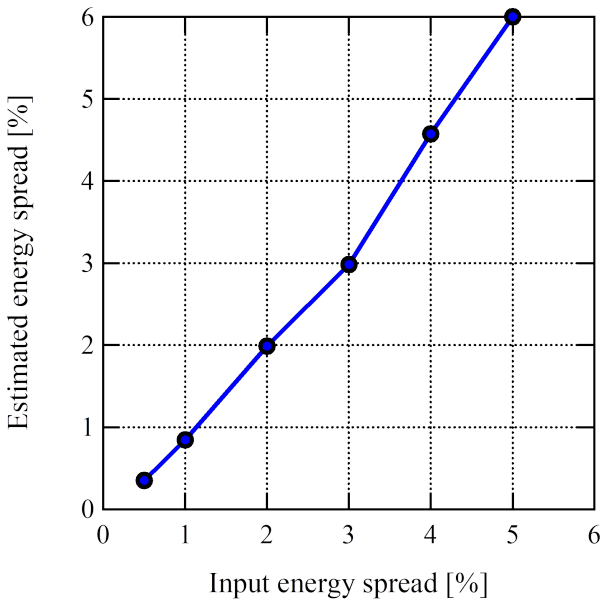

Figure 6.15: Estimated energy spread versus the input value in the simulation.

It is important to mention that the energy spread in Eq. (6.21) represents only half the Gaussian energy distribution and it should be multiplied by two to get the entire energy spread. However the energy spread is estimated rather good within 0.5% and 3% that is close to the value that we have at COXINEL, so I continue using it for the next sections and for chapter 9.

6.2.2 Effect of the divergence on the photon beam transverse shape

This section studies the effect of the electron beam divergence on the transverse photon beam shape. Fig. 6.16 presents the transverse beam shape with different optical range using the reference beam (see Table 6.3) while changing the divergence in both planes simultaneously. The transverse beam size is significantly broadened in both planes as the divergence is increased regardless of the optical filter case.

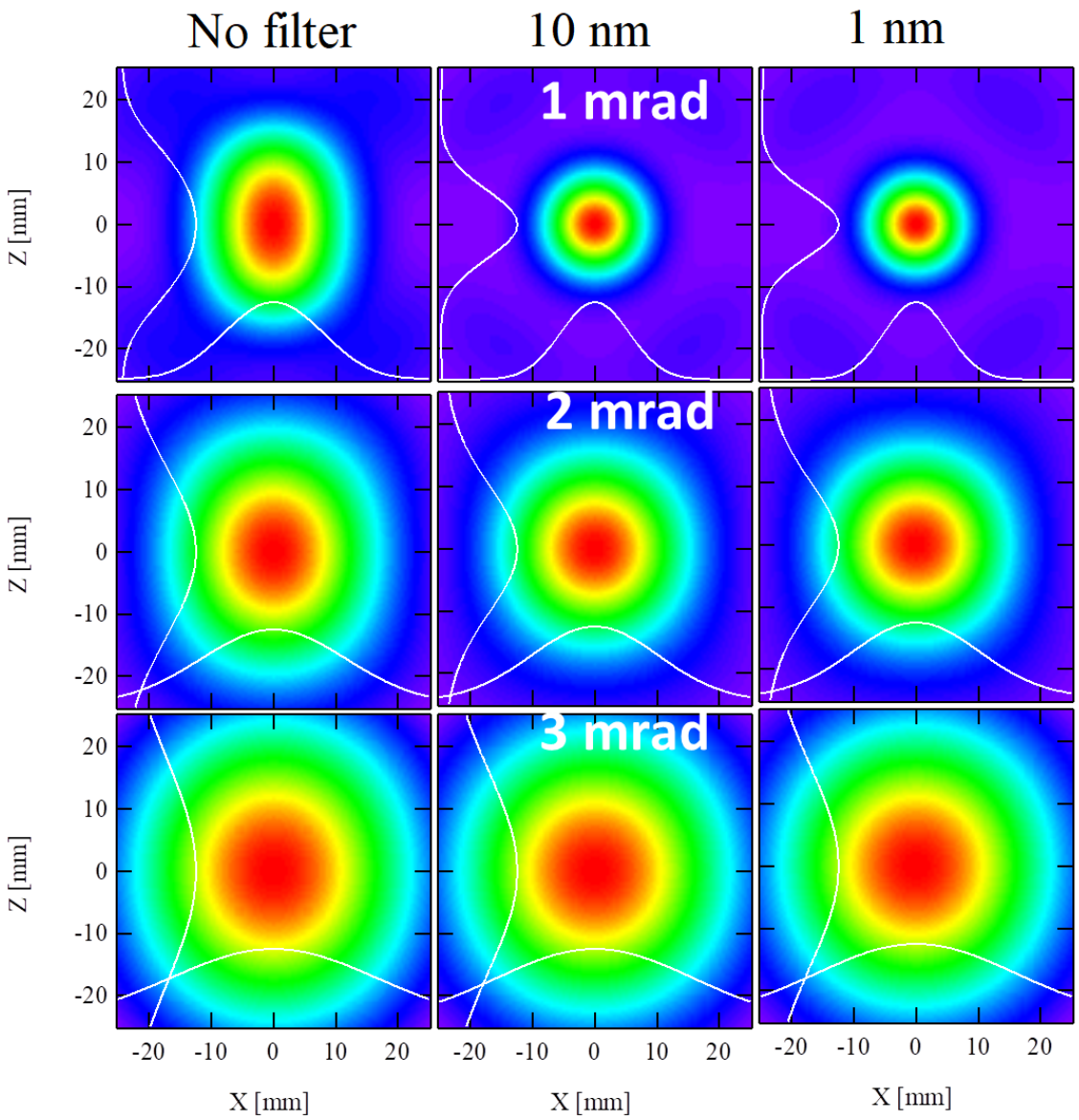

Figure 6.16: Transverse beam shape with integrated flux for different divergences: (left) wavelength range between 205 nm to 310 nm, (middle) a 10 nm optical filter, (right) 1 nm optical filter. Window aperture of dimensions 50 mm x 50 mm placed at a distance of 5 m from the undulator center. Electron beam: E = 161 MeV, σ_γ = 0.1%, $\sigma_{x,z}$ = 0.1 mm. Undulator: λ_u = 18.16 mm, B = 1 T, K_u = 1.7, N_u = 110.

Table 6.12 presents the beam size of the spectra shown in Fig. 6.16 with an additional case of 0.5 mrad divergence. For large divergence, the photon beam transverse size becomes independent of the optical filter applied, because the electron beam divergence dominates the spectra over the natural off-axis radiation.

	No filter		10 nm filter		1 nm filter	
Divergence mrad	$\sigma_{p,x}$ mm	$\sigma_{p,z}$ mm	$\sigma_{p,x}$ mm	$\sigma_{p,z}$ mm	$\sigma_{p,x}$ mm	$\sigma_{p,z}$ mm
0.5	15.5	25.6	8.2	8.4	6.5	6.5
1	18.7	25.7	13	13.1	12.1	12.2
2	28.4	33	25.1	25.8	24.6	25.2
3	40.6	44.2	38.6	39.9	38.2	39.5

Table 6.12: FWHM of the cut at the center of the transverse beam shape. Window aperture of dimensions 50 mm x 50 mm placed at a distance of 5 m from the undulator center. Electron beam: E = 161 MeV, σ_γ = 0.1%, $\sigma_{x,z}$ = 0.1 mm, $\sigma'_{x,z}$ = 0.1 mrad. Undulator: λ_u = 18.16 mm, B = 1 T, K_u = 1.7, N_u = 110.

By using the quadratic sum, the divergence can be estimated:

$$\sigma'_{x,z} = \frac{1}{D}\sqrt{(\sigma_{p,x,z})^2 - (\sigma'_n D)^2} \tag{6.22}$$

Using the above equation, the divergence is calculated in both planes and presented in Fig. 6.17. For $\sigma'_{x,z} > 1$ mrad, the discrepancy between the estimated value and the input one increases.

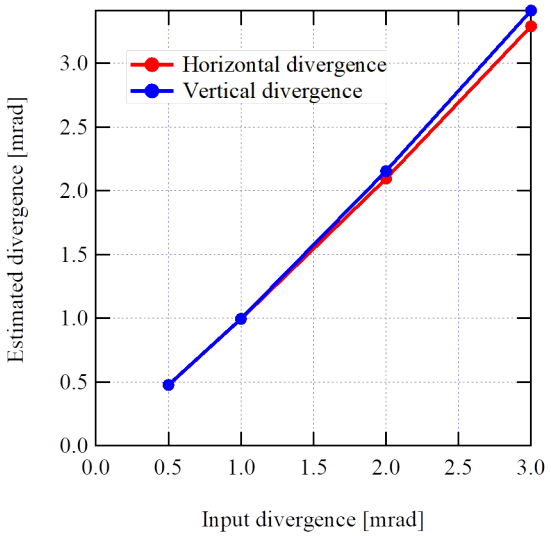

Figure 6.17: Estimated energy spread using Eq. (6.22) versus the input value in the simulation.

6.2.3 Effect of the beam size on the transverse shape

This section studies the effect of the electron beam size on the transverse photon beam shape. Fig. 6.18 presents the transverse beam shape with different optical range using the reference beam (see Table 6.3) while changing the beam size in both planes simultaneously.

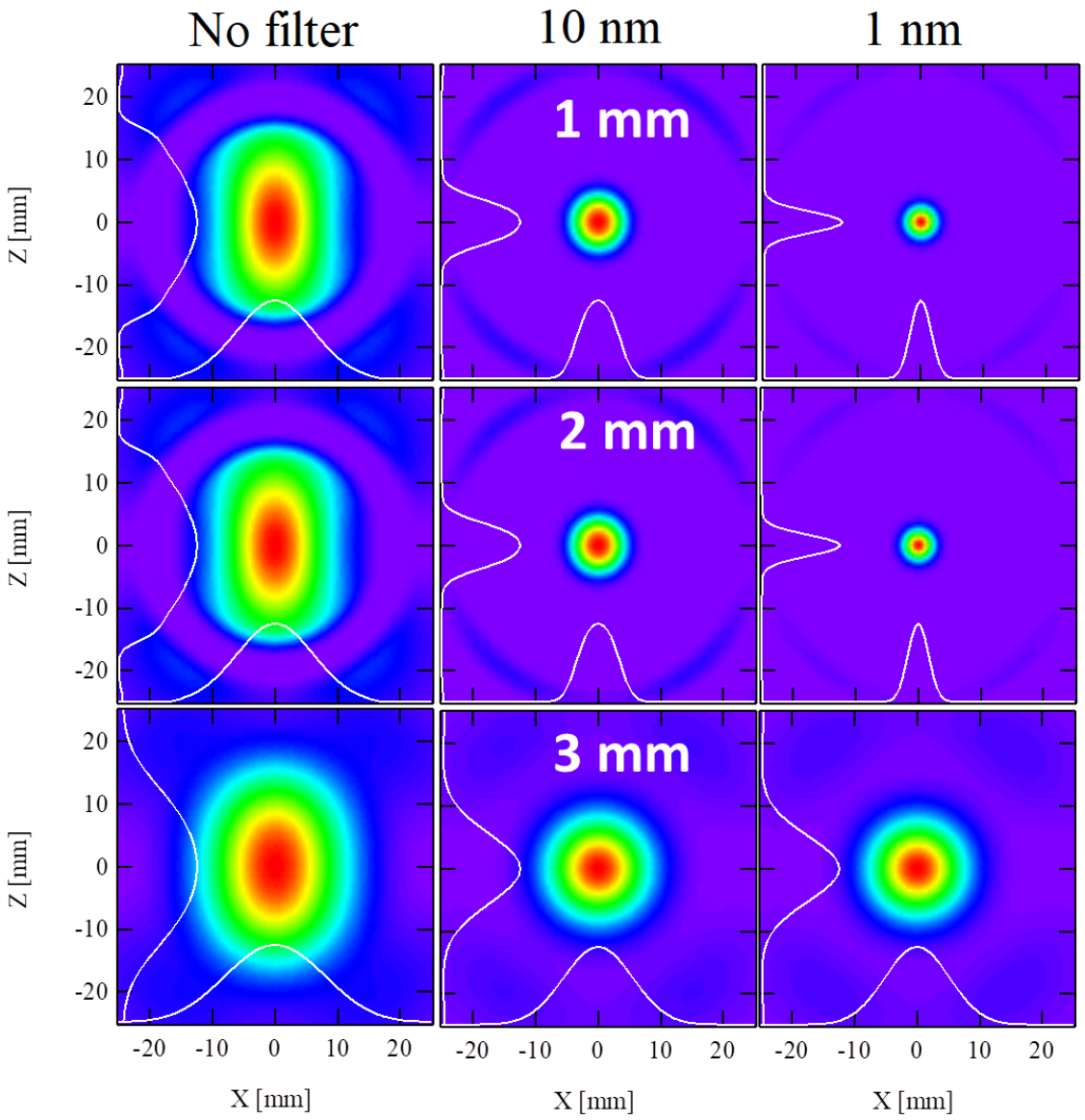

Figure 6.18: Transverse beam shape as the beam size in both planes is varied with the value appended. (Left) integrated flux between 205 nm and 310 nm (left) covering the first harmonic, (middle) optical filter of 10 nm bandwidth applied, (right) optical filter of 1 nm bandwidth applied. Window aperture of dimensions 50 mm x 50 mm placed at a distance of 5 m from the undulator center. Electron beam: E = 161 MeV, σ_γ = 0.1%, $\sigma'_{x,z}$ = 0.1 mm. Undulator: λ_u = 18.16 mm, B = 1 T, K_u = 1.7, N_u = 110.

By using the values of Table 6.13 in the following quadratic sum:

$$\sigma_{x,z} = \sqrt{(\sigma_{p,X})^2 - (D\sigma'_n)^2} \tag{6.23}$$

the beam size is estimated to a very good precision for large beam size as shown in Fig. 6.18.

	No filter		10 nm filter		1 nm filter	
Electron Beam size mm	$\sigma_{p,x}$ mm	$\sigma_{p,z}$ mm	$\sigma_{p,x}$ mm	$\sigma_{p,z}$ mm	$\sigma_{p,x}$ mm	$\sigma_{p,z}$ mm
1	14.4	26.7	7.1	7.4	3.8	3.9
2	15.1	25.9	7.6	7.9	5.6	5.6
3	16.2	25.4	9.1	9.3	7.7	7.7
4	17.4	25.4	11	11.1	9.9	10.0
5	18.7	25.7	13	13.1	12.2	12.2

Table 6.13: FWHM of the cut at the center of the transverse beam shape. Window aperture of dimensions 50 mm x 50 mm placed at a distance of 5 m from the undulator center. Electron beam: E = 161 MeV, σ_γ = 0.1%, $\sigma'_{x,z}$ = 0.1 mm. Undulator: λ_u = 18.16 mm, B = 1 T, K_u = 1.7, N_u = 110.

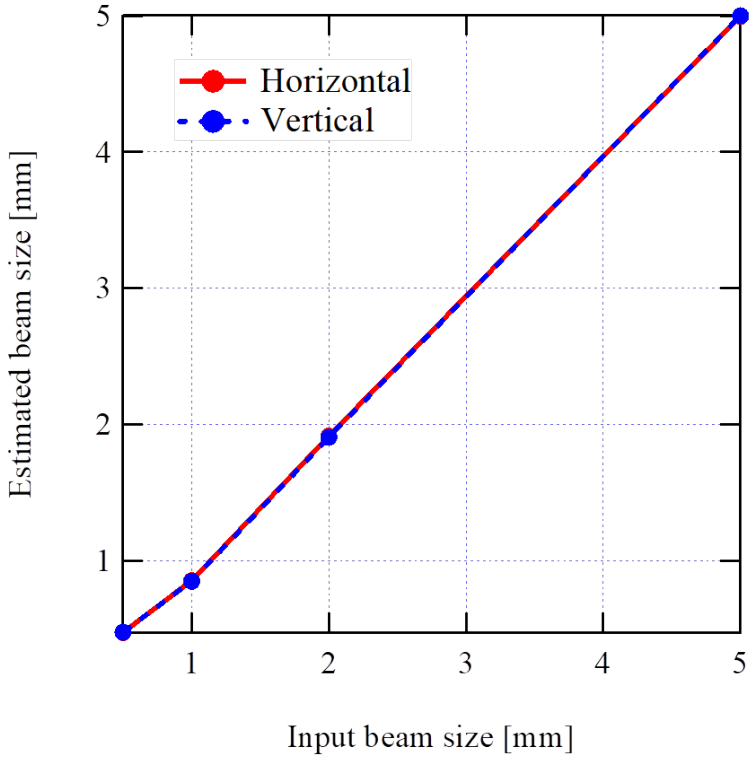

Figure 6.19: Estimated beam size using Eq. (6.23) versus the input value in the simulation.

6.3 Angular spectral flux

The radiation in the vertical axis versus energy, what we call angular spectral flux also referred to as the moon shape [165, 285, 286], is examined. In SRW, the angular spectrum is computed with a horizontal pinhole observation. The angular spectra generated as the reference electron beam (see Table 6.3) traverses the U18 undulator is presented in Fig. 6.20 using the near field (a) and far field (b) approximations. One can also compute the radiation at different horizontal positions of the observation window and then add the intensities, and thus acquire the angular spectra seen by an aperture as shown in Fig. 6.21-c. The moon-shapes are fitted with Eq. (6.2) (black curve) that exhibit a parabolic shape due to the term $\gamma^2\theta^2$.

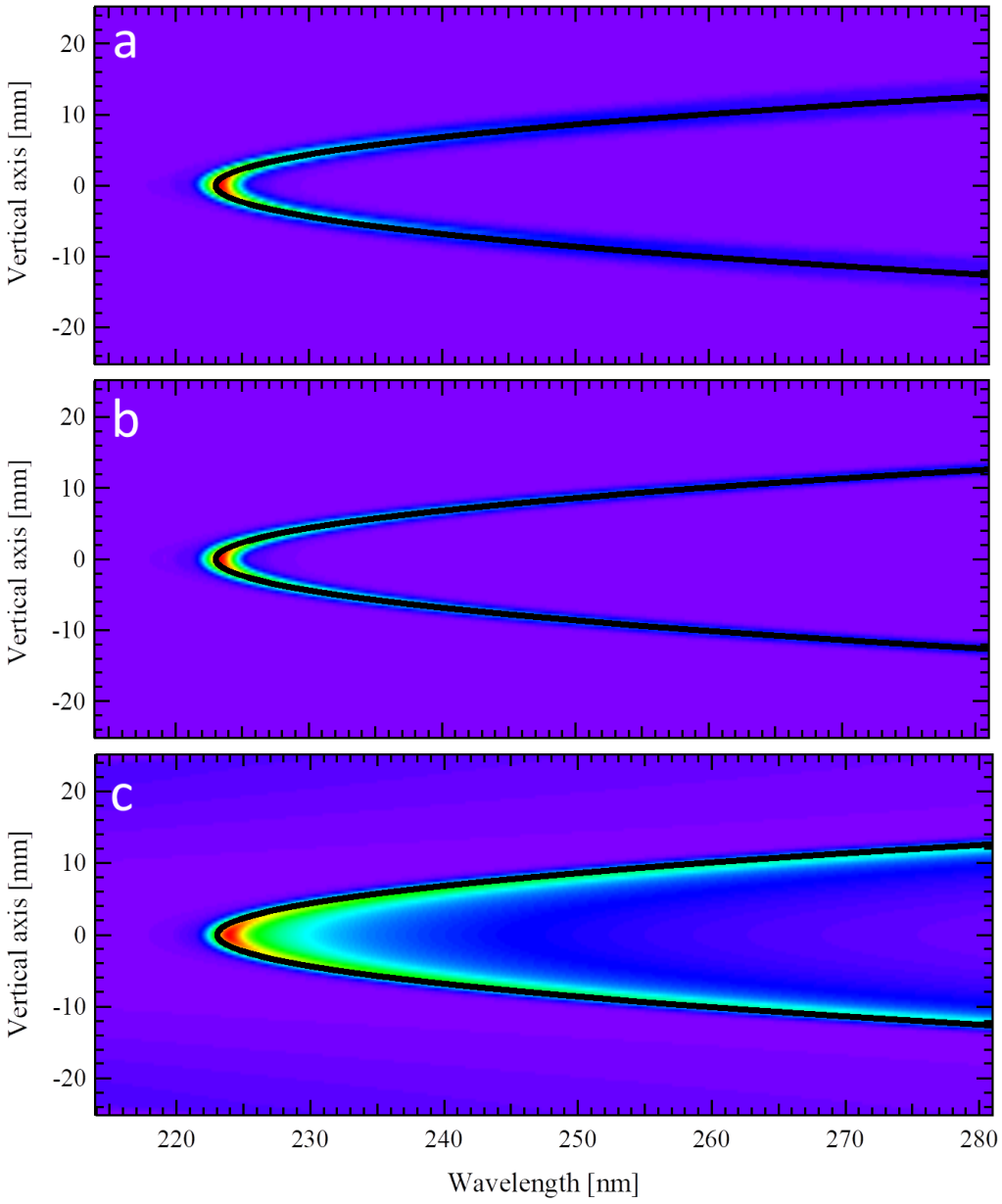

Figure 6.20: Angular spectral flux generated by the reference electron beam with parameters presented in Table 6.3 with a horizontal pinhole observation using the near field (a) and far field (b) approximations. (c) spectra computed in the far-field approximation with a horizontal window aperture of 50 mm. Black curve is the fit using Eq. (6.2). Window aperture of dimensions 50 mm x 50 mm placed at a distance of 5 m from the undulator center. Electron beam: E = 161 MeV, σ_γ = 0.1%, $\sigma_{x,z}$ = 0.1 mm, $\sigma'_{x,z}$ = 0.1 mrad. Undulator: λ_u = 18.16 mm, B = 1 T, K_u = 1.7, N_u = 110.

Figure 6.21-a shows the integrated intensity of the angular spectral flux over the vertical angles presented in Fig. 6.20. A cut at the center of the moon shape is presented in Fig. 6.21-b. The near-field and far-field computations show very good agreement ensuring that a 5 m distance of the window aperture from the undulator center is considered to be in the far-field region for the operating wavelength (223 nm).

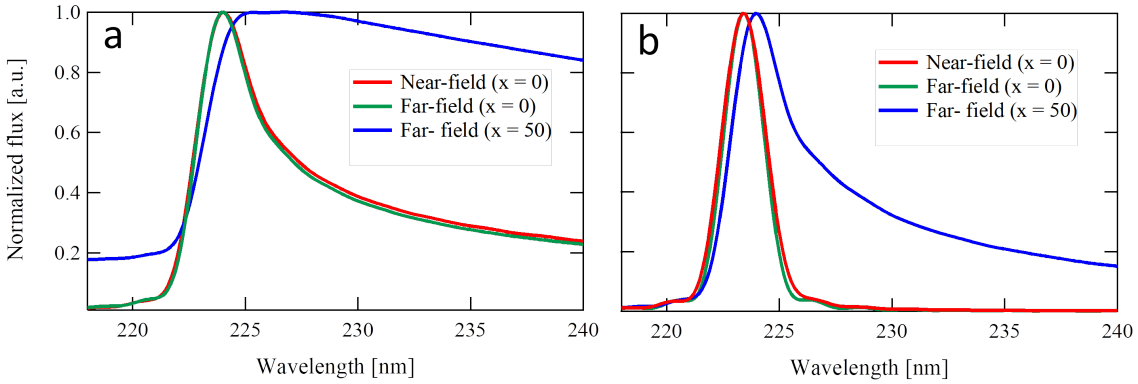

Figure 6.21: Integrated flux (a) and cut at z = 0 (b) for the spectra presented in Fig. 6.20. Window aperture of a horizotal pinhol (x = 0 mm) and 50 mm vertical aperture (red, green) and an aperture of 50 mm x 50 mm (blue) placed at a distance of 5 m from the undulator center. Electron beam: E = 161 MeV, σ_γ = 0.1%, $\sigma_{x,z}$ = 0.1 mm, $\sigma'_{x,z}$ = 0.1 mrad. Undulator: λ_u = 18.16 mm, B = 1 T, K_u = 1.7, N_u = 110.

Table 6.14 shows the spectra characteristics of Fig. 6.21. The bandwidth of the z = 0 cut is equal to the natural linewidth which is expected in the case of x = 0 (pinhole observation). In the case of the horizontal aperture, the wavelength is slightly red shifted and the bandwidth is increased by a factor of 2. A vertical cut is done at the resonace wavelength, and it is found to be ~3.8 mm FWHM close to the one computed in the transverse beam shape.

	Method	**Horizontal aperture** mm	**Wavelength** nm	**FWHM** nm	**Relative BW** %
Integrated intensity	Near-field	x = 0	224.0	4.75	2.12
	Far-field	x = 0	223.9	4.46	1.99
	Far-field	x = 50	226.7	59	26
z = 0 mm	Near-field	x = 0	223.3	2.26	1.01
	Far-field	x = 0	223.4	2.07	0.93
	Far-field	x = 50	223.9	4.08	1.82

Table 6.14: Peaked wavelength and bandwidth of the angular spectra presented in Fig. 6.21. Window aperture of dimensions 50 mm x 50 mm placed at a distance of 5 m from the undulator center. Electron beam: E = 161 MeV, σ_γ = 0.1%, $\sigma_{x,z}$ = 0.1 mm, $\sigma'_{x,z}$ = 0.1 mrad. Undulator: λ_u = 18.16 mm, B = 1 T, K_u = 1.7, N_u = 110.

Figure 6.22-a shows cuts at different vertical position of the angular spectra of Fig. 6.20-c. The off-axis radiation at vertical position (|z| > 0) is red-shifted due to the $\gamma^2\theta^2$ term in the resonance wavelength relationship. At z = 0 mm, the peaked intensity is at the resonance wavelength with a relative bandwidth of 1.8%. At z = 8 mm, the intensity is reduced by a factor of 2 with respect to the z = 0 mm cut, peaked wavelength is shifted to 248 nm with a wider relative bandwidth of 5.3%.

Figure 6.22-b shows cuts at different wavelength of the angular spectra of Fig. 6.20-c. The vertical radiation profiles for increasing wavelengths exhibit first a Gaussian type distribution at the resonance wavelength followed by a hole dip in the center (donut shape). At $\lambda = \lambda_{res}$, the FWHM of the vertical radiation profile is found to be 3.8 mm equal to the photon transverse beam size $\sigma_{p,z}$ discussed in section 6.2.

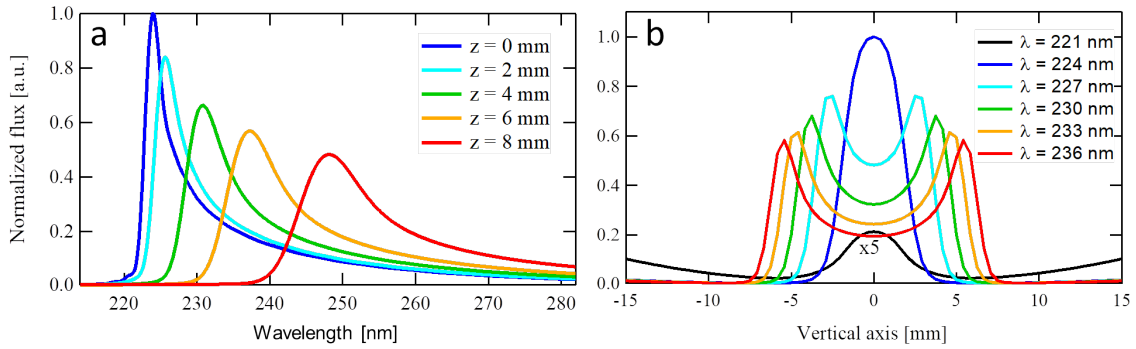

Figure 6.22: Moon shape analysis of Fig. 6.20-c. (a) Cuts at different vertical positions. (b) Cuts at different wavelengths.

6.3.1 Effect of the energy spread on the angular spectra

The energy spread effect on the angular spectral flux is examined. Fig. 6.23 displays the spectra computed using the reference beam (see Table 6.3) for different RMS energy spread with the cuts at z = 0 (blue) and integrated intensity (red). Table 6.15 shows the values of the bandwidth of Fig. 6.23 as well as the vertical cut at the resonance wavelength corresponding to the photon vertical beam size ($\sigma_{p,z}$).

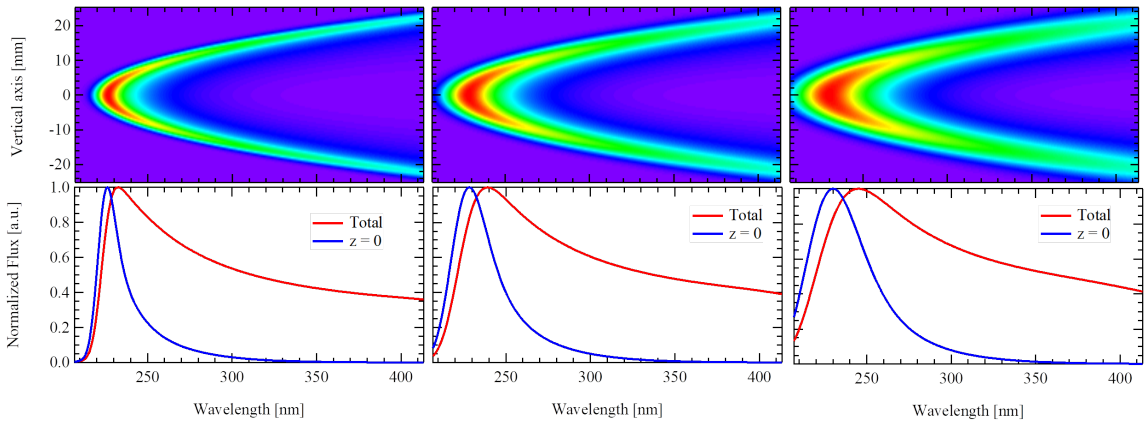

Figure 6.23: Angluar spectral flux for different energy spread (rms): (left) 1%, (middle) 2%, (right) 3%. Bottom figures are the cuts at z = 0 (blue) and the integrated intensity (red). Window aperture of dimensions 50 mm x 50 mm placed at a distance of 5 m from the undulator center. Electron beam: E = 161 MeV, $\sigma_{x,z}$ = 0.1 mm, $\sigma'_{x,z}$ = 0.1 mrad. Undulator: λ_u = 18.16 mm, B = 1 T, K_u = 1.7, N_u = 110.

Energy spread %	λ_{peak} nm	**Bandwidth** nm	$\frac{\Delta\lambda}{\lambda}$ %	$\frac{\Delta\lambda}{\lambda}\|_{blue}$ %	$\frac{\Delta\lambda}{\lambda}\|_{red}$ %	$\sigma_{p,z}$ mm
0.5	225	9.8	4.36	1.59	2.77	6.4
1	226	16.8	7.43	2.81	4.63	8.4
2	229	29.7	13.01	5.36	7.64	11.7
3	230	41.9	18.23	7.56	10.66	13.9
4	231	53.8	23.29	9.7	13.58	15.8
5	232	65.9	28.42	11.81	16.61	17.6

Table 6.15: Peaked wavelength and bandwidth of the angular spectra presented in Fig. 6.23. Window aperture of dimensions 50 mm x 50 mm placed at a distance of 5 m from the undulator center. Electron beam: E = 161 MeV, $\sigma_{x,z}$ = 0.1 mm, $\sigma'_{x,z}$ = 0.1 mrad. Undulator: λ_u = 18.16 mm, B = 1 T, K_u = 1.7, N_u = 110.

Fig. 6.24 shows the estimated rms energy spread using the two methods introduced in the previous sections presented in Eqs. (6.19) (blue) and (6.11) (green). The energy spread can be estimated to a good value using both methods, however Eq. (6.19) starts to degrade for an energy spread larger than 3%.

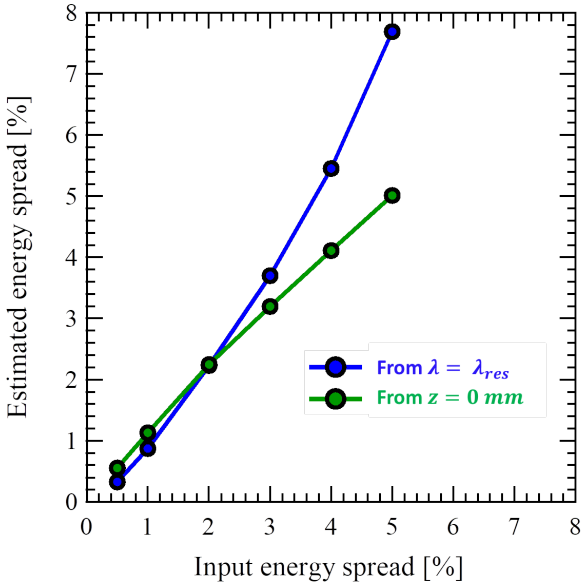

Figure 6.24: Estimated energy spread versus input value. (Blue curve) the estimated energy spread using Eq. (6.19) as done in the transverse beam shape section. (Green curve) energy spread estimated from the cut at z = 0 using Eq. (6.11).

6.3.2 Effect of the divergence on the angular spectra

The divergence effect on the angular spectral flux is examined. Fig. 6.25 displays the spectra computed using the reference beam (see Table 6.3) for different rms horizontal and vertical divergence. Table 6.16 shows the characteristics of the spectra presented in Fig. 6.25. The horizontal divergence has a slight effect on the angular spectral shape due to the large aperture, however it adds a tail at long wavelength without affecting the bandwidth as presented in the spectral flux section (see Table 6.16). The vertical divergence spoils the moon shape pattern by adding kind of a "bubble glow" around the resonance wavelength.

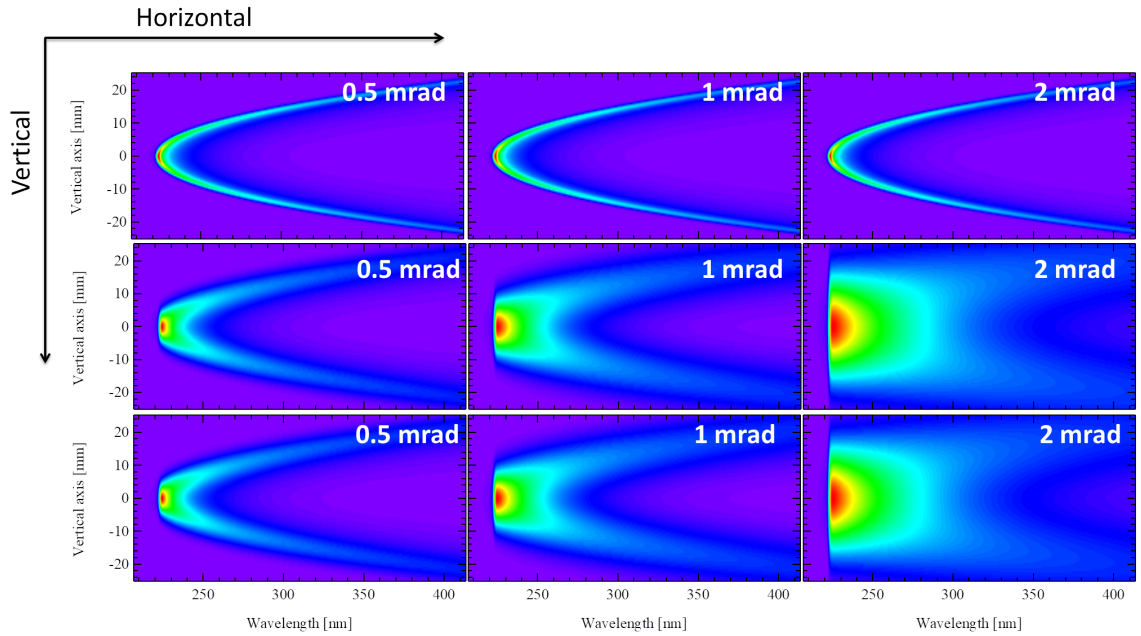

Figure 6.25: Angluar spectral flux for different horizontal and vertical divergences (rms): (Top) horizontal divergence, (middle) vertical divergence, (Bottom) both divergence while keeping the rest of the parameters the case of the reference beam. Window aperture of dimensions 50 mm x 50 mm placed at a distance of 5 m from the undulator center. Electron beam: E = 161 MeV, σ_γ = 0.1%, $\sigma_{x,z}$ = 0.1 mm. Undulator: λ_u = 18.16 mm, B = 1 T, K_u = 1.7, N_u = 110.

σ'_x mrad	σ'_z mrad	λ_{peak} nm	$\Delta\lambda$ nm	$\frac{\Delta\lambda}{\lambda}$ %	$\frac{\Delta\lambda}{\lambda}\|_{blue}$ %	$\frac{\Delta\lambda}{\lambda}\|_{red}$ %	$\sigma_{p,z}$ mm
0.5	0.1	224	4.0	1.78	0.57	1.21	3.9
1	0.1	224	3.9	1.75	0.59	1.16	3.9
2	0.1	224	3.8	1.68	0.48	1.2	3.9
0.1	0.5	225	9.6	4.28	0.79	3.49	6.7
0.1	1	225	20.4	9.08	0.91	8.17	12.4
0.1	2	225	38.4	17.04	0.92	16.12	25
0.5	0.5	225	9.5	4.22	0.79	3.43	7.0
1	1	225	20.1	8.92	0.9	8.02	12.5
2	2	225	36.2	16.09	0.91	15.18	24.8

Table 6.16: Peaked wavelength and bandwidth of the angular spectra presented in Fig. 6.25. Window aperture of dimensions 50 mm x 50 mm placed at a distance of 5 m from the undulator center. Electron beam: E = 161 MeV, σ_γ = 0.1%, $\sigma_{x,z}$ = 0.1 mm. Undulator: λ_u = 18.16 mm, B = 1 T, K_u = 1.7, N_u = 110.

The vertical divergence can be estimated using the following:

$$\sigma'_z = \frac{1}{D}\sqrt{\sigma^2_{p,z} - (\sigma'_n D)^2} \tag{6.24}$$

Figure 6.26-a shows the vertical profile at the resonant wavelength for different input divergence. The estimated values using Eq. (6.24) are very close to the input one as shown in Fig. 6.26-b.

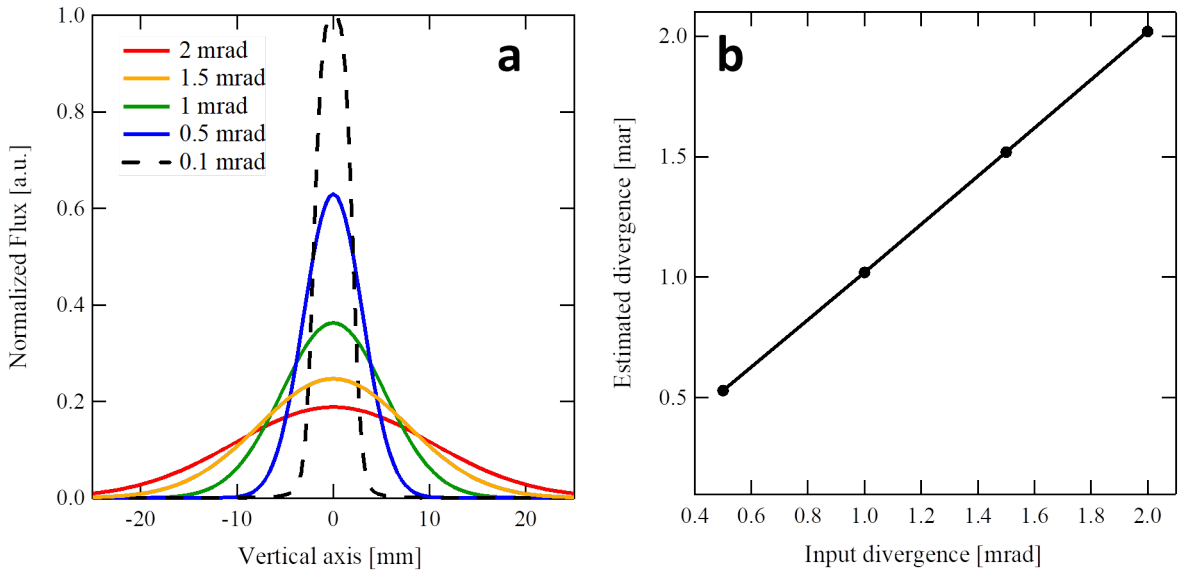

Figure 6.26: (a) vertical cut at the resonance wavelength 223 nm for different vertical divergence. (b) Estimated vertical divergence using Eq. 6.24.

As presented before with the spectral flux section, the divergence estimation using Eq. (6.11) is not efficient when looking at the bandwidth of the spectra. Thus a different approach is examined by looking at the flux integration. The integrated flux at the blue side I_{blue} and red side I_{red} of the spectrum are introduced as:

$$I_{blue} = \frac{1}{\lambda_{peak}} \int_{-\infty}^{\lambda_{peak}} f(\lambda) d\lambda \tag{6.25}$$

and

$$I_{red} = \frac{1}{\lambda_{peak}} \int_{\lambda_{peak}}^{+\infty} f(\lambda) d\lambda \tag{6.26}$$

respectively, where $f(\lambda)$ is the flux distribution at $z = 0$ mm. The integration of a Gaussian function is given by:

$$\int_{-\infty}^{+\infty} e^{-cx^2} = \sqrt{\frac{\pi}{c}}$$

Using this identity and approximating that Eqs. (6.25) and (6.26) are half Gaussians, one gets:

$$\begin{cases} I_{blue} = \frac{\sqrt{2\pi}}{2} \sigma_{blue} \\ I_{red} = \frac{\sqrt{2\pi}}{2} \sigma_{red} \end{cases} \tag{6.27}$$

where σ_{blue} is the standard deviation on the blue side of the spectrum and σ_{red} the one on the red side of the spectrum. Assuming that the horizontal divergence contribution is only on the red side of the spectrum, one gets:

$$\left[\frac{\Delta\lambda}{\lambda}\right]_{\sigma'_x} = \sqrt{\sigma^2_{red} - \sigma^2_{blue}} \tag{6.28}$$

and thus:

$$\sigma'^2_{tot} = \sigma'^2_x + \sigma'^2_z = \frac{(1 + K_u^2/2)}{\gamma^2} \sqrt{\frac{2}{\pi}} \sqrt{I^2_{red} - I^2_{blue}} \tag{6.29}$$

Table 6.17 presents the spectrum characteristics at the center of the moon shape computed in the near-field approximation. The bandwidth on the red side and vertical size between the two computations change depending on the divergence, as for the bandwidth on the blue side, it remains the same. Figure 6.27 presents a comparison between the near and far field approximations for the reference electron beam with 1 mrad divergence.

σ'_x mrad	σ'_z mrad	λ_{peak} nm	$\frac{\Delta\lambda}{\lambda}$ %	$\frac{\Delta\lambda}{\lambda}\|_{blue}$ %	$\frac{\Delta\lambda}{\lambda}\|_{red}$ %	σ'_{tot} mrad	$\sigma_{p,z}$ mm
0.5	0.1	224	1.4	0.6	0.8	0.52	3.9
0.1	0.5	224	1.3	0.6	0.7	0.54	8.4
0.5	0.5	225	3.1	0.8	2.3	0.75	8.5
0.5	1	225	4.1	0.7	3.3	1.04	11.3
1	0.5	226	4.1	1.4	2.7	0.93	8.6
1	1	225	8	0.8	7.2	1.4	14.3

Table 6.17: Peaked wavelength and bandwidth of the angular spectra using the near field approximation. Window aperture of a horizotal pinhole ($x = 0$ mm) and 50 mm vertical aperture placed at a distance of 5 m from the undulator center. σ'_{tot} calculated using Eq. (6.29). Electron beam: E = 161 MeV, $\sigma_\gamma = 0.1\%$, $\sigma_{x,z} = 0.1$ mm. Undulator: $\lambda_u = 18.16$ mm, B = 1 T, $K_u = 1.7$, $N_u = 110$.

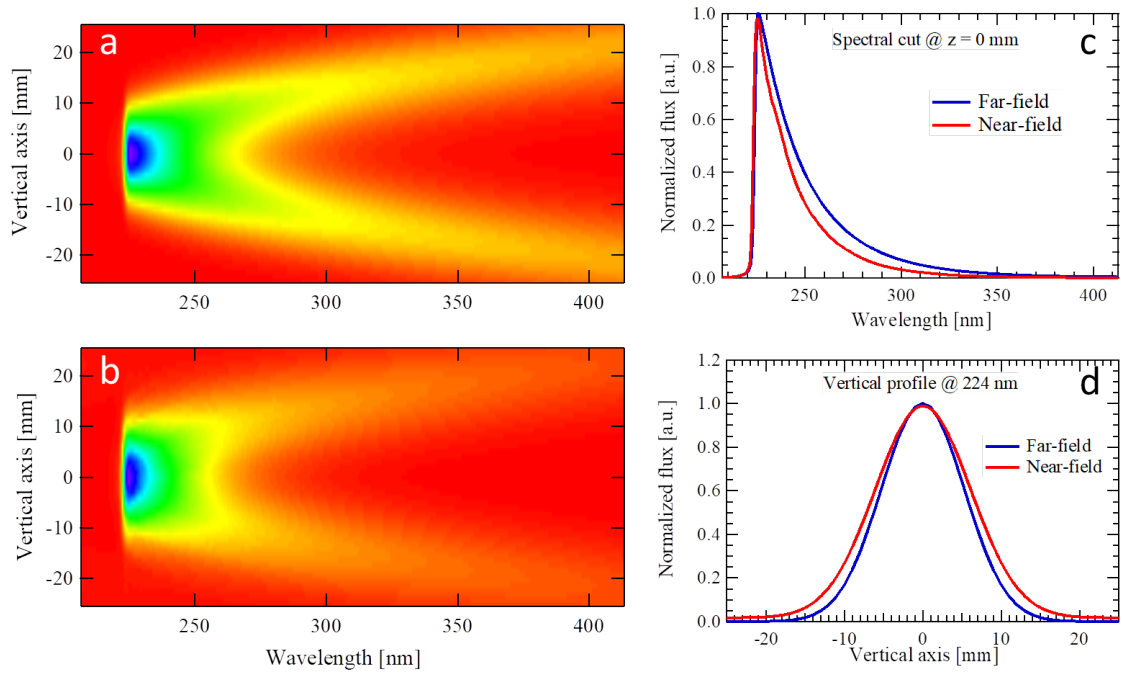

Figure 6.27: Computed spatio-spectral flux using the far field (a) and near field (b) approximations, with their corresponding spectral profile at $z = 0$ (c) and vertical profile at the resonance wavelength (d). Window aperture of a horizotal pinhole ($x = 0$ mm) and 50 mm vertical aperture placed at a distance of 5 m from the undulator center. Electron beam: E = 161 MeV, $\sigma_\gamma = 0.1\%$, $\sigma_{x,z} = 0.1$ mm, $\sigma'_{x,z} = 1$ mrad. Undulator: $\lambda_u = 18.16$ mm, B = 1 T, $K_u = 1.7$, $N_u = 110$.

Table 6.18 shows the estimated vertical divergence using Eq. (6.24) and horizontal divergence using Eq. (6.29) in the case of the near field computation. Both divergences are estimated rather well.

Input		Estimate		Difference	
σ'_x mrad	σ'_z mrad	σ'_x mrad	σ'_z mrad	σ'_x %	σ'_z %
0.5	0.1	0.51	-	2	-
0.1	0.5	-	0.63	-	26
0.5	0.5	0.4	0.63	-20	26
1	0.5	0.66	0.65	-34	30
0.5	1	0.52	0.9	4	-10
1	1	0.85	1.1	-15	10

Table 6.18: Input and estimated values of the horizontal and vertical divergence.

6.3.3 Effect of the beam size on the angular spectra

The horizontal beam size has no effect on the angular spectral flux especially when the observation window has a horizontal aperture larger than the horizontal beam size. The vertical beam size, however, has an effect similar to that of the vertical divergence where the "bubble" glow appear around the resonance as shown in Fig. 6.28.

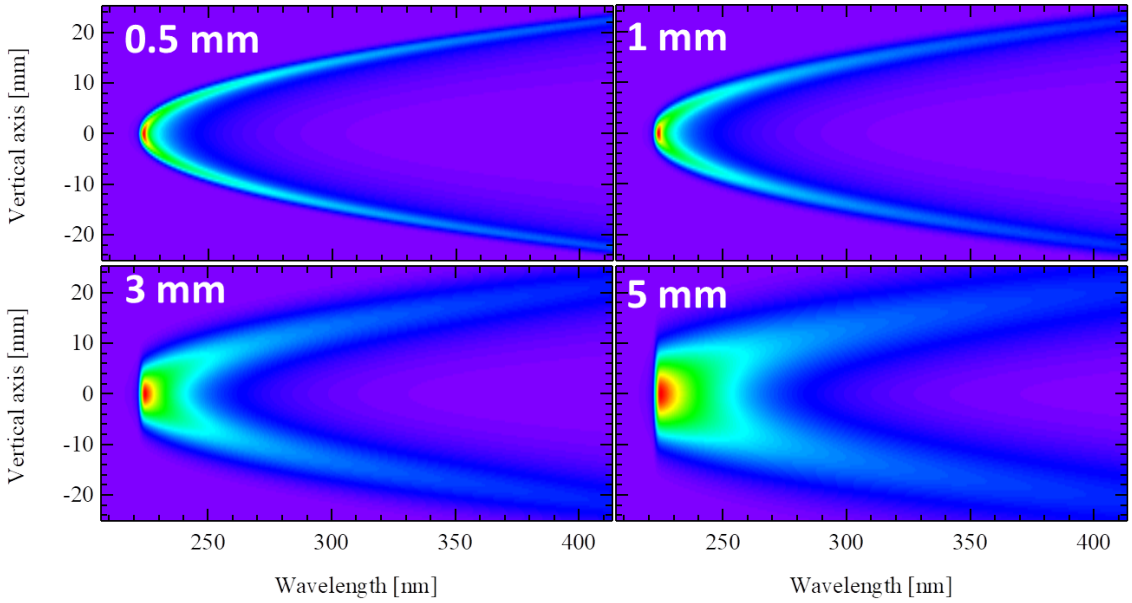

Figure 6.28: Angluar spectral flux for different vertical beam size (rms) with value appended. Bottom figures are the cuts at z = 0 (blue) and the integrated intensity (red). Window aperture of dimensions 50 mm x 50 mm placed at a distance of 5 m from the undulator center. Electron beam: E = 161 MeV, σ_γ = 0.1%, $\sigma'_{x,z}$ = 0.1 mrad. Undulator: λ_u = 18.16 mm, B = 1 T, K_u = 1.7, N_u = 110.

Table 6.19 presents the spectra at $z = 0$ characteristics for different vertical beam sizes.
The vertical beam size can be estimated using the following:

$$\sigma_z = \sqrt{\sigma^2_{p,z} - (\sigma'_n D)^2} \tag{6.30}$$

Figure 6.29-a shows the vertical profile at the resonant wavelength for different input beam size. The estimated beam size using Eq. (6.30) is very close to the input one as shown in Fig. 6.29-b.

σ_z mrad	**Peak** nm	**FWHM** nm	$\frac{\Delta\lambda}{\lambda}$ %	$\frac{\Delta\lambda}{\lambda}\|_{blue}$ %	$\frac{\Delta\lambda}{\lambda}\|_{red}$ %
0.5	224	4.1	1.81	0.61	1.2
1	224	4.8	2.15	0.58	1.58
3	225	11.7	5.21	0.78	4.43
5	225	20.2	8.96	0.9	8.06

Table 6.19: Peaked wavelength and banwidth of the angular spectra presented in Fig. 6.25. Window aperture of dimensions 50 mm x 50 mm placed at a distance of 5 m from the undulator center. Electron beam: E = 161 MeV, σ_γ = 0.1%, $\sigma'_{x,z}$ = 0.1 mrad. Undulator: λ_u = 18.16 mm, B = 1 T, K_u = 1.7, N_u = 110.

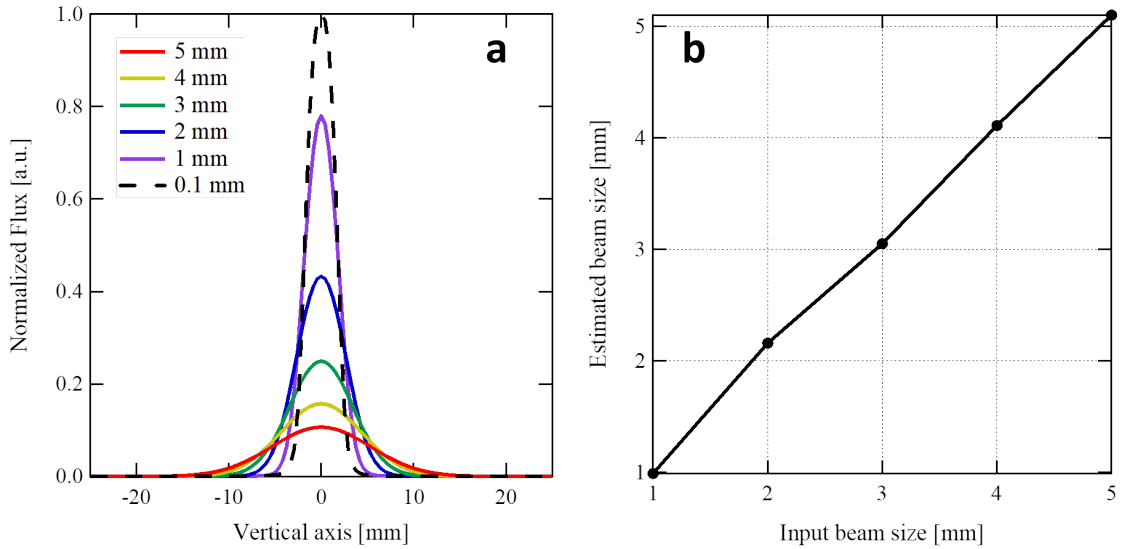

Figure 6.29: (a) Vertical profile of Fig. 6.28 at the resonant wavelength. (b) Estimated vertical beam size versus imput value.

6.3.4 Simultaneous effect of the energy spread and divergence on the angular spectra

This section is to try to deduce the energy spread and divergence simultaneously by observing the angular spectra. Figure 6.30 shows the angular spectral flux computed in the far-field approximation, using the reference beam parameters (see Table 6.3) while changing the energy spread rms and divergence in both transverse planes. The energy spread and vertical divergence widen the moon shape in spectral bandwidth and vertical profile, as for the horizontal divergence it mainly affect the spectral width.

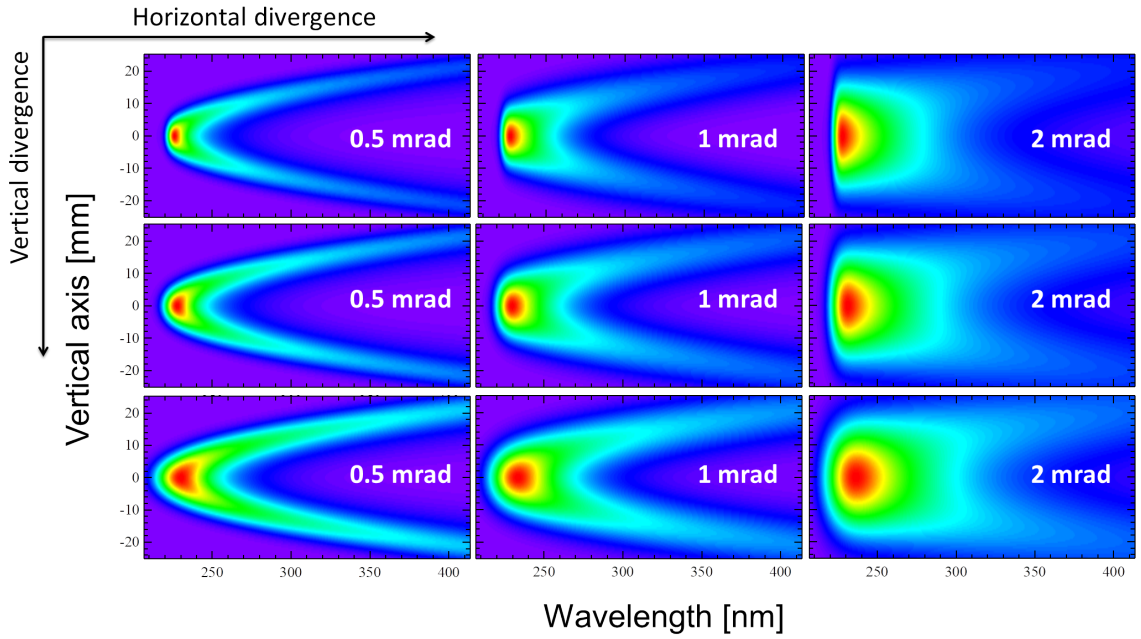

Figure 6.30: Angluar spectral flux computed in the far-field approximation for different energy spread (rms) and divergence: (Top) 0.5%, (middle) 1%, (Bottom) 2%. Window aperture of dimensions 50 mm x 50 mm placed at a distance of 5 m from the undulator center. Electron beam: E = 161 MeV, $\sigma_{x,z}$ = 0.1 mm. Undulator: λ_u = 18.16 mm, B = 1 T, K_u = 1.7, N_u = 110.

Table 6.20 presents the properties of the spectra cut at z = 0 for different electron beam parameters. The blue spectra is dominated by the energy spread and receives more contribution from the divergence when the value increases. The photon vertical beam size at the resonance wavelength is also presented, and it increases with the vertical divergence as seen in section 6.3.2.

σ_γ %	$\sigma'_{x,z}$ mrad	λ_{peak} nm	$\Delta\lambda/\lambda$ %	$\frac{\Delta\lambda}{\lambda}\|_{blue}$ %	$\frac{\Delta\lambda}{\lambda}\|_{red}$ %	$\sigma_{p,z}$ mm
	0.5	226	5.97	1.83	4.14	8.6
0.5	1	228	9.98	2.13	7.84	13.4
	2	228	16.03	2.35	13.67	24.6
	0.5	228	8.48	3.16	5.32	10.3
1	1	230	12.37	3.53	8.85	14.5
	2	231	19.49	3.92	15.56	25.1
	0.5	230	13.64	5.47	8.17	12.8
2	1	234	16.81	6.16	10.65	16.5
	2	236	24.01	6.79	17.22	26.3
	0.5	231	17.59	7.64	9.95	14.9
3	1	236	21.68	8.51	13.17	19.1
	2	240	29.23	9.69	19.53	29.8

Table 6.20: Relative bandwidth of the moon shape cut at z = 0 while changing the divergence and energy spread of the spectra computed in the far-field. $\sigma_{p,z}$ the FWHM for the vertical cut at the resonance wavelength. Window aperture of dimensions 50 mm x 50 mm placed at a distance of 5 m from the undulator center. Electron beam: E = 161 MeV, $\sigma_{x,z}$ = 0.1 mm. Undulator: λ_u = 18.16 mm, B = 1 T, K_u = 1.7, N_u = 110.

Computations have been done using the near-field approximation for different electron beam parameters with characteristics shown in Table 6.21.

σ_γ %	σ'_x mrad	σ'_z mrad	λ_{peak} nm	$\Delta\lambda/\lambda$ %	$\frac{\Delta\lambda}{\lambda}\|_{blue}$ %	$\frac{\Delta\lambda}{\lambda}\|_{red}$ %	σ'_{tot} mrad	$\sigma_{p,z}$ mm
0.5	0.5	0.5	227	3.7	1.8	1.9	0.55	8.8
1	0.5	0.5	227	7	3.4	3.7	0.66	9.8
1	0.5	1	228	8	3.1	4.9	1.13	15.8
1	1	0.5	228	6.9	2.6	4.3	0.9	9.5
1	1	1	231	11.1	3.9	7.2	1.28	15.7
2	0.5	0.5	233	12.1	7.1	5	0.99	14.4
2	1	1	231	12.6	5.3	7.2	1.31	17.7

Table 6.21: Spectra characteristics computed in the near field approximation, while changing the divergence and energy spread . $\sigma_{p,z}$ the FWHM for the vertical cut at the resonance wavelength. Window aperture of a horizotal pinhole (x = 0 mm) and 50 mm vertical aperture placed at a distance of 5 m from the undulator center. Electron beam: E = 161 MeV, $\sigma_{x,z}$ = 0.1 mm. Undulator: λ_u = 18.16 mm, B = 1 T, K_u = 1.7, N_u = 110.

With the methods presented previously, it is possible to extract the energy spread, horizontal and vertical divergence in a single shot measurement of the spatio-spectral flux for a negligible electron beam sizes. From section 6.2, we have seen that the energy spread widens the photon vertical size ($\sigma_{p,z}$), so $\sigma_{p,z}$ at the resonant wavelength can be expressed as:

$$\sigma_{p,z} = \sqrt{(\sigma'_n D)^2 + (\theta_H D)^2 + (\sigma'_z D)^2} \tag{6.31}$$

First the energy spread is estimated from the blue side of the spectrum using Eq. (6.11) and replaced in Eq.(6.19), where θ_H is determined. Then θ_H is substituted in Eq. (6.31), and the vertical divergence is calculated. Finally, Eq. (6.29) is used to determine the horizontal divergence:

$$\sigma'_x = \sqrt{\sigma'^2_{tot} - \sigma'^2_z} \tag{6.32}$$

Table 6.22 presents the calculated electron beam parameters using the described method. This approach works quite well especially in determining the vertical divergence. As for the energy spread and horizontal divergence, the difference with respect to the input value is a bit far in most cases.

Input			**Estimate**			**Difference**		
σ_γ %	σ'_x mrad	σ'_z mrad	σ_γ %	σ'_x mrad	σ'_z mrad	σ_γ %	σ'_x %	σ'_z %
0.5	0.5	0.5	0.74	-	0.57	48	-	14
1	0.5	0.5	1.4	0.3	0.59	40	-40	18
1	0.5	1	1.3	-	1.2	30	-	20
1	1	0.5	1.1	0.7	0.6	10	-30	20
1	1	1	1.6	0.49	1.2	60	-51	20
2	0.5	0.5	3	0.28	0.95	50	-44	90
2	1	1	2.24	-	1.34	12	-	34

Table 6.22: Input and estimated values of the energy spread, divergence and their difference with respect to the input values from the spectra computed using the near-field approximation.

Another attempt is done using the same approach, but instead of getting the blue and red side bandwidth with respect to the peak wavelength, we now get it with respect to the resonant wavelength (see Fig. 6.31).

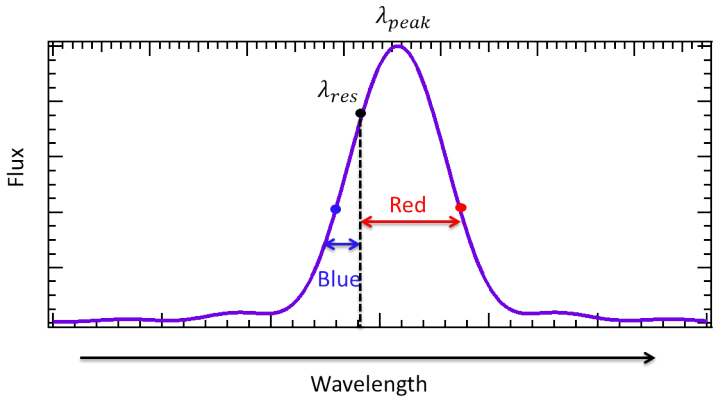

Figure 6.31: Scheme describing the blue and red bandwidth with respect to the resonant wavelength.

Table 6.23 presents the characteristics of the spectra already displayed in Table 6.21 but by taking the bandwidth with respect to the resonant wavelength. The bandwidth on the blue side of the spectrum is decreased and increased on the red side. The electron beam parameters are estimated to a better value especially the energy spread, as shown in Table 6.24. One can notice that σ'_{tot} is well extracted using Eq. (6.29) and agrees with the input values ($\sigma'^2_x + \sigma'^2_z$), however Eq. (6.31) is not that sufficient, where it estimates a larger vertical divergence and thus induces a large deviation of the estimated horizontal divergence in some cases (see Table 6.24).

σ_γ %	σ'_x mrad	σ'_z mrad	λ_{res} nm	$\Delta\lambda/\lambda$ %	$\frac{\Delta\lambda}{\lambda}\|_{blue}$ %	$\frac{\Delta\lambda}{\lambda}\|_{red}$ %	σ'_{tot} mrad	$\sigma_{p,z}$ mm
0.5	0.5	0.5	225	4.2	1.1	3.2	0.81	8.8
1	0.5	0.5	225	7.6	2.8	4.8	0.91	9.8
1	0.5	1	225	9.4	2.8	6.7	1.23	15.8
1	1	0.5	226	8.4	2.1	6.3	1.05	9.5
1	1	1	229	11.8	3.2	8.6	1.38	15.7
2	0.5	0.5	231	12.7	6.4	6.3	0.77	14.4
2	1	1	229	13.9	4.8	9.2	1.42	17.7

Table 6.23: Relative bandwidth of the moon shape cut at z = 0 while changing the divergence and energy spread computed using the near field approximation. $\sigma_{p,z}$ the FWHM for the vertical cut at the resonance wavelength. Window aperture of a horizotal pinhol (x = 0 mm) and 50 mm vertical aperture placed at a distance of 5 m from the undulator center. Electron beam: E = 161 MeV, $\sigma_{x,z}$ = 0.1 mm. Undulator: λ_u = 18.16 mm, B = 1 T, K_u = 1.7, N_u = 110.

Input			Estimate			Difference		
σ_γ %	σ'_x mrad	σ'_z mrad	σ_γ %	σ'_x mrad	σ'_z mrad	σ_γ %	σ'_x %	σ'_z %
0.5	0.5	0.5	0.4	0.5	0.6	-20	1	20
1	0.5	0.5	1.2	0.7	0.6	20	40	20
1	0.5	1	1.2	0.1	1.2	20	-80	20
1	1	0.5	0.9	0.8	0.6	-10	-20	20
1	1	1	1.3	0.7	1.2	30	-30	20
2	0.5	0.5	2.7	-	1	35	-	100
2	1	1	2	0.4	1.4	1	-60	40

Table 6.24: Input and estimated values of the energy spread and divergence and their difference with respect to the input values of the spectra computed in the near-field approximation.

The method has been introduced with simulations using a horizontal pinhole observation. However more tests have been done for different horizontal apertures and show that it is still valid, to a certain extent, for horizontal apertures no larger than ~5 mm.

6.4 Summary

The COXINEL radiation generated in the baseline reference beam have been examined using SRW simulation code. Analytical approaches have been introduced to extract some electron beam parameters from the observed undulator radiation.

When looking at the transverse beam shape, the energy spread can be estimated when the vertical beam emittance is rather small. However a small bandpass filter (around 10 nm FWHM) before the measurement device should be implemented otherwise the off-axis radiation will dominate the spectra. The divergence can also be estimated when the energy spread and beam size are quite small. However, the different contributions can not be distinguished from each other.

As for the spatio spectral shape or the moon shape pattern, the energy spread and divergence in both transverse planes can be estimated in a single shot, however the vertical beam size should be small or the observation window should be placed far from the undulator so that its effect is negligible.

The methods described here are used in chapter 8 to estimate the beam parameters at the center of the undulator and compared to the ones found using the beam optics code, where the measured LPA electron beam characteristics are used.

Chapter 7

COXINEL Experiment

The beam time from the 30 TW laser used for the generation of electrons at Laboratoire d'Optique Appliquée is ditributed over different applications. Dedicated experimental sessions, noted as RUNs in the PhD, were devoted to COXINEL. COXINEL first two runs (RUN1 and RUN2) objective was to control and transport the electron beam. The transport was not as easy as expected due to the presence of alignment issues, drifts along the line and pointing fluctuations. First undulator radiation was measured during RUN3 [287] using a CCD camera. In RUN4 and RUN5, a UV spectrometer was installed at the end of the line to measure the spatio-spectral distribution of the undulator radiation. In this chapter, the COXINEL line elements are reported alongside electron beam transport and measurements during RUN4 and RUN5, focusing mainly on the days where undulator radiation is observed.

7.1 COXINEL line

The COXINEL transport line [287–289], as shown in Fig. 7.1, starts with a triplet of QUAPEVAs [131] that strongly focuses the LPA electron beam and permits to handle the divergence. The electron beam is then sent through a four-dipole-magnet chicane where the beam is longitudinally stretched. The presence of a variable width slit in the middle of the chicane enables to select an energy range of interest [290–292]. A second set of quadrupoles placed after the chicane ensures that the transverse beam size is minimized at the undulator center. The U18 n°2 undulator, presented in chapter 5, is installed and operating at room temperature. Transfer line components and LPA laser are aligned within ±100 µm on the reference axis using a laser tracker.

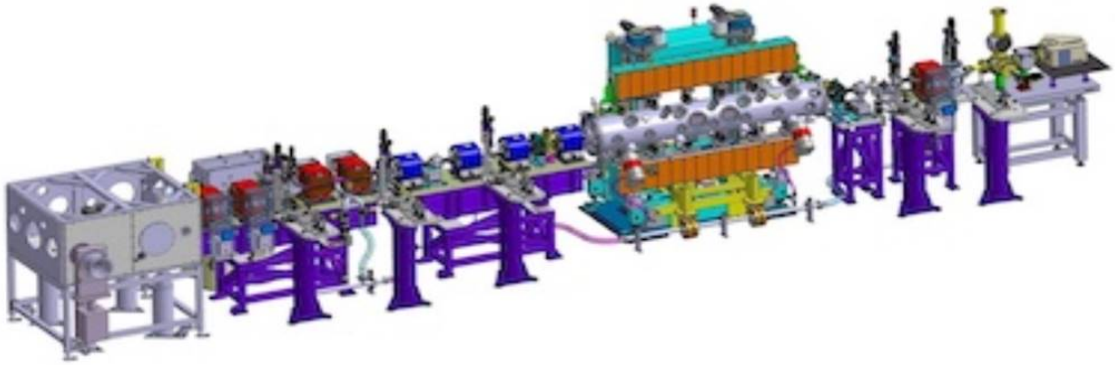

Figure 7.1: COXINEL experimental setup. laser hutch (grey), QUAPEVAs placed inside the laser hutch, electro-magnet dipoles (red), electro-magnet quadrupoles (blue), undulator (gray), dipole dump (red), UV spectrometer (light grey).

7.1.1 Electron source

The LPA is driven by a Titanium:Sapphire laser system at Laboratoire d'Optique Appliquée, which delivers 30 fs (FWHM) pulses of 1.5 J energy at a central wavelength of 800 nm with a repetition rate of 1 Hz (see Table 7.1). The laser beam is focused by an off-axis parabola into a gas mixture composed of 99% He and 1% N_2.

Parameter	Value	Unit
Material	Ti:Sapphire	-
Wavelength	800	nm
Pulse duration	30	fs
Power	30	TW
Energy	1.5	J

Table 7.1: Laser characteristics.

The LPA was tested in two regimes, the ionization injection [293] and shock injection [44], where the same laser parameters are used for both techniques. In the shock injection technique, the power is slightly reduced (~ factor of 2) and a 500 µm thick silicon wafer is inserted into the supersonic gas flow [44]. This technique produced electron beams with a smaller energy spread but displayed a poor stability and lower charge. Hence it was decided to operate the LPA in the ionization injection regime due to its robustness.

7.1.2 Electron beam optics

The COXINEL line was designed to enable wide tuning and manipulation of the electron beam. Thanks to the tunable high gradient QUAPEVAs, different beam optics can be adopted. Electron beam transport is tuned with BETA code [294] up to the second order, with home-made multiparticle tracking code for high order non-linear effects and collective effects like coherent synchrotron radiation [201]. Hard edge models are used for the magnets and apertures of the vacuum chamber along the beam line are included.

As discussed previously, the supermatching optics has been developed for the FEL demonstration, where the nominal energy slice is well focused at the center of the undulator, and the lower and higher energies are focused before and after, respectively, as shown in Fig. 7.2.

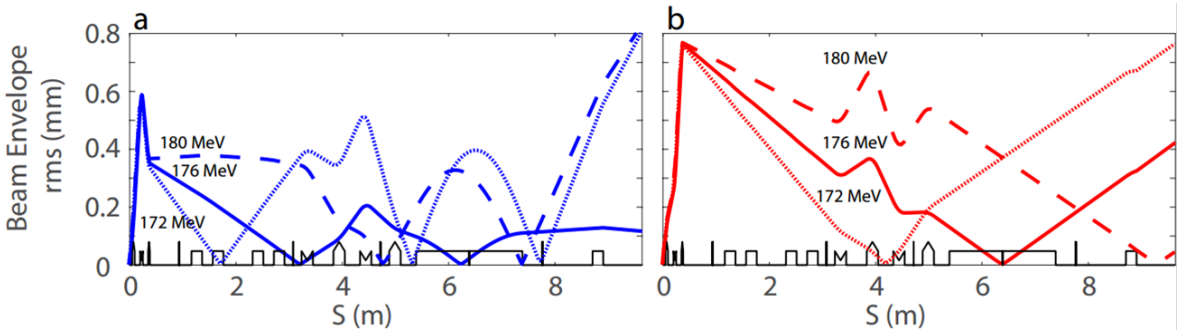

Figure 7.2: Simulation of vertical (a) and horizontal (b) RMS beam envelope evolution for different energies with an initial σ'_z = 2 mrad (RMS) and σ'_x = 3 mrad (RMS) along the beam line using the supermatching optics.

Another optics has been adopted, what we call the slit optics, optimized to focus firstly at the center of the chicane, where an adjustable slit is placed to help us control the energy range. Figure 7.3 shows the beam envelope evolution in horizontal and vertical for different energy slices. The nominal energy of 176 MeV is well focused at chicane slit and then at the undulator center.

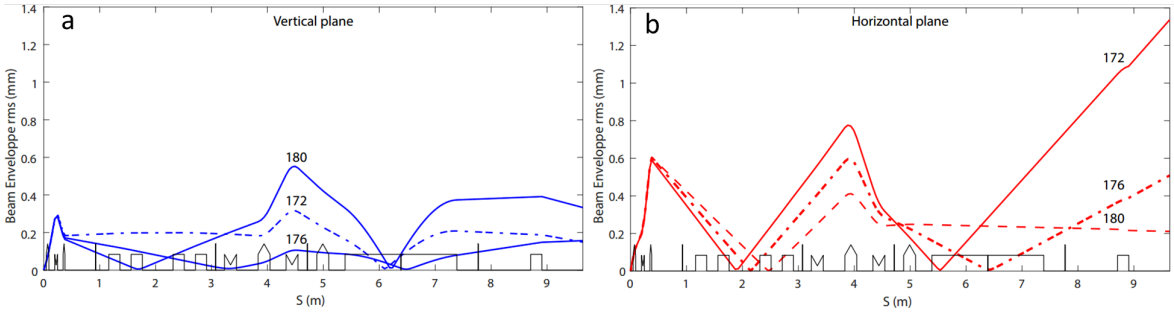

Figure 7.3: Simulation of horizontal (a) and vertical (b) RMS beam envelope evolution along the beam line for a flat-top beams with an initial σ'_z = 2 mrad (RMS) and σ'_x = 3 mrad (RMS) using the supermatching optics.

During the electron beam transport, optimization is done along the way to make sure the electron beam is well controled. Two other optics are implemented that allow us to focus the beam at two imagers placed before and after the undulator. For these optics, the gradient of the QUAPEVAs is slightly tuned. Figure 7.4 summarizes the different optics configurations (Figure 7.4a-d) and the associated beam transverse shape before, at the center of and after the undulator (Figure 7.4a1-d3) [283]. The envelope is modeled in the case of a 176±0.3 MeV flat-top energy distribution electron beam.

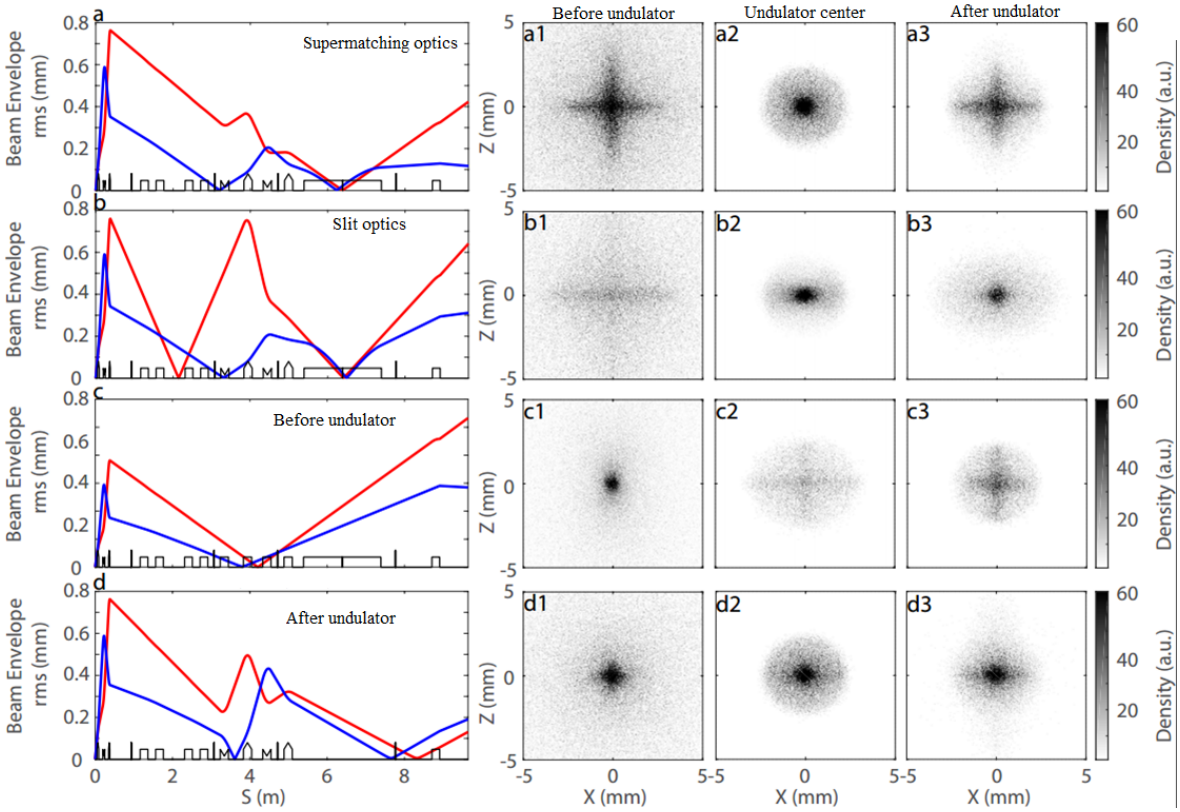

Figure 7.4: Simulation of horizontal (red) and vertical (blue) RMS beam envelope evolution (a-d) along the beam line for a beam of energy spectrum flat-top of 176±0.3 MeV, with an initial σ'_z = 2 mrad (RMS) and σ'_x = 3.12 mrad (RMS). Transversal distribution of the electron beam at the undulator entrance (a1-d1), center (a2-d2) and exit (a3-d3).

7.1.3 Magnetic elements of the transport line

In this section, the magnetic elements and their characteristics that enable us to control and manipulate the electron beam phase space are presented.

7.1.3.1 QUAPEVAs

The first magnetic element is a triplet QUAPEVAs [131, 132] introduced in chapter 6. The QUAPEVAs are located 5 cm from the electron generation source. The high gradient enables to focus the beam and handle the divergence at an early stage mitigating the emittance growth. In addition, the tunability allow for fine tuning of the machine as well as focusing different energies at the center of the undulator. Table 7.2 presents the operating gradient of the three QUAPEVAs for the two optics cases during RUN4 and RUN5.

Optics	Parameter	QUAPEVA 1	QUAPEVA 2	QUAPEVA 3	Unit
	Magnetic length	40.7	44.7	26	mm
Super Matching	Gradient for 176 MeV	102.7	-101.1	89.1	T/m
	Gradient for 161 MeV	105.5	-109.1	95.71	T/m
Slit	Gradient for 176 MeV	104.1	-103.1	96.4	T/m
	Gradient for 161 MeV	113.5	-111.3	103.4	T/m

Table 7.2: QUAPEVAs gradient for the two optics and operating energies at RUN4 and RUN 5.

Fig. 7.5 shows a picture of the QUAPEVA triplet installed in the vacuum chamber, where the electrons are produced.

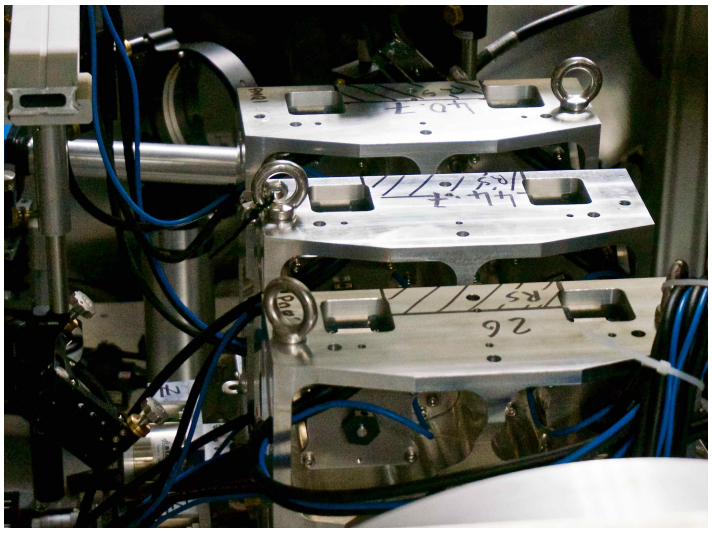

Figure 7.5: QUAPEVA triplet installed at COXINEL beam line in the laser chamber.

7.1.3.2 Chicane

The chicane is composed of four electro-magnet dipoles to stretch the beam longitudinally and sorts electrons in energy. The dipoles equipped with water-cooling infrastructure, are manufactured by SEF providing 0.55 T when powered at 150 A (Sigmaphi Electronics bipolar power supplies, 8 V, 30 ppm, calibrated at SOLEIL) for 25 mm yoke gap. The dipoles have been measured on

a SOLEIL magnetic measurement bench including a Hall probe system (consisting of three single-axis Hall probes (FW Bell GH-701) with a 1 V/T sensibility) and a rotating coil (a 20 turn 3.5 m long coil made of a 0.1 mm diameter copper wire, reproducibility of 1.5%). The field measurements of one of the dipoles at 150 A with two other systems (a Group3 Teslameter and a Metrolab PT2025 NMR system) show an agreement of 10 mT, corresponding to a relative error of 1.8%, which can be explained by the relative position and orientation of the different probes, and by the hysteresis influence. Table 7.3 shows some of the dipole characteristics. A removable Aluminium slit of variable width (up to 4 mm) is also inserted in the middle of the chicane at 32 ± 0.5 mm horizontal position corresponding to the nominal energy.

Parameter	**Value**	**Unit**
Current	150	A
Magnetic field	0.55	T
Integrated gradient	120	T·mm
ΔB/B	0.2	%
Current density	5.2	A/mm^2
Resistance	45	m·Ω
Impedance	10	mH
Number of turns	44	

Table 7.3: Dipole characteristics

Figure 7.6 shows the dipoles installed at COXINEL beam line.

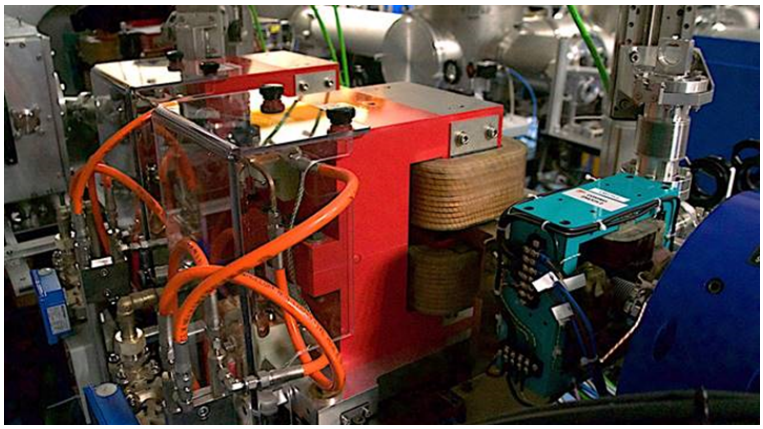

Figure 7.6: Chicane dipoles installed at COXINEL transport line.

7.1.3.3 Quadrupoles

After the beam traverses the chicane, energy-position correlation is achieved. By taking advantage of this correlation, another set of quadrupoles is implemented to enable the supermatching optics. Table 7.4 presents the electro-magnet quadrupoles characteristics. Table 7.5 presents the gradient strength of the quadrupoles for the two optics and operating energies of RUN4 (176 MeV) and RUN5 (161 MeV).

Parameter	Value	Unit
Maximum gradient	20	$T \cdot m^{-1}$
Gradient tunability	100	%
B_6	0.4×10^{-2}	
B_{10}	0.07×10^{-2}	
B_{14}	0.02×10^{-2}	
Bore radius	12	mm
Pole length	200	mm
Pole thickness	20	mm
Section	70×12	mm^2
Current density	1.6	$A \cdot mm^2$
Current (I)	1.6	A
Number of turns (N)	14×10	
Pole width	20	mm
Pole height	93	mm

Table 7.4: Quadrupole characteristics. B_6, B_{10} and B_{14} the systematic multipoles defined in chapter 6.

Optics		Quad 1	Quad 2	Quad 3	Quad 4	Unit
Super	Gradient for 176 MeV	-0.52	0.85	-1.23	0.46	T/m
Matching	Gradient for 161 MeV	-1.346	3.267	-5.132	1.895	T/m
Slit	Gradient for 176 MeV	-0.01	4.7	-4.4	0.29	T/m
	Gradient for 161 MeV	4.15	-3.45	-0.13	1.7	T/m

Table 7.5: Quadrupoles characteristics.

Figure 7.7 presents a model with the CATIA software of an electromagnetic quadrupole alongside two quadrupoles installed at COXINEL.

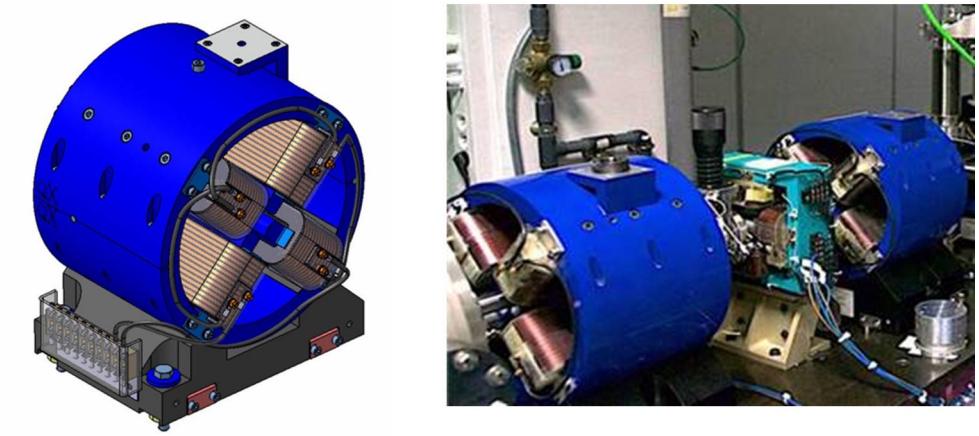

Figure 7.7: Electron magnet quadrupoles: CATIA software model (left), device installed at COXINEL.

7.1.3.4 Steerer

Four steerers, also known as correctors, are installed along the beam line: before the chicane, before the electromagnet quadrupoles, before and after the undulator. The steerers allow the vertical and horizontal positions of the electron beam to be adjusted. The properties of the correctors are summarized in Table 7.6.

Parameter	Value	Unit
Magnetic field	0.035	T
Field integral	31	G·m
Gap	340	mm
Section	30 × 15	mm^2
Current density	1.6	$A \cdot mm^2$
Current	10	A
Voltage	3	V
Conductor	5 × 1.25	mm^2
Number of turns (N)	72	
NI	720	A·t

Table 7.6: Steerer characteristics.

Figure 7.8 illustrates an ISO view under the CATIA software of a corrector and the built system.

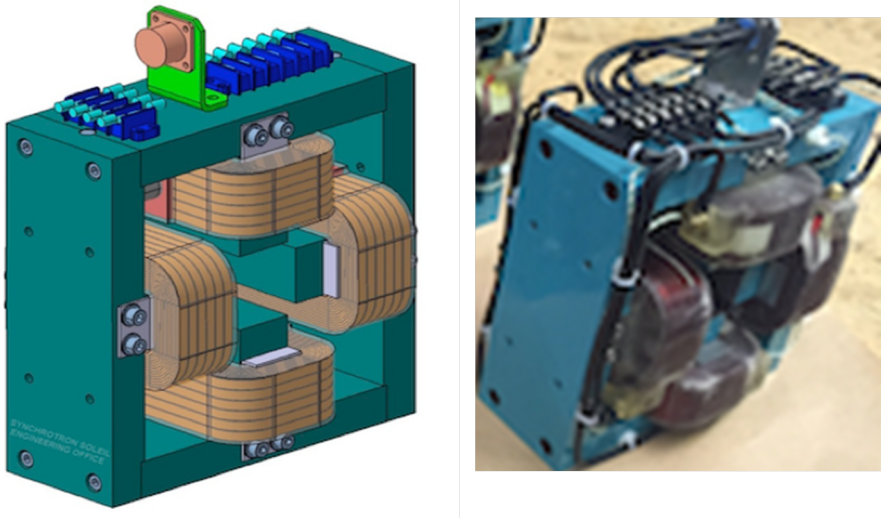

Figure 7.8: CATIA model of the steerer (left), the real device (right).

7.1.3.5 Dipole Dump

The electron beam dump dipole powered at 300 A provides a magnetic field of 0.84 T to get rid of the beam and allow for photon beam diagnostics.

7.1.4 Undulator

The U18n°2 undulator presented in chapter 5 is installed at LOA for the COXINEL project and operating at room temperature due to infrastructure reasons as shown in Fig. 7.9.

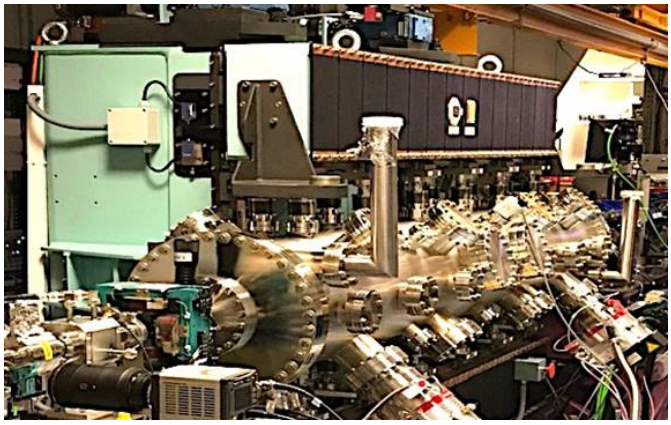

Figure 7.9: U18 undulator installed at COXINEL beam line.

Figure 7.10 presents the measured magnetic field versus gap at room temperature.

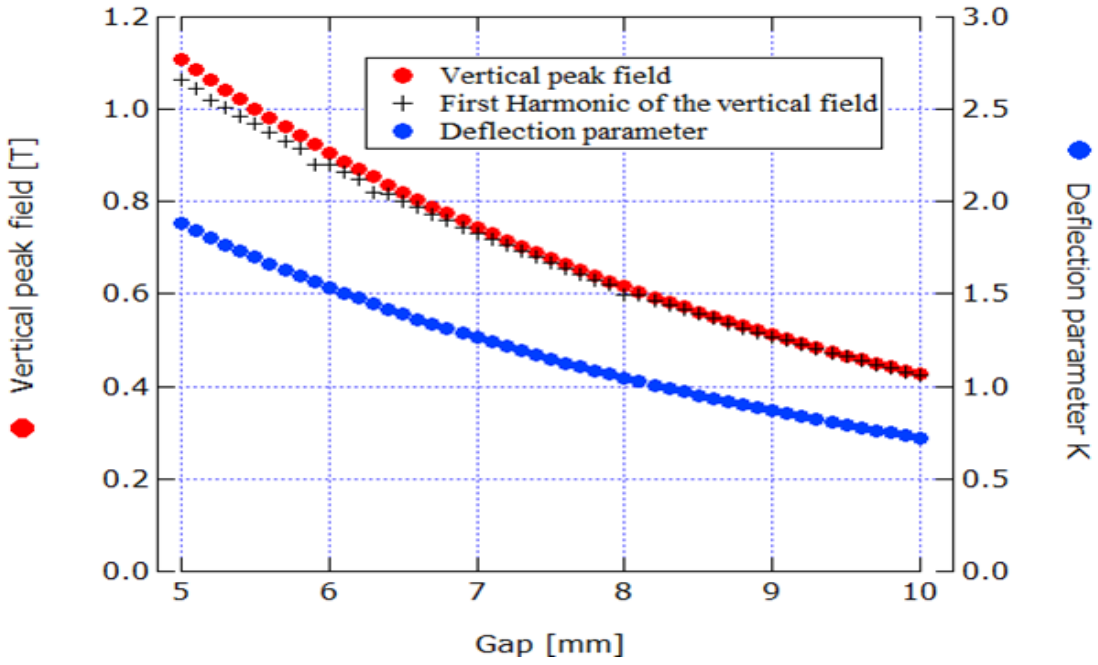

Figure 7.10: Measured magnetic field (red in left axis), its first harmonic (dark on left axis) and corresponding deflection parameter (blue on right axis) versus undulator gap deduced from magnetic measurements at room temperature.

The peak field at gaps smaller than 5 mm have been estimated by extrapolating from the measured field. B_{peak} versus g can be expressed as:

$$B_{peak} = 3.37 \exp\left[-4.34\frac{g}{\lambda_u} + 1.12\left(\frac{g}{\lambda_u}\right)^2\right] \tag{7.1}$$

where the fit has been done for gaps 5 mm to 10 mm.

7.1.5 Electron beam diagnostics

Figure 7.11 presents the electron beam diagnostics installed along the transport line [295]:

- Electron spectrometer (black)

- Imager 1 installed 64 cm from the last QUAPEVA. (blue)
- Integrated current transformer (ICT1) placed after imager 1 (grey)
- Imager 2 placed in the middle of the chicane (blue)
- Imager 4 placed after the chicane and in between the electro-magnet quadrupoles (blue)
- ICT2 placed after the undulator (grey)
- Imager 5 placed after the ICT2 (blue)
- Imager 6 placed after the dipole dump (blue)

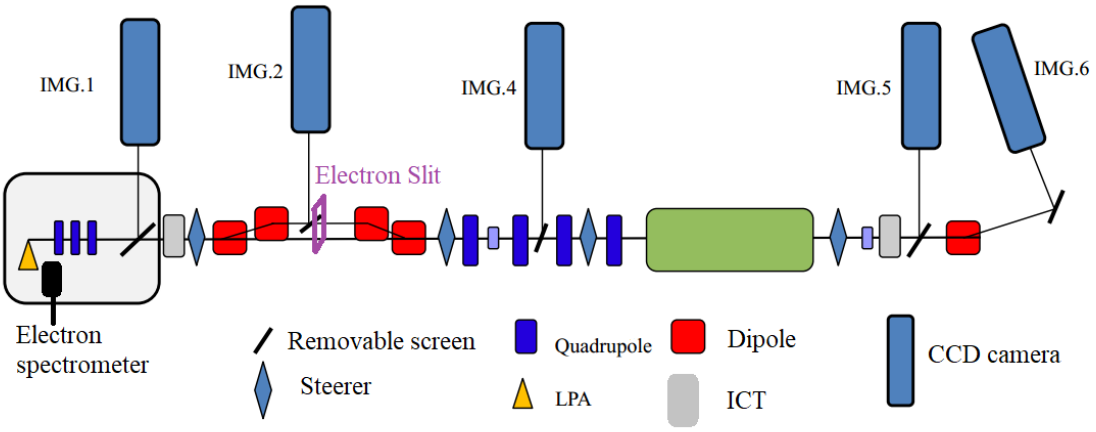

Figure 7.11: Different electron beam diagnostics installed along the COXINEL beam line [295].

7.1.5.1 Electron spectrometer

An electron spectrometer installed in the laser chamber allows us to mesure the energy spectrum of the electron beam immediately after the plasma exit. The spectrometer consists of a removable permanent magnet dipole of 10 cm length and 1.1 T magnetic field. The electrons are dispersed towards a phosphor screen and imaged on a CCD camera, with a spectral resolution of 2.7% at 50 MeV and 3.8% at 280 MeV. A spectrometer scheme is shown in Fig. 7.12.

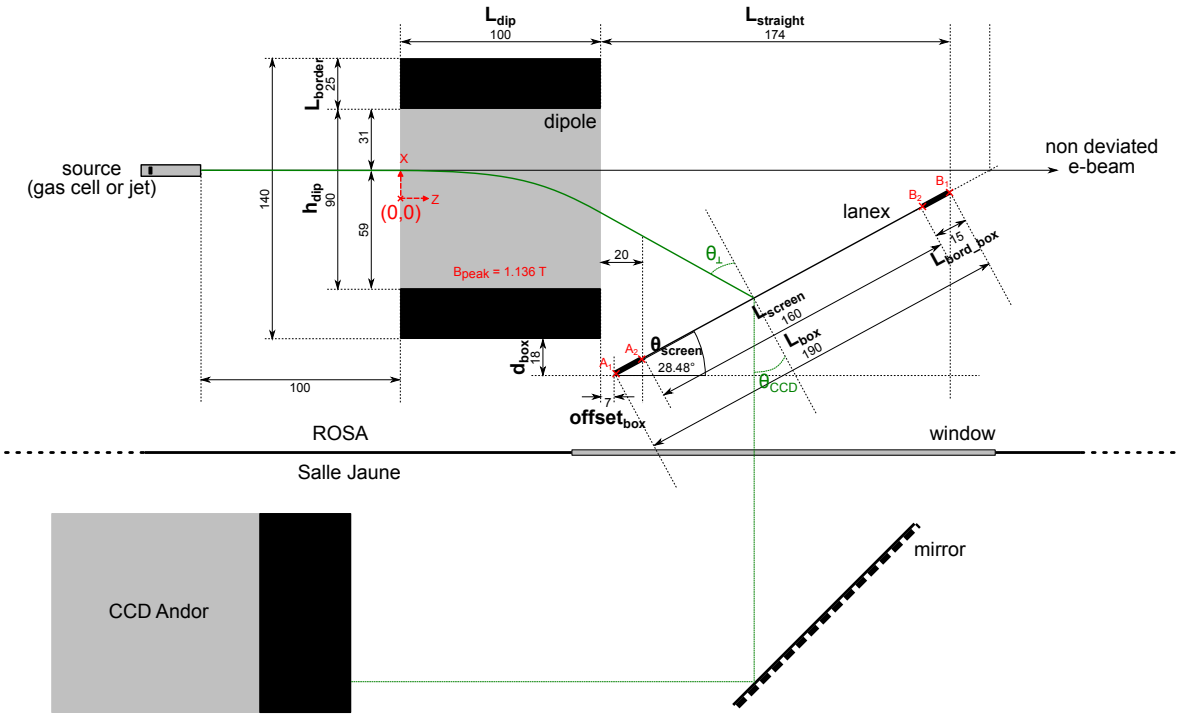

Figure 7.12: Electron spectrometer schematic view.

7.1.5.2 Imagers

Five electron beam imagers installed along the beam line consist of a scintillating screen mounted on a motorized stage for insertion on the electron beam axis, in combination with an imaging optics and a CCD camera. The screens are back-side imaged. On the first imager (LPA exit), a LANEX type screen protected by a 75 µm black ionized Aluminium foil is used together with a pair of simple focusing lenses and a 12 bit Basler scA640 CCD camera. The magnification ratio (0.12 and 0.17 resp. in the horizontal and vertical plane) together with the screen lead to a resolution of about 150 µm. For the downstream imagers, a LANEX or YAG:Ce screen protected by a 25 µm black ionized Aluminium foil can be inserted while the imaging optics is a commercial objective (f/2 100 mm focal length ZEISS MACRO or f/2.8 105 mm focal length SIGMA MACRO) and the camera is a 16 bit ORCA Flash 4.0 cMOS from Hamamatsu. The magnification ratio (0.35 and 0.5 resp. in the horizontal and vertical plane) together with the screen grain size allow to reach a resolution of 100 µm using a LANEX and of 30 µm using a YAG:Ce.

7.1.5.3 Integrated current transformers

Integrated Current Transformers (ICTs) are based on electronics which integrate the charge over a time window of hundreds of microseconds. ICTs are not well adapted to the LPA strong electromagnetic pulse environment, low-charge beams and single-shot requirement. Nevertheless, ICTs from Bergoz (http://www.bergoz.com/en) were implemented on LPAs and compared with LANEX screen measurements. For beam charge measurements, the beam line is equipped with two turbo Integrating Current Transformers (ICTs) from Bergoz (specified for 10 fC noise) calibrated with the SOLEIL linac, one after the electron generation chamber and one at the undulator exit.

7.2 Electron beam characterization

In this section, the electron beam measurements are presented.

7.2.1 Electron beam energy distribution

Figure 7.13 presents typical electron beam distribution single shot measurements observed on the spectrometer CCD camera. The energy spread is quite broad and spans over a range between 50 MeV up to 200 MeV, much larger than the one presented in the baseline reference case.

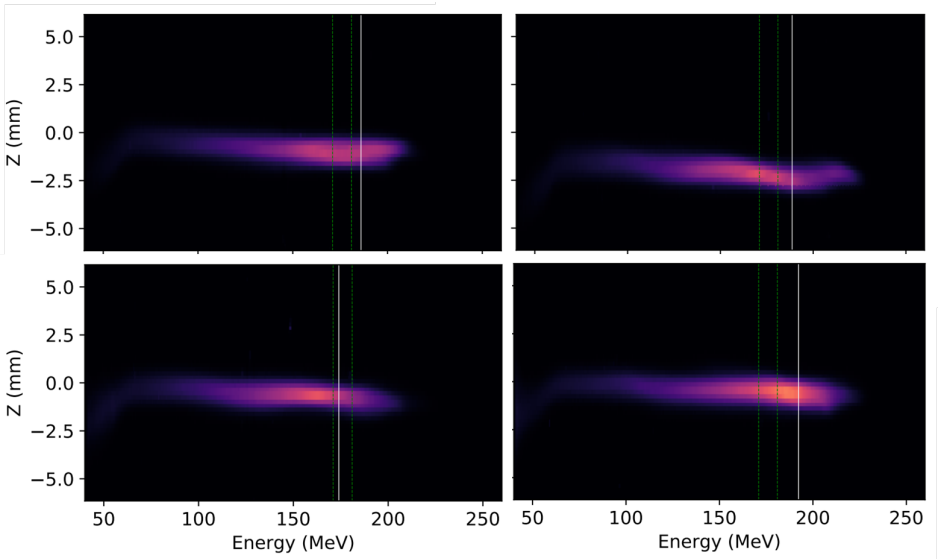

Figure 7.13: Single shot measurements of the electron beam distribution using the electron spectrometer. Data taken in RUN4.

Figure 7.14 presents the energy distribution or charge density for all the shots taken during RUN4. One can see that the beam is dominated by shot-to-shot fluctuations, where the electron energy distribution highly depends on the daily performance of the laser and the gas jet.

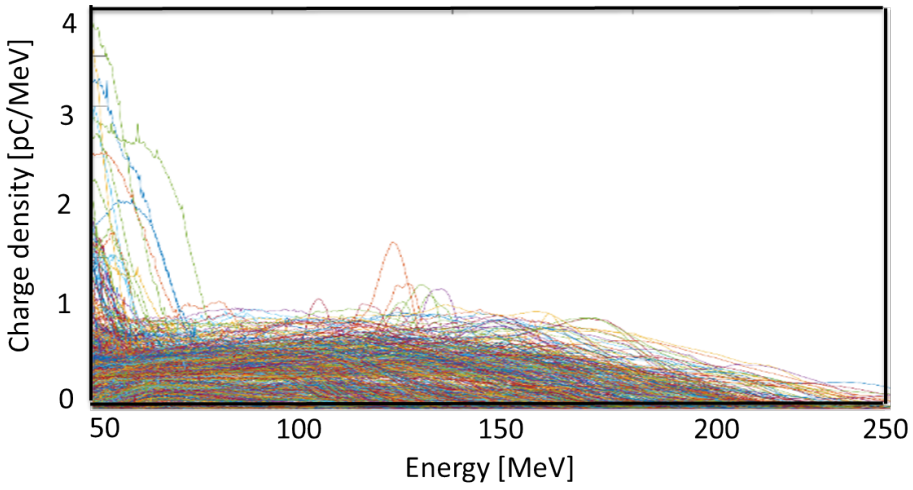

Figure 7.14: Single shot measurements of the electron beam distribution using the electron spectrometer taken in RUN4 for all the days.

Figure 7.15 shows the electron beam charge distribution averaged over 20 shots for RUN4 (a) and RUN5 (b), on the days that we did undulator radiation measurements. In RUN5, the electron beam operation energy has been reduced to 161 MeV (down from 176 MeV) to attain a higher charge density.

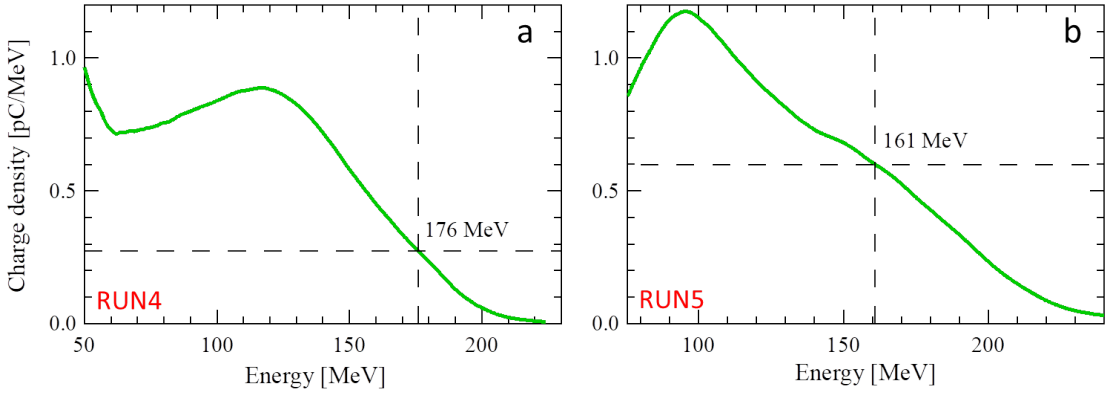

Figure 7.15: Charge density distribution of the electron beam averaged over 20 measurements for RUN4 (a) and RUN5 (b) on the days where undulator radiation was measured.

7.2.2 Electron beam charge

The beam charge can be measured using the electron spectrometer. The CCD camera is calibrated and a conversion is applied on the counts to deduce the charge. Figure 7.16 presents the total beam charge (a) and slice charge (b) during RUN4, where it fluctuates from day to day depending on the laser performance. An average charge of 150±95 pC and a slice charge of 0.3±1 pC are measured.

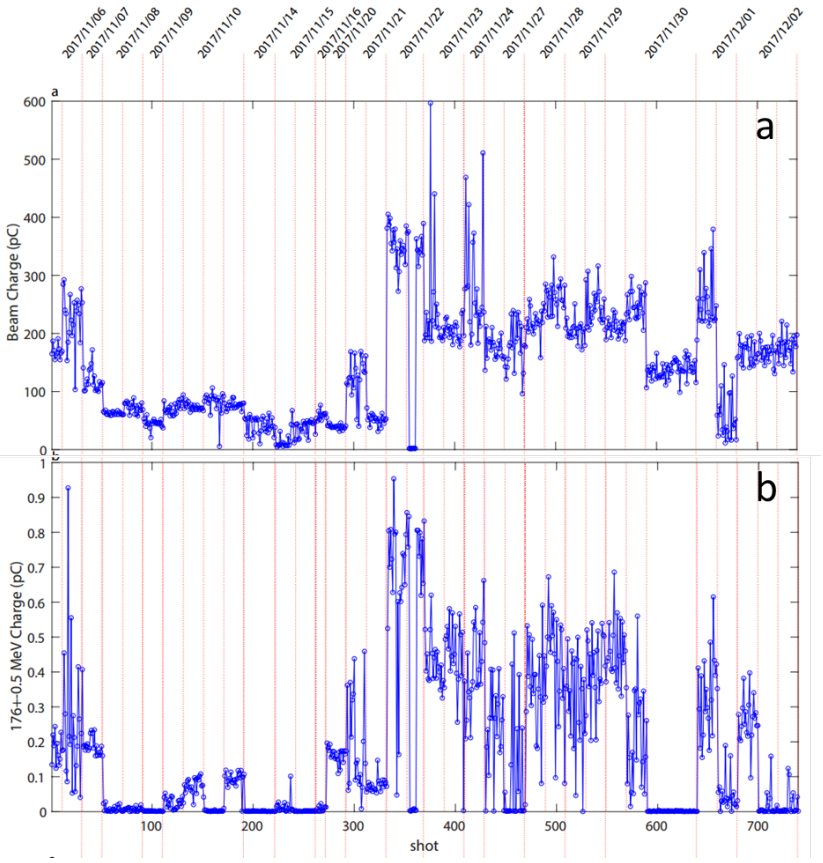

Figure 7.16: Electron beam charge measured on the electron spectrometer (a) and the charge for an energy slice of 1 MeV for all the measured shots during RUN4.

Figure 7.17 presents the total beam charge measured using ICT1 and ICT2 during RUN4, where an average charge of 33±25 pC and 3±4 pC are measured.

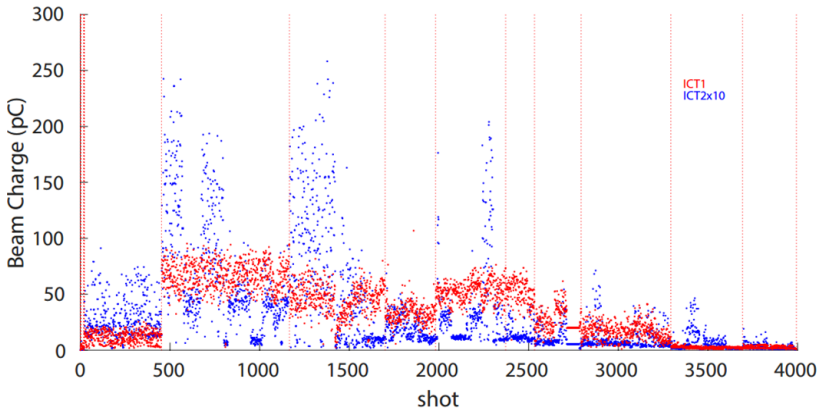

Figure 7.17: Electron beam charge measured on ICT1 (red) and ICT2 x 20 (blue) during RUN4.

7.2.3 Electron beam divergence and pointing

Using the geometry of the electron spectrometer (see Fig. 7.18), the initial vertical divergence σ'_{z0} can be calculated from the measured vertical beam size at the CCD image divided by the distance from the source to the spectrometer. Figures 7.18-a and b display the vertical divergence averaged over 20 shots during RUN4 and RUN5, respectively, on the days of undulator radiation measurements. The rms vertical divergence is calculated to ~2 mrad for both RUNs.

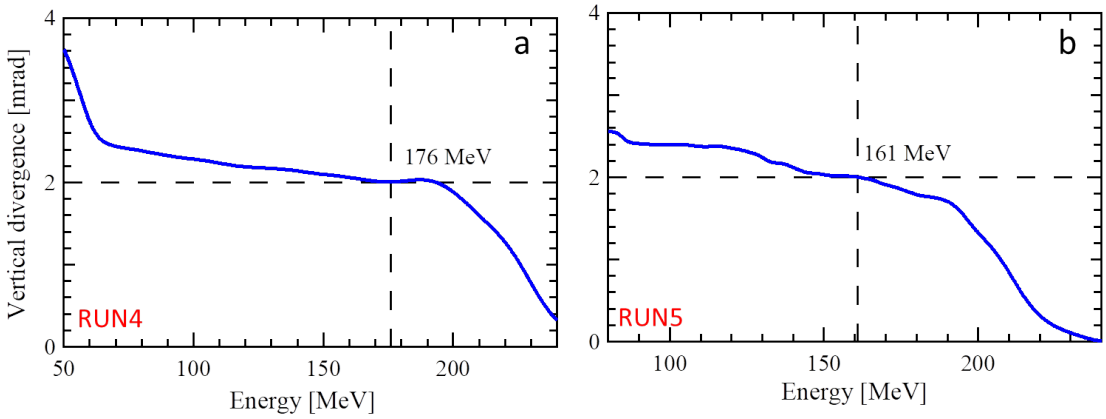

Figure 7.18: Vertical divergence measured during RUN4 (a) and RUN5(b).

Fig. 7.19 presents typical measurements of the transverse shape of the electron beam on the first imager without inserting the QUAPEVAs, where the beam pointing stability is quite poor. The electron beam size can give a clue about the initial divergence. For example by measuring the ratio r expressed as:

$$r = \frac{\sigma_z}{\sigma_x} = \frac{\sigma'_{z0}}{\sigma'_{x0}} \tag{7.2}$$

for a given energy slice, one is able to deduce the horizontal divergence by using the extracted vertical divergence from the electron spectrometer measurements.

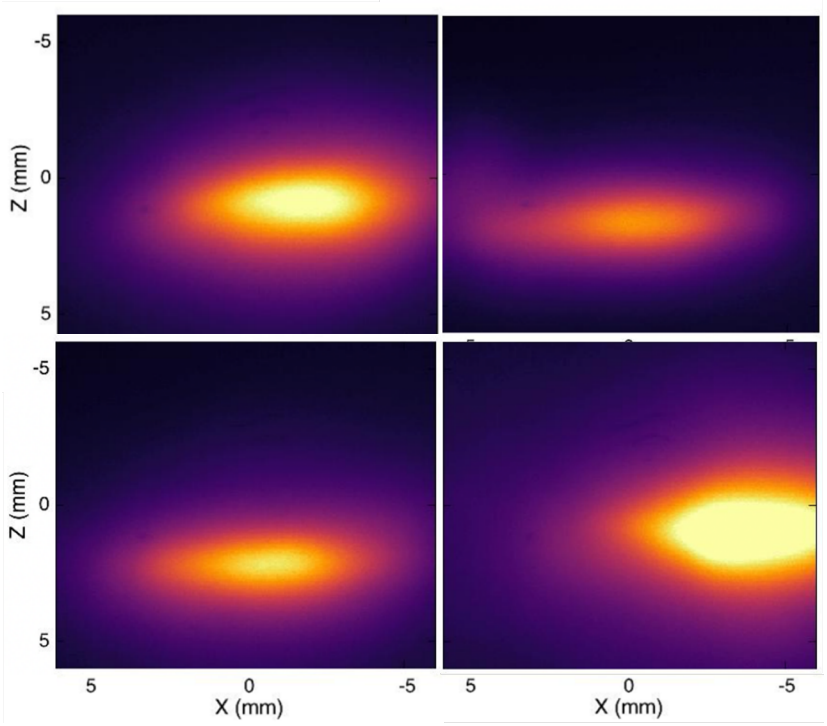

Figure 7.19: Electron beam transverse shape measured with imager 1.

Figure 7.20-a presents the measured horizontal and vertical divergence that are found to be 2.6±0.4 mrad and 2±0.3 mrad, respectively. The electron beam pointing is calculated as well to be 2875 2.9±1.4 mrad and 2.5±0.7 mrad in horizontal and vertical planes, respectively (as shown in Figure 7.20-b).

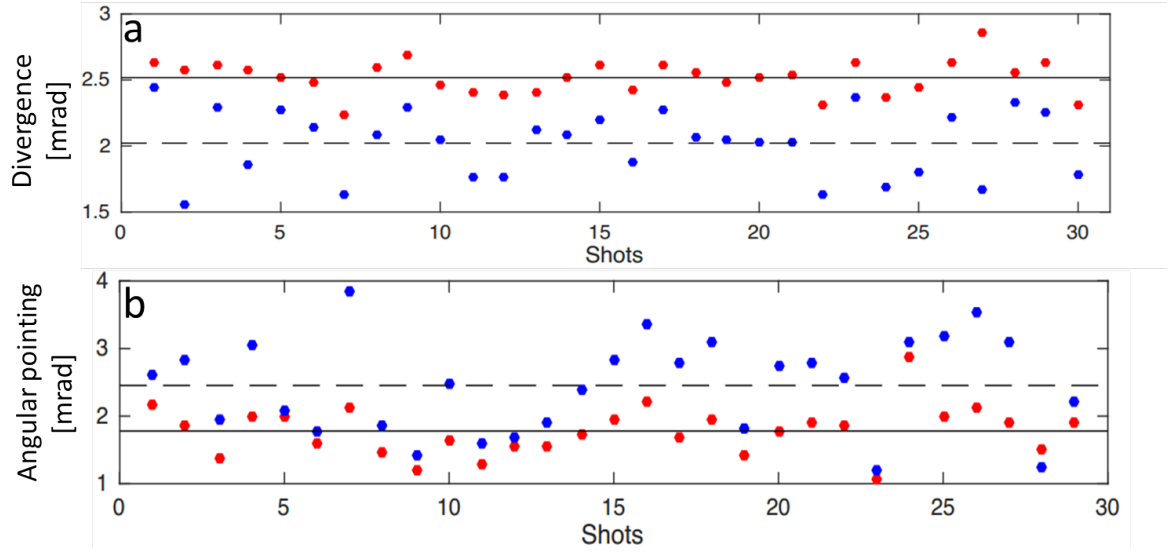

Figure 7.20: Measured electron beam divergence in horizontal (red) and vertical (blue) (a) alongside the beam pointing (b) during RUN4.

7.2.4 Beam pointing alignment compensation

The beam pointing alignment compensation (BPAC) method consists in compensating the initial pointing of the electron beam as well as the possible misalignments of the three QUAPEVAs with respect to the transport line axis, by displacing the magnetic centers of the QUAPEVAs thanks to the translation tables. To apply this method, it is necessary to calculate the response matrix A, linking the position X and the dispersion D_X of the beam to a transverse displacement of the QUAPEVAs $\Delta\vec{X}_{quap}$:

$$\begin{pmatrix} X \\ D_X \end{pmatrix} = A\Delta\vec{X}_{quap} \tag{7.3}$$

After the determination of the response matrix, one can invert Eq. (7.3) to calculate the translation of the QUAPEVAs needed to correct the position and dispersion of the beam seperately:

$$\Delta\vec{X}_{quap} = A^{-1}\begin{pmatrix} X \\ D_X \end{pmatrix} \tag{7.4}$$

During the COXINEL run, the electron beam position and dispersion are corrected by observing the beam profile along the beam line with slightly tuned optics to focus the electron beam at a specific screen. According to these measurements, the values of the necessary corrections are estimated by calculating the response matrix, and the translations are then applied to the QUAPEVAs.

7.2.4.1 BPAC example

The first BPAC is done on IMAGER 2 located at the center of the chicane. Figure 7.21-a illustrates a correction of position and vertical dispersion. In this example the initial beam **I** is dispersed in both planes. A vertical translation is applied to the QUAPEVAs resulting in beam **II**, where it is horizontally flat indicating that the beam vertical dispersion is quite null.

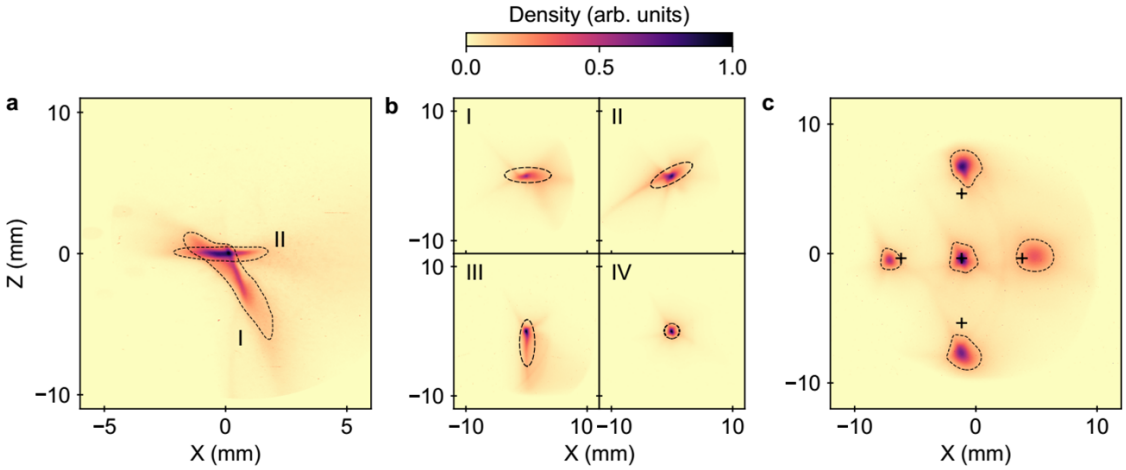

Figure 7.21: Super-imposed images with the appropriate adjustment of the QUAPEVAs magnetic axis. (a) Case of screen in the middle of the chicane where the beam is horizontally dispersed, correction of the vertical dispersion (from **I** to **II**) (b) Screen located at the undulator entrance: initial beam **I**, with artificial vertical dispersion introduced **II**, with horizontal dispersion corrected **III**, with artificial vertical dispersion removed **IV**. (c) Beam experimental transverse position control with respect to expected displacements from the model (black crosses).

The second beam correction is done on IMAGER 4 placed in the middle of the second set of quadrupoles, between the chicane and undulator (see Fig. 7.21-b). The initial beam arriving on

the screen is dispersed all around the center. An artificial vertical dispersion is added to tilt the beam along the *s* axis and arrive to beam **II**. This tilt indicates that there is a correlation between the virtual dispersion and the original one, which implies that the beam has horizontal dispersion. Beam **III** displays the beam after correction of the horizontal dispersion, where the beam exhibits a vertical flat shape. Finally the artificial vertical dispersion is removed to achieve the well focused round beam **IV**. Figure 7.21 compares the applied position corrections of the dispersion-free electron beam from the model to the experimental measurements. BPAC enables to control the electron beam position and dispersion just at the exit of the QUAPEVA all along the downstream line even in presence of electron pointing and residual equipment misalignment.

7.2.5 Quadrupoles gradient variation

The combination of both the QUAPEVAs and the quadrupoles enables to focus different energies at the undulator center by varying the gradient. This method allows one to select a specific energy while retaining all the adjustments previously made to correct the focusing defects and without having to re-optimize the process for generating the electrons. Figure 7.22 presents the numerical simulations as well as the experimental transversal profiles measured on IMG5 while varying the gradient. The relative change of the QUAPEVAs and quadrupoles strength corresponds to the same change in electron beam energy.

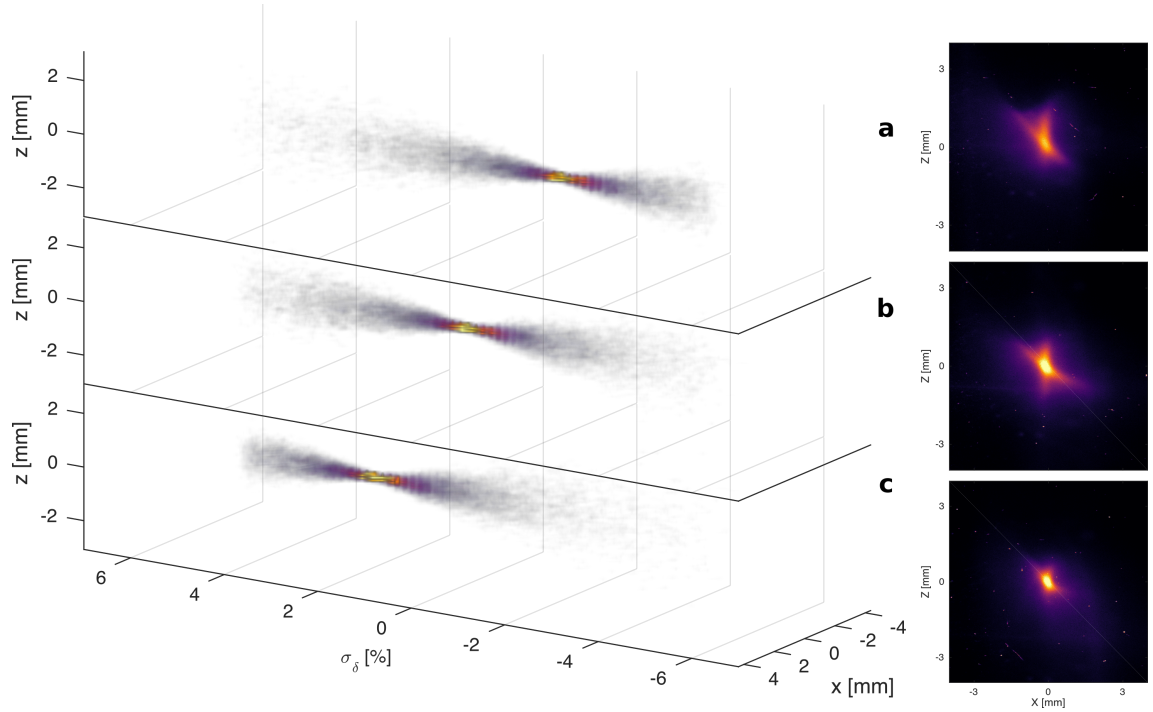

Figure 7.22: 6D electron beam phase space modeled as the gradient of the quadrupoles is varied. **(a)** gradients changed by a relative value of -2%, **(b)** nominal gradients, **(c)** gradients changed by a relative value of 2%. Measured electron beam shape from RUN4. Figure from [128].

7.3 Electron beam transport

Fig. 7.23 illustrates the electron beam transverse shape measured with the different imagers during transport. The electron beam measured on imager 1 (after the QUAPEVAs) has a cross-shape due to chromatic effects induced by the large energy spread, where the nominal energy is well

focused at the center, the low energies are dispersed vertically and the high energies in the horizontal. At imager 2 (middle of the chicane), the electron beam is dispersed horizontally due to the first two dipoles of the chicane. The electron beam measured on imager 4 (before the undulator) and imager 5 (after the undulator) still exhibits a cross-shape due to the large energy spread.

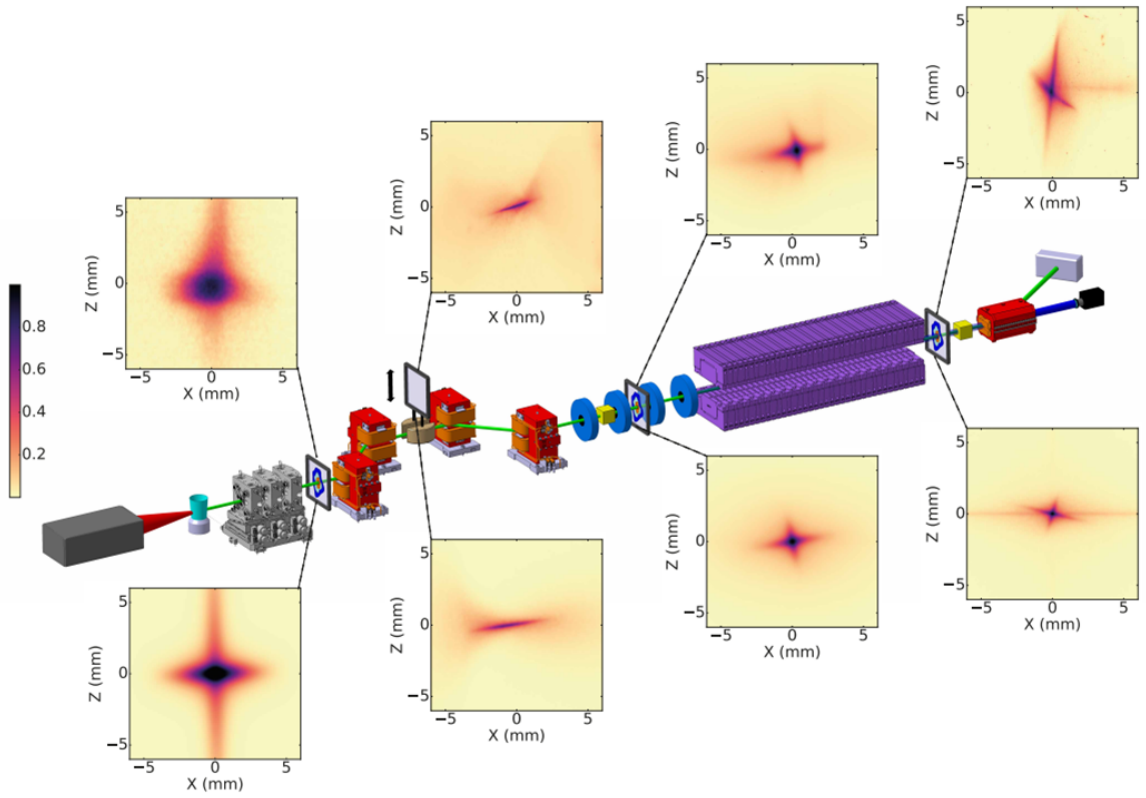

Figure 7.23: Measured (top) and simulated (down) electron beam transverse profiles. Figure from [284].

The initial beam parameters measured (energy distribution and divergence) are inserted in the beam optics code with a normalized emittance of 1 mm.mrad, and the particles are tracked along the transport line. The beam tracking for measured electron beam distribution has been benchmarked with ELEGANT code [296]. Figure 7.23 compares the simulations to the measurements at COXINEL where they show a very good agreement.

To characterize the undulator radiation, the large energy spread reaching the undulator has to be reduced. The adjustable slit introduced in the middle of the chicane helps us to control the range of energies arriving at the undulator (results are presented in chapter 9). Figure 7.24 shows the beta Twiss parameter and dispersion along the beam line for the two Runs using the measured electron parameters.

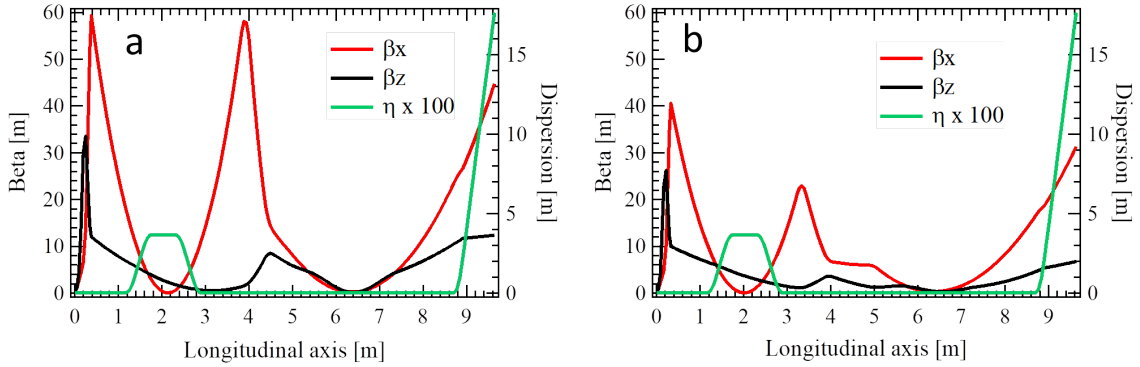

Figure 7.24: Horizontal (red) and vertical (black) beta Twiss parameter along the line and horizontal dispersion (green). (a) Run4 176 MeV, (b) Run5 161 MeV.

Figure 7.25 presents the energy distribution at the center of the undulator for different electron slit cases. The energy spread is reduced as the slit is closes (see Table 7.7 for values).

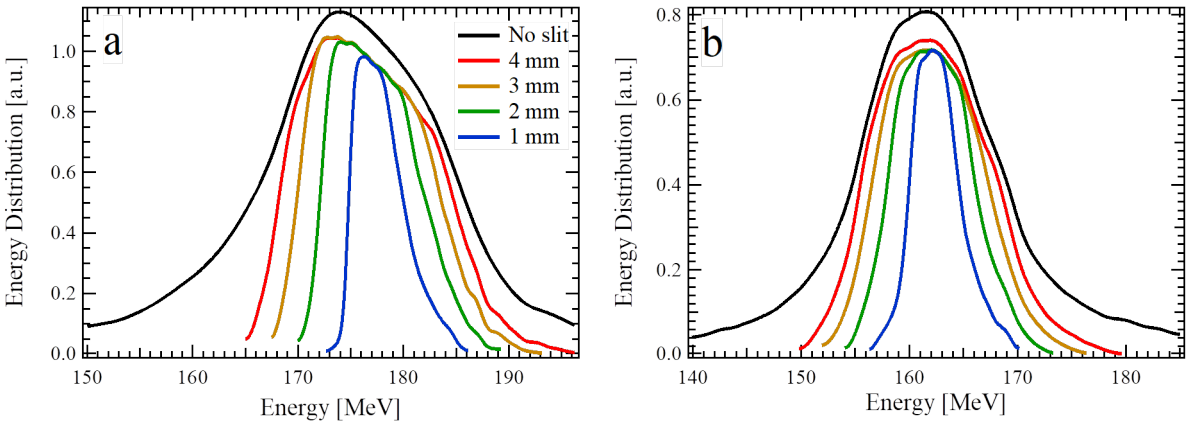

Figure 7.25: Energy distribution at the center of the undulator for different slit widths. (a) RUN4 with energy centered at 176 MeV, (b) RUN5 with energy centered at 161 MeV.

Table 7.7 shows the electron beam parameters computed at the center of the undulator using the distributions and vertical divergences presented in Figs. 7.18 and 7.15. The energy distributions of Fig. 7.25 are fitted with a Gaussian to determine the mean energy and energy spread rms.

	Slit mm	E MeV	σ_γ %	σ_x mm	σ_z mm	σ'_x mrad	σ'_z mrad	σ_l µm	Q transmission %
Run4	No Slit	175	3.7	1.01	0.46	0.63	1.08	200	11.4
	4	177	3.3	0.88	0.30	0.61	0.98	86	5.4
	3	177	2.9	0.81	0.27	0.59	0.89	72	4.4
	2	177	2.3	0.72	0.23	0.55	0.75	55	3.1
	1	178	1.2	0.59	0.21	0.46	0.55	35	1.7
Run5	No Slit	168	4.7	1.02	0.33	0.51	1.54	262	18.1
	4	162	3.9	0.92	0.12	0.55	1.51	85	9.8
	3	162	3.3	0.86	0.12	0.54	1.45	70	8.4
	2	162	2.5	0.80	0.12	0.54	1.35	56	6.4
	1	162	1.1	0.73	0.14	0.51	1.14	40	3.5

Table 7.7: Electron beam characteristics for different electron slit width at the center of the undulator. The charge at the undulator center deduced from the transport for different chicane slit widths.

7.3.1 FEL calculation with the real electron beam

Table 7.8 presents the average electron beam parameters measured compared to the baseline reference case. The real beam quality is quite poor compared to the baseline reference case.

Parameters	**RUN4**	**RUN5**	**Baseline case**	**Unit**
Energy	176	161	200	MeV
Charge	50	-	200	pC
ε_N	1	1	1	mm.mrad
σ_γ	> 10	> 10	1	%
σ'_x	3	3	1	mrad
σ'_z	2	2	1	mrad
Slice charge	3	-	34	pC

Table 7.8: Beam parameters at the generation point in the gas jet. Divergence, beam size and beam length in rms.

The FEL calculations using Ming Xi equations [154] showed that the FEL amplification is not possible with such parameters. The charge per energy slice is quite low reducing the current and the Pierce parameter. More importantly, the slice divergence and beam size are quite larger than the ones presented in the baseline reference case (chapter 3) causing the main setback of the FEL performance.

7.3.2 Conclusion

The electron beam quality at the source is quite different from the baseline reference case presented in chapter 3, where the divergence and energy spread are larger by a factor of ~5. A beam pointing alignment compensation method enabled a full control the electron beam from source to the undulator, by correcting the position and dispersion of the beam. A slit is introduced in the middle of the chicane to select a smaller range of energy, enabling to characterize undulator radiation and achieve a rather small spectral bandwidth (to be discussed in the next chapter). Concerning the FEL, the slice charge is quite low with large beam size and divergence at the center of the undulator preventing any amplification.

Chapter 8

COXINEL Undulator Radiation

As discussed in chapter 3, proof-of-principle LPA based undulator emission does not yet exhibit the full specific radiation properties due to the large energy spread, divergence and shot-to-shot fluctuations. The first undulator radiation observation was during RUN3 with a CCD camera. In RUN4 and RUN5, undulator radiation has been observed using a UV spectrometer. In this chapter, I present some brief results of RUN3, and focus mainly on the new results that we acquired on RUN4 and RUN5.

8.1 Description of the photon beam diagnostic line

During RUN3, a CCD camera is placed at the end of the transport line to measure the photon transverse shape. In RUN4 and RUN5, a spectrometer composed of a grating and a CCD camera has been installed to measure the spatio-spectral distribution.

8.1.1 X-ray CCD camera

The undulator radiation transverse beam shape was imaged with a Princeton Instruments PIXIS XO 2048 B camera, located directly under vacuum at the exit of the beam line, with a 75 mm fused silica biconvex lens (Newport SBX052) in front of it, limiting the detected wavelengths above 150 nm.

8.1.2 Spectrometer

Figure 8.1: iHR 320 horiba spectrometer.

The emitted radiation is measured using a UV imaging spectrometer, shown in Fig. 8.1 and its characteristics are shown in Table 8.1). It consists of an adjustable entrance slit and is equipped

with three gratings (600, 1200, 3600 grooves/mm) and a CCD camera that enables to map the radiation vertical angular-spectral distribution.

Parameter	Value	Unit
Model	Horiba iHR320	
Focal length	320	mm
Aperture	78	mm
Gratings	600 - 1200 - 3600	grooves/mm
Grating size	68 x 68	mm^2
Repeatability	0.075	nm
Slit	0.08 - 2	mm
Magnification	1.1	
Length	417	mm
Width	422	mm
Height	192	mm
Camera Model	SYNAPSE - 354308	
Camera format	1024 x 256	
Camera Pixel size	26	µm
Camera Image area	26.6 x 6.7	mm^2

Table 8.1: Spectromer characteristics. The magnification is from the spectrometer entrance slit to the CCD camera.

The resolution is improved with higher number of grooves/mm but on the expense of the total window acquisition, so the 3600 and 1200 gr/mm gratings have not been used due to the broad-band radiation of COXINEL. Fig. 8.2 presents the spectrometer response, i.e. the 600 gr/mm grating reflectivity and CCD camera quantum efficiency, as a function of the wavelength.

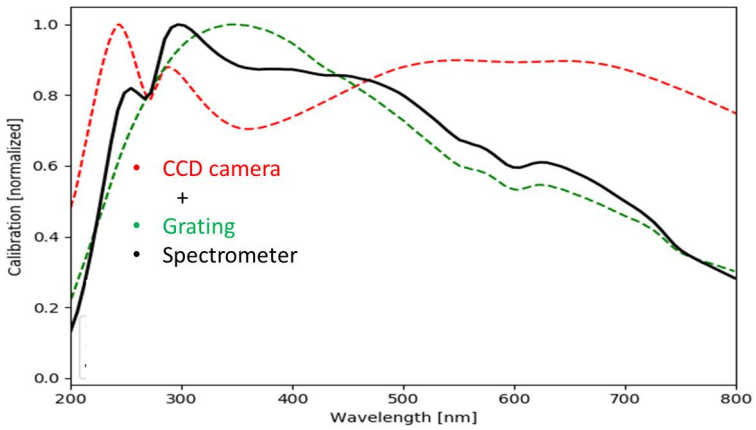

Figure 8.2: Spectrometer response by taking the grating calibration of Horiba plus the CCD camera.

8.1.2.1 Spectrometer resolution

The radiation enters the spectrometer slit and is reflected by a collimating mirror (with ~99% reflectivity) towards the grating where it is diffracted. The grating dispersion equation is expressed as:

$$\sin\alpha + \sin\beta = kn\lambda \tag{8.1}$$

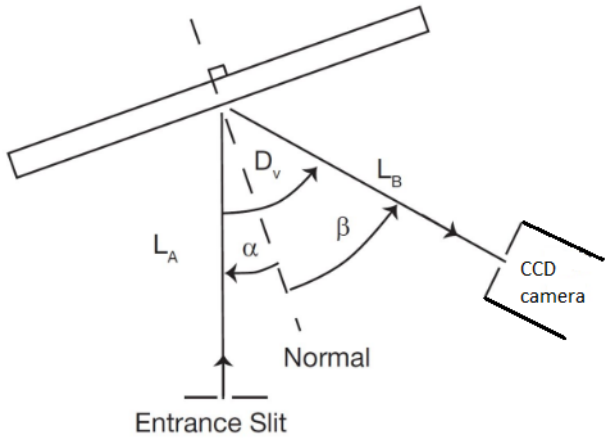

Figure 8.3: Spectrometer configuration.

where α / β is the angle between the incident ray / diffracted ray and the grating normal, k the diffraction order, n the groove density and λ the radiation wavelength (see Fig. 8.3). The location of the entrance slit and the CCD camera are fixed and the grating rotates around a plane through the center of its face to focus different wavelengths at the camera. By replacing the constant deviation angle $D_\upsilon = \beta - \alpha$ in Eq. (8.1), one gets:

$$\begin{cases} \alpha = sin^{-1}\left[\frac{nk\lambda}{2cosD_\upsilon/2}\right] - \frac{D_\upsilon}{2} \\ \beta = sin^{-1}\left[\frac{nk\lambda}{2cosD_\upsilon/2}\right] + \frac{D_\upsilon}{2} \end{cases} \tag{8.2}$$

In general, most imaging spectrometers are not used at the limit of their resolution so the influence of the entrance slit dominates the line profile. The theoretical bandpass $\Delta\lambda^{th}$ is expressed as:

$$\Delta\lambda^{th} = w_s \frac{d\lambda}{dx} = w_s 10^6 \frac{\cos\beta}{knL_B} \quad [\text{nm/mm}] \tag{8.3}$$

where w_s is the spectrometer entrance slit, $\frac{d\lambda}{dx}$ the linear dispersion and L_B is the distance from the grating to the CCD camera (see Fig. 8.3).

Two lasers were used: a green one of wavelength 532 nm (CPS532-C2 Thorlabs) and a red one of wavelength 635 nm (He-Ne NEC corporation) to measure the resolution (full width half maximum) of the spectra captured by the camera versus slit width. Fig. 8.4-a,b show the measured resolution of the two lasers compared with the theory presented in Eq. (8.3).

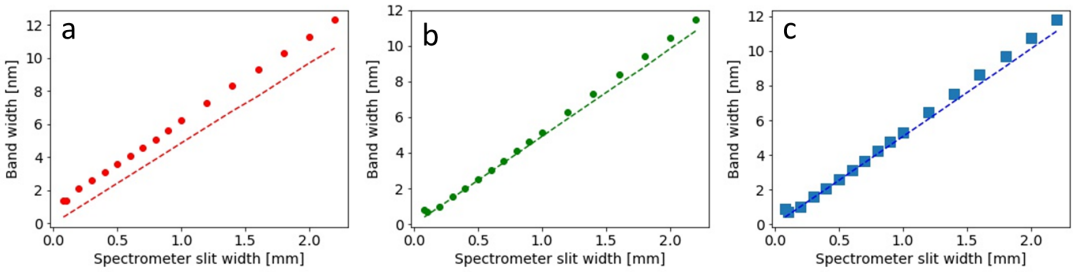

Figure 8.4: (○) Experimental data, (- -) theoretical data and (■) predicted data of the bandwidth of the laser measured at the CCD camera. (a): green laser, (b): red laser, (c) 220 nm. L_B = 40 cm and D_υ = 10.63°.

The slit resolution for 220 nm wavelength is presented in Fig. 8.4-c. The predicted resolution

at 220 nm $\Delta\lambda_{220}^{pred}$ is attained by:

$$\Delta\lambda_{220}^{pred} = \Delta\lambda_{532}^{cal}\frac{\Delta\lambda_{220}^{th}}{\Delta\lambda_{532}^{th}} \tag{8.4}$$

where 'cal' is the calculated, 'th' the theoretical, $\Delta\lambda_{220}$ the 220 nm resolution and $\Delta\lambda_{532}$ the 532 nm resolution. With the predicted data at wavelength 220 nm, one is able now to determine the real bandwidth $\Delta\lambda_{real}$ of the spectra measured by the camera using a quadratic substraction:

$$\Delta\lambda_{real} = \sqrt{\Delta\lambda_{meas}^2 - (\Delta\lambda_{220}^{pred})^2} \tag{8.5}$$

where $\Delta\lambda_{meas}$ is the measured bandwidth.

8.1.3 Optical lens

The radiation is focused at the entrance slit of the spectrometer with a CaF_2 lens (eSource Optics CF5025LCX) with a schematic view presented in Fig. 8.5.

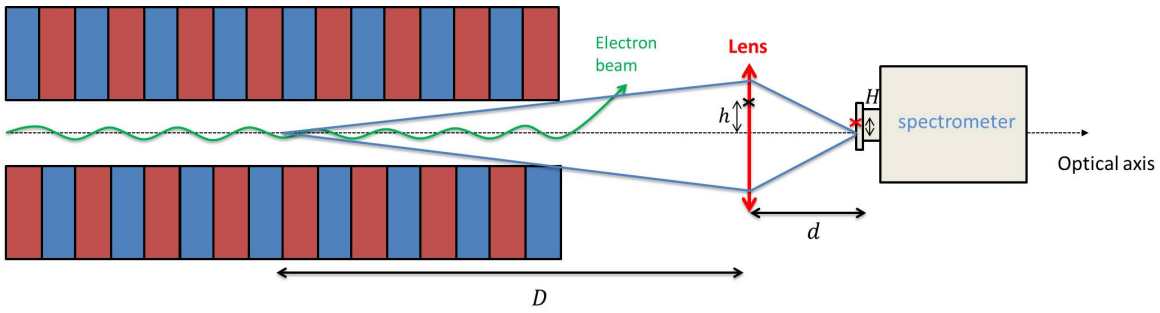

Figure 8.5: Undulator radiation imaging setup. The undulator radiation is focused at the entrance slit of the spectrometer using a lens, located at a distance D from the undulator center and d from the spectrometer with a vertical offset h with respect to the optical axis. H the vertical offset of the spectrometer with respect to the optical axis.

Due to the chromatic dispersion of the CaF_2 [297], the conversion from observation angle to position on the CCD of the spectrometer is not trivial and includes chromatic aberration effect. Using Table 8.2 the focal length can be determined:

$$\begin{cases} n(\lambda)^2 - 1 = \frac{B_1\lambda^2}{\lambda^2 - C_1^2} + \frac{B_2\lambda^2}{\lambda^2 - C_2^2} + \frac{B_3\lambda^2}{\lambda^2 - C_3^2} \\ f(\lambda) = \frac{R}{n(\lambda)-1} \end{cases}$$

with R = 108.5 mm the radius of curvature of the lens, n the refractive index of the CaF_2 and $B_{1,2,3}, C_{1,2,3}$ the Sellmeier coefficients (see Table 8.2 for values).

Table 8.2: Sellmeir coefficients of CaF_2 [298].

B_1	0.5675888
B_2	0.4710914
B_3	3.8484723
C_1	0.050263605 µm
C_2	0.1003909 µm
C_3	34.649040 µm

Fig. 8.6 shows the focal length $f(\lambda)$ of the lens as a function of the wavelength, where it varies by 2 cm from 200 nm to 300 nm.

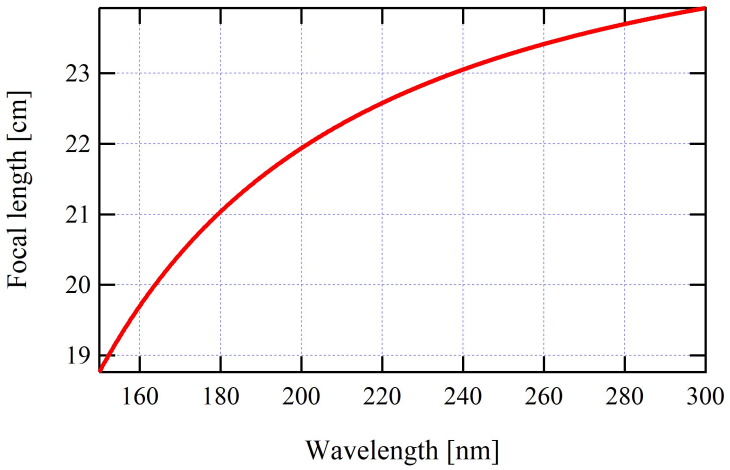

Figure 8.6: The focal length of the CaF_2 lens versus wavelength.

One can use a geometric optics approach to apply the chromatic effects of the lens considering the far-field radiation. The radiation emitted by the electrons impinges the lens at a position:

$$z_0 = \theta_0 D + h$$

with θ_0 being the angle of the radiation and h the vertical offset of the lens w.r.t. the optical axis (see Fig. 8.5). A matrix response M, to convert the radiation at the center of the undulator to the spectrometer CCD camera, can be expressed as:

$$M = \begin{pmatrix} 1 & d \\ 0 & 1 \end{pmatrix} \cdot \begin{pmatrix} 1 & 0 \\ -\frac{1}{f(\lambda)} & 1 \end{pmatrix} \cdot \begin{pmatrix} z_0 \\ \theta_0 \end{pmatrix}, \tag{8.6}$$

where d is the distance between the lens and the entrance slit of the spectrometer.

Taking into account the spectrometer magnification G, the vertical displacement z_c observed on the CCD camera is expressed as:

$$z_c = G \times \left[(D_{lens}\theta_0 + h) \cdot \left(1 - \frac{d}{f(\lambda)}\right) + \theta_0 d \right] + H, \tag{8.7}$$

with H the vertical offset of the spectrometer CCD.

8.1.4 Bandpass filters

To study the spectral content of the synchrotron radiation pattern, band pass filters can be inserted on the light path just before the CCD camera or spectrometer. The filters characteristics are given in Fig. 8.7.

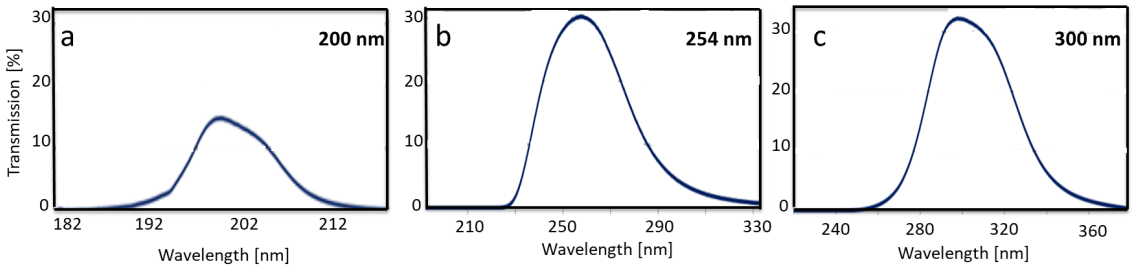

Figure 8.7: Transmission curves of the optical bandpass filters purchased from Edmund optics. (a) centered at 200 nm with a bandwidth of 10nm, (b) centered at 254 nm with a bandwidth of 40 nm, (c) centered at 300 nm with a bandwidth of 40 nm.

8.2 Photon beam transverse shape measurements

During RUN3 a CCD camera was installed at the end of the beam line as shown in Fig. 8.8. The optical filters can be automatically inserted in the path of the photon beam.

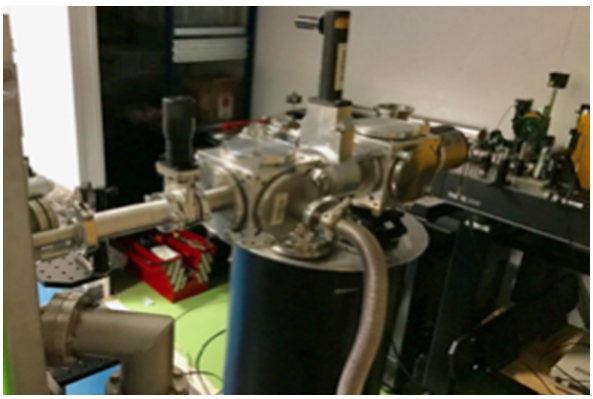

Figure 8.8: CCD camera installed at the end of the beam line with adjustable and removable optical filters.

Figure 8.9-a and b display the measured and simulated transverse profiles of the radiation, respectively, for an undulator gap of 5 mm and without electron slit nor optical filter. Simulations of undulator radiation are performed using LPA test particle beam with a broad energy spectrum, 0.5 mm.mrad emittance, 3 mrad vertical and 5 mrad horizontal divergences. The 12000 test particles are propagated in the undulator with $\Delta s = \lambda_u$=50 steps, using the second order Boris method [299]. Orbits are recorded and integrated to compute the spectral-angular distribution of radiation energy using classical far-field approach (see Fig. 8.9-b). A good agreement is achieved, where they exhbit a similar shape in terms of signal level and beam size.

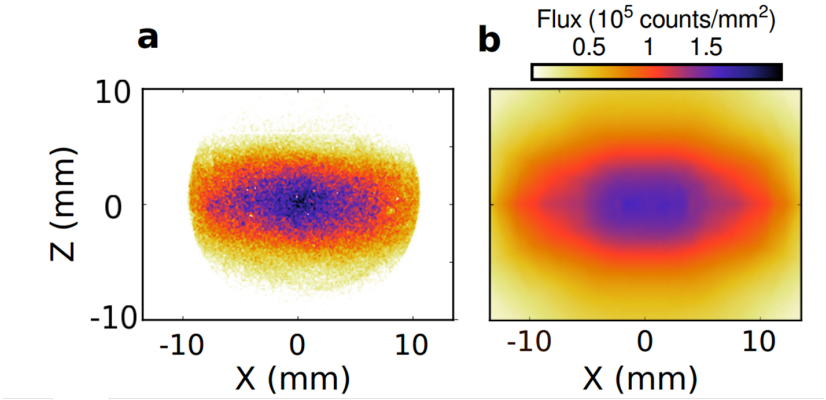

Figure 8.9: Photon transverse shape measured with a CCD camera (a) and computed (b) for an undulator gap of 5 mm, no filter applied and no electron slit.

Figure 8.10 shows measurements of the integrated flux observed on the CCD camera as the undulator gap is varied and by applying the optical filters with characteristics presented in Fig 8.7. The measurements (points) are compared to simulations (curves). The simulated spectra are treated with the optics characteristics, i.e. quantum-efficiency curve of camera, transmission of the band-pass filters to reproduce the measurements. When opening the gap, the signals decrease both for measurements and simulations. In the case when the electron beam is not spectrally filtered (black stars), the camera receives the on-axis and the red-shifted off-axis radiation, associated with the resonant wavelengths and its harmonics. The signal follows qualitatively the dependence of the undulator total power, decreasing as the intensity collected in the detection spectral range. The measurements with the bandpass filters inserted (colored markers) provide a further insight on the spectral behaviour. With the 253 and 300 nm filters, mainly off-axis light is collected exhibiting a similar gap dependance as the total power. Alternatively, with the 200 nm narrow-band filter on-axis (at low gaps) and off-axis radiation is seen, leading to slightly different evolutions versus gap. At 5 mm gap the camera collects the purely on-axis 200 nm light that has a lower flux than the off-axis. At 6 mm gap, the resonant wavelength decreases, and the 200 nm filter band mainly gets the red-shifted off-axis radiation resulting in a maximum on the gap curve. More details about the presented measurements can be found in article [284].

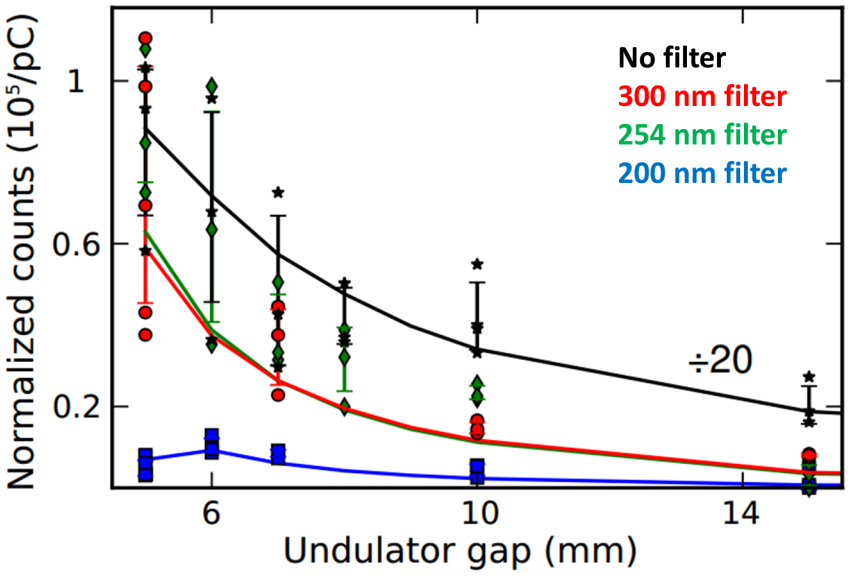

Figure 8.10: Total photon count measured by the camera in case of no filters (black stars) downscaled by a factor of 20, and with the optical filters: 300 nm (red circles), 253 nm(green diamonds), 200 nm (blue squares). Error bars: mean values and deviations of acquired data sets, solid curves: numerical simulation.

8.3 Spatio-spectral flux measurements

Figure 8.11 presents the installation of the spectrometer at the end of the transport line. During RUN4 (a), the spectrometer was operated under nitrogen gas to allow for a better transmission in the 160-190 nm range.

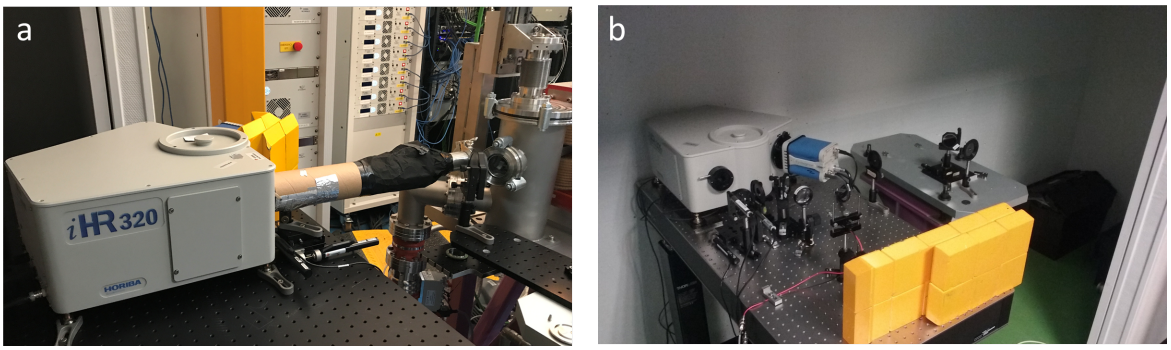

Figure 8.11: Spectrometer installed at 3.3 m from the undulator center during RUN4 (a) and 3.5 m during RUN5 (b).

8.3.1 Measurement analysis

The measurements with the spectrometer are treated in three steps as shown in Fig. 8.12. First, the background noise of the raw data (a) is removed by averaging over 20 rows (10 rows top and 10 row bottom), where there is no signal, and then subtracting it from the image (b). Then a filter is applied to the spectra by taking the median over 3 points that corresponds to 0.3 nm (c). Finally the spectrometer response is added to the spectra (d).

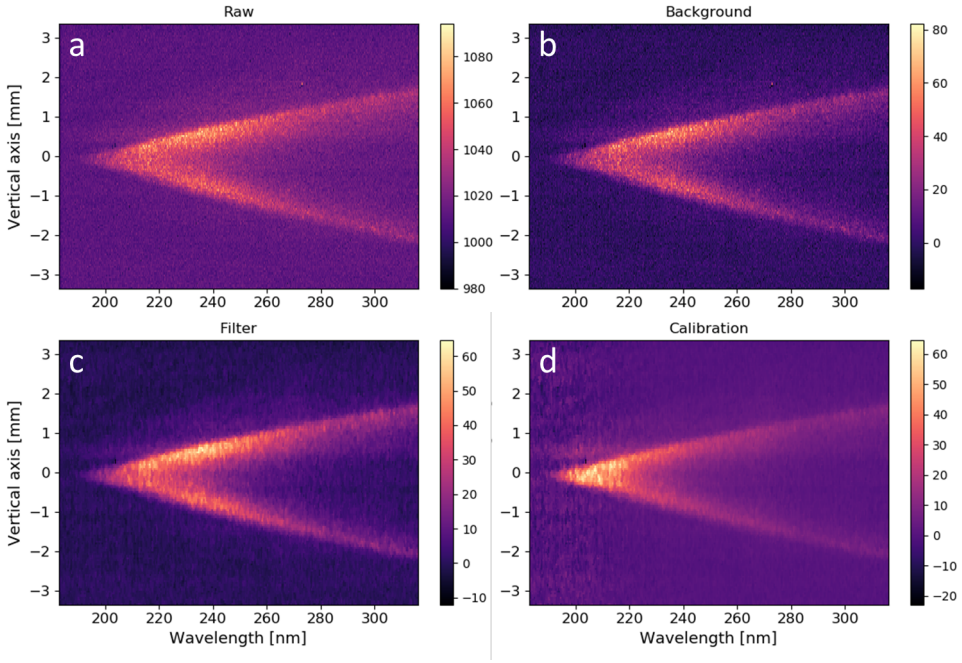

Figure 8.12: Angular spectra data treatment: after removing the high pixels (a), after removing the background noise (b), after applying the median filter (c), after adding the spectrometer response (d). Measurement conditions: 4 mm electron slit, 2.2 mm spectrometer slit and 5 mm undulator gap.

The spectrum shows a similar "moon-shape" pattern, but with a more defined triangular shape, slightly deviating from the usual parabolic behaviour, due to the chromatic effects of the lens.

Figure 8.13-a shows the vertical angular dependance of the spectra with the image cuts at various z for the calibrated image (see Fig. 8.12-d). The on-axis ($z = 0$) spectrum is peaked at the
3070 resonance wavelength of 208 nm with a 13.1% relative FWHM bandwidth, larger than natural homogeneous linewidth of 0.84%, due to the emittance and energy spread contributions. Figure 8.13-b presents the vertical radiation profiles for increasing wavelengths that exhibit first a Gaussian type distribution ($\lambda = 208$ nm) followed by a hole dip in the center ($\lambda = 228$ nm) and a donut shape ($\lambda = 268$ nm and above), as typically observed for undulator radiation.

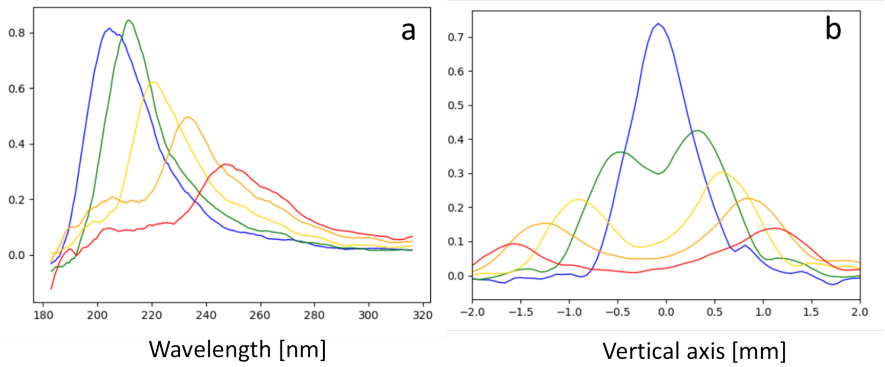

Figure 8.13: (a): Undulator spectra for different vertical positions at $z = 0$ (blue), 0.2 mm (green), 0.4 mm (yellow), 0.6 mm (orange), 0.8 mm (red). (b): Vertical radiation profiles with cuts at different wavelengths λ = 208 nm (blue), 228 nm (green), 248 nm (yellow), 268 nm (orange), 288 nm (red).

8.3.2 Wavelength tunability and stability

The undulator radiation tunability, one of the major undulator properties, has been explored at COXINEL. The radiated wavelength is independently varied either by changing the undulator gap or the electron beam energy. Such an undulator wavelength control corresponds to what is currently achieved with conventional accelerators. Figure 8.14 shows the measured spatio-spectral distribution for different undulator gaps during RUN5. The smaller the gap, the larger the wavelength.

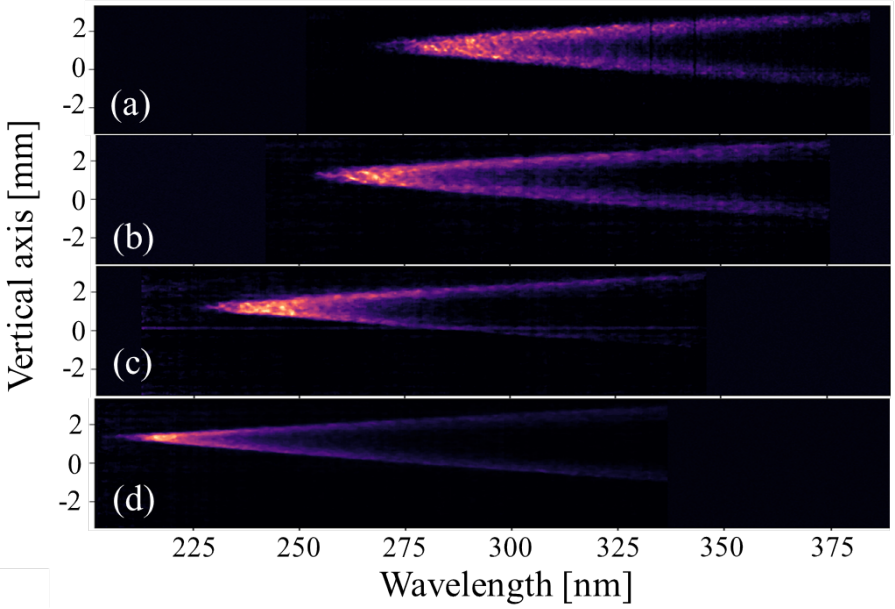

Figure 8.14: Spatio-spectral profile single shots measurements for different undulator gaps: (a) 4.7 mm, (b) 5 mm, (c) 5.5 mm, (d) 6 mm. Shots taken from RUN5 for an electron slit of 3 mm and a spectrometer slit of 2.2 mm.

The resonant wavelength is measured by doing a cut at the center of the moon shape and taking the wavelength at which the intensity is peaked. Figure 8.15 displays the resonant wavelength measured during RUN4 (a) and RUN5 (b) as a function of the undulator gap. The behaviour shows a good agreement with the theoretical curves (dashed) using the measured magnetic field gap dependence especially in the case of RUN4 (blue) and RUN5 (green). In the case of RUN4 (red), the measurements drift from the theoretical value at gaps >6 mm, due to the degradation of the laser at the end of the day that reduced the electron beam energy. In summary, a wavelength tunability around 120 nm is achieved.

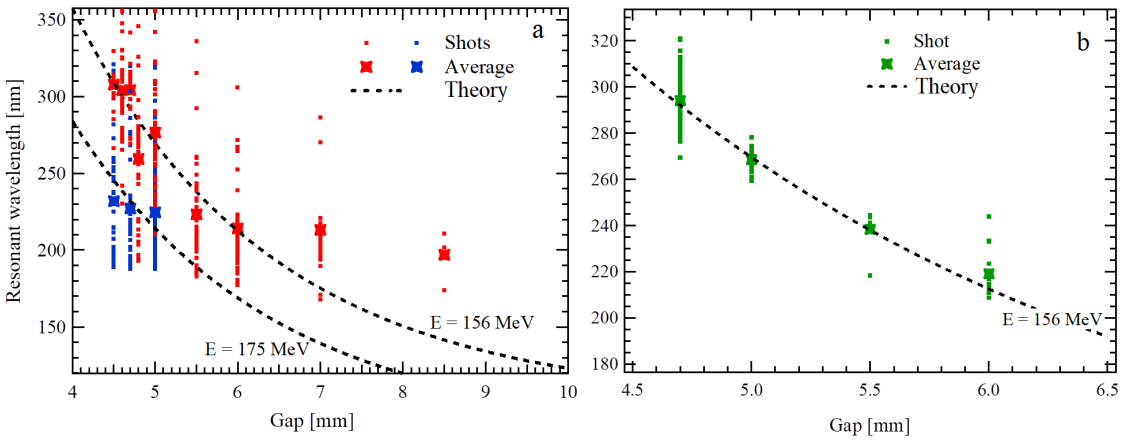

Figure 8.15: Wavelength tunability by undulator gap and energy change. (a) Measurements during RUN4 where the (red) and (blue) correspond to two consecutive days. (b) Measurements during RUN5 (green). (Dashed) theoretical values using the measured field, (star) the average resonance for a given gap.

Table 8.3 presents the resonant wavelength shown in Fig. 8.15 alongside the wavelength stability. The best stability achieved is 1.5% over 31 shots.

	Gap mm	number of shots	Resonant wavelength nm	Standard deviation nm	Stability %
RUN4 Red	4.5	20	307	29	9.4
	4.6	42	304	33	10.8
	4.7	17	304	19	6.3
	4.8	48	259	37	14.3
	5	66	277	39	17.2
	5.5	45	223	32	14.3
	6	50	214	32	14.9
	7	34	213	31	14.6
	8.5	4	197	31	15.7
RUN4 Blue	4.5	45	232	42	18.1
	4.7	46	227	43	18.9
	5	190	225	34	15.1
RUN5 Green	4.7	84	294	11	3.7
	5	31	269	4	1.5
	5.5	6	238	9	3.8
	6	21	219	8	3.7

Table 8.3: Average resonant wavelength and stability for both runs as a function of the gap. The colors correspond to the data shown in Fig. 8.15.

Figure 8.16 displays the undulator resonant wavelength versus time during RUN5 for an undulator gap of 4.7 mm. The 2.4% wavelength stability over 3 hours of operation confirms a good handling and transport of the electron beam. This value is different from the one presented in Table 8.3 (3.7%), because for this calculation, I selected spectra with good moon shape pattern and strong signal. Regarding the previous calculation, I took all the measurements and a lot of them were dominated by the background noise due to the weak signal and thus the resonant wavelength tends to drift more when applying a fit or a smoothing to the spectrum.

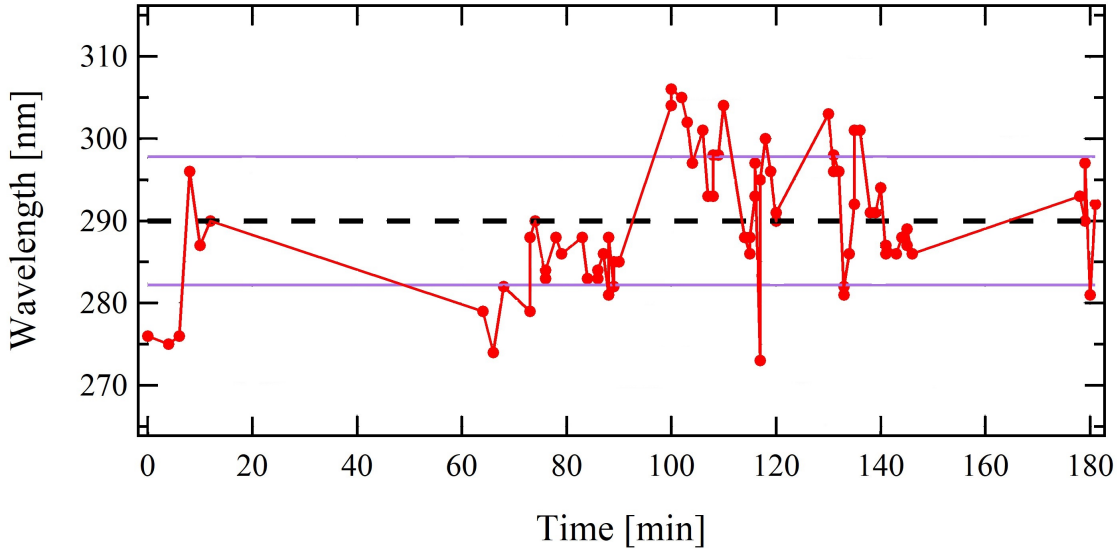

Figure 8.16: Undulator resonant wavelength measured during over 3 hours for an undulator gap of 4.7 mm and different electron slit widths. Average value (dashed), standard deviation (purple).

8.3.3 Electron beam energy

Using the magnetic field dependence on the gap as presented in Eq. (7.1), the electron beam energy is calculated by:

$$E = \frac{1}{2}\sqrt{\frac{\lambda_u}{2\lambda}\left(1 + K_u^2/2\right)} \tag{8.8}$$

Figure 8.17 presents the deduced electron beam energy from the measured spectra. In RUN 4 (a), the average beam energy (red) is found to be 156 MeV with a standard deviation of 12 MeV over 313 shots lower than the operational energy of 176 MeV. This is due to the laser degradation at that given day as a result of mirrors contamination and misalignment of the optical transport of the laser. The day after, the mirrors were cleaned and alignement was corrected resulting in an average energy of 175 MeV with a standard deviation of 13 MeV over 280 shots. In RUN5 (b), the beam was more stable (green), where an average energy of 156 MeV with a standard deviation of 2.5 MeV over 146 shots.

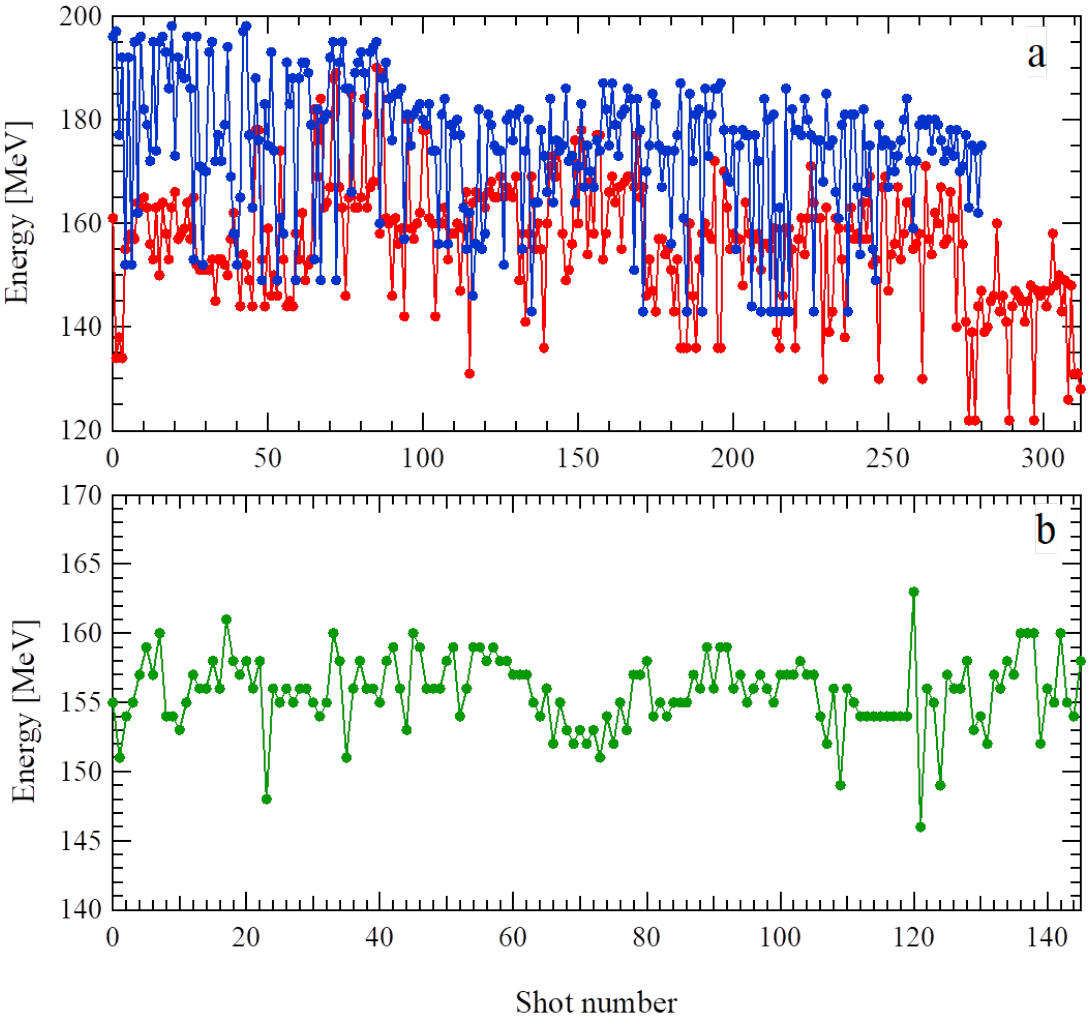

Figure 8.17: Electron beam energy deduced from the resonant wavelength extracted from the measured spectra. (a) RUN4 for two consecutive days (blue) and (red), (b) RUN5 (green).

Figure 8.18 presents the electron beam energy calculated for the high signal spectra. The average beam energy is found to be 156 MeV (red) with a standard deviation of 6.7 MeV over 23 shots. For the (blue), an average energy of 177 MeV with a standard deviation of 4.6 MeV over 27 shots. In RUN5 (b), the average energy is found to be of 156 MeV with a standard deviation of 3.1 MeV over 95 shots.

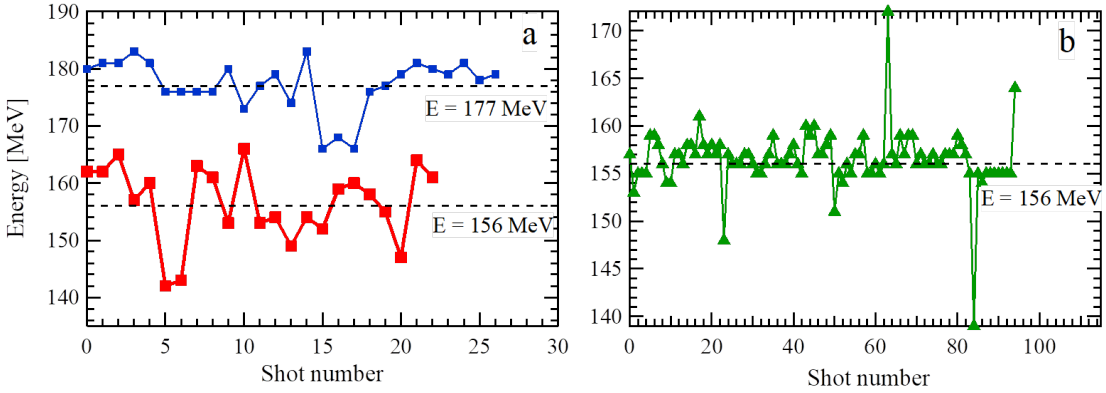

Figure 8.18: Electron beam energy deduced from the resonant wavelength extracted from the measured spectra. (a) RUN4 for two consecutive days (blue) and (red), (b) RUN5 (green).

Figure 8.19 presents spectra with good (left) and weak (right) signals. For the resonant wavelength, we are still able to measure it to a good extent even in the weak signal case, however any analysis related to the bandwidth is dominated by the noise. Hence, in the rest of the chapter, only the high signal spectra are analyzed.

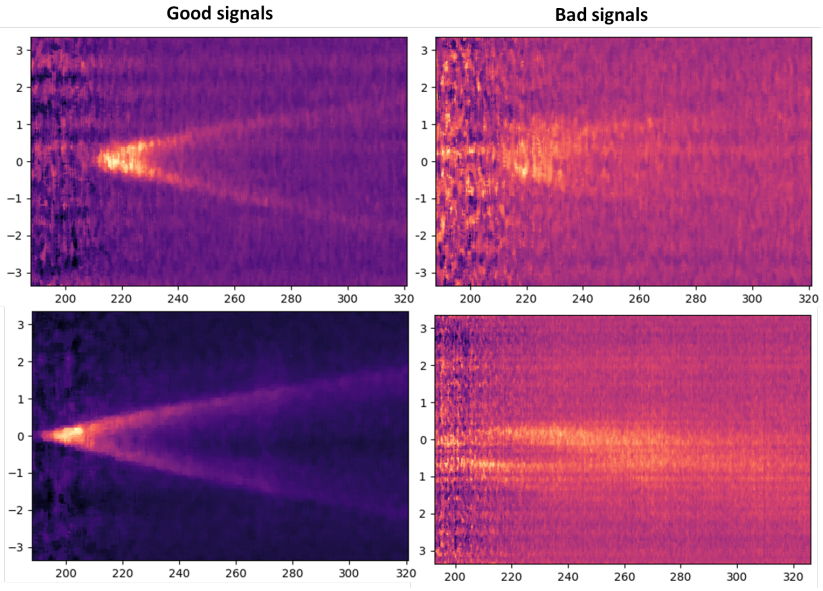

Figure 8.19: The good signals spectra (left) and bad ones (right).

8.3.4 On-axis spectral width control with the electron slit

The spectral width of the on-axis radiation is examined by measuring the bandwidth of the spectral cut at the center of the moon shape for RUN4 and RUN5 for different electron slit cases. The bandwidth decreases with the slit width as shown in Fig. 8.20. A minimum relative bandwidth of 5% is achieved for a slit width of 1 mm during RUN5 (b).

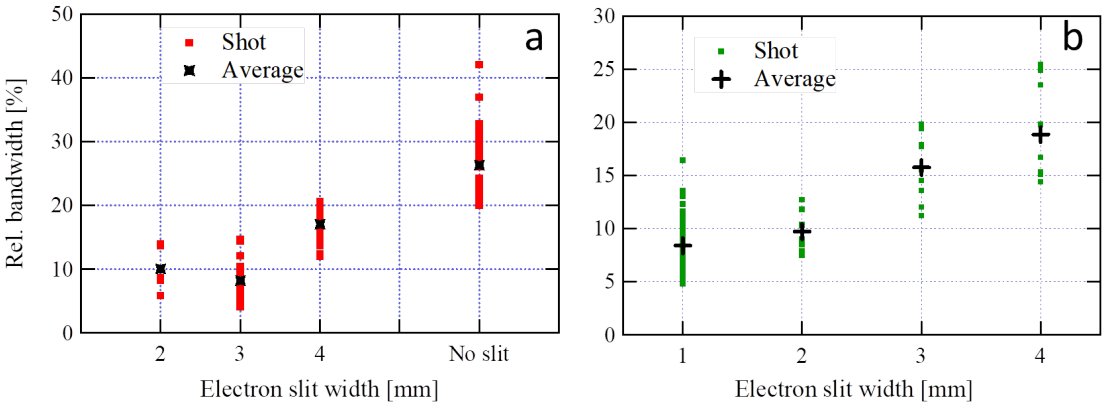

Figure 8.20: Relative bandwidth versus electron slit width during RUN4 (a) and RUN5 (b).

Table 8.4 presents the average relative bandwidth with its corresponding standard deviation, where it is reduced from 26% down to 8% as the slit is inserted and closed at 1 mm.

	Slit width mm	**Average Rel. BW** %	Standard deviation %
	No slit	26.3	5.2
RUN4	4	17.0	2.6
	3	8.2	2.7
	2	10.1	3.2
	4	18.8	4.7
RUN5	3	15.7	2.9
	2	9.7	1.7
	1	8.4	2.4

Table 8.4: Relative bandwidth versus electron slit width for the two runs.

8.4 Beam parameters extraction

Recall from chapter 7 the following equations to extract beam parameters:

The first approach estimates the energy spread and total divergence by looking at the bandwidth on the blue and red side of the spectrum using the following:

$$\sigma_\gamma = \frac{1}{2}\sqrt{4\left[\frac{\Delta\lambda}{\lambda}\right]^2_{Blue} - \left[\frac{1}{N_u}\right]^2} \tag{8.9}$$

$$\sigma'_{tot} = \left[\frac{1+K_u^2/2}{\gamma^2}\sqrt{\left[\frac{\Delta\lambda}{\lambda}\right]^2_{Red} - \left[\frac{\Delta\lambda}{\lambda}\right]^2_{Blue}}\right]^{1/2} \tag{8.10}$$

The divergence in both planes is determined by considering them equal ($\sigma'_{x,z} = \sigma'_{tot}/\sqrt{2}$). This method is not very efficient to estimate a large divergence (>0.5 mrad).

Thus another approach has been introduced. We start by extracting the energy spread using Eq. (8.9) and replacing it in Eq. (6.18) to get:

$$\theta_H = \frac{1}{\gamma}\sqrt{(1+K_u^2/2) - \frac{1+K_u^2/2}{(1+2\sigma_\gamma)^2}} \tag{8.11}$$

Then by substituting θ_H in:

$$\sigma'_z = \frac{1}{D}\sqrt{\sigma^2_{p,z} - (\sigma'_n D)^2 - (\theta_H D)^2 + \sigma^2_z} \tag{8.12}$$

the vertical divergence is estimated. Note that in Eq. (8.12) the electron beam size contribution is added where it was neglected in chapter 7.

Finally Eq. (6.29) is used to get the horizontal divergence:

$$\sigma'^2_x = \frac{(1+K^2_u/2)}{\gamma^2}\sqrt{\frac{2}{\pi}}\sqrt{I^2_{red} - I^2_{blue}} - \sigma'^2_z \tag{8.13}$$

The second approach could not be used efficiently due to the fact that there is a lens between the undulator and the spectrometer preventing us from extracting the vertical profile size at the resonant wavelength. Also it is very sensitive to the spectral profile shape at high wavelength that is dominated mainly by the CCD camera background noise. Thus this approach has been tested for very few good signal shots, where the measured spatio-spectral flux at the camera is converted to an image at the lens.

8.4.1 Energy spread and divergence estimation

Fig. 8.21 shows the estimated values of the energy spread and divergence using Eqs. (8.9) and (8.10), respectively, during RUN4 (a and b) and RUN5 (c and d).

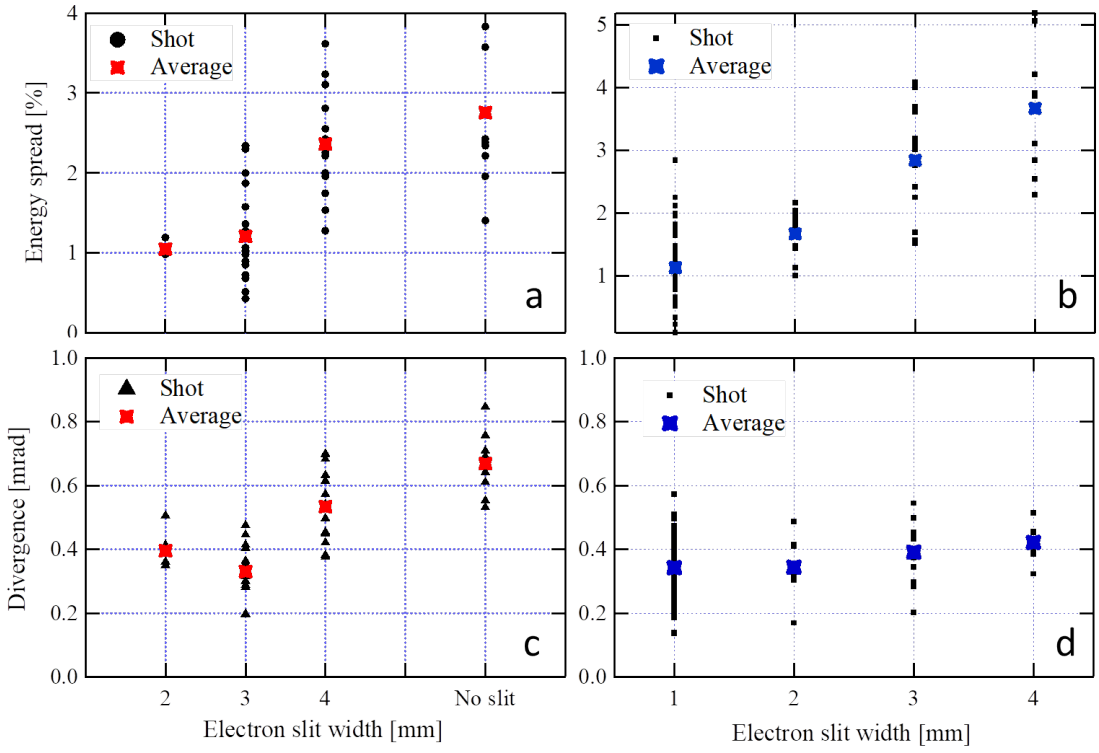

Figure 8.21: Estimated energy spread (a) and horizontal divergence (b) of the measurements taken during RUN4 for different slit cases. Estimated energy spread (c) and horizontal divergence (d) of the measurements taken during RUN5 for different slit cases.

Table 8.5 presents the estimated divergence and energy spread for measurements of RUN4 and RUN5. The "Difference" column corresponds to the deviation of the estimated value from the ones computed with the beam optics code (see Table 7.7). The estimated energy spread in the case

of RUN5 is very close to the beam optics simulations. During RUN4, in the 3 mm and 2 mm cases the estimated energy spread is quite far, and this might be due to an angle offset on the slit at that given day, where a 1° misalignment changes the slit width by ~1 mm.

		Estimate			Difference		
	Slit mm	σ_γ %	σ'_x mrad	σ'_z mrad	σ_γ %	σ'_x %	σ'_z %
	No slit	2.8±1	0.7±0.1	0.7±0.1	-24	11	-35
RUN4	4	2.4±0.6	0.5±0.1	0.5±0.1	-27	-18	-49
	3	1.2±0.6	0.3±0.1	0.3±0.1	-58	-49	-66
	2	1.0±0.1	0.4±0.1	0.4±0.1	-57	-27	-46
	4	3.7±1	0.42±0.1	0.42±0.1	-5	-23	-72
RUN5	3	2.8±0.9	0.4±0.1	0.4±0.1	-15	-26	-72
	2	1.7±0.4	0.35±0.1	0.35±0.1	-32	-35	-74
	1	1.1±0.5	0.34±0.1	0.34±0.1	1	-33	-71

Table 8.5: Average energy and bandwidth over the measured spectra with the standard deviation value after the ±. Estimated parameters and their deviation with respect to the beam optics simulations from Table 7.7.

8.4.2 Spatio-spectral flux construction at the lens

An attempt to re-construct the image at the lens is done to be able to use the second approach and extract the electron beam parameters more precisely. Figure 8.22 displays two spectra from RUN4 with an electron slit width of 4 mm that are tested.

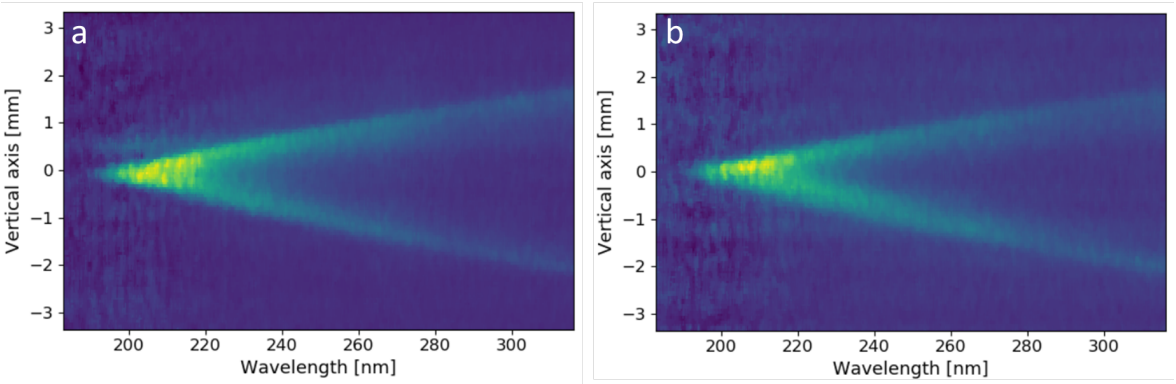

Figure 8.22: spectra from RUN4 with an electron slit width of 4 mm and undulator gap of 5 mm.

The lens parameters are deduced by substituting the undulator radiation resonant wavelength in Eq. (8.7) and fitting it to the spectra as shown in Fig. 8.23. The average values found are d = 22.2 cm, h = -2 mm and H = 0.02 mm.

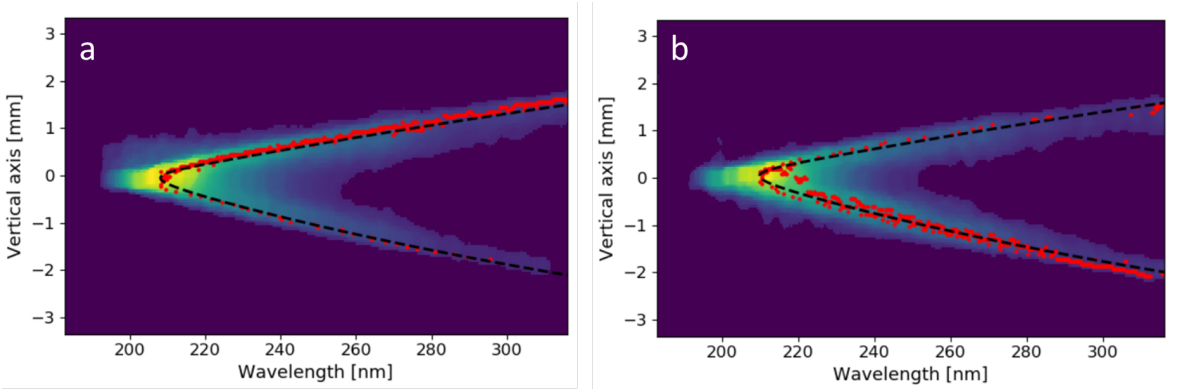

Figure 8.23: Spectra of Fig. 8.22 fitted with Eq. (8.7).

The vertical axis at the lens z_{lens} can be written as a function of the lens parameters and the CCD axis and is expressed as:

$$z_{lens} = \frac{\frac{z_c - \mathrm{H}}{\mathrm{G}} - h\left(1 - \frac{d}{f(\lambda)}\right)}{1 - \frac{d}{f} - \frac{d}{\mathrm{D}}} \tag{8.14}$$

The average lens parameters (d = 22.2 cm, h = -2 mm, H = 0.02 mm) are used to transfer the spectra of Fig. 8.22 and the image is re-constructed at the lens using Eq. (8.14) as shown in Fig. 8.24.

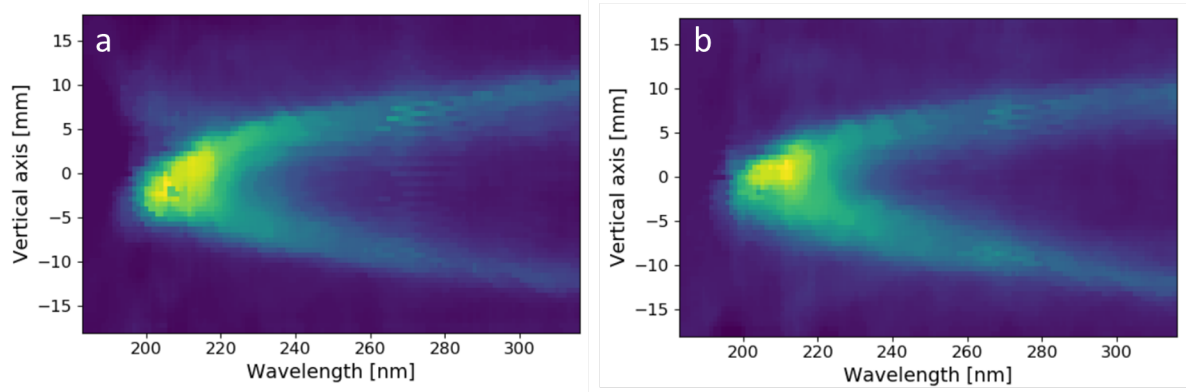

Figure 8.24: Image of Fig. 8.22 spectra measured at the CCD camera converted at the lens.

Fig. 8.25 shows the spectra cuts at the center of the moon shape z = 0 of the images in Fig. 8.24.

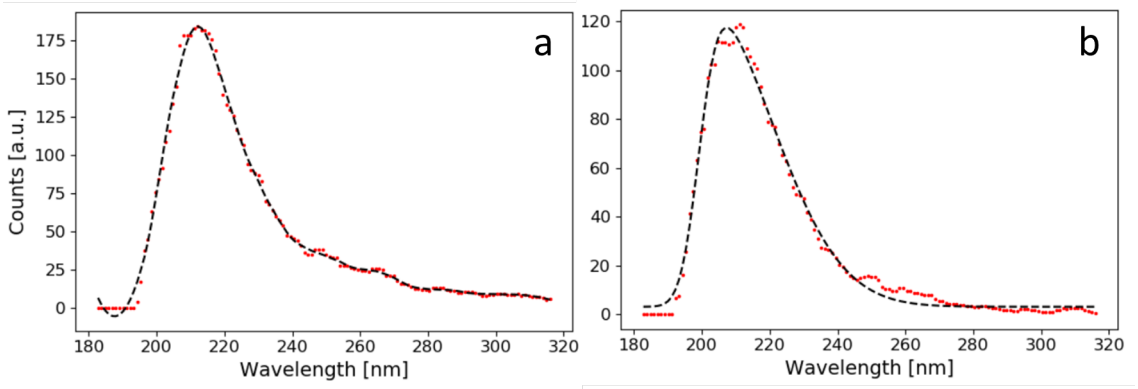

Figure 8.25: Spectral profile at $z = 0$ of the images in Fig. 8.24 (red) fitted with a skew gaussian (black).

Fig. 8.26 shows the vertical profile cuts at the resonant wavelength ~210 nm of the images in Fig. 8.24.

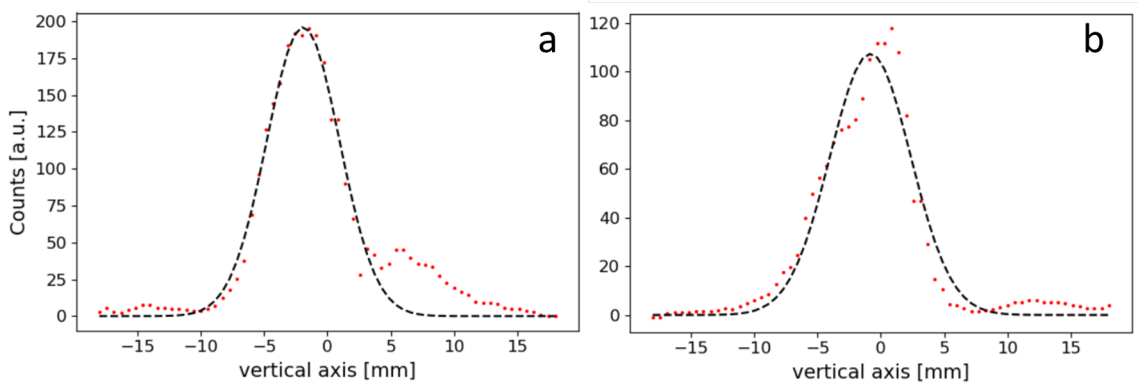

Figure 8.26: Vertical radiation profile at $\lambda = \lambda_{res}$ (red) fitted with a gaussian function (black).

Table 8.6 presents the spectrum characteristics for the two shots of Fig. 8.24 after the re-
3170 construction at the lens, where the bandwidth of the blue and red side vary by around ~20%. The estimated vertical divergence agree with the simulations (see Table 7.7), as for the horizontal divergence, the difference is large, which is due to the sensitivity of this approach on the flux integral that is dominated by the background noise at large wavelength.

	Characteristics			**Estimate**			**Difference**		
Shot	$\frac{\Delta\lambda}{\lambda}\|_{blue}$ %	$\frac{\Delta\lambda}{\lambda}\|_{red}$ %	$\sigma_{p,z}$ mm	σ_γ %	σ'_x mrad	σ'_z mrad	σ_γ %	σ'_x %	σ'_z %
1	3.8	8.4	9.5	1.62	1.54	0.91	-50	152	-7
2	3.1	9.0	8.2	1.32	1.78	0.74	-60	191	-25

Table 8.6: Spectra characteristics of the constructed images in Fig. 8.24 alongside the estimated beam parameters the second approach.

This image re-construction at the lens is also applied on RUN5 measurements for the 1 mm
3175 electron slit case, while neglecting the vertical beam size contribution due to its small value at the center of the undulator (see Table 7.7). The estimated vertical divergence is calculated to be 0.5 mrad with a standard deviation of 0.2 mrad over 31 shots. The difference with respect to the beam optics simulation is still quite large ~98%. For this method to work efficiently, the spectrometer should be placed at the position of the lens, and also the undulator radiation signal has to be quite

high compared to the camera noise.

8.4.3 Comparison with simulations

Figure 8.27-left shows the undulator spatio-spectral patterns, with the corresponding appended on-axis spectra, measured while shaping the beam parameters during RUN5. As the slit is closed in the magnetic chicane, the beam energy spread, size and divergence in the undulator are reduced (see Table 7.7) and, accordingly, the corresponding measured moon-shape thickness decreases. The electron beam parameters deduced from the measured distribution and transported along the line are used for the undulator radiation modeling using SRW code [194] in the far-field region as shown in Fig. 8.27-right. A so-called slicing method is used, where radiation of each electron energy slice is computed separately with its corresponding parameters (divergence and size), and then all the spectra are added up taking into account the slice energy distributions. Ray optics is finally applied to the computed undulator radiation to include the chromatic effects induced by the lens.

The difference of the resonant wavelength between the experiment (290 nm) and the simulation (275 nm) is because the electron beam energy at COXINEL was slightly lower (156 MeV) than the simulated one (161 MeV). One explanation could be due to a beam pointing issue at the entrance of the chicane, lower energy electrons pass through the slit. Another explanation could be due to beam pointing at the entrance of the undulator, where the electron beam is not well centered at the undulator axis ($z = 0$). For example, if we consider that the electron beam during COXINEL was indeed 161 MeV, we can calculate how much the electron beam has to be deviated from the undulator axis, to attain a resonant wavelength of 290 nm. It is found that the electron beam has to experience a larger magnetic field of 1.23 T. The on-axis undulator field at gap 4.7 mm is 1.18. Substituting these two values in the following equation:

$$\mathrm{B} = \mathrm{B}_0 \cosh(k_u z)$$

we get a vertical deviation of 0.85 mm, which is far-fetched but not entirely impossible.

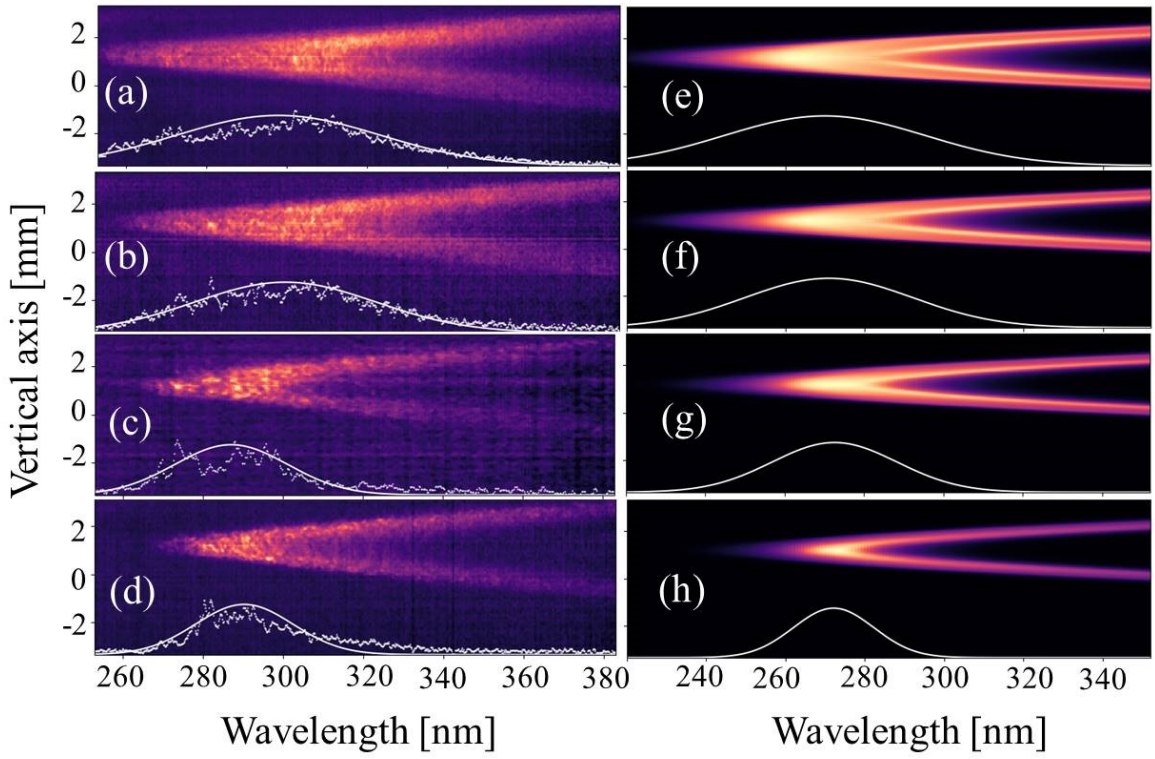

Figure 8.27: Single shot measured spatio-spectral distributions during RUN5 for a 4.7 mm undulator gap while varying the electron slit width: 4 (a), 3 (b), 2 (c) and 1 mm (d) with a 2.2 mm spectrometer entrance slit. Simulated spectra using SRW for a magnetic field of 1.17 T, with beam parameters taken from the simulations of the corresponding electron beam distribution transported along the line (see Table 7.7 for 161 MeV) for slit widths of 4 (e), 3 (f), 2 (g) and 1 mm (h) with their corresponding appended on-axis spectra (white curves)

Figure 8.28 presents a comparison of the relative bandwidth between the experiment (RUN5) and simulations for different slit widths. The agreement is quite good especially for the 1 mm slit case, where we have the most number of shots.

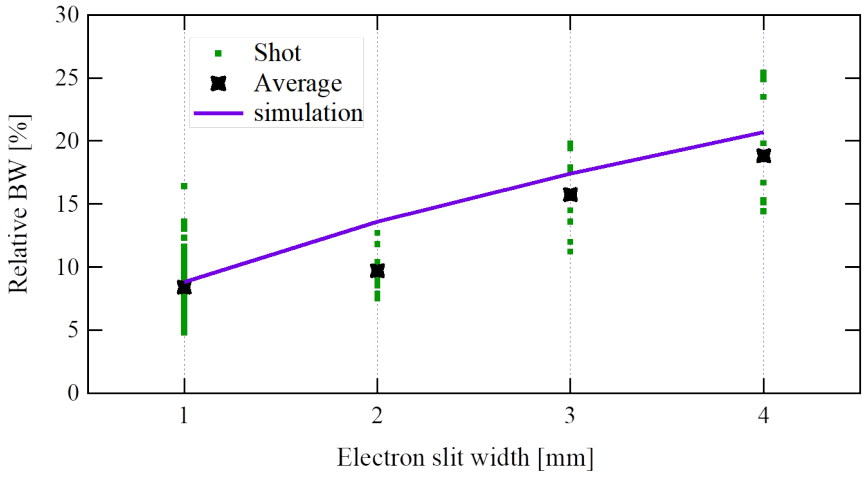

Figure 8.28: Relative bandwidth of the spectrum profile at the center of the moon shape pattern

8.4.4 Observation of the second harmonic

One of the main features of planar undulators is the high intensity emission on the harmonics, provided the deflection parameter is not too small. Considering the limited spectral range of the used spectrometer, the emission on the second harmonics is explored. Figures 8.29-a,b present a simulation using the average beam parameters for the 4 mm slit case (see Table 7.7). The second harmonic is visible on-axis (175 nm) because of the multi-electron contribution. Figure 8.29-d shows a measurement of undulator radiation, where the moon shape of the second harmonic is twisted (closed onto itself) due to chromatic effects of the lens forming a "ribbon" type pattern. The maximum intensity is observed at ~225 nm, where the focal length of this particular wavelength is equal to the distance between the lens and the spectrometer slit. Figure 8.29-c displays the simulated undulator radiation of (b) after introducing the chromatic effects. A good agreement is found with the measurement.

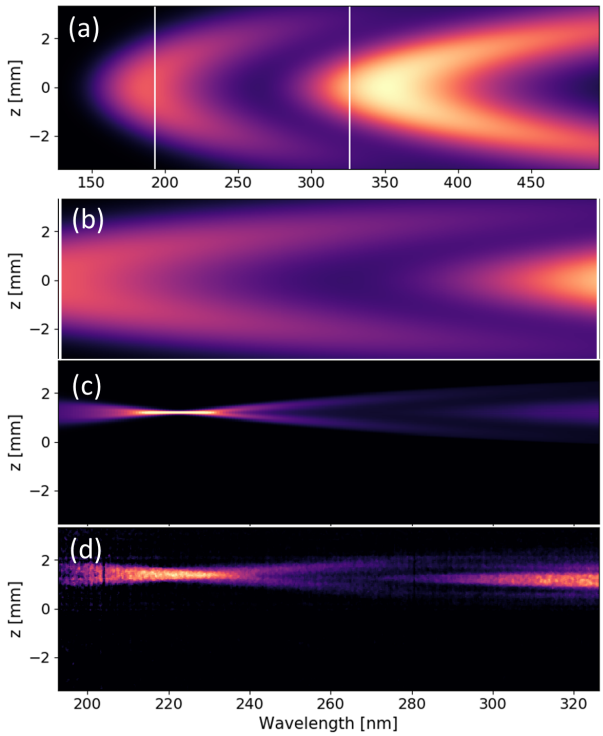

Figure 8.29: Undulator radiation spatio-spectral distribution at a gap of 4.7 mm, electron slit opened at 4 mm and spectrometer slit at 2.2 mm. (a) simulation showing the first and second harmonic, (b) zoom of (a), (c) simulation including chromatic effects of the lens on (b), (d) calibrated measurement.

8.5 Seeding

The main 800 nm laser is split in to two, one for the generation of the electron beam, and the other for seeding at a wavelength of ~275 nm attained by high harmonic in gas. The seed was spectrally tuned and aligned with the undulator radiation as shown in Fig. 8.30. Tranvserse spatial alignment was also done by looking at the imagers 4 and 5, before and after the undulator. In RUN6, we focused mainly on the synchronization and alignment of the seed laser with the electron beam aiming at measuring coherent emission but without any success.

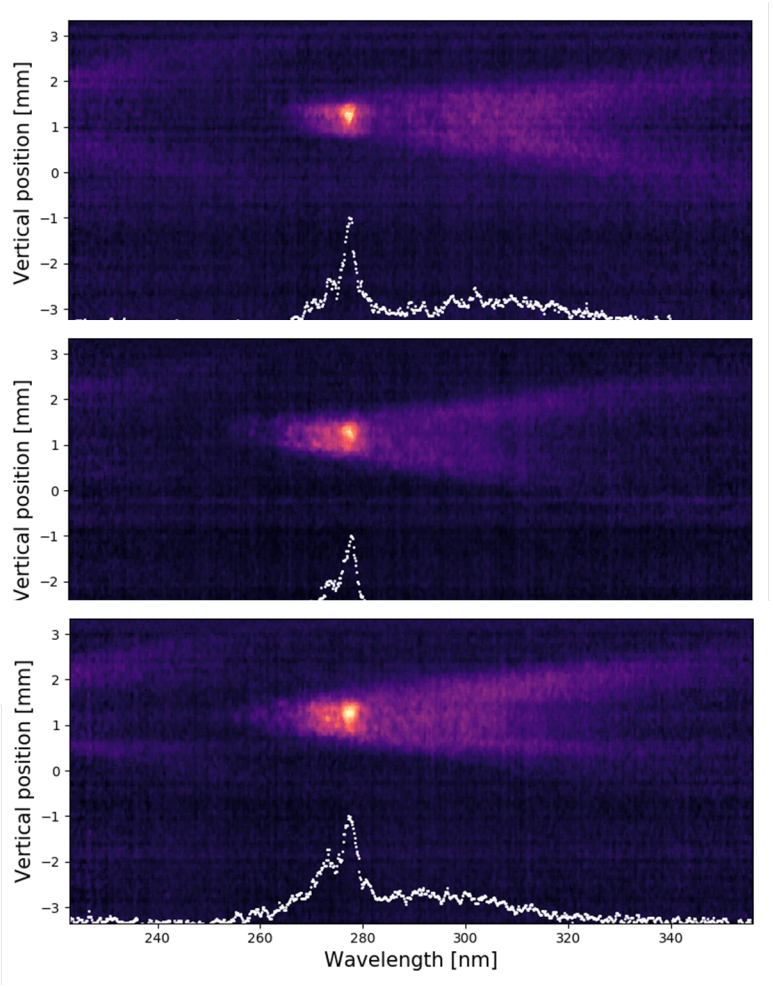

Figure 8.30: Single shots measured with the spectrometer showing the spectral alignment of the seed and the undulator radiation.

8.6 Conclusion

The undulator radiation measurements at COXINEL have been presented. The photon transverse beam shape is measured using a CCD camera while applying different optical filters. The measurements are in good agreement with the simulations in terms of power dependence on undulator gap. The angular spectral flux has been also examined during two runs with different operating energy. A ~120 nm tunability of LPA based undulator radiation has been achieved by varying the undulator gap and electron beam energy. A wavelength stability of 2.4% has also been recorded. Furthermore, the control of the undulator radiation has been accomplished via chicane and slit combination, resulting in a small radiation bandwidth down to 5% FWHM. The achieved agreement demonstrates a new capability in handling the LPA electron beam and transporting it to the undulator for a high photon beam brilliance.

Chapter 9

Echo-Enabled Harmonic Generation

In this chapter, the other approach for compact FEL line is examined. The FEL advanced scheme of Echo-Enabled Harmonic Generation is discussed. The line characteristics of LUNEX5 test experiment are examined to achieve amplification at different wavelengths. In addition the successful experimental results achieved at FERMI@Elettra are presented.

9.1 Introduction

FELs have seen tremendous developements over the past years, where they are now capable of producing coherent ultra short pulses radiation down to hard x-rays. Two approaches are mainly used, the SASE [116] and the HGHG [124]. In SASE, the radiation has an excellent transverse coherence but poor temporal coherence due to the electron beam shot noise start. Even though self-seeding is developing [117, 118, 120], HGHG main advantage over the SASE FEL is the up-frequency conversion of the initial seed signal, where temporally coherent pulses at higher harmonics are generated. HGHG has the advantages of using a shorter undulator section, due to the smaller saturation length, and achieving a temporal coherence at higher harmonics. However, the frequency up-conversion efficiency is limited to an intermediate harmonic number (≤10) due to the large energy modulation required and shot noise degradation [124].

The up-frequency conversion efficiency can be enhanced with the recently proposed echo-enabled harmonic generation (EEHG) technique [127, 300]. Echo-Enabled Harmonic Generation (EEHG) FEL scheme uses two laser modulators in combination with two dispersion sections to generate a high-harmonic density modulation in the electron beam (see Fig. 9.1). The echo scheme has a remarkable up-frequency conversion efficiency and allows for generation of high harmonics with a relatively small energy modulation [127]. The beam energy is tuned at frequency ω_1 in the first modulator by interacting with the first laser beam. After passing through the first dispersion section, the beam energy is then modulated in the second modulator tuned to frequency ω_2. The beam then passes through the second dispersion section, and finally into the radiator to achieve large gain at a high harmonic of the first laser seed. The amplification occurs at the wavenumber k_{ECHO} expressed as:

$$k_{\mathrm{ECHO}} = nk_1 + mk_2 \tag{9.1}$$

Thus the echo wavelength λ_{ECHO} is written as:

$$\lambda_{\mathrm{ECHO}} = \frac{\lambda_1\lambda_2}{n\lambda_2 + m\lambda_1} \tag{9.2}$$

where k_1 (λ_1) and k_2 (λ_2) are the wavenumbers (wavelengths) of the first and second laser seeds, respectively, with n and m being integers.

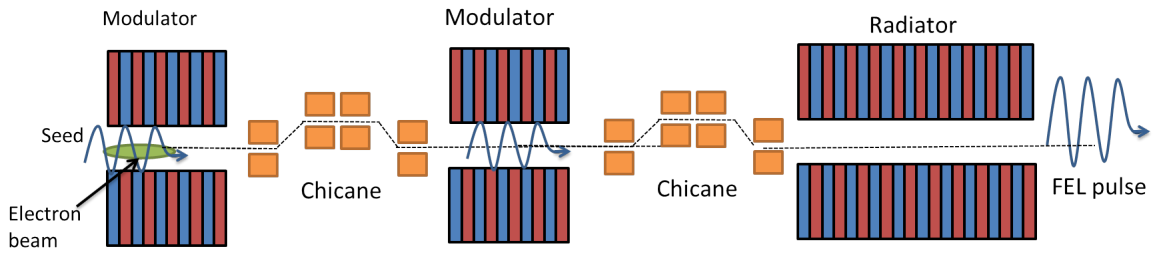

Figure 9.1: Scheme representing the echo-enabled harmonic generation configuration.

9.2 State-of-art

The first experimental measurements of the EEHG technique has been demonstrated on NLCTA at SLAC in 2010 [301]. The EEHG cofiguration uses two different lasers in the modulators, a 795 nm and 1590 nm wavelength. The FEL amplification was achieved at the 3^{rd} (530 nm) and 4^{th} (397 nm) harmonics of the second seed. An FEL lasing using the EEHG scheme was demonstrated at the SDUV-FEL facility in 2012 [302]. The two lasers of wavelength 1047 nm are used for seeding and a bunching was achieved at the 3^{rd} harmonic of 350 nm wavelength. The measurements also showed that the same power can be generated by the EEHG compared to the HGHG with a narrower radiation bandwidth. At SLAC's NLCTA, a 120 MeV electron beam enters the EEHG line composed of three chicanes and three undulators. The first chicane is used to generate an orbit bump to inject the first laser seed of wavelength 795 nm. The second laser seed is at wavelength of 1590 nm. Finally the electron beam is sent to the third undulator tuned at the seventh harmonic of the second laser (227 nm) to generate coherent radiation. In 2014, generation of highly coherent and stable vacuum ultraviolet radiation at the 15^{th} harmonic (160 nm) of an infrared seed laser by the EEHG technique has been observed [303]. In 2016, demonstration of EEHG bunching at the 75^{th} harmonic of the seed laser (2400 nm) was achieved at NLCTA-SLAC [304]. Up to the year 2019, neither FEL amplification nor coherent emission has been reported in the soft x-ray region, where the seed laser phase errors alongside electron beam instabilities strongly affect the bunching process and set a limitation on the EEHG configuration at very high harmonics. At FERMI user facility, the electron beam generated has a high energy and reliability with quite good quality resulting from the daily operation for users. Thus, it was possible to measure coherent radiation at very high harmonics [305]. The result at FERMI will be discussed in more details later on considering that I contributed to the experiment as a part of my PhD. Figure 9.2 presents a summary of the harmonic number attained using EEHG.

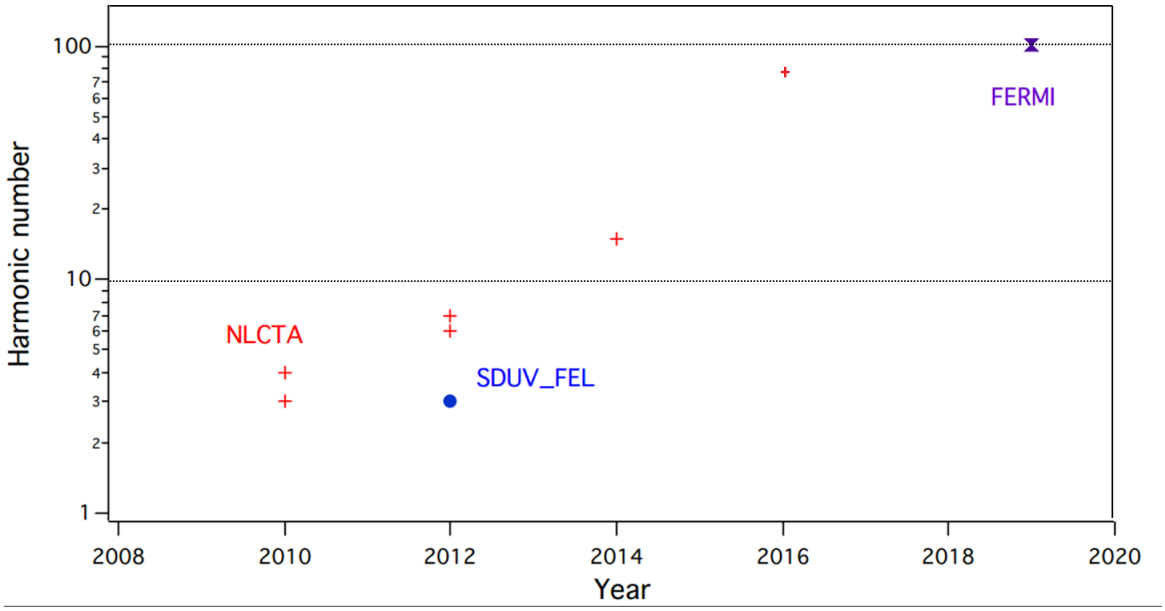

Figure 9.2: EEHG harmonic number achieved over the years.

9.3 EEHG Theory

Consider an initial Gaussian beam energy distribution generated at the source with an average energy E_0 and an rms energy spread σ_E. The energy distribution can be expressed as:

$$f_0(p) = \frac{N_0}{\sqrt{2\pi}} \exp\left[-\frac{p^2}{2}\right] \tag{9.3}$$

where N_0 is the number of electrons per unit length of the beam and $p = \frac{E-E_0}{\sigma_E}$.

As the electron beam passes through the first undulator and interacts with the first laser seed, the beam energy is modulated with an amplitude ΔE_1. The new energy deviation p' is expressed as:

$$p' = p + A_1 \sin(k_1 s)$$

where $A_1 = \Delta E_1/\sigma_E$ and k_1 the wavenumber of the first laser seed. Introducing the dimensionless $\zeta = k_1 s$, the longitudinal phase space distribution becomes:

$$f_1(\zeta, p) = \frac{N_0}{\sqrt{2\pi}} \exp\left[-\frac{\left(p - A_1 \sin(\zeta)\right)^2}{2}\right] \tag{9.4}$$

Passing through the first dispersion section of strength $R_{56}^{(1)}$, the longitudinal coordinate s is converted to s' by:

$$s' = s + R_{56}^{(1)} \frac{p\sigma_E}{E_0}$$

Introducing $B_1 = R_{56}^{(1)} \frac{k_1 \sigma_E}{E_0}$, the longitudinal phase space after the first dispersive section thus becomes:

$$f_2(\zeta, p) = \frac{N_0}{\sqrt{2\pi}} \exp\left[-\frac{1}{2}\left(p - A_1 \sin(\zeta - B_1 p)\right)^2\right] \tag{9.5}$$

Integrating Eq. (9.5) over p gives the density distribution as a function of ζ:

$$N(\zeta) = \int_{-\infty}^{+\infty} f(\zeta, p)\, dp \tag{9.6}$$

Noting that the density is a periodic function of ζ, one thus can expand it into Fourier series:

$$\frac{N(\zeta)}{N_0} = 1 + \sum_{n=1}^{\infty} b_n \cos(n\zeta + \Phi_n) \tag{9.7}$$

where the coefficient b_n is the amplitude of the harmonic n.

After some calculations (see [306]), one gets an analytical expression for b_n:

$$|b_n| = \exp(-\frac{1}{2}B_1^2 n^2)|J_n(A_1 B_1 n)| \tag{9.8}$$

where J_n is the Bessel function of order n. Figure 9.3 presents the bunching factor magnitude as a function of the normalized paramaters A_1 and B_1 for different harmonic numbers. To achieve up-frequency conversion at a high harmonic, the A_1 parameter should be quite large ~10 for m = 10 and ~15 for m = 20. This would result in a significant increase in the energy spread of the beam after the passage through the first modulator.

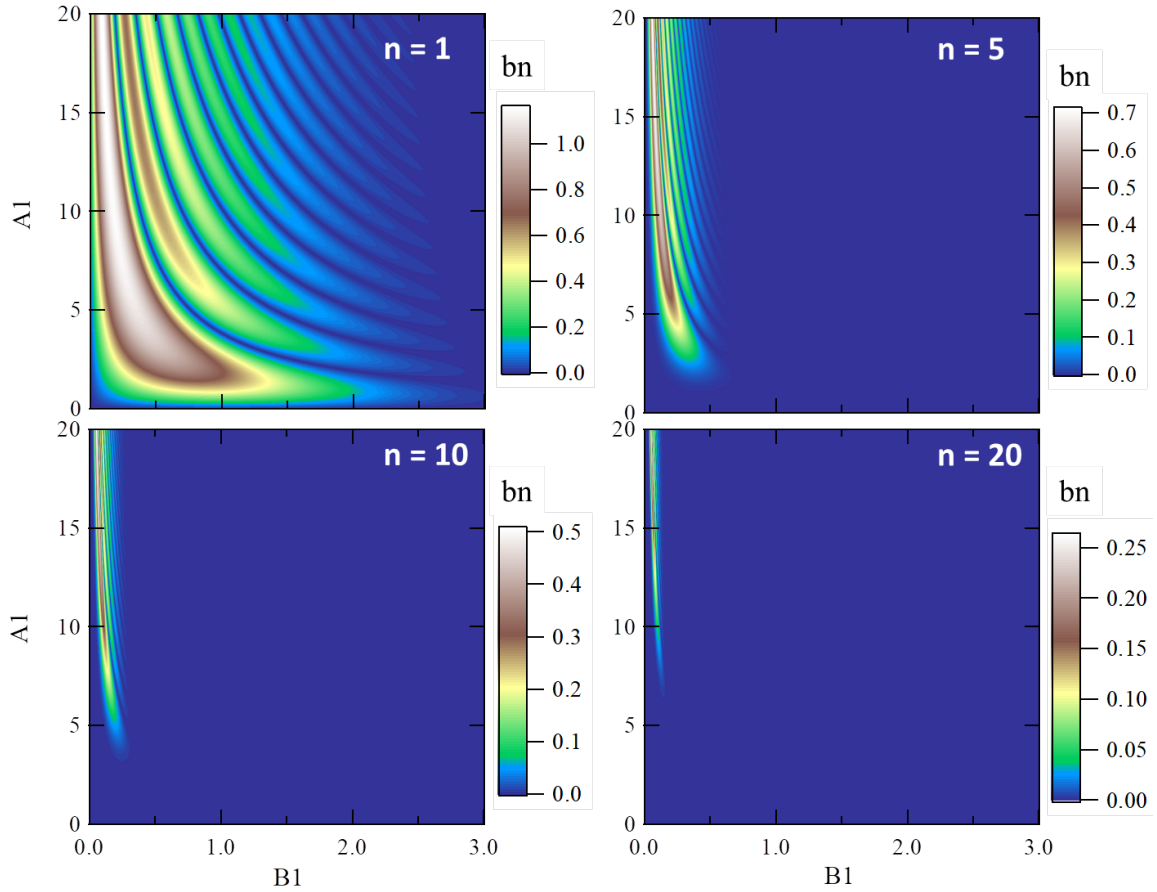

Figure 9.3: The bunching factor ($|b_n|$) calculated using Eq. (9.8) as a function of A_1 and B_1 for different harmonic numbers.

The beam then interacts with the second laser seed of wavenumber k_2 and is modulated with

an amplitude ΔE_2. Same as before, the new energy deviation p' is expressed as:

$$p' = p + A_2 \sin(k_2 s + \phi)$$

where ϕ is the phase difference of the second laser beam with respect to the first one. The longitudinal phase space distribution after the second modulator $f_3(\zeta, p)$ is:

$$f_3(\zeta, p) = \frac{N_0}{\sqrt{2\pi}} \exp\left[-\frac{1}{2}\left[p - A_2 \sin(k_2 s + \phi) - A_1 \sin\left(\zeta - B_1 p + A_2 B_1 \sin(k_2 s + \phi)\right)\right]^2\right] \tag{9.9}$$

Passing through the second dispersion section of strength $R_{56}^{(2)}$, the longitudinal coordinate s is converted to s' by:

$$s' = s + R_{56}^{(2)} \frac{p\sigma_E}{E_0}$$

Introducing $B_2 = R_{56}^{(2)} \frac{k_1 \sigma_E}{E_0}$ and $K = \frac{k_2}{k_1}$, the final longitudinal phase space $f(\zeta, p)$ before entering the radiator is expressed as:

$$f_4(\zeta, p) = \frac{N_0}{\sqrt{2\pi}} \exp\left[-\frac{1}{2}\left[p - A_2 \sin(K\zeta - KB_2 p + \phi) - A_1 \sin\left(\zeta - (B_1 + B_2) p + A_2 B_1 \sin(K\zeta - KB_2 p + \phi)\right)\right]^2\right] \tag{9.10}$$

The electron beam is well bunched after the modulator and dispersive sections and has a density $N(\zeta)$ that is expressed as:

$$N(\zeta) = \int_{-\infty}^{+\infty} f(\zeta, p)\, dp \tag{9.11}$$

The bunching factor $b_{n,m}$ is defined as:

$$b_{n,m} = \frac{1}{N_0} | < e^{-ih\zeta} N(\zeta) > | \tag{9.12}$$

where the brackets denote averaging over ζ. $b_{n,m}$ is different than zero only in the case where $h = n + Km$ with h being an integer. The echo wavenumber k_E is expressed as:

$$k_E = hk_1 = nk_1 + mk_2 \tag{9.13}$$

where h becomes the harmonic number of the first seed laser. The final expression of the bunching factor is (details are presented in [300]):

$$b_{n,m} = \left| J_m\left(-(mK + n) A_2 B_2\right) J_n\left(-nA_1 B_1 - (mK + n) A_1 B_2\right) e^{-\frac{1}{2}[nB_1 + (mK+n)B_2]^2} \right| \tag{9.14}$$

By removing the second chicane and modulator ($A_2 = 0$ and $B_2 = 0$), one arrives at the HGHG bunching factor presented in Eq. (9.8).

Analysis shows that the bunching factor attains its maximum when $n = \pm 1$ and decreases as the absolute value of n increases. Using two chicanes as dispersive mediums, the n and m should have opposite signs in order for B_1 and B_2 to have the same sign. We now consider the case of n = -1, and thus the bunching factor becomes:

$$b_{-1,m} = \left| J_m\left((mK - 1) A_2 B_2\right) J_1\left(A_1 B_1 - (mK - 1) A_1 B_2\right) e^{-\frac{1}{2}[B_1 - (mK-1)B_2]^2} \right| \tag{9.15}$$

Figure 9.4-a presents the maximum value of the Bessel function $|J_m|$ versus the Bessel order m

and is fitted with:

$$|\mathrm{J}_m|_{max} = 0.63 m^{-1/3} \tag{9.16}$$

Figure 9.4-b shows the argument Y_{max} corresponding the maximal values of $|\mathrm{J}_m|$ and is fitted with:

$$\mathrm{Y}_{max} = m + 0.81 m^{1/3} \tag{9.17}$$

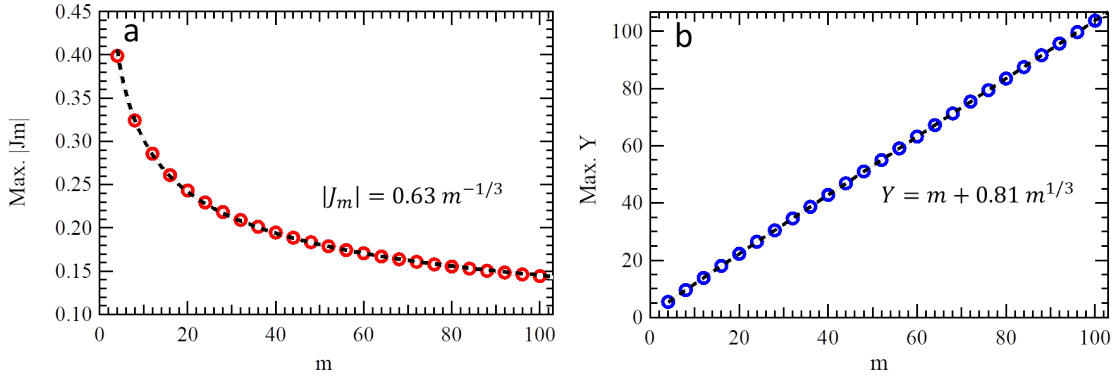

Figure 9.4: The maximum value of $|\mathrm{J}_m|$ versus m (a) and its corresponding argument Y_{max} (b).

Thus to maximize the J_m factor in Eq. (9.15), one takes the following:

$$\mathrm{Y} = (m\mathrm{K} - 1)\mathrm{A}_2\mathrm{B}_2 = m + 0.81 m^{1/3} \tag{9.18}$$

3340 Taking $\zeta_m = \mathrm{B}_1 - (m\mathrm{K} - 1)\mathrm{B}_2$, the term $\mathrm{F}(\zeta_m) = \mathrm{J}_1(\mathrm{A}_1\zeta_m)e^{-\frac{1}{2}\zeta_m^2}$ is examined to find the parameters to achieve the maximum bunching value. Figure 9.5-a displays the maximum value of $|\mathrm{F}(\zeta_m)|_{max}$ as a function of A_1 fitted with:

$$|\mathrm{F}(\zeta_m)|_{max} = 0.57 - 0.59 e^{-0.7\mathrm{A}_1} \tag{9.19}$$

Figure 9.5-b shows the corresponding argument fitted with a third degree polynomial:

$$\zeta_m = \mathrm{B}_1 - (m\mathrm{K} - 1)\mathrm{B}_2 = 1.13 - 0.275\mathrm{A}_1 + 0.029\mathrm{A}_1^2 - 0.0011\mathrm{A}_1^3 \tag{9.20}$$

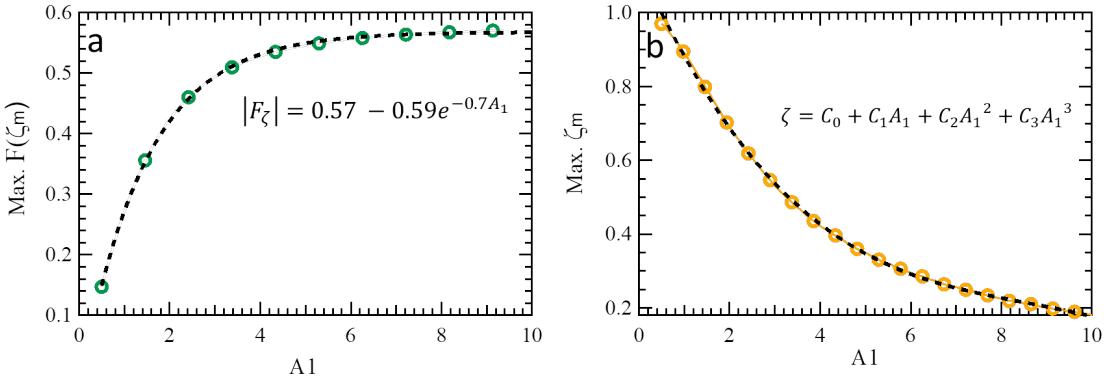

Figure 9.5: The maximum value of $\mathrm{F}(\zeta_m)$ versus m fitted with an exponential (a) and its corresponding argument fitted with a third degree polynomial (b). (c_0, c_1, c_2, c_3) = (1.13, -0.275, 0.029, -0.0011).

Combining Eqs. (9.16) and (9.20), one gets the maximum bunching factor expressed as:

$$|b_{-1,m}| = 0.36 m^{-1/3} \tag{9.21}$$

Using Eqs. (9.17)-(9.20), the EEHG components parameters can be optimized to achieve a bunching at a specific harmonic number using the following relations:

$$\begin{cases} \mathrm{B}_1 - (m\mathrm{K}-1)\mathrm{B}_2 = +c_0 + c_1\mathrm{A}_1 + c_2\mathrm{A}_1^2 + c_3\mathrm{A}_1^2 \\ \mathrm{A}_2\mathrm{B}_2(m\mathrm{K}-1) = m + 0.81\, m^{1/3} \end{cases} \tag{9.22}$$

9.4 Longitudinal phase space evolution

Starting with Gaussian beam of mean energy 400 MeV and relative energy spread of 0.02% (80 keV), the initial electron beam phase space is shown in Fig. 9.6 using Eq. (9.3).

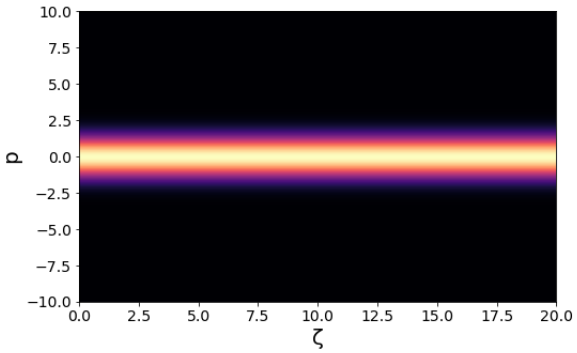

Figure 9.6: Phase space of a Gaussian beam.

Figure 9.7 presents the electron beam phase space distribution as it propagates through the modulators and dispersive sections. The first seed laser induces a sinusoidal energy modulation with a normalized amplitude A_1 as the electron beam passes through the first modulator (a). After passing through the strong dispersive chicane of strength $\mathrm{R}_{56}^{(1)}$, the energy modulation becomes a density modulation, where the electrons with a deviated energy $\Delta\mathrm{E}$ from the nominal energy E_0 are displaced according to $\Delta s = \mathrm{R}_{56}^{(1)}\Delta\mathrm{E}/\mathrm{E}_0$ and thus the longitudinal phase space splits into many separated energy bands (b). The electrons then pass through another modulator, where their energy is again periodically modulated using a second seed laser λ_2, with a phase difference ϕ with respect to the first laser (c). Finally the electron beam traverse a weak chicane of strength $\mathrm{R}_{56}^{(2)}$, where the separated energy bands are converted into separated current bands resulting high frequency components.

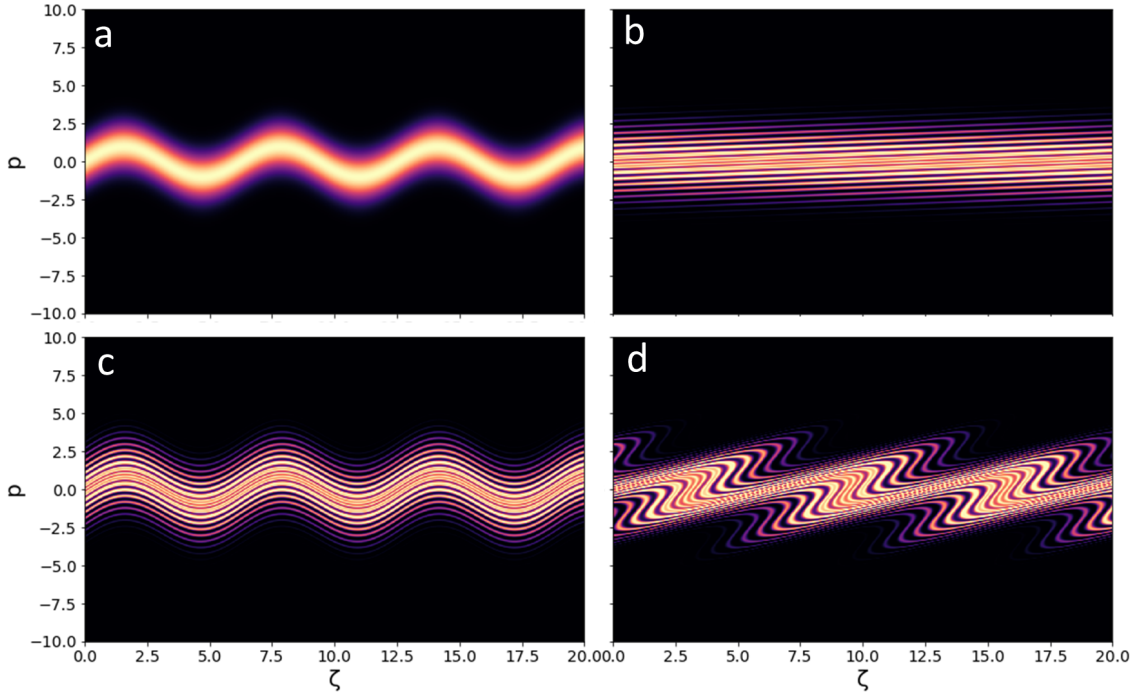

Figure 9.7: The phase distribution as the electron beam passes through the first modulator (a) (Eq. (9.4)), the first chicane (b) (Eq. (9.5)), the second modulator (c) (Eq. (9.9)) and the second chicane (d) (Eq. (9.10)). $\lambda_1 = \lambda_2 = 800$ nm, energy modulation amplitudes $A_1 = A_2 = 1$. $R_{56}^{(2)} = 10$ mm and $R_{56}^{(2)} = 1$ mm.

Figure 9.8-a shows the density distribution of the electron beam from the phase space of Fig. 9.7-d (before the radiator). By applying the Fourier transformation on the density distribution, one gets all the harmonic contents of the electron beam bunching, as shown in Fig. 9.8-b (green curve). The bunching at different harmonic contents can be calculated analytically by summing up Eq. (9.14) (blue curve in Fig. 9.8-b). The small difference of the bunching factor between the analytical and from the longitudinal phase space is due to the resolution of the phase space distribution.

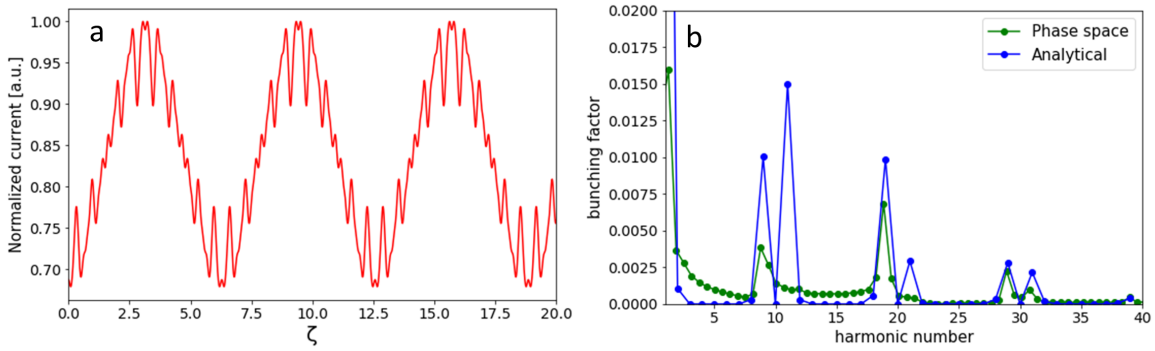

Figure 9.8: (a) Density distribution after the second dispersive section. (b) Bunching factor from the phase space (green) and from Eq. (9.14). $\lambda_1 = 800$ nm, $\lambda_2 = 800$ nm, $\Delta E_1 = \sigma_E$, $\Delta E_2 = \sigma_E$, $\phi = 0$, $R_{56}^{(1)} = 10$ mm, $R_{56}^{(1)} = 1$ mm.

One can notice that the bunching factor is quite compelling at the harmonics lying close to the optimized one. Thus, multi-color FEL operation is possible using EEHG with the appropriate radiator configurations, such as setting some of the radiators at the optimized harmonic and the

others at the one lying close to it.

9.4.1 ECHO applied to LUNEX5

In the case of LUNEX5 Linac accelerator, recalling the beam parameters from Table 3.1, where a Gaussian beam of mean energy 400 MeV and relative energy spread of 0.02% (80 keV) is introduced. The two laser seeds are of wavelength 266 nm.

9.4.2 Bunching at 20 nm

The two modulators are tuned on the seed laser wavelength (266 nm). The first laser power is chosen to modulate the electron energy with an amplitude about 5 times the energy spread with 15 MW power. The first chicane strength is $R_{56}^{(1)} = 2$ mm. Then the second laser power modulates the electron energy with an amplitude about 5 times the energy spread with 30 MW power. The second chicane of strength $R_{56}^{(2)} = 0.16$ mm tuned to maximize the bunching factor at the desired wavelength of 20 nm which corresponds to the 13^{th} harmonic.

Figure 9.9-a shows the density distribution of the electron beam after the second dispersive section using Eq. (9.10). Figure 9.9-b presents the bunching factor, where it is maximum ~0.06 at the 13^{th} harmonic (20.5 nm).

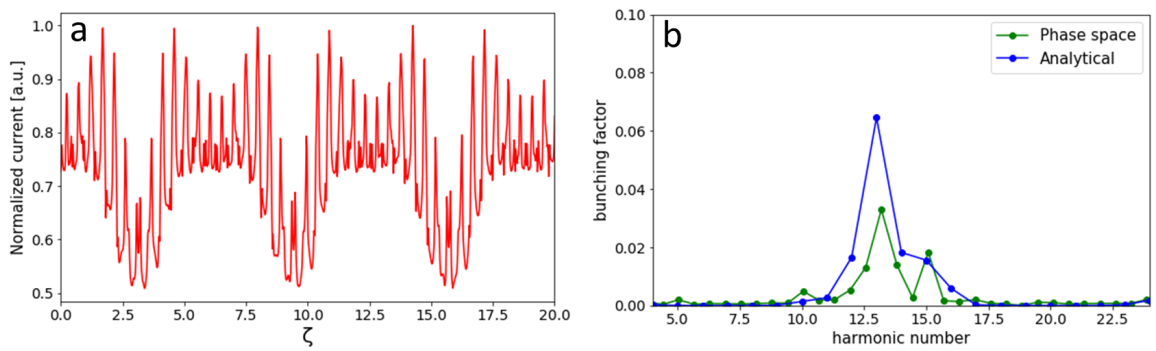

Figure 9.9: (a) Density distribution after the second dispersive section. (b) Bunching factor from the phase space (green) and Eq. (9.14). $\lambda_1 = 266$ nm, $\lambda_2 = 266$ nm, $\Delta E_1 = 5\sigma_E$, $\Delta E_2 = 5\sigma_E$, $\phi = 0$, $R_{56}^{(1)} = 2$ mm, $R_{56}^{(1)} = 0.16$ mm.

Figure 9.10 presents the power along the undulator axis (a) and the spectral profile power simulated using GENESIS [167]. At the entrance of the radiator (i.e. at the exit of the second chicane), the bunching factor at 20 nm is non-null along the overlapping of the two seed laser pulse (of width 30 fs FWHM). The saturation is reached within two undulator sections tuned at 20 nm, and the maximum peak power is of 70 MW, with a RMS width of about 10 fs.

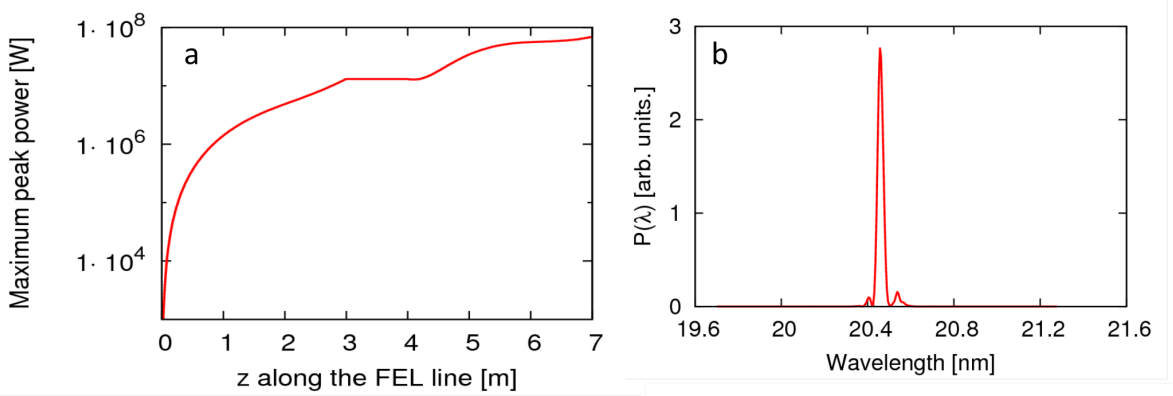

Figure 9.10: GENESIS simulation: Power growth along the undulator section (a) and the power profile (b).

9.4.3 Bunching at 11 nm

The first laser power and the first chicane have the same characteristics that for the 20 nm case (P = 15 MW and $R_{56}^{(1)}$ = 2 mm). The second laser power and the second chicane strength are tuned to maximize the bunching factor at 11 nm (24^{th} harmonic of the seed laser), where they are found to be P_2 = 90 MW and $R_{56}^{(2)}$ = 0.08 mm. Figure 9.11-a shows the density distribution of the electron beam after the second dispersive section, where it exhibits a rather noisy shape due to the high frequency contents and insufficient resolution. Figure 9.9-b presents the bunching factor, where it is ~0.02 at the 24^{th} harmonic (11 nm).

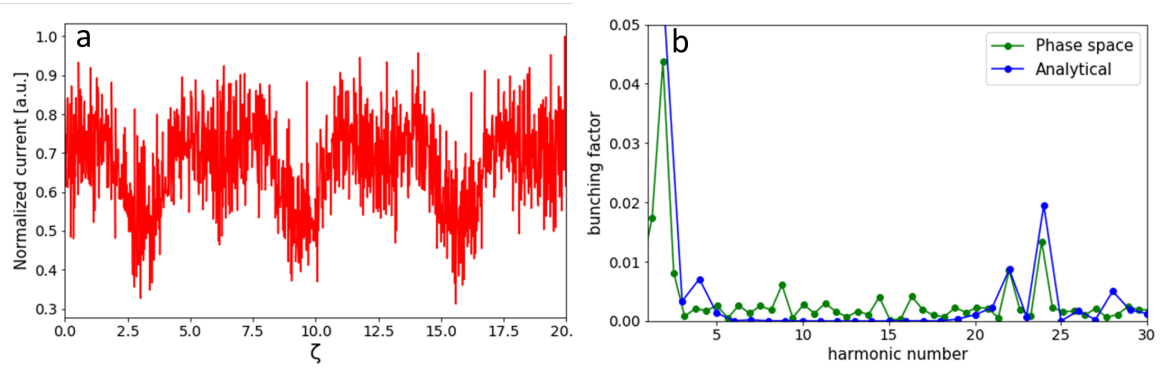

Figure 9.11: (a) Density distribution after the second dispersive section. (b) Bunching factor from the phase space (green) and Eq. (9.14). λ_1 = 266 nm, λ_2 = 266 nm, $\Delta E_1 = 5\sigma_E$, $\Delta E_2 = 9\sigma_E$, $\phi = 0$, $R_{56}^{(1)}$ = 2 mm, $R_{56}^{(1)}$ = 0.08 mm.

Figure 9.12 presents the power along the undulator axis (a) and the spectral profile power simulated using GENESIS. At the entrance of the radiator, the maximum bunching factor at 11 nm is about of 2%. The saturation is reached within only one undulator section tuned at 36 nm, and the maximum peak power is of 30 MW, with a RMS width of about 3 fs. This ultra-short pulse is obtained because the initial bunching factor is only significant when the second laser power is near its maximum.

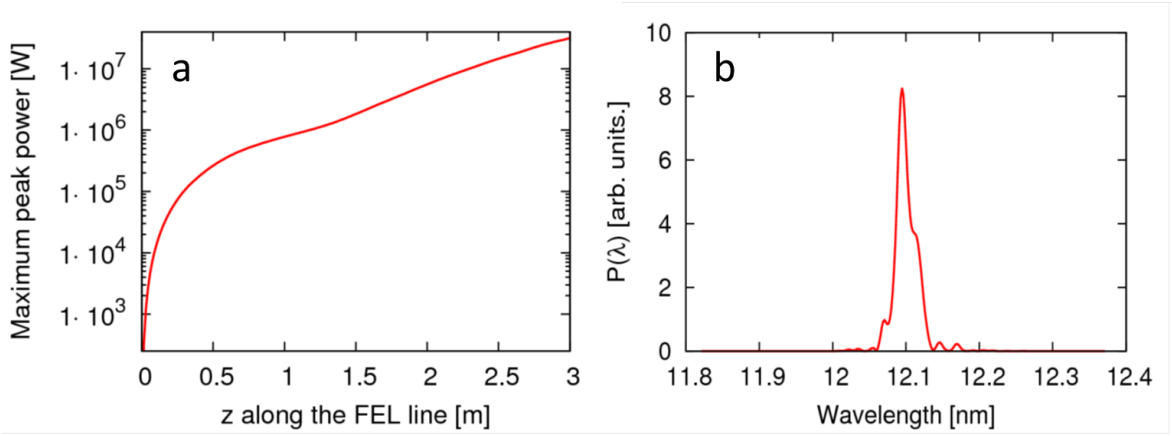

Figure 9.12: GENESIS simulation: Power growth along the undulator section (a) and the power profile (b).

9.4.4 Bunching at 4 nm

An energy modulation amplitude of 5 times the energy spread is set for both modulators. Using Eqs. (9.22) for n = -1 tune, the first and second chicane strength are calculated to be 8.4 mm and 0.13 mm, respectively, to achieve a bunching at the 66^{th} harmonic. Figure 9.13-a shows the density distribution of the electron beam after the second dispersive section. Figure 9.13-b presents the bunching factor, where it is ~3% at the 66^{th} harmonic (4 nm).

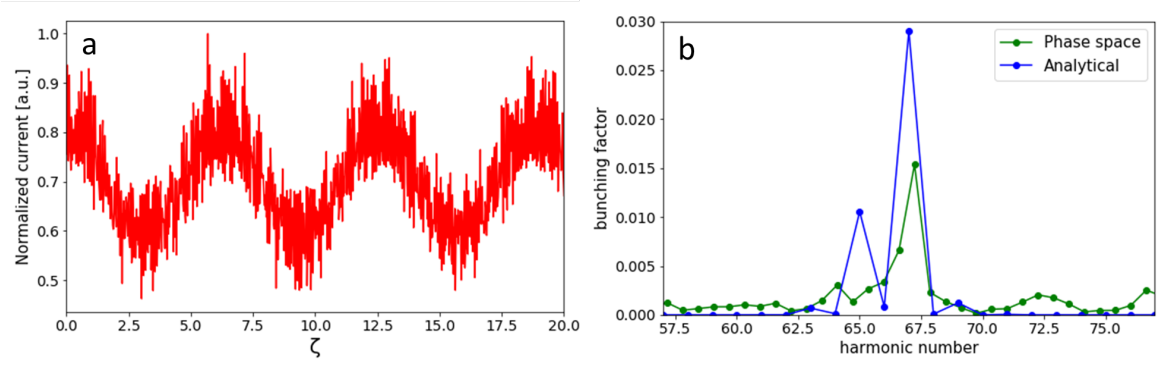

Figure 9.13: (a) Density distribution after the second dispersive section. (b) Bunching factor from the phase space (green) and Eq. (9.14). λ_1 = 266 nm, λ_2 = 266 nm, $\Delta E_1 = 5\sigma_E$, $\Delta E_2 = 5\sigma_E$, $\phi = 0$, $R_{56}^{(1)}$ = 8.4 mm, $R_{56}^{(1)}$ = 0.13 mm.

9.5 FERMI

The comparison between EEHG and HGHG configurations has been explored experimentally at FERMI, Trieste, the first seed FEL user facility.

A photo-injector composed of a photo-cathode gun and a booster Linac generates ~1.3 GeV electron beams [307]. The slice normalized emittance and relative energy spread rms at the Linac end are 1 mm.mrad and 0.01%, respectively. The energy can be varied to 1.1 GeV and 1.5 GeV by the radio-frequency Linac. The seeds are produced by a Ti:Sapphire laser system incorporating a single mode-locked oscillator and two separate regenerative amplifiers. The system delivers 792 nm wavelength and 5 mJ energy pulses with a repetition rate of 50 Hz. The first amplifier is frequency-tripled (UV - 264 nm) and sent to the first modulator. The infrared pulse generated by the second amplifier is transported and then frequency-tripled close to the second modulator. The

two UV pulses have a near Gaussian shape with a FWHM duration of 175 fs and 130 fs, respectively. The peak laser powers of the two seeds are estimated to be 43 MW and 90 MW, respectively, resulting in energy modulation amplitudes $A_1 = A_2 \approx 3$. The first chicane strength is set at $R_{56}^{(1)} = 2.38$ mm, and the second one is optimized depending on the operating harmonic using the following:

$$R_{56}^{(2)} = \frac{|n|}{h} R_{56}^{(1)} \tag{9.23}$$

Figure 9.14 presents the FEL gain at 7.3 nm. The gain curve exhibits an exponential growth with a gain length of ~1.9 m. An output peak power of 0.4 GW is estimated by dividing the pulse energy of 25 μJ over the estimated pulse duration (60 fs) obtained from simulations.

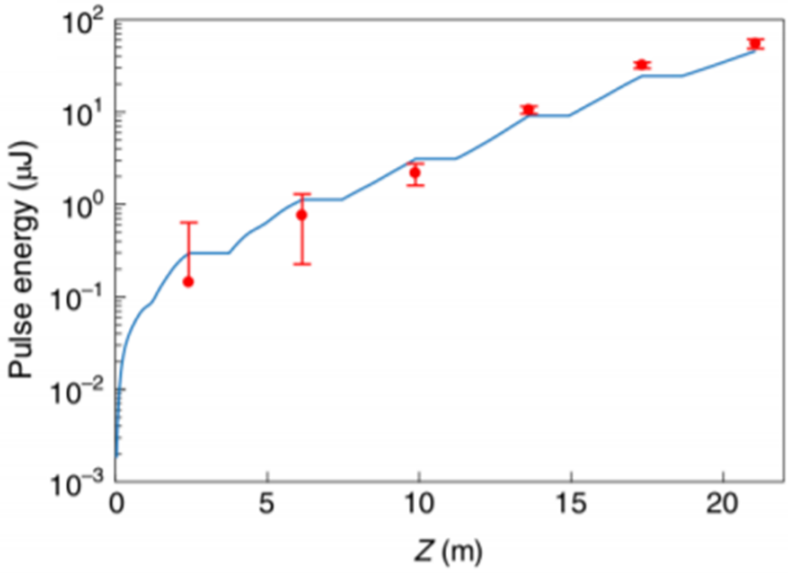

Figure 9.14: Simulated (blue line) and measured (red circles) FEL pulse energy at 7.3 nm wavelength.

Figure 9.15 shows a detailed data analysis of the spectra measured at the harmonics 36 (7.3 nm) and 45 (5.9 nm). The spectra exhibits a Gaussian shape with a relative central wavelength stability of $\sim 7 \times 10^{-5}$ and a relative spectral bandwidth of ~0.04% for the two harmonics. In comparison with the two-stage HGHG at the FERMI FEL, the EEHG configuration produces a much better spectra properties in terms of central wavelength stability and spectral bandwidth. This is especially true for high harmonics ($h = 45$), where the performance is affected by electron-beam imperfections that have a stronger influence in the HGHG operation scheme.

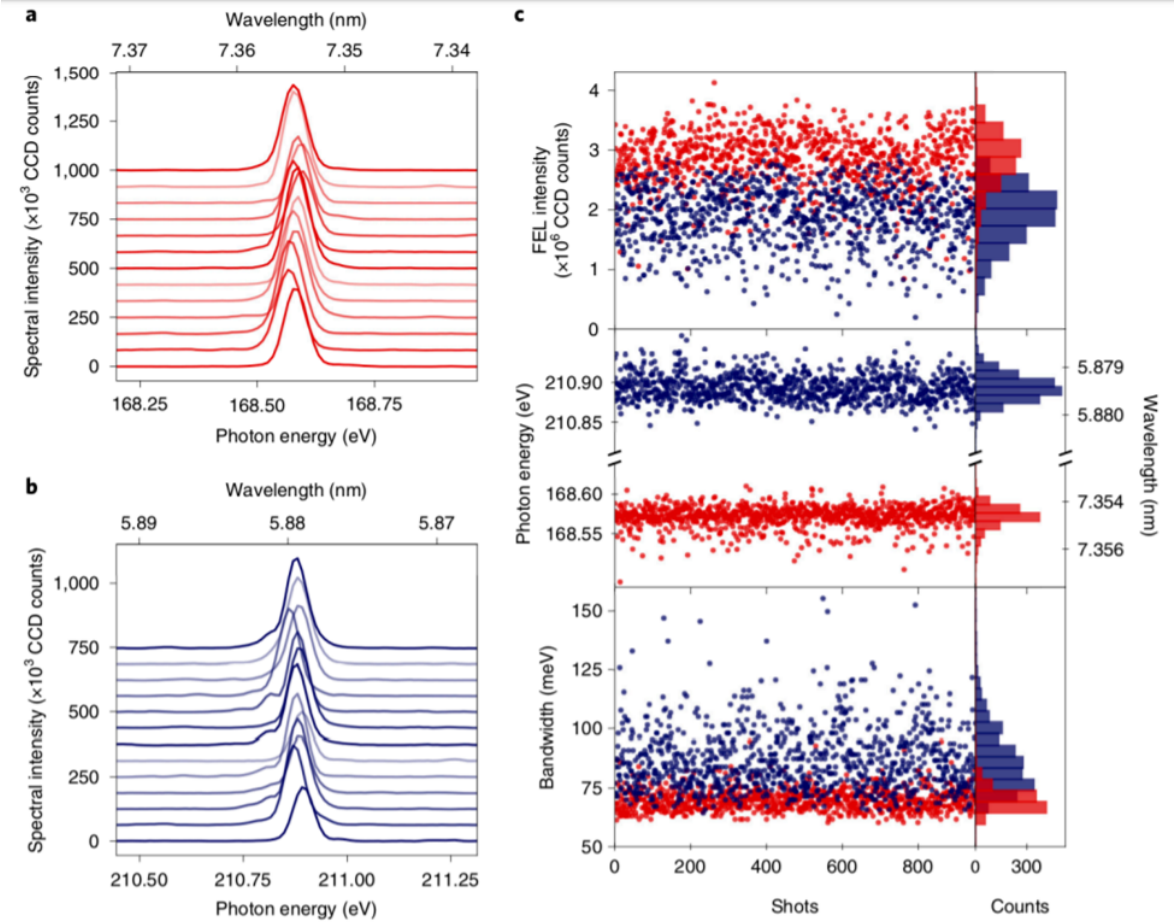

Figure 9.15: Single-shot spectra randomly chosen in a sequence of 1000 consecutive shots at 7.3 nm (a) and 5.9 nm (b) in the n = -1 tune. (c): Intensity (top), wavelength (middle) and bandwidth (bottom) for 7.3 nm (red) and 5.9 nm (blue).

For harmonics higher than 45, the undulator section does not allow for FEL saturation due to the increase in the gain length. So the electron beam energy is increased to 1.5 GeV to observe coherent emission with clean spectra at higher harmonics. Figure 9.16-a shows the spectrum at h = 84 of wavelength 3.1 nm with an insert of the raw measurement using a CCD camera. Emission at the 101 harmonic (i.e. 2.6 nm) was successfully observed as presented in Fig. 9.16-b. Due to the limited seed power and dispersive strength of the first chicane, we had to operate EEHG at n = -4 tune, resulting in a reduction of the bunching factor. Moreover, due to the absence of gain, the EEHG signal becomes comparable to the broadband spontaneous emission coming from the whole electron beam (see inset figure).

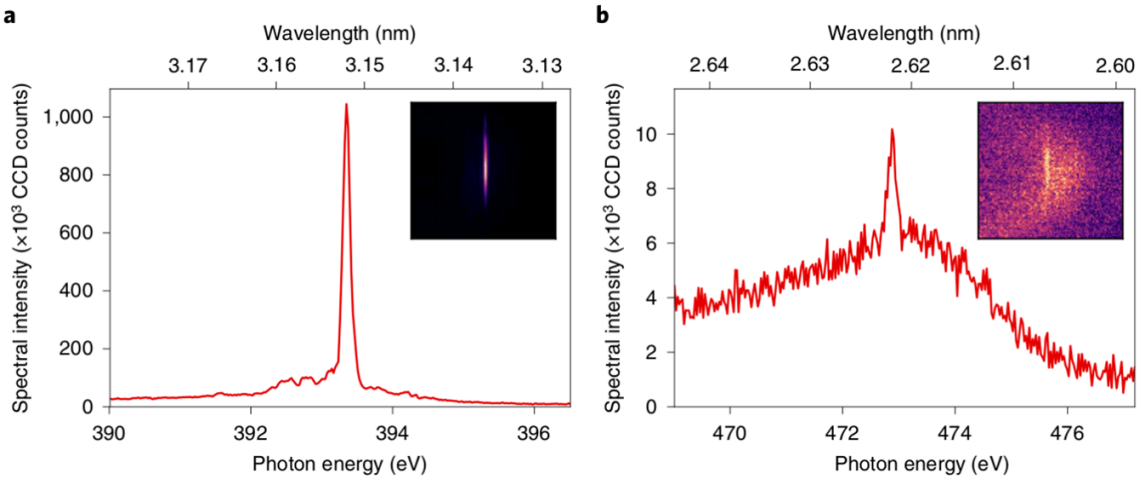

Figure 9.16: EEHG FEL signal at 3.1 nm (a) and 2.6 nm (b). Insets show the raw image measured with the CCD, where the background is dominated by the sponteneous emission in the 2.6 nm case.

3445 Fig. 9.17 displays measurements in the two-color operation, where the EEHG line was optimized for emission at $h = 45$ with the first four radiator sections tuned at 5.9 nm and the last two at 5.7 nm ($h = 46$). The spectra illustrates a similar shape and wavelength stability but with a lower pulse energy, because only part of the radiator was used for amplification of each harmonic.

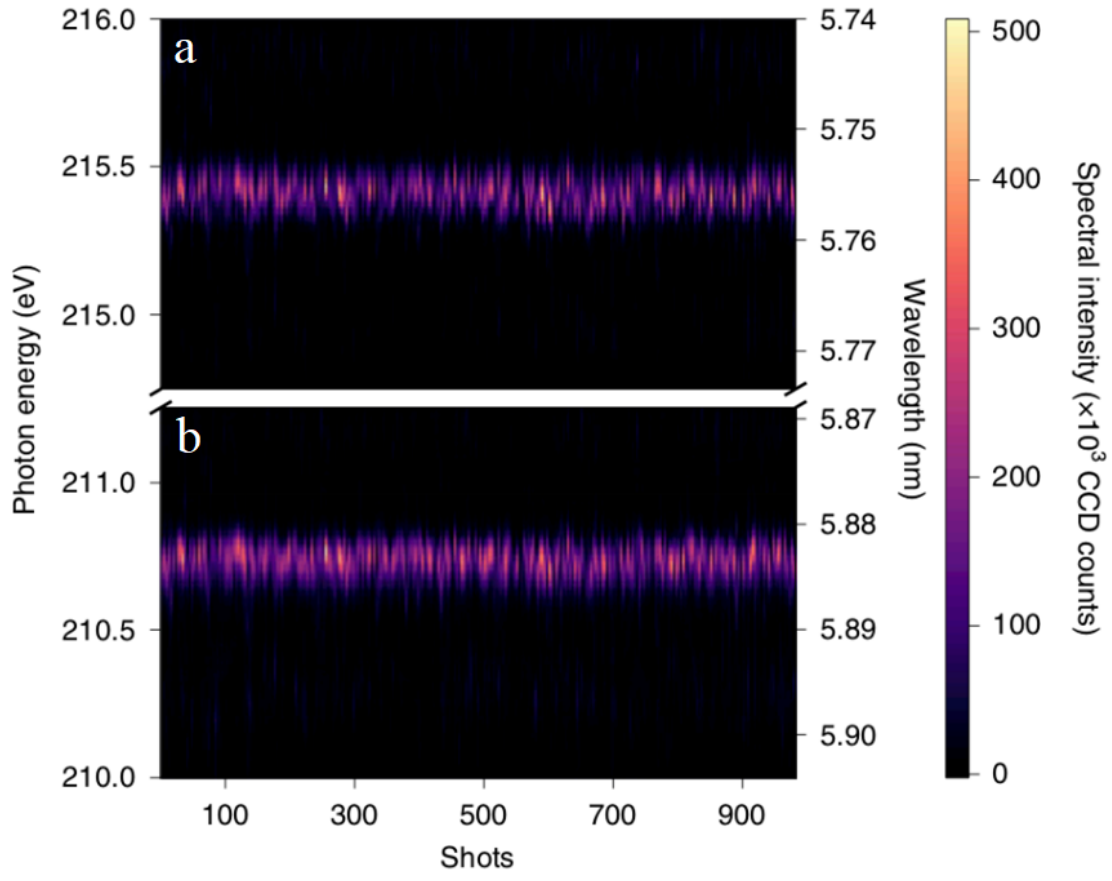

Figure 9.17: Consecutive single-shot spectra centered at 5.7 nm (a) and 5.9 nm (b) with n = -2 tune.

9.6 Conclusion

The EEHG FEL configuration enables to operate at high harmonics to achieve coherent emission at the 13^{th} and 24^{th} harmonics corresponding to wavelength of 20 nm and 11 nm, respectively, in the LUNEX5 test facility. At FERMI, Trieste, we were able to achieve an efficient bunching at the 36 and 45 harmonics of the seed laser using EEHG, resulting in the generation of intense, nearly fully coherent and stable pulses at 7.3 nm and 5.9 nm. A bunching at the 101 harmonic of wavelength 2.6 nm was also successful but due to the lack of flexibility on the first chicane strength and the available seed power, the emission experienced no gain but with a better spectral purity. In conclusion, FERMI FEL user facility in Trieste, Italy, was able to demonstrate the first high gain lasing using EEHG FEL in the soft X-ray region [305].

Chapter 10

Conclusion

My PhD work aimed at progressing towards advanced and compact free electron laser in the short wavelength region. It followed a three-fold approach :

- The qualification of laser plasma acceleration with the Free Electron Laser application.
- The development of ancillary equipments such as compact undulators (in the particular case of my PhD, cryogenic permanent magnet ones) and variable high gradient compact quadrupoles for handling the LPA divergence, that can be of interest as well for all accelerators requiring high focusing strength.
- The exploration of a particular Free Electron Laser configuration: the echo enabled harmonic generation using a mature conventional linear accelerator.

10.1 Review of the general context underlying my PhD work

First, the context on which my work relies on was drawn in chapter 1. The advent of laser made possible two essential ingredients of my work: the free electron laser (FEL) and the laser plasma acceleration (LPA). Indeed, the laser paved the way to the discovery of the FEL, where a combination of an electron beam and an undulator can act as gain medium generating intense coherent radiation with tunable wavelength. The first FEL concept examined was the so-called low gain FEL, where the electrons interact with an optical wave and get bunched in the longitudinal axis on the radiation wavelength scale, and transmit a portion of their energies to the wave in a coherent emission to achieve a small gain signal. Further studies on the high gain FEL theory showed that after a lethargy regime, the amplification enters a regime exhibiting an exponential growth, where the coherent radiation emitted by the bunched electrons enhances the bunching process furthermore and a positive feed-up is accomplished commonly knows as collective instability. Different configurations that improve the bunching by the use of an external laser seed have been discussed. For example echo-enabled harmonic generation (EEHG) can bunch the electron beam at high frequency contents and generate amplification at very short wavelength.

The laser discovery led also the concept of LPA five years later after the FEL invention. This new kind of electron source is based on focusing a high power laser on to a gas, where a plasma with intense electric field is induced, and electrons can achieve GeV energies in few cm scale. LPA has demonstrated its high potential advancing the accelerator field towards compactness.

The theoretical basis (analytical approach), on which my work relies on, has then been presented in chapter 2. The electron equation of motion in the presence of a magnetic field, describing the different paths that it undergoes as it passes through different magnetic structures, has been reported. A single energy electron beam is then taken into account, where the so-called Twiss parameters and beam emittance, that characterize the beam transport and quality along an

accelerator, have been introduced. The equations have been further expanded to include the electron beam dispersion and chromaticity that occur with a real beam having a spread in energy. The equations of motion can be described easily in a 6D phase space matrix as well as the effect of a dipole and quadrupole magnetic devices transformation matrices. The magnetic field produced by a planar undulator is derived alongside the orbit of the electrons traversing it. As electrons propagate in an undulator, the radiation adds constructively from one period to another resulting in a harmonic spectrum. The radiation intensity scales as N_u number of undulator periods with a relative bandwidth $\approx 1/N_u$. Afterwards, the low gain FEL pendulum equation has been derived starting with the Vlasov equation. As for the high gain, a more traditional classical approach is applied using Maxwell equations.

Then, I have introduced in chapter 3 the particular framework of my PhD, within the context of the LUNEX5 project and its associated R&D programs. The LUNEX5 test facility is composed of two kinds of accelerators, a conventional linear accelerator (Linac) and an LPA. The beam line is composed of two FEL seeding configurations, the high gain harmonic generation (HGHG) and EEHG, allowing for a comparison of the radiation quality. The state-of-art LPA electron source and problems have been discussed especially for FEL based applications, where the high energy spread and divergence require a specific beam line to manipulate the electron beam phase space to satisfy the FEL requirements and generate coherent emission. Different solutions to handle the divergence and energy spread have been presented. Concerning the divergence, high gradient quadrupoles can be used at an early stage to mitigate the emittance growth. A plasma lens can also be implemented. Regarding the energy spread, a magnetic chicane can be used to sort electrons in energy and thus reduce the energy slice or a transverse gradient undulator generating a linear deviation of the magnetic field along the horizontal axis can compensate the energy spread effect on the FEL performance. The first step of the FEL is to characterize the undulator radiation also referred to as spontaneous emission. A brief state-of-art of the different measurements of spontaneous emission based LPA at different laboratories have been introduced with properties that do not yet reach the achievable properties using a Linac. The COXINEL experiment is considered as a small LUNEX5 test experiment, where an LPA source is used to produce electrons around 200 MeV and try to demonstrate FEL in the UV range. The beam line is equipped with compact high gradient permanent magnet based quadrupoles to handle the high divergence, a de-mixing chicane to reduce the slice energy spread and a compact cryogenic undulator. Another set of quadrupoles are added between the chicane and the undulator. They take advantage of the electron beam energy-position correlation induced by the chicane and allow for the so-called supermatching optics, where each energy slice is focused at a different location inside the undulator. This focusing slippage can be synchronized with the FEL wave achieving a larger FEL power. Finally quick FEL evaluation is done using Ming Xi equations, which showed that FEL amplification is quite possible using the COXINEL baseline reference case, which turned out to be rather too optimistic.

10.2 Progress with performing compact ancillary equipment

I have studied two specific ancillary equipments. I have discussed in chapter 4, the progress of cryogenic permanent magnet undulators (CPMUs) at synchrotron SOLEIL, with optimization techniques to ensure a good magnetic field quality before the undulator commissioning, magnetic design modeling, measurements methods to characterize the undulator field (Hall probe connected to a rail for the local field, a rotating coil or stretched wire for the field integrals). Three CPMUs of period 18 mm and 2 m long have been constructed and optimized, in which two of them are installed at SOLEIL storage ring and one is used at COXINEL. Another CPMU of period 15 mm and 3 m long is still under construction and will be used later on in the LUNEX5 project. A study on the first CPMU of period 18 mm is done at the Nanoscopium beamline of SOLEIL. Measurements displayed that the undulator field quality is very good.

As mentioned above, the highly divergent electron beam generated from an LPA source can be handled with high gradient quadrupoles. In chapter 5, different permanent magnet based quadrupoles are examined, alongside new models designed using RADIA. The QUAPEVA, which is a tunable high gradient permanent magnet based quadrupole is also presented. The QUAPEVAs are intended for the COXINEL project and the LUNEX5 test facility in the case of the LPA. Modeling using RADIA and TOSCA softwares have been done alongside the magnetic field characterization using three measurements: rotating coil, stretched wire and pulsed wire. The design achieves a maximum gradient of 200 T/m with 90 T/m tunability. Seven systems with different magnetic lengths have been manufactured so far, a prototype, a first triplet currently under commisioning at COXINEL for an operation energy of 200-400 MeV, and a second triplet for a 400-800 MeV. These systems could also be of interest for other types of applications, such as diffraction limited storage ring, provided a better quality in terms of mulipole components, while relaxing the range of tunability.

10.3 Progress with the LPA qualification with the FEL application

For a proper understanding of the undulator radiation produced by the electrons at the end of the beam line, I started by examining it for the COXINEL baseline reference case with simulations using SRW code in chapter 6. I analyzed the dependence of the radiation properties (spectral flux, transverse shape and angular-spectral distribution) versus different observations conditions, and electron beam characteristics. I tried, as far as I can, to interpret with the analytic approach that I have introduced in Chapter 2. Having in mind the qualification of the LPA beam with the produced undulator radiation, I tested with simulations and different methods to estimate the electron beam parameters from the undulator radiation, in view of using them later on to extract the parameters from a real electron beam at COXINEL experiment.

Then, I discussed what we could achieve experimentally, starting first by describing in chapter 7 the COXINEL line, the electron beam quality and transport, leading to new parameters different from the ones used in the baseline reference case for the undulator radiation. The transport line is equipped with compact high gradient permanent magnet based quadrupoles to handle the high divergence, a de-mixing chicane to reduce the slice energy spread and a compact cryogenic undulator. Another set of quadrupoles are added between the chicane and the undulator. The electrons at the source, characterized with an electron spectrometer, exhibit a broad spectrum ranging from 50 MeV up to 200 MeV, which is very far from the baseline reference case. The divergence is also measured to be ~2-3 mrad. The charge arriving at the center of the undulator is one order of magnitude lower as well. Nevertheless, such a beam was first transported properly along the beam line, in adjusting independently position, dispersion and energy by taking advantage of interesting feature of the QUAPEVAs, i. e. adjustable magnetic center thanks to translation tables on which they are mounted, allowing for a beam pointing alignment compensation (BPAC), and to variable gradient, enabling for energy adjustment. Thanks to the corrected beam position and dispersion at any location in the transport line, it was then possible to step further for undulator radiation measurements. Due to the broad energy spread, a slit is introduced in the center of the chicane that helped us select a smaller range of energies and be able to characterize the undulator radiation.

Then, the measured LPA undulator radiation after a manipulation beam line has been discussed in chapter 8. The photon beam diagnostic line consists of a lens placed around 3.5 m from the undulator center that focuses the radiation into a UV spectrometer, equipped with a variable entrance slit, two concave mirrors, three gratings and finally a CCD camera. We have shown that the measured undulator radiation exhibits the distinguished properties currently observed on conventional accelerator light sources, with the particular spatio-spectral dependance leading to a moon-shape pattern. The proper handling of the energy of interest along the COX-

INEL line ensures a stability of the resonant wavelength within 2.4%. A 120 nm tunability of LPA based undulator radiation has been achieved by varying the undulator gap and electron beam energy. Furthermore, the control of the undulator radiation has been accomplished via chicane and slit combination, resulting in a small radiation bandwidth down to 5% FWHM. Furthermore, the methods introduced in chapter 6 to recover the electron beam properties are tested. In one particular day, the LPA laser had a low performance due to mirror pollution and misalignment in the laser optical transport, so the undulator radiation that exhibits a moon shape pattern, was spoiled and the spectra was dominated by shot-to-shot fluctuations. Thus, not much analysis could be done except for the wavelength tunability by adjusting the undulator gap. For other days, the laser was operating quite better, and the moon shape pattern was much defined and allowed us to do some analysis and extract some beam parameters up to a good estimation in comparison with the beam optics tracking code using the measured electron beam parameters at the source. Even though there is a satisfactory comparison between measurements and simulations using electron beam longitudinal and transverse distributions, that make us confident in future predictions of undulator radiation, the electron beam parameters are found to be slightly better from the ones deduced from the average of the distributions measured in conditions close to the photon measurements, and are reasonable considering the shot-to-shot fluctuations, the possible electron beam drifts and pointing changes, combined to uncertainties on the alignment. Undulator radiation can appear as a fine measurement tool of the electron beam quality, and a system that can provide a deeper insight on the transported electron beam along the line.

Because of the electron beam characteristics far from the baseline reference case, only low gain free electron laser type coherent emission could be possibly expected. A 266 nm seed and the undulator radiation were synchronised, transversely overlapped and spectrally tuned, but no coherent emission signal was observed. Further analysis indicates that the charge/MeV level is still not sufficient. An upgrade of the laser at LOA is under way, and possibilities offered with the electron beam performance achieved at CALA and Dresden HZDR are considered.

10.4 Progress with the EEHG configuration

The EEHG configuration was targeted from the beginning on the LUNEX5 project. It was aimed at being compared to the high gain harmonic generation (HGHG) since the very efficient up frequency conversion can provide a very compact solution for reaching short wavelengths. Unfortunately, the LUNEX5 is not funded yet and the experiment comparing EEHG and HGHG could not be done in France. Meanwhile, a EEHG / HGHG test experiment was in preparation at FERMI (Italy), and we could join the collaboration. The experiment took place in Spring and Summer 2018, and gave very promising results. High-gain and high-quality lasing using EEHG at the FERMI FEL down to wavelengths as short as 5.9 nm (211 eV, i.e. harmonic 45) was demonstrated. In comparison to the output produced via a two-stage HGHG scheme, EEHG shows both narrower and cleaner spectra with significantly less shot-to-shot central wavelength jitter and at the same time a comparable energy per pulse. Coherent emission was observed on harmonics from 84 to 10, indicating the possibility to extend the lasing to wavelengths as short as 2 nm (620 eV) or less in a more optimised setup, either by using EEHG directly, or with a cascade employing both EEHG and HGHG schemes. Such a scheme could also be considered for the LUNEX5 project. Besides, multi-color operation was also made possible with the EEHG, without the limitations due to the harmonic conversion of the first stage; EEHG appears, thanks to these results, very promising for achieving high quality compact FEL, via the interaction configuration.

10.5 Synthèse en français

L'avènement du laser a rendu possibles deux ingrédients essentiels de mon travail: le laser à électrons libres (LEL) et l'accélération du plasma laser (LPA). Les lasers à électrons libres (LEL) X sont aujourd'hui des sources lumineuses cohérentes et intenses utilisées pour des investigations multidisciplinaires de la matière.

Le laser a ouvert la voie à la découverte du laser à électrons libres, où la combinaison d'un faisceau d'électrons et d'un onduleur peut jouer le rôle de milieu amplificateur générant un rayonnement cohérent intense à longueur d'onde variable. Les études LEL ont d'abord porté sur les système à faible gain, où les électrons interagissent avec une onde optique, échangent en énergie, se regroupent en micro-paquets séparés par la longueur d'onde du rayonnement, émettent de façon cohérente et cèdent une partie de leur énergie à l'onde de lumière, qui est amplifiée. Des études théoriques ultérieures sur le régime de fort gain du LEL ont montré qu'après un régime de léthargie, l'amplification entre dans un régime présentant une croissance exponentielle, où le rayonnement cohérent émis par les électrons groupés renforçait la mise en micro-paquet et rétro-agissant ainsi sur le système d' instabilité collective. Différentes configurations peuvent être utilisées, comme l'oscillateur, l'injection externe d'une onde cohérente accordée spectralement à l'onduleur (seeding),ou l'émission spontanée auto-amplifiée (SASE : Self Amplified Spontaneous Emission). Le SASE présente une cohérence longitudinale limitée, car l'émission est générée à partir du bruit, tandis qu'un LEL injecté présente une haute pureté spectrale. Dans le cas de la génération d'harmoniques à gain élevé (HGHG : High Gain Harmonic Generation), le faisceau d'électrons passe à travers un onduleur où il est modulé en énergie, puis dans une chicane qui convertit la modulation d'énergie en modulation de densité, et permet l'émission cohérente dans le module d'onduleur suivant qui est accordé sur une harmonique du premier onduleur. La conversion en fréquence ne peut être d'ordre très élevé, car le processus nécessite une modulation trop importante de l'énergie qui conduirait à détériorer les performances du LEL. Un autre système de seeding avancé, l'echo (Echo Enabled Harmonic Generation, EEHG), composé de deux modulateurs et de deux chicanes, permet d'induire une modulation en densité d'électrons à haute fréquence et de générer une amplification à très courte longueur d'onde sans nécessiter de modulation importante de l'énergie et donc de puissance laser importante.

La découverte du laser a aussi ouvert la voie au concept d'accélération laser plasma (LPA) cinq ans plus tard après l'invention de la LEL. Ce nouveau type de source d'électrons est basé sur la focalisation d'une impulsion laser ultra-courte de haute puissance dans un milieu gazeux qui induit un champ de sillage suivant le trajet du laser, dans lesquels les électrons sont éloignés de l'impulsion laser, alors que les ions ne sont pas affectés en raison de leur masse importante. Les électrons piégés dans le les champ de sillage du laser subissent un champ électrique intense et peuvent atteindre des énergies GeV à une échelle de quelques cm. Ce nouveau schéma d'accélération est maintenant capable de produire une accélération de quelques GeV/cm, bien supérieure à celle des accélérateurs linéaires radiofréquence. Il ouvre la voie vers des accélérateurs compacts.

L'équation du mouvement des électrons en présence d'un champ magnétique est décrite lors du passage à travers différentes structures magnétiques. Les paramètres de Twiss et l'émittance du faisceau, qui caractérisent le transport et la qualité d'un faisceau mono-énergétique le long d'un accélérateur, sont introduits. Les équations sont étendues pour inclure la dispersion et la chromaticité du faisceau d'électrons qui se produisent avec un faisceau réel ayant une dispersion d'énergie. Les équations de mouvement peuvent être décrites avec une matrice d'espace de phase 6D, les matrices de transfert associées aux dispositifs magnétiques dipolaires et quadripolaires. Le champ magnétique périodique permanent produit par un onduleur plan est ensuite décrit et la trajectoire des électrons le traversant calculée. Lorsque les électrons se propagent dans un onduleur, le rayonnement s'ajoute de manière constructive d'une période à l'autre, conduisant à

un spectre de raies avec une longueur d'onde fondamentale et ses harmoniques. L'intensité de rayonnement est exprimée en N_u nombre de périodes d'onduleur avec une largeur de bande relative $\sim 1/N_u$. Ensuite, l'équation du pendule LEL à faible gain a été dérivée en commençant par l'équation de Vlasov. En ce qui concerne le gain élevé, une approche classique plus traditionnelle est appliquée en utilisant les équations de Maxwell.

Ce travail de thèse a été mené dans le cadre des programmes de R&D du projet LUNEX5 (Laser à électrons libres Utilisant un Nouvel accélérateur pour l'Exploitation du rayonnement X de 5e génération) de démonstrateur LEL avancé et compact avec applications utilisatrices pilotes.

L'installation de test LUNEX5 est composée de deux types d'accélérateurs, un accélérateur linéaire conventionnel (Linac) et un LPA. LUNEX5 comprend un linac supraconducteur de 400 MeV de haute cadence (10 kHz) pour l'étude de schémas LEL avancés, et un LPA pour sa qualification par une application LEL. La ligne LEL utilise une configuration d'injection avancée dans la plage spectrale 40-4 nm par génération d'harmoniques à gain élevé (HGHG) et le schéma d' écho (EEHG), ermettant de comparer la qualité du rayonnement. Des onduleurs compacts cryogéniques à champ élevé de courte période courte sont employés. L'étude de solutions adaptées aux applications LEL compactes et avancées est donc examinée. La source d'électrons LPA à la pointe de la technologie et ses problèmes ont été discutés en particulier pour les applications basées sur la LEL, où la dispersion d'énergie élevée et la divergence nécessitent une ligne de faisceau spécifique pour manipuler l'espace de phase du faisceau d'électrons afin de satisfaire les exigences de la LEL et de générer une émission cohérente. Différentes solutions pour gérer la divergence et la propagation de l'énergie ont été présentées. En ce qui concerne la divergence, des quadripôles de haut gradient jusqu'à 100 T / m peuvent être utilisés à juste après la source pour prévenir la croissance de l'émittance. Une lentille plasma peut également être mise en œuvre, elle présente un champ magnétique azimutal généré à partir du faisceau d'électrons, atteignant des gradients allant jusqu'à kT / m. En ce qui concerne la dispersion en énergie, une chicane magnétique peut être utilisée pour trier les électrons en énergie et réduire ainsi la dispersion en énergie par tranche. Une autre solution consiste à installer un onduleur à gradient transverse (TGU) générant une déviation linéaire du champ magnétique le long de l'axe horizontal. En plaçant un dipôle devant le TGU, le faisceau d'électrons est dispersés horizontalementet chaque tranche d'énergie subit un champ magnétique différent et émet à la longueur d'onde de résonance. Cette technique peut compenser l'effet de la dispersion en énergie sur les performances LEL. La première étape vers la démonstration LEL consiste à caractériser le rayonnement de l'onduleur, également appelé émission spontanée. Un bref état de l'art des différentes mesures de LPA à base d'émissions spontanées dans différents laboratoires est introduit, avec des propriétés qui n'atteignent pas encore celles obtenues avec un linac. L'expérience COXINEL est considérée comme une petite expérience de test LUNEX5, dans laquelle une source de LPA est utilisée pour produire des électrons d'environ 200 MeV et pour essayer de démontrer un effet LEL dans l' UV. La ligne de faisceau est équipée de quadripôles à aimants permanents compacts à gradient élevé pour gérer la divergence élevée, d'une chicane de dcomprssion pour réduire la dispersion d'énergie par tranche et d'un onduleur cryogénique compact. Un autre ensemble de quadripôles est ajouté entre la chicane et l'onduleur. Ils tirent parti de la corrélation position-énergie du faisceau d'électrons induite par la chicane pour focaliser chaque tranche d'énergie à un emplacement différentselon la direction logitudinale de l'onduleur, dans l'optique dite"chromatic matching". Le glissement de focalisation peut être synchronisé avec l'onde optique pour obtenir une puissance LEL plus grande. Des calculs analytiques ont été effectués pour différents paramètres initiaux du faisceau d'électrons et une évaluation rapide de la LEL est effectuée à l'aide d'équations de Ming Xi afin d'étudier les effets de chaque paramètre individuellement sur les performances duLEL. Le cas de référence dde COXINEL a montré que l'amplification LEL est tout à fait possible.

J'ai d'abord étudié deux équipements spécifiques.

Un premier aspect concerne la réduction du milieu de gain du LEL (électrons dans l'onduleur), le raccourcissement de la période se faisant au détriment du champ magnétique. Les onduleurs cryogéniques compacts à base d'aimants permanents cryogéniques (CPMU), dans lesquels les performances de l'aimant sont améliorées à température cryogénique sont étudiés. Je discute d'abord l'évolution des onduleurs cryogéniques au synchrotron SOLEIL, ainsi que les techniques d'optimisation permettant de garantir une bonne qualité de champ magnétique avant la mise en service de l'onduleur, la modélisation magnétique et les méthodes de mesure permettant de caractériser le champ de l'onduleur (sonde de Hall connecté à un rail pour le champ local, bobine rotative ou un fil tendu pour les intégrales de champ). Trois CPMU de 18 mm et de 2 m de long ont été construits et optimisés. Deux d'entre eux sont installés sur l'anneau de stockage SOLEIL et un est utilisé dans l'expérience COXINEL. Pour le premier CPMU, deux types de modules ont été utilisés: un module avec un aimant seul ou un aimant entouré de deux pôles. Les autres CPMU utilisent un seul type de module, un aimant entouré de deux demi-pôles. De plus, le processus de shimming est effectué avant l'assemblage, ce qui nous a permis d'atteindre une petite erreur de phase sans qu'il soit nécessaire d'effectuer un shimming individuel après l'assemblage. Actuellement, une unité CPMU de 15 mm et de 3 m de long est en construction et sera utilisée ultérieurement dans le projet LUNEX5. Une étude sur le premier CPMU de période 18 mm fut réalisée sur la ligne de lumière Nanoscopium de SOLEIL. Les spectres de la ligne de faisceau comparés aux spectres simulés (SRW) à partir des mesures magnétiques présentent un bon accord prouvant que nos mesures magnétiques à température cryogénique sont bien précises. Une autre comparaison entre les spectres mesurés et les spectres simulés d'un onduleur idéal confirment que les CPMU ont une très haute qualité de champ.

De plus, omme mentionné ci-dessus, le faisceau d'électrons généré à partir d'une source de LPA est très divergent et recquiert l'emploi de quadripôles de haut gradient. Après avoir examiné différents quadripôles à aimants permanents, j'ai conçu de nouveaux modèles à l'aide de RADIA. Le QUAPEVA, qui est un quadripôle à aimant permanent accordable à gradient élevé, est également présenté. Les QUAPEVA sont destinés au projet COXINEL et à l'installation de test LUNEX5 dans le cas de la ligne de lumière LPA. Le QUAPEVA consiste en un anneau hybride de Halbach à gradient fixe (155 T / m) entouré de quatre aimants cylindriques capables de tourner autour de leur axe pour assurer l'accordabilité du gradient (50%). La modélisation à l'aide des logiciels RADIA et TOSCA a été effectuée parallèlement à la caractérisation du champ magnétique à l'aide de trois mesures: bobine tournante, fil nedu et fil pulsé. La conception atteint une pente maximale de 200 T / m avec une adaptabilité de 90 T / m. Jusqu'à présent, sept systèmes de longueurs magnétiques différentes ont été fabriqués: un prototype, un premier triplet actuellement mis en service à COXINEL pour une énergie de fonctionnement de 200 à 400 MeV et un second triplet pour un fonctionnement à 400-800 MeV. Les calculs analytiques du gradient produit sont présentés et comparés à des simulations. Avant l'installation du triplet QUAPEVA à COXINEL, les aimants cylindriques doivent être étalonnés pour garantir une excursion du centre magnétique faible. Avant l'étalonnage, il était de l'ordre de ± 100 µ m et a chuté à ± 10 µ m après étalonnage.

Une partie du travail est développée dans le cadre l'expérience de R&D COXINEL visant à démontrer l'amplification LEL à l'aide d'un LPA. La ligne permet de manipuler les propriétés des faisceaux d'électrons produits (dispersion en énergie, divergence, variation de pointé) avant d'être utilisées pour des applications de sources lumineuses. Le faisceau d'électrons généré est très divergent et nécessite une bonne manipulation juste après la source avec des quadrupôles forts placés immédiatement après la génération d'électrons. Ainsi, des quadrupôles innovants à aimants permanents de gradient élevé réglable appelés QUAPEVA, sont développés. Ils sont optimisés avec le code RADIA et caractérisées avec trois mesures magnétiques. Un gradient de 200 T/m avec une variabilité de 50% est obtenu tout en maintenant une excursion du centre magné-

tique réduite à ± 10 µm, qui a permis un alignement par compensation de pointé du faisceau dans COXINEL grâce au centre magnétique variable des systèmes, avec un faisceau bien focalisé sans dispersion. Les QUAPEVA constituent des systèmes originaux dans le paysage des quadrupôles à de gradient élevé et variable développés jusqu'à présent.

Pour bien comprendre le rayonnement de l'onduleur produit par les électrons à la fin de la ligne de faisceau, j'ai commencé par examiner le cas de référence de COXINEL au moyen de simulations utilisant le code SRW. J'ai analysé la dépendance des propriétés du rayonnement (flux spectral, distribution transversale et distribution angulo-spectrale) selon différentes conditions d'observation et caractéristiques du faisceau d'électrons. J'ai essayé, dans la mesure du possible, d'interpréter avec l'approche analytique que j'ai introduite précédemment. Gardant à l'esprit la qualification du faisceau LPA avec le rayonnement produit par l'onduleur, j'ai testé en simulations différentes méthodes pour estimer les caractéristiques du faisceau d'électrons à partir des paramètres du rayonnement de l'onduleur, en vue de leur utilisation ultérieure pour extraire les paramètres d'un faisceau d'électrons réels dans le cas de l'expérience COXINEL.

Ensuite, j'ai discuté de ce que nous pouvions réaliser expérimentalement, en commençant par décrire la ligne COXINEL, la qualité et le transport du faisceau d'électrons, ce qui a conduit à des paramètres bien différents de ceux utilisés dans le cas de référence pour le rayonnement de l'onduleur. La ligne de transport est équipée de quadripôles à aimant permanent compacts à gradient élevé pour gérer la divergence élevée, d'une chicane de décompression pour réduire la dispersion d'énergie par tranche et d'un onduleur cryogénique compact. Un autre ensemble de quadripôles est ajouté entre la chicane et l'onduleur. Les électrons à la source, caractérisés par un spectromètre à électrons, présentent un large spectre allant de 50 MeV à 200 MeV, ce qui est très éloigné du cas de référence de base de 1% rms. La divergence est également mesurée à $2-3$ mrad, soit le double de la valeur dans le cas de référence. La charge qui arrive au centre de l'onduleur est également inférieure d'un ordre de grandeur. Néanmoins, un tel faisceau a tout d'abord été correctement transporté le long de la ligne de faisceau, en ajustant indépendamment la position, la dispersion et l'énergie en tirant parti des caractéristiques intéressantes des QUAPEVA, à savoir un centre magnétique réglable grâce aux tables de translation sur lesquelles ils sont montés, permettant ainsi de mettre en œuvre une méthode de compensation d'alignement et de pointé (BPAC) et au gradient variable permettant l'ajustement de l'énergie. Grâce à la position et à la dispersion du faisceau corrigées à n'importe quel endroit de la ligne de transport, il était alors possible de poursuivre par la mesure du rayonnement des onduleurs. En raison de la large dispersion en énergie, une fente est introduite au centre de la chicane, ce qui nous a permis de sélectionner une gamme d'énergies plus petite et de pouvoir caractériser le rayonnement de l'onduleur.

Les résultats majeurs de mes travaux portent sur l'observation du rayonnement d'onduleur monochromatique ajustable sur la ligne COXINEL.

Le rayonnement mesuré de l'onduleur LPA après une ligne de faisceau de manipulation est ensuite présenté.

Au cours de RUN3, une caméra CCD a été installée à l'extrémité de la ligne de faisceau pour imager la distribution transverse du faisceau de photons. Trois filtres interférentiels optiques ont été appliqués à la caméra et des mesures ont été effectuées pour différents entrefers d' onduleurs. Les mesures ont été comparées aux simulations et ont montré une bonne dépendance de l'intensité intégrée par rapport à l'entrefer de l' onduleur. En l'absence de filtre, l'intensité présente une décroissance exponentielle en fonction de l'entrefer. Pour les deux filtres centrés autour de 256 nm et 300 nm, le même comportement est mesuré, mais avec une intensité inférieure à celle du cas sans filtre. Pour le filtre centré autour de 200 nm, qui est la longueur d'onde de résonance pour un enterfer de 5 mm à 5.5 mm, l'évolution est assez différente : il commence avec une intensité plus faible puis augmente en raison du plus grand flux de rayonnement hors axe que ceux sur l'axe.

Au cours des runs suivants, la ligne de diagnostic à faisceau de photons a consisté en un spectromètre UV, équipé d'une fente d' entrée variable, de deux miroirs concaves, de trois réseaux et enfin d'une caméra CCD installée à l'extrémité de la ligne de faisceau. En raison de la faible charge du faisceau d'électrons atteignant l'onduleur, une lentille a été placée à environ 3,5 m du centre de l'onduleur afin de focaliser le rayonnement dans le spectromètre. Nous avons montré que le rayonnement de l'onduleur mesuré présente les propriétés caractéristiques actuellement observées sur les sources lumineuses sur accélérateur classiques, la dépendance spatio-spectrale particulière conduisant à un pattern en forme de lune dû au rayonnement excentré décalé vers le rouge. Le traitement correct de l'énergie d'intérêt le long de la ligne COXINEL assure une stabilité de la longueur d'onde résonante inférieure à 2.4% qui a été améliorée d'un facteur 5 par rapport au run précédent. Une accordabilité de 120 nm du rayonnement de l'onduleur sur LPA a été obtenue en faisant varier l'intervalle de l'onduleur et l'énergie du faisceau d'électrons. Les données mesurées ont été comparées à la théorie et montrent un bon accord. En outre, le contrôle du rayonnement de l'onduleur a été réalisé via une combinaison chicane-fente, ce qui a permis d'obtenir une faible largeur de bande de raie pouvant atteindre 5% FWHM, valeur minimale obtenue jusqu'à présent avec un faisceau d'électrons à base de LPA. De plus, les méthodes présentées auparavant pour estimer les propriétés du faisceau d'électrons sont testées. Un jour en particulier, les performances du laser LPA étaient médiocres en raison de la pollution des miroirs et du désalignement du transport optique du laser. La distribution spatio-spectrale en forme de lune de l'onduleur était altéré. Ainsi, peu d'analyses pouvaient être effectuées à l'exception de l'accordabilité en longueur d'onde en ajustant l' entrefer de l' onduleur. Pour les autres jours, le laser fonctionnait plutôt mieux et la forme de la lune était bien définie et nous permettait de faire une analyse et d'extraire certains paramètres du faisceau jusqu'à obtenir une bonne estimation par rapport au code de l'optique du faisceau.

Même s'il existe un accord satisfaisant entre les mesures et les simulations utilisant des distributions longitudinales et transverses d'un faisceau d'électrons, ce qui nous laisse confiants dans les prévisions futures du rayonnement des onduleurs, les paramètres du faisceau d'électrons se révèlent légèrement supérieurs à ceux déduits de la moyenne des distributions mesurées dans des conditions proches des mesures de photons, et sont raisonnables compte tenu des fluctuations coup par coup, des dérives possibles du faisceau d'électrons et des changements de pointé, combinés à des incertitudes sur l'alignement. Le rayonnement de l'onduleur peut apparaître comme un outil de mesure précis de la qualité du faisceau d'électrons et un système capable de fournir des informations plus détaillées sur le faisceau d'électrons transporté le long de la ligne.

En raison des caractéristiques du faisceau d'électrons éloignées du cas de référence, seule une émission cohérente du type laser à électrons libres à gain libre pourrait éventuellement être attendue. Une seed à 266 nm et le rayonnement de l'onduleur ont été synchronisés, superposés transversalement et spectralement accordés, mais aucun signal d'émission cohérent n'a été observé. Une analyse plus poussée indique que le niveau de charge / MeV n'est toujours pas suffisant. Une mise à niveau du laser à LOA est en cours et les possibilités offertes par les performances du faisceau d'électrons obtenues à CALA et à Dresden HZDR sont envisagées.

Pour terminer, je rapport les avancées obtenues en vue d' un LEL compact avec un linac conventionnel. La configuration EEHG a été ciblée dès le début sur le projet LUNEX5. Il visait à être comparé au HGHG car la conversion très efficace en fréquence peut fournir une solution très compacte pour atteindre de courtes longueurs d'onde. Malheureusement, le projet LUNEX5 n'est pas encore financé et l'expérience de comparaison entre EEHG et HGHG n'a pas pu être réalisée en France. Pendant ce temps, une expérience de test EEHG / HGHG était en préparation à FERMI (Italie) et nous pouvions nous joindre à la collaboration. L'expérience a eu lieu au printemps et à l'été 2018 et a donné des résultats très prometteurs. Un amplification laser avec gain élevé et

de haute qualité utilisant la configuration EEHG à FERMI LEL jusqu'à des longueurs d'onde aussi courtes que 5,9 nm (211 eV, c'est-à-dire harmonique 45) ont été démontrés. En comparaison avec le schéma HGHG à deux étages, l'EEHG présente des spectres plus étroits, avec une gigue de longueur d'onde centrale coup sur coup nettement inférieure, ainsi qu'une énergie comparable par impulsion. Une émission cohérente a été observée sur les harmoniques de 84 à 10 nm, indiquant la possibilité d'étendre le laser à des longueurs d'onde aussi courtes que 2 nm (620 eV) ou moins dans une configuration plus optimisée, soit en utilisant directement le mode EEHG, soit avec une cascade utilisant une configuration EEHG suivie d'un schéma HGHG. En outre, un gain faible de LEL a été observé à l'harmonique 101 (2.8 nm) à l'aide du schéma EEHG. Un tel schéma pourrait également être envisagé pour le projet LUNEX5. De plus, le fonctionnement multicolore a également été rendu possible avec la configuration EEHG, sans les limitations dues à la conversion harmonique du premier étage; Grâce à ces résultats, le schéma EEHG semble très prometteur pour obtenir une LEL compact de haute qualité, via la configuration d'interaction.

Bibliography

[1] Test infrastructure and accelerator research area preparatory phase. http://www.eu-tiara.eu/Phocea/Vie_des_labos/News/index.php?id_news=26. Accessed: 2010-09-30. 5

[2] Couprie, M.-E. & Filhol, J.-M. X radiation sources based on accelerators. *Comptes Rendus Physique* **9**, 487–506 (2008). 5

[3] Chen, J. *et al.* The uses of synchrotron radiation sources for elemental and chemical micro-analysis. *Nuclear Instruments and Methods in Physics Research Section B: Beam Interactions with Materials and Atoms* **49**, 533–543 (1990). 5

[4] Helliwell, J. Protein crystallography with synchrotron radiation. *Journal of Molecular Structure* **130**, 63–91 (1985). 5

[5] Suortti, P. & Thomlinson, W. Medical applications of synchrotron radiation. *Physics in Medicine & Biology* **48**, R1 (2003). 5

[6] Rugg, D. Synchrotron use for materials science and engineering—the next decade. *Philosophical Transactions of the Royal Society A: Mathematical, Physical and Engineering Sciences* **373**, 20130160 (2015). 5

[7] Madey, J. M. Stimulated emission of bremsstrahlung in a periodic magnetic field. *Journal of Applied Physics* **42**, 1906–1913 (1971). 5

[8] Emma, P. *et al.* First lasing and operation of an ångstrom-wavelength free-electron laser. *nature photonics* **4**, 641 (2010). 5

[9] Bostedt, C. *et al.* Linac coherent light source: The first five years. *Reviews of Modern Physics* **88**, 015007 (2016). 5

[10] Van De Graaff, R. J., Compton, K. & Van Atta, L. The electrostatic production of high voltage for nuclear investigations. *Physical Review* **43**, 149 (1933). 5

[11] Ising, G. Arkiv för matematik. *Astronomi och Fysik* **18** (1924). 5

[12] Paszkiewicz, J., Burrows, P. & Wuensch, W. Spatially resolved dark current in high gradient traveling wave structures. In *10th Int. Partile Accelerator Conf.(IPAC'19), Melbourne, Australia, 19-24 May 2019*, 2956–2959 (JACOW Publishing, Geneva, Switzerland, 2019). 5

[13] Döbert, S. Gradient limitations for high-frequency accelerators. Tech. Rep., SLAC National Accelerator Lab., Menlo Park, CA (United States) (2018). 5

[14] Lawrence, E. O. & Livingston, M. S. The production of high speed light ions without the use of high voltages. *Physical Review* **40**, 19 (1932). 5

[15] Tajima, T. & Dawson, J. M. Laser electron accelerator. *Physical Review Letters* **43**, 267 (1979). 7

[16] Malka, V. *et al.* Electron acceleration by a wake field forced by an intense ultrashort laser pulse. *Science* **298**, 1596–1600 (2002). URL http://science.sciencemag.org/content/298/5598/1596. http://science.sciencemag.org/content/298/5598/1596.full.pdf. 7

[17] Esarey, E., Schroeder, C. B. & Leemans, W. P. Physics of laser-driven plasma-based electron accelerators. *Rev. Mod. Phys.* **81**, 1229–1285 (2009). URL http://link.aps.org/doi/10.1103/RevModPhys.81.1229.

[18] Malka, V. Laser plasma accelerators. *Physics of Plasmas* **19**, 055501 (2012). URL http://dx.doi.org/10.1063/1.3695389. http://dx.doi.org/10.1063/1.3695389. 7

[19] Mangles, S. *et al.* Monoenergetic beams of relativistic electrons from intense laser-plasma interactions. *Nature* **431**, 535–538 (2004). 7, 8

[20] Geddes, C. *et al.* High-quality electron beams from a laser wakefield accelerator using plasma-channel guiding. *Nature* **431**, 538–541 (2004). 8

[21] Faure, J. *et al.* A laser-plasma accelerator producing monoenergetic electron beams. *Nature* **431**, 541–544 (2004). 7, 8

[22] Pukhov, A. & Meyer-Ter-Vehn, J. Laser wake field acceleration: the highly non-linear broken-wave regime. *Appl. Phys. B* **74**, 355 (2002). URL https://link.springer.com/article/10.1007/s003400200795. 7

[23] Faure, J. *et al.* A laser-plasma accelerator producing monoenergetic electron beams. *Nature* **431**, 541–544 (2004). URL http://dx.doi.org/10.1038/nature02963.

[24] Lu, W., Huang, C., Zhou, M., Mori, W. B. & Katsouleas, T. Nonlinear theory for relativistic plasma wakefields in the blowout regime. *Phys. Rev. Lett.* **96**, 165002 (2006). URL https://link.aps.org/doi/10.1103/PhysRevLett.96.165002. 7

[25] Sprangle, P., Tang, C.-M. & Esarey, E. Relativistic self-focusing of short-pulse radiation beams in plasmas. *IEEE Trans. Plasma Sci.* **15**, 145 (1987). URL http://ieeexplore.ieee.org/document/4316677/. 7

[26] Sun, G., Ott, E., Lee, Y. C. & Guzdar, P. Self-focusing of short intense pulses in plasmas. *The Physics of Fluids* **30**, 526–532 (1987). URL http://aip.scitation.org/doi/abs/10.1063/1.866349. http://aip.scitation.org/doi/pdf/10.1063/1.866349. 7

[27] Kalmykov, S., Yi, S. A., Khudik, V. & Shvets, G. Electron self-injection and trapping into an evolving plasma bubble. *Phys. Rev. Lett.* **103**, 135004 (2009). URL http://link.aps.org/doi/10.1103/PhysRevLett.103.135004. 7

[28] Kalmykov, S. Y. *et al.* Electron self-injection into an evolving plasma bubble: Quasi-monoenergetic laser-plasma acceleration in the blowout regime. *Physics of Plasmas* **18**, 056704 (2011). URL http://dx.doi.org/10.1063/1.3566062. http://dx.doi.org/10.1063/1.3566062. 7

[29] Esarey, E., Hubbard, R. F., Leemans, W. P., Ting, A. & Sprangle, P. Electron injection into plasma wakefields by colliding laser pulses. *Phys. Rev. Lett.* **79**, 2682–2685 (1997). URL https://link.aps.org/doi/10.1103/PhysRevLett.79.2682. 7

[30] Faure, J. *et al.* Controlled injection and acceleration of electrons in plasma wakefields by colliding laser pulses. *Nature* **444**, 737–739 (2006). 8

[31] Rechatin, C. *et al.* Observation of beam loading in a laser-plasma accelerator. *Phys. Rev. Lett.* **103**, 194804 (2009). URL https://link.aps.org/doi/10.1103/PhysRevLett.103.194804. 7, 8

[32] McGuffey, C. *et al.* Ionization induced trapping in a laser wakefield accelerator. *Phys. Rev. Lett.* **104**, 025004 (2010). URL http://link.aps.org/doi/10.1103/PhysRevLett.104.025004. 7, 8

[33] Pak, A. *et al.* Injection and trapping of tunnel-ionized electrons into laser-produced wakes. *Phys. Rev. Lett.* **104**, 025003 (2010). URL https://link.aps.org/doi/10.1103/PhysRevLett.104.025003.

[34] Pollock, B. B. *et al.* Demonstration of a narrow energy spread, ~ 0.5 GeV electron beam from a two-stage laser wakefield accelerator. *Phys. Rev. Lett.* **107**, 045001 (2011). URL http://link.aps.org/doi/10.1103/PhysRevLett.107.045001.

[35] Golovin, G. *et al.* Tunable monoenergetic electron beams from independently controllable laser-wakefield acceleration and injection. *Phys. Rev. ST Accel. Beams* **18**, 011301 (2015). URL https://link.aps.org/doi/10.1103/PhysRevSTAB.18.011301. 8

[36] Couperus, J. *et al.* Demonstration of a beam loaded nanocoulomb-class laser wakefield accelerator. *Nature communications* **8**, 487 (2017). 7

[37] Bulanov, S., Naumova, N., Pegoraro, F. & Sakai, J. Particle injection into the wave acceleration phase due to nonlinear wake wave breaking. *Phys. Rev. E* **58**, R5257–R5260 (1998). URL http://link.aps.org/doi/10.1103/PhysRevE.58.R5257. 7

[38] Faure, J., Rechatin, C., Lundh, O., Ammoura, L. & Malka, V. Injection and acceleration of quasimonoenergetic relativistic electron beams using density gradients at the edges of a plasma channel. *Physics of Plasmas* **17**, 083107 (2010). URL http://dx.doi.org/10.1063/1.3469581. http://dx.doi.org/10.1063/1.3469581. 8

[39] Geddes, C. G. R. *et al.* Plasma-density-gradient injection of low absolute-momentum-spread electron bunches. *Phys. Rev. Lett.* **100**, 215004 (2008). URL http://link.aps.org/doi/10.1103/PhysRevLett.100.215004.

[40] Gonsalves, A. J. *et al.* Tunable laser plasma accelerator based on longitudinal density tailoring. *Nat Phys* **7**, 862–866 (2011). URL http://dx.doi.org/10.1038/nphys2071. 8

[41] Samant, S. A., Upadhyay, A. K. & Krishnagopal, S. High brightness electron beams from density transition laser wakefield acceleration for short-wavelength free-electron lasers. *Plasma Physics and Controlled Fusion* **56**, 095003 (2014). URL http://stacks.iop.org/0741-3335/56/i=9/a=095003. 7

[42] Schmid, K. *et al.* Density-transition based electron injector for laser driven wakefield accelerators. *Phys. Rev. ST Accel. Beams* **13**, 091301 (2010). URL https://link.aps.org/doi/10.1103/PhysRevSTAB.13.091301. 7, 8

[43] Buck, A. *et al.* Shock-front injector for high-quality laser-plasma acceleration. *Phys. Rev. Lett.* **110**, 185006 (2013). URL https://link.aps.org/doi/10.1103/PhysRevLett.110.185006. 8

[44] Thaury, C. *et al.* Shock assisted ionization injection in laser-plasma accelerators. *Scientific Reports* **5**, 16310 (2015). URL http://dx.doi.org/10.1038/srep16310. 8, 168

[45] Massimo, F., Lifschitz, A. F., Thaury, C. & Malka, V. Numerical studies of density transition injection in laser wakefield acceleration. *Plasma Physics and Controlled Fusion* **59**, 085004 (2017). URL http://stacks.iop.org/0741-3335/59/i=8/a=085004. 7

[46] Leemans, W. P. *et al.* Multi-gev electron beams from capillary-discharge-guided subpetawatt laser pulses in the self-trapping regime. *Phys. Rev. Lett.* **113**, 245002 (2014). URL http://link.aps.org/doi/10.1103/PhysRevLett.113.245002. 7, 8

[47] Gonsalves, A. *et al.* Petawatt laser guiding and electron beam acceleration to 8 GeV in a laser-heated capillary discharge waveguide. *Phys. Rev. Lett.* **122**, 084801 (2019). 7

[48] Kim, H. T. *et al.* Enhancement of electron energy to the multi-gev regime by a dual-stage laser-wakefield accelerator pumped by petawatt laser pulses. *Phys. Rev. Lett.* **111**, 165002 (2013). URL https://link.aps.org/doi/10.1103/PhysRevLett.111.165002. 8

[49] Steinke, S. *et al.* Multistage coupling of independent laser-plasma accelerators. *Nature* **530**, 190–193 (2016). URL http://dx.doi.org/10.1038/nature16525. 8

[50] Faure, J. *et al.* A laser–plasma accelerator producing monoenergetic electron beams. *Nature* **431**, 541 (2004). 8

[51] Leemans, W. P. *et al.* GeV electron beams from a cm-scale accelerator. *Nature Phys.* **2**, 696–699 (2006).

[52] Kneip, S. *et al.* Near-gev acceleration of electrons by a nonlinear plasma wave driven by a self-guided laser pulse. *Phys. Rev. Lett.* **103**, 035002 (2009). URL https://link.aps.org/doi/10.1103/PhysRevLett.103.035002.

[53] Wang, X. *et al.* Quasi-monoenergetic laser-plasma acceleration of electrons to 2 gev. *Nature communications* **4**, 1988 (2013).

[54] Guillaume, E. *et al.* Electron rephasing in a laser-wakefield accelerator. *Phys. Rev. Lett.* **115**, 155002 (2015). URL https://link.aps.org/doi/10.1103/PhysRevLett.115.155002. 8

[55] Hansson, M., Aurand, B., Ekerfelt, H., Persson, A. & Lundh, O. Injection of electrons by colliding laser pulses in a laser wakefield accelerator. *Nuclear Instruments and Methods in Physics Research Section A: Accelerators, Spectrometers, Detectors and Associated Equipment* **829**, 99 – 103 (2016). URL http://www.sciencedirect.com/science/article/pii/S0168900216002461. 2nd European Advanced Accelerator Concepts Workshop - EAAC 2015. 8

[56] Burza, M. *et al.* Laser wakefield acceleration using wire produced double density ramps. *Phys. Rev. ST Accel. Beams* **16**, 011301 (2013). URL https://link.aps.org/doi/10.1103/PhysRevSTAB.16.011301. 8

[57] Hansson, M. *et al.* Down-ramp injection and independently controlled acceleration of electrons in a tailored laser wakefield accelerator. *Phys. Rev. ST Accel. Beams* **18**, 071303 (2015). URL https://link.aps.org/doi/10.1103/PhysRevSTAB.18.071303. 8

[58] Thaury, C. *et al.* Demonstration of relativistic electron beam focusing by a laser-plasma lens. *Nature communications* **6**, 6860 (2015). 8, 60

[59] M.E. Couprie, A. G. e. a. Undulator design for laser plasma based free electron laser. In preparation to be submitted to Physics Report journal. 9

[60] Elder, F., Gurewitsch, A., Langmuir, R. & Pollock, H. Radiation from electrons in a synchrotron. *Physical Review* **71**, 829 (1947). 9

[61] Onuki, H. & Elleaume, P. *Undulators, wigglers and their applications* (CRC Press, 2003). 9, 36

[62] Einstein, A. Zur quantentheorie der strahlung. *Phys. Z.* **18**, 121–128 (1917). 10

[63] Gordon, J. P., Zeiger, H. J. & Townes, C. H. The maser—new type of microwave amplifier, frequency standard, and spectrometer. *Physical Review* **99**, 1264 (1955). 10

[64] Townes, C. & Schawlow, A. Infrared and optical masers. *Phys. Rev* **112**, 1940–1949 (1958). 10

[65] Maiman, T. H. *et al.* Stimulated optical radiation in Ruby (1960). 10

[66] Jaegle, P. *et al.* X-ray laser experiment with a long recombining-plasma column. *EPL (Europhysics Letters)* **7**, 337 (1988). 10

[67] Corkum, P. B. Plasma perspective on strong field multiphoton ionization. *Physical review letters* **71**, 1994 (1993). 10

[68] L'Huillier, A. & Balcou, P. High-order harmonic generation in rare gases with a 1-ps 1053-nm laser. *Physical Review Letters* **70**, 774 (1993). 10

[69] Madey, J. M. Stimulated emission of bremsstrahlung in a periodic magnetic field. *Journal of Applied Physics* **42**, 1906–1913 (1971). 10, 47, 48

[70] Colson, W. Theory of a free electron laser. *Physics Letters A* **59**, 187–190 (1976). 10

[71] Palmer, R. B. Interaction of relativistic particles and free electromagnetic waves in the presence of a static helical magnet. *Journal of Applied Physics* **43**, 3014–3023 (1972). 10

[72] Courant, E., Pellegrini, C. & Zakowicz, W. High-energy inverse free-electron laser accelerator. In *AIP Conference Proceedings*, vol. 127, 849–874 (AIP, 1985). 10

[73] Trovo, M. *et al.* Operation of the european storage ring fel at elettra down to 190 nm. *Nuclear Instruments and Methods in Physics Research Section A: Accelerators, Spectrometers, Detectors and Associated Equipment* **483**, 157–161 (2002). 11

[74] Elias, L. R., Fairbank, W. M., Madey, J. M., Schwettman, H. A. & Smith, T. I. Observation of stimulated emission of radiation by relativistic electrons in a spatially periodic transverse magnetic field. *Physical Review Letters* **36**, 717 (1976). 11, 12

[75] Deacon, D. A. *et al.* First operation of a free-electron laser. *Physical Review Letters* **38**, 892 (1977). 11, 12

[76] Billardon, M. *et al.* First operation of a storage-ring free-electron laser. *Physical review letters* **51**, 1652 (1983). 11

[77] Newnam, B. E., Warren, R. W., Sheffield, R. L., Goldstein, J. C. & Brau, C. A. The los alamos free electron laser oscillator: Optical performance. *Nuclear Instruments and Methods in Physics Research Section A: Accelerators, Spectrometers, Detectors and Associated Equipment* **237**, 187–198 (1985). 11

[78] Couprie, M., Garzella, D. & Billardon, M. Operation of the Super-ACO free-electron laser in the UV range at 800 MeV. *EPL (Europhysics Letters)* **21**, 909 (1993). 11

[79] Prazeres, R., Glotin, F. & Ortega, J. Optical mode analysis on the CLIO infrared FEL. *Nuclear Instruments and Methods in Physics Research Section A: Accelerators, Spectrometers, Detectors and Associated Equipment* **341**, 54–58 (1994). 11

[80] Oepts, D., Van der Meer, A. & Van Amersfoort, P. The free-electron-laser user facility FELIX. *Infrared physics & technology* **36**, 297–308 (1995). 11

[81] Litvinenko, V. N., Park, S. H., Pinayev, I. V. & Wu, Y. Operation of the OK-4/Duke storage ring FEL below 200 nm. *Nuclear Instruments and Methods in Physics Research Section A: Accelerators, Spectrometers, Detectors and Associated Equipment* **475**, 195–204 (2001). 11

[82] Marsi, M. *et al.* Operation and performance of a free electron laser oscillator down to 190 nm. *Applied physics letters* **80**, 2851–2853 (2002). 11

[83] Couprie, M.-E. Historical survey of free electron lasers. *CERN Yellow Reports: School Proceedings* **1**, 195 (2018). URL https://e-publishing.cern.ch/index.php/CYRSP/article/view/473. 12

[84] Dobiasch, P., Meystre, P. & Scully, M. Optical wiggler free-electron x-ray laser in the 5 angstrom region. *IEEE journal of quantum electronics* **19**, 1812–1820 (1983). 12

[85] Girard, B. *et al.* Optical frequency multiplication by an optical klystron. *Physical review letters* **53**, 2405 (1984). 12

[86] Litvinenko, V., Burnham, B., Madey, J. & Wu, Y. Giant laser pulses in the DUKE storage ring UV FEL. *Nuclear Instruments and Methods in Physics Research Section A: Accelerators, Spectrometers, Detectors and Associated Equipment* **358**, 334–337 (1995). 12

[87] De Ninno, G. *et al.* Generation of ultrashort coherent vacuum ultraviolet pulses using electron storage rings: a new bright light source for experiments. *Physical review letters* **101**, 053902 (2008). 12

[88] Labat, M. *et al.* Coherent harmonic generation on UVSOR-II storage ring. *The European Physical Journal D* **44**, 187–200 (2007). 12

[89] Labat, M., Hosaka, M., Shimada, M., Katoh, M. & Couprie, M. Optimization of a seeded free-electron laser with helical undulators. *Physical review letters* **101**, 164803 (2008). 12

[90] Thorin, S., Brandin, M., Werin, S., Goldammer, K. & Bahrdt, J. Start-to-end simulations for a seeded harmonic generation free electron laser. *Physical Review Special Topics-Accelerators and Beams* **10**, 110701 (2007). 12

[91] Fauchet, A.-M., Feinstein, J., Gover, A. & Pantell, R. Visible and ultraviolet radiation generation using a gas-loaded free-electron laser. *IEEE journal of quantum electronics* **20**, 1332–1341 (1984). 12

[92] Kroll, N. M. & McMullin, W. A. Stimulated emission from relativistic electrons passing through a spatially periodic transverse magnetic field. *Physical Review A* **17**, 300 (1978). 12

[93] Dattoli, G., Marino, A., Renieri, A. & Romanelli, F. Progress in the hamiltonian picture of the free-electron laser. *IEEE Journal of Quantum Electronics* **17**, 1371–1387 (1981).

[94] Bonifacio, R., Casagrande, F. & Casati, G. Cooperative and chaotic transition of a free electron laser hamiltonian model. *Optics Communications* **40**, 219–223 (1982).

[95] Bonifacio, R., Casagrande, F. & Pellegrini, C. Hamiltonian model of a free electron laser. *Optics communications* **61**, 55–60 (1987). 12

[96] Kondratenko, A. & Saldin, E. Generating of coherent radiation by a relativistic electron beam in an ondulator. *Part. Accel.* **10**, 207–216 (1980). 12

[97] Bonifacio, R., Pellegrini, C. & Narducci, L. Collective instabilities and high-gain regime free electron laser. In *AIP Conference Proceedings*, vol. 118, 236–259 (AIP, 1984). 50

[98] Kim, K.-J. Three-dimensional analysis of coherent amplification and self-amplified spontaneous emission in free-electron lasers. *Physical review letters* **57**, 1871 (1986). 12

[99] Gold, S., Hardesty, D., Kinkead, A., Barnett, L. & Granatstein, V. High-gain 35-GHz free-electron laser-amplifier experiment. *Physical review letters* **52**, 1218 (1984). 13

[100] Orzechowski, T. *et al.* Microwave radiation from a high-gain free-electron laser amplifier. *Physical review letters* **54**, 889 (1985). 13

[101] Ayvazyan, V. *et al.* Generation of GW radiation pulses from a VUV free-electron laser operating in the femtosecond regime. *Physical review letters* **88**, 104802 (2002). 13

[102] Bonifacio, R. *et al.* Physics of the high-gain fel and superradiance. *La Rivista del Nuovo Cimento (1978-1999)* **13**, 1–69 (1990). 13, 50, 52, 69

[103] Hogan, M. *et al.* Measurements of gain larger than 10^5 at 12 μm in a self-amplified spontaneous-emission free-electron laser. *Physical Review Letters* **81**, 4867 (1998). 13

[104] Babzien, M. *et al.* Observation of self-amplified spontaneous emission in the near-infrared and visible wavelengths. *Physical Review E* **57**, 6093 (1998). 13

[105] Milton, S. *et al.* Observation of self-amplified spontaneous emission and exponential growth at 530 nm. *Physical review letters* **85**, 988 (2000). 13

[106] Andruszkow, J. *et al.* First observation of self-amplified spontaneous emission in a free-electron laser at 109 nm wavelength. *Physical Review Letters* **85**, 3825 (2000). 13

[107] Tremaine, A. *et al.* Experimental characterization of nonlinear harmonic radiation from a visible self-amplified spontaneous emission free-electron laser at saturation. *Physical review letters* **88**, 204801 (2002). 13

[108] Emma, P. *et al.* Demonstration of self-seeding in a hard-X-ray free-electron laser. In *Nat. Photonics*, vol. 6, 693 (2012). 13

[109] Ishikawa, T. *et al.* A compact X-ray free-electron laser emitting in the sub-ångström region. *nature photonics* **6**, 540 (2012). 13

[110] Kang, H.-S. *et al.* Fel performance achieved at PAL-XFEL using a three-chicane bunch compression scheme. *Journal of Synchrotron Radiation* **26** (2019). 13

[111] Milne, C. *et al.* SwissFEL: the Swiss X-ray free electron laser. *Applied Sciences* **7**, 720 (2017). 13

[112] Decking, W. & Weise, H. Commissioning of the european xfel accelerator. Tech. Rep. (2017). 13

[113] Yu, L.-H. *et al.* High-gain harmonic-generation free-electron laser. *Science* **289**, 932–934 (2000). 14, 16

[114] Zholents, A. A. Method of an enhanced self-amplified spontaneous emission for x-ray free electron lasers. *Physical Review Special Topics-Accelerators and Beams* **8**, 040701 (2005). 14

[115] Marinelli, A. Towards attosecond science at LCLS and LCLS-II. Presentation at Greece workshop titled Physics and Applications of High Brightness Beams (2019). 14

[116] Feldhaus, J., Saldin, E., Schneider, J., Schneidmiller, E. & Yurkov, M. Possible application of x-ray optical elements for reducing the spectral bandwidth of an X-ray SASE FEL. *Optics Communications* **140**, 341–352 (1997). 14, 211

[117] Geloni, G., Kocharyan, V. & Saldin, E. A novel self-seeding scheme for hard X-ray FELs. *Journal of Modern Optics* **58**, 1391–1403 (2011). 15, 211

[118] Amann, J. *et al.* Demonstration of self-seeding in a hard-x-ray free-electron laser. *Nature photonics* **6**, 693 (2012). 15, 211

[119] Ratner, D. *et al.* Experimental demonstration of a soft x-ray self-seeded free-electron laser. *Physical review letters* **114**, 054801 (2015). 15

[120] Yabashi, M. & Tanaka, T. X-rays: Self-seeded FEL emits hard x-rays. *Nature Photonics* **6**, 648 (2012). 15, 211

[121] Doyuran, A. *et al.* Characterization of a high-gain harmonic-generation free-electron laser at saturation. *Physical review letters* **86**, 5902 (2001). 15

[122] Yu, L.-H. *et al.* First ultraviolet high-gain harmonic-generation free-electron laser. *Physical review letters* **91**, 074801 (2003). 15, 16

[123] Wu, J. & Yu, L. H. Coherent hard x-ray production by cascading stages of high gain harmonic generation. *Nuclear Instruments and Methods in Physics Research Section A: Accelerators, Spectrometers, Detectors and Associated Equipment* **475**, 104–111 (2001). 16

[124] Saldin, E., Schneidmiller, E. & Yurkov, M. Study of a noise degradation of amplification process in a multistage HGHG FEL. *Optics Communications* **202**, 169–187 (2002). 16, 211

[125] Gover, A. & Dyunin, E. Collective-interaction control and reduction of optical frequency shot noise in charged-particle beams. *Physical review letters* **102**, 154801 (2009). 16

[126] Allaria, E. *et al.* Highly coherent and stable pulses from the fermi seeded free-electron laser in the extreme ultraviolet. *Nature Photonics* **6**, 699 (2012). 16

[127] Stupakov, G. Using the beam-echo effect for generation of short-wavelength radiation. *Physical review letters* **102**, 074801 (2009). 16, 211

[128] Thomas, A. *Transport et manipulation d'électrons produits par interaction laser plasma sur la ligne COXINEL* (PhD, 2018). 18, 68, 182

[129] Chubar, O., Elleaume, P. & Chavanne, J. A three-dimensional magnetostatics computer code for insertion devices. *Journal of synchrotron radiation* **5**, 481–484 (1998). 19, 75, 83, 101, 105, 106, 117

[130] Benabderrahmane, C. *et al.* Development and operation of a Pr_2Fe_14B based cryogenic permanent magnet undulator for a high spatial resolution x-ray beam line. *Physical Review Accelerators and Beams* **20**, 033201 (2017). 19, 75, 82, 87, 95

[131] Marteau, F. *et al.* Variable high gradient permanent magnet quadrupole (QUAPEVA). *Applied Physics Letters* **111**, 253503 (2017). 20, 167, 170

[132] Ghaith, A. *et al.* Tunable high gradient quadrupoles for a laser plasma acceleration based FEL. *Nuclear Instruments and Methods in Physics Research Section A: Accelerators, Spectrometers, Detectors and Associated Equipment* **909**, 290–293 (2018). 20, 113, 170

[133] Ghaith, A. *et al.* Permanent magnet-based quadrupoles for plasma acceleration sources. *Instruments* **3**, 27 (2019). 20

[134] Chubar, O., Elleaume, P., Kuznetsov, S. & Snigirev, A. A. Physical optics computer code optimized for synchrotron radiation. In *Optical Design and Analysis Software II*, vol. 4769, 145–152 (International Society for Optics and Photonics, 2002). 20, 71, 131

[135] Hill, J. M. *Differential equations and group methods for scientists and engineers* (CRC Press, 1992). 25

[136] Chauvin, N. Transverse beam dynamics (2016). 25

[137] Bukov, M., D'Alessio, L. & Polkovnikov, A. Universal high-frequency behavior of periodically driven systems: from dynamical stabilization to floquet engineering. *Advances in Physics* **64**, 139–226 (2015). 25

[138] Roser, T., Chao, A. & Tigner, M. Handbook of accelerator physics and engineering. *edited by A. Chao and M. Tigner* 150 (2002). 26

[139] Halbach, K. Permanent magnet undulators. *Le Journal de Physique Colloques* **44**, C1–211 (1983). 30, 77

[140] Meeker, D. Finite element method magnetics. *FEMM* **4**, 32 (2010). 30, 116

[141] Jackson, J. D. Classical electrodynamics (1999). 33

[142] Kim, K.-J. Brightness, coherence and propagation characteristics of synchrotron radiation. *Nuclear Instruments and Methods in Physics Research Section A: Accelerators, Spectrometers, Detectors and Associated Equipment* **246**, 71–76 (1986). 36

[143] Coisson, R. & Walker, R. Phase space distribution of brilliance of undulator sources. In *Insertion Devices for Synchrotron Sources*, vol. 582, 24–31 (International Society for Optics and Photonics, 1986). 36

[144] Kim, K.-J. Brightness and coherence of radiation from undulators and high-gain free electron lasers (1987).

[145] Walker, R. P. Insertion devices: undulators and wigglers (1998).

[146] Lindberg, R. R. & Kim, K.-J. Compact representations of partially coherent undulator radiation suitable for wave propagation. *Physical Review Special Topics-Accelerators and Beams* **18**, 090702 (2015).

[147] Walker, R. P. Undulator radiation brightness and coherence near the diffraction limit. *Physical Review Accelerators and Beams* **22**, 050704 (2019). 36

[148] Clarke, J. A. *The science and technology of undulators and wigglers*, vol. 4 (Oxford University Press on Demand, 2004). 38, 39, 134

[149] Bonifacio, R., De Salvo, L., Pierini, P., Piovella, N. & Pellegrini, C. Spectrum, temporal structure, and fluctuations in a high-gain free-electron laser starting from noise. *Physical review letters* **73**, 70 (1994). 50, 52

[150] Huang, Z. & Kim, K.-J. Review of x-ray free-electron laser theory. *Physical Review Special Topics-Accelerators and Beams* **10**, 034801 (2007).

[151] Pellegrini, C., Marinelli, A. & Reiche, S. The physics of X-ray free-electron lasers. *Reviews of Modern Physics* **88**, 015006 (2016). 50

[152] Ding, Y. *et al.* Measurements and simulations of ultralow emittance and ultrashort electron beams in the linac coherent light source. *Physical review letters* **102**, 254801 (2009). 52

[153] Saldin, E. L., Schneidmiller, E. A. & Yurkov, M. Statistical properties of radiation from vuv and x-ray free electron laser. *Optics communications* **148**, 383–403 (1998). 52

[154] Xie, M. Design optimization for an x-ray free electron laser driven by slac linac. In *Proceedings Particle Accelerator Conference*, vol. 1, 183–185 (IEEE, 1995). 52, 185

[155] Pellegrini, C. Free electron lasers: development and applications. *Part. Accel.* **33**, 159–170 (1990). 53

[156] Huang, Z. & Kim, K.-J. Three-dimensional analysis of harmonic generation in high-gain free-electron lasers. *Physical Review E* **62**, 7295 (2000). 54

[157] Couprie, M. *et al.* The lunex5 project in france. In *Journal of Physics: Conference Series*, vol. 425, 072001 (IOP Publishing, 2013). 55, 58

[158] Couprie, M. *et al.* The lunex5 project in france. In *X-Ray Lasers 2012*, 55–62 (Springer, 2014).

[159] Couprie, M. *et al.* Strategies towards a compact xuv free electron laser adopted for the lunex5 project. *Journal of Modern Optics* **63**, 309–323 (2016). 55

[160] Freericks, J., Krishnamurthy, H. & Pruschke, T. Theoretical description of time-resolved photoemission spectroscopy: application to pump-probe experiments. *Physical review letters* **102**, 136401 (2009). 55

[161] Azima, A. *et al.* Time-resolved pump-probe experiments beyond the jitter limitations at flash. *Applied Physics Letters* **94**, 144102 (2009). 55

[162] Wang, T. *et al.* Femtosecond single-shot imaging of nanoscale ferromagnetic order in co/pd multilayers using resonant x-ray holography. *Physical review letters* **108**, 267403 (2012). 55

[163] Rechatin, C. *et al.* Controlling the phase-space volume of injected electrons in a laser-plasma accelerator. *Physical review letters* **102**, 164801 (2009). 56

[164] FELs of europe. https://www.fels-of-europe.eu/fel_facilities/test_facilities/lunex_5/. 56

[165] Lambert, G. *et al.* Injection of harmonics generated in gas in a free-electron laser providing intense and coherent extreme-ultraviolet light. *Nature physics* **4**, 296 (2008). 57, 153

[166] Evain, C. *et al.* Study of high harmonic generation at synchrotron SOLEIL using echo enabling technique. In *Proceedings of the First International Particle Accelerator Conference*, 2308 (2010). 57

[167] Reiche, S. Genesis 1.3: a fully 3d time-dependent FEL simulation code. *Nuclear Instruments and Methods in Physics Research Section A: Accelerators, Spectrometers, Detectors and Associated Equipment* **429**, 243–248 (1999). 58, 219

[168] Migliorati, M. *et al.* Intrinsic normalized emittance growth in laser-driven electron accelerators. *Physical Review Special Topics-Accelerators and Beams* **16**, 011302 (2013). 58

[169] Floettmann, K. & Paramonov, V. V. Beam dynamics in transverse deflecting rf structures. *Physical Review Special Topics-Accelerators and Beams* **17**, 024001 (2014).

[170] Floettmann, K. Some basic features of the beam emittance. *Physical Review Special Topics-Accelerators and Beams* **6**, 034202 (2003).

[171] Antici, P. *et al.* Laser-driven electron beamlines generated by coupling laser-plasma sources with conventional transport systems. *Journal of Applied Physics* **112**, 044902 (2012). 58

[172] Leemans, W. *et al.* Laser-driven plasma-based accelerators: Wakefield excitation, channel guiding, and laser triggered particle injection. *Physics of Plasmas* **5**, 1615–1623 (1998). 59

[173] Lin, C. *et al.* Long-range persistence of femtosecond modulations on laser-plasma-accelerated electron beams. *Physical review letters* **108**, 094801 (2012). 59

[174] Bennett, W. H. Magnetically self-focussing streams. *Physical Review* **45**, 890 (1934). 59

[175] Rosenzweig, J., Breizman, B., Katsouleas, T. & Su, J. Acceleration and focusing of electrons in two-dimensional nonlinear plasma wake fields. *Physical Review A* **44**, R6189 (1991). 60

[176] Chen, P. Grand disruption: A possible final focusing mechanism for linear colliders. *Part. Accel.* **20**, 171–182 (1986). 60

[177] Lehe, R., Thaury, C., Guillaume, E., Lifschitz, A. & Malka, V. Laser-plasma lens for laser-wakefield accelerators. *Physical Review Special Topics-Accelerators and Beams* **17**, 121301 (2014). 60

[178] Panofsky, W. K. H. & Baker, W. R. A focusing device for the external 350-mev proton beam of the 184-inch cyclotron at berkeley. *Review of Scientific Instruments* **21**, 445–447 (1950). 60

[179] Röckemann, J.-H. *et al.* Direct measurement of focusing fields in active plasma lenses. *Physical Review Accelerators and Beams* **21**, 122801 (2018). 60

[180] Tauschwitz, A. *et al.* Plasma lens focusing and plasma channel transport for heavy ion fusion. *Fusion engineering and design* **32**, 493–502 (1996). 60

[181] Nakanii, N. *et al.* Transient magnetized plasma as an optical element for high power laser pulses. *Physical Review Special Topics-Accelerators and Beams* **18**, 021303 (2015). 60

[182] Van Tilborg, J. *et al.* Active plasma lensing for relativistic laser-plasma-accelerated electron beams. *Physical review letters* **115**, 184802 (2015).

[183] Van Tilborg, J. *et al.* Nonuniform discharge currents in active plasma lenses. *Physical Review Accelerators and Beams* **20**, 032803 (2017).

[184] Marocchino, A. *et al.* Experimental characterization of the effects induced by passive plasma lens on high brightness electron bunches. *Applied Physics Letters* **111**, 184101 (2017).

[185] Pompili, R. *et al.* Focusing of high-brightness electron beams with active-plasma lenses. *Physical review letters* **121**, 174801 (2018). 60

[186] Seggebrock, T., Maier, A., Dornmair, I. & Grüner, F. Bunch decompression for laser-plasma driven free-electron laser demonstration schemes. *Physical Review Special Topics-Accelerators and Beams* **16**, 070703 (2013). 60

[187] Maier, A. *et al.* Demonstration scheme for a laser-plasma-driven free-electron laser. *Physical Review X* **2**, 031019 (2012). 60

[188] Loulergue, A. *et al.* Beam manipulation for compact laser wakefield accelerator based free-electron lasers. *New Journal of Physics* **17**, 023028 (2015). 60, 68, 69

[189] Liu, T., Zhang, T., Wang, D. & Huang, Z. Compact beam transport system for free-electron lasers driven by a laser plasma accelerator. *Physical Review Accelerators and Beams* **20**, 020701 (2017). 60

[190] Huang, Z., Ding, Y. & Schroeder, C. B. Compact x-ray free-electron laser from a laser-plasma accelerator using a transverse-gradient undulator. *Physical review letters* **109**, 204801 (2012). 60

[191] Schlenvoigt, H.-P. *et al.* A compact synchrotron radiation source driven by a laser-plasma wakefield accelerator. *Nature Physics* **4**, 130 (2008). 60, 61, 62, 67

[192] Fuchs, M. *et al.* Laser-driven soft-x-ray undulator source. *Nature physics* **5**, 826 (2009). 62, 63, 64, 67

[193] Lambert, G. *et al.* Progress on the generation of undulator radiation in the uv from a plasma-based electron beam. In *Proceed. FEL conf., Nara, Japan*, 2 (2012). 64, 65, 67

[194] Chubar, O. & Elleaume, P. Accurate and efficient computation of synchrotron radiation in the near field region. In *proc. of the EPAC98 Conference*, 1177–1179 (1998). 65, 206

[195] Anania, M. P. *et al.* An ultrashort pulse ultra-violet radiation undulator source driven by a laser plasma wakefield accelerator. *Applied Physics Letters* **104**, 264102 (2014). 65, 66, 67

[196] Loulergue, A. *et al.* Experiment preparation towards a demonstration of laser plasma based free electron laser amplification. In *Advances in X-ray Free-Electron Lasers Instrumentation III*, vol. 9512, 95121G (International Society for Optics and Photonics, 2015). 67

[197] Brown, K. L. First-and second-order matrix theory for the design of beam transport systems and charged particle spectrometers. Tech. Rep., Stanford Linear Accelerator Center, Calif. (1971). 68

[198] Payet, J. *et al.* Beta code. *CEA, SACLAY* . 70

[199] Labat, M. *et al.* Robustness of a plasma acceleration based free electron laser. *Physical Review Accelerators and Beams* **21**, 114802 (2018). 70

[200] Floettmann, K. *et al.* Astra: A space charge tracking algorithm. *Manual, Version* **3**, 2014 (2011). 70

[201] Khojoyan, M. *et al.* Transport studies of lpa electron beam towards the fel amplification at coxinel. *Nuclear Instruments and Methods in Physics Research Section A: Accelerators, Spectrometers, Detectors and Associated Equipment* **829**, 260–264 (2016). 70, 168

[202] Borland, M. & APS, E. A flexible sdds-compliant code for accelerator simulation, report no. *APS LS-287* (2000). 70

[203] Agapov, I., Geloni, G., Tomin, S. & Zagorodnov, I. Ocelot: a software framework for synchrotron light source and fel studies. *Nuclear Instruments and Methods in Physics Research Section A: Accelerators, Spectrometers, Detectors and Associated Equipment* **768**, 151–156 (2014). 70

[204] Huang, Z. & Kim, K.-J. Formulas for coherent synchrotron radiation microbunching in a bunch compressor chicane. *Physical Review Special Topics-Accelerators and Beams* **5**, 074401 (2002). 71

[205] Elleaume, P., Chavanne, J. & Faatz, B. Design considerations for a 1 å sase undulator. *Nuclear Instruments and Methods in Physics Research Section A: Accelerators, Spectrometers, Detectors and Associated Equipment* **455**, 503–523 (2000). 71, 78, 86

[206] Hara, T. *et al.* Cryogenic permanent magnet undulators. *Physical Review Special Topics-Accelerators and Beams* **7**, 050702 (2004). 75, 79, 80

[207] Ghaith, A. *et al.* Progress of $Pr_2Fe_{14}B$ based hybrid cryogenic undulators at SOLEIL (2017). 75

[208] Valléau, M. *et al.* Construction and optimization of cryogenic undulators at SOLEIL. In *60th ICFA Advanced Beam Dynamics Workshop on Future Light Sources (FLS'18), Shanghai, China, 5-9 March 2018*, 193–198 (JACOW Publishing, Geneva, Switzerland, 2018).

[209] Valléau, M. *et al.* Development of cryogenic permanent magnet undulators at SOLEIL. *Synchrotron Radiation News* **31**, 42–47 (2018). 75

[210] García, L., Chaboy, J., Bartolomé, F. & Goedkoop, J. Orbital magnetic moment instability at the spin reorientation transition of nd 2 fe 14 b. *Physical review letters* **85**, 429 (2000). 75, 79

[211] Walker, R. P. Interference effects in undulator and wiggler radiation sources. *Nuclear Instruments and Methods in Physics Research Section A: Accelerators, Spectrometers, Detectors and Associated Equipment* **335**, 328–337 (1993). 75, 77

[212] Wollmann, D. *A novel concept for phase error correction in superconductive undulators: theory and experimental verification.* Ph.D. thesis, KIT-Bibliothek (2008). 76

[213] Elleaume, P. & Marechal, X. B2e: A software to compute synchrotron radiation from magnetic field data. *ESRF-SR/lD-91-54* (1991). 77

[214] Ilinski, P. P., Dejus, R. J., Gluskin, E. S. & Morrison, T. I. Practical aspects of undulator radiation properties. In *Optics for High-Brightness Synchrotron Radiation Beamlines II*, vol. 2856, 16–26 (International Society for Optics and Photonics, 1996). 77

[215] Li, Y., Faatz, B. & Pfluger, J. Study of phase tolerances for the european xfel undulator system. Tech. Rep. (2007). 77

[216] Moog, E. *et al.* Development status of a superconducting undulator for the advanced photon source (aps). *IPAC10, Kyoto* (2010). 77

[217] Tatchyn, R. *et al.* Design considerations for a 60 meter pure permanent magnet undulator for the slac linac coherent light source (lcls). In *Proceedings of International Conference on Particle Accelerators*, 1608–1610 (IEEE, 1993). 77

[218] Robinson, K. *et al.* Hybrid undulator design considerations. *Nuclear Instruments and Methods in Physics Research Section A: Accelerators, Spectrometers, Detectors and Associated Equipment* **250**, 100–109 (1986). 77

[219] Coey, J. M. D. *Rare-earth iron permanent magnets*. 54 (Oxford University Press, 1996). 78

[220] Pan, S. The first generation rare earth permanent-magnet alloys. In *Rare Earth Permanent-Magnet Alloys' High Temperature Phase Transformation*, 27–93 (Springer, 2013). 78

[221] Magnetic properties of $Y_2Fe_{14}B$ and $Nd_2Fe_{14}B$ single crystals, author=Givord, D and Li, HS and De La Bâthie, R Perrier, journal=Solid state communications, volume=51, number=11, pages=857–860, year=1984, publisher=Elsevier . 78, 105

[222] Sagawa, M., Hirosawa, S., Yamamoto, H., Fujimura, S. & Matsuura, Y. Nd–fe–b permanent magnet materials. *Japanese journal of applied physics* **26**, 785 (1987). 78

[223] Bizen, T. *et al.* Baking effect for ndfeb magnets against demagnetization induced by high-energy electrons. *Nuclear Instruments and Methods in Physics Research Section A: Accelerators, Spectrometers, Detectors and Associated Equipment* **515**, 850–852 (2003). 78

[224] Bizen, T. *et al.* High-energy electron irradiation of ndfeb permanent magnets: Dependence of radiation damage on the electron energy. *Nuclear Instruments and Methods in Physics Research Section A: Accelerators, Spectrometers, Detectors and Associated Equipment* **574**, 401–406 (2007). 78

[225] Yan, G., McGuiness, P., Farr, J. & Harris, I. Optimisation of the processing of Nd-Fe-B with dysprosium addition. *Journal of Alloys and Compounds* **491**, L20–L24 (2010). 78

[226] Gudat, W., Pflüger, J., Chatzipetros, J. & Peatman, W. An undulator/multipole wiggler for the bessy storage ring. *Nuclear Instruments and Methods in Physics Research Section A: Accelerators, Spectrometers, Detectors and Associated Equipment* **246**, 50–53 (1986). 79

[227] Tanaka, T. *et al.* In-vacuum undulators. In *Proceedings of the 27th International Free Electron Conference*, 370–377 (2005).

[228] Yamamoto, S. *et al.* Construction of an in-vacuum type undulator for production of undulator x rays in the 5–25 kev region. *Review of scientific instruments* **63**, 400–403 (1992). 79

[229] Yamamoto, S. Undulator development towards very short period lengths. *Synchrotron Radiation News* **28**, 19–22 (2015). 79

[230] Yamamoto, S. Development of undulator magnets towards very short period lengths. In *AIP Conference Proceedings*, vol. 1741, 020029 (AIP Publishing, 2016). 79

[231] Dufeu, D. & Lethuillier, P. High sensitivity 2 t vibrating sample magnetometer. *Review of scientific instruments* **70**, 3035–3039 (1999). 79

[232] Huang, J.-C. *et al.* Challenges of in-vacuum and cryogenic permanent magnet undulator technologies. *Physical Review Accelerators and Beams* **20**, 064801 (2017). 80

[233] Marcouille, O. *et al.* In vacuum permanent magnet wiggler optimized for the production of hard x rays. *Physical Review Special Topics-Accelerators and Beams* **16**, 050702 (2013). 80

[234] Kersevan, R., Hahn, M., Parat, I. & Schmied, D. Machine operation issue related to the vacuum system of the ESRF. *EPAC08* 3705 (2008). 80

[235] Tanaka, T., Seike, T. & Kitamura, H. Measurement of spring-8 xfel undulator prototype with the safali system. In *FEL*, vol. 8, 371 (2008). 80

[236] Tanaka, T. *et al.* In situ correction of field errors induced by temperature gradient in cryogenic undulators. *Physical Review Special Topics-Accelerators and Beams* **12**, 120702 (2009). 80

[237] Chavanne, J. *et al.* Construction of a cryogenic permanent magnet undulator at the ESRF. *EPAC08, Genoa* 2243–2245 (2008). 80, 81

[238] Benabderrahmane, C. *et al.* Development of a PrFeB cryogenic undulator at SOLEIL. In *Proceedings of the 1st International Particle Accelerator Conference (IPAC'10), Kyoto, Japan*, 3096–3098 (2010). 80, 82

[239] Tanaka, T., Tsuru, R., Nakajima, T. & Kitamura, H. Magnetic characterization for cryogenic permanent-magnet undulators: a first result. *Journal of synchrotron radiation* **14**, 416–420 (2007). 80

[240] Kuhn, C., Baecker, H.-J., Bahrdt, J., Gaupp, A. & Schulz, B. Hall-probe bench for cryogenic in-vacuum-undulators. *Proceedings of IPAC2013, Shanghai, China* 2126–2128 (2013). 80

[241] Murokh, A. *et al.* Textured dysprosium and gadolinium poles for high-field, short-period hybrid undulators. *Nuclear Instruments and Methods in Physics Research Section A: Accelerators, Spectrometers, Detectors and Associated Equipment* **735**, 521–527 (2014). 81

[242] O'Shea, F., Palmowski, A., Spranza, E., Agustsson, R. & Chen, Y.-C. Development of a short period cryogenic undulator at radiabeam 995–997 (2017). 81

[243] Chavanne, J., Penel, C. & Elleaume, P. Development and operation of a prototype cryogenic permanent magnet undulator at the ESRF (2009). 81

[244] Chavanne, J., Lebec, G., Penel, C., Revol, F. & Kitegi, C. First operational experience with a cryogenic permanent magnet undulator at the ESRF. In *The 23rd Particle Accelerator Conference*, 2414–2416 (2009). 81

[245] Calvi, M. *et al.* Commissioning results of the u14 cryogenic undulator at SLS. In *Journal of Physics: Conference Series*, vol. 425, 032017 (IOP Publishing, 2013). 82

[246] Schmidt, T. & Reiche, S. Undulators for the SwissFEL. In *Proceedings of the FEL Conference* (2009). 82

[247] Benabderrahmane, C. *et al.* Development of a 2 m $Pr_2Fe_{14}B$ cryogenic permanent magnet undulator at SOLEIL. In *Journal of Physics: Conference Series*, vol. 425, 032019 (IOP Publishing, 2013). 82

[248] Weitkamp, T. *et al.* The tomography beamline anatomix at synchrotron SOLEIL. In *Journal of Physics: Conference Series*, vol. 849, 012037 (IOP Publishing, 2017). 82

[249] Schouten, J. & Rial, E. Electron beam heating and operation of the cryogenic undulator and superconducting wigglers at diamond. In *Proceedings of the 2nd International Particle Accelerator Conference, San Sebastián, Spain*, 3323 (2011). 82

[250] Ostenfeld, C. & Pedersen, M. Cryogenic in-vacuum undulator at danfysik. In *IPAC* (2010). 82

[251] Bahrdt, J. & Kuhn, C. Cryogenic permanent magnet undulator development at hzb/bessy ii. *Synchrotron Radiation News* **28**, 9–14 (2015). 82

[252] Bahrdt, J. *et al.* Measurements of the lattice modifications for the cryogenic undulator cpmu17. In *7th International Particle Accelerator Conference (IPAC'16), Busan, Korea, May 8-13, 2016*, 4031–4034 (JACOW, Geneva, Switzerland, 2016). 82

[253] Huang, J.-C. *et al.* Design of a magnetic circuit for a cryogenic undulator in taiwan photon source. In *AIP Conference Proceedings*, vol. 1741, 020016 (AIP Publishing, 2016). 82

[254] Huang, J.-C., Yang, C.-S., Kohda, T., Kitamura, H. & Yang, C.-K. Performance of tps cryogenic permanent magnet undulators at nsrrc 1559–1561 (2019).

[255] Huang, J.-C. *et al.* Development of cryogenic permanent magnet undulators at nsrrc. In *AIP Conference Proceedings*, vol. 2054, 030022 (AIP Publishing, 2019). 82

[256] Wang, H. *et al.* The magnetic field measurement systems for a cryogenic undulator and a superconducting undulator at ssrf. In *Journal of Physics: Conference Series*, vol. 1067, 082016 (IOP Publishing, 2018). 82

[257] Chavanne, J., Penel, C. & Van Vaerenbergh, P. Construction of apple ii and in vacuum undulators at ESRF. In *PACS2001. Proceedings of the 2001 Particle Accelerator Conference (Cat. No. 01CH37268)*, vol. 4, 2459–2461 (IEEE, 2001). 87

[258] Chubar, O. *et al.* Application of genetic algorithms to sorting, swapping and shimming of the SOLEIL undulator magnets. In *AIP Conference Proceedings*, vol. 879, 359–362 (AIP, 2007). 92

[259] Walckiers, L. Cern accelerator school CAS 2009: Specialised course on magnets (2009). 102

[260] Halbach, K. Design of permanent multipole magnets with oriented rare earth cobalt material. *Nuclear instruments and methods* **169**, 1–10 (1980). 105

[261] Benabderrahmane, C. *et al.* $Nd_2Fe_{14}B$ and $Pr_2Fe_{14}B$ magnets characterisation and modelling for cryogenic permanent magnet undulator applications. *Nuclear Instruments and Methods in Physics Research Section A: Accelerators, Spectrometers, Detectors and Associated Equipment* **669**, 1–6 (2012). 105, 130

[262] Hiroyoshi, H. *et al.* High-field magnetization and crystalline field of $R_2Fe_{14}B$ and $R_2Co_{14}B$. *Journal of magnetism and magnetic materials* **70**, 337–339 (1987). 105, 130

[263] Mihara, T., Iwashita, Y., Kumada, M., Evgeny, A. & Spencer, C. M. Super strong permanent magnet quadrupole for a linear collider. *IEEE transactions on applied superconductivity* **14**, 469–472 (2004). 110

[264] Eichner, T. *et al.* Miniature magnetic devices for laser-based, table-top free-electron lasers. *Physical Review Special Topics-Accelerators and Beams* **10**, 082401 (2007). 110, 113

[265] Lou, W., Hartill, D., Rice, D., Rubin, D. & Welch, J. Stability considerations of permanent magnet quadrupoles for cesr phase-iii upgrade. *Physical Review Special Topics-Accelerators and Beams* **1**, 022401 (1998). 110, 113

[266] Lim, J. *et al.* Adjustable, short focal length permanent-magnet quadrupole based electron beam final focus system. *Physical Review Special Topics-Accelerators and Beams* **8**, 072401 (2005). 110, 113

[267] N'gotta, P., Le Bec, G. & Chavanne, J. Hybrid high gradient permanent magnet quadrupole. *Physical Review Accelerators and Beams* **19**, 122401 (2016). 110, 113

[268] Mihara, T., Iwashita, Y., Kumada, M. & Spencer, C. M. Variable permanent magnet quadrupole. *IEEE transactions on applied superconductivity* **16**, 224–227 (2006). 110, 113

[269] Tosin, G., Sanchez, P. P., Citadini, J. F. & Vergasta, C. C. Super hybrid quadrupoles. *Nuclear Instruments and Methods in Physics Research Section A: Accelerators, Spectrometers, Detectors and Associated Equipment* **674**, 67–73 (2012). 110, 111

[270] Gottschalk, S. C. & Taylor, D. J. Magnetic and engineering analysis of an adjustable strength permanent magnet quadrupole. In *Particle Accelerator Conference, 2005. PAC 2005. Proceedings of the*, 2122–2124 (IEEE, 2005). 111, 113

[271] Modena, M. *et al.* Design, assembly and first measurements of a short model for clic final focus hybrid quadrupole qd0. In *Conf. Proc.*, vol. 1205201, THPPD010 (2012). 111, 113

[272] Shepherd, B., Clarke, J. & Collomb, N. Construction and measurement of novel adjustable permanent magnet quadrupoles for clic (2016). 111, 112, 113

[273] Easton, M. J. *et al.* Permanent-magnet quadrupoles for an interdigital h-mode drift tube linear accelerator: Optimization code and adjustable magnet design. *Physical Review Accelerators and Beams* **21**, 122401 (2018). 112, 113

[274] Iwashita, Y., Mihara, T., Antokhin, E., Kumada, M. & Aoki, M. Permanent magnet quadrupole for final focus for linear collider. *PAC03, May* 12–16 (2003). 113

[275] Cesar, D. *et al.* Demonstration of single-shot picosecond time-resolved mev electron imaging using a compact permanent magnet quadrupole based lens. *Physical review letters* **117**, 024801 (2016). 113

[276] Zhou, Z. *et al.* Compact high energy electron radiography system based on permanent magnet quadrupole (2017). 113

[277] Pompili, R. *et al.* Compact and tunable focusing device for plasma wakefield acceleration. *Review of Scientific Instruments* **89**, 033302 (2018). 113

[278] Benabderrahmane, C., Couprie, M., Forest, F. & Cosson, O. Adjustable magnetic multipole (2016). URL https://patentscope.wipo.int/search/en/detail.jsf?docId=WO2016034490. Europe : PCT/EP2015/069649 of 27/08/2015, WOBL14SSOQUA / CA. 114

[279] Simkin, J. & Trowbridge, C. Three-dimensional nonlinear electromagnetic field computations, using scalar potentials. In *IEE Proceedings B-Electric Power Applications*, vol. 127, 368–374 (IET, 1980). 117

[280] Le Bec, G., Chavanne, J. & Penel, C. Stretched wire measurement of multipole accelerator magnets. *Physical Review Special Topics-Accelerators and Beams* **15**, 022401 (2012). 120

[281] Madur, A. Contribution à la métrologie magnétique des multipôles d'accélérateurs: les quadrupôles du synchroton SOLEIL. *Institut National Polytechnique de Lorraine* (2006). 120

[282] Preston, D. W. & Warren, R. W. Wiggler field measurements and corrections using the pulsed wire technique. *Nuclear Instruments and Methods in Physics Research Section A: Accelerators, Spectrometers, Detectors and Associated Equipment* **318**, 794–797 (1992). 123

[283] Oumbarek Espinos, D. *et al.* Skew quadrupole effect of laser plasma electron beam transport. *Applied Sciences* **9**, 2447 (2019). 128, 169

[284] André, T. *et al.* Control of laser plasma accelerated electrons for light sources. *Nature communications* **9**, 1334 (2018). 130, 183, 193

[285] Giannessi, L. *et al.* Superradiant cascade in a seeded free-electron laser. *Physical review letters* **110**, 044801 (2013). 153

[286] Desjardins, K. *et al.* The diagon: an undulator diagnostic for SOLEIL low energy beamlines. In *2008 IEEE Nuclear Science Symposium Conference Record*, 2571–2574 (IEEE, 2008). 153

[287] André, T. *et al.* Electron transport on coxinel beam line (2017). 167

[288] Couprie, M.-E. *et al.* An application of laser plasma acceleration: towards a free-electron laser amplification. *Plasma Physics and Controlled Fusion* **58**, 034020 (2016).

[289] Couprie, M.-E., Andre, T. & Andriyash, I. Coxinel: Towards free electron laser amplification to qualify laser plasma acceleration. *Reza Kenkyu* **45**, 94–98 (2017). 167

[290] Emma, P. *et al.* Femtosecond and Subfemtosecond X-Ray Pulses from a Self-Amplified Spontaneous-Emission–Based Free-Electron Laser. *Phys. Rev. Lett.* **92**, 074801 (2004). URL https://link.aps.org/doi/10.1103/PhysRevLett.92.074801. 167

[291] Scisciò, M., Migliorati, M., Palumbo, L. & Antici, P. Design and optimization of a compact laser-driven proton beamline. *Scientific Reports* **8**, 6299 (2018).

[292] Zhu, X., Broemmelsiek, D. R. & Shin, Y.-M. Theoretical and numerical analyses of a slit-masked chicane for modulated bunch generation. *Journal of Instrumentation* **10**, P10042 (2015). 167

[293] Chen, M., Sheng, Z.-M., Ma, Y.-Y. & Zhang, J. Electron injection and trapping in a laser wakefield by field ionization to high-charge states of gases **99**, 056109 (2006). 168

[294] Payet, J. Beta code. CEA, SACLAY, http://irfu.cea.fr/Sacm/logiciels/index6.php. 168

[295] Labat, M. *et al.* Electron and photon diagnostics for plasma acceleration-based fels. *Journal of synchrotron radiation* **25**, 59–67 (2018). 174, 175

[296] Borland, M. Elegant: A flexible SDDS-compliant code for accelerator simulation. Tech. Rep., Argonne National Lab., IL (US) (2000). 183

[297] Polyanskiy, M. N. Refractive index database (2016). 190

[298] Malitson, I. H. A redetermination of some optical properties of calcium fluoride. *Applied Optics* **2**, 1103–1107 (1963). 190

[299] Boris, J. P. Relativistic plasma simulation-optimization of a hybrid code. In *Proc. 4th Conf. Num. Sim. Plasmas*, 3–67 (1970). 192

[300] Xiang, D. & Stupakov, G. Echo-enabled harmonic generation free electron laser. *Physical Review Special Topics-Accelerators and Beams* **12**, 030702 (2009). 211, 215

[301] Xiang, D. *et al.* Demonstration of the echo-enabled harmonic generation technique for short-wavelength seeded free electron lasers. *Physical review letters* **105**, 114801 (2010). 212

[302] Zhao, Z. *et al.* First lasing of an echo-enabled harmonic generation free-electron laser. *Nature Photonics* **6**, 360 (2012). 212

[303] Hemsing, E. *et al.* Highly coherent vacuum ultraviolet radiation at the 15th harmonic with echo-enabled harmonic generation technique. *Physical Review Special Topics-Accelerators and Beams* **17**, 070702 (2014). 212

[304] Hemsing, E. *et al.* Echo-enabled harmonics up to the 75th order from precisely tailored electron beams. *Nature Photonics* **10**, 512 (2016). 212

[305] Ribič, P. R. *et al.* Coherent soft x-ray pulses from an echo-enabled harmonic generation free-electron laser. *Nature Photonics* 1 (2019). 212, 225

[306] Yu, L. H. Generation of intense UV radiation by subharmonically seeded single-pass free-electron lasers. *Physical Review A* **44**, 5178 (1991). 214

[307] Trovo, M. *et al.* Status of the fermi@ elettra photoinjector. *Proceedings of EPAC08, Genoa, Italy* 247–249 (2008). 221

Titre : Vers un laser à électrons libres compact et avancé

Mots clés : Onduleur, laser à électrons libres, rayonnement synchrotron, accélération laser plasma, quadrupôles

Résumé : Les lasers à électrons libres (LEL) X sont aujourd'hui des sources lumineuses cohérentes et intenses utilisées pour des investigations multidisciplinaires de la matière. Un nouveau schéma d'accélération, l'accélérateur laser plasma (LPA), est maintenant capable de produire une accélération de quelques GeV/cm, bien supérieure à celle des linacs radiofréquence. Ce travail de thèse a été mené dans le cadre des programmes de R&D du projet LUNEX5 (laser à électrons libres utilisant un nouvel accélérateur pour l'exploitation du rayonnement X de 5e génération) de démonstrateur LEL avancé et compact avec applications utilisatrices pilotes. Il comprend un linac supraconducteur de 400 MeV de haute cadence (10 kHz) pour l'étude de schémas LEL avancés, et LPA pour sa qualification par une application LEL. La ligne LEL utilise une configuration d'injection
avancée dans la plage spectrale 40-4 nm par génération d'harmoniques à gain élevé (HGHG) et schéma d' écho (EEHG) avec des onduleurs compacts cryogéniques à champ élevé de courte période courte. L'étude de solutions adaptées aux applications LEL compactes et avancées est donc examinée. Un premier aspect concerne la réduction du milieu de gain du LEL (électrons dansl'onduleur), le raccourcissement de la période se faisant au détriment du champ magnétique.
Les onduleurs cryogéniques compacts à base d'aimants permanents cryogéniques (CPMU), dans lesquels les performances de l'aimant sont améliorées à la température cryogénique sont étudiés. Une deuxième partie du travail développée dans le cadre l'expérience de R&D COXINEL visant à démontrer l'amplification LEL à l'aide d'un LPA. La ligne permet de manipuler les propriétés des faisceaux d'électrons produits (dispersion en énergie, divergence, variation de pointé) avant d'être utilisées pour des applications de sources lumineuses.
Le faisceau d'électrons généré est très divergent et nécessite une bonne manipulation juste après la source avec des quadrupôles forts placés immédiatement après la génération d'électrons. Ainsi, des quadrupôles innovants à aimants permanents de gradient élevé réglable appelés «QUAPEVA», sont développés. Ils sont optimisés avec le code RADIA et caractérisées avec trois mesures magnétiques. Un gradient de 200 T/m avec une variabilité de 50 Une troisième partie des travaux concerne l'observation du rayonnement d'onduleur monochromatique ajustable sur la ligne COXINEL. Le faisceau d'électrons d'énergie de 170 MeV est transporté et focalisé dans un CPMU de 2 m et de période de 18 mm émettant à 200 nm. Le flux spectral est caractérisé à l'aide d'un spectromètre UV et le flux angulaire mesuré par une caméra CCD. La longueur d'onde est accordée avec l'entrefer. Les distributions spatio-spectrales mesurées en forme de lune du rayonnement de l'onduleur sont bien reproduites par les simulations de rayonnement utilisant les distributions d'électrons mesurées et transportées le long de la ligne. Elles permettent aussi de renseigner sur la qualité du faisceau d'électrons, de son transport et d'en estimer les paramètres tels que la dispersion en énergie et la divergence. Le dernier aspect du travail est lié à la comparaison entre la génération des harmoniques en gain élevé et le schéma d'écho, dans le cadre de ma participation à une expérience réalisée à FERMI @ ELETTRA. Nous avons pu démontrer un LEL de type écho à 5.9 nm, avec spectres plus étroits et une meilleure reproductibilité que le schéma HGHG à deux étages. Cette thèse constitue un pas en avant vers les lasers à électrons libres compacts et avancés.

Université Paris-Saclay
Espace Technologique / Immeuble Discovery
Route de l'Orme aux Merisiers RD 128 / 91190 Saint-Aubin, France

Title : Towards advanced and compact Free Electron Laser

Keywords : Undulator, free electron laser, synchrotron radiation, laser plasma acceleration, quadrupole

Abstract : X-ray Free Electron Lasers (FEL) are nowadays unique intense coherent fs light sources used for multi-disciplinary investigations of matter. A new acceleration scheme such as Laser Plasma Accelerator (LPA) is now capable of producing an accelerating gradient of few GeV/cm far
superior to that of conventional RF linacs. This PhD work has been conducted in the framework of R&D programs of the LUNEX5 (free electron Laser Using a New accelerator for the Exploitation of X-ray radiation of 5th generation) project of advanced and compact Free Electron laser demon strator with pilot user applications. It comprises a 400 MeV superconducting linac for studies of advanced FEL schemes, high repetition rate operation (10 kHz), multi-FEL lines, a Laser Wake Field Accelerator (LWFA) for its qualification by a FEL application. The FEL lines comports enables advanced seeding in the 40-4 nm spectral range using high gain harmonic generation (HGHG) and echo-enabled harmonic generation (EEHG) with compact short period high field cryogenic undulators. The study of compact devices suitable for compact FEL applications is thus examined. One first aspect concerns the reduction of the Free Electron Laser gain medium (electrons in undulator) where shortening of the period is on the expense of the magnetic field leading to an intensity reduction at high harmonics. Compact cryogenic permanent magnet based undulators (CPMUs), where the magnet performance is increased at cryogenic temperature making them suitable for compact applications, are studied. Three CPMUs of period 18 mm have been built: two are installed at SOLEIL storage ring and one at COXINEL experiment. A second part of the work is developed in the frame of the R&D programs is the COXINEL experiment with an aim at demonstrating FEL amplification using an LPA source. The line enables to manipulate the properties of the produced electron beams (as energy spread, divergence, induced dispersion due) before being used for light source applications. The electron beam generated is highly divergent and requires a good handling at an early stage with strong quadrupoles, to be installed immediately after the electron generation source. Hence, the development of the so-called QUAPEVAs, innovative
permanent magnet quadrupoles with high tunable gradient, is presented. The QUAPEVAs are optimized with RADIA code and characterized with three magnetic measurements. High tunable gradient is achieved while maintaining a rather good magnetic center excursion that allowed for beam pointing alignment compensation at COXINEL, where the beam is well-focused with zero
dispersion at any location along the line. The QUAPEVAs constitute original systems in the landscape of variable high gradient quadrupoles developed so far. A third part of the work concerns the observation of tunable monochromatic undulator radiation on the COXINEL line. The elec tron beam of energy of 170 MeV is transported and focused in a 2-m long CPMU with a period of 18 mm emitting radiation light at 200 nm. The spectral flux is characterized using a UV spectrometer and the angular flux is captured by a CCD camera. The wavelength is tuned with the undulator gap variation. The spatio-spectral moon shape type pattern of the undulator radiation provided an insight on the electron beam quality and its transport enabling the estimation of the electron beam parameters such as energy spread and divergence. The final aspect of the work is related to the comparison between the echo and high gain harmonic generation, in the frame of my participation to an experiment carried out at FERMI@ELETTRA. At FERMI, we have demonstrated a
high gain lasing using EEHG at a wavelength of 5.9 nm where it showed a narrower spectra and better reproducibility compared to a two-stage HGHG. This PhD work constitutes a step forward towards advanced compact Free Electron Lasers.

Université Paris-Saclay
Espace Technologique / Immeuble Discovery
Route de l'Orme aux Merisiers RD 128 / 91190 Saint-Aubin, France